AD-A241 323

CONFERENCE PROCEEDINGS

DTIC
ELECTE
OCT 0 9 1991
S D
D

7th Annual Review of Progress in APPLIED COMPUTATIONAL ELECTROMAGNETICS

at the

Naval Postgraduate School

Monterey, CA

March 18-22, 1991

SYMPOSIUM PROGRAM COMMITTEE CHAIRMAN

Frank Walker

Sponsored by

The Applied Computational Electromagnetics Society

and DOD/USA ECOM, USAISEC, NOSC, NPS, DOE/LLNL

REPRODUCED BY
U.S. DEPARTMENT OF COMMERCE
NATIONAL TECHNICAL
INFORMATION SERVICE
SPRINGFIELD, VA 22161

THE NAVAL POSTGRADUATE SCHOOL

91 7

91-06085

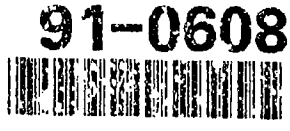

1992 **CALL FOR PAPERS** **1992**

The 8th Annual Review of Progress in Applied Computational Electromagnetics

SUBMISSION OF PAPERS

Suggested topics for papers include

NUMERICAL METHODS	CODE DEVELOPMENT	APPLICATIONS
Differential methods	EM Field Codes	Antenna analysis
Integral methods	NEC	EMC/EMI
Method of Moments	GEMACS	EMP/shielding/radiation effects
Finite Element methods	System Compatibility Codes	Impulse and transient analysis
Finite Difference methods	IEMCAP	Propagation and scattering
GTD/FTD methods	SEMCAP	Microwave, mm-wave components
Spectral Domain techniques	AAPG	EM machines and devices
Low/High frequency issues	COEDS	Power transmission
Time Domain techniques	Time Domain codes	Accelerator design
Hybrid techniques	Code validation	Biological interpretation
Perturbation multipole methods	CAD/automesh generation	Data interpretation
New algorithms	Graphical I/O techniques	Code studies of basic physics

TIMETABLE

October 1st 1991:- Abstract Submission
Refereeing is carried out on the abstract which must not be more than a single page including figures. Please supply four copies.

November 1st 1991:- Authors notified of acceptance

January 15th 1992:- Submission of camera-ready copy, not more than 8 pages including figures. All submissions become the property of the SYMPOSIUM and will not be returned. The author of each paper accepted for publication will be required to provide Copyright Releases from the author and the sponsoring organisation to the Symposium. Copyright Release forms will be supplied at time of acceptance. The author and sponsoring organisation will retain the right to free use of the copy protected material.For both abstract and final paper, please supply the following data for the lead author - Full name, address, telephone and FAX number for both work and home and a brief professional biography

Cost per person for the Symposium will be $180.0 ($195.0 after March 9th 1992).

SHORT COURSES

These will cover numerical techniques, computational methods, surveys of EM analysis and code usage instruction. Fee for a short course is expected to be $70.00 per person for a half-day course and $120.0 for a full day, if booked before March 2nd 1992. Full details will be published by October 1st 1991.

DEMONSTRATIONS

These will cover computer demonstrations, software demonstrations, poster papers and key-note speakers.

VENDOR BOOTHS

These will cover product distribution, small company capabilities, new commercial codes.

The Applied Computational Electromagnetics Society

1992 CALL FOR PAPERS 1992

The 8th Annual Review of Progress
in Applied Computational Electromagnetics

March 17 - 19, 1992

Naval Post Graduate School, Monterey, California

Share your knowledge and expertise with your colleagues
at the Applied Computational Electromagnetics Society's
8th Annual Review of Progress

The Annual ACES Symposium is an ideal opportunity to participate in a large gathering of EM analysis enthusiasts. Whether your interest is to learn or to share your knowladge, this symposium is aimed at you. In addition to technical publication, the Symposium organises live demonstrations and short courses. All aspects of electromagnetic computational analysis are represented.

The purpose of the Symposium is to bring analysts together to share information and experience about the practical application of EM analysis using computational methods. There are four areas, Symposium papers, short courses, demonstrations and vendor booths. The NSF/IEEE CAEME (Computer Applications in Electromagnetics Education) Center will organise a special session of technical presentations on Compute. Applications. This special session will cover topics of interest in education/training, evolving computer technologies and the latest in electromagnetics computation and analysis. In conjunction with the special session, there will be booths dedicated to the interchange of ideas and software. Please contact Magdy Iskander for CAEME details. Contact Pat Foster for details of the other events.

1992 ACES	**Symposium**	**CAEME**
Symposium Chairman	**Administrator**	**Director**
Pat Foster	Richard W Adler	Magdy Iskander
Microwave and	Naval Postgraduate School	University of Utah
Antenna Systems	Code EC/AB	E E Department
16 Peachfield Road	Monterey	Salt Lake City
Malvern, WORCS	CA 93943	UT 84112
WR14 4AP, UK		
Tel 010 44 684 574057	Tel (408) 646-2352	Tel (801) 581-6944
FAX 010 44 684 5/3509	FAX (408) 646-2955	FAX (801) 581-5281

1992 ACES Symposium	
Sponsored by:	ACES, DOD/USA CECOM, USAIESA,NOSC, NPS and DOE/LLNL
In cooperation with:	The IEEE Antennas and Propagation Society, the IEEE Electromagnetic Compatibility Society and USNC/URSI

1991 Symposium Program Committee
for the
7th Annual Review of Progress in
APPLIED COMPUTATIONAL ELECTROMAGNETICS
at the
Naval Postgraduate School
Monterey, CA

Symposium Chairman: Frank Ellis Walker
Boeing Aerospace & Electronics
P.O. Box 3999; M/S 85-84
Seattle, WA. 98124-2499
(206) 773-5023

Symposium Administrator: Dr. Richard W. Adler
Naval Postgraduate School
Code EC/AB
Monterey, CA. 93943
(408) 646-2352

Symposium Short Course Chairman: Dr. John Rockway
Naval Ocean Systems Center
NOSC/Code 805
San Diego, CA. 92152-5000
(619) 553-3791

CAEME Director: Dr. Magdy Iskander
Electrical Engineering Dept.
University of Utah
Salt Lake City, UT. 84112
(801) 581-6944

Vendor Booth Co-Chairman: Kathy Lee
C3I & Countermeasures
The MITRE Corp.
Bedford, MA. 01730
(617) 271-8555

1992 Symposium Chairman: Dr. Patricia Foster
Microwave and Antenna Systems
16 Peachfield Rd.
Great Malvern, Worcestershire WR14 4AP, U.K.

Conference Secretary: Mrs. Pat Adler

Advisory Committee:. Dr. Ed Miller, Los Alamos Labs.
Dr. Robert Bevensee, Consultant
Dr. Harold Sabbagh, Sabbagh Assoc., Inc.
Jim Logan, NOSC (Univ. of South Carolina)
Dr. Ray Luebbers, Penn State Univ.
Dr. Andrew Peterson, Georgia Inst. of Tech.

Accesion For
NTIS CRA&I
DTIC TAB
Unannounced
Justification
By
Distribution /
Availability Codes
Dist | Avail and/or Special
A-1

Statement A per telecon
Dr. Richard Adler
NPC/Code EC/AB
Monterey, CA 93943
NWW 10/8/91

VENDOR BOOTHS

Commercial Companies:

Hewlett Packard

Compact Software

EEsof

CAE Soft Corp.

Sonnet Software

Antenna Software Ltd.

Denmar Inc.

Wave Tracer

CAEME Associates:

Dr. Magdy Iskander, CAEME Director, NSF/IEEE CAEME Center

Dr. Markus Zahn, CAEME Faculty, Michigan Institute of Technology (MIT)

Dr. Zvonko Fazarinc, CAEME Faculty, Stanford University

Dr. Rodney Cole, CAEME Faculty, University of California at Davis

Dr. Bob Shin, CAEME Faculty, Lincoln Lab

Dr. Jovan Lebaric, CAEME Faculty, Rose-Hulman Institute of Technology

CONFERENCE CHAIRMAN'S SUMMARY

In this year's conference we have made modest gains in planning and organization. The most obvious change is the publication of the conference proceedings in time for distribution at the conference. This is due primarily to the conscientious delivery of the papers by the authors and a super effort on the part of Dick and Pat Adler in organizing the volume and getting it to the printer in time for publication.

We have also arranged for advanced notice of next year's conference complete with Program Committee. Dr. Patricia Foster of the United Kingdom will be the 1992 Symposium Chairman and Dr. Perry Wheless, Jr, of the University of Alabama is providing stateside support as the Conference Co-Chairman. The 1992 Conference "Call for Papers" is published in these proceedings.

It has been the interest of ACES to promote international participation at ACES conferences. This year we have initiated an "International Forum" by recruiting representatives from each of eight international regions to address the conference and discuss topics of technical significance in their region of the world. We sincerely hope that these addresses will promote international dialog on technical issues of computational electromagnetics.

As many of you know, ACES has matured with the incorporation of the society last year. With this expansion comes the responsibility of economic self sufficiency. ACES has been sponsored for many years by the donations of facilities and financial support from such organizations as the Naval Postgraduate School and Lawrence Livermore Labs. In the future, like competing technical organizations, ACES will be required to undergo long range fiscal planning and sound financial operations. This year's conference is a start. Care has been taken to minimize conference costs and improve revenues. We conservatively project more than $5,000.00 in cost savings and additional revenues compared to past conferences. These results bring ACES closer to total self sufficiency and allow us to consider new and novel activities such as sponsored international attendees and funded computational competitions.

As a result of negotiations with MIT, CAEME will offer a 120 minute version of the MIT video on "Experimental Demonstrations for Teaching Electromagnetic Fields and Energy". In cooperation with CAEME, ACES has purchased the video at cost for free distribution to each registered conference attendee. Additional copies of the video will be available from CAEME at the conference for $10.00 ($25.00 after the conference). This is a substantial discount compared to the commercial value of the MIT material. Dr. Magdy Iskander, CAEME director, is to be commended for his efforts in successfully arranging for the generous contribution of this MIT video material to the technical community.

With the gracious efforts of Dr. Magdy Iskander, CAEME director, and Kathy Lee, the Vendor Booth Co-Chairman, we have organized fourteen vendor booths at this year's conference. Six are CAEME associates and eight are commercial product vendors. These vendor booths provide exposure to products and services of interest to ACES attendees in addition to generating conference revenues.

Another feature is repeated this year with the offering of two full day and four half day short courses on the Monday of conference week. We wish to express our appreciation to the 1991 Short Course Chairman, Dr. John Rockway, for organizing the short course curriculum. The lecturers are to be commended for the excellent quality of the short course material offered this year.

We do not have news to report at the time of this printing concerning inclusion of ACES papers in technical library data bases. Dialog has been initiated with the IEEE and we hope to have progress to report at the conference.

As a result of the material offered in the technical papers this year, we have several new sessions. There are three sessions relating to time domain analysis techniques and solutions. A second new topic is the low frequency session that has resulted from international papers dealing with transformer analysis and electrical power problems.

An added feature in the table of contents are two or three letter keys to indicate topic associations for each paper. This is as a result of the screening process used to place each paper into a technical session. These are in addition to the more general session titles and are intended to help minimize confusion over the probability that a technical paper contains multiple topics of interest to an ACES reviewer. As an example there is a session of "NEC Antenna Analysis". In addition all conference papers in which NEC was used are labelled with the (NEC) key for quick identification. We hope that these keys will assist the reader in more quickly finding topics of interest.

In conclusion let us welcome you as a conference attendee and wish you success in your search for knowledge in the growing field of computational electromagnetics.

Frank Ellis Walker
1991 Symposium Chairman

ACES PRESIDENT'S STATEMENT

The exhilarating spring beauty and charm of the Monterey Peninsula and the hospitality of the Naval Postgraduate School have become synonymous with the Annual Reviews of Progress in Computational Electromagnetics of our Society. I take pleasure in welcoming you to this 7th review. I hope that you will once more share with me the appreciation of this environment while obtaining the practical benefits of a rich technical program of papers, short courses, and display booths that Frank Walkor and his team have prepared for us this year.

Let me assure you that the officers and directors of ACES appreciate your participation. Your attendance at the symposium helps to make a viable and thriving technical society. To the authors, instructors, and chairmen my thanks for your efforts and willingness to participate in this important capacity. We are most interested in the reaction of companies and individuals participating in vendor displays. We should like to take advantage of your experience to improve our offerings in the years to come.

I also invite you to consider increasing your involvement with ACES activities. But it is my hope that you will leave this year's event with your expectations fulfilled and with a resolve to make plans to attend in 1992.

Dr. Stan Kubina
ACES President

1992 CONFERENCE CHAIRMAN'S STATEMENT

As chairman for the 1992 Symposium, I would like to welcome you to that event. The primary aim of the Symposium is the interchange of information and, although the centerpiece of the Symposium remains in the sessions given by you, the authors, there are other ways in which we can all gain. The good work of the 1991 Symposium will continue in 1992 with more short courses to bring you all up to date with the latest techniques or teach those starting out in this field the basic tools of the trade. We will identify those courses suitable for training purposes. We also hope to run another exhibition as I believe it is in the interests of ACES to know what programs are available commercially and for software interchange. No amount of reading promotional literature can replace conversation with suppliers and other users.

After seven years of the ACES Symposium, we can claim that it has become a notable feature of the electromagnetic year but that does not mean that it cannot be improved upon. I hope all of you will consider what help you can give in organizing the Symposium to be more suitable for you. You do not have to volunteer to work on a committee but you can write to me to specify what you like about this Symposium or have noticed as an omission.

Pat Foster
1992 Symposium Chairman

MONDAY MARCH 18

SHORT COURSES

FULL-DAY COURSES: (Approximately 6 hour Course)

0830 "The ESSENCE of Electromagnetic Radiation"
by Dr. Robert M. Bevensee, Consultant

0830 "The Electromagnetic Analysis of Microstrip"
by Dr. James C. Rautio, Sonnet Software

MORNING HALF-DAY COURSES:

0830 "UTD and Its Practical Applications"
by Dr. Ronald J. Marhefka, The Ohio State University Electroscience Laboratory

0830 "An Overview of Several Topics in Electromagnetic Modeling"
by Dr. Edmund K. Miller, Los Alamos National Laboratory
and Gerry Burke, Lawrence Livermore National Laboratory

AFTERNOON HALF-DAY COURSES:

1300 "Introduction to GEMACS"
by Dr. Edgar L. Coffey III

1300 "Volume Integral Equations and Conjugate Gradient Methods in Electromagnetic Non destructive Evaluation"
by Dr. Harold A. Sabbagh, Sabbagh Associates, Inc.

1800 - 2030	REGISTRATION	101A Spanagel
1830	ACES BOARD OF DIRECTORS DINNER	
2000	ACES BOARD OF DIRECTORS MEETING (Members invited to observe)	122 Ingersoll

TABLE OF CONTENTS

SESSION 1: USER INTERFACES AND PC APPLICATIONS FOR EM MODELING CODES
Moderator: Ronald Marhefka

"A Portable Interactive-Graphics Pre-Processor for Use with Wire-Grid Modelling Software"
P.S. Excell and A.F. Armanious (I/O,WG,MOM) 1

"Progress: Development of an Interactive Graphics Program for EM Codes"
J. Peng, J. Choi, C.A. Balanis, and G.C. Barber (I/O) 10

"GEMCOP: An Expert System for GEMACS and GAUGE"
R. Fisher, E.L. Coffey III, and T. Timmerman (I/O,PC,GEM) 20

"Implementation of the NEC - Basic Scattering Code on a PC"
R.J. Marhefka (PC) 21

"NEC, FERM and GEMACS on the Macintosh"
P.E. Bussey and R.W. Taylor (PC,ANT,NEC,GEM) 29

SESSION 2: CAEME SPECIAL SESSION ON COMPUTER APPLICATIONS IN ELECTROMAGNETIC EDUCATION"
Moderator: Magdy Iskander

"NSF/IEEE-CAEME Center Activities: Progress Report, Software Projects, and Future Focus"
M.F. Iskander 37

"Simulation of Electromagnetic Phenomena Using a Finite Difference - Time Domain Technique"
K. Li, M.A. Tassoudji, R.T. Shin, and J.A. Kong (TD,FD,SC,PC) 38

"Electromagnetic Code for Solving Static and Dynamic 2 - D Field Problems on a Personal Computer"
J.E. Lebaric, M. Melton, and J. Engel (PC) 56

"The High Frequency Electromagnetic Simulation of Arbitrary Two and Three Dimensional Structures"
B. Brim (MM,FE,AX,I/O) 57

"Software for Antenna Modeling and Radar Applications"
R.J. Hancock (ANT,PC) 58

"Microwave Explorer: An Electromagnetics Program for the Analysis of High Frequency Integrated Microstrip Circuits"
A. Hill, J. Burke, and K. Kottapalli (MM,SC,MAT,MOM) 59

"A Case for Realism in Scientific Animation"
Z. Fazarinc (I/O) 67

"Educational Uses of GEMAC"
E.L. Coffey III (GEM,MOM) 68

"Experimental Demonstrations for Teaching Electromagnetic Fields and Energy"
M. Zahn, J. Melcher, and H.A. Haus 72

"Lienard-Wiechert Field Generator and HyperCard Tutorials for Visual Electromagnetics"
R. Cole and D. Krull 73

SESSION 3: INVERSE PROBLEM SOLUTIONS — Moderator: Margaret Cheney

"An Inverse Boundary Value Problem for Maxwell's Equations"
E. Somersalo, D. Isaacson, and M. Cheney (BV) 74

A Layer-Stripping Approach to Impedance Imaging"
M. Cheney, D. Isaacson, E. Somersalo, and E. Isaacson (BV) 79

"Electric Current Computed Tomography"
D. Isaacson, M. Cheney, J.C. Newell, D.G. Gisser, and J.C. Goble (BV,MAT) 87

"Use of Electrical Impedance Imaging in Two-Phase, Gas-Liquid Flows"
J.T. Lin, T. Suzuki, L. Ovacik, O.C. Jones, J.C. Newell, and M. Cheney (BV,MAT,BIO) 94

SESSION 4: ASYMPTOTIC SOLUTIONS — Moderator: Andrew J. Terjuoli Jr.

"Primitive Target Validation for the Signature Prediction Tools Software Package"
D.J. Young and A.J. Terzuoli Jr. (ASY,SC,NM) 115

"High Frequency Scattering Code in a Distributed Processing Environment"
S. Suhr, A.J. Terjuoli Jr, and G.B. Lamont (ASY,SC) 130

"Simulation of Site Obstruction Effects on the Performance of a High Gain Antenna Using NEC-BSC2"
A.M. Bucceri, J.C. Herper, and E. Mertz (ASY,ANT,NEC) 139

"Bistatic Physical Optics Scattering from a Surface Described by an Electromagnetic or Acoustic Impedance Boundary Condition"
R.T. Brown (ASY,SC,BV) 146

INTERNATIONAL FORUM

Reports from International Regional Representatives concerning topics of technical importance in each region.

Great Britain:	Dr. David Lidius, AEA Industrial Technology, Culham, U.K.
Western Europe:	Dr. Ruediger Anders, ACES Europe Committee Chairman, Applied Electromagnetic Engineering, Germany
Eastern Europe:	Dr. Mihaela Morega, Polytechnic Institute of Bucharest
Australia:	Dr. Gregory Haack, Surveillance Research Laboratory, South Australia
Japan:	Dr. Chiyo Hamamura, Mitsubishi Electronic Corporation, Japan
China:	Dr. Yuanren Qiu, Xi'an Jiaotong University, P.R. China
South America:	Dr. J.P.A. Bastos, Universidate Federal de Santa Catarina, Brazil
Africa:	Dr. Duncan Baker, University of Pretoria, South Africa

SESSION 5: NEW TECHNIQUES — Moderator: Ronald Pogorzelski

"A Hybrid Finite Element and Moment Method for Electromagnetic Scattering from Inhomogeneous Objects"
W.E. Boyse and A.A. Seidl (FE,SC,MAT,MOM) 160

"A New Expansion Function of GMT: The Ringpole"
J. Zhang (NM,BV) 170

"An Application of Symbolic Manipulation Software in Computational Electromagnetics"
R.J. Pogorzelski (NM,ASY) 174

"Efficient Solution of Matrix Equations in Finite Element Modeling of Eddy Current NDE"
A. Mahmood, D.J. Lynch, G.H. Nguyen, and L.D. Philipp (NM,FE) 184

"An Approximate (Symmetric) Combined Field Integral Equation for the Analysis of Scattering by Conducting Bodies in the Resonance Region"
L.M. Correia and A.M. Barbosa (NM,SC) 190

"New Expansion Functions for Long Structures in the MMP-Code"
P. Leuchtmann (NM) 198

"Direct Solution of the Wave Equation Using Parallel Computational Techniques"
R.G. Hohlfeld, S.M. Sparagna, and C. Sandi (NM,ANT,MAT,FD) 203

"On Using a Conceptual Model for Deriving the Electromagnetic Statistics of Complex Cavities"
T.H. Lehman and E.K. Miller (NM) 222

SESSION 6: FINITE ELEMENT AND FINITE DIFFERENCE FREQUENCY DOMAIN SOLUTIONS
Moderator: Glenn Crabtree

"Solution of Multi-Media Wave Propagation and Scattering Problems Using Finite Elements"
E.T. Moyer Jr. and E. Schroeder (FE,SC,MAT) 234

"Finite Element Solutions to the Mass-Tensor Form of the Ginzburg-Landau Equations"
K.G. Herd and G. Theodossiou (FE,MAT) 235

"Characterization of Anechoic Chambers by Finite Difference Method"
S. Halfa, D. Hollmann, and W. Wiesbeck (FD,SC) 244

SESSION 7: MOMENT METHOD THEORY
Moderator: Allen Glisson

"A Multi-level Enhancement of the Method of Moments"
K. Kalbasi and K. Demarest (MOM,SC,NM) 254

"On the Applicability of Pulse Expansion and Point Matching in the Moment Method Solution of Three Dimensional Electromagnetic Boundary-Value Problems"
B.C. Ahn, K. Mahadevan, and A.W. Glisson (MOM,SC,BV,NM) 265

"Recursive Algorithms to Reduce the Computational Complexity of Scattering Problems"
W.C. CHew, Y.M. Wang, L. Gurel, and J.H. Lin (MOM,SC,NM) 278

"Numerical Solution of the EFIE Using Arbitrarily Shaped Quandrangular and Triangular Elements"
T. Madsen and H. Singer (MOM,NM) 292

SESSION 8: MODELING EM INTERACTIONS IN MATERIALS
Moderator: Kenneth Demarest

"General Approach for Treating Boundary Conditions on Multi-Regional Scatterers Using the Method of Moments"
J.M. Putnam (MAT,SC,MOM,BV) 304

"Comparison of Computed and Measured Results for a Simple Man-with-Radio Model"
A.W. Glisson, D. Kajfez, W.P. Wheless Jr., and K.H. Agar (MAT,BIO,NM) 320

"Toolbox for Characterization of Materials"
J.R. Dornfest (MAT,SC) 329

"Polarimetric Scattering and Control of Radar Cross Section of Chiral Targets of Simple Geometrics and Associated Code Development"
A.K. Bhattacharyya (MAT,SC,BV) 344

SESSION 9 HIGH FREQUENCY APPLICATIONS AND WIRE GRID MODELING TECHNIQUES
Moderator: Christopher Trueman

"Scattering By Sectioned Cylinders"
B Rulf (SC) 351

"RCS of Fundamental Scatterers in the HF Band"
C W Trueman, S R Mishra, and S J Kubina (SC,WG,I/O) 369

"Automated Radius Calculation for Wire Grid Models"
C W Trueman and S J Kubina (SC,WG,I/O) 380

SESSION 10 MICROWAVE CIRCUITS AND MICROSTRIP ANTENNA ANALYSIS
Moderator: Fabrice Huret

"Full Wave Modeling of a Multi Layer Microstrip Array with a Superconducting Microstrip Feed Network"
J S Herd (MM,SC,MOM) 389

"Modeling of an Anisotropic Stripline"
M Kamarei, N Dib, R Sabatar, and M Boutheiche (MM,SD) 396

"Analysis of the Behavior of Quasi Complex Modes on Lossy Substrate Boxed Microstrip Lines"
F Huret, P Pribetich, and P Kennis (MM,MMIC) 403

"Computer Modelling of Helical Slow Wave Structures for Use in Travelling Wave Tubes"
A J Morrison (WG,NEC) 409

"Electrically Trimmed Array Synthesis for Solid State Radar Applications"
M A Hussain, B Noble, and M McKee (ANT,NM) 419

"Guided Wave Propagation on Two Dimensional Clusters of Directly Coupled Cavity Resonators"
R A Speciale (MM,SC,NM) 428

SESSION 11 ANTENNA ANALYSIS
Moderator: Asoke Bhattacharyya

"Method of Moments Analysis of Cavity Backed Wire Antennas"
D C Jenn and E E Barber (ANT,WG,MOM) 432

"Moment Method Modeling of the Normal Mode Helical Antenna"
Y J Guo and P S Excell (ANT,WG,MOM) 446

"Intercomparison of Several Moment Method Models of Dipoles and Folded Dipoles"
P S Excell and A F Armanious (ANT,WG,MOM) 451

"Simplified Horn Antenna Parameter Estimation Using Selective Criteria"
P D Ewing (ANT,NM) 456

"Far-Field Patterns of Ultra High Gain Antenna Arrays of Finite Size"
R A Speciale (ANT,NM) 471

SESSION 12: NEC ANTENNA ANALYSIS
Moderator: Peter Excell

"Modeling a Shipboard Fan Antenna"
L Koyama (ANT,WG,NEC) 474

"Optimizing Sidelobe Levels of an Array Using NEC"
R L Haupt, C J McCormack, and W F Brandow III (ANT,WG,NEC) 487

"Using the Numerical Electromagnetics Code (NEC) to Calculate Magnetic Field Strength Close to a Sommerfeld Ground"
G. Haack (ANT,NEC) 493

"Refinement of HF Vertical Half Rhombic Characterization"
W.P. Wheless Jr., M.O. Fanning, D.L. Faust, and M.B. King (ANT,WG,NEC) 507

SESSION 13: ELECTROMAGNETIC COMPATIBILITY (EMC) Moderator: David P. Millard

"A Survey of Numerical Techniques for Modeling Sources of Electromagnetic Interference"
T.H. Hubing (EMC) 516

"Computer Aided Electromagnetic Compatibility Analysis"
D.P. Millard, J.K. Daher, R.M. Herkert, and J.A. Moody (EMC,I/O,PC) 520

SESSION 14: LOW FREQUENCY APPLICATIONS Moderator: Perry Wheless, Jr.

"Transient Leakage Field in Transformers With Saturable Magnetic Core"
M.I. Morega and A.M.I. Morega (LF,TD) 529

"Finite Element Analysis of Magnetic Field Distribution in Ferromagnetic Shields"
C.V. Bala, O.C. Cralu, and M.I. Morega (LF,TD) 534

"A Model for Dynamic Analysis of AC Contactor"
P.I. Kottermann, J.P.A. Bastos, and S.R. Arruda (LF,FE) 540

"Eddy Current Analyses of the Core Plate in a Large Power Transformer"
Y. Qiu, W. Wang, Q. Zhang, G. Xiao, and X. Li (LF,FE) 545

"Engineering Resolvability of Engineering Eddy-Current Problems"
Z. Cheng, S. Gao, D. Zhang, J. Wang, and C. Ye (LF,FE) 551

SESSION 15: TIME DOMAIN METHODS Moderator: Gerald Burke

"Comparison of GTD and MoM Scattering Computations and Transformation to the Time Domain"
P.G. Elliot and T. Kohlberg (TD,MOM) 557

"Evaluation of Modified Log-Periodic Antennas for Transmission of Wide-Band Pulses"
G.J. Burke (TD,NEC) 567

"The Pulsed Response from a Parabolic Reflector Antenna"
G.R. Sato (TD,ASY) 577

"A Ray-Tracing Model to Predict Time-Domain RCS Performance of a Compact Range"
N. Carey, S. Brumely, and A. Jain (TD,SC) 586

SESSION 16: TRANSMISSION LINE MATRIX (TLM) TIME DOMAIN APPLICATIONS POSTER
Moderator: Lloya Riggs

"A Transmission Line Matrix (TLM) Method Analysis of the Separated Aperture Buried Dielectric Anomaly Detection Scheme"
P.R. Hayes, L.S. Riggs, and C.A. Amazeen (TD,TLM,NEC) 599

"The Modelling of Lossy Materials with the Symmetrical Condensed Node TLM Method"
F.J. German, G.K. Gothard, and L.S. Riggs (TD,TLM,MAT) 612

"The Analysis of Passive Microwave Components Using the TLM Method"
P.R. Conway, F.J. German, and L.S. Riggs (TD,TLM,MAT) 627

SESSION 17: FINITE ELEMENT AND FINITE DIFFERENCE TIME DOMAIN SOLUTIONS
Moderator: Raymond Luebbers

"A New Weighted Residual Finite Element Method for Computational Electromagnetics in the Time Domain"
J. Ambrosiano, S.T. Brandon, and R. Lohner (TD,FE) 642

"'Virtual Particle' Electromagnetic Particle-Mesh Algorithms for Microwave Tube Modelling"
J.W. Eastwood (FE,TD,NM) 655

"A New Magnetic Field Analysis for Dynamical Problem Involving Relative Displacement with Time"
C. Hamamura, M. Okabe, T. Ohmura, and K. Sato (TD,FE) 661

"A Time Domain to Calculating Radar Cross Sections"
D.W. Harmony and G.R. Sato (TD,FD,SC,MAT) 656

"A 2-D Finite-Volume Time-Domain Technique for RCS Evaluation"
R. Holland, V.P. Cable, and L. Wilson (TD,FE,SC) 667

"RCS Calculation for Smooth Bodies of Revolution Using FDTD"
R. Luebbers, D. Steich, K. Kunz, and F. Hunsberger (TD,FD,SC,MAT) 682

"FDTD Waveguide Coupling Modeling and Experimental Validation"
P. Allnikula, S. Kunz, and R. Luebbers (TD,FD,V) 691

Authors Index 702

© 1991 The Applied Computational Electromagnetics Society

KEY:

DOMAINS

TD	Time Domain
SD	Spectral Domain
MM	Millimeter wave (microwave, microstrip, antennas)
LF	Low Frequency (power systems)

METHODS

MOM	Method of Moments
FE	Finite Element method
FD	Finite Difference method
BV	Boundary Value method
TLM	Transmission Line Modeling
WG	Wire Grid modeling
ASY	Asymptotic solution applications
NM	New Method

APPLICATIONS

SC	Scattering (RCS)
MAT	Materials
BIO	Biological applications
ANT	Antenna analysis
MMIC	Monolithic Microwave Integrated Circuitry
EMC	Electromagnetic Compatibility, Electromagnetic Interference (EMC/EMI)
V	Validation
I/O	Input/Output interfaces
PC	Personal Computer applications

CODES

NEC	Numerical Electromagnetics Code (NEC)
GEM	GEMACS/GAUGE

SESSION 1 – "USER INTERFACES AND PC APPLICATIONS FOR EM MODELING CODES"

Moderator: Ronald Marhefka

A PORTABLE INTERACTIVE-GRAPHICS PRE-PROCESSOR FOR USE WITH WIRE-GRID MODELLING SOFTWARE

P S Excell & A F Armanious*

Electrical Engineering Department, University of Bradford, West Yorkshire, UK
*now at Sultan Qaboos University, Oman

Abstract

An interactive-graphics input program for wire-grid moment-method modelling packages is described. This was written in Fortran-77, using the standard GKS (Graphical Kernel System) graphics commands in order to maximise the portability and maintainability of the software. The program contains several features to ease the inputting of the physical structure of the wire-grid object and its subsequent sub-division into segments of appropriate length. The object can be visualised on a graphics screen, with or without annotations. The output data may be formatted to conform to the input requirements of a number of standard moment-method packages.

1. Introduction

Wire-grid modelling involves the fictitious replacement of continuous metallic surfaces in an arbitrary metallic structure with wire meshes having aperture perimeters that are small compared with a half-wavelength at the frequency of interest. The input into a computer of the topology of a complex metallic structure, and its conversion into a corresponding wire-grid model, is a tedious procedure that is prone to many sources of error. This problem has been widely recognised, and interactive graphics input programs such as IGUANA [1] and GAUGE [2] have been developed to aid input to specific modelling programs. In addition, certain other programs designed to run on personal computers incorporate integral input graphics routines [3,4]. While these programs have many merits, they have the limitation that they can only be used on one display device (an IBM-type personal computer), and they each produce output data in a format specific to one solution program.

The lack of an all-pervading standard for computer graphics remains a very serious impediment to many applications. The Graphical Kernel System (GKS) was an attempt to rectify this situation and, although its uptake has been less widespread than might have been desired, it remains one of the few widely-used graphics standards: at the time the work reported here was commenced, it was effectively the only graphics standard.

It is well known to practitioners of wire-grid moment-method modelling that it is seldom possible to place a high degree of confidence in the first results from any attempt to model a complex structure. The normal heuristic approach is to compare the initial prediction with the nearest available analytical solution in order to check that it is fundamentally physically reasonable, and then to re-run the model with changed values of some of the arbitrary parameters in order to check that the results remain stable. Despite commendable attempts by some to improve the rigour and reliability of the method, strategies of this type are likely to continue and it was felt that it would be very desirable if variation of the moment-method formulation and the solution method were available as an alternative to variation of the wire-grid parameters. To this end, it was decided that the program described here should incorporate a menu of several different well-known moment-method packages such that the output data from this pre-processor could be formatted in such a way that it was immediately usable as input to the chosen solution package.

2. The Graphical Kernel System (GKS)

The Graphical Kernel System is a set of graphical software library routines, written by an international working group in the early 1980s, and published as an international standard by ISO in 1985 [5].

GKS is a device-independent system which has the facility to support a wide variety of graphical devices. Thus the source program may be transferred from one computer to another without the need for modifications, since it is independent of device drivers (which exist as commercial software for a wide variety of computers). The object of the device drivers is to drive the device concerned within the operating system rather than making it dedicated to the program, hence the program uses normalised device coordinates. The GKS version used was only implemented for two-dimensional coordinates. However, three-dimensional structures may easily be projected onto two dimensions. The next sections introduce some of the features of GKS used in the program, known as Wire Grid Modelling (WGM).

2.1 Workstations

Instead of considering individual input and output devices, GKS introduced the concept of a 'workstation' (not to be confused with the normal understanding of this word as a piece of computing hardware). The idea of using workstations in a program is try to relate all of the graphics calculations to a system of normalised device coordinates. The device coordinates may be applied to a display, plotter, digitizer, etc. Thus a program which uses the GKS library may define all the workstations which may be used at the run time. These workstations are labelled with common names (e.g. display, printer, plotter, digitizer, etc.). Each workstation name may be opened for different devices, by loading the appropriate device within the operating system. For example, in using GKS on an IBM-PC-type computer, assuming the workstation used is called 'DISPLAY', then different devices for the display may be used, e.g. colour graphics adapter (CGA), enhanced colour graphics adapter (EGA), etc. The same principle is applied for the printer workstation, etc. The workstation must be activated before it is used, and deactivated before it is closed.

2.2 Segment Storage and Attributes

During the execution of a program, graphical output can be saved for later use in the execution session. In GKS, this operation has the concept of a 'segment' (not to be confused with wire segments, as used in the Moment Method). The segments have a number of attributes associated with them. The operation of storing graphical output during execution is achieved by creating a new segment: whenever graphical output is issued, it will not be displayed on the screen until the segment is closed. Once the segment is closed, it can be copied, deleted or renamed and its attributes can be changed. The segment attributes control the following:

1. Rotating and translating the whole set of coordinates which are stored in the requested segment, using a segment transformation matrix.
2. The segment may be set as visible or hidden.
3. The segment may be highlighted to draw the operator's attention to a certain object.
4. Segments may have different priorities to control which segment number appears in front of the others on a display.
5. Segments may be set to be detectable or not detectable for input pickup.

2.3 Scaling

As mentioned above, the 'world' coordinates (i.e. user x,y coordinates) are normalised to the device coordinates. In general, the scale is defined by the coordinates of a rectangular window. Thus in GKS, different transformation numbers may be set to each appropriate window and the requested scale may be referred to by its transformationnumber. The maximum number of transformation numbers is installation-dependent.

2.4 GKS Methods for Input

GKS offers six different methods for interactive input. Each method may be used through an appropriate input device (e.g. cursor control keys; a track-ball; a joystick; a graphics tablet (digitizer); a mouse; or a lightpen).

1. LOCATOR: used to input (x,y) coordinates.
2. PICK: used to pick (select) a displayed object on the screen.
3. CHOICE: used to select an item from a set (menu) of alternatives.
4. VALUATOR: used like a potentiometer for inputting a numerical value from a quasi-continuous linear distribution
5. STROKE: used to input a sequence of (x,y) positions.
6. STRING: used to input a string of characters from the keyboard.

These logical devices need to be initialised before they are used.

3. The Interactive-Graphics Pre-Processor

The pre-processor program for wire grid modelling, named WGM, was developed using standard Fortran-77 with GKS graphics commands. Fig. 1 shows the display format, three windows being used within this. The first window is used for menus, the second for warning messages and string input and the third is the main window for display of the structure. These windows are set to occupy the whole display, thus each window is set to a certain portion of the maximum view port (i.e. the whole screen). Thus three transformation scales have to be used for the three windows. The CHOICE logical input device is set for selection of an option from the menu. An item from the menu can be selected by one of the standard set of ten function keys on a Personal Computer. The program uses a small number of workstations, these being: WISS, DISPLAY, and PRINTER. The Workstation-Independent Segment Storage (WISS) is used to enable the copying of segment storage to other workstations (e.g. printer or plotter).

3.1 Menu Structure

The menu consists of a root menu and menu trees. Thus each option in the root menu is a sub-menu and each option in a sub-menu is another sub-menu. The function keys F9 and F10 in the sub-menus are always used to return to the last or the root menu respectively. A program was written for creating or modifying a fixed database menu system which was then used as a data file by the WGM program.

In order to solve and simplify the geometry input problem, the program should be rich with different options. Table 1 shows the menu structure created: although the program does not, at present, contain all of the options listed, the main options were developed and the program thus provides a structure for further development and improvement. Implemented options are described below.

3.1.1 DEFINE

The start of any problem should be its definition. The definitions include any of the following:

1. The axis orientations and the location of the origin on the screen. Also the axes can be set to be either displayed or hidden.
2. The scales of the structure: these are simply the range of dimensions of the rectangular prism which completely surrounds the whole structure.
3. The operating frequency or the wavelength, required to control the wire segment length.
4. The output format, determined by the choice of electromagnetics software package which will use the generated data. Outputs feeding the following codes were implemented: NEC [6]; GEMACS [7]; Richmond's code [8]; Chao & Strait's code [9]; and TWC [10] (a code by the present authors, based on the same formulation as MININEC [3]).
5. The wire radii used in the wire model: during the interaction session any radius may be referred to by its index number.

3.1.2 ATTRIBUTE

The graphical attributes are: colour, line type, and point marker type.

3.1.3 DRAW

This is the most important part of the menu and consists of the following:

1. Draw point with label given by the program. The point can be entered in cartesian, cylindrical polar, or spherical polar coordinates. Relative coordinates can also be entered (i.e. relative to previous point).
2. Define a structure boundary. The user may start from a point in space and then automatically draw a continuous boundary (which may be open or closed) through any other points specified.
3. Line utilities, requiring knowledge of the coordinates of one end, line (wire) length and some other parameter such as: line parallel to another line or a plane; line perpendicular to another line or a plane; or direction angles of the line.
4. Wires may be created by connecting a line between two points, or between one point and a number of points.
5. A wire may be automatically divided into a specified number of equal segments.

3.1.4 EDIT

Editing the geometry is an essential feature to aid rapid building of the structure.
The edit menu consists of:

1. Erasing a point or segment, or all segments having a given tag number.
2. Changing a segment tag number or its radius; changing a point number or segment number; changing attributes (e.g. segment colour, and displayed line type (dotted etc.) of a wire segment).
3. Rotating and duplicating the structure.

3.1.5 DISPLAY

This option is designed to aid the user to exploit the maximum degree of visualisation possible. It has the following options:

1. The structure can be viewed in one of the three major planes (i.e. $x=0$, $y=0$, or $z=0$). Alternatively the elevation angle or the view angle may be changed.
2. Zoom to fit the whole structure into the whole working window.
3. Display the labels of either points, or wire segments, or both.

3.1.6 PLOT

With the concept of the workstation, any part of the structure may be plotted easily. Thus the user may plot the whole structure, or any selected parts (selected by tag number, or block etc.).

3.1.7 END

This option is used to write all the segment coordinates into a file (with a format determined by the chosen electromagnetics code). It also saves all the data entered during the interaction session and exits from the WGM program.

3.2 Two-Dimensional Display of Three-Dimensional Structures

Since the structures modelled are relatively compact, the use of perspective is not essential and a simple method for projection was used. In this method any three-dimensional point will be projected on the plane of the screen (which is defined by spherical view angles θ and ϕ, these being the polar angles of the normal to the plane relative to the origin).

3.3 Database Storage of Wire Segment Parameters

To avoid the problem of memory limitation when storing the wire segment parameters, a binary random-access file was used. The use of such a direct-access file means that the limit for the maximum number of segments is determined by the available disk space. Using the concept of GKS segment storage, any point marker with its label and any line representing a wire segment are stored in separate graphics segments. To maximise the use of available storage, data for a point and a wire with the same input sequence number are stored together in a single record, even though, in general, they will not be connected with each other.

Note that the program always remembers the current total numbers of wire segments and points which have been entered. At the end of a session, the numbers of wire segments and points are saved in some reserved records in the file, together with the current scale in use and the current segment attributes for new wire segments.

3.4 WGM Program Structure

The WGM program starts with a menu of three options. These are to select whether to start a fresh model, to retrieve data built in a previous session, or to build a model from a NEC geometry data input file.

As explained above, the three-dimensional coordinates are mapped into two-dimensional coordinates. Thus any basic operation (e.g. dividing, rotating, duplication) on the structure will be performed first on the three-dimensional representation and then the resulting three-dimensional coordinates will be mapped into two dimensions as explained. Once the structure has been modelled, the program can generate all the geometrical input data in the format required by the chosen Method of Moments computer program.

An example of the modelling of a simple structure is given in Fig. 2, which shows a box (an idealised vehicle) with a monopole antenna mounted on the top. This model was run with NEC, using a lossy ground plane to simulate a real environment. Figs. 3 and 4 show the electric field pattern for the structure in the theta and phi polarizations respectively.

4. Conclusion

A computer-aided technique for inputting and displaying large geometrical data sets has been described. This uses device-independent graphical software commands from the Graphical Kernel System (GKS), chosen as the most flexible method of achieving this. Several methods of inputting the geometrical data set are desirable and these are provided in GKS. The geometry input problem was tackled by combining a database system for the model with an interactive graphics CAD-type program such that the user interaction was translated into database query, add and update commands. As shown above, the WGM program was provided with a very detailed database menu which may be extended for further work and requirements.

The use of GKS involves an additional software library resource, but this is compensated by the potential portability, giving a uniform input system on any computer for which GKS drivers are available.

References

1. 'NEEDS, The Numerical Electromagnetic Engineering Design System', Monterey, ACES, 1988.

2. Lockyer, A & Tulyathan P: 'Graphical Aids for Users of GEMACS (GAUGE)', Proc. 4th Annual Review of Progress in Applied Computational Electromagnetics, Monterey, 1988.

3. Rockway, J W et al: 'The MININEC System: Microcomputer Analysis of Wire Antennas', Boston: Artech House, 1988.

4. Djordjevic, A R et al: 'Analysis of Wire Antennas and Scatterers', Boston: Artech House, 1990.

5. Hopgood, F R A et al: 'Introduction to the Graphical Kernel System (GKS)', New York: Academic Press, 1986.

6. Burke, G J & Poggio, A J: 'Numerical Electromagnetics Code (NEC)', Lawrence Livermore Nat. Lab., Report No. UCID-18834, 1981.

7. Coffey, E L & Kadlec, D L: 'General Electromagnetic Model for the Analysis of Complex Systems (GEMACS)', USAF Rome Air Development Center, Report. No. RADC-TR-87-68, 1987.

8. Richmond, J H: 'Computer Program for Thin Wire Structures in a Homogeneous Conducting Medium', NASA Report No. CR-2399, 1974.

9. Chao, H H & Strait, B J: 'Computer Programs for Radiation and Scattering by Arbitrary Configurations of Bent Wires', Air Force Cambridge Research Labs., Report No. AFCRL-70-0374, 1970.

10. Armanious, A F & Excell, P S: 'Enhancements to Moment-Method Field Computation Packages', IERE Conf. on EMC, York University, 1986, pp. 191-196.

Acknowledgements

This work was funded by a studentship grant from the University of Bradford Research Committee. Some software and hardware was provided by the UK Science & Engineering Research Council.

Menu name	Function Keys							
	F1	F2	F3	F4	F5	F6	F7	F8
ROOT	DEFINE	ATTRIB	DRAW	EDIT	DISPLAY	LAYERS	BLOCK	INQUIRY
DEFINE	AXIS	SCALES	FREQ.	CODE	RADII	PLANE	SURFACE	AUTO S.
ATTRIB.	COLOUR	LINE T.	MARK T.	HIDE				
DRAW	POINT	BOUND.	LINE	ARC	RECT.	PATCH	DIVIDE	CONNECT
EDIT	ERASE	CHANGE	ROTATE	MOVE	MIRROR	CYL. R.		
DISPLAY	VIEW	ZOOM	FIT	WIRES	POINTS	TAG	RADIUS	2D
LAYERS	X=0	Y=0	Z=0	PLANE	SURF.			
BLOCK	DEFINE							
INQUIRY	POINT	SEGMENT						
PLOT	ALL	WIRES	POINTS	TAG	RADIUS	SCALE		
END	SEG(S)	QUIT						
AXIS	SHOW	HIDE	ORIGIN	CREATE				
SCALES	ALL	X SCALE	Y SCALE	Z SCALE	CM.	METRE	INCH	WAVE
FREQ.	GHZ	MHZ	KHZ	WAVE/M				
CODE	NEC	GEMACS	RICHM	CHAOS	TWC			
RADII	A1	A2	A3	A4	A5	A6	A7	A8
PLANE	A X	B Y	C Z	D				
SURF.	CYL.	CONE	SPHERE					
AUTO	DEL	.25 LAM	.125 LA	.1 LAM.	.01 LAM	.02 LAM	.025LAM	.001LAM
COLOUR	LINE	TEXT	TAG NO.	BLOCK				
LINE T.	SOLID	L-DASH	DOTTED	DASH.D	M-DASH	DASH..		
MARK T.	S. BOX	+	*	REC.B	x	DIAM.		
HIDE	ALL	TAG	BLOCK					
RES.								
RES.								
RES.								
RES.								
POINT	X Y Z	RO PH Z	R TH PH	D XYZ	D CYL.	D SPH.		
BOUND.	NEW	START						
LINE			PAR. L.	PAR PL.	PER. L.	PER. PL	INTR.	ANGLE L
ARC	CENTRE	FIRST P	SECOND					
RECT.	PICK	PROMPT	CORNER1	CORNER2				
PATCH	REC.	TRIANG.	AREA,NO					
DIVIDE	PICK	PROMPT	M REC.	M TRI.	M SQU.			
CONNECT	TAG NO.	RADIUS	LINE B.	LINE TO	P1-P2	G-MP	PROMPT	PICK
ERASE	POINT	LINE	TAG NO.	RADIUS				
CHANGE	RADIUS	TAG NO.	L COLOU	T COLOU	LINE T	MARK T	PROMPT	PICK
ROTATE	TAG NO.	BLOCK	X	Y	Z	XYZ	CYL. R	
MOVE	TAG NO.	BLOCK	X	Y	Z	XYZ	LEAVE	
MIRROR	PLANE							
CYL. R	ANGLE							
RES.								
RES.								

Table .1 The menu structure used by the WGM program.

(Continued overleaf)

Menu name	Function Keys							
	F1	F2	F3	F4	F5	F6	F7	F8
VIEW ZOOM FIT WIRES POINTS TAG RADIUS 2D	THETA X-0	PHI Y-0	DEFAULT Z-0	TH,PH				
X-0 Y-0 Z-0 PLANE SURF. RES. RES. RES.	LAYER 1 LAYER 1 LAYER 1 LAYER 1 LAYER 1	LAYER 2 LAYER 2 LAYER 2 LAYER 2 LAYER 2	LAYER 3 LAYER 3 LAYER 3 LAYER 3 LAYER 3	LAYER 4 LAYER 4 LAYER 4 LAYER 4 LAYER 4	LAYER 5 LAYER 5 LAYER 5 LAYER 5 LAYER 5	LAYER 6 LAYER 6 LAYER 6 LAYER 6 LAYER 6	LAYER 7 LAYER 7 LAYER 7 LAYER 7 LAYER 7	LAYER 8 LAYER 8 LAYER 8 LAYER 8 LAYER 8
DEFINE RES. RES. RES. RES. RES. RES. RES.	NAME							
POINT SEGMENT RES. RES. RES. RES. RES. RES.	NUMBER LENGTH	COORD. NUMBER	DIRECT.					

N.b. F9 and F10 call up the last menu and the root menu respectively, except in root menu itself, where F9 and F10 are used for the PLOT and END menus. The word 'RES.' indicates an option reserved for a future addition.

Table 1 (Continued).

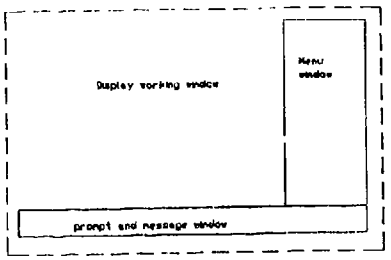

Fig. 1 The three-window display

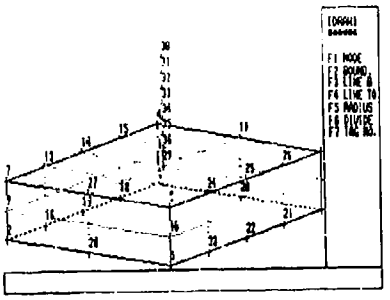

Fig. 2 Typical display (monopole mounted on a box)

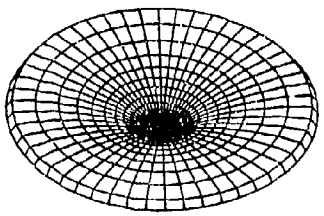

Fig. 3 Vertically-polarised field pattern for object in Fig. 2

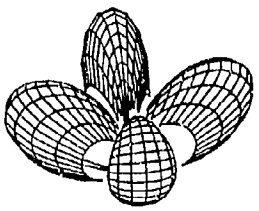

Fig. 4 Cross-polar field pattern

PROGRESS: DEVELOPMENT OF AN INTERACTIVE GRAPHICS PROGRAM FOR EM CODES

J. Peng, J. Choi, and C. A. Balanis
Department of Electrical Engineering
Telecommunications Research Center
Arizona State University
Tempe, AZ 85287-7206

G. C. Barber
Joint Research Program Office
NASA Langley Research Center
Hampton, VA 23665

Abstract

In this paper, progress in developing an interactive graphics program (GEOM) for the numerical electromagnetics computer codes, such as NEC[1] and ESP[2], at Arizona State University is described. By using the interactive graphics program, one can not only save time and effort to create geometry data, but also have better understanding of the EM problem under investigation by visualizing objects on the screen. To validate the usage of the interactive graphics program GEOM, the geometry of a NASA helicopter scale model is generated based on the cross sectional information. Radiation patterns of a monopole mounted on the scaled helicopter model are then calculated using the NEC and ESP codes, and their results are compared to the measured data provided by NASA.

I Introduction

The interactive usage between the electromagnetics computer program and the graphics program provides some advantages to the electromagnetics researchers. When it involves complex geometries such as a helicopter, an accurate computer model of the real object is essential for the valid prediction of the EM characteristics. By using the interactive graphics program, one can not only save time and effort to create accurate geometry data, but also to have better understanding of the EM problem under investigation by displaying objects on the screen. In addition, the availability of a graphics program allows the user to make very easily changes or modifications in the geometry of the structure or position of the source. As part of such an effort, the GEOM[3,4] was developed to be

used interactively between the EM computer codes, such as the NEC and ESP, and the Macintosh Super-3D[5] graphics program. The progress made at the Telecommunications Research Center of Arizona State University can be summarized as follows:

(1) Developed a solid surface generating program based on cross sectional data of complex objects.
(2) Developed and completed a Fortran program (GEOM) to convert the geometry data from Super-3D to the NEC and ESP input format.
(3) Developed a user-friendly EM control command program to specify the excitation, frequency of operation, pattern cut, impedance loading, segment size, wire radius, etc..

The detailed capability of the interactive program GEOM is illustrated in Figure 1.

In the following sections, an entire NASA helicopter scale model is generated based on cross sectional geometry information. Representative radiation patterns of a monopole mounted on the helicopter scale model are then calculated by the NEC and ESP codes which are interactively used with the GEOM. Finally, numerical predictions are compared to measured data obtained at NASA.

II Input Data Generation for the NEC and ESP Codes Using the GEOM

The input data for the NEC and ESP can be created very easily by using the GEOM. To generate the complete input data for the NEC and ESP codes, two sets of input data are necessary. They are the geometry data and the EM control command data. First, the geometry input data for a scaled helicopter model is constructed using the solid surface generating program, as illustrated in Figure 1. The input geometry data required to construct the scaled helicopter model are 13 cross sections for the main body, two wings, two tail wings, the tail cross section, rotor blades simulated by two wires, and a monopole of length 0.1m. Once these cross sectional geometry data are input into the solid surface generating program (see Figure 1), the geometry data for the solid urface scale model of a NASA

helicopter is generated, as shown in Figure 2. Second, EM control data (labeled as 'user input' in Figure 1), which consist of the excitation type, frequency of operation, pattern type, pattern cut, impedance loading, segment size, wire radii of the segment, and so on, need to be specified by the user.

The solid surface geometry data along with the EM control data can now be used as an input of the GEOM main program to generate the input data for either the ESP surface patch model (Figure 2) or the NEC wire-grid model (Figure 3). Note that the wire-grid model for the NEC code is generated automatically in the GEOM main program. For the NASA helicopter scale model shown in Figures 2 and 3, the ESP surface patch model contains 107 surface patches and three wires, and the NEC wire-grid model consists of the total of 853 wires using the segment size of 0.05λ.

III Radiation Patterns of a Monopole Mounted on the NASA Helicopter Scale Model

The radiation patterns of a 0.1m monopole mounted on the NASA helicopter scale model are calculated using the NEC and the ESP codes. The overall dimensions of the scaled helicopter model are illustrated in Figure 2. In both NEC and ESP codes, 0.05λ segment length is used. After the segmentation, the NEC wire-grid model has 853 wire current modes, and the ESP codes has 1,062 plate current modes and 22 wire current modes.

In Figures 4-6 the radiation patterns (normalized gain in dB) of a 0.1m monopole antenna placed at the MP1 location (36.5 inches aft of nose) of the helicopter body are presented as a function of aspect angles. Both the NEC (dashed line) and the ESP codes (solid line) are used interactively with the GEOM, and their results are compared to measured data provided by NASA (dotted curve) in the three major pattern planes; i.e., roll, pitch, and yaw planes. For each pattern plane, only the co-polarized patterns are plotted. Note that each data set is normalized to its own maximum.

There exists reasonably good agreement between the calculated and measured data. However, in the roll and pitch planes

the agreement between the measured data and the NEC calculated data is better than that between measurements and predictions by the ESP code. One can also notice that the symmetry property of the radiation patterns of the ESP code in the roll plane has deteriorated. This is believed to be due to the non-symmetric positioning of the overlap current modes on the two joining patches[6]. Also, numerical efficiency of the NEC is superior to that of the ESP. In general, this statement is true whenever a surface patch model of the ESP code requires many overlap current modes. To obtain the entire patterns using the NEC code, it takes 1,278 CPU seconds on a CRAY X-MP/18se super computer. On the other hand, the ESP code requires 13,000 CPU seconds on the same machine.

IV Conclusions

The interactive graphics program GEOM developed at the Telecommunications Research Center of Arizona State University was used to generate the geometry of a NASA helicopter scale model. By using the GEOM, we not only saved time and effort to generate the complex geometry data but also avoided the error prone direct input process. In order to validate the interactive graphics program GEOM, radiation patterns are calculated using the NEC and ESP codes which were used interactively with the GEOM. Despite of the complexity of a NASA helicopter geometry under investigation, the numerical predictions and measurements are in excellent agreement.

Presently, only a limited number of geometry and EM control commands are incorporated into the GEOM. More general control commands will be included in the code in the near future.

Acknowledgement

This work is supported by the Advanced Helicopter Electromagnetics Industrial Associates Program and NASA Grant NAG-1-1082.

References

[1] J. Burke and A. J. Poggio," Numerical Electromagnetics Code (NEC)-Methods of Moments Part 1, 2, and 3," Naval Ocean Systems Center, San Diego, CA, NOSC TD 116, 1980.

[2] E. H. Newman, "A User's Manual for Electromagnetic Surface Patch Code: ESP Version 4," The Ohio State University, ElectroScience Lab., Rep. 716199-11, Dept. of Electrical Engineering prepared under contract No. NSG-1498 for NASA, Langley Research Center, Hampton, VA. Aug. 1988.

[3] C. A. Balanis et al., " Advanced Electromagnetics for Helicopter Applications," Arizona State University, Telecommunications Research Center, Annual Report prepared under NASA research grant NAG-1-1082 and Advanced Helicopter Electromagnetics Industrial Associates Program, Oct. 1990.

[4] J. Peng, J. Choi, and C. A. Balanis, " Automation of the Geometry Data for the NEC and the ESP Using the Super-3D," Proceedings of 6th Annual Review of Progress in Applied Computational Electromagnetics, pp. 33-38, March 1990.

[5] Super 3D, copy righted by Silicon Beach Software, 9770 Carroll Center, Suite J, San Diego, CA 92126.

[6] C. A. Balanis et al., "Advanced Helicopter Electromagnetics Associates Program," Quarterly Progress Report, Arizona State University, Telecommunications Research Center, June 1990.

Figures

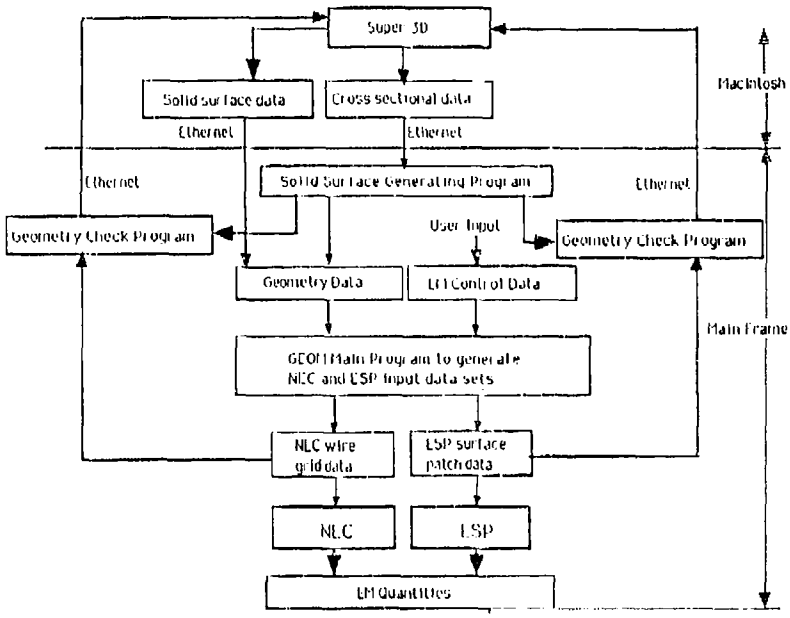

Figure 1 Block diagram for the interactive usage of GEOM and the EM codes.

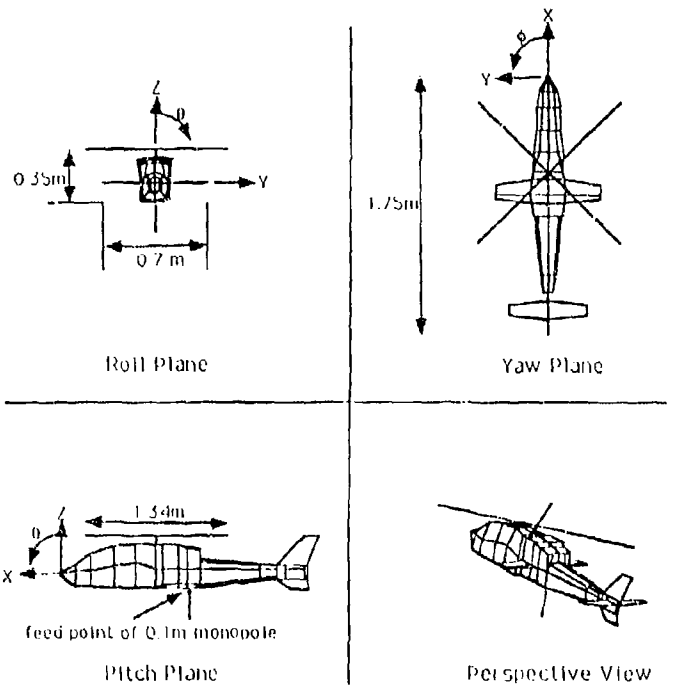

Figure 2 Solid surface model of the NASA helicopter based on the cross sectional data.

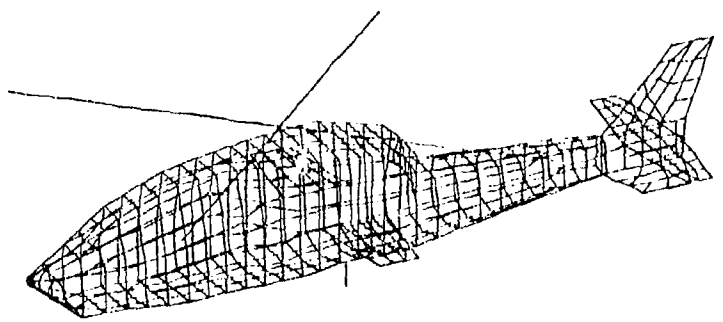

Figure 3 NEC wire-grid model of the NASA helicopter generated by the GEOM.

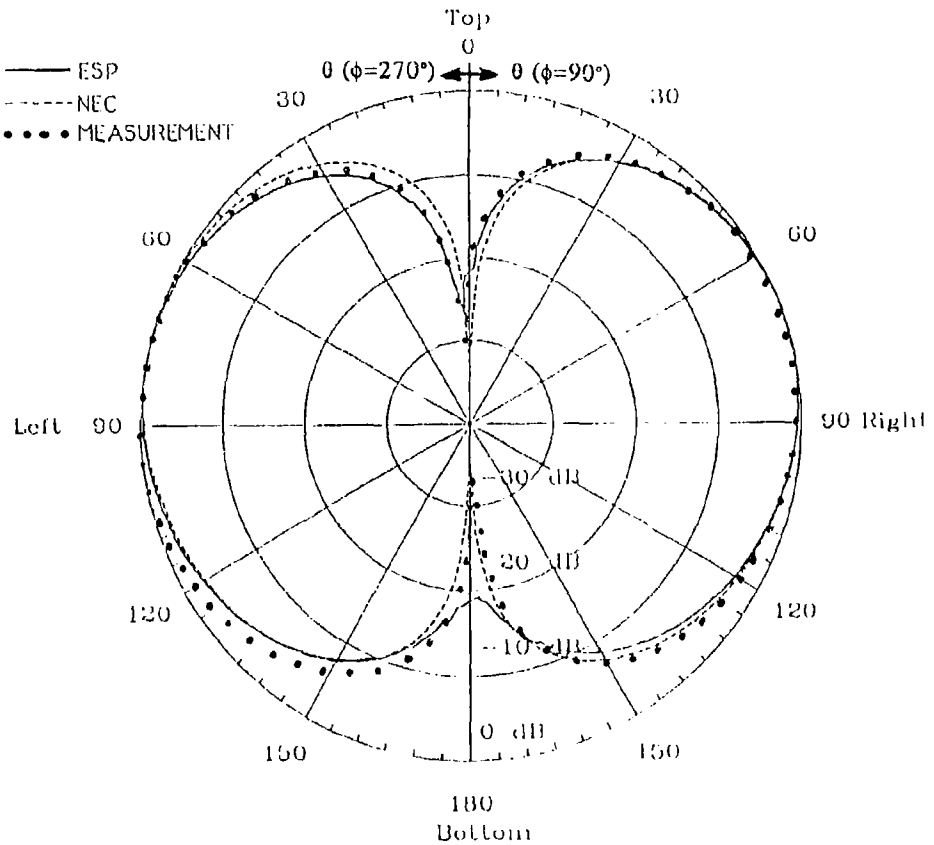

Figure 4 Radiation patterns of 0.1m monopole antenna mounted on the NASA helicopter scale model at a frequency of 200 MHz. Roll plane (YZ-plane), co-polarization.

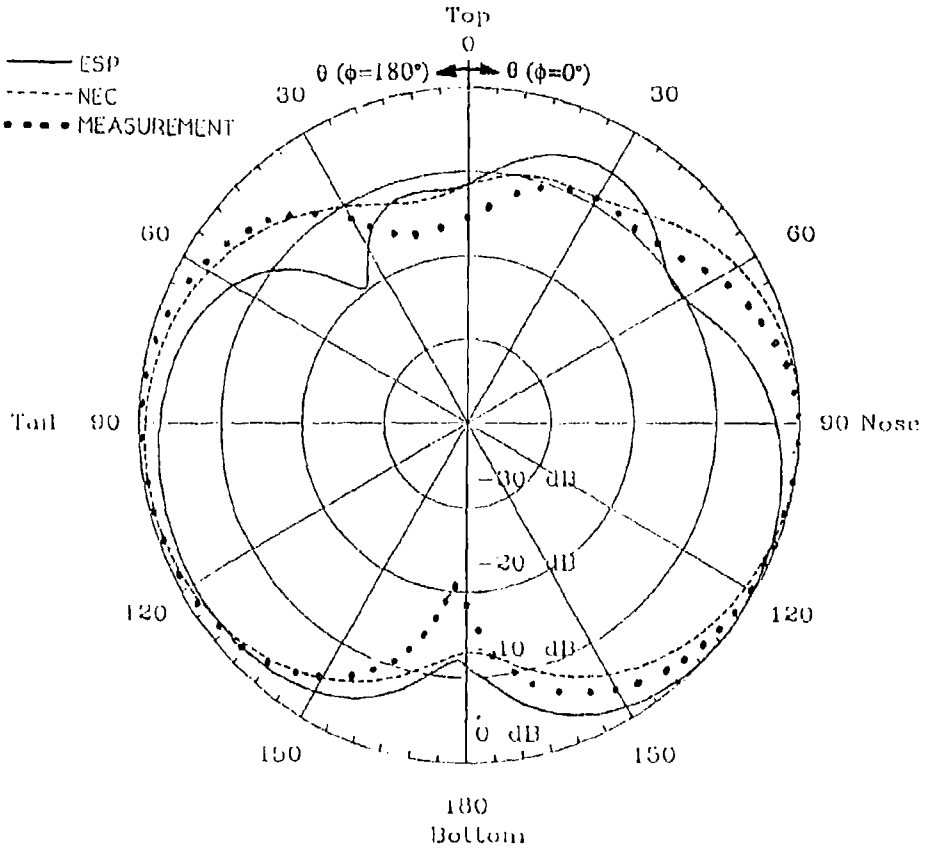

Figure 5 Radiation patterns of 0.1m monopole antenna mounted on the NASA helicopter scale model at a frequency of 200 MHz. Pitch plane (XZ-plane) co-polarization.

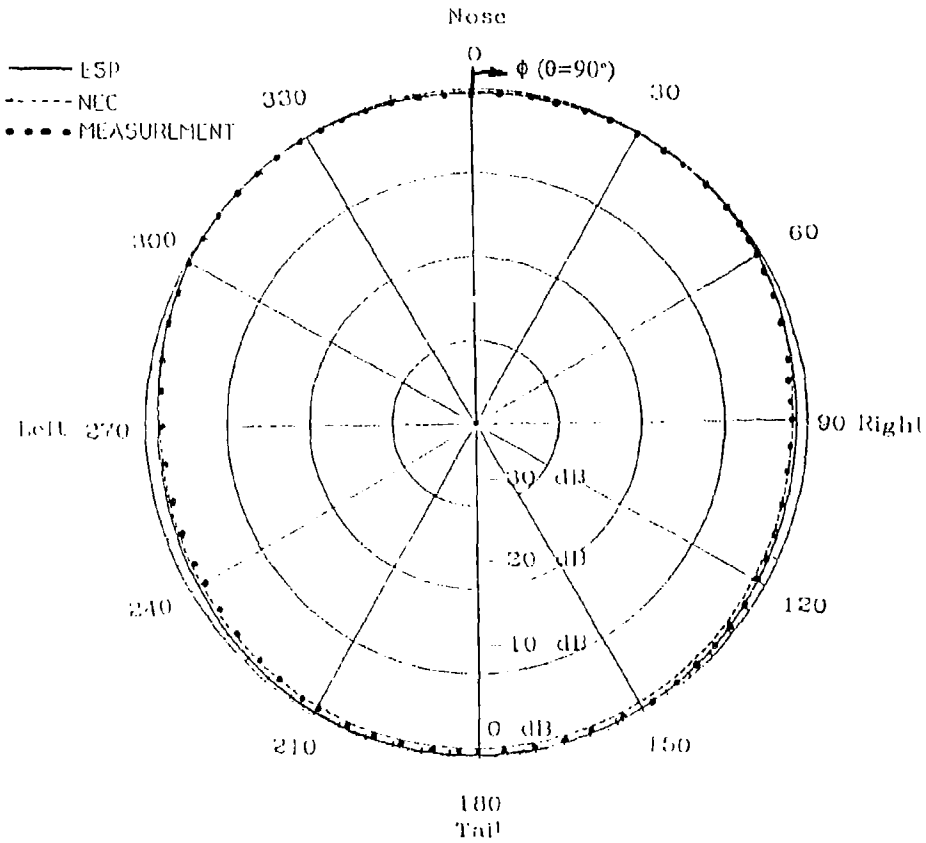

Figure 6 Radiation patterns of 0.1m monopole antenna mounted on the NASA helicopter scale model at a frequency of 200 MHz. Yaw plane (XY-plane) co-polarization.

R. Fisher - Science & Engineering Associates
6100 Uptown Blvd. NE, Suite 700
Albuquerque, NM 87110

E. L. Coffey - Advanced Electromagnetics
5617 Palomino Dr. NW
Albuquerque, NM 87120

Lt. T. Timmerman - Phillips Laboratory/AWE
Kirtland AFB, NM 87117-6008

Overview/Status of GEMCOP

The primary objectives of the GEMCOP program are:

- Develop a user friendly, menu driven control program for GEMACS/GAUGE
- Minimize the requirements for user's knowledge of GEMACS/GAUGE
- Provide pre/post processing support for GEMACS/GAUGE
- Support script file development for execution of user applications
- Simplify user development of complex topologies

The original development of GEMCOP was intended for the PC/DOS environment. Due to increasing demands placed on computer memory by programs such as GEMACS and GAUGE, as well as the graphical nature of the GEMCOP program, the development has been shifted from DOS to OS/2. Since OS/2 operates with a linear address space, code and problems requiring more than the old DOS 640 KB limit can be supported. However, this migration to the OS/2 environment place new requirements on the hardware necessary to run GEMCOP. An 80286, 80386, 80486 processor is required, or a workstation capable of supporting OS/2. The computer must have at least 2.5 MB of RAM with 4 MB recommended. In addition, the computer will need a hard disk of from 40 to 60 MB with 100 MB or more recommended.

The development of GEMCOP is continuing on schedule after the decision to make it an OS/2 application. The program is due for completion and checkout by May, 1991 and should be released sometime around mid-summer. Sample OS/2 Presentation Manager screens for the program are illustrated in Figures 1 and 2. The first figure is the main GEMCOP menu, the second is the GEMACS input data file development screen. More information on the types of GEMCOP menus and their content can be found in the previous paper on GEMCOP presented at the 6th ACES conference (**Development of GEMCOP, an Expert System for GEMACS and GAUGE**).

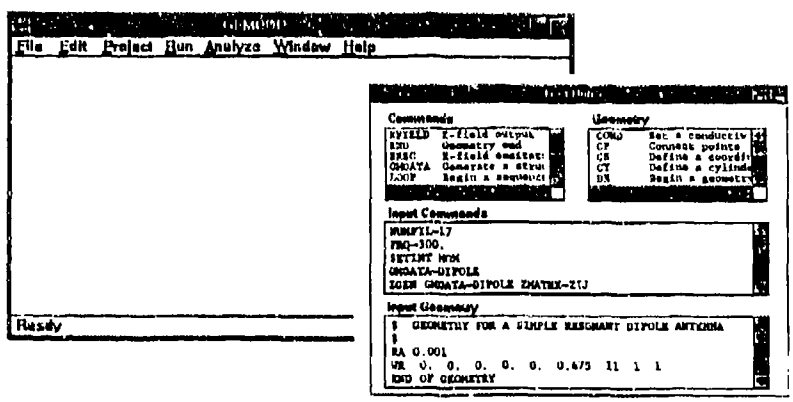

Figure 1. GEMCOP Main Menu

Figure 2. GEMACS Input File Development Screen

IMPLEMENTATION OF THE NEC - BASIC SCATTERING CODE ON A PC

Ronald J. Marhefka
The Ohio State University
ElectroScience Laboratory
1320 Kinnear Road
Columbus, Ohio 43212-1191
Phone: (614)292-5752

Abstract

It is desirable to have general purpose user oriented codes run on as many machines and compilers as possible. Users prefer to change as little as possible in the codes to get them to run on their computers. This is especially desirable for large codes like the NEC-BSC. Changes made to the NEC-BSC to make it more easily implemented on PC type computers will be presented. The talk will center primarily on IBM compatible computers and several compilers, though other types and sizes of machines will be discussed. Benchmarks for the code on large and small computers will be compared.

Recent technical enhancements to the code will also be outlined. They include third order plate interactions and double diffraction along with a dielectric curved surface capability (without surface waves). These changes will be available in version 3.2 of the NEC-BSC.

I Introduction

A new version of the NEC-BSC has been slightly modified to take into consideration implementation on personal computers (PC). Modern PC hardware and software has progressed in recent years to the point that they can easy be used for running electromagnetic codes. It is therefore, the premise of this discussion that the full version of the NEC-BSC is to be implemented on the PC. No special version for the PC is attempted. The code is Fortran 77 and only modifications to make it easier to run on the PC without causing difficulties on bigger machines are made.

First a brief overview of the capabilities of the code is presented. Specific changes that took place for PC operation is detailed next. The hardware and software used

in the benchmarks are then presented. The benchmarks first compare various VAX compiler options, then two IBM types and three VAX machines are compared.

II Background

The Numerical Electromagnetic Code - Basic Scattering Code (NEC-BSC) is a user-oriented computer code for the electromagnetic analysis of the radiation from antennas in the presence of complex structures at high frequency. For many practical sized structures this corresponds to UHF and above. The code can be used to predict near or far zone patterns of antennas in the presence of scattering structures, to provide the EMC or coupling between antennas in a complex environment, and to determine potential radiation hazards. Simulation of the scattering structures is accomplished by using combinations of perfectly conducting multiple flat plates, finite elliptic cylinders, composite cone frustums, and finite composite ellipsoids. The code, also, has a limited finite thin dielectric capability for both plates and curved surfaces. The analysis is based on uniform asymptotic techniques formulated in terms of the Uniform Geometrical Theory of Diffraction (UTD) [1,2]. This version of the NEC-BSC is an update to version 2 [3] and the more recent version 3.1 [4].

A summary of the capabilities of Version 3.2 [5] is listed here:

- User oriented command word based input structure.
- Pattern calculations.
  - Near zone source fixed or moving.
  - Far zone observer.
  - Near zone observer.
- Single or multiple frequencies.
- Antenna to antenna spacial coupling calculations.
  - Near zone receiver fixed or moving.
- Efficient representation of antennas.
  - Infinitesimal Green's function representation.
  - Six built in antenna types.
  - Interpolation of table look up data.
  - Method of Moments code or Reflector Code interface.

- Multiple sided flat plates.
  - Separated or joined.
  - Infinite ground plane.
  - Limited dielectric plate capability (no surface waves).
- Multiple curved surfaces.
  - Finite elliptic cylinders.
  - Multiple sectioned elliptic cone frustums.
  - Composite ellipsoids.
  - Limited dielectric curved surface capability (no surface waves).
- UTD multiple interactions included.
  - Second order plate terms including double diffraction. (restricted to PEC).
  - Third order plate terms:
    - triple reflections
    - reflection - reflection - diffraction
    - reflection - diffraction - reflection
    - diffraction - reflection - reflection
  - First order curved surface terms only (creeping waves for PEC cylinder only).
  - Presently no plate - cylinder interactions.
- Individual control of every UTD term.
- GKS graphical codes for geometry and patterns.

III Changes made for PC

The premise as mentioned above is that PCs have gotten large enough to handle essentially the same code as bigger machines. The changes needed are, therefore, rather minimal. The major task has been to reduce the size of the larger subroutines. Many PC compilers such as Microsoft and NDP have a limit on the number of lines that can be compiled at one time. This limit is proportional to the amount of memory in the computer. The PCs used have 4MB of memory. The practical size for compilation of each file seems to be around 3000 lines. Several subroutines, that

were originally designed to directly share information by using entry points, needed to be changed into individual subroutines. This required using more common blocks to transport the shared information.

Next, the code needs to be broken up into many different files. Usually when sending the code out, we put all our codes into one file. This makes documentation easier, since all that needs to be done to the codes is Fortran, Link, and Run a single file. When breaking the code up into files, it is necessary to decide whether to do this simply alphabetically or group files by functions. Putting subroutines together by functions seems better, at least for the code developer, since changes to the code usually will be confined to fewer files. For the NEC-BSC this turns out, presently to be 16 different files of various sizes.

Fortran specific changes seemed to have been unnecessary, since the code has been written in standard Fortran 77 as much as can be determined. Of course there are always variations between compilers, but the PC compilers used seemed to be striving for as much compatibility with the standard options of the VAXes on which the code was developed. One extended feature of the VAX that is used is tabs in the beginning of lines. These can easily be removed and usually are depending on distribution format. The new version 2.0 NDP compiler seems to be 100 percent compatible with this feature, where as the previous version would not work in all cases.

The other change made centered around associating the logical unit numbers with the input and output files. In previous versions of the NEC-BSC, the assignments are left up to the user. For example, on a VAX the ASSIGN or DEFINE commands could be used. In the new version, OPEN statements are used in the code. The input file name is obtained after the start of the code.

On output for the PC, it is assumed that the operating system does not support version numbers for files. If the user is requesting more than one output, than the code will inquire for a new name for an output file when one already exists on the disk. This can be changed by the user if a different naming convention is desired.

IV Hardware Considerations

The suitability of PCs for many engineering applications has greatly progressed. It is not necessary to restrict the code to accomodate the hardware limitations. It is assumed for an IBM compatible that a 386 type machine or better will be give best results.

The primary machine used in this study is a 386SX, 16MHz, 4MB IBM type computer with 80387SX math co-processor and 60MB hard disk. In addition, a

full 386, 20MHz, 4MB IBM compatible with 80387 co-processor is also used in the benchmarks. The VAX computers used for comparisons are a VAXstation 2000, VAXstation 3100 M30, and a VAX 8550. The workstations had 8MB of memory and are diskless being clustered into the VAX 8550. The working set size for the VAXes are set at 1000.

The size requirements of the NEC-BSC version 3.2 on the disk are 668KB for the Fortran source code. The NDP compiled object modules took 984KB of space and the execute module took 673KB. The memory requirements for running the code are 983KB.

V Software Considerations

Several PC compilers for IBM's have been investigated. It is assumed that DOS 4.0 is the operating system for the PCs. The Microsoft compiler appears to be very good, however, it presently does not allow the code to go beyond the 640KB range. In order to accomodate the size of the NEC-BSC V3.2, it would be necessary to use the OS2 operating system. It would also have been possible to reduce the size of the code by removing subroutines or reducing the array sizes, however, this was not done.

The Lahey Fortran 77 Version 2.0 compiler with AI extended memory operating environment was tried. This was successfully used on Version 3.1 by someone using DOS 3. It has the advantage that the compiler is very fast and does not require that the code be broken up into small files sizes. Unfortunately, the version of Lahey tried would not work on the machines used here. The extender would hang up all the machines tried by us. As near as can be determined, this is due to a incompatibility with DOS 4.0. New versions of DOS or the Lahey product may remove this problem.

The compiler used for the benchmarks here is the NDP compiler and PHAR LAP 386 ASM 2.2 linker and extender. Two versions of the NDP Fortran compiler has been tried. First, Version 1.4E/5 was used and then updated to Version 2.0.8. There was no difference in time or accuracy detected between the two versions. The newer version, however, is much easier to use since it is more compatible with the VAX's use of tabs. Version 2 is used here in the benchmarks. It should be noted that it takes exactly 1 hour to compile the code on the 386SX. Presumably most of that time is spent in the assembler stage.

One problem arose when Windows 3.0 was installed on the 386SX machine. The new windows environment requires that the HIMEM driver be installed. There presently is a conflict between the memory handlers in NDP and Windows. It is necessary to reboot the machine without the HIMEM driver to use the compiler and

linker. This problem is being addressed by NDP and hopefully will be improved in the future.

Various individuals are working on implementing versions of the NEC-BSC on MACs. Unfortunately, no data is available here. It has been determined that some versions of compilers for MACs (Absoft MacFortran/020) do not initialize variables to zero. The NEC-BSC has been checked using a product called LINT to find undefined variables, however, it did not detect one in the subroutine SOURCP. The variable was defined at some place in the subroutine, but the IF THEN ELSE logic would bypass it in certain cases [6]. This caused rather large errors, however, it has been corrected in this version.

For the VAX computers, various compiler options are compared. They presently are running VMS 5.4 with DECwindows installed on the workstations. The first compiler configuration is suited for the code developer. It has the debug option, no optimization, bounds checks, and all warnings options included. The second and third configuration compares the optimizer versus no optimizer. All other checks and warnings are turned off. In certain past instances, the VAX optimizer appeared to give some trouble. No difficulties are presently being encountered. For comparison, it should be noted that it takes around 4-5 minutes to compile the code on the VAXstation 3100.

VI Benchmarks

Two examples from the NEC-BSC User's Manuals are used in the benchmarking procedure. The first is Example 6 which calculates the pattern of a dipole in the presence of an eight sided box. The second is Example 19 which calculates the pattern of a slot on the wing of a model of a B737 aircraft. In both of these case, a far zone pattern of 361 data points in 1 degree increments is computed. The UTD terms automatically obtained from the **XQ** command are used.

The CPU times are obtained by using the "SEC_100" function for the NDP compiler and "SYS$GETJPI" function for the VAX. The times are converted and presented in minutes. The CPU times are the difference between the samples taken after the input data is read and echoed back to the user and before the fields are output to the disk. The values, therefore, represent only the time it takes to do the EM field calculations and does not included any IO.

In terms of accuracy, all VAXes produce exactly the same results. The PC's produced the same accuracy compared to the VAX over the five digits displayed for all significant results. The exception being the noise level cross polarized results in Example 6, which is normal and expected.

Compiler Options	Example 6	Example 19
No opt, all checks	3.29	2.25
No opt, no checks	1.28	1.09
Opt, no checks	0.94	0.89

Table 1: Table comparing various compiler options using a VAXstation 3100 M30. CPU times are in minutes.

Computer	Example 6	Example 19
PC 386SX	3.26	3.14
VAX 2000	3.10	3.01
PC 386	2.20	2.00
VAX 3100	0.94	0.89
VAX 8550	0.40	0.38

Table 2: Table comparing various computers. The VAXes are run using the optimizer with no checks. CPU times are in minutes.

The first benchmarks for the two examples are run using the VAXstation 3100. Three compiler options are used. First all checks, debug, and no optimization is used. Second all checks and the debug options are turned off with no optimizations. In the last case, all checks and debug options are off but the optimizer is on. The results for the three cases are shown in Table 1. Amazingly the CPU times with the checks on differ by over a factor of 2. The optimizer helps by about another 25%. Of course when first running the code, it is safer to use the bounds checks. For production runs, it would appear clear that these should be turned off and the optimizer used.

For comparison between the various computers, the optimized case with the bounds checks off is used in all cases. The results are shown in Table 2. The VAX 2000 is slightly slower than a VAX 780, this means that the 386SX is running very close to the speed of a VAX 780. The 386SX machine has a 25% slower clock speed than the 386 and has addition overhead due to the 16 bit bus compared to the 32 bit bus. This properly accounts for the indicated time differences. The VAX's times also are accounted for by the published difference in CPU speeds within reasonable bounds.

VII Conclusions

The experience of implementing the NEC-BSC V3.2 on PC is presented. Various hardware and software configurations are discussed. Benchmarks for two examples from the user's manual are used to compare the PCs to VAXes. It appears that PCs can be effectively used to run the full up NEC-BSC.

References

[1] P. H. Pathak, "Techniques for high-frequency problems," in *Antenna Handbook: Theory, Applications, and Design*, (Y. T. Lo and S. W. Lee, eds.), ch. 4, New York: Van Nostrand Reinhold Co. Inc., 1988.

[2] W. D. Burnside and R. J. Marhefka, "Antennas on aircraft, ships, or any large, complex environment," in *Antenna Handbook: Theory, Applications, and Design*, (Y. T. Lo and S. W. Lee, eds.), ch. 20, New York: Van Nostrand Reinhold Co. Inc., 1988.

[3] R. J. Marhefka and W. D. Burnside, "Numerical electromagnetic code - basic scattering code (version 2), Part I: user's manual," Technical Report 712242-14, The Ohio State University ElectroScience Laboratory, Department of Electrical Engineering, Dec. 1982. Prepared under Contract No. N00123-79-C-1469 for Naval Regional Contracting Office.

[4] R. J. Marhefka and J. W. Silvestro, "Near zone - basic scattering code, user's manual with space station applications," Technical Report 716199-13, The Ohio State University ElectroScience Laboratory, Department of Electrical Engineering, March 1989. Prepared under Grant No. NSG 1613 for National Aeronautics and Space Administration.

[5] R. J. Marhefka, "NEC - basic scattering code, user's manual (version 3.2)," Final Report 718422-4, The Ohio State University ElectroScience Laboratory, Department of Electrical Engineering, Dec. 1990. Prepared under Contract No. N60530-85-C-0249 for Naval Weapons Center.

[6] G. J. Burke, "Personal communications," Aug. 1990.

NEC, FERM & GEMACS on the Macintosh

by
Paul E Bussey & Dr. Russell W. Taylor

Introduction, Motivation and Objective

Our objective is to simplify the development of reliable EM models for the three analysis codes, NEC, FERM, and GEMACS by creating a interactive program to analyze these models. Our experience with other data analysis/visualization codes designed to support these three codes has been less than completely successful. McDonnell Douglas Helicopter Company has had problems with IGUANA and GUAGE. The data analysis/visualization code which supports FERM was not available.

Other similar codes do not have the same same objective as ours. They present the geometric representation, but do not easily alert the user of the potential problems with the model. We have endeavored to include features that will make debugging easier. Our verification code indicates situations which can result in incorrect interaction matrix elements, or cause misleading results.

The Macintosh CPUs were chosen because we have developed codes on them for other purposes, an excellent development environment is available, and the graphical user interface is easier for new users to learn. The alternative platforms for most of our projects are MicroVAX IIs. The newer Macs are much less expensive (especially for large amounts of memory), as well as faster than the MicroVAXs, and they provide greater precision for floating point calculations because they use the IEEE standard 80 bits for real and complex calculations.

Code Installation on the Macintosh

Installation of the three analysis codes on the Macintosh is planned, but this task is not yet complete. NEC installed very easily with essentially no modifications, but GEMACS and FERM both contain code that does correctly execute on the Mac. Further information will be available at the conference regarding these installation problems. Our approach to generating the input data for our verification code is to first use the input data interpretation part of the analysis code without modification.

We have slightly modified the analysis codes so that a file is automatically written containing the data we need as input. Reproducing the data interpretation portions of the analysis codes has not been attempted; we believe this approach is less prone to errors.

Benchmarks

The benchmark results will be presented at the Conference.

"Good Practice" Violations Tests

Calculating the interaction matrix requires several integrations to be performed involving the Green's function (Equations 88 & 92 of NEC manual, Vol. 1). Since there is no closed-form solution for these integrations, several series expansions are used (the number of terms is determined by the thin versus extended-thin wire approximations). These integrals are expanded in terms of two variables, a and ρ, where a is the radius of the source segment and ρ is the radial distance to the observation segment. The expansion in terms of ρ is used only for the self-interaction term, while the expansion in a is used for all other interactions. The expansion in ρ was developed for the special case when the observation point falls inside the "cylinder" of the source segment, the expansion in a is not valid in this case; however, this expansion is only used to compute the self-interaction terms. Unfortunately, it is possible to build models in which observation points fall within the volume of other segments. Then, during the calculation of the interaction terms, the wrong expansion is used to determine the interaction, thus producing erroneous results. We have decided to divide the modelling errors of this type into three groups - adjacent segments which intersect at angles which are too small, unintentional intersections (not in connections table), and duplicate segments (often generated by computer gridding routines).

Acutes: Connected wires (identified in the connection list) were examined, the midpoint of the wire with smallest radius is found, and the distance to the other segment is computed. If the distance is less than or equal to the larger radius, then the angle is too acute and the interaction evaluation will be flawed.

Bad intersections: This test only involves wires not in the connection lists. The shortest distance between the two segments is first calculated under test. If this

distance is less than the sum of the two radii, then an inadvertent intersection is present.

Coincident segments: As this test is conducted on each segment, the connection list of each end point is searched for segments connected at both ends of another segment.

Incompatible radii: For this test, radii of connected segments are compared; radii ratios (a_{large}/a_{small}) greater than five are identified.

Short, fat segments: Here, the length of the segment is compared to its radius; if this ratio is less than eight for the thin wire kernel, or two for the extended-thin wire kernel, it is brought to the attention of the user.

Bad sources: Segments are identified that are both connected to a plate and excited by a source.

Other tests are also performed which are not necessarily problems, but can indicate that the data is not being interpreted as intended by the user.

Opens: Checks connection lists for both ends. If a connection list for either end is empty, then the segment is added to the opens list.

Long segments: Here, the length of each wire is calculated and compared to $\lambda/10$ of the highest frequency. Any wires longer than this will be highlighted.

How Visualization/Analysis Code Works

At this time, the code MacVerify has been developed to test wire frame models for GEMACS and NEC. In the future, it will be expanded to test surface patch models, and optics/diffraction models. The code is a typical Macintosh application; it is window based, and event driven. We have attempted to give the user as much freedom as possible without making the interface too complicated.

After running the model through the input interpretation stage of the desired

analysis code, the resulting test file can be examined using MacVerify.

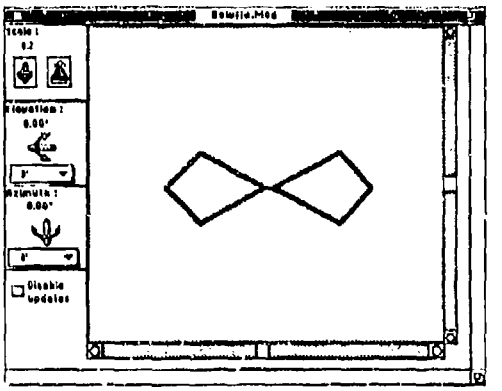

Figure 1. Model display window

After reading in the selected model, a model display window is opened, as shown in Figure 1. The information and controls on the left side of the window allow the user to change the scale and the viewing angle of the model. The scale is adjusted by clicking the mouse in either of the arrow buttons; the arrow coming out (Zoom In) causes the scale to increase, while the arrow going in (Zoom Out) causes the scale to decrease. The amount of change can be regulated with the use of modifier keys as shown in Table I. The elevation and azimuth controls work in a similar fashion. By pressing on the desired side of the "axis", the model will rotate in that direction. Again, Table I shows how the amount of change can be regulated with the use of the modifier keys. In addition to the rotator controls, we have provided pop-up menus which can be used to quickly set the view to one of the predefined angles (see Figure 2). In its default condition, the model will be redrawn each time one of the controls is activated; however, for larger, more involved models, this activity can be quite time consuming. In order to bypass this problem, we have added a checkbox which will disable the redrawing of the model so that specific scales or viewing angles

Table I. Model display viewing control options

	nominal	with modifier keys				
Function		⌘	*shift*	*option*	⌘*shift*	⌘*option*
Zoom In	200%	150%	125%	110%	105%	175%
Zoom Out	50%	$66\frac{2}{3}$%	80%	90%	95%	57%
Elevation & Azimuth	1°	15°	5°	10°	0.1°	0.01°

can be set. The model will be redrawn according to the final settings when the box is unchecked. The model is shown to the right of the display controls. The scroll bars on the model display allow the user to pan across the model.

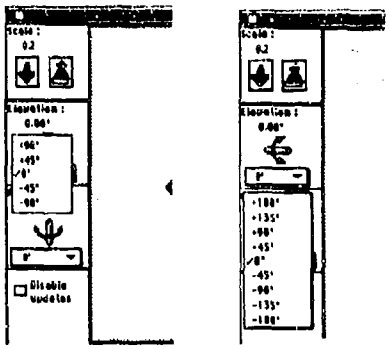

Figure 2. Preset rotation angle pop-up menus

In order to check the model against the various modelling practices, the user must activate the diagnostics window by selecting the **Diagnostics window** option in the **Diagnostics** menu, or by pressing the key combination ⌘/. The diagnostics window, shown in Figure 3, currently has selections for eight common modelling errors found in wire models. Since performing these tests can be quite time consuming, the default condition is set for all of the tests to be off. Any combination of the tests can be selected by checking the appropriate boxes; the tests are then performed when the mouse is clicked in the **Apply** button, or when the Return or Enter keys are pressed. Each test has an associated color which can be changed by double-clicking the mouse inside the colored box. Any wire segments which violate a particular modelling rule will be drawn in the corresponding color. If a segment violates more than one rule, it will be drawn in the color of the last rule tested (top to bottom in the diagnostics window).

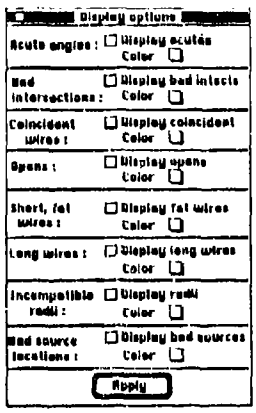

Figure 3. Diagnostics window

If the user wishes to change the model related colors, he may do so via the model display dialog shown in Figure 4. This dialog is accessible through the **Edit** menu as the **Preferences** selection. Colors can be selected for the basic model, the background, "connected" wires, and the buried wires. The colors are changed by double-clicking with the mouse in the desired color square. The standard color-picker dialog will appear and the user is free to choose any available color.

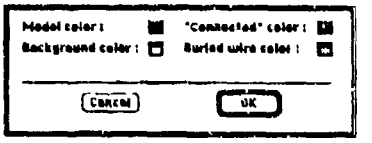

Figure 4. Model display dialog

The model statistics window is activated by selecting the **Model stats** option in the **Diagnostics** menu, or by pressing **⌘S**. As shown in Figure 5, this window lists the various statistics relevant to the model, and the results of any tests performed on the model. If a certain test has not yet been performed, then "**???**" appears as the error count, and the total error count reflects only those tests which have been performed.

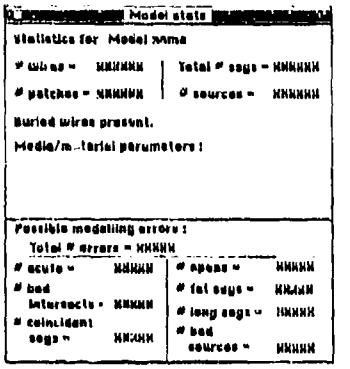

Figure 5. Model statistics window

Detailed information about individual wire segments is available through the wire data dialog (Figure 6). To obtain this information, a wire segment must first be selected; wires are selected by clicking on them with the mouse in the model display. The selected wire will then be highlighted, after which the dialog displaying the wire data can be obtained by selecting **Show wire data** from the **Diagnostics** menu, or by pressing **⌘D**. The wire data includes such information as the end points, radius, loading, sources, length (in meters and shortest wavelength), etc... The user must click in the OK box, and press Return (or Enter) to continue.

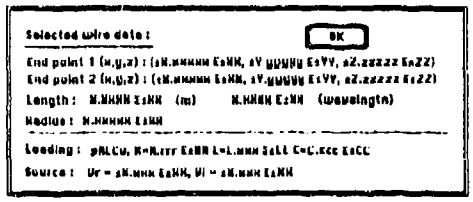

Figure 6. Wire data dialog

To show all segments connected to a selected segment, the desired segment is selected as previously described and any connected segments are highlighted by selecting **Show connections** from the **Diagnostics** menu, or by pressing **⌘H**. The highlighted connections are cleared by clicking elsewhere in the model display area, or by pressing **Apply** in the display options dialog.

In order to facilitate model comparisons, multiple models can be read in and displayed. Depending on the available memory, up to nine models can be read in at one time. As each file is read in, the file name is added as a new item to the windows menu. The display window for the last model read in becomes the active window, and the last active model window is deactivated. Only one model display window can be active at a time. Other windows can be activated by clicking the mouse in each window, by selecting the file name from the **Windows** menu, or by pressing the **⌘#** key combination with the number as shown in the **Windows** menu.

Several means of generating graphical output have been incorporated into MacVerify. Printing can be performed interactively or files can be generated with HPGL commands, or in the PICT format. Printing is accomplished using standard Macintosh methods and is selected via the **Print** option in the **Files** menu. HPGL files are generated by selecting the **Save HPGL** option in this menu. This option creates a text file of HPGL commands to draw the current model in the current view. These files can be ported to other systems for output to HPGL compatible devices. Choosing the **Save PICT** option in the **Files** menu allows a PICT file of the current model display to be created. This format can be read in by many Macintosh applications for inclusion to reports or other documents.

Future enhancements

The code will be enhanced to interpret closed wire frames as surfaces. These surfaces will be shaded to indicate their normal direction for easier interpretation. Verification will be expanded to include tests for:

- wires that are too fine
- wires too close together
- wires too close to a plate or ground plane
- plates too close together
- plates with too large an aspect ratio
- duplicate plates
- plate surfaces that are not closed

A FERM interface, capable of providing error checking, will also be created. Additionally, capability for rendering GTD models will be added.

SESSION 2 – "CAEME SPECIAL SESSION ON COMPUTER APPLICATIONS IN ELECTROMAGNETIC EDUCATION"

Moderator: Magdy Iskander

"THE NSF/IEEE CAEME CENTER ACTIVITIES: PROGRESS REPORT, SOFTWARE PROJECTS, AND FUTURE FOCUS"

Magdy F. Iskander
Electrical Engineering Department
University of Utah
Salt Lake City, Utah 84112

The NSF/IEEE Center for Computer Applications in Electromagnetics Education (CAEME) was established to stimulate, accelerate, and lead efforts in utilization of computers and software tools to boost electromagnetics education. The Center provides seed funds for development of educational software, publishes books of developed software and a catalog of available packages, sponsors workshops, and organizes special sessions in conferences, and provides an effective mechanism for distribution. Thus far, the Center has funded a wide variety of software development projects in all areas of educational electromagnetics, including fundamentals and visualization tools, transmission lines, antennas, numerical techniques, waveguides, and other special topics in EM interactions.

In this paper, the Center's activities will be reviewed and examples of developed EM educational software and videos will be demonstrated. The Center's plans for becoming self-supporting will be reviewed.and curriculum needs and future funding opportunities will be discussed.

This project is funded by the Division of Science, Engineering, and Mathematics Education, National Science Foundation Grant No. USE-9048469. The Center is managed by the Executive Office of IEEE on behalf of the Antennas and Propagation Society. Other participating societies and participating companies include the IEEE Microwave Theory and Techniques Society, the Applied Computational EM Society, Hewlett Packard, Motorola, and EEsof.

Simulation of Electromagnetic Phenomena Using a Finite Difference-Time Domain Technique

K. Li, M. A. Tassoudji, R. T. Shin, and J. A. Kong

Department of Electrical Engineering and Computer Science
and Research Laboratory of Electronics
Massachusetts Institute of Technology
Cambridge, MA 02139

Abstract

A finite difference-time domain (FD-TD) code for Maxwell's equations was developed and implemented on an IBM 386 personal computer and used to simulate and examine various electromagnetic phennomena. The FD-TD technique has potential to become a very useful tool for students who are learning electromagnetics. This technique is especially useful in visualizing electromagnetic phenomena, since fields are calculated everywhere within the computational domain in time. The FD-TD code was implemented for two-dimensional geometries using rectangular grids in conjunction with a second-order absorbing boundary condition. Both E and H-field polarizations were analyzed. Scatterers consisting of dielectric, magnetic and conducting materials were modeled and plane wave and line current sources were implemented. The code was used to generate color animation of various electromagnetic phenomena on a personal computer: leading edge, trailing edge, and slit diffraction, creeping waves, and cavity mode excitation. Through the visualization of electromagnetic fields, the FD-TD technique can be used effectively as an educational tool for students learning electromagnetic wave theory.

1 Introduction

Currently, tools which students can use to aid them in understanding and visualizing electromagnetic phenomena are difficult to find. In an attempt to rectify this problem, we applied the finite difference-time domain (FD-TD) technique to Maxwell's equations in order to examine various electromagnetic phenomena [1-6]. This particular method is especially helpful in visualizing electromagnetic phenomena, since electric and magnetic fields are calculated everywhere within a computational domain in time. Thus, it is possible to observe how electromagnetic fields propagate through space as a function of time. By allowing students to visualize various electromagnetic phenomena, they can develop some intuition regarding electromagnetics.

The finite difference-time domain technique was applied in the following manner. Maxwell's equations in differential form are approximated using centered differences

in space and time. The locations at which electric and magnetic fields are calculated are positioned on some sort of grid. Typically, the grid is either a rectangular [1] or triangular mesh [3]. The scatterer is discretized on the grid. To begin the FD-TD simulation, all the fields within the computational domain are initially set to zero and then the excitation is started. The electric fields are calculated in terms of the electric and magnetic fields of the previous time step. Next, the magnetic fields are calculated in a similar manner. Boundary conditions are enforced at the outer boundary of the computational domain and at all dielectric and conducting interfaces. At the outer boundary a second-order absorbing boundary condition is utilized in order to simulate unbounded space beyond the computational domain [7]. The tangential electric fields are set to zero at the conducting surfaces, and the tangential electric and magnetic fields are kept continuous at the dielectric/magnetic boundaries. These steps are essentially repeated until steady state is reached for a sinusoidal excitation, or until transient scattered fields have propagated out of the computational domain for a Gaussian pulse excitation.

In order to keep the program simple, only two-dimensional problems were examined using a uniform rectangular grid. Despite the fact that only two-dimensional geometries are considered, valuable insight can be gained through the observation of FD-TD simulations of electromagnetic phenomena. Also, in order to allow wide distribution of this program, the program was written for IBM 386 personal computers. Both electric and magnetic field polarizations were implemented and examined. Scatterers can have arbitrary geometries of finite size which consist of perfect conductors, dielectrics with finite conductivity, and magnetic materials with finite magnetic conductivity. The excitation sources include a sinusoidal plane wave, a Gaussian pulse plane wave, and a line current source. It is possible to store any field component at a point, a line, or in the entire plane. When the field values over an entire plane are stored, the fields can be displayed using color plots. By displaying the fields for successive time steps in rapid succession, the propagation of the fields can be animated.

2 Finite Difference-Time Domain Technique

2.1 Maxwell's Equations on Rectangular Grids

In implementing the finite difference-time domain technique, Maxwell's equations must be discretized in space and time. In this case, Yee's lattice, which is a rectangular grid, is utilized because of the grid's simplicity [1]. Maxwell's equations in vector differential form in a dielectric and magnetic material are

$$\nabla \times \vec{E} = -\frac{\partial \vec{B}}{\partial t} - \sigma_m \vec{H} \tag{1}$$

$$\nabla \times \vec{H} = \frac{\partial \vec{D}}{\partial t} + \sigma \vec{E} \tag{2}$$

$$\vec{B} = \mu \vec{H} = \mu_r \mu_0 \vec{H} \tag{3}$$

$$\vec{D} = \epsilon \vec{E} = \epsilon_r \epsilon_0 \vec{E} \tag{4}$$

where σ and σ_m are electric and magnetic conductivities, respectively.

For two-dimensional problems, which are assumed to be uniform and infinite in the $\hat{y}$ direction, all the partial derivatives with respect to y are equal to zero. Maxwell's equations in arbitrary homogeneous, isotropic media, for two-dimensional problems in a rectangular coordinate system, decouple into the H-field polarization,

$$\mu_r \mu_0 \frac{\partial H_y}{\partial t} = \frac{\partial E_x}{\partial x} - \frac{\partial E_z}{\partial z} - \sigma_m H_y \tag{5}$$

$$\epsilon_r \epsilon_0 \frac{\partial E_x}{\partial t} = -\frac{\partial H_y}{\partial z} - \sigma E_x \tag{6}$$

$$\epsilon_r \epsilon_0 \frac{\partial E_z}{\partial t} = \frac{\partial H_y}{\partial x} - \sigma E_z \tag{7}$$

and the E-field polarization which has dual equations [See Section 2.3].

The following notation for any function of time and space will be used in the finite difference equations.

$$f(i\Delta x, k\Delta z, n\Delta t) = f^n(i,k) \tag{8}$$

The partial derivatives in space and time, within Maxwell's equations, are approximated using center differences.

$$\frac{\partial f(\xi)}{\partial \xi} \approx \frac{f(\xi + \Delta\xi/2) - f(\xi - \Delta\xi/2)}{\Delta\xi} \tag{9}$$

Thus, the electric and magnetic field components are interlaced in time, and are calculated in a leap frog manner (i.e. first the electric fields are calculated, then the magnetic fields are calculated, and repeat). The electric and magnetic field components are interlaced spatially a half grid cell apart.

Only the H-field polarization will be treated explicitly because the E-field polarization can be treated very easily through the use of duality.

2.2 Finite Difference Equations for the H-Field Polarization

2.2.1 Treatment of Free Space

For the H-field polarization, the finite difference equations in free space, where $\epsilon_r = \mu_r = 1$ and $\sigma = \sigma_m = 0$ are

$$H_y^{n+\frac{1}{2}}(i+\tfrac{1}{2}, k+\tfrac{1}{2}) = H_y^{n-\frac{1}{2}}(i+\tfrac{1}{2}, k+\tfrac{1}{2})$$

$$+\frac{1}{\eta_0}\frac{\Delta\tau}{\Delta x}\left[E_z^n(i+1,k+\tfrac{1}{2})-E_z^n(i,k+\tfrac{1}{2})\right]$$
$$-\frac{1}{\eta_0}\frac{\Delta\tau}{\Delta z}\left[E_x^n(i+\tfrac{1}{2},k+1)-E_x^n(i+\tfrac{1}{2},k)\right] \quad (10)$$

$$E_x^{n+1}(i+\tfrac{1}{2},k) = E_x^n(i+\tfrac{1}{2},k) \quad (11)$$
$$-\eta_0\frac{\Delta\tau}{\Delta z}\left[H_y^{n+\frac{1}{2}}(i+\tfrac{1}{2},k+\tfrac{1}{2})-H_y^{n+\frac{1}{2}}(i+\tfrac{1}{2},k-\tfrac{1}{2})\right]$$

$$E_z^{n+1}(i,k+\tfrac{1}{2}) = E_z^n(i,k+\tfrac{1}{2}) \quad (12)$$
$$+\eta_0\frac{\Delta\tau}{\Delta x}\left[H_y^{n+\frac{1}{2}}(i+\tfrac{1}{2},k+\tfrac{1}{2})-H_y^{n+\frac{1}{2}}(i-\tfrac{1}{2},k+\tfrac{1}{2})\right]$$

where

$$\eta_0=\sqrt{\frac{\mu_0}{\epsilon_0}} \quad (13)$$

$$\tau = ct = \frac{t}{\sqrt{\mu_0\epsilon_0}} \quad (14)$$

The locations of the field components on a unit cell of the rectangular grid for the H-field polarization are shown in Figure 1.

2.2.2 Treatment of Dielectric and Magnetic Material

The finite difference equations in a dielectric and magnetic material are

$$H_y^{n+\frac{1}{2}}(i+\tfrac{1}{2},k+\tfrac{1}{2}) = H_y^{n-\frac{1}{2}}(i+\tfrac{1}{2},k+\tfrac{1}{2})\left(\frac{2\mu_r-\sigma_m\Delta\tau/\eta_0}{2\mu_r+\sigma_m\Delta\tau/\eta_0}\right)$$
$$+\frac{1}{\eta_0}\left[\frac{2\Delta\tau}{\Delta(2\mu_r+\sigma_m\Delta\tau/\eta_0)}\right]\left\{\left[E_x^n(i+1,k+\tfrac{1}{2})-E_x^n(i,k+\tfrac{1}{2})\right]\right.$$
$$\left.-\left[E_z^n(i+\tfrac{1}{2},k+1)-E_z^n(i+\tfrac{1}{2},k)\right]\right\} \quad (15)$$

$$E_x^{n+1}(i+\tfrac{1}{2},k) = E_x^n(i+\tfrac{1}{2},k)\left(\frac{2\epsilon_r-\sigma\eta_0\Delta\tau}{2\epsilon_r+\sigma\eta_0\Delta\tau}\right) \quad (16)$$
$$-\eta_0\left[\frac{2\Delta\tau}{\Delta(2\epsilon_r+\sigma\eta_0\Delta\tau)}\right]\left[H_y^{n+\frac{1}{2}}(i+\tfrac{1}{2},k+\tfrac{1}{2})-H_y^{n+\frac{1}{2}}(i+\tfrac{1}{2},k-\tfrac{1}{2})\right]$$

$$E_z^{n+1}(i,k+\tfrac{1}{2}) = E_z^n(i,k+\tfrac{1}{2})\left(\frac{2\epsilon_r-\sigma\eta_0\Delta\tau}{2\epsilon_r+\sigma\eta_0\Delta\tau}\right) \quad (17)$$
$$+\eta_0\left[\frac{2\Delta\tau}{\Delta(2\epsilon_r+\sigma\eta_0\Delta\tau)}\right]\left[H_y^{n+\frac{1}{2}}(i+\tfrac{1}{2},k+\tfrac{1}{2})-H_y^{n+\frac{1}{2}}(i-\tfrac{1}{2},k+\tfrac{1}{2})\right]$$

2.2.3 Treatment of Interfaces Between Two Media

At the interface between two dielectric and magnetic materials, the finite difference equation for E_x must be treated carefully [See Figure 2]. Using the integral form of Equation (2) to calculate E_x, yields

$$\begin{aligned}\oint_C \vec{H}\cdot d\vec{l} &= \iint_{S_1+S_2}\left(\frac{\partial \vec{D}}{\partial t}+\sigma\vec{E}\right)\cdot d\vec{S} \\ &= \iint_{S_1}\left(\epsilon_1\frac{\partial \vec{E}}{\partial t}+\sigma_1\vec{E}\right)\cdot d\vec{S}+\iint_{S_2}\left(\epsilon_2\frac{\partial \vec{E}}{\partial t}+\sigma_2\vec{E}\right)\cdot d\vec{S} \qquad (18)\end{aligned}$$

Changing Equation (18) to a finite difference equation, yields

$$E_x^{n+1}(i+\tfrac{1}{2},0)=E_x^n(i+\tfrac{1}{2},0)\left[\frac{2(\epsilon_{r1}+\epsilon_{r2})-(\sigma_1+\sigma_2)\eta_0\Delta\tau}{2(\epsilon_{r1}+\epsilon_{r2})+(\sigma_1+\sigma_2)\eta_0\Delta\tau}\right] \qquad (19)$$
$$-\eta_0\left[\frac{4\Delta\tau}{\Delta\left(2(\epsilon_{r1}+\epsilon_{r2})-(\sigma_1+\sigma_2)\eta_0\Delta\tau\right)}\right]\left[H_y^{n+\frac{1}{2}}(i+\tfrac{1}{2},\tfrac{1}{2})-H_y^{n+\frac{1}{2}}(i+\tfrac{1}{2},-\tfrac{1}{2})\right]$$

2.2.4 Treatment of Perfect Electric Conductor

The boundary condition at the perfect electric conductor states that the tangential electric field must be zero. The interface between any two media always occurs at integer nodes (i,k) [See Figure 3]. The field locations for the H-field polarization with respect to the integer nodes (i,k) are shown in Figure 1. The electric fields, calculated at points on the surface of the perfect electric conductor, are always tangential to the surface. Thus, in the finite difference-time domain scheme, the boundary condition at the perfect electric conductor can be satisfied by simply setting these electric fields equal to zero at each time step.

2.2.5 Treatment of Perfect Magnetic Conductor

At a perfect magnetic conductor the tangential magnetic field must be zero. This boundary condition is satisfied when the tangential electric field at the surface of the perfect magnetic conductor is calculated. One way of obtaining a difference equation for E_x is to simplify the original problem [See Figure 4] by using image theory [See Figure 5]. The difference equation for E_x at the interface between a perfect magnetic conductor and a dielectric and magnetic material is given by

$$E_x^{n+1}(i+\tfrac{1}{2},k)=E_x^n(i+\tfrac{1}{2},k)\left(\frac{2\epsilon_r-\sigma\eta_0\Delta\tau}{2\epsilon_r+\sigma\eta_0\Delta\tau}\right) \qquad (20)$$
$$-\eta_0\left[\frac{2\Delta\tau}{\Delta\left(2\epsilon_r+\sigma\eta_0\Delta\tau\right)}\right]2H_y^{n+\frac{1}{2}}(i+\tfrac{1}{2},k+\tfrac{1}{2})$$

The implementation of perfect magnetic conductors is of particular importance in the E-field polarization because by duality the perfect magnetic conductor becomes the perfect electric conductor.

2.3 Finite Difference Equations for the E-Field Polarization

All the difference equations needed for the E-field polarization can be easily obtained through the use of duality. The difference equations used for the H-field polarization can be directly applied for the E-field polarization with the following substitutions.

$$\vec{E} \rightarrow \vec{H} \tag{21}$$
$$\vec{H} \rightarrow -\vec{E} \tag{22}$$
$$\mu \rightarrow \epsilon \tag{23}$$
$$\epsilon \rightarrow \mu \tag{24}$$
$$\eta_0 \rightarrow 1/\eta_0 \tag{25}$$
$$\sigma \rightarrow \sigma_m \tag{26}$$
$$\sigma_m \rightarrow \sigma \tag{27}$$
$$\tag{28}$$

All the other variables remain the same.

2.4 Stability and Accuracy

The choices of Δx, Δz, and $\Delta \tau$, are motivated by reasons of accuracy and stability [3,6]. In general, to obtain accurate results, Δx and Δz must be a small fraction of the smallest wavelength in any media expected in the model or of the smallest dimension of the scatterer. For this problem, the spacing in the x and z directions will be equal in size.

$$\Delta x = \Delta z = \Delta \tag{29}$$

To ensure the stability of this time stepping algorithm, $\Delta \tau$ must satisfy the following condition [3].

$$\Delta \tau \leq \left(\frac{1}{\Delta x^2} + \frac{1}{\Delta z^2} \right)^{-\frac{1}{2}} = \frac{1}{\sqrt{2}\Delta} \tag{30}$$

2.5 Implementation of Excitation Source

The two basic types of sources, which are plane waves and current line sources, are treated differently. When the excitation source is assumed to be either a sinusoidal or Gaussian pulse plane wave, the computational domain is separated into an inner

and outer region in order to facilitate the treatment of the excitation source. Within the inner region, total fields are calculated, while in the outer region, only scattered fields are calculated. The scattered fields are defined to be the total fields minus the incident plane wave.

The incident fields are subtracted from field quantities just within the inner regions, when they are used to calculate field quantities just beyond the inner region. The incident fields are added to field quantities just outside the inner regions, when they are used to calculate field quantities just within the inner region.

For the H-field polarization, some sample finite difference equations in the vicinity interface between the two regions are [See Figure 6]

$$\begin{aligned} H_{sy}^{n+\frac{1}{2}}(i+\tfrac{1}{2},k+\tfrac{1}{2}) &= H_{sy}^{n-\frac{1}{2}}(i+\tfrac{1}{2},k+\tfrac{1}{2}) + \frac{1}{\eta_0}\frac{\Delta\tau}{\Delta x}\left[E_{sz}^{n}(i+1,k+\tfrac{1}{2})\right. \\ &\quad \left. - E_{sz}^{n}(i,k+\tfrac{1}{2})\right] - \frac{1}{\eta_0}\frac{\Delta\tau}{\Delta z}\left\{E_{sx}^{n}(i+\tfrac{1}{2},k+1)\right. \\ &\quad \left. - \left[E_{tx}^{n}(i+\tfrac{1}{2},k) - E_{ix}^{n}(i+\tfrac{1}{2},k)\right]\right\} \end{aligned} \tag{31}$$

$$\begin{aligned} E_{tx}^{n+1}(i+\tfrac{1}{2},k) &= E_{tx}^{n}(i+\tfrac{1}{2},k) - \eta_0\frac{\Delta\tau}{\Delta z}\left\{\left[H_{sy}^{n+\frac{1}{2}}(i+\tfrac{1}{2},k+\tfrac{1}{2})\right.\right. \\ &\quad \left.\left. + H_{ty}^{n+\frac{1}{2}}(i+\tfrac{1}{2},k+\tfrac{1}{2})\right] - H_{ty}^{n+\frac{1}{2}}(i+\tfrac{1}{2},k-\tfrac{1}{2})\right\} \end{aligned} \tag{32}$$

The implementation of a current line source is more straightforward. In this situation, total fields are calculated within the entire computational domain. The current line source is essentially a point source in this two-dimensional simulation. For the E-field polarization, an electric line current in the y direction is the source, while for the H-field polarization a magnetic line current in the y direction is the source. Hence, the value of either E_y or H_y, depending on the polarization, is imposed at single point for each time step. For example, the line current source could be a sinusoidal or Gaussian pulse time function.

2.6 Absorbing Boundary Condition

An absorbing boundary condition at the outer boundary is needed to make the computational domain finite, and to simulate unbounded space beyond the computational domain [See Figure 7] [7-10]. The absorbing boundary condition used for this problem is the second-order approximation derived by Engquist and Majda [7].

$$\left(\frac{\partial^2}{\partial n\partial\tau} + \frac{\partial^2}{\partial\tau^2} - \frac{1}{2}\frac{\partial^2}{\partial T^2}\right) w = 0 \tag{33}$$

where w is a field quantity which is tangential to the absorbing boundary, n is the normal direction, T is the tangential direction, and τ is time normalized with respect

to the speed of light. The second-order absorbing boundary condition works very well for waves which are at or near normal incidence, and not as well for waves which are incident at grazing angles. This second-order absorbing boundary condition can be applied to all the edges of the computational domain.

At the corners of the computational domain, the second-order absorbing boundary condition cannot be used, since the normal and tangential directions are not defined. In treating the corners, an average of the two limiting cases for the normal direction is used with a first-order absorbing boundary condition.

$$\frac{1}{2}\left[\left(\frac{\partial}{\partial n_1}+\frac{\partial}{\partial \tau}\right)+\left(\frac{\partial}{\partial n_2}+\frac{\partial}{\partial \tau}\right)\right]w=0 \tag{34}$$

where $\hat{n}_1$, and $\hat{n}_2$ are the two limiting cases for the normal direction at the corner. The absorbing boundary condition at the corners is not as important as at the edges, because there is only one point at each corner, while there are many points on the edges. Thus, in general, using the first-order absorbing boundary condition at the corners will not cause significant deterioration in the accuracy of the algorithm.

The absorbing boundary is not required to absorb the incident plane wave, because the scattered fields, from which the incident plane wave has been analytically removed, are calculated outside the inner region. Since the scattered field radiates from the target, the outgoing scattered fields will not be incident on the absorbing boundary at grazing angles, which allows the absorbing boundary condition to absorb a large percentage of the outgoing scattered fields.

3 Numerical Results and Discussion

Various electromagnetic phenomena were examined and animated utilizing the FD-TD code. A few of the electromagnetic phenomena which are examined in this paper include: leading and trailing edge diffractions from a conducting strip and their dependence on polarization, creeping waves around a conducting cylinder, and radiation from a line source. In each of the surface plots shown in Figures 8-11, the outlines of the targets and the line sources will be represented by a uniform small positive height. The size of the computational domain used to perform these simulations was 200 nodes by 200 nodes large. The physical size of the computational domain was chosen to be 10 meters by 10 meters.

The target in the first two cases is a thin perfectly electrically conducting strip which is in the center of the computational domain. The strip is 3.5 meters wide and 0.1 meters thick. The excitation source is a Gaussian pulse plane wave which is incident at 7 degrees above the plane of the strip. The pulse width is 0.354 meters and is defined to be equal to two standard deviations of the Gaussian pulse. The first case involves the E-field polarization and is illustrated in Figure 8. For Figure

8, the electric field, E_y, which is pointing out of the paper, is plotted. The Gaussian pulse plane wave appears as a fairly uniform hill which stretches across the entire computational domain. The surface plot was recorded when the Gaussian pulse plane wave had already propagated near the end of the strip. The ring, which is centered at one edge of the strip, is the leading edge diffraction from the edge of the strip which was struck first by the plane wave. The diffraction from the leading edge, in this case, is strong because there is a strong discontinuity in the electric field when the pulse strikes the leading edge. The perfect electric conductor requires the tangential electric field at the surface to be zero. Hence, when the incident electric field, which is parallel to the strip's surface, strikes the strip, a rtrong reflected wave is generated in order to satisfy the boundary conditions. At the trailing edge, the boundary condition of importance states that the current must be continuous. Since the magnetic field is almost perpendicular to the strip, the tangential magnetic fields at the surface will be weak. Thus, the surface currents will also be weak, and there will be little diffraction at the trailing edge. The second case, which is illustrated in Figure 9, involves the H-field polarization. In this case, the magnetic field, H_y, which is also pointing out of the paper, is plotted. The Gaussian pulse plane wave has propagated past the strip, and now two circular rings can be seen. The larger ring is the leading edge diffraction, which is weaker than the previous case because the electric field of the incident plane wave points nearly perpendicularly to the strip, and causes a less severe discontinuity in the tangential electric field at the strip's surface. The smaller ring represents the trailing edge diffraction. In this case, the surface currents will be particularly strong because the magnetic field is always parallel to the strip's surface. The strong trailing edge diffraction is due to the large discontinuity in the surface current at the trailing edge of the strip.

The third scatterer is a perfectly conducting cylinder. The excitation source is again a Gaussian pulse plane wave which is incident at 90 degrees for the H-field polarization. The cylinder has a diameter of 2.5 meters, and the pulse width is again 0.354 meters. Figure 10 illustrates the magnetic field, H_y, as the plane wave scatters off the cylinder. Again the incident plane wave can be seen after it has propagated past the cylinder. The circular arc is travelling outward away from the cylinder and is the specular reflection from the cylinder. In the vicinity of the shadow region, where the cylinder blocks the incident plane wave, the circular arc is still attached to the conducting cylinder and travels around the back of the cylinder. This phenomena is known as a creeping wave. Creeping waves occur much more strongly for the H-field polarization because stronger surface currents are generated which essentially allow the fields to remain attached to the cylinder.

The last case simply illustrates radiation from a simple line source interacting with two perfectly conducting strips. The two strips lie on the same line and are 1.65 meters wide and 0.1 meters thick, and are separated by 0.4 meters. The line source

is 2 meters directly above the space inbetween the two strips. The line source has a Gaussian pulse time dependence with a pulse width of 0.354 meters. In this cas the H-field polarization is examined, and Figure 11 shows the magnetic field H_y. In this figure, a uniform cylindrical wave can be seen emanating from the line source. The reflection off the perfectly conducting strips simply illustrates how the curvature of the wavefront reverses itself. The fields that pass between the two strips radiate cylindrically from the aperture illustrating slit diffraction phenomena.

An additional capability of this code is to examine resonant structures (e.g. cavities). Due to the limitations of the surface plots and the inability to include color plots, it was not possible to show the resonant behavior of any cavities in this paper. One extremely useful aspect of this code is to calculate and display the fields in color successively in order to visually produce the propagation of electromagnetic waves in real time. The typical computational time for animation consisting of 500 time steps and 100 color plots is less than 1 hour on an IBM 386 personal computer. After the FD-TD computation has been completed, the actual animation can be played back at about 5 frames per second.

4 Summary

The FD-TD code developed can be used to examine various electromagnetic phenomena. The code successfully and accurately predicted the interaction between various sources and targets. Because the FD-TD technique has the capability to animate propagation, diffraction and scattering of electromagnetic waves, it is well suited as an educational tool for students learning electromagnetic wave theory.

References

[1] Yee, K. S. (1966), "Numerical Solution of Initial Boundary Value Problems Involving Maxwell's Equations in Isotropic Media," *IEEE Trans. Antennas Propag., Vol. AP-14, No. 8, pp. 302-307.*

[2] Li, K. (1990), "Electromagnetic Wave Scattering by Surface Discontinuities in a Perfectly Conducting Ground Plane," Master's Thesis, Department of Electrical Engineering and Computer Science, M. I. T., Cambridge, Massachusetts.

[3] Taflove, A. and M. E. Brodwin (1975), "Numerical Solution of Steady-State Electromagnetic Scattering Problems Using the Time-Dependent Maxwell's Equations," *IEEE Trans. Microwave Theory Tech.*, Vol. MTT-23, No. 8, pp. 623-630.

[4] Lee, C. F., R. T. Shin, J. A. Kong and B. J. McCartin (1989), "A Finite Difference - Time Domain Technique on Triangular Grids," *J. of Electromagn. Waves and Appl.*, to be published.

[5] Morgan, M. A. ed. (1990), *PIER 2: Finite Element and Finite Difference Methods in Electromagnetic Scattering*, Elsevier Science Publishing Co., Inc., New York.

[6] Bayliss, A., C. I. Goldstein, and E. Turkel (1985), "On Accuracy Conditions for the Numerical Computation of Waves," *J. of Computational Physics*, Vol. 59, pp. 396-404.

[7] Engquist, B. and A. Majda (1977), "Absorbing Boundary Conditions for the Numerical Simulation of Waves," *Math. of Comp.*, Vol. 31, No. 139, pp. 629-651.

[8] Mur, G. (1981), "Absorbing Boundary Conditions for the Finite-Difference Approximation of the Time-Domain Electromagnetic-Field Equations," *IEEE Trans. Electromagn. Compat.*, Vol. EMC-23, No. 4, pp. 377-382.

[9] Bayliss, A. and E. Turkel (1980), "Radiation Boundary Conditions for Wave-Like Equations," *Comm. on Pure and Appl. Math.*, Vol. 33, pp. 707-725.

[10] Trefethen, L. N. and L. Halpern (1985), "Well-Posedness of One-Way Equations and Absorbing Boundary Conditions," NASA Contractor Report No. 172619, Institute for Computer Applications in Science and Engineering, NASA Langley Research Center, Hampton, Virginia.

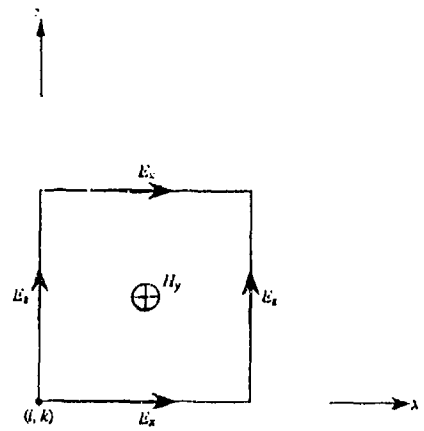

Figure 1: Field locations on rectangular grid for H-field polarization.

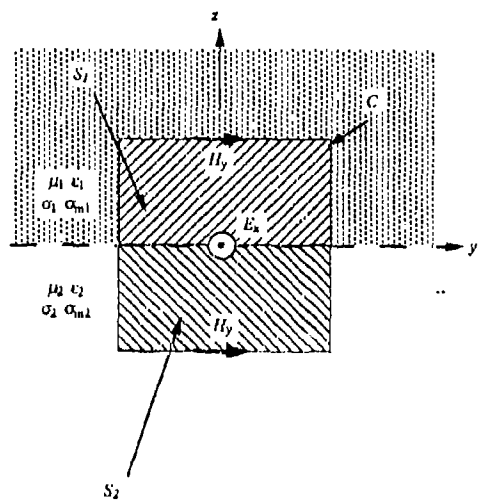

Figure 2: Interface between two dielectric and magnetic media for H-field polarization.

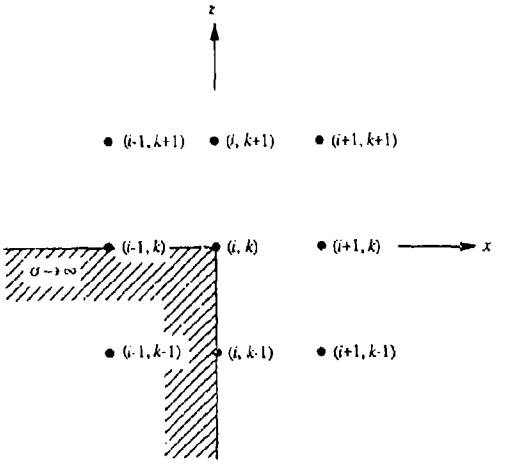

Figure 3: Positioning of the perfect conductor.

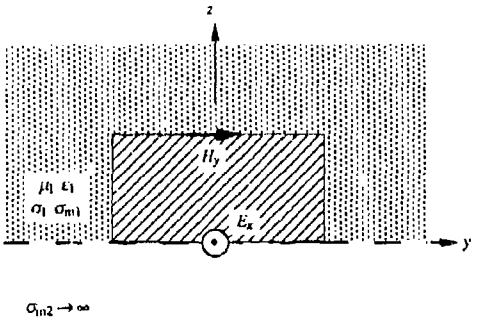

Figure 4: Interface between a media and a perfect magnetic conductor.

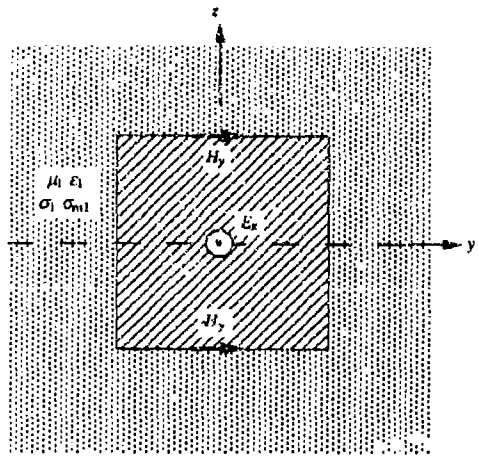

Figure 5: Image problem of interface between a media and a perfect magnetic conductor.

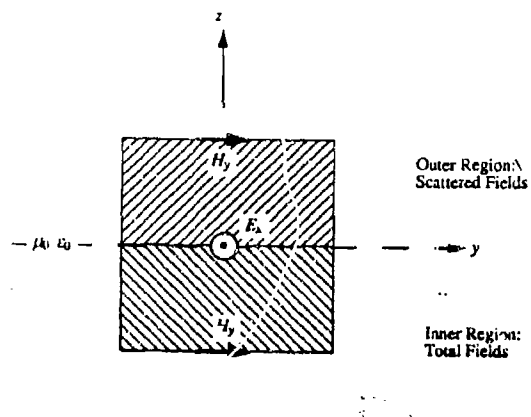

Figure 6: Interface between inner and outer regions.

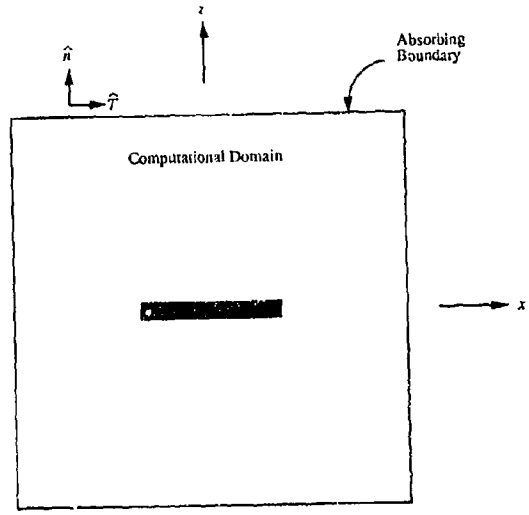

Figure 7: Absorbing boundary and computational domain.

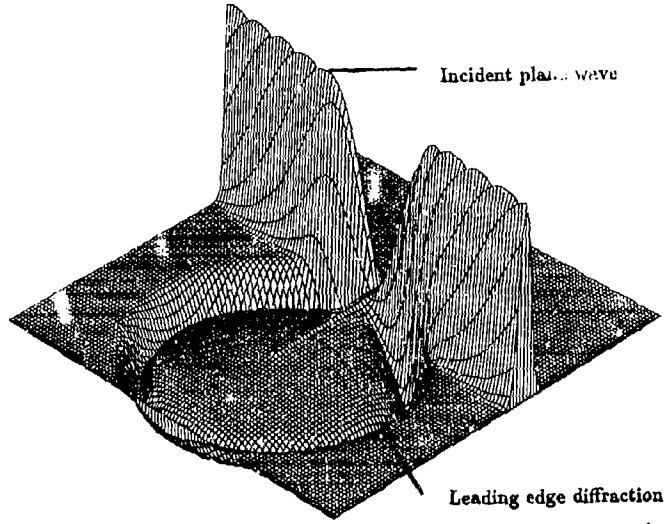

Figure 8: Leading edge diffraction from a perfectly conducting strip for E-field polarization.

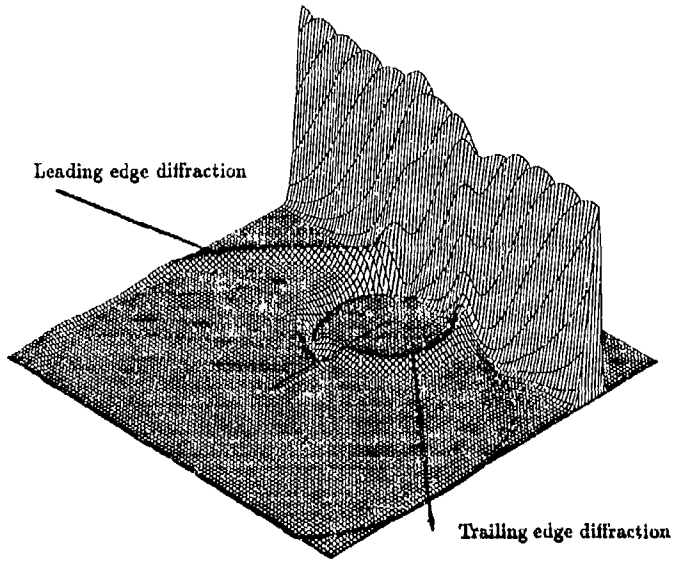

Figure 9: Trailing edge diffraction from a perfectly conducting strip for H-field polarization.

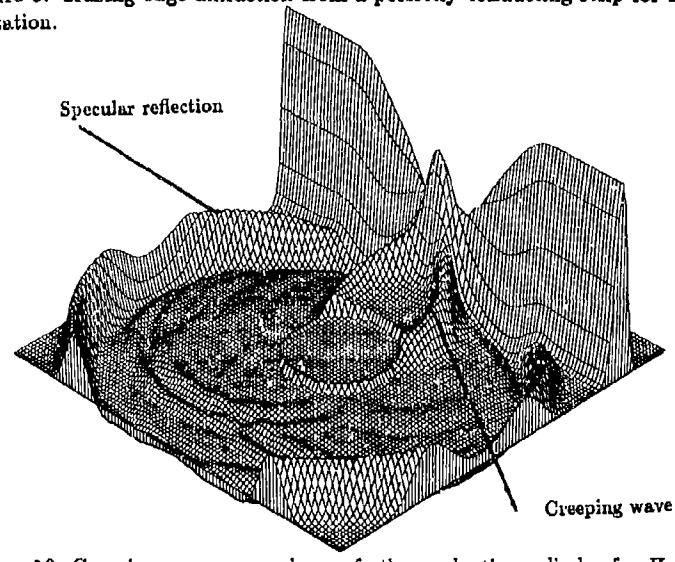

Figure 10: Creeping waves around a perfectly conducting cylinder for H-field polarization.

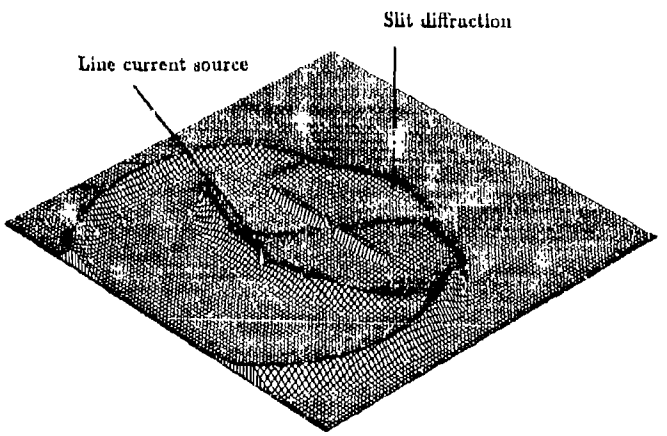

Figure 11: Interaction between a line source and two perfectly conducting strips for H-field polarization.

Kevin Li received his BS and SM degrees in electrical engineering from the Massachusetts Institute of Technology where he is currently pursuing his PhD in electrical engineering. Since 1990, he has been the recipient of an Air Force Laboratory Graduate Engineering Fellowship. His main research interests include electromagnetic scattering, radar cross section prediction, and numerical techniques. Mr. Li is a member of Tau Beta Pi.

M. Ali Tassoudji received his BS (1987) and MS (1989) degrees in electrical engineering from the University of Michigan, Ann Arbor. Since 1989, he has been a research assistant at the Massachusetts Institute of Technology, where he is currently working towards his PhD in electrical engineering. His research interests include electromagnetic scattering and propagation, modeling of microwave circuits, and numerical techniques. Mr. Tassoudji is a member of IEEE and Eta Kappa Nu.

Robert T. Shin received his SB (1977), SM (1980), and PhD (1984) in Electrical Engineering from the Massachusetts Institute of Technology. Since 1984 he has been a member of the Air Defense Techniques Group at MIT Lincoln Laboratory, as a Research Staff and as a Senior Staff from 1989. His research interest is in the areas of electromagnetic wave scattering and propagation and theoretical model development and data interpretation for microwave remote sensing. He is the coauthor of *Theory of Microwave Remote Sensing* (Wiley, 1985). Dr. Shin is a member of The Electromagnetics Academy, IEEE, American Geophysical Union, Tau Beta Pi, Eta Kappa Nu and Commission F of the International Union of Radio Science.

Jin Au Kong is a Professor of Electrical Engineering and Chairman of Area IV on Energy and Electromagnetic Systems in the Department of Electrical Engineering and Computer Science at the Massachusetts Institute of Technology. His research interest is in the field of electromagnetic wave theory and applications. He has published 7 books and over 300 refereed journal and conference papers, and is the Editor of the Wiley Series in Remote Sensing, and Chief Editor of the Elsevier book series of Progress in Electromagnetics Research (PIER).

ELECTROMAGNETIC CODE FOR SOLVING STATIC AND DYNAMIC 2-D FIELD PROBLEMS ON A PERSONAL COMPUTER

Dr. Jovan E. Lebaric, Mark Melton and Jens Engel
Rose-Hulman Institute of Technology, 5550 Wabash Av., Terre Haute, IN 47803

The Graphical Electromagnetics Code (GEC) was developed at Rose-Hulman Institute of Technology with funding from the NSF/IEEE CAEME program. The objective of GEC is to provide a user friendly graphical environment for the formulation and numerical solution of general 2-D electromagnetic field problems including static, harmonic, and transient analysis. The code is geared towards being an educational tool for the demonstration of electromagnetic field principles using the graphical capabilities of the computer to aid in the visualization of field problems. However, the code also has advanced features that make it useful as a research tool for practicing electromagnetics engineers and scientists.

GEC is targeted for 286 and 386 class DOS personal computers with EGA/VGA graphics capabilities, mouse, and 640k memory, but will operate on 8086 machines as well. GEC uses a graphical environment with mouse and keyboard support. A field problem can be described by drawing the geometry of the problem on the screen with the aid of a mouse, in a manner similar to some of the "paint" programs common on PCs. There is support for the basic shapes such as: dot (point source), box, line, circle, ellipse, polygon, and pie slice. The materials used in the geometry can have arbitrary permittivity, permeability, and conductivity. The materials are differentiated on the screen by color and pattern where they can be selected, moved, copied. etc. In addition, there is support for creating material libraries of often used materials. Furthermore, there a several types of default prototype sources to choose from including DC, AC, and transient type sources. GEC writes the geometry and material files to disk in ASCII format for easy access and modification by 3rd parties.

The static and harmonic analysis use FD methods to solve for electric potentials on a regular rectangular grids. Similarly, the transient analysis uses a Finite Difference Time Domain (FD-TD) algorithm to calculate the time history of the electric and magnetic field on interlaced ("dual") regular rectangular grids ("Yee-lattice"). The grid used for the computations is independent of the grid used to describe the problem geometry. Thus, it is easy to start with quick coarse solutions to a problem and then refine the computation grid if necessary with no modifications to the problem geometry.

The computation grid is terminated by coupling the interior grid to a radiation integral formulation for the infinite exterior region. The solution process matches the FD (or FD-TD) and radiation integral equation solutions along the grid boundary using an iterative process. In addition, GEC also supports the use of infinite ground planes by using image theory in the different analyses.

THE HIGH FREQUENCY ELECTROMAGNETIC SIMULATION OF ARBITRARY TWO AND THREE DIMENSIONAL STRUCTURES

Brad Brim
Hewlett Packard Company
Network Measurements Division
Santa Rosa, CA 95401
(707) 577-4798 bradb@hpnmd.hp.com

In the distant past most electromagnetic analyses were carried out analytically for canonical structures. Integral equation techniques were preferred since approximate source distributions (current or charge) or asymptotic analyses could often lead to the dominant behavior of the true solution. This preference endured as numerical electromagnetic codes were developed. Differential equation based and time domain algorithms have not received as much attention in research and commercial applications. The recent significant speed improvements in readily available computers has caused a refocusing of attention toward these long neglected techniques.

Recently, many authors have reported implementation of the Finite Element Method (FEM) free of spurious solutions [1]. Commercially available software packages are beginning to incorporate these new solution techniques. One such software package available from Hewlett Packard (HP85180A) is referred to as the High Frequency Structure Simulator (HFSS). This product is biased toward the solution of arbitrary two (propagating) and three dimensional RF, microwave, and mm-wave circuits type geometries.

The goal of this presentation is to present to the numerical electromagnetics researcher the capabilities of such commercially available products. A brief history of numerical electromagnetics will be discussed to set the stage for the development of FEM algorithms. A block diagram will be presented to inform the audience of the many technical disciplines that constitute these numerical tools. The main focus of the talk will be the sorts of applications that have been analyzed with HFSS. The results are not just propagation constants, characteristic impedances, and scattering parameters. In addition, any examples of the graphical display of two and three dimensional electromagnetic fields will be presented. These graphical displays lead both research and design users to develop a much higher understanding of the physical solution or how the design must be perturbed to function properly. The types of problems that HFSS presently addresses will be classified and characterized through example solutions and comparison with measurements. Problems that HFSS does not currently address will also be presented. The advances in the implementation of the FEM to achieve these solutions will be discussed.

Groups such as ACES represent the pool of talent from which theoretical advances will come to further develop numerical electromagnetic tools. The talk will conclude with a discussion of research topics that should be addressed. The applicability to general areas of numerical techniques and the relative difficulty of these suggested topics will also be addressed.

[1] "The Transfinite Element Method for Modeling MMIC Devices," Z. J. Cendes and J. F. Lee, IEEE MTT-S, Vol. 36, No. 12, Dec. 1988, pp. 1639-49.

SOFTWARE FOR ANTENNA MODELING AND RADAR APPLICATIONS

Robert J. Hancock
CAE Soft Corporation
P. O. Box 818
Rockwall, Texas 75087

The CAE Soft-Phased Array Analysis System (CS-PAAS) computer program enables students and practicing engineers to model phased array antennas quickly, accurately, and inexpensively using a personal computer or VAX computer system. CS-PAAS simplifies antenna model development for the novice while offering complete flexibility and advanced techniques for the experienced user. CS-PAAS can be used to design and analyze specific phased array configurations and determine performance sensitivity to component tolerances and other error sources.

The program is primarily used for the evaluation of discrete planar arrays. These planar arrays represent either electronically scanned phased array antennas or sampled dish antenna illumination functions evaluated in a reference plane. The program's emphasis is on speed, accuracy, and versatility with easily evaluated results. The program is in a modular structure which allows easy incorporation of additional capabilities. CS-PAAS is a detailed antenna simulation computer program. Written for the systems engineer, it is a valuable tool for the design and evaluation of phased array antenna systems.

A phased array antenna system consists of a group of subsystems which are composed of various functional elements, such as power dividers, phase shifters, and radiators. In CS-PAAS emphasis is placed on accurately simulating the functional elements because the same functional elements are used in many phased array antennas -- only the parameters change. For example, most phased arrays have phase shifters but the number of bits varies from one system to another.

The simulation is comprehensive. Currently, a number of different feed networks can be modeled. The main array can be a variety of generic shapes. A number of amplitude tapers for side lobe control are also available. The element layout and radiator type can be specified and a host of systematic and random errors can be included. CS-PAAS is ideally suited for predicting phased array performance sensitivity to component tolerances and other errors.

In the paper an overview of the CS-PAAS computer program and its capabilities will be provided. Following that the results from selected antenna system analyses that were performed using CS-PAAS will be presented. Among those examples will be the analysis of an interferometer antenna system and an evaluation of phased array performance sensitivity to correlated phase and amplitude errors in a corporate feed power distribution network.

Microwave Explorer: An Electromagnetics Program for the Analysis of High Frequency Integrated Microstrip Circuits

A. Hill, J. Burke, K. Kottapalli
Compact Software
483 McLean Blvd
Paterson NJ 07504

Abstract

This contribution describes a general electromagnetics simulator EXPLORER for rectangular microstrip geometries. The analytical formulation is based on the electric field integral equation which is solved by the Method of Moments. The general geometry to be analyzed consists of a metallization interface that is situated between various dielectric layers. The entire structure is enclosed in a rectangular box. The electromagnetics code contains an automatic generator for the current subsections which allows the convenient definition of the microstrip geometry. A number of examples are shown in order to demonstrate the effect of losses, mutual coupling and box resonances.

Introduction

Accurate characterization of passive microstrip components is essential for the design of microwave and millimeter wave components such as filters, couplers and delay lines. Typically these circuits have been modeled by subdividing them into functional blocks like microstrip bends, junctions and transmission lines. Models for these individual elements are well developed and are readily available in circuit analysis programs. The performance of an entire circuit is obtained by cascading the individual functional blocks. The access time for the electrical characteristics of each element is rather small which allows complex circuits to be analyzed within seconds on a personal computer. In addition, the approach of cascading individual circuit elements allows for optimization and statistical circuit analysis within acceptable time frames.

However, as circuit density increases certain circuit elements can no longer be treated as isolated components and their interaction with adjacent structures needs to be taken into account for accurate prediction of circuit performance. A treatment of interacting elements that is based on curve fitting techniques is impractical due to the large number of parameters associated with interacting structures. Accurate characterization of these cases requires a rigorous solution to Maxwell's Equations. A number of full wave solutions have

been developed in the past. [1-6]. The analytical foundation of most solvers is based on the integral equation approach. The unknown represents the surface current on the microstrip which is solved for by the Method of Moments. The evaluation of the Moment Matrix and the solution of the resulting linear system requires computation times that exceed run times of conventional circuit analysis programs considerably.

Theory

The structure of interest consists of a microstrip metallization pattern that is situated between multiple dielectric substrate layers. We analyze the configuration in a conducting box with possible lossy top and bottom cover. The tangential electric field on the microstrip is derived from the transverse magnetic and transverse electric field components. For the lossy, multilayered structure the related Green's function is derived using the immitance approach [7]. After applying the appropriate boundary conditions the integral equation for the electric field is found to be:

$$\mathbf{E}_{inc}(x,y)=Z\mathbf{J}(x,y)-\iint \mathbf{G}(x\,|\,x',y\,|\,y')\cdot\mathbf{J}(x',y')ds' \quad (1)$$

where J represents the surface current on the metal, Z represents the surface impedance of the metal and G is the associated dyadic Green's function of the geometry[7]. In the Moment Method we employ roof top functions[8] for basis and testing functions. Thanks to the evaluation of the roof top functions in the spectral domain the convergence of the double infinite series is obtained at acceptable limits. More precisely, the upper limit for the summation is chosen to be

$$M=\frac{2a}{d} \quad (2)$$

where a represents the length of one side of the box and d represents the desired spatial resolution.

An efficient technique for the evaluation of the elements of the Moment Matrix has been published previously [9]. The double summations in the formulation of the elements in the Moment Matrix are rewritten in such a form that they are

suited for the application of two dimensional discrete fast Fourier transforms.

In order to alleviate the burden on the part of the user an algorithm has been developed that computes the location of the current subsections from a minimum set of information that is provided by the user. Instead of specifying the location of all the current subsections, the user is only required to specify the corners of the polygons which describe the metalization structure. The program divides the metalization pattern in such a way that larger subsections are used on transmission line regions and smaller sections are used in discontinuity areas. A sample grid for a microstrip right angle bend is shown in figure 1. Note that as the edges of the transmission line region are approached the grid spacing is decreased. Also, in the discontinuity region of the right angle bend a higher grid density is maintained. Due to the application of fast Fourier transforms all grid spacings need to be a multiple integer of the minimum grid spacing.

Results

In order to demonstrate the application of the program we analyzed three examples. The first case demonstrates mutual coupling effects using a microstrip filter. A next example shows the effect of package resonances on the performance of a microstrip gap discontinuity. For the final example we compute the s parameters of a lossy transmission line and compare the results to those obtained from a two dimensional spectral domain program (see appendix).

The circuit characteristics of the filters shown in figure 2 are compared in figure 3. We show the transmission of a microstrip filter for three cases. These include the fullwave results obtained from EXPLORER for the structures of figure 2 and the results obtained from an idealized circuit analysis. For the idealized case interaction of the stubs is neglected. Note that the orientation of the stubs and the interaction between them has a significant effect on the bandwidth of the filter. These effects cannot be described with conventional circuit simulators that assume idealized conditions e.g. isolation between various circuit elements. For this example we used a 50 Ohm line on an Alumina substrate. The substrate thickness and the cover height were 0.1323mm and 2.646mm, respectively. The planar substrate dimensions were chosen to be 3.429mm by 6.985mm and the reference planes were placed at an offset 0.889mm from the wall. The stubs were 2.921mm long and were separated by s=0.762mm.

The next example shows the transmission of a microstrip gap within a frequency range where box resonances become a

matter of concern. The transmission is shown in figure 4. EXPLORER determines possible package resonant frequencies before the structure is analyzed and for this case predicts the resonant TM_{110} mode at f_r = 10.343 Ghz. This situation is reflected in figure 4. Notice the perfect transmission around 10.4 GHz which is due to the resonant package mode. We include the simulated results for the case where no package effects are considered and the trace for this idealized case is smooth indead. For this example we selected a 50 Ohm microstrip line on 25 mil Alumina enclosed in a box of dimensions 19.02mm by 19.02mm. The gap with was 2/3 W. The substrate and cover height were 0.635mm and 3.81mm respectively.

Figure 5 compares results for the magnitude and phase of the transmission s parameter for a lossy microstrip line using EXPLORER to results obtained from a two dimensional spectral domain approach (see appendix). The agreement in the frequency range up to 15 GHz is excellent. For the microstrip line with w/h=1 we used a 25mil Alumina substrate with a loss tangent of 1.0. The planar substrate dimensions were chosen to be 10mm by 6mm. The line was deembeded with the location of the reference planes at a 2.5mm offset from the walls. The cover height was 3.81mm.

Conclusion

The electromagnetics code EXPLORER has been introduced which is based on the fullwave solution for a boxed, multilayered microstrip geometry. The code was applied to demonstrate the effect of losses, coupling and package resonances on the electrical characteristics of selected microstrip structures. It became apparent that the application of fullwave electomagnetics computation improves the modeling accuracy as compared to conventional circuit analysis where the interactions between various circuit components are neglected. The efficient numerical treatment and the fact that modern workstation computers reach larger processing speeds makes electromagnetics simulation a realistic option in Microwave Integrated Circuit Design.

Appendix

Since the two dimensional spectral domain method is well known and the derivation of the Green's function follows a similar approach as used in EXPLORER, it will only be outlined briefly.

The one dimensional currents on the strips are expanded using sinusoidal basis functins modified by an edge condition term. Applying Galerkin's method along with Parseval's theorem, we obtain a set of algebraic equations

for the unknown current coefficients. The complex value of beta which makes the determinant of the characteristic matrix equal to zero is the propagation constant.

Once the propagation constant and the expansion coefficients are determined, the complex power flow is calculated. The complex impedance of the transmission line is related to the ratio of the complex power flow to the total longitudinal current.

References

[1] T. Itoh, Ed., Numerical Techniques for Microwave and Millimeter Wave Passive Structures. New York: Wiley, 1989.

[2] J. C. Rautio and R. F. Harrington, "An electromagnetic time-harmonic analysis of shielded microstrip circuits, "IEEE Trans. Microwave Theory Tech., vol. MTT-35, pp. 726-730, Aug. 1987.

[3] R. W. Jackson, "Full-wave, finite element analysis of irregular microstrip discontinuities," IEEE Trans. Microwave Theory Tech., vol. 37, pp. 81-89, Jan. 1989.

[4] J. R. Mosig, "Arbitrarily shaped microstrip structures and their analysis with a mixed potential integral equation, "IEEE Trans. Microwave Theory Tech., vol. 36, pp. 314-323, Feb. 1988.

[5] L. P. Dunleavy and P. B. Katehi, "Shielding effects in microstrip discontinuities," IEEE Trans. Microwave Theory Tech., vol. 36, pp. 1767-1774, Dec. 1988.

[6] W. Wertgen and R. H. Jansen, "Spectral iterative techniques for the full-wave 3D analysis of (M)MIC structures," in IEEE MTT-S Int. Microwave Symp. Dig., 1988, pp. 709-712.

[7] T. Itoh, "Spectral Domain Immitance Approach for Dispersion Characteristics of Generalized Printed Transmission Line," IEEE Trans. Microwave Theory Tech., Vol. MTT-28, No 7, July 1986.

[8] A. W. Glisson and D. R. Wilton, "Simple and efficient numerical methods for problems of elctromagnetic radiation and scattering from surfaces, " IEEE Trans. Microwave Theory Tech., vol. 37, pp. 81-89, Jan. 1989.

[9] A. Hill, V. U. Tripathi, "An Efficient Algorithm for the Three-Dimensional Analysis of Passive Microstrip Components and Discontinuities for Microwave and Millimeter-Wave Integrated Circuits," IEEE Trans. Microwave Theory Tech., vol. 39, No 1, January 1991.

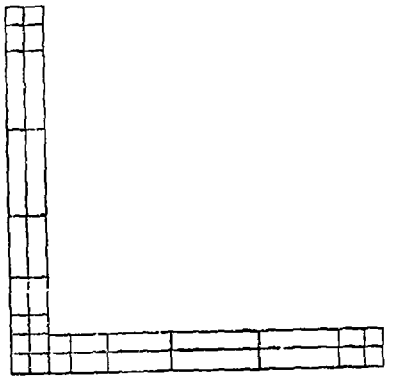

Figure 1: Sample grid for a microstrip right angle bend

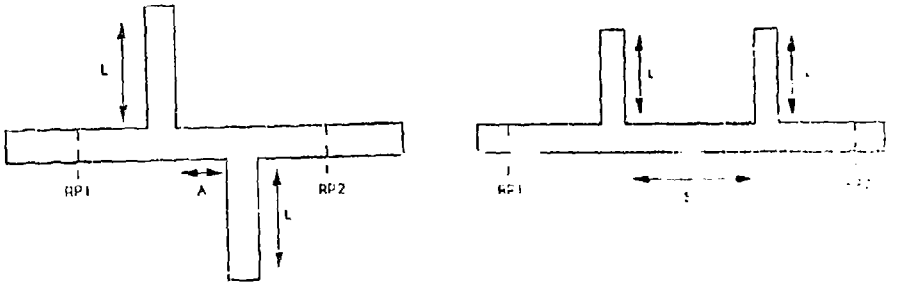

(a) (b)

Figure 2: Microstrip stub filter used to demonstrate the coupling effect of the stubs

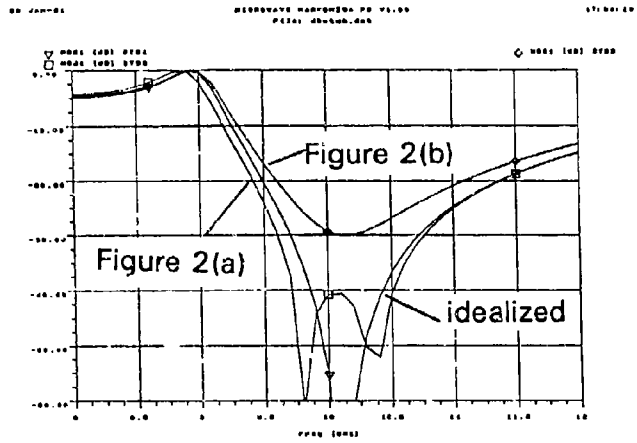

Figure 3: Transmission S_{21} for microstrip stub filter

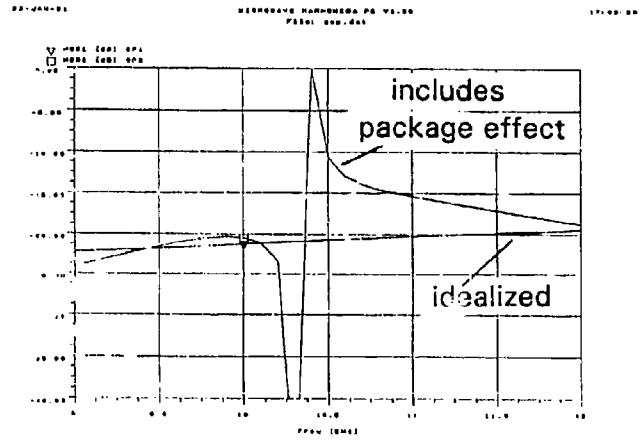

Figure 4: Effect of package resonance on the transmission S_{21} of a microstrip gap

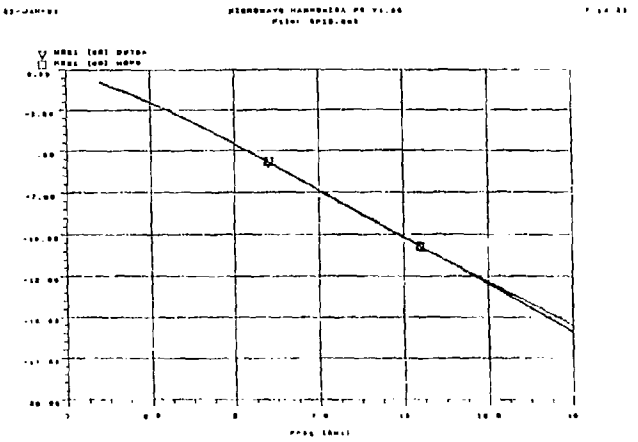

(a) Magnitude

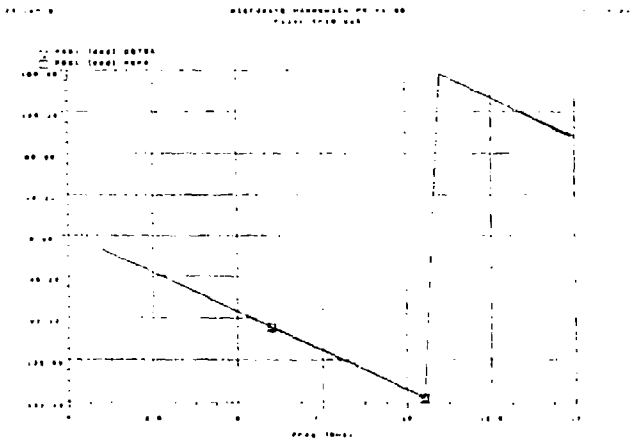

(b) Phase

Figure 5: Comparison of the transmission for a lossy microstrip line

A CASE FOR REALISM IN SCIENTIFIC ANIMATIONS

Zvonko Fazarinc,
Consulting Professor, Stanford University, California
Consultant to Hewlett-Packard Laboratories, Palo Alto, California

The author discusses the pitfalls of scientific animations performed in two-dimensional space. One supporting example is collisional interaction of neutral particles. The equipartition of energy or the Maxwellian velocity distribution cannot be expected from two-dimensional simulations or from random selection of the bounce after the collision even if the energy and momentum conservation principles are imposed. The second supporting example is the mutual interaction of charged particles. Neither Coulomb's law nor Gauss's law are satisfied in two-dimensional animations and peculiar behaviour is observed. In the future when scientific animations become widely accepted as the "nature's behaviour" their deviation from the truth may create serious damage to the student-explorer.

Three-dimensional animations are compute intensive and not very prone to visualization. The author outlines efficient algorithms for realistic three-dimensional interaction of neutral and charged particles and offers hints for their implementation in visualization software packages.

Demonstrations of behaviour of such algorithms on a UNIX workstation will be offered after the lecture.

Educational Uses of GEM. S

by

Edgar L. Coffey, III

Advanced Electromagnetics
5617 Palomino Dr. NW
Albuquerque, New Mexico 87120

The GEMACS (General Electromagnetic Model for the Analysis of Complex Systems) computer program is well-suited to educational uses. Students can access a wide variety of physics techniques and solution methods from a single input format. They can examine data in a consistent output format. The purpose of this paper is to describe some of the capabilities of GEMACS and its suitability to use in the engineering classroom.

Capabilities

Version 5.0 of GEMACS is a highly integrated program that supports the more common electromagnetic solution methods: (1) method of moments (MOM), (2) geometrical theory of diffraction (GTD), and (3) finite differences (FD). The abundance of methods in one computer program facilitates its use for instructional purposes.

Method of moments supports both wire segment and surface patch elements as well as wire-patch connections. MOM wire segments can be loaded with lumped or distributed loads. The GTD capability supports multiple ray tracing interactions among a structure composed of plates, cylinders, and cylinder end caps. There are no hard limits to the number of interactions or the number of GTD modeling elements in GEMACS. GTD elements can also be loaded with an arbitrary surface impedance if desired. Finite differences is implemented in the frequency domain for compatibility with the other GEMACS modeling techniques. At present FD is restricted to interior (cavity) regions.

GEMACS also supports combinations of methods. The two most important combinations are MOM/GTD and MOM/GTD/FD. A MOM/GTD problem contains both MOM and GTD modeling elements in the geometry. A MOM interaction matrix is generated among the line-of-sight interactions among the MOM elements and is then augmented by a GTD interaction matrix obtained from ray paths that interaction with the GTD elements of the structure. This is shown in figure 1.

The MOM/GTD/FD hybrid permits the analysis of multiple region problems such as the one shown in Figure 2. The physics quantities (interaction matrix, excitation vector) are computed for each region of the hybrid problem, then boundary conditions are matched at the aperture interfaces to obtain the total problem solution.

Code Structure

GEMACS 5.0 has been structured so that the details of peripheral files, data management, symbol tables, and other non-engineering items are all taken care of by the GEMACS overhead routines. This frees the user to concentrate on the problem at hand

and not be concerned about data input formats, opening and closing devices, etc. In fact, the user is presented with an English language command set and a CAD-like geometry language.

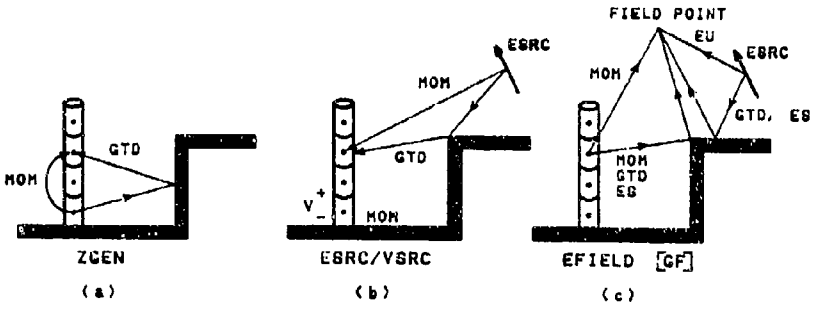

Figure 1. MOM/GTD Hybrid Concept as Implemented in GEMACS.

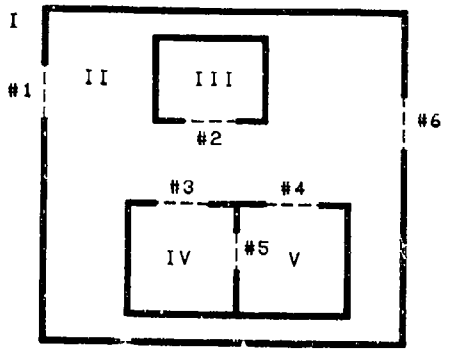

Figure 2. Multiple Region MOM/GTD/FD Hybrid Problem for GEMACS.

The command language is rich with features that permit the user to simulate nearly any problem he can conceive. Though it is not an RCS computer code, GEMACS can compute the backscatter and bistatic RCS by using **LOOP** and **LABEL** commands with look angle as the loop variable. Another user can study effects of ground conductivity on antenna performance using conductivity as the loop variable.

The geometry language contains the basic modeling elements of wire segments, surface patches, GTD plates, cylinders, and end caps. GTD elements can have apertures placed on them so that a multiple region problem can be worked. GTD elements can also

contain one or more surface impedance areas. In addition to these basic elements, the geometry processor allows CAD-like manipulation of the elements. A group of element can be defined as a modeling entity which can then be replicated by translation, rotation, or reflection. The result is a compact description of a structure that can be more easily maintained than a structure described by a series of simple commands.

GEMACS also has the ability to restart in the middle of an execution. The GEMACS checkpoint (CHKPNT) command saves the state of GEMACS at any point in the execution. GEMACS can then be restored with the restart (RSTART) command and the execution will continue where GEMACS left off. This feature permits the user to correct errors without re-running an entire problem. But perhaps a more valuable use of this feature is the ability to utilize data from earlier runs (decomposed matrices, currents, etc.) to generate new data in later runs (different field pattern cuts). Thus an instructor can generate the basic physics data for a class and have the students utilize that data via CHKPNT/RSTART to produce the observables of interest without severely tying up computer resources.

Portability

GEMACS is written in ANSI standard FORTRAN. As such it has been easily hosted on a wide variety of host computers from an IBM PCjr to a CRAY mainframe. Thus the identical code that is hosted on a university's central computer (for large problems) can also reside on a student's personal computer (subject to export control restrictions) for smaller (homework) problems. We have had no problem in hosting GEMACS on DOS, UNIX, and OS/2 operating systems. I must emphasize that it is the same identical source code for all machines and all operating systems.

Common User Interface

GEMACS users interface with the code through the same command set regardless of solution method or physics techniques selected. This provides consistency in teaching and gives the user confidence that a particular command stream will indeed describe the problem desired. Figure 3 shows sample command sets for MOM and GTD problems. Notice the similarity of the inputs.

```
$ GEMACS MOM INPUT EXAMPLE
NUMFIL = 17
FRQ = 300.
SETINT MOM
GNDATA = MOMEX
ZGEN GNDATA=MOMEX ZMATRX=ZIJ
SRC = ESRC(MOMEX) DW=1.,0. R=10. THETA=90. PHI=30.
SOLVE ZIJ*I = SRC
FLD = EFIELD(MOMEX) T1=0. P1=0. DP=2. P2=360.
END OF COMMANDS

$ GEMACS GTD INPUT EXAMPLE
NUMFIL = 9
FRQ = 300.
SETINT GTD
GNDATA = GTDEX
SRC = ESRC(GTDEX) DW=1.,0. R=10. THETA=90. PHI=30.
FLD = EFIELD(MOMEX) T1=0. P1=0. DP=2. P2=360.
END OF COMMANDS
```

Figure 3. Sample Inputs for MOM and GTD GEMACS Simulations.

A GEMACS Control Program (GEMCOP) is due to be released in the summer of 1991. The purpose of GEMCOP is to make GEMACS input language generation and output results extraction even easier than it is now. For example, GEMCOP will allow the user to extract parametric data from a collection of runs and plot those results to the user's specifications. For instance, one user may wish to plot current vs. frequency while another user may desire current vs. conductivity. If the data exist on the computer, then GEMCOP will find the data, sort the data, and format them for plotting. Hence, multiple users may make use of the same basic physics data and not have to re-run GEMACS just because the data are scattered about among many simulations.

Graphics Support

Though not a part of GEMACS proper, there is available a powerful graphics processor that works in conjunction with the GEMACS input and output streams. The GAUGE (Graphical Aids for Users of GEMACS) package contains routines for displaying, creating, and editing geometry inputs for MOM, GTD, and FD. There are other routines for displaying currents and fields, including the ability to color map currents onto wires, patches, and GTD solids. Extensive visual aids such as contouring and skeleton plots permit the user to more easily grasp the significance of the physics results. For example, a log periodic antenna can be run with GEMACS at several frequencies. By color mapping the current results back onto the antenna structure, the user can see how the longer antenna elements resonate at lower frequencies while the shorter elements work at higher frequencies.

There are also other utilities with GAUGE that let the user define his own geometry elements via an extensive macro language and to even translate NEC and BSC geometry inputs into a form that can be displayed with GAUGE and executed by GEMACS.

Finally there is a new graphics companion to GAUGE called MODELED (Model Editor). MODELED among other things takes an existing GEMACS model and scales it to other frequencies by adding wire segments and/or patches.

Summary

We feel that GEMACS is an ideal teaching tool at the advanced undergraduate and graduate levels. Its richness of physics, its simple user interface, and its extensive graphics support make it possible for students to simulate complex problems without worrying about the mechanics of the underlying computer software.

EXPERIMENTAL DEMONSTRATIONS FOR TEACHING ELECTROMAGNETIC FIELDS AND ENERGY

Markus Zahn, James R. Melcher and Hermann A Haus
Massachusetts Institute of Technology
Department of Electrical Engineering and Computer Science
Cambridge, MA 02139

Abstract

The MIT course, "Electromagnetic Fields and Energy" is the first in a two semester sequence that simplifies Maxwell's equations into their electroquasistatic (EQS) and magnetoquasistatic (MQS) forms and takes a structured approach that leads to electrodynamics giving a physical overview while developing mathematical skills to solve engineering problems. At first electromagnetic waves are unimportant, yet the electric and magnetic fields are never static with media often introducing their own dynamics. The dynamics allow for a wealth of lecture demonstrations to be used throughout the course to make the mathematical analysis take on physical meaning. Based upon relatively simple configurations and arrangements of equipment, the demonstrations make a direct connection between what has been analytically derived and what is observed. Often accompanied by a plot of the theoretical predictions that can be compared to data taken in the classroom, they give the opportunity to test the range of validity of the theory and to promulgate a quantitative approach to dealing with the physical world. In our course the lecture demonstrations are generally presented "live" but most of the demonstrations have also been videotaped presenting enough overview of the theory, documentation of the experimental procedure and data, and summary graphics to stand alone from the textbook. These tapes are used to train new teaching staff and for review at the students convenience in the departmental video room and campus library and at scheduled times on campus cable television. The undergraduate students in the course are urged to view the videotapes as study aids before exams while graduate students are urged to view the videotapes in their preparation for qualifying exam . These tapes are used as supplements to the electromagnetism urse at many universities throughout the world. The first author can be contacted for information concerning acquisition of the videotapes.

Liénard-Wiechert Field Generator
&
HyperCard Tutorials for Visual Electromagnetics

Rodney Cole & David Krull
Physics Department
University of California, Davis

Because we cannot taste, feel, or smell electric and magnetic fields, it is extremely difficult for a student to develop an intuitive feel for the subject. It often takes years of study to be able to conceptually arrive at a solution without using the powerful mathematics of Maxwell's theory. This is a major contribution to the decrease in the number of students choosing electromagnetics as a career. This state of affairs led us to develop HyperCard computer tutorials containing animated graphics and animated derivations of equations. The goal is to link the computed graphical solutions for various arrangements of charge with the standard mathematical techniques. The series of HyperCard tutorials starts with electrostatics and builds to cover radiation from charged particles. In using graphics that students are likely to encounter in current research projects, we are building graphical visual skills a student is likely to use the rest of his life as well as building a visual intuition for electromagnetics. We will describe a computer simulator that is under development for static and radiated electric fields.

SESSION 3 – "INVERSE PROBLEM SOLUTIONS"

Moderator: Margaret Cheney

AN INVERSE BOUNDARY VALUE PROBLEM FOR MAXWELL'S EQUATIONS

Erkki Somersalo[1], David Isaacson[2] and Margaret Cheney[2]

[1] Department of Mathematics
University of Helsinki, Hallituskatu 15, 00100 Helsinki
[2] Department of Mathematical Sciences
Rensselaer Polytechnic Institute, Troy, NY 12180

ABSTRACT

We consider the problem of determining the electromagnetic properties of a body from measurements made on the surface of the body. We study the full set of Maxwell's equations that govern time-harmonic electric and magnetic fields. The unknown parameters that we seek to reconstruct from boundary measurements are the magnetic permeability μ, the electric permittivity ε and the electric conductivity σ. The boundary measurement is exhibited in form of a boundary mapping, specifically the mapping from the tangential components of the electric field to the tangential components of the magnetic field. This data can be used to reconstruct μ, ε and σ approximately, provided they deviate only slightly from known constants. We give an estimate for the reconstruction error.

In his paper [2], Calderón considered the problem of determining an approximation to the electrical conductivity in a bounded region Ω of $\mathbf{R}^3$ from electrical measurements made on the surface $\partial\Omega$. This *impedance imaging* problem has recently been studied by a number of authors: Uniqueness results can be found e.g. in [9], [10], [12] and [15], and numerical reconstruction methods have been discussed in [1], [3], [4], [5], [6], [7], [8], [11], [13] and [16]. In these works, the time variation of the electromagnetic fields is neglected, so that the electric state of Ω is governed by a single second-order elliptic partial differential equation of electrostatics,

$$\nabla \cdot \sigma \nabla u = 0,$$

where σ is the conductivity and u is the electric potential. The data in the static problem is the Dirichlet-to-Neumann map (or its inverse) that assigns to each surface potential distribution the corresponding current density (or vice versa).

In [14], we study the full set of Maxwell's equations that govern time-harmonic electric and magnetic fields. The inverse problem therefore involves three unknown coefficients. We consider the case in which Ω is a bounded domain in $\mathbf{R}^3$. For simplicity, we assume that Ω has a C^2 boundary, i.e., each point of the boundary $\partial\Omega$ has a neighborhood U such that $U \bigcap \overline{\Omega}$ is C^2-isomorphic with the upper half space $\overline{\mathbf{R}^3_+} = \{x = (x_1, x_2, x_3) \mid x_3 \geq 0\}$. We shall consider the electromagnetic fields (E, H) in Ω satisfying frequency domain Maxwell's equations

$$\begin{aligned} \nabla \wedge E &= i\omega\mu H \\ \nabla \wedge H &= -\omega\varepsilon E + \sigma E \end{aligned} \tag{1}$$

in Ω, $\omega > 0$ being the fixed time harmonic frequency of the fields. The magnetic permeability μ, the electric permittivity ε and the conductivity σ are assumed to satisfy the following regularity conditions in Ω:

$$\mu, \varepsilon, \sigma \in C^1(\overline{\Omega}) \cap C^2(\Omega), \tag{2}$$

$$\mu, \varepsilon > 0, \sigma \geq 0$$

Let ν denote the unit normal vector on the surface $\partial\Omega$ pointing outwards from Ω. We seek to recover the unknown functions μ, ε and σ from the knowledge of the surface mapping

$$\Lambda : \nu \wedge E|_{\partial\Omega} \mapsto \nu \wedge H|_{\partial\Omega}.$$

Thus, Λ is the mapping that assigns to the tangential components of the electric field at the boundary the tangential components of the corresponding magnetic field. We suggest an approximate constructive procedure to recover the electromagnetic parameters ε, μ and σ from the knowledge of Λ. The method is similar to the distorted plane wave aprroximation given by Calderón. As in his work, this approximate linearization scheme is expected to work well in the case where the electromagnetic parameters deviate only slightly from constant values.

In the following, the approximate method is briefly summarized.

Assume that the coefficient functions μ,ε and σ can be written as

$$\mu(x) = \mu_0 + \delta\mu(x), \quad \varepsilon(x) = \varepsilon_0 + \delta\varepsilon(x), \quad \sigma(x) = \sigma_0 + \delta\sigma(x),$$

where ε_0, μ_0 and σ_0 are constants, ε_0, $\mu_0 > 0$ and $\sigma_0 \geq 0$, and the perturbations $\delta\mu$, $\delta\varepsilon$ and $\delta\sigma$ are small. Consider first the constant medium equations

$$\nabla \wedge E_0 = i\omega\mu_0 H_0$$

$$\nabla \wedge H_0 = -i\omega\varepsilon_0 E_0 + \sigma_0 E_0. \tag{3}$$

For any $\xi \in \mathbf{R}^3$, assume that we can always find a pair (E_0, H_0) and (E_0^*, H_0^*) of solutions to the system (3) with the following properties: (E_0, H_0) and (E_0^*, H_0^*) are of the form

$$E_0(x) = \alpha e^{i\zeta \cdot x},$$

$$H_0(x) = \beta e^{i\zeta \cdot x}, \tag{4}$$

and

$$E_0^*(x) = \alpha^* e^{i\zeta^* \cdot x},$$

$$H_0^*(x) = \beta^* e^{i\zeta^* \cdot x}, \tag{5}$$

for some α, β, ζ and α^*, β^*, ζ^* in $\mathbf{C}^3$, where the complex wave vectors satisfy the extra condition

$$\zeta + \zeta^* = \xi.$$

Next, suppose that the complete equations (1) have a solution (E, H) of the form

$$E(x) = E_0(x) + \delta E(x),$$

$$H(x) = H_0(x) + \delta H(x),$$

where (E_0, H_0) is the constant medium solution (4), and δE satisfies the boundary condition

$$\nu \wedge \delta E(x)|_{\partial\Omega} = 0, \tag{6}$$

and what is more, the correction terms δE and δH are small to first order in the perturbations $\delta\mu$, $\delta\varepsilon$ and $\delta\sigma$, denoted as

$$\delta E(x) = \mathcal{O}(\delta\mu, \delta\varepsilon, \delta\sigma)$$

$$\delta H(x) = \mathcal{O}(\delta\mu, \delta\varepsilon, \delta\sigma).$$

Then a straightforward calculation gives

$$\int_{\partial\Omega} \nu\cdot(E \wedge H_0^* - E_0^* \wedge H)dS = \int_\Omega \nabla\cdot(E \wedge H_0^* - E_0^* \wedge H)dx$$

$$= \int_\Omega ((\nabla \wedge E)\cdot H_0^* - (\nabla \wedge H_0^*)\cdot E - (\nabla \wedge E_0^*)\cdot H + (\nabla \wedge H)\cdot E_0^*)dx$$

$$= \int_\Omega (i\omega\delta\mu H\cdot H_0^* - i\omega\delta\varepsilon E\cdot E_0^* + \delta\sigma E\cdot E_0^*)dx \tag{7}$$

$$= \int_\Omega (i\omega\delta\mu H_0\cdot H_0^* - i\omega\delta\varepsilon E_0\cdot E_0^* + \delta\sigma E_0\cdot E_0^*)dx + \mathcal{O}((\delta\mu, \delta\varepsilon, \delta\sigma)^2),$$

the notation above meaning that the error term is second order in the perturbations $\delta\mu$, $\delta\varepsilon$ and $\delta\sigma$. Using the definition of the fields (4)-(5) together with the boundary condition (6) we obtain from (7) the formula

$$d(\xi) = \int_{\partial\Omega} ((\nu \wedge \alpha)\cdot\beta^* e^{i\zeta\cdot x} + \Lambda(\nu \wedge \alpha e^{i\zeta\cdot x})\cdot\alpha^* e^{i\zeta^*\cdot x})dS$$

$$= \int_\Omega (i\omega\delta\mu\beta\cdot\beta^* - i\omega\delta\varepsilon\alpha\cdot\alpha^* + \delta\sigma\alpha\cdot\alpha^*)e^{i\zeta\cdot x}dx + \mathcal{O}((\delta\mu, \delta\varepsilon, \delta\sigma)^2) \tag{8}$$

$$= \omega\beta\cdot\beta^*\widehat{\delta\mu} - \omega\alpha\cdot\alpha^*\widehat{\delta\varepsilon} + \alpha\cdot\alpha^*\widehat{\delta\sigma} + \mathcal{O}((\delta\mu, \delta\varepsilon, \delta\sigma)^2),$$

the hats denoting the Fourier transforms of the corresponding functions.

The approximate linearized solution of the inverse problem is obtained by the following steps:

(i) From the knowledge of Λ, compute the left hand side of formula (8).

(ii) We show that the choice of the complex vectors α, β, α^* and β^* is not unique for a given pair ζ, ζ^*. Therefore, we can solve for the Fourier transforms of the functions $\delta\mu$ and $\delta\varepsilon + i\delta\sigma/\omega$ in terms of the data and the residual term.

(iii) Apply the inverse Fourier transform to these equations to get an approximate solution for $\delta\mu$ and $\delta\varepsilon + i\delta\sigma/\omega$.

The crucial point that makes the above linearization possible is that one can prove estimates for the error term that is due to the second order residual term $\mathcal{O}((\delta\mu, \delta\varepsilon, \delta\sigma)^2)$ in equation (8). The error estimate obtained in [14] for the reconstruction procedure is summarized in the theorem below.

In the following, ψ denotes a smooth mollifier, i.e., $\psi \in C^\infty(\mathbb{R}^3)$, $\operatorname{supp} \psi \subset \{\xi \in \mathbb{R}^3 \mid |\xi| \leq 1\}$ and $\int \psi dx = 1$. If $N > 0$, we write $\psi_N(x) = N^3\psi(x/N)$. We denote by $*$ the convolution product of functions, i.e., $f * g(x) = \int f(x-y)g(y)dy$. Under the smoothness assumption (2), the convolutions $\psi_N * \delta\mu$, $\psi_N * \delta\varepsilon$ and $\psi_N * \delta\sigma$ are reasonable approximations of the perturbations $\delta\mu$, $\delta\varepsilon$ and $\delta\sigma$ if N is large.

Theorem. *Assume that*

$$\|Q\|_\infty = \sup|Q(x)| = \sup\left|\begin{pmatrix} \delta\varepsilon + i\dfrac{\delta\sigma}{\omega} & 0 \\ 0 & \delta\mu \end{pmatrix}\right|$$

is small, and for some η, $0 < \eta < 1$, N is a large number of the order $(1-\eta)\log(1/\|Q\|_\infty)$. Then the above linearization yields an approximation of the functions $\psi_N * \delta\mu$, $\psi_N * \delta\varepsilon$ and $\psi_N * \delta\sigma$ where the error is of the order of magnitude $\|Q\|_\infty^{1+\eta}$.

References

[1]: D. C. Barber and B. H. Brown: Applied potential tomography. J. Phys. E. Sci. Instrum. 17 (1984) 723–733.

[2]: A. P. Calderón: On an inverse boundary value problem. *Seminar on Numerical Analysis and its Applications to Continuum Physics*, Soc. Brasileira de Matemática, Rio de Janeiro, 65–73, 1980.

[3]: M. Cheney, D. Isaacson, J. C. Newell, S. Simske and J. Goble: NOSER: An algorithm for solving the inverse conductivity problem. To appear in Internat. J. Imaging Systems and Technology.

[4]: D. G. Gisser, D. Isaacson and J. C. Newell: Theory and performance of an adaptive current tomography system. Clin. Phys. Physiol. Meas. 9, Suppl. A (1988) 35–41.

[5]: D. G. Gisser, D. Isaacson and J. C. Newell: Electric current computed tomography and eigenvalues. SIAM J. Appl. Math. 50 (1990) 1623–1634.

[6]: D. Isaacson: Distinguishability of conductivities by electric current computed tomography. IEEE Trans. Med. Imaging MI-5 (1986) 91–95.

[7]: D. Isaacson and M. Cheney: Effects of measurement precision and finite numbers of electrodes on linear impedance imaging algorithms. To appear in SIAM J. Appl. Math.

[8]: R. V. Kohn and A. McKenney: Numerical implementation of a variational method for electrical impedance imaging. Preprint.

[9]: R. Kohn and M. Vogelius: Determining conductivity by boundary measurements. Comm. pure Appl. Math. 37 (1984) 113–123.

[10]: A. Nachman: Reconstructions from boundary measurements. Annals of Math. 128 (1988) 531–576.

[11]: J. C. Newell, D. G. Gisser and D. Isaacson: An electric current tomograph. IEEE Trans. Biomed. Eng. BME-35 (1988) 828–833.

[12]: A. G. Ramm: Multidimensional inverse problems and completeness of products of solutions to PDE. J. Math. Anal. Appl. 134 (1988) 211–253.

[13]: F. Santosa and M. Vogelius: A backprojection algorithm for electrical impedance imaging. SIAM J. Appl. Math. 50 (1990) 216–243.

[14]: E. Somersalo, D. Isaacson and M. Cheney: A linearized inverse boundary value problem for Maxwell's equations. Manuscript (1991)

[15]: J. Sylvester and G. Uhlmann: A global uniqueness theorem for an inverse boundary value problem. Annals of Math. 125 (1987) 153–169.

[16]: T. J. Yorkey, J. G. Webster and W. J. Tompkins: Comparing reconstruction algorithms for electrical impedance tomography. IEEE Trans. Biomed. Eng. BME-34 (1987) 843–852.

A LAYER-STRIPPING APPROACH TO IMPEDANCE IMAGING

Margaret Cheney and David Isaacson,
Department of Mathematical Sciences
Rensselaer Polytechnic Institute
Troy, New York 12180-3590

Erkki Somersalo,
University of Helsinki
Department of Mathematics
Hallituskatu 15
00100 Helsinki, Finland

and

Eli L. Isaacson
Department of Mathematics
University of Wyoming
Laramie, Wyoming 82071

ABSTRACT

Impedance imaging systems apply currents to the surface of a body, measure the induced voltages on the surface, and from this information reconstruct an approximation to the electrical impedance in the interior of the body. This paper proposes a layer-stripping approach to solving the reconstruction problem. The idea is to first find the impedance on the boundary, and then use this information to "strip away" the outermost layer. The process is then repeated, and the medium is stripped away, layer-by-layer.

1. INTRODUCTION.

Impedance imaging systems apply currents to the surface of a body, measure the voltages on the surface, and from this information reconstruct an approximation to the electrical impedance in the interior of the body [BB, GIN]. Such systems have a variety of possible applications. The first is in medical imaging [BB, CINGS]. This arises because the electrical conductivity and permittivity of different organs in the body are different [SK], so an image of the electrical impedance should also be an image of the different organs in the body. A second application is in the nondestructive testing of materials. For example, a crack in a metal has very different electrical properties from those of the surrounding metal. It is therefore possible to locate cracks in metals with impedance imaging systems [ESIC]. Other possible applications are multiphase fluid flow [XPB] and geophysical prospecting [P, DL].

The problem can be formulated mathematically as follows. We denote the electrical conductivity by σ and the permittivity by ϵ. Then at frequency ω, the admittivity γ is defined by

$$\gamma = \sigma + i\omega\epsilon. \tag{1.1}$$

We assume [IC1] that the electric potential u satisfies the boundary value problem

$$\nabla \cdot \gamma \nabla u = 0 \quad \text{inside the body } \Omega \tag{1.2}$$

$$\gamma \frac{\partial u}{\partial \nu} = j \quad \text{on the surface } \partial\Omega \tag{1.3}$$

For existence of a solution, we need also the conservation of charge condition

$$\int_{\partial\Omega} j = 0. \tag{1.4}$$

To obtain a unique solution, we need to choose a ground or reference potential. This can be done by means of the condition

$$\int_{\partial\Omega} u = 0. \tag{1.5}$$

We may make any boundary measurements we like. This means that we may specify any j and measure the corresponding u on the boundary. The restriction of u to the boundary we denote by v. Equivalently, we assume that we can obtain from measurements the map R that takes j to v. We call this map the resistive map. From knowledge of the map R, we would like to find γ.

Sylvester and Uhlmann have shown [SU] that the map R does indeed determine γ if the body is n-dimensional with n greater than two, and in the two-dimensional case R determines γ provided that γ is close to a constant. Nachman [N] used the Sylvester-Uhlmann ideas to develop a constructive method for determining γ from R. This method, however, has yet to be implemented numerically.

Most of the methods that have actually made images have been of two kinds, those based on linearization and those based on optimization. One type of method based on linearization is the backprojection method [BB, SV], which is essentially an approximate solution of the linearized problem. Another approach to the linearized problem is to convert it to a moment problem [CW, BAG, AS]. Detailed analyses of the linearized problem are given in [IC2] and [AS]; limitations of the linear theory are discussed in [II] and [CII], which give exact solutions of the linearized problem. Examples of the optimization approach are [CINGS, KM, YWT]. In this paper, however, we pursue a different method ([CI1, CI2]) that has its roots in invariant imbedding [CDK, CoK, ChK].

2. THE METHOD

First, we derive a formula that allows us to compute the resistive map in the interior from boundary data. We then outline the layer-stripping algorithm. Section 3 contains an explanation of the other key idea needed.

For simplicity, we will assume throughout that the body Ω is a disk of radius r. Our layer-stripping algorithm is based on understanding how the resistive map R changes as r changes. Below, we obtain a formula for the derivative $\partial R/\partial r$.

We begin by extending the definition of R to all r:

$$R(r)(\gamma(r,\theta)\frac{\partial u(r,\theta)}{\partial r}) = u(r,\theta). \tag{2.1}$$

We then differentiate (2.1) with respect to r:

$$\frac{\partial R(r)}{\partial r}(\gamma\frac{\partial u}{\partial r}) + R(r)\frac{\partial}{\partial r}(\gamma\frac{\partial u}{\partial r}) = \frac{\partial u}{\partial r}. \tag{2.2}$$

In the second term of (2.2), we use the differential equation (1.2), written in polar coordinates:

$$\frac{\partial}{\partial r}(\gamma\frac{\partial u}{\partial r}) + \frac{\gamma}{r}\frac{\partial u}{\partial r} + \frac{1}{r^2}\frac{\partial}{\partial\theta}(\gamma\frac{\partial u}{\partial\theta}) = 0. \tag{2.3}$$

Finally, we multiply the resulting equation by γ, use definition (2.1), and extract the operator equation

$$\frac{\partial R(r)}{\partial r} = \frac{1}{\gamma(r,\theta)} + \frac{R(r)}{r} + \frac{R(r)}{r^2}\frac{\partial}{\partial\theta}(\gamma(r,\theta)\frac{\partial R(r)}{\partial\theta}). \tag{2.4}$$

This formula suggests the following algorithm for solving the inverse problem. We call it a "layer-stripping" algorithm because it essentially works by stripping away the medium, one layer at a time. The admittivity of each layer is found before it is stripped away.

1) Make measurements $R(r_0)$ on the boundary of the body.

2) Find γ on the boundary at r_0.

3) Make a finite difference approximation to the layer-stripping formula (2.4): for some small Δ, write

$$R(r_0 - \Delta) = R(r_0) - \Delta\frac{\partial R}{\partial r}. \tag{2.5}$$

4). Replace r_0 by $r_0 - \Delta$ and repeat, starting with step 2.

To complete the discussion of this algorithm, we need to show how to do step 2).

3. HOW TO GET γ ON THE BOUNDARY

There are a number of ways to find γ on the boundary from R. For example, it was shown rigorously by Kohn and Vogelius [KV] and Sylvester and Uhlmann [SU] that γ and all its derivatives on the boundary can be obtained from boundary measurements. Kohn and Vogelius did this by applying localized, highly oscillatory boundary data. Such boundary data is insensitive to variations in γ far from the boundary (see also [I]). This is essentially equivalent to the technique used by Sylvester and Uhlmann, which was to obtain an asymptotic expansion of the boundary map R^{-1}.

Here we give a formal description of how one may recover γ from the singular behavior of the kernel of the map R. First we see that this kernel is the Green's function G defined by the following boundary value problem.

$$\nabla\cdot\gamma\nabla G = -\delta \text{ in } \Omega \tag{3.1}$$

$$\gamma\frac{\partial G}{\partial\nu} = -\frac{1}{|\partial\Omega|} \text{ on } \partial\Omega \tag{3.2}$$

$$\int_{\partial\Omega} G = 0. \tag{3.3}$$

To see how G and R are related, we multiply (3.1) by u, multiply (1.2) by G, subtract and integrate over Ω. This gives us

$$\int_\Omega (G\nabla \cdot \gamma \nabla u - u\nabla \cdot \gamma \nabla G) = u(x), \tag{3.4}$$

where x is in Ω. Using and the divergence theorem, we obtain

$$\int_{\partial\Omega} (G\gamma \frac{\partial u}{\partial \nu} - u\gamma \frac{\partial G}{\partial \nu}) = u(x). \tag{3.5}$$

The first term of (3.5), however, vanishes by (3.2) and (1.5). This leaves

$$u(x) = \int_{\partial\Omega} G(x,y) j(y) dy, \tag{3.6}$$

which shows that for x and y on $\partial\Omega$, $G(x,y)$ must be the kernel of R.

The leading order singularity of G can be understood by writing (3.1) as

$$\gamma \nabla^2 G + \nabla\gamma \cdot \nabla G = -\delta. \tag{3.7}$$

Thus a parametrix [G, SU] for (3.7) is G_0, which satisfies

$$\gamma \nabla^2 G_0 = -\delta, \tag{3.8}$$

which, in the case when Ω is a disk, can be found explicitly:

$$G_0(x,y) = const. \frac{\log \mid x-y \mid}{\gamma(x)}. \tag{3.9}$$

Thus G can be written

$$G(x,y) = const. \frac{\log \mid x-y \mid}{\gamma(x)} + \text{(smoother stuff)}. \tag{3.10}$$

This allows us to recover γ as

$$\gamma(x) = \lim_{y \to x} const. \frac{\log \mid x-y \mid}{G(x,y)}. \tag{3.11}$$

4. CONCLUSIONS

The layer-stripping algorithm has a number of possible advantages over the approximate linearizations and iterative methods that have been tried so far. First, it has no difficulty with extraneous local minima as do optimization-type methods. Second, in principle at least, it solves the full nonlinear problem. Third, the ill-posedness of the problem appears in an explicit, isolated way. Fourth, it requires fewer computations (order L^4,

where L is the number of electrodes) than realistic optimization-type methods, which typically require order L^6 operations. Fifth, it requires less storage (the matrices are $L \times L$) than optimization-type methods, which involve matrices of size $\frac{L(L-1)}{2} \times \frac{L(L-1)}{2}$.

The chief difficulty, of course, stems from the fact that the inverse problem is ill-posed: large changes in the admittivity can correspond to very small changes in the boundary measurements. This ill-posedness appears in the above algorithm as instability: the reconstructed admittivity tends to oscillate wildly, and some sort of regularization is necessary. This is not discussed here.

Below we show results of reconstructions made with this method. The following figures show rotationally invariant conductivity distributions and reconstructions made from simulated data.

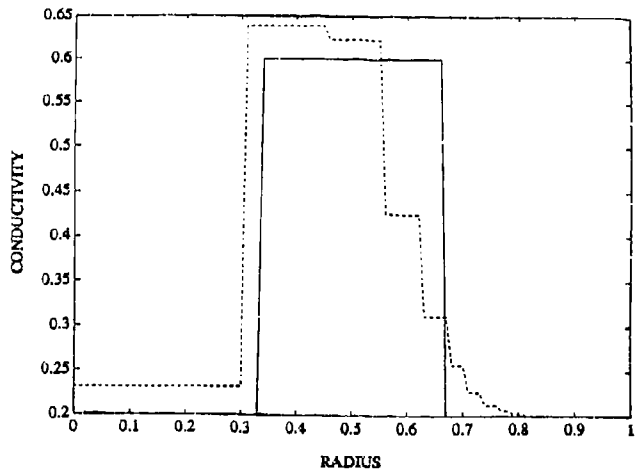

Figure 1. The solid line denotes the true conductivity distribution. For this conductivity distribution, the boundary map R was computed analytically. This data was then fed into the layer-stripping reconstruction algorithm described above. The resulting conductivity is plotted as a dotted line.

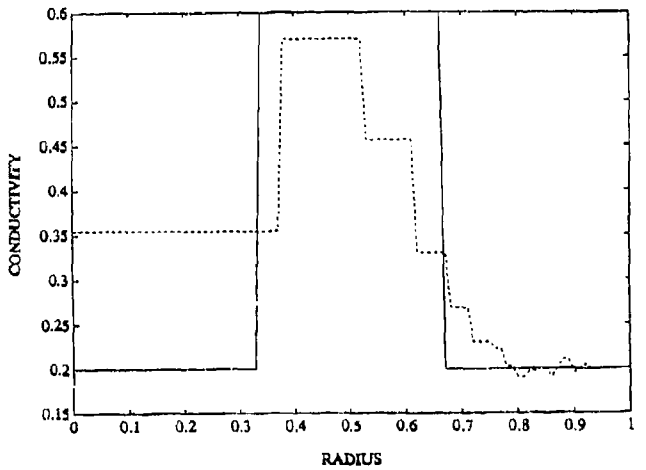

Figure 2. This shows the same conductivity distribution as in Fig. 1. Again the boundary data was computed analytically, but this time .01% noise was added. The reconstruction is plotted with a dotted line.

ACKNOWLEDGMENTS

We would like to thank D.G. Gisser, J.G. Goble, J.C. Newell, G. Saulnier, and the many students involved in our project for their work in building impedance imaging systems that continues to inspire and enlighten us. We would especially like to thank E. Coffey for assisting in numerical experiments to test the ideas set forth in this paper.

We would also like to thank John Sylvester for sharing with us his ideas on a related approach to this problem.

This work was supported by the National Science Foundation Grant EI 8706340, by the National Institutes of Health Research Grants GM39388 and GM42935, and by the Office of Naval Research Grant N-00014-89-J-1129.

REFERENCES

[AS] A. Allers and F. Santosa. "Stability and resolution analysis of a linearized problem in electrical impedance tomography", Technical Report No. 90-13, Dept. of Math. Sciences, Univ. of Delaware.

[BB] D.C. Barber and B.H. Brown, "Applied potential tomography", J. Phys. E. Sci. Instrum. 17 (1984) 723-733.

[BAG] S. Berntsen, J.B. Andersen, and E. Gross, "A general formulation of applied potential tomography", preprint.

[CDK] J.P. Cerones, M.E. Davison, and R.J. Krueger, "Direct and inverse scattering in the time domain via invariant imbedding equations", J. Acoust. Soc. Am. 74 (1983) 1535-1541.

[CF] P. Colli Franzone, "Il probleme inverso dell'elettrocardiografia", Boll. U.M.I. 15-A (1978) 30-51; and P. Colli Franzone, L Guerri, B. Taccardi, and C. Viganotti, "The direct and inverse potential problems in electrocardiology. Numerical aspects of some regularization methods and application to data collected in isolated dog heart experiments", Pub. 222, laboratorio di Analisi Numerica del Consiglio Nazionale delle Ricerche, Pavia (1979).

[ChK] M. Cheney and G. Kristensson, "Three- dimensional inverse scattering: layer-stripping formulae and ill posedness results", Inverse Problems 4 (1988) 625-642.

[CI1] M. Cheney and D. Isaacson, "Layer- stripping, Invariant Imbedding, and Impedance Imaging", Conference Proceedings for AMS Special Session in memory of Bob Krueger, Albuquerque, NM, April, 1990 (SIAM, Philadelphia, 1991).

[CI2] M. Cheney and D. Isaacson, "An Overview of Inversion Algorithms for Impedance Imaging", Proceedings of the AMS Summer Research Conference, Amherst, MA, June 1990.

[CII] M. Cheney, D. Isaacson, and E.L. Isaacson, "Exact solutions to a linearized inverse boundary value problem", Inverse Problems 6, 923-934 (1990).

[CINGS] M. Cheney, D. Isaacson, J. Newell, J. Goble, and S. Simske, "NOSER: An algorithm for solving the inverse conductivity problem", to appear in Internat. J. Imaging Systems and Technology.

[CoK] J.P. Cerones and R.J. Krueger, "Obtaining scattering kernels using invariant imbedding", J. Math. Anal. App. 95 (1983) 393-415.

[CW] T.J. Connolly and D.J.N. Wall, "On an inverse problem, with boundary measurements, for the steady state diffusion equation". *Inverse Problems* 4 (1988) pp. 995-1012.

[DL] K.A. Dynes and R.J. Lytle, "Analysis of electrical conductivity imaging", Geophys. 46 (1981) 1025- 1036.

[ESIC] M.R. Eggleston, R.J. Schwabe, D. Isaacson, and L.F. Coffin, "The application of electric current computed tomography to defect imaging in metals", in Review of Progress in Quantitative NDE, vol. 9A, 455-462 ed. D.O. Thompson and D.E. Chimenti (Plenum, New York, 1989).

[G] P.R. Garabedian, Partial Differential Equations (Chelsea, New York, 1986).

[GIN] D.G. Gisser, D. Isaacson, and J.C. Newell, "Theory and performance of an adaptive current tomography system", Clin. Phys. Physiol. Meas. 9, Suppl. A (1988) 35- 41.

[I] D. Isaacson, "Distinguishability of conductivities by electric current computed tomography", IEEE Trnas. Med. Imaging MI-5, 91-95 (1986).

[IC1] D. Isaacson and M. Cheney, "Current problems in impedance imaging", in Inverse Problems in Partial Differential Equations, ed. D. Colton, R. Ewing, and W. Rundell (SIAM, Philadelphia, 1990).

[IC2] D. Isaacson and M. Cheney, "Effects of measurement precision and finite numbers of electrodes on linear impedance imaging algorithms", SIAM J. Appl. Math., in press (1991).

[II] D. Isaacson and E.L. Isaacson, "Comment on Calderón's paper: 'On an inverse boundary value problem' ", Math. of Comp. 52, 553-559 (1989).

[N] A. I. Nachman, "Reconstruction from boundary measurements", Ann. of Math. 128 (1988) 531-576.

[NGI] J.C. Newell, D.G. Gisser, and D. Isaacson, "An electric current tomograph", IEEE Trans. Biomed. Engr. 35 (1988) 828-833.

[K] R. J. Krueger, "Inverse problems for nonabsorbing media with discontinuous material properties", J. Math. Phys. 23 (1982) 396-404 and "Numerical aspects of a dissipative inverse problem", IEEE Trans. Antennas and Propagation, AP-29 (1981) 253-261.

[KK] G. Kristensson and R.J. Krueger, "Direct and inverse scattering in the time domain for a dissipative wave equation", Parts 1-4, J. Math. Phys. 27 (1986) 1667-1693; 28 (1987) 360-370; Inverse Problems 5 (1989) 375-388.

[KM] R.V. Kohn and A. McKenney, "Numerical implementation of a variational method for electrical impedance imaging", preprint.

[KV] R.V. Kohn and M. Vogelius, "Determining conductivity by boundary measurements", Comm. Pure and Appl. Math. 37 (1984) 289-298.

[P] R.L. Parker, "The inverse problem of resistivity sounding", Geophysics 42 (1984) 2143-2158.

[SK] H.P. Schwann and C.F. Kay, "The conductivity of living tissues", Ann. of the NYAS 65 (1957) 1007-1013.

[SU] J. Sylvester and G. Uhlmann, "A uniqueness theorem for an inverse boundary value problem in electrical prospection", Comm. Pure Appl. Math. 39 (1986) 91-112; "A global uniqueness theorem for an inverse boundary value problem", Ann. of Math., 125 (1987) 153-169; "Inverse boundary value problems at the boundary — continuous dependence", Comm. Pure and Appl. Math. 41 (1988), 197-221.

[SV] F. Santosa and M. Vogelius, "A backprojection algorithm for electrical impedance imaging", Technical Note BN 1081 (Dept. of Math., Univ. of Maryland 1988)

[YWT] T.J. Yorke, J.G. Webster, and W.J. Tompkins, "Comparing reconstruction algorithms for electrical impedance tomography", IEEE Trans. Biomed. Eng. BME-34 (1987) 843-52.

[XPB] C.G. Xie, A. Plaskowski, and M.S. Beck, "8-electrode capacitance system for two-component flow identification", Parts 1 and 2, IEE Proc. 136, Pt. A (1989) 173-190.

ELECTRIC CURRENT COMPUTED TOMOGRAPHY

D. Isaacson[1], M. Cheney[1], J.C. Newell[2], D.G. Gisser[3], and J.C. Goble[4]
Rensselaer Polytechnic Institute
Troy, New York 12180-3590

[1] Department of Mathematical Sciences
[2] Department of Biomedical Engineering
[3] Department of Electrical and Computer Systems Engineering
[4] Department of Computer Science

ABSTRACT

Electric current computed tomography (ECCT) systems apply electric currents to the exterior of a body and measure the voltages that result on the body's surface. Using these measurements as data, these systems make and display reconstructions of the electrical conductivity and permittivity inside the body.

We will discuss a simple mathematical model for this problem. We then show how mathematical considerations can improve the design of the data-collection aspect of ECCT systems. Finally, we describe a reconstruction algorithm that computes approximations to the electrical conductivity and permittivity inside the body. We will also present images made with this algorithm.

There are many situations in which one would like to know the electrical conductivity and permittivity inside a body from measurements made on the body's surface. Such information is useful, for example, for the detection of cracks or flaws in metals [ESIC]. The ability to obtain such information about the interior of a human body could lead to the design of better electrocardiographs and defibrillators [CF, IC]. The ability to image the electrical properties of material flowing in a pipe could lead to a better understanding of multiphase fluid flow [XPB].

At present, there is only one commercial system that images the conductivity inside the human body. This is the Applied Potential Tomography (APT) system invented by David Barber and Brian Brown [BB]. This pioneering system uses sixteen electrodes placed around the circumference of the body. First a pair of electrodes is connected to a current source, so that current flows in through one electrode and out through the adjacent electrode. These two electrodes are the "driver pair". While current is flowing through these two electrodes, the voltages at all the other electrodes are measured. Then the current source is connected to the next pair of electrodes (a new driver pair) and the voltages measured on all the others. This process is repeated until all pairs of adjacent electrodes have served as driver pair. This data is then fed into a reconstruction algorithm based on backprojection, and a low resolution image is obtained of conductivity changes inside the body.

One way to improve this system would be to improve its resolution. How can this be done? A naive guess would be to use more electrodes. We can see whether this will work by studying the following mathematical model.

First we describe a model for the propagation of electromagnetic fields in the body. Such a model can be obtained from Maxwell's equations as follows. Maxwell's equations are

$$\nabla \wedge E = -\partial_t B \tag{1}$$

$$\nabla \wedge H = J + \partial_t D \tag{2}$$

$$\nabla \cdot B = 0 \tag{3}$$

$$\nabla \cdot D = \rho, \tag{4}$$

and we assume constitutive relations of the form

$$D = \epsilon(E, H) \tag{5}$$

$$B = \mu(H, E) \tag{6}$$

$$J = \sigma(E, H). \tag{7}$$

Here E is the electric field, B the magnetic field, ρ the charge density, J the current density, ϵ the electric permittivity, μ the magnetic permeability, and σ the conductivity.

In our experiments, we will apply current densities to the boundary of the form

$$J^{\text{source}} = J^{\text{source}}(x)\cos\omega t = Re\{J^{\text{source}}(x)e^{i\omega t}\}. \tag{8}$$

We therefore look for solutions E and B of the form $E(x)e^{i\omega t}$ and $B(x)e^{i\omega t}$. Equations (1) and (2) are then

$$\nabla \wedge E = -i\omega B \tag{9}$$

$$\nabla \wedge H = J + i\omega D. \tag{10}$$

Since the currents applied are small, we assume that the linear constitutive relations $D = \epsilon(x,\omega)E$, $B = \mu(x,\omega)H$, $J = \sigma(x,\omega)E$ hold inside the body. In living tissue, the electric permittivity , the magnetic permeability μ, and the conductivity σ are frequency-dependent. However, the magnetic permeability μ is very small. If we are interested in biological applications, we can therefore simplify Maxwell's equations by expanding all quantities about $\mu = 0$ as

$$E = E_0 + \mu E_1 + \mu^2 E_2 + \cdots \tag{11}$$

$$B = B_0 + \mu B_1 + \mu^2 B_2 + \cdots. \tag{12}$$

Substituting these expansions into the preceding two equations (9) and (10) yields

$$\nabla \wedge B_0 = 0. \tag{13}$$

Since from (3), we also have

$$\nabla \cdot B_0 = 0, \tag{14}$$

we conclude that $B_0 = 0$. This, in turn, when substituted together with (11) and (12) into (9), gives us

$$\nabla \wedge E_0 = 0. \tag{15}$$

The zero-order electric field E_0 is therefore the gradient of a function u which we call the electric potential:

$$E_0 = -\nabla u. \tag{16}$$

Because the divergence of a curl is zero, we have from (10), (5) and (7) that

$$\nabla \cdot [\sigma(x,\omega) + i\omega\epsilon(x,\omega)]E = 0. \tag{17}$$

Using (11) and (16) in (17), we obtain

$$\nabla \cdot (\sigma + i\omega\epsilon)\nabla u = 0 \tag{18}$$

for the electric potential inside the body Ω. We will use the letter γ for the admittivity:

$$\gamma = \sigma + i\omega\epsilon.$$

Next we describe the approximations we use to determine electric fields on the body's surface. In practice, we apply currents to electrodes on the surface of the body. These currents produce a current density on the surface whose inward pointing normal component is denoted by j. Thus

$$\gamma \frac{\partial u}{\partial \nu} = j \text{ on } \partial\Omega. \tag{19}$$

In this paper we take j to be given by

$$j = \begin{cases} I_l/A_l \text{ on electrode } e_l, & l = 1, 2, \cdots, L \\ 0 \text{ off } \bigcup_{l=1}^{L} e_l. \end{cases} \tag{20}$$

where I_l is the current sent to the lth electrode and A_l is the area of the lth electrode. This model for the boundary conditions we call the "gap" model. Other, more realistic models for the boundary conditions are discussed in [CING].

If currents $I = (I_1, \cdots, I_L)$ are sent to electrodes $e_1, \cdots, e_L$, and the corresponding voltages $V = (V_1, \cdots, V_L)$ are measured, then V and I are related by

$$V = RI, \tag{22}$$

where R is an $L \times L$ matrix called the resistance map. To study the question of whether more electrodes will improve the resolution of an impedance imaging system, we introduce a quantitative measure of a current density's ability to distinguish two different admittivities γ and τ. We define [I, GIN1] the "distinguishability" δ of γ from τ by a current density j to be

$$\delta(j) = \frac{\|R(\gamma)j - R(\tau)j\|}{\|j\|}, \tag{23}$$

where $R(\gamma)j$ denotes the electric potential or voltage on $\partial\Omega$ resulting from the application of the current density j to a body containing the admittivity distribution γ. The norm

is, say, the $L^2(\partial\Omega)$ norm [CI]. The distinguishability of γ from τ by j is just a normalized measure of the difference in the voltages (or signals) that would result from the application of j to the two different admittivity distributions γ and τ. This difference must be larger than the smallest voltage difference our system can detect in order for us to be able to distinguish γ from τ by j. We see from the following theorem [GIN1] that as the number L of electrodes increases, the distinguishability decreases if one applies current only on a finite number of electrodes. Here we assume that all L electrodes have the same size; since they must all fit on the same body, their size A must decrease as L increases to infinity.

Theorem. *Suppose there are constants σ_- and σ_+ such that $0 < \sigma_- \leq \sigma \leq \sigma_+$, and suppose $\partial\Omega$ is smooth. If j_{finite} denotes the current density from a finite number of current generators applied to L electrodes, then*

$$\lim_{L\to\infty} \delta(j_{finite}) = 0.$$

This result suggests that in order to improve resolution by increasing the number of electrodes, one should apply current to all the electrodes. This, in turn, raises the question of which patterns of current are best to use. These best current patterns are described in [I, GIN1]. To test these ideas, our group at Rensselaer has designed and built an Adaptive Current Tomography (ACT) system [NGI, GIN2]. This system applies currents through all of the 32 or 64 electrodes attached to the surface of the body and measures the resulting voltages. It uses these electrical measurements to reconstruct and display approximate pictures of the electrical conductivity and permittivity inside the body. The reconstruction is made by the following process. For simplicity, we discuss only the reconstruction of the conductivity; the reconstruction of the permittivity is similar. Rather than reconstructing the conductivity, in fact, we reconstruct the resistivity ρ, which is the reciprocal of the conductivity.

From a finite number of measurements, we can only hope to obtain a finite number of values of the resistivity. We assume that the resisitivity is a piecewise constant of the following form: at a point p in the body,

$$\rho(p) = \sum_{n=1}^{N} \rho_n \chi_n(p), \tag{24}$$

where χ_n is the characteristic function that is one for p contained in the nth mesh element and zero otherwise. Most of our reconstructions are done on a mesh with N = 496 = 32×31/2 elements. This is the maximum number of degrees of freedom obtainable from a 32-electrode system.

Given a resisitivity of the form (24), we could solve (18) with boundary data given by (20), where I^k is one of L-1 current patterns. The corresponding voltages measured at the electrodes we denote by

$$U^k(\rho_1, \cdots, \rho_N) = (U_1^k(\rho_1, \cdots, \rho_N), \cdots, U_L^k(\rho_1, \cdots, \rho_N)). \tag{25}$$

Our goal is to find $\rho_1, \cdots, \rho_N$ so that

$$U^k(\rho_1, \cdots, \rho_N) = V^k, \tag{26}$$

where V^k denotes the vector of measured voltages.

We do this by considering the functional

$$E(\rho_1, \cdots, \rho_N) = \sum_{k=1}^{L-1} \|U^k(\rho) - V^k\|^2 = \sum_{k=1}^{L-1} \sum_{l=1}^{L} (U_l^k(\rho_n) - V_l^k)^2. \tag{27}$$

To minimize this functional, we differentiate with respect to each variable ρ_n and set each derivative equal to zero. This gives us the system of N equations

$$0 = \frac{\partial E(\rho)}{\partial \rho_n} = 2 \sum_{k=1}^{L-1} \sum_{l=1}^{L} (U_l^k(\rho_n) - V_l^k) \frac{\partial U_l^k(\rho)}{\partial \rho_n}. \tag{28}$$

A standard method for solving such a system of nonlinear equations is Newton's method. Our algorithm [CINSG] does one Newton iteration and displays the result. Because this algorithm takes only one step, it never has to solve the variable-coefficient version of (18). Thus finite difference or finite element methods are not needed. Clearly, the algorithm does not actually give us a solution of (26), but it yields useful images. Some of these images are exhibited in the figures below.

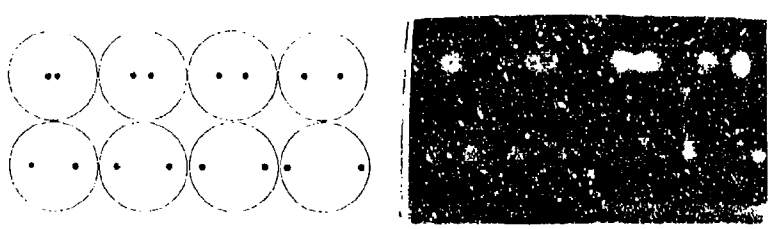

Figure 1. This shows images made of insulators in a test tank. The tank has a diameter of 30cm and is filled with a saline solution. Each teflon insulator is 22mm in diameter. The first two rows are drawings of what is actually in the tank: the insulators are placed 3, 6, 9, 12, 15, 18, 21, and 25 cm apart, respectively. The second two rows are reconstructions made by the algorithm described in the text. Each image is scaled so that the minimum conductivity is white and the maximum is black.

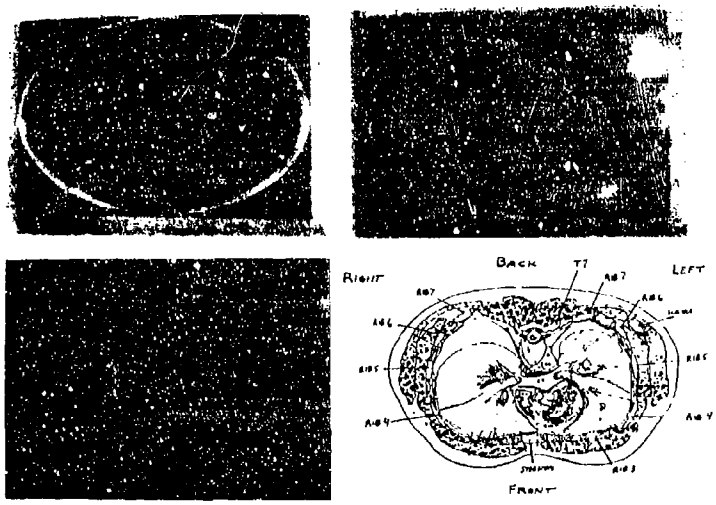

Figure 2. This shows images of the interior of the chest of a human volunteer. Thirty-two karaya gum electrodes were place around the chest at the level of the seventh thoracic vertebra (T7). The bottom right picture is a drawing of the interior of a human chest at level T7. Note the locations of the lungs. The top left image is a reconstruction at complete expiration. The top right image is a reconstruction with 1500 ml of inhaled air. Note the decrease in conductivity in the region of the lungs. Also visible in both pictures is a circumferential layer of low conductivity. This presumably represents skin and fat, which have low conductivity. The light spots at the bottom of each image may be ribs passing through the image plane. The image on the bottom left is a difference image, obtained by subtracting the top left image from the top right one. Features that are the same in both top images cancel out in this process, and only features that are different remain. This difference image shows conductivity changes in the lung regions as the lungs inflate.

Acknowledgments

The work described in this talk was done in collaboration with a large number of other people. We would especially like to thank S. Simske, L. F. Coffin, M. R. Eggelston, and R. Schwabe. This work was supported in part by NIH(GM 39388, GM 42935), NSF(BCS-8706340), ONR(N00014-89-J-1129), GE, and RPI.

References

[DB] D. C. Barber and B. H. Brown, "Applied potential tomography," J. Phys. E. Sci. Instrum. 17, 723-733 (1984).

[CI] M. Cheney and D. Isaacson, "Distinguishability in Impedance Imaging," RPI preprint.

[CINSG] M. Cheney, D. Isaacson, J.C. Newell, S. Simske, and J.G. Goble, "NOSER: An Algorithm for Solving the Inverse Conductivity Problem", to appear in Internat. J. Imaging Systems and Technology.

[CING] K.-S. Cheng, D. Isaacson, J. C. Newell, and D. G. Gisser, "Electrode models for electric current computed tomography," IEEE Trans. Biomed Engr. 36, 918-924 (1989).

[CFGTV] P. Colli Franzone, "Il probleme inverso dell'elettrocardiografia," Boll. U.M.I. 15-A, 30-51 (1978); and P. Colli Franzone, L. Guerri, B. Taccardi, and C. Viganotti, "The direct and inverse potential problems in electrodcardiology. Numerical aspects of some regularization methods and application to data collected in isolated dog heart experiments," Pub. 222, laboratorio di Analisi Numerica del Consiglio Nazionale delle Ricerche, Pavia (1979).

[ESIC] M. R. Eggleston, R. J. Schwabe, D. Isaacson, and L. F. Coffin, "The application of electric current computed tomography to defect imaging in metals," to appear in Review of Progress in Quantitative NDE, vol. 9A, 455-462, ed. D.O. Thompson and D.E. Chimenti (Plenum, New York, 1989).

[I] D. Isaacson, "Distinguishability of conductivities by electric current computed tomography," IEEE Trans. Med. Imaging MI-5, 91-95 (1986).

[ISC] D. Isaacson, E. Somersalo, and M. Cheney, "Existence and uniqueness for an electrode model for electric current computed tomography," RPI preprint.

[GIN1] D. G. Gisser, D. Isaacson, and J. C. Newell, "Electric current computed tomography and eigenvalues," SIAM J. Appl. Math 50, 1623-1634 (1990).

[GIN2] D. G. Gisser, D. Isaacson, and J. C. Newell, "Theory and performance of an adaptive current tomography system," Clin. Phys. Physiol. Meas. 9, Suppl. A, 35-41 (1988).

[NGI] J. C. Newell, D. G. Gisser, and D. Isaacson, "An electric current tomograph", IEEE Trans. Biomed. Engr. 35, 828-833 (1983).

[XPB] C.G. Xie, A. Plaskowski, and M.S. Beck, "8-electrode capacitance system for two-component flow identification", Parts 1 and 2, IEE Proc. 136, Pt. A (1989) 173-190.

USE OF ELECTRICAL IMPEDANCE IMAGING IN TWO-PHASE, GAS-LIQUID FLOWS

by

J.T. Lin[1], H. Suzuki[2], L. Ovacik[3], O.C. Jones[4], J.C. Newell[5], M. Cheney[6]
Center for Multiphase Research
Rensselaer Polytechnic Institute
Troy, New York 12180-3590 U.S.A.

ABSTRACT

The determination of interfacial area density in two-phase, gas-liquid flows is one of the major elements impeding significant development of predictive tools based on the two-fluid model. Currently, these models require coupling of liquid and vapor at interfaces using constitutive equations which do not exist in any but the most rudimentary form. Work described herein represents the first step towards the development of electrical impedance computed tomography (EICT) for nonintrusive determination of interfacial structure and evolution in two-phase, gas-liquid flows.

This paper summarizes the work accomplished to date towards the development of electrical impedance imaging methods for use in two-phase, gas-liquid flows. The basis for the method is presented and algorithms for implementation are described. Both Gauss elimination and modified Jacobi conjugate gradient methods are used for matrix inversion to calculate the electrical field from a given complex conductivity distribution and known distribution of applied current. Results of numerical simulations and the first, non-iterative real images are encouraging.

It is felt that tomographic methods such as described herein will at the least provide rapid, nonintrusive area-averaged gas volume fraction and volume fraction profiles within a cross section, and at best yield definitive data on interfacial area density, interfacial structure, and evolution, and interfacial motions.

INTRODUCTION

Virtually all present methods of predicting two-phase, gas-liquid flow behavior for design, optimization, and safety analyses use computer-based, two-fluid models where field equations are written for each phase separately describing the conservation of mass, momentum, and energy. The two-fluid model is generally constructed by considering separately (usually with some degree of spatial and temporal averaging to eliminate phasic fluctuation effects) the field equations for the phases. Closure is obtained by using

[1] Post Doctoral Research Associate
[2] Visiting Researcher, Energy Research Laboratory, Hitachi, Ltd., Japan
[3] Graduate Student
[4] Professor of Nuclear Engineering and Engineering Physics, Director--Center for Multiphase Research
[5] Professor of Biomedical Engineering
[6] Associate Professor of Mathematical Sciences

appropriate constitutive equations to describe interactions at phase bonudaries--both solid and fluid.

Reasonable descriptions are currently in hand for steady-state fluid-solid boundary interactions because of their representation in terms of global behavior which is readily measured. Nothing of practical value is known in general about fluid-fluid boundary interactions except in the most simple of cases involving fixed geometric elements such as planes or spheres. This is because of a complete lack of measurement ability relative to complex interfacial interactions.

Description of interfacial structure and evolution, as well as the gradients which control transfer of mass, momentum, and energy at these phase boundaries is the single most important key element and the challenge for the future of two-phase flow analysis. Indeed, measurement and prediction of phase boundary structure and gradients at these boundaries is one of the major factors impeding development of true predictive capability for systems involving flows of liquid and vapor or gas mixtures.

There are no methods available today which allow determination of interfacial structure and evolution in any but the most simplistic cases. It is the purpose of this paper to describe a concept which appears to hold promise for determining the distribution and evolution of interfacial area density in two-phase, gas-liquid flows.

BACKGROUND

Importance of Interfacial Area Density

On a fundamental level, it can be shown that phase change is the result of a combined effect of interfacial area and its evolution, and the potential gradient normal to the interface which leads to energy transfer. Both are expected to change with time and both are equally important in the determination of the rate of phase change per unit volume in liquid-vapor flows. Thus, both the potential and the interfacial area density must be accurately specified in order to correctly specify the phase change rates. In addition, it can be stated a priori that the distribution of the interfacial structure (traditionally termed the flow regime) is intimately involved with the processes which affect evolution. At present, there are no methods to either accurately predict or measure interfacial structure in liquid-vapor flows.

Measurement Techniques

There are no methods which exist to date which have proven to be adequate for general measurement of interfacial area density in two-phase, gas-liquid flows. There are no methods known for the measurement of interfacial area density in any other field which can be adapted to measurements in gas-liquid flowing systems. Traditional two-phase measurement techniques have been summarized in various papers, monographs and symposium volumes [e.g., Jones and Delhaye, 1976; Hewitt, 1978; Banerjee and Lahey, 1981; and Hetsroni, 1982]. Many different physical principles have been applied in making local measurements, including the use of impedance, optical, mechanical, thermal, and electro-chemical techniques. These have been adequately discussed elsewhere and will not be reiterated herein. While some methods are well developed, most others are based on ad hoc application with little understanding and application of the actual physical mechanisms involved.

Moreover, most techniques are intrusive and in some cases can substantially affect the flows, esspecially in metastable situations.

Light scattering, chemical, photographic, and interfacial velocity measurement methods have been proposed and/or utilized to obtain interfacial area density. The light scattering method can be used only in pre-calibrated conditions where the flow field is a dilute suspension of one phase homogeneously dispersed in the other. Chemical methods actually determine the integral effect of the product between potential gradient and interfacial area and can provide no definitive information on local interfacial area density or evolution. Photographic methods are also applicable only to dilute suspensions of generally spherical elements. At this time, measurement of interfacial velocities itself is extremely difficult in all but the most simple low-speed systems and has not been utilized for direct determination of interfacial area density.

Electrical Impedance Computed Tomography

Research in the development of EICT has been undertaken in the geological area [c.f. Dynes and Lytle, 1981] and in the biomedical field [c.f. Seagar, Barber, and Brown, 1987]. Most methods have used the resistive field because the resistivities of relevant materials are low. To date, the best of applications applied to real systems produce a very fuzzy planar "picture" of resistivity or permittivity variations but the results are encouraging.

Most EICT methods can be classified by the number of poles used to make a single measurement, and the method of excitation. Two-pole methods use only two electrodes for both excitation and measurement whereas four-pole methods separate excitation electrodes from those used for measurement, the measurement generally being a potential difference. Some feel that the four-pole method eliminates errors due to contact resistance at excitation electrodes, but this is not clearly a benefit [Newell et al., 1988, 1989].

Price [1979], although unsuccessful, appears to have been the first in the biomedical field to attempt obtaining impedance tomographs using the three-pole method but his reported work failed. His suggestion of the use of "guarding" methods was followed by others, all of whom were unsuccessful [Bates et al., 1980; Schneider, 1981; Seagar et al., 1987]. Furthermore, in the three-pole method, small voltage differences are obtained by subtracting the measured voltages leading to substantial errors [Smith, 1985].

Contact impedance was minimized by Barber et al. [1983] using a two-pole method and high-impedance measurement methods, but results were quite blurred. Two-pole methods were also used with little success by Dynes and Lytle [1981] and by Starzyk and Dai [1985].

Seagar et al. [1984] contend that the blurring of two-dimensional results in a continuously variable conservative field is due to nonzero effective wave number (infinite wave length) of the applied signal. They show, however, that successful reconstructions can be made for certain classes of piecewise constant media (similar to two-phase systems), and that the process is relatively simple when the discrete zones are circular in shape.

There can be orders of magnitude differances between the sensitivity of a given boundary measurement to a fixed size body depending on its location. Similar orders difference can thus occur in the eigenvalues of the solution matrix thereby making the inversion problem severely ill-posed and difficult to solve [Tarassenko and Rolph, 1984; Murai and Kagawa, 1985, 1986]. In spite of ill conditioning, good results were obtained by Wexler [1985] using a four-pole potential method with real domain reconstructions even where

there were widely varying conductivities in an overall conducting medium--i.e., metal and plastic shapes in a conducting water field.

Isaacson and coworkers [Isaacson, 1986; Isaacson and Cheney, 1989; Gisser, Isaacson, and Newell, 1987] described a method to estimate the conditions necessary to distinguish a homogeneous cylindrical body of one size, centered in a cylinder of a larger size with the region between the two also of homogeneous electrical field structure. This was followed by Fuks et al. [1989] who also provided methods of estimating the degree of accuracy to be obtained with digital conversion of data.

Barber and Brown [1984, 1985] developed an iterative back-projection method based on linearization around a constant conductivity. This method was subsequently improved upon by Santosa and Vogelius [1988] but with mixed results. Beck and his co-workers (Huang, et al., 1989; Beck and Williams, 1990) have also developed back-plane projection methods for analysis of gas-liquid pipe flows of gas and oil. A variational method developed by Kohn and Vogelius [1987] is similar to that of Wexler [1985] but guaranteed to converge. It was shown by Kohn and McKenney [1989], however, to produce results no better than those of Wexler. Murai and Kagawa [1985] used a "matrix regularization" method based on Akaike's information criterion and eliminated altogether the problem of ill-conditioning.

Yorkey, Webster, and Tompkins (YWT) followed a different approach using Marquardt's conditioning method which they stated to be better than Akaike's method. Their results appear singularly successful in inversion of two carefully-chosen numerical experiments [Yorkey, 1986; Yorkey and Webster, 1987; Yorkey, Webster, and Tompkins, 1985, 1986, 1987a, 1987b]. Finite element methods were used to obtain accurate reconstructions in four iterations. No reconstruction of real situations has yet been reported and Kohn and McKenney [1989] indicate the YWT tests were "biased by the nature of the synthetic data."

Very slow transient results were obtained by Brown, Barber, and Seagar [1985] when a dish of heated saline solution was reconstructed showing the thermal patterns of convection. From comparison of their results with Price's estimates of resistivity [Price, 1979] it seems that changes of the order of 1.5-10 Ω-cm were easily resolved. These results also indicate that there is a good potential for application of EICT methods to natural convection studies.

Finite element methods seem to have been singularly useful in reconstruction tomography of electrical fields. Starting with the suggestions of Kim, Tompkins, and Webster [1981], this work has been the basis for the most successful inversions reported on to date [Dynes and Lytle, 1981; Murai and Kagawa, 1985; Yorkey (and coworkers), 1985, 1986, 1987a, 1987b].

Yorkey et al. examined several other methods including the perturbation method used by Kim et al. [1983], the equipotential lines method used by Barber et al. [1983] and by Barber and Brown [1985], the iterative equipotential lines method (the original one proposed did not iterate), and the method used by Wexler et al., and similarly by Kohn and Vogelius [1987] (referenced by YWT). Of the five methods tried, only the YWT method converged to zero error in overall resistivity, and seemed to obtain the correct result locally, in spite of the fact that they only utilized adjacent electrodes for excitation--a pattern guaranteed to produce the most difficult problems with sensitivity. Other methods either did not converge or converged with some error.

On a completely separate track, Newell, Gisser, and Isaacson and their coworkers at Rensselaer have been developing the multi-pole current

distribution (MPCD) method. This method has resulted from mathematical analysis showing the "best" application of electrical current in a radially-symmetric system to be sin(kθ) and cos(kθ), k=1...K where K is half the number of circumferential electrodes [Gisser et al. 1987; Newell et al., 1988, 1989; Fuks et al., 1989; Isaacson and Cheney, 1989; Cheng et al., 1989]. This distribution is optimum in effect because at any instant all electrodes are simultaneously excited and the total input current is the sum of individual electrode-pair currents thereby increasing the sensitivity and decreasing the effects of noise in the system. Results on two-dimensional electrode arrays without iteration (NOSER method) are quite fuzzy but are the equal of others described in the literature.

ANALYSIS

Reconstruction Method

The best iterative method to present rapid convergence (Yorkey's resistive network or YWT method) is being extended to complex reactive networks. The computational logical includes two parts. The first part is the forward problem which is used to generate a voltage distribution using a given distribution of complex conductivity. The second part is the inverse problem which uses the simulated (calculated) experimental boundary voltages in comparison with the measured values to reconstruct the conductivity/permittivity distribution.

The theoretical basis for the algorithm is given as follows. The steady-state governing equation for the voltage distribution within the inhomogeneous and isotropic field is given by Laplaces's equation:

$$(1) \qquad \vec{\nabla} \cdot (\sigma \vec{\nabla} V) = 0$$

Finite element methods (FEM) are utilized where they are nodalized by squares. It is assumed that each square has constant complex conductivity/permittivity σ. It is known that this method converges to the exact solution where the element size becomes infinitesimal.

The FEM is defined for a reactive network (Fig. 1) as $\mathbf{YV} = \mathbf{C}$, where $\mathbf{Y}$ is the N x N indefinite admittance-matrix, and $\mathbf{V}$ and $\mathbf{C}$ are N x P matrices. The other parameters are defined as

N : the number of the total nodes.
P : the number of the current excitations.
M : the number of total elements.
E : the number of measured electrodes on the periphery.

For the given conductivity/permittivity, the admittance-matrix can be calculated by the assumptions of linear shape functions in the finite element analysis. Then the matrix representation is

$$(11) \qquad \mathbf{V}_{N \times P} = \mathbf{Y}^{-1} \mathbf{C}_{N \times P}.$$

While $\mathbf{V}$ represents the voltages of the nodes both inside and on the periphery of the body, only the voltages on the periphery can be measured. A transformation T should be made to pick up the calculated voltages on the periphery from the calculated voltages matrix $\mathbf{V}_{N \times P}$ to form a new vector $\mathbf{f}_{EP \times 1}$. The measured voltages on the E electrodes with P current excitations are collected to form the matrix $\mathbf{V}_{0,EP \times 1}$, which $\mathbf{V}_0$ is also a vector. There are errors between the calculated voltages $\mathbf{f}_{EP \times 1}$ and measured voltages

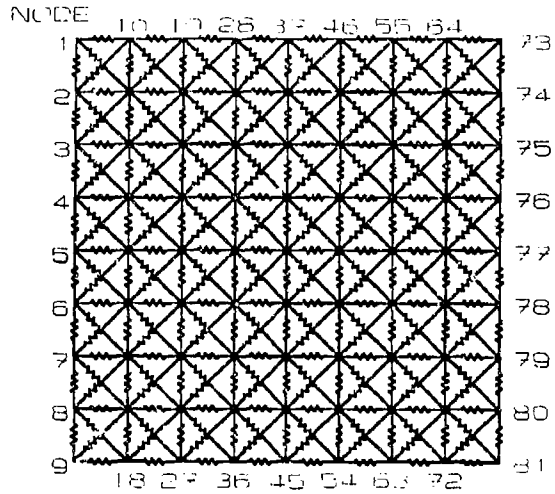

Figure 1. Schematic of an 8 × 8 impedance network.

$\mathbf{V}_{0,\,8P\times 1}$ on the measured electrodes.
A scalar error function is then defined as

(2) $$\phi = (^1/_2)(\mathbf{f} - \mathbf{V}_0)^T(\mathbf{f} - \mathbf{V}_0)$$

In order to get the minimum error, the derivative of ϕ relative to σ should be zero. Thus,

(3) $$\phi' = \frac{d\phi}{d\sigma} = [\mathbf{f}']^T[\mathbf{f} - \mathbf{V}_0] = 0$$

where $\mathbf{f}' = df/d\sigma$. The quantity ϕ' can be expressed as a Taylor expansion as

(4) $$\phi' = \phi'(\sigma^K) + \phi''(\sigma^K)\nabla(\sigma^K)$$

Therefore,

(5) $$\nabla\sigma^K = -[\phi''(\sigma^K)]^{-1}\,\phi'(\sigma^K)$$

where

(6) $$\phi' = \mathbf{f}'(\sigma^K)[\mathbf{f}(\sigma^K) - \mathbf{V}_0]$$

and where

(7) $$\phi''(\sigma^K) = [\mathbf{f}'(\sigma^K)]^T\,\mathbf{f}'(\sigma^K).$$

The corrections to σ^K can be obtained after every iteration, until the convergence criteria is achieved.

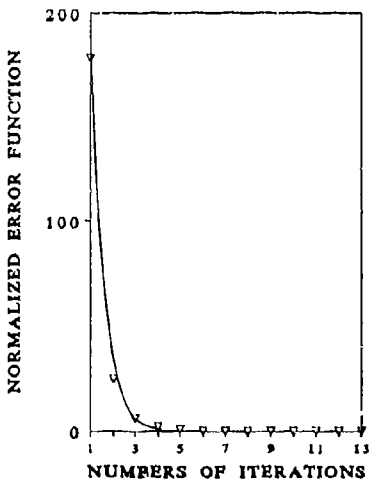

Figure 2. Typical convergence of error function for square-array FEM, with real conductivity.

A complex geometry will need many current excitations and so the matrices required in the inversions can be very large. Since the forward computation of the field potential for a given complex resistivity pattern involves inversion of a sparse matrix, Gaussian elimination methods used are computationally expensive. Thus, the Jacobi conjugate gradient (JCG) method similar to that described by Carey and Oden (1984) has been utilized for real domain inversions. In the case of a matrix having eigenvalues separated by orders of magnitude, preconditioning is obtained by pre-multiplying with the inverse of the diagonal of the original matrix. The JCG method is both extremely fast and absolutely convergent for positive definite matrices such as are anticipated in this problem. Since it is not necessary to calculate and store zeros in the matrix, the computational CPU time is decreased substantially.

The accuracy for both methods are similar. Hestenes and Stiefel (1952) have shown that if the conjugate directions are chosen as the unit basis vectors, then the conjugate gradient will be equivalent to Gaussian Elimination method. Round-off error can also be corrected in the JCG algorithm.

RESULTS

Numerical

Square-element conductive arrays. Implementation of the method using square elements in the resistive mode only indicates that convergence is very rapid. As shown in Fig. 2, the error function (Eq. 12) for an 8 x 8 array converges to two significant figures occurs within 4-5 iterations in

agreement with the results of Yorkey (1986), and within 1 part in 10^4 within 12 iterations where the contrast ratio is as large as 10,000:1. Aitken's method is also used to improve convergence speed more than a factor of 3.

Quadrilateral-element arrays. An automatic, quadrilateral-grid, mesh generator was added to convert simulations of arbitrary geometries to equivalent square element arrays. Figure 3 shows the iteration sequence results for a 25-element body having a central element of high resistivity and surrounding elements of low resistivity. Gauss elimination was used to perform matrix inversions. The small square patterns are used to visually represent the degree of variation in resistivity. The dense pattern represents material with high conductivity and low resistivity. The less dense the fill pattern, the lower the conductivity. This selection was used since, with air/vapor and liquid systems, the air regions are called "voids." The last iteration shown is that after which no visual detection of changes can be made.

Figure 4 shows the variation of error function with iteration is not uniformly convergent. Nevertheless, convergence within 10^{-6} is obtained for contrast ratios up to 100:1 within 15 iterations and convergence was obtained with all contrast ratios tested up to 10^5:1 in the real case. However, using Gauss elimination for the case of complex conductivities, convergence could not be obtained for contrast ratios much over 100:1 and the results are erratic and not well understood at this point. However, it appears that part of the problem is associated with distorted quadralateral elements where angles become quite obtuse or acute. It is expected that implementation of the JCG method for inversion will substantially alter this picture.

The relatively rapid reduction in the numerical value of the error function does not, however, tell the whole story. Figure 5 shows the local error for central, middle-ring, and outer-ring elements as a function of iteration. Convergence in this case is not quadratic and significant local error can exist even with very low error in ϕ. Furthermore, the elements farthest from the boundary are the slowest to converge due to the low degree of sensitivity to boundary effects.

Figure 6 shows the iterative sequence for a 64-element, near-circular body having a ring-shaped region of high resistivity with contrast ratio of 3:1. Note that the starting pattern is of uniform conductivity, identical to that shown in Fig. 3. Convergence results are similar to those for the 25-element body. Note that while only 11 iterations were required for "visual convergence," in Fig. 3, 15 iterations are required in this case.

Figure 7 simulates a case where liquid hugs the wall of a pipe and gas occupies the central region, again to a resolution of 64 elements. The starting pattern was identical to that shown in Fig. 3. It is seen that the outer ring of low resistivity material converges rapidly due to the high sensitivity of electrode reaction to nearby material whereas the central core zones take approximately 25 iterations for visual convergence.

The results shown in Fig. 8 are for a relatively random arrangement of the two resistivities resistivities in a circular, 64-element array. Again, 25 iterations are required for visual convergence of the pattern. Global convergence is compared in Fig. 9 for this case (Case 1) and those shown in Fig. 6 (Case 2) and Fig. 7 (Case 3). All three cases are for the 3:1 real contrast ratio. It appears that the more complex the pattern, the more difficult it is to obtain accurate solutions.

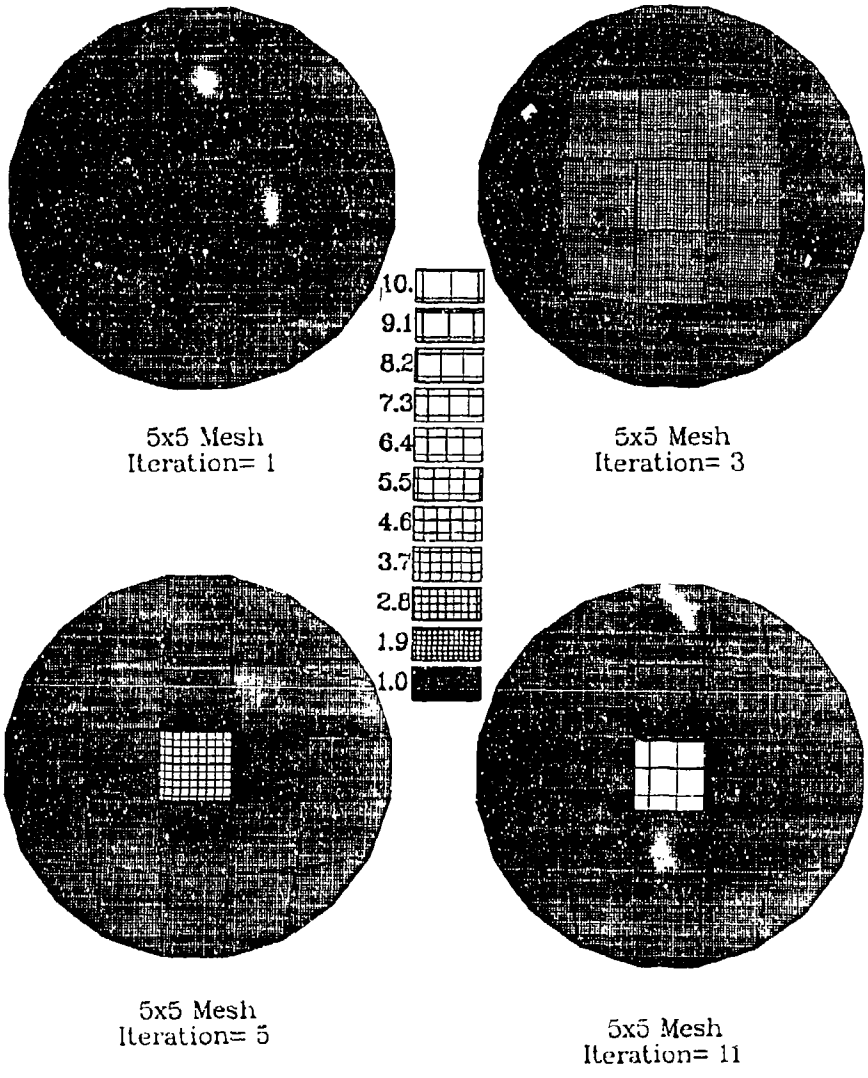

Figure 3. Iteration patterns for a 25-element, quadrilateral array.

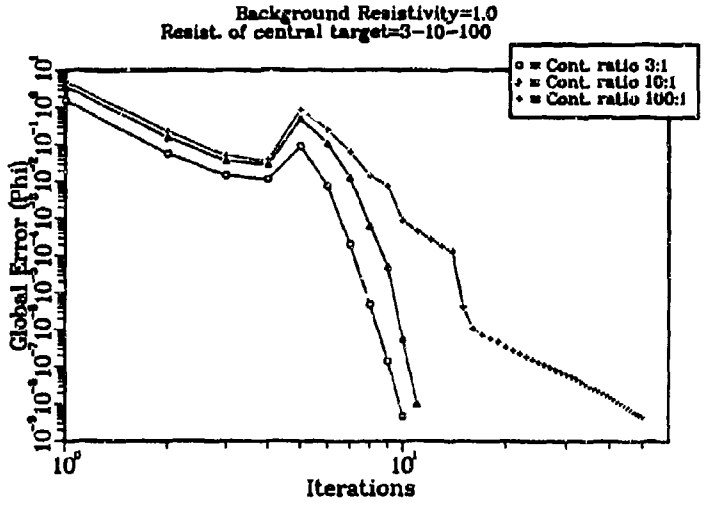

Figure 4. Global convergence for a 25-element quadrilateral array having only real conductivity components.

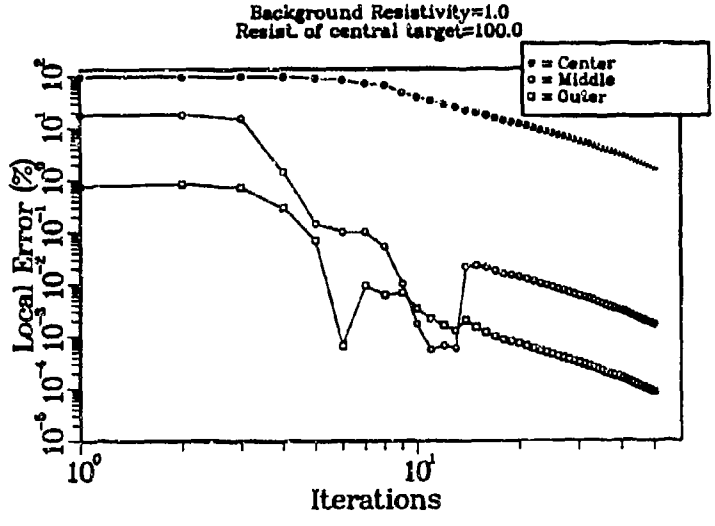

Figure 5. Local convergence for a 25-element quadrilateral array having only real conductivity components.

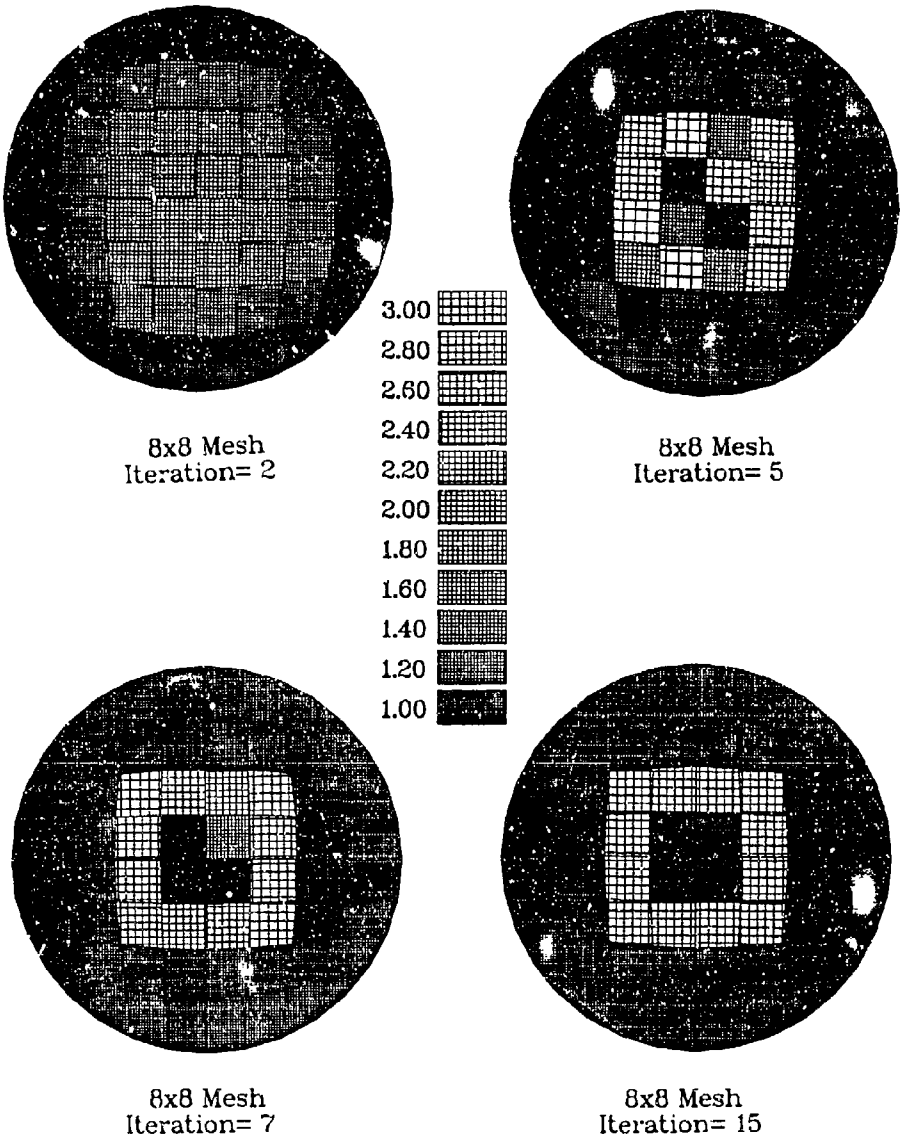

Figure 6. Iteration patterns for a 64-element array of quadrilateral elements having only real conductivity elements. Ring pattern, 3:1 contrast.

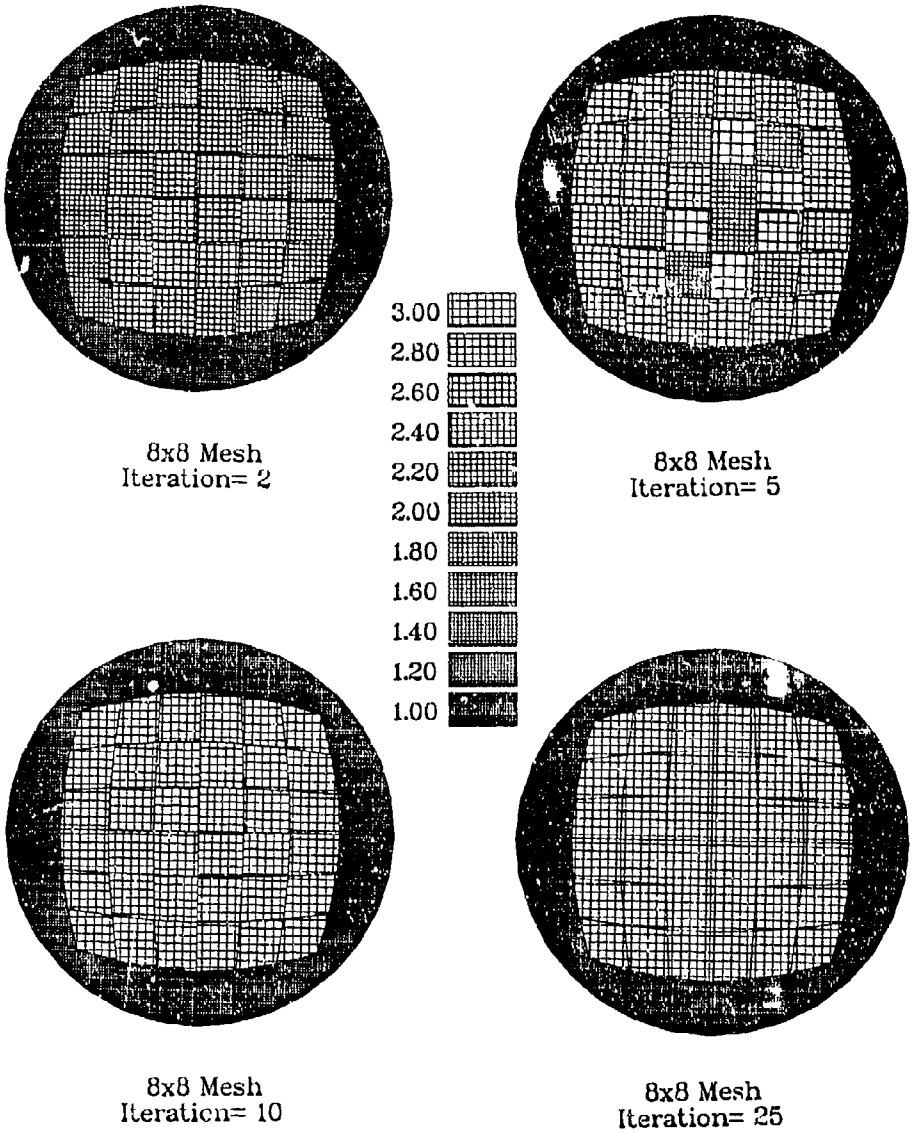

Figure 7. Iteration patterns for a 64 element array of quadrilateral elements having only real conductivity elements.
Annular pattern, 3:1 contrast.

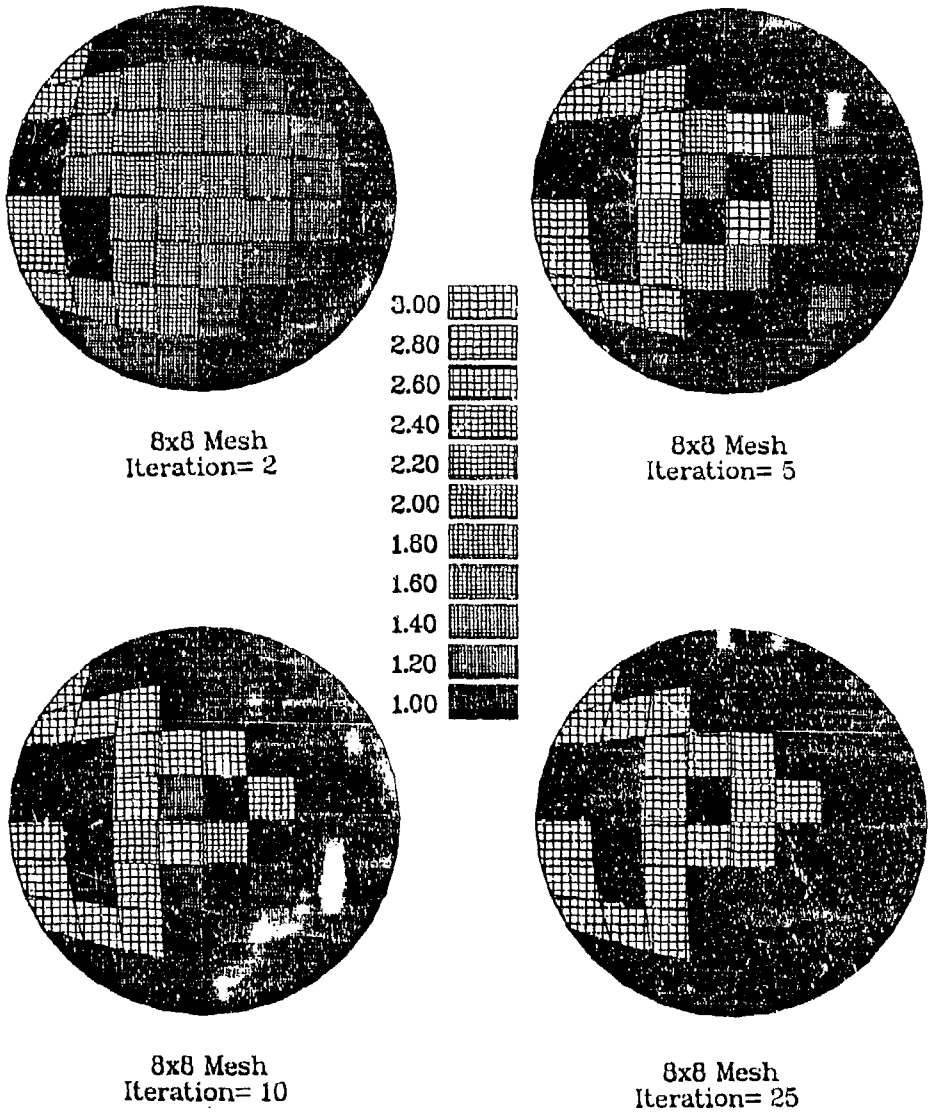

Figure 8. Iteration patterns for a 64-element array of quadralateral elements having only real conductivity elements. Random pattern, 3:1 contrast.

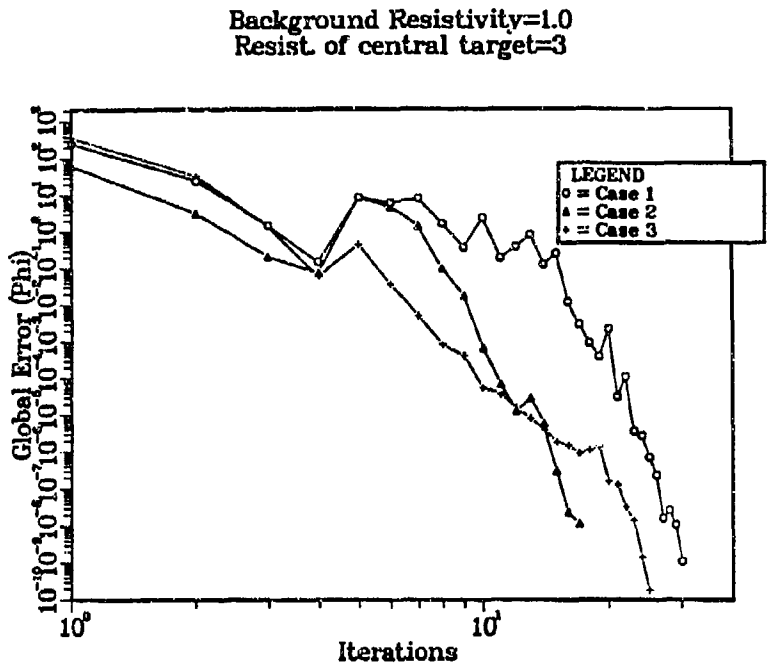

Figure 9. Global convergence for a 64-element quadrilateral array having patterns shown in Fig. 9 (Case 1), Fig. 6 (Case 2), and Fig. 7 (Case 3), for the case of 3:1 real contrast ratio.

Experimental

An example of a electrical impedance tomographic image obtained using sinusoidal current excitation patterns and complex conductivity inversion is shown in Fig. 10 (NOSER method, Newell et al., 1989). The test geometry used is a rather shallow, two-dimensional bath 500-mm in diameter. Water fills the dish to a depth of approximately 12 mm except for an empty, 50-mm-diameter beaker placed in the center of the dish.

The NOSER method, described elsewhere in this meeting, is a noniterative reconstruction which uses exact solution of the uniform field problem and exact computation of the first corrections in the iterative process. Results are shown in Fig. 10(b) where the darker regions are higher impedance associated with air. It is expected that with improved sensitivity algorithms and iteration, the reconstructed image will be much improved. The results show that it is clearly possible to separately identify large separate regions of gas-phase surrounded by water in a large geometry. What must yet be shown is if the inverse is true--separate water regions surrounded by air. Also, the capability for discrimination in smaller overall geometry with relatively smaller, multiple zones of the discrete phase remains to be demonstrated.

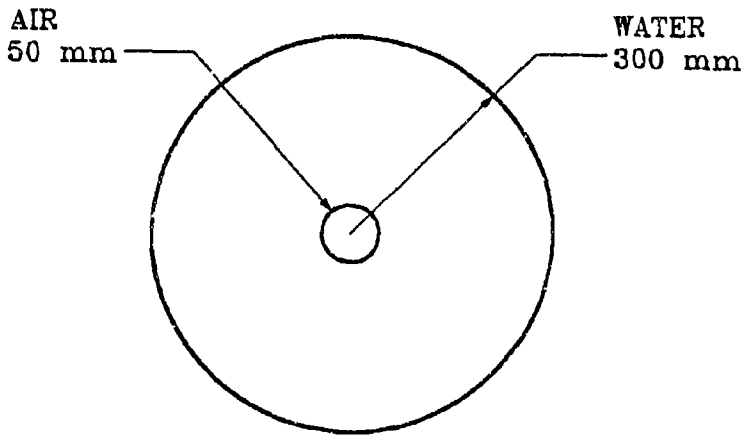

(a)

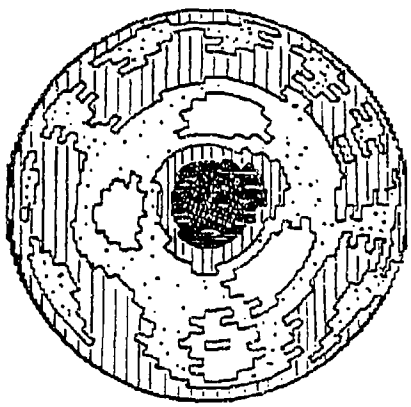

(b)

Figure 10. Example of electrical impedance reconstruction in an air water system using noniterative, complex conductivity methods. (a) geometry

CONCLUSIONS

A method of using electrical impedance for imaging of two-phase fluid distributions using inverse computational methods has been discussed with the following conclusions.

1. It has been shown that the internal distribution of complex electrical impedance can be determined within a body by using only boundary excitation and measurement.
2. Square-element FEM modeling of a resistive body allows iterative convergence to 1% within 4-5 iterations and within 0.01% within 12 iterations for all contrast ratios up to 10^5.
3. Quadralateral-element, adaptive grid, FEM modeling was slower to iterate and more sensitive to resistivity ratio, perhaps due to the presence of highly acute or obtuse angles distorting the equivalent square-element conductivity. Local error in a given element was shown to be considerably slower to converge to a reasonable error. Elements farthest from the boundary showed slowest convergence, and more complex situations appear to require more interations for convergence.
4. Complex contrast ratios as large as 10^7 were found to converge using Gauss elimination for matrix inversion. Situations with larger contrast diverged.
5. Application to a practical, laboratory situation shows that even without iteration, reasonable results can be obtained for complex conductivity fluids.
5. Considerable development effort remains before the method will be of general utility for two-phase, gas-liquid flows.

ACKNOWLEDGEMENTS

This research was supported by the Energy Research Laboratory, Hitachi, Ltd., Hitachi-shi, Ibaraki-ken, Japan, and by the U.S. Department of Energy under contract number DE-FG07-90ER13032.

NOMENCLATURE

English

A	Area (flow area if not subscripted)
G	Mass flux
i	Enthalpy
j	Square root of (-1)
$\vec{n}$	Unit outward normal on the surface of a region
$\vec{q}$	Heat flux
t	Time or generalized Jacobian matrix
$\vec{v}$	Velocity
V	Volume
z	Flow direction general coordinate

Greek

α	Void fraction
Δ	Difference indicator
ϵ	Permittivity
ϕ	Flux of conserved quantity
Ψ	Generalized state equation

Γ Volumetric source term
ψ Intensive conserved quantity
ρ Density
σ Surface tension or conductivity
$\underline{\underline{T}}$ Stress tensor
ω Frequency

Subscripts and Superscripts and Others

fg Saturated liquid-vapor difference
i Interfacial
k Refers to phase-k
ℓ Liquid
r Relative (between liquid and vapor)
s Refers to surface at interface
v Vapor

REFERENCES

Banerjee, S. and Lahey, R.T., Jr., [1984], "Advances in Two-Phase Flow Instrumentation," **Advances in Nuclear Science and Technology, 13**.

Barber, D.C., Brown, B.H., and Freeston, I.L., [1983] "Imaging spatial distributions of resistivity using applied potential tomography," **Elec. Lett., 19**, pg. 933-935.

Barber, D.C., and Brown, B.H., [1984] "Applied Potential Tomography," **J. Phys. E: Sci. Instrum., 17**, pg. 723-733.

Barber, D.C., and Brown, B.H., [1985] "Recent developments in applied potential tomography--APT," in **Proc. 9th Int. Conf. Info. Proc. Med. Imaging**, Washington, D.C.

Bates, R.H.T., Mckinnon, G.C., and Seager, A.D., [1980] "A limitation on systems for imaging electrical conductivity distributions," **IEEE Trans. Biomed. Eng., BME-27**, 7, pg. 418-420.

Bates, R.H.T., [1984] "Full-wave computed tomography Pt. 1: Fundamental theory," **IEE Proc. A, 131**, pg. 610-615.

Beck, M., and Williams, R., [1990] "Looking into Process Plant," **The Chem. Engr.**, 26 July, pg. 14-15.

Brown, B.H., Barber, D.C., and Seagar, A.D., [1985] "Applied potential tomography - clinical applications," **IEEE Conf. Publ. (Inst. Electr. Eng.)**, No. 257, pg. 74-78.

Brown, B.H., and Barber, D.C., [1987] "Electrical impedance tomography; the construction and application to physiological measurement of electrical impedance images," **Medical Prog. Through Technology, 13**, pg. 69-75.

Brown, B.H., Karatzas, T., Nakielny, R., and Clarke, R.G., [1988] "Determination of upper arm muscle and fat areas using electrical impedance measurements," **Clin. Phys. Physiol. Meas. (UK), 9**, 1, pg. 47-55.

Carey, G.F., and Oden, J.T., [1984] **Finite Element Computational Aspects: Vol. 3**, Prentice-Hall, Englewood Cliffs, N.J.

Cheng, K-S, Isaacson, D., Newell, J.C., and Gisser, D.G., [1989] "Electrode Models for Electric Current Computed Tomography," **IEEE-Trans. Biomed. Eng., 36**(9), pg. 918-924.

Dines, K.A., and Lytle, R.J., [1981] "Analysis of electrical conductivity imaging," **Geophysics, 46**, pg. 1025-1036.

Fuks, L.F., Isaacson, D., Gisser, D.G., and Newell, J.C., [1989] "Tomographic Images of Dielectric Tissue Properties," **IEEE-Trans. Biomed. Eng.**, in review.

Gilbert, P., [1972] "Iterative methods for the reconstruction of three-dimensional objects from projections," **J. Theoret. Biol., 36**, pg. 105-117.

Gisser, D.G., Isaacson, D., and Newell, J.C., [1987] "Current Topics in Impedance Imaging," **Clin. Phys. Physiol. Meas., 8**, Suppl. A, pg. 39-46.

Griffiths, H., [1987] "The importance of phase measurement in electrical impedance tomography," **Phys. Med. Biol., 32**, 11, pg. 1435-1444.

Hestenes, M.R., and Stiefel, E., [1952] "Methods of Conjugate Gradients for Solving Linear Systems," **J. Res. NBS, 49**, 6, pg. 409-436.

Henderson, R.P., and Webster, J.G., [1978] "An Impedance camera for spatially specific measurements of thorax," **IEEE Trans. Biomed. Eng., BME-25**, pg. 250-254.

Hewitt, G.F., [1978], **Measurement of Two-Phase Flow Parameters**, Academic Press.

Huang, S.M., Plaskowski, A.B., Xie, G.C., and Beck, M.S., [1989] "Tomographic Imaging of Two-Component Flow using Capacitance Sensors," **J. Phys. E: Sci. Instrum., 22**, pg 173-177.

Isaacson, D., [1986] "Distinguishability of Conductivities by Electric Current Computed Tomography," **IEEE Med. Imaging MI-5**, 91-95.

Isaacson, D., and Cheney, M., [1990] "Current Problems in Impedance Imaging," in **Inverse Problems in Partial Differential Equations**, D. Colton, R. Ewing, and W. Rundell, Eds., SIAM, Philadelphia.

Ishii, M., [1971]. "Thermally Induced Flow Instabilities in Two-Phase Mixture in Thermal Equilibrium," PhD Thesis, Georgia Institute of Technology.

Ishii, M., [1975]. **Thermo-Fluid Dynamic Theory of Two-Phase Flow**, Eyrolle, Paris.

Jones, O.C., Jr. and Delhaye, J.M., [1976], "Transient and Statistical Measurement Techniques for Two-Phase Flows: A Critical Review," **Int. J. Multiphase Flow, 3**, 89-116.

Kagawa, Y., Murai, T., and Matsumoto, O., [1983] "Finite element iterative technique for determining the interface boundary between Laplace and Poisson domains--characteristic analysis of field effect transistor," **Int. J. Numer. Methods Eng.**, **19**, pg. 315-329.

Kardous, G., [1987] "Etude de la distribution de la sensibility d'un systeme circulaire multi-electrodes en vue de la reconstruction d'images d'impedance bio-electrique," PhD Thesis, Institute National des Sciences Appliquees de Lyon, Villeirbanne, France.

Kim, Y., Webster, J.G., and Tompkins, W.J., [1983] "Electrical impedance imaging of the thorax," **J. Microwave Power**, **18**, 3, pg. 245-257.

Kim, Y., Tompkins, W.J., and Webster, J.G., [1982] "Medical body imaging using electrical impedance and nonlinear reconstruction," **Ann. Northwest Bioeng. Conf.**, **10**, pg. 298-303.

Kohn, R.V., and Vogelius, M., [1987] "Relaxation of a Variational Method for Impedance Computed Tomography," **Comm. Pure Appl. Math.**, **40**, pg. 745-777.

Kohn, R.V., and McKenney, A., [1989] "Numerical Implementation of a Variational Method for Electrical Impedance Tomography," Courant Institute of Mathematical Sciences, private communication.

Kocamustafaogullari, G., [1971]. "Thermo-Fluid Dynamics of Separated Two-Phase Flow," PhD Thesis, Georgia Institute of Technology.

Lin, T.F., Block, R.C., Lahey, R.T., Jr., Jones, O.C., Jr. and Murase, M., [1985], "Measurement of Flow in a Horizontal Pipe Using the Pulsed Photon Activation Technique," **Nucl. Sci. Eng.**, **91**, 3.

Murai, T., and Kagawa, Y., [1985] "Electrical impedance computed tomography based on a finite element model," **IEEE Trans. Biomed. Eng.**, **BME-32**, 3, pg. 177-184.

Murai, T., and Kagawa, Y., [1986] "Boundary element iterative techniques for determining the interface boundary between two Laplace domains-a basic study of impedance plethysmography as an inverse problem," **Int. J. Numer. Methods Eng. (GB)**, **23**, 1, pg. 35-47

Newell, J.C., Isaacson, D., and Gisser, D.G. [1989] "Rapid Assessment of Electrode Characteristics for Impedance Imaging," **IEEE-Trans., Biomed. Eng.**, in press.

Newell, J.C., Gisser, D.G., and Isaacson, D., [1988] "An Electric Current Tomograph," **IEEE-Trans. Biomed. Eng.**, **35** (10), pg. 828-833.

Nakayama, K., Yagi, W., and Yagi, S., [1981] "Fundamental study on electrical impedance plethsmography," in **Proc. Vth Int. Conf. Elect. Bio-Impedance**, Tokyo, August, pg. 99-102.

Pfeiler, M., [1981] "New development in computed tomography with reference to computed tomographic non-x-ray processors, [Neiere entwicklungen der computertomographie (unter einbeziehung computertomographischer nicht-Röntgenverfahren)]," **Röentgenpraxis (FRG), 34**, 1, pg. 3-13

Price, L.R., [1979] "Electrical impedance computed tomography (ICT): a new CT imaging technique," **IEEE Trans. Nucl. Sci. (USA), NS-26**, 2, pg. 2736-2739.

Pfeiler, M., and Steiner, K., [1982] "Computer tomographic methods using different information carriers," **J. Belge. Radiol., 65**, 2, pg. 95-102.

Powell, H.M., Freeston, I.L., and Barber, D.C., [1985] "Impedance imaging using a linear electrode array," **IEEE Conf. Publ. (Inst. Electr. Eng.)**, No. 257, pg. 88-92.

Sakamoto, K., and Kanai, H., [1983] "A fundamental study of an electrical impedance CT algorithm," in **Proc. Vth Int. Conf. Elect. Bio-Impedance**, Tokyo, August, pg. 349-352.

Santosa, F., and Vogelius, M., [1988] "A Backprojection Algorithm for Electrical Impedance Imaging," Institute for Physical Science & Technology, Univ. Maryland, Tech. Note BN-1081, July.

Seagar, A.D., Yeo, T.S., and Bates, R.H.T.,[1984] "Full wave computed tomography, part 2: Resolution limits," **Proc. IEE, part A, 131**, pg. 616-622.

Seagar, A.D., Barber, D.C., and Brown, B.H., [1987] "Electrical Impedance Imaging," **IEE Proc. 134**, Pt. A, No. 2, pg. 201-210.

Shomberg, H., and Tasto, M., [1981] "Reconstruction of spatial resistivity distribution," Phillips GMDI, Hamburg, Germany (FRG), MS-H 2715/81.

Smith, D.N., [1985] "Determination of impedance using numerous simultaneous currents (DINSC) - system design and practical applications," **IEEE Conf. Publ. (Inst. Electr. Eng.)**, No. 257, pg. 69-73

Starzyk, J.A., and Dai, H., [1985] "Element evaluation in the resistive networks," **Midwest Sym. Circuits Syst., 28**, pg. 178-181

Tarassenko, L., and Rolfe, P., [1984] "Imaging spatial distributions of resistivity - an alternative approach," **Electron. Lett., 20**, 14, pg. 574-576.

Trusdell, C., and Toupin, R., 1960. "The Classical Field Theories," in **Handbuch der Physik**, S. Flugge, Ed., **3**, 1.

Vernier, P., and Delhaye, J.M., 1968. "General Two-Phase Flow Equations Applied to the Thermodynamics of Boiling Nuclear Reactors," **Energie Premaire, IV**, 1-2.

Wexler, A., Fry, B., and Neiman, M.R., [1985] "Impedance-computed tomography algorithm and system," **Appl. Opt., 24**, 23, pg. 3985-3992.

Woo, H.W., and Kim, Y., [1986] "A medical imaging system with electrical impedance," **Proc. Ann. Conf. IEEE Eng. Med. Biol. Soc., 8,** 1, pg. 343-346.

Yorkey, T.J., [1986] "Comparing reconstruction methods for electrical impedance tomography," Ph.D. Thesis, Dep. Elec. Comput. Eng., Univ. Wisc., Madison, WI 53706, August.

Yorkey, T.J., and Webster, J.G., [1987] "A comparison of impedance tomographic reconstruction algorithms," **Clin. Phys. Physiol. Meas., 8,** suppl. A, pg. 55-62.

Yorkey, T.J., Webster, J.B., and Tompkins, W.J., [1985] "Errors caused by contact impedance in impedance imaging,' **Proc. Ann. Conf. IEEE Eng. Med. Biol. Soc., 7,** 1, pg. 632-637

Yorkey, T.J., Webster, J.G., and Tompkins, W.J., [1986] "An optimal impedance tomographic reconstruction algorithm," **Proc. Ann. Conf. IEEE Eng. Med. Biol. Soc., 8,** 1, pg. 339-342.

Yorkey, T.J., Webster, J.G., and Tompkins, W.J., [1987a] "An improved perturbation technique for electrical impedance imaging with some criticisms," **IEEE Trans. Biomed. Eng., 34,** 11, pg. 898-901.

Yorkey, T.J., Webster, J.G., and Tompkins, W.J., [1987b] "Comparing reconstruction algorithms for electrical impedance tomography," **IEEE Trans. Biomed. Eng., 34,** 11, pg. 843, 852.

SESSION 4 – "ASYMPTOTIC SOLUTIONS"

Moderator: Andrew Terzuoli

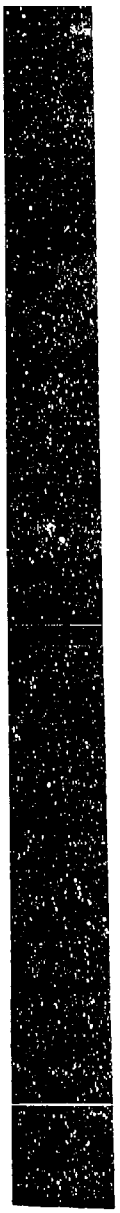

Primitive Target Validation for the Signature Prediction Tools Software Package

D. J. Young, A. J. Terzuoli Jr.
Air Force Institute of Technology
Wright-Patterson AFB Ohio

February 18, 1991

1 Abstract

The Signature Prediction Tools software package[1] is the part of the Synthetic Aperture Radar (SAR) prediction Tool (SarTool) that generates radar signature predictions of objects such as ground vehicles and aircraft. SarTool employs the geometric representations of these objects and the parametric descriptions of sensors to calculate the full polarimetric, complex-valued radar signature data of individual scattering components through the use of physical optics models of radar backscattering. SarTool is a major component in a model-based vision concept of constructing synthetic SAR images of objects and comparing these images with actual sensor data of the real objects for target identification.

This paper[2] presents a technique to validate the individual scattering components of SarTool. The technique consists of using SarTool to calculate the signature data of primitive radar targets which are constructed from the scattering components and then comparing this data to the scattering data of the well known physical optics (PO) equations for these radar targets with the same input parameters. These targets consist of flat plates, right dihedral and square trihedral corner reflectors, and tophats. The results of the validation show close agreement to the PO equations for the circular plate target, the scattering components consisting of the double bounce tophat, triple bounce trihedral, and single bounce magnitude for the rectangular plate.

[1] Sensor Algorithm Research Expert System. Contract F33615-87-C-1404, The Analytic Sciences Corporation.

[2] This research is sponsored by WRDC/AARA WPAFB OH

2 Introduction

The only target recognition system currently in use is the human which employs photo or television visual imaging systems to discern targets from the surrounding terrain. The limitations of a human target recognition system when presented with images generated at wavelengths other than optical frequencies, produce a requirement for an automatic target recognition system which is a part of the Synthetic Aperture Radar (SAR) or infrared imaging systems. A proposed automatic target recognition system for SAR systems employs a computer program that compares an unknown SAR image to a database of SAR target images to find a match. The problem with this system is the acquisition of the target image database.

A proposal to solve this problem is the Model Based Vision (MBV) concept, which is based on the calculation of synthetic SAR target image displays by a computer program that simulates the SAR sensor and the target/background radar returns. The first part of the MBV system is the construction of a three dimensional computer model of a radar target by a solid modeling computer aided design (CAD) package. This model is constructed of radar reflectors from a list that consists of single bounce reflectors; flat plate, cone, ellipsoid, ogive, and torus, as well as multiple bounce interactions; dihedral, trihedral, tophat, and cavity. From the model, which is a database of reflectors and their position, a computer program calculates the polarimetric complex radar cross section (RCS) in matrix form with respect to the angles from the SAR sensor position for each of these simple reflectors. The RCS is then used to calculate the magnitude and phase of the response of each reflector and places this response on the SAR image with respect to the range and range-rate coordinate frame [7]. This synthetic image is a database entry of the target model at one aspect angle. A target image database is then constructed from the computer models of all possible targets by calculating synthetic SAR image for a multitude of aspect angles.

The one key requirement for the success of the MBV concept is the correct implementation of the physical optics (PO) equations for the single and multiple bounce reflectors. This paper validates the implementation of the polarimetric PO equations in the Signature Prediction Tools software package for a set of simple radar targets consisting of flat plates, dihedrals, trihedrals, and top hats.

3 Validation

Since the procedure for validating radar targets has not been defined explicitly in the radar community, this validation effort is limited to:

1. PO Equations. The research for validating the PO approximation for the simple targets has already accomplished by many researchers. These PO equations [6], [3], [4], [2], [5], [1] are encoded in FORTRAN programs that

generate data in the form of RCS and phase vs. aspect angle for differing polarizations for the primitives listed above.

2. SarTool Data. Primitives in SarTool are constructed to duplicate the parameters in the PO equations data set. The resulting data from SarTool will be presented in the same format as the PO data.

3. Analysis. The plots of the PO and SarTool for the same polarization are superimposed. This technique shows the similarities and differences between the PO equations and the SarTool implementation for the same input parameters.

4 Results

The orientation and conventions of the sensor viewing angles are shown in figures 1- 4. Figures 5 and 7 show that the PO equations for the RCS of these flat plates agree perfectly with the SarTool calculations. Figure 6 reveals differences in the phase calculations in SarTool for the rectangular plate when complared to the PO equations. The dihedral RCS plots in figures 9 and 11 also reveal differences in the implementation of the PO equations and SarTool. The elevation viewing angle ($\theta = 55.0$ degrees) corresponds to the maximum response of a square trihedral. Figures 13 and 15 show a near perfect agreement in the PO and SarTool equations for the trihedral. The tophat plots in figures 17 and 19 show a sizeable difference in the SarTool response and the PO equations. Investigation into this problem reveals that SarTool does not add the single bounce response of the base of the tophat to the rest of the scattering components.

5 Conclusions

This paper presents the preliminary work in the validation of the SarTool computer package. The conclusions of the validation of the primitive targets are presented for SarTool version 7.03.

5.1 Flat Plates

The analysis on the rectangular and circular plates shows that the RCS and phase of the circular plate agrees with the PO equations available in the literature. The phase characteristics of the rectangular plate do not agree with the PO equations, but the magnitude does agree. This difference in the phase especially at the broadside aspect angle reveals a possible problem with the implementation of the PO equations for polygonal plates in SarTool.

5.2 Dihedral

The analysis of the dihedral at the maximum return angles $\theta = 90$ (89.9) degrees and $\phi = 45$ degrees agrees with the PO equations. The differences in the RCS and phase plots can be attributed to the addition of the two rectangular plate responses which have incorrect phase relationships to the double bounce dihedral response.

5.3 Trihedral

The response of the trihedral at maximum response angle $\theta = 55$ degrees shows very close agreement in the plots of SarTool and PO equations for the RCS for phi angles from 12 to 78 degrees. At this theta angle and phi angles, the triple bounce trihedral scattering response dominates the total target RCS. These plots reveal an agreement in the triple bounce equation implementation for SarTool. Once again, the phase relationship of the flat plates combined with the three double bounce dihedral responses and the triple bounce response results in the small disagreement of SarTool and PO calculations.

5.4 Tophat

The failure of SarTool to calculate the flat plate response of the base disc of the tophat results in big disagreements with the PO equations. The section of the RCS plot where the double bounce tophat response dominates reveals a general agreement of SarTool with the PO equations. Further study of this problem is also required for a validation of this primitive.

References

[1] Balanis, Constantine A. *Advanced Engineering Electromagnetics*. New York: John Wiley and Sons, Inc., 1989.

[2] Blejer, Dennis J. *Physical Optics Polarization Scattering Matrix for a Top Hat Reflector*. Unpublished report, Lexington MA: MIT Lincoln Laboratory.

[3] Blejer, Dennis J. *Physical Optics Polarization Scattering Matrix and Impulse Response of a Right Dihedral Corner Reflector*. Unpublished report No. 47PM ADT-0052, Lexington MA: MIT Lincoln Laboratory, 1986.

[4] Blejer, Dennis J. *Physical Optics Polarization Scattering Matrix of a Square Trihedral Corner Reflector*. Unpublished report No. 47PM-ADT-0059, Lexington MA: MIT Lincoln Laboratory, 1987.

[5] Blejer, Dennis J. *Scattering Matrix Transformations for Polarimetric Target Modeling*. Unpublished report No. 47PM-ADT-0057, Lexington MA: MIT Lincoln Laboratory, 1987.

[6] Knott, Eugene F. and others. *Radar Cross Section*. Norwood, MA: Artech House, Inc., 1985.

[7] Pinto, Robert and others. *Sensor Algorithm Research Expert System, Interim Technical Report, Volume 8*. Contract F33615-87-C-1404, Reading MA: The Analytic Sciences Corporation, May 1989.

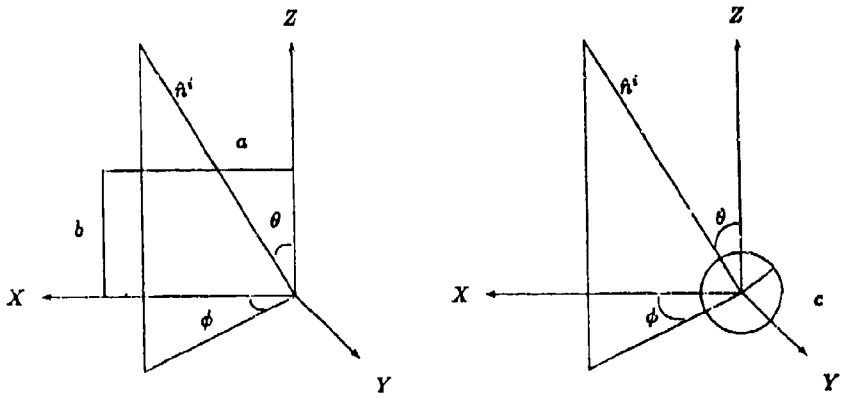

Figure 1: Rectangular and Circular Plates

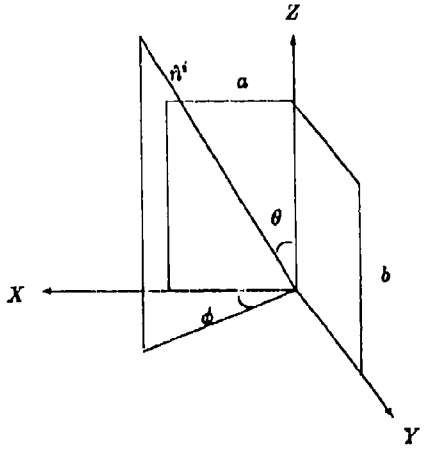

Figure 2: Right Dihedral

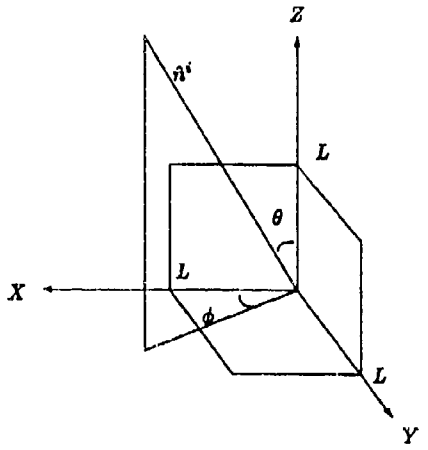

Figure 3: Square Trihedral

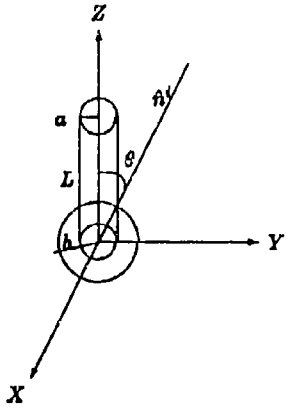

Figure 4: Tophat

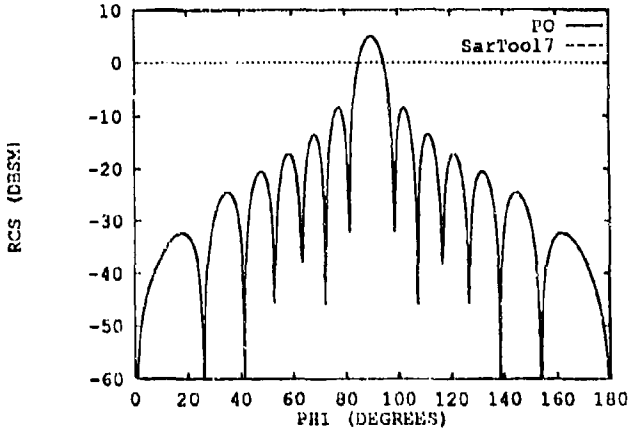

Figure 5: RCS RECT. PLATE A=10 CM B=15 CM F=10 GHz THETA=89.9 DEG

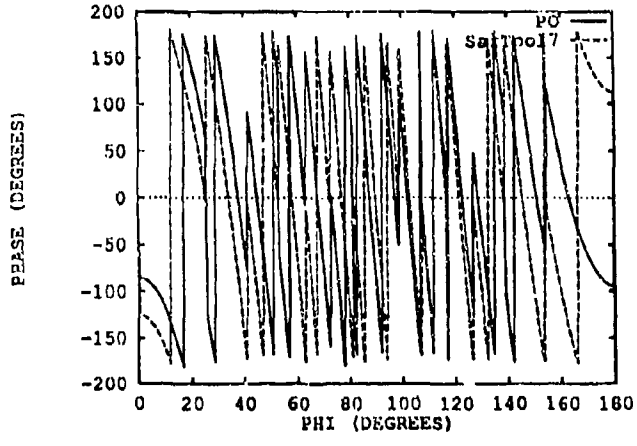

Figure 6: PHASE RECT. PLATE A=10 CM B=15 CM F=10 GHz THETA=89.9 DEG

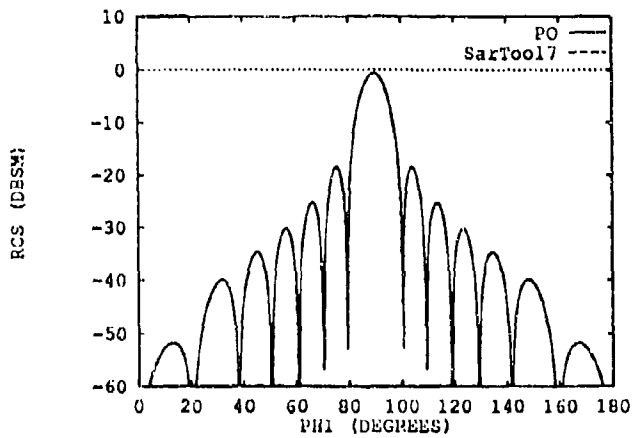

Figure 7: RCS CIRC. PLATE RADIUS=5 CM F=10 GHz THETA=89.9 DEG

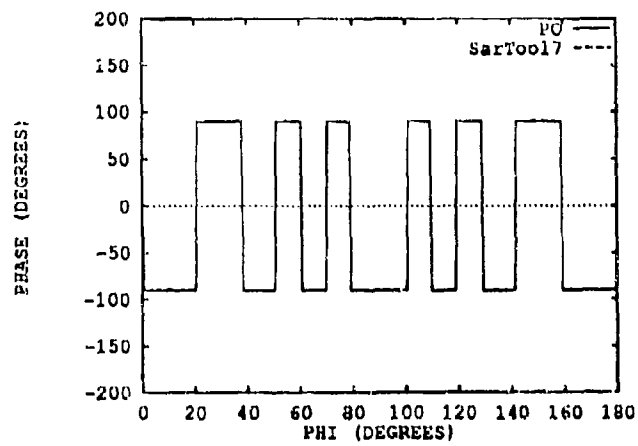

Figure 8: PHASE CIRC. PLATE RADIUS=5 CM F=10 GHz THETA=89.9 DEG

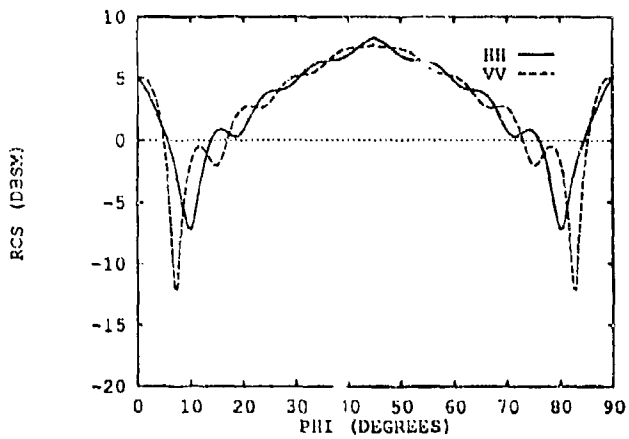

Figure 9: RCS RT DIHEDRAL A=10 CM B=15 CM F=10 GHz THETA=89.9 DEG PO EQNS

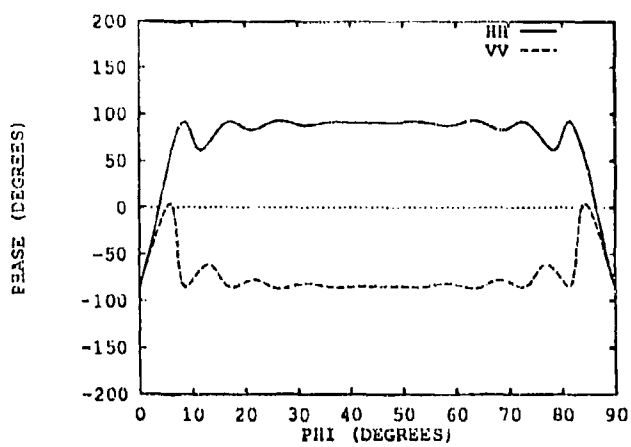

Figure 10: PHASE RT DIHEDRAL A=10 CM B=15 CM F=10 GHz THETA=89.9 DEG PO EQNS

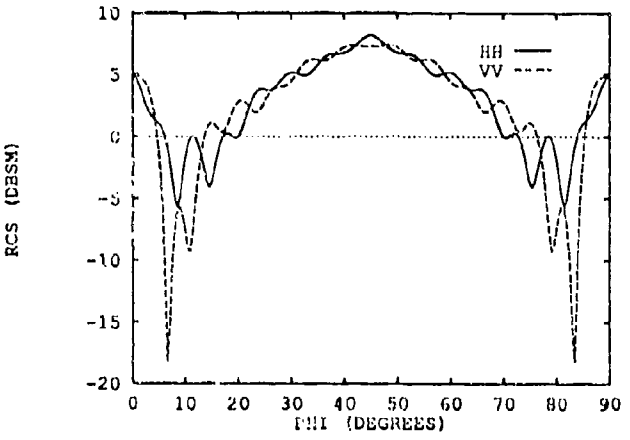

Figure 11: RCS RT DIHEDRAL A=10 CM B=15 CM F=10 GHz THETA=89.9 DEG SarTool7

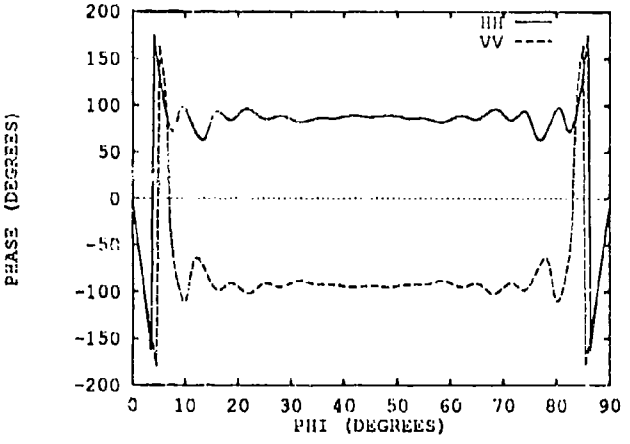

Figure 12: PHASE RT DIHEDRAL A=10 CM B=15 CM F=10 GHz THETA=89.9 DEG SarTool7

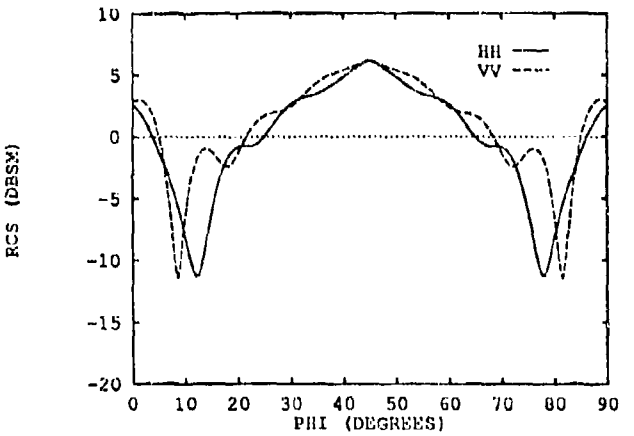

Figure 13: RCS SQ TRIHEDRAL L=10 CM F=10 GHz THETA=55.0 DEG PO EQNS

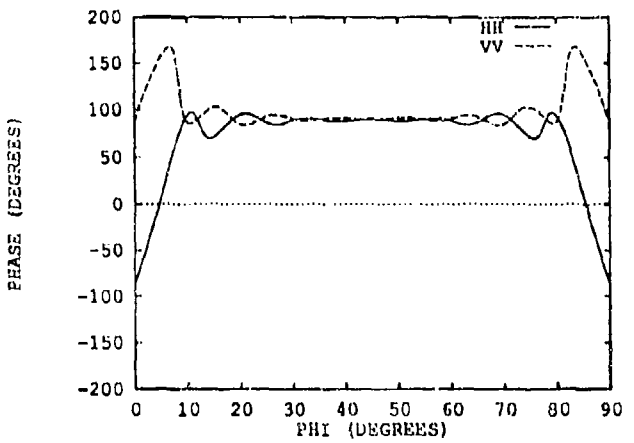

Figure 14: PHASE SQ TRIHEDRAL L=10 CM F=10 GHz THETA=55.0 DEG PO EQNS

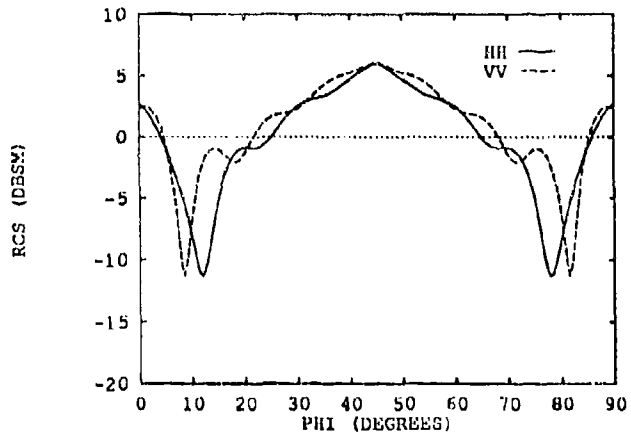

Figure 15: RCS SQ TRIHEDRAL L=10 CM F=10 GHz THETA=55.0 DEG SarTool7

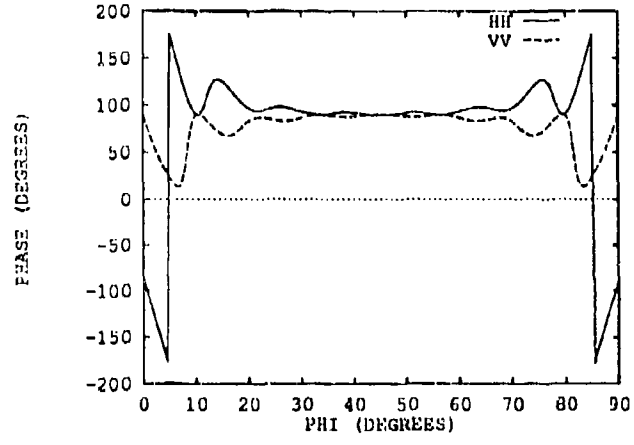

Figure 16: PHASE SQ TRIHEDRAL L=10 CM F=10 GHz THETA=55.0 DEG SarTool7

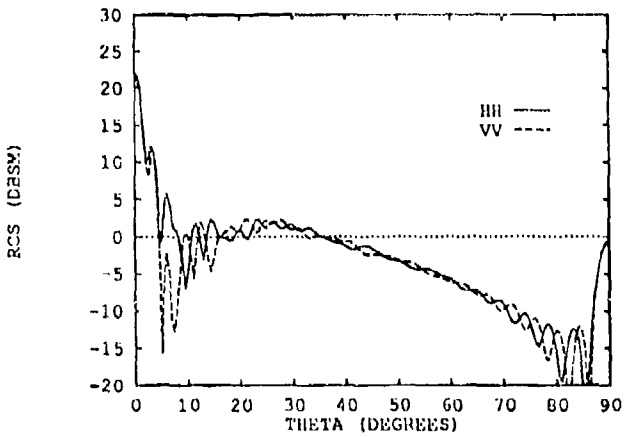

Figure 17: RCS CIRC BASE TOPHAT A=10.16 CM B=20.32 CM L=20.32 CM F=10 GHz PO EQNS

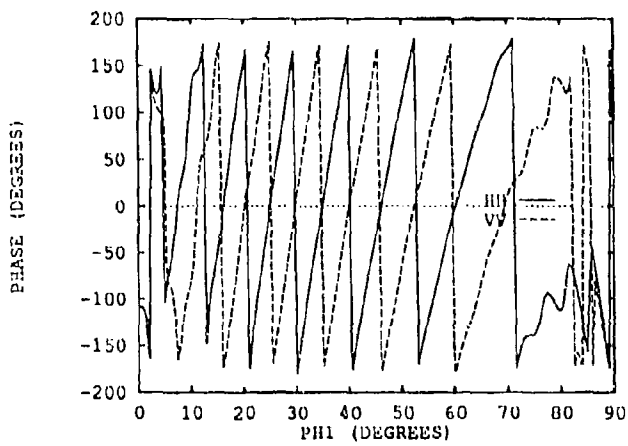

Figure 18: PHASE CIRC BASE TOPHAT A=10.16 CM B=20.32 CM L=20.32 CM F=10 GHz PO EQNS

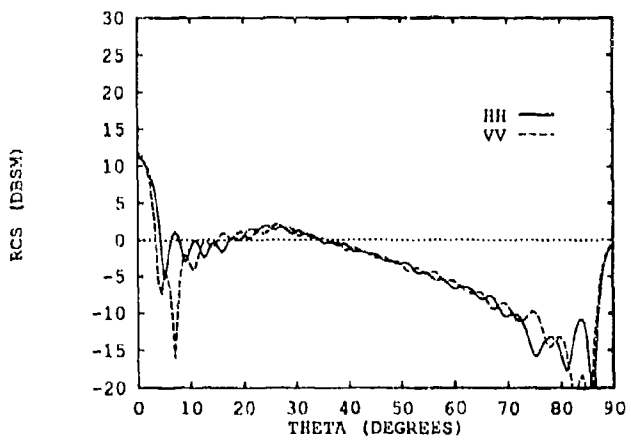

Figure 19: RCS CIRC BASE TOPHAT A=10.16 CM B=20.32 CM L=20.32 CM F=10 GHz SarTool7

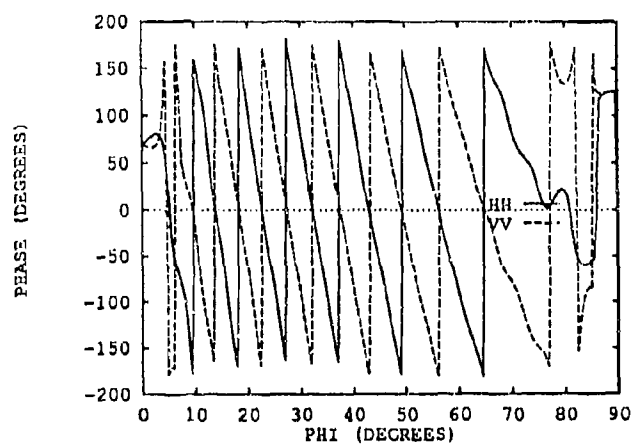

Figure 20: PHASE CIRC BASE TOPHAT A=10.16 CM B=20.32 CM L=20.32 CM F=10 GHz SarTool7

High Frequency Scattering Code in a Distributed Processing Environment *

S. Suhr, A. J. Terzuoli Jr., G. B. Lamont
School of Engineering
Air Force Institute of Technology
Wright-Patterson AFB OH 45433-6583
(513) 255-3576

Abstract

This paper describes the transformation of serial computer codes for use in a concurrent processing environment, with in-progress results of the specific task of porting the NECBSC sequential FORTRAN source code to the intel iPSC©/2 and iPSC©/860 hypercubes. Improved efficiency and effectiveness should result from the use of concurrent processing on multiple processors. The sequential code is examined and modified in stages in an attempt to minimize the changes to the program interface and output, while maximizing performance. At each step of the transformation, the modified code is executed, efficiencies compared to those of previous steps, and effectiveness compared to VAX serial benchmarks.

1 Introduction

The Air Force is conducting research into quicker, more cost effective methods for predicting the electromagnetic scattering from complex objects of interest. One of the computer codes currently in use is the Numerical Electromagnetic Code - Basic Scattering Code (NECBSC)[1]. This code was developed for the VAX minicomputer and written in FORTRAN-77 for portability to most standard mainframe computers. However, even on potent mainframes, any but the simplest of problems takes considerable execution time (~hours), at a relatively high cost. This research centers on the modification of the NECBSC for execution by a distributed processing computer. Before we examine this specific problem, we need to examine the generic problem of porting existing serial code to concurrent processing environments.

*This work is sponsored by Jeffrey L. Fath of the Target Recognition Branch at the Wright Laboratory(WL/AARA), Wright-Patterson AFB OH

[1]NECBSC was developed by R.J. Marhefka and J.W. Silvestro of the Ohio State University ElectroScience Laboratory, Columbus OH.

2 Concurrent Computers

Characteristics of the target computer have a large impact on the approach taken for decomposition of the source program. Concurrent processing computers come in many varieties. Single instruction, multiple data (SIMD) computers have multiple processors each with identical code, working on different data elements in "lock-step". These machines are very appropriate for problems involving matrix/array solutions such as finite-difference methods where each processor would calculate the results for a single location in the grid. Multiple instruction, multiple data (MIMD) computers have processors which may operate independently on different parts of the problem and/or different parts of the data.

When the computer has a single block of memory addressable by all of the processors, it is referred to as "shared-memory". Each processor can freely exchange data with the others through the intervening memory. This type of architecture lends flexibility to the programmer at the expense of hardware complexity/cost and fixed overhead due to memory contention and address decoding time. When each processor has a dedicated block of memory to which it has exclusive access, it is called "distributed memory". This architecture is simpler, but may require data to be passed between the processors via messages, imposing overhead. The distributed-memory architecture is appropriate for tasks that involve routines with large amounts of processing relative to data sharing.

Given a distributed memory MIMD computer, the physical interconnection topology of the processors has a large impact on the suitability of the machine to the task. Each processor can be connected to all others, but the complexity of the hardware for even tens of processors is impractical. A four interconnection scheme where each processor can communicate with each of four neighbors is ideal for two-dimensional problems, but communications in a problem with three or more dimensions become burdensome. The hypercube is a compromise architecture with a high degree of flexibility. A hypercube of dimension d has 2^d processors nodes each connected to d neighbors. This interconnection scheme becomes unwieldy when the dimension exceeds eight (256 nodes) or so. Stated without proof: the hypercube architecture has considerable flexibility in mapping the processors to different types of problem-spaces[2, 49].

3 Program Decomposition

From a user's point of view, a vectorizing compiler is the simplest way to adapt an existing program to run on a concurrent computer. The details of the conversion are hidden from the user by the compiler itself. The compiler attempts to identify sections of the code that are appropriate for predetermined forms of concurrent computation. Some experts believe that vectorizing compilers produce code that is more efficient than that of skilled programmers [6, 237]. This

may be true for the limited concurrency of multiprocessor computers such as the Cray XMP, but a compiler cannot make the sweeping changes that a programmer could implement for more complex architectures [2, 27], and a compiler does not generally run a program with actual data, and this can affect performance.

There are two basic methods of manual program translation: domain decomposition and control decomposition. Domain decomposition consists of loading identical programs on each node and segmenting the data among the processors, allowing each to perform the task on part of the data. This method is particularly effective when there are loops in the serial program and the data in each loop is not dependent on the results of earlier iterations of that loop. If there is no need for interprocessor communication during the calculations, the overhead is minimized and high efficiencies are achievable. Presuming one has a very large data set, one attempts to divide the data into equal sections and map each to a different node. This also would seem to be the correct approach when the data-set is small, but the data-transfer time to load different data sets may negate any parallelism gains, resulting in an inefficient configuration.

Control decomposition consists of dividing the program into sections, and putting different code on each processor. If there are multiple data to be processed, a pipeline can be effected, allowing concurrent processing and speedup. However, because a large data set must pass through all the nodes, there is a communications penalty which negates potential speedup unless the computations are very time-consuming relative to the data-passing required.

Once control-decomposition is chosen, a problem can be mapped to the nodes in two fundamental ways. The first is a static configuration, where all the routines are divided among the nodes and remain fixed throughout the lifetime of the program. The second is where "slave" nodes are loaded with programming and data as needed by one or more "master" nodes. This type of configuration is most appropriate when the selection and order of execution of the various pieces of code cannot be determined until run time, especially when all the routines cannot be loaded on a node simultaneously due to memory constraints. The master-slave approach is one of the fundamental forms of dynamic load balancing.

There are many tools available to aid in the decomposition, analysis, and evaluation of parallel programming efforts. One tool which assists in FORTRAN code conversion is FORGE^{TM}, an analysis tool available from Intel/Pacific-Sierra Research Corp. FORGE^{TM} creates a database of program and data entities and displays them in coherent formats to the programmer/analyst [3]. Other tools range from conventional automated flowchart creators, to sophisticated concurrent visual debugging systems [5].

Debugging concurrent programs is quite a bit more difficult to accomplish than ordinary sequential programs. Since different processes are occurring simultaneously and independently, it is possible to have a properly executing program give different answers on consecutive runs using the same input data. This is because the processors could be finishing in a different order after each

run or they could be finishing at the same time and competing for communications bus permission, the transmitted data simply arriving in a different order for each run. If the order of results is significant to the algorithm, "random" results may occur. Thus, in a complex problem, little can be directly deduced about the specific causes of a case of erratic behavior. The difficulty of the problem is further complicated by a manifestation of the Heisenburg uncertainty principle. Trying to actively record the behavior and timing of system events influences the results obtained. Passive event-recording systems are relatively non-intrusive and available, but they only store limited amounts of data [5, 594].

4 Measures of Merit

There are four major standards that will be used to evaluate the desirability of this concurrent processing implementation: speedup, efficiency, accuracy, and relative cost-efficiency.

Speedup is the ratio of the execution time in the sequential implementation to the fastest parallel implementation (n nodes) and therefore is a measure of merit of the success of the concurrent implementation vs the serial version (normal maximum: n). Efficiency is speedup divided by the number of processors used. Efficiency is the proportion of time that the average node is spending to further the task at hand, relative to the serial implementation, with a theoretical maximum of 1 (which requires a speedup of n). Computationally idle time during overhead/message passing functions degrade this result.

Accuracy is used in a normal subjective sense. In general: does the implementation produce results that match the actual RCS? For the purposes of these investigations, accuracy refers to the number of digits of accuracy, relative to NECBSC run on a VAX computer. Relative cost-efficiency is speedup normalized by the ratio of the operating (or purchase) costs of the computers being compared.

5 Generic Porting to MIMD Computers

The first task in porting a program to any computer is to understand the problem. On concurrent computers, the structure of the code and data is especially important. As discussed earlier, different combinations of data and code topology require different decomposition approaches. The previously mentioned FORGE^{TM} analysis tool is a suitable analysis tool for FORTRAN source code destined for Intel hypercubes.

Based on the code analyses, target computer architecture, and other less tangible factors one chooses a basic form for the decomposition (control or domain) and proceeds. As alluded to previously, control decomposition is nor-

mally used when there is little independence among the various data elements, the routines used for a given element cannot fit in the available memory, and/or the routines used vary depending on the data input. Domain decomposition is more appropriate for situations where different data elements may be processed independently, and the routines called are similar (or they can all reside simultaneously in each node's memory).

Given a generic decomposition method, in general, a host routine must be written which loads the node routine(s) and passes the input and output data to/from the individual nodes. The routines from the serial code must be divided, and control routines added to control the timing of their execution, the receiving and sending of data, and error handling. Extreme care must be taken to understand the changes made, or erratic results may occur which have no apparent cause.

6 The Task

The Air Force Institute of Technology and the Wright Laboratory have Intel iPSC©/2 and iPSC©/860 hypercubes. These computers are based on up to 128 interconnected nodes consisting of: an Intel 80386 or i860 microprocessor, a numeric coprocessor, a separate communications processor, and 8-16 Mbytes of memory. Each node can operate as an independent, self-contained computer, autonomously performing as many tasks as its memory will allow. In addition, it can communicate with its neighbors through the communications processor and interconnection network. This allows it to coordinate its activities, share data, and, if necessary, load/execute new programming in order to work on a different piece of a given problem. This hardware allows flexibility and high total throughput while maintaining relatively low cost.

The iPSC©'s nodes are also connected to a "front-end" 80386-based computer. The host has the responsibility of sending programming and data to each of the nodes, collecting any returned data, and serving as the conduit for all communications between the nodes and external entities such as the user, disk drives, and other computers.

On the iPSC©, if a node needs to use data that is resident on a different node, it must first request the data. Then the possessing node must explicitly receive and interpret the request, and be programmed to retrieve and send the requested data back to the requesting node in a like manner. The requesting node must, again, explicitly receive the data [1, 32]. The overhead incurred in setting up an appropriate data-link can be a hundred times longer than the time for a typical sequential FORTRAN statement execution.

The code to be modified is NECBSC, a high-frequency scattering code initially written to evaluate antenna placement on the space station. As such, it allows multiple objects, antennas, and radiation sources to interact. It makes far- or near-field calculations of the energy reaching a specified observation point

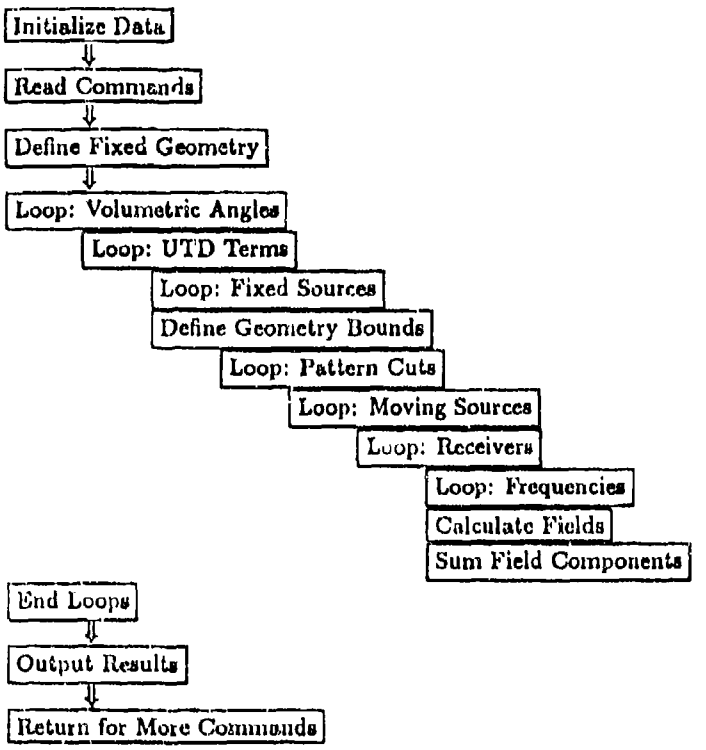

Figure 1: Block Diagram of NECBSC

from specified angles, or can compute antenna coupling. The code traces the path from each far-zone receiving direction backwards through each possible scattering path to each of the sources. It also has the capability to measure the total near-zone fields for a series of points along a specified path through space. Antenna coupling is accomplished similarly with the receiver antenna defined in terms of its free-field antenna pattern, the intensity of the fields arriving in a given direction modified by the appropriate gain. Shadowing is taken into account, and diffraction terms are calculated to smooth discontinuities.

The NECBSC code is organized with a lengthy input parsing routine followed by a computation section composed of a series of nested do-loops, with the outer loops varying the pattern points. Inner loops calculate all the relevant scattering terms for all of the objects and sources. A block diagram is included as Figure 1 [4, 24]. Input is from a disk file containing two-letter command codes, followed

by the required data for that object, pattern, choice, etc. Multiple "runs" can be stacked in the input deck to allow unattended continuous computing Output is normally tabular in format with header information which echoes the input deck in a presentable format. This standard output can be sent to the screen, printer or disk. Optionally, a file of plot data in a standard binary form can be selected.

Given the iPSC© computers as the target environment and NECBSC as the software to be translated, the task is to distribute the problem among the processors such that the processors are efficiently and continually tasked (maximum efficiency), with a minimum of modification to the inherent structure of NECBSC and maintaining the program accuracy and interface.

7 Methodology

For this task, an incremental approach to modification is indicated, in order to minimize the potential for introducing errors into the algorithm. After each successive stage, several of the test cases provided with the NECBSC documentation are executed and timed for comparison. The generic stages of the analysis/modification are shown below:

- Run sequentially on VAX & iPSC© host.
- Run sequentially on single iPSC© node.
- Develop host control program.
- Incorporate node timing routines.
- Divide domain by sweep angle, output data into n files, postprocess multiple data files on host.

Optional, depending on previous performance:

- Output individual lines of data via messages, concurrent insert sort on host.
- Burst transmit output data, sort on host or free node.
- Passive balancing - rotation of starting index between nodes.
- Overt load balancing: Message sent on node completion, free node works backwards on working node's data, etc.

8 In-Progress Results

The serial NECBSC code compiled and ran successfully on a VAX, the iPSC©/2 host, and a single node of each of the /2 and the /860 computers. The only anomalies were that the timing routines were incompatible with all these computers, and the iPSC©/860 32 bit precision is better than the VAX example runs in the documentation. Formal timing runs will be completed when the basic parallel implementation is operational.

An attempt to analyze NECBSC with FORGE^{TM} was disappointing. The manual claims it is compatible with FORTRAN 77, yet will not allow the inclusion of data statements with complex arguments–which are allowed by all of the compilers used to date. The offending routines must be excluded or modified to conform to FORGE^{TM} F77 before a database can be created. Even so, FORGE^{TM} has another bug that causes a core dump when processing some of the larger NECBSC files (6 files, largest: 218KB), presumably somehow related to the code length or memory requirements.

The basic host program development is almost complete, with run-time user input for the name of the input file, timing routines, and message passing to the nodes implemented. Only the output data-file collation routine remains to be written to complete a basic implementation. The node routines contain most of the original NECBSC routines with message passing and timing routines added and the outer loop variable indexed by node number, creating separate output files for each node.

Perhaps the most disappointing result to date is that indexing the outer loop which spans the "volumetric angles" does not result in evenly divided output files, as it should. The file from the first node is, consistently, approximately five times as large as the remaining files. Further investigation disclosed that the azimuth sweep index was incremented in a loop three levels deeper in the nest ("pattern cuts" in Fig 1). Dividing the work at this point in the code was successful, but the output files were indexed by other variables, depending on the input deck; a simple fix was not evident.

Due to the large number of modifications apparently necessary, and the rising risk of introducing an error into the code, we elected to back up a step and introduce the indexing in the command processor section. This involves modifying several routines which initialize the indexed variables such that each node processes only the data points desired. With this approach, the input deck for each node is modified to request only a portion of the problem be computed on each node. The indexing is such that each successive angular increment is on a different node in an attempt to divide up any computationally intensive regions. An appropriate method for decomposition of the antenna coupling option remains.

A lesser problem is that the Green Hills F77 compiler has no capability for recording elapsed time on the host. Getting a true elapsed time would involve an assembly-language or C routine, which may not be portable between machines.

The timing data will therefore reflect only the process time on the host, not the total elapsed time.

9 Conclusions

Concurrent computers and the iPSC© hypercubes have many ideosyncracies that have to be taken into account when writing or modifying code for them, but there are tools available to help in this process. One can code from scratch, take the domain- or control-decomposition approach to sequential program conversion, or allow a commercially-available vectorizing compiler to control the parallelization task. In the end, it is up to the individual programmer to analyze the problem, its data, and make the controlling decisions about how to effect the required parallelization. The specific task of modifying NECBSC for the AFIT and Wright Laboratory hypercubes is progressing, with an estimated completion date of 15 May 91.

References

[1] Beard, Andrew and Gary B. Lamont, "AFIT/ENG Intel Hypercube Quick Reference Manual Version 1.1." Class handout - EENG 689, School of Engineering, Air Force Institute of Technology (AU), Wright-Patterson AFB OH, 6 February 1990.

[2] Geoffrey C. Fox, et al. *Solving Problems on Concurrent Processors, Vol I*. Englewood Cliffs NJ: Prentice Hall, 1988.

[3] *iPSC©/2 and iPSC©/860 FORGE™ Users Guide (The FORGE™ User's Guide)*. Beaverton OR: Intel Scientific Computers, April 1990.

[4] Marhefka, R. H. and J. W. Silvestro. "Near Zone - Basic Scattering Code User's Manual with Space Station Applications." Preliminary Version, March 1989.

[5] McDowell, Charles E and David P. Helmbold. "Debugging Concurrent Programs," *ACM Computing Surveys*, 4:593–622 (December 1989).

[6] Polychronopoulous, Constantine D. "Loop Coalescing: A Compiler Transformation for Parallel Machines." In *The Proceedings of the 1987 International Conference on Parallel Processing*, pages 235–241, University Park PA: Penn State University Press, 1987.

SIMULATION OF SITE OBSTRUCTION EFFECTS ON THE PERFORMANCE OF A HIGH GAIN ANTENNA USING NEC-BSC2

A.M. Bucceri, J.C. Herper and E. Mertz
Unisys Defense Electronics
Great Neck, NY 11020

Abstract - Obstructions in the field of view of an antenna result in degraded sidelobe performance and loss of gain. The degradation is caused by antenna blockage and scattered fields. For obstacles larger than one wavelength in cross section these fields may be efficiently calculated using a combination of geometric optics and GTD/UTD as implemented in NEC-BSC2 code.

The evaluation of high gain antenna performance in the presence of obstacles is presented. Modelling techniques are discussed for a specified site and for antennas with large apertures. An example is presented which shows the effects of site modifications with simple radar absorbing materials. In addition, a computer graphic simulation is presented which shows the far-field pattern perturbations as the antenna is rotated in azimuth 360°.

Introduction - Modern radar applications often require high gain antennas with low sidelobe performance. However the placement of the antenna on a site with obstructions can severely degrade the realized antenna performance. Typically, for high gain antennas, this performance degradation can be attributed to obstructions in the near field which are large compared to wavelength. For these obstacles which are in the optical region, utilization of the Geometric Optics and Geometric Theory of Diffractions/Uniform Theory of Diffraction (GTD/UTD) are the most efficient computational approaches. These techniques have been implemented in the Numerical Electromagnetic Code - Basic Scattering Code (NEC-BSC2) developed at Ohio State University ElectroScience Laboratory and sponsored by NOSC.

NEC-BSC2 and NEC-MOM as well as other codes form the computational core for the antenna analysis workstation. Pre- and post-processing routines aid in generating input files and perform far-field pattern analysis and data reduction. The edit and graphic capabilities of the Apollo computer networked with the Alliant super-minicomputer as an interactive workstation permits efficient parametric studies for the realized antenna performance in a realistic site environment. Automated input file editing and run stream management generates a sequence of far-field calculations producing a striking visualization of the antenna performance as it is rotated through 360 degrees in azimuth.

Antenna Workstation Implementation - Techniques available for the solution to the scattering of electromagnetic fields by an object include: Geometric Optics (GO), Geometric Theory of Diffraction/Uniform Theory of Diffraction (GTD/UTD), Plane Wave Spectra (PWS), and the Method of Moments (MOM). These techniques rely on certain physical assumptions, each with advantages and disadvantages in its applicability to various classes of problems. Low frequency methods such as the Method of Moments are effectively used for objects (or sources) whose characteristic size is in the Rayleigh (small compared to wavelength) or Mie (resonant) regions. High frequency methods such a GTD/UTD are used for objects whose characteristic size is in the optical region (larger than a wavelength). Here input models for objects can be constructed from simple canonical shapes (plates, cylinders, etc).

NEC-BSC2 and NEC-MOM are among the "engines" for the antenna analysis workstation. The Apollo/Alliant computing environments are combined with the advantages of page editing, program control scripts, and graphics along with the significantly reduced execution times for computationally intensive simulations. An interactive workstation environment was implemented and is flow charted in Figure 1. Several "Shell" routines or scripts invoke utility programs for execution, data transfer and reduction, pattern analysis, and graphics. For example, the shell script used to generate a sequence of input files for a visualization requires for input the seed file name, the range of antenna pointing angles and the angle increment. Subsequently, when executed, the input files together with the respective NEC-BSC2 code command data will be automatically generated for the visualization input file sequence. This and other scripts significantly reduce the instruction set needed by the user to display results graphically, generate visualizations and thereby allow concentration on the design process in a time efficient manner.

Performance Evaluation for High Gain Antenna - To demonstrate the capabilities of the antenna analysis workstation concept a generic topside naval arrangement, shown in Figure 2 was chosen. The dominant contributors to antenna sidelobe degradation are large objects located close to the antenna. For the determination of sidelobe performance in the azimuth plane, the scatterers are the ship's mast and two obstacles located aft. The characteristic size for these obstructions is grater than a wavelength allowing the use of optical methods. The NEC-BSC2 code is well suited to this task. These obstacles are specified as conducting cylinders and located relative to the antenna as shown in the figure.

Evaluating the geometric relationship of the obstacles and the antenna performance requirements, it was determine that azimuth sidelobes would be most perturbed by the scattered fields. Since this geometry limits the interaction calculations to the azimuthal plane, the problem is simplified to a two-dimensional analysis and the aperture of the antenna may be collapsed to an equivalent line source. The line source model is arrayed with 52 Taylor weighted dipole sources to realize -35dB peak sidelobe level. The line source array may be further subdivided into subapertures provided that each obstacle is in

the far-field of the subaperture for which interactions are being considered. Through this technique further significant savings in computer run-time were achieved. Figure 3 illustrates the ideal far-field azimuth pattern simulated by this antenna computer model and the printed data from the automated post-processing analysis.

Pattern calculations for antenna/obstacle interactions are shown in Figure 4 for the antenna directed at each of the three dominant scatterers. These results show that significant performance degradation occurs when the antenna is looking directly at the mast which is relatively large and closely located. Contributions from those obstacles which are smaller and more remotely located are appreciably less.

In considering the mast as the most significant antenna performance degrader, Figure 5 compares the realized antenna performance to the ideal far-field pattern. The degradation observed in this comparison is attributed to two dominant mechanisms. First, high near-in sidelobes and gain loss result from the physical blockage in the antenna's field of view. Second, high far-out sidelobes arise from the scattered field of the mast. For this case, the antenna gain loss is calculated to be -3.7 dB, the near-in sidelobes increase from -35 dB to -11.2 dB, and the RMS value for the far-out sidelobes over the region from 30^{0} to 180^{0} off the beam-pointing direction increase significantly from -58 dB to -33 dB.

A simple planar absorber mounted between the antenna and mast is modeled into the computer simulation providing a far-field pattern for comparison with the antenna/mast pattern in Figure 6. Although there is little improvement in gain loss or near-in sidelobe levels, the RMS sidelobe level for the far-out region significantly improves by -12 dB to -45 dB. The variation in RMS sidelobe level with the mast bearing angle relative to the antenna is plotted in Figure 7 for the antenna/mast interactions, both with and without the inclusion of the absorbing panel, and shows the improvement in far out sidelobes when the mast is near broadside to the antenna.

Conclusion - The Numerical Electromagnetic Codes; NEC-BSC2 and NEC-MOM are integrated into the workstation environment providing efficient simulation for a high gain antenna and its interactions with local scatterers. The siting study demonstrates the viability of this computer tool for analyses and graphic visualizations as well as demonstrating realized performance of a common shipboard siting situation.

References

1. R.J. Marhefka and W.D. Burnside, "Numerical Electromagnetic Code - Basic Scattering Code NEC-BSC (Version 2) Part I and II", The Ohio State University ElectroScience Laboratory, Columbus, Ohio, 1982.

2. G.J. Burke and A.J. Poggio, "Numerical Electromagnetic Code - Method of Moments NEC-MOM Parts, I, II and III". Naval Ocean Systems Center, San Diego, CA, NOSC TD116 (revised), 1980.

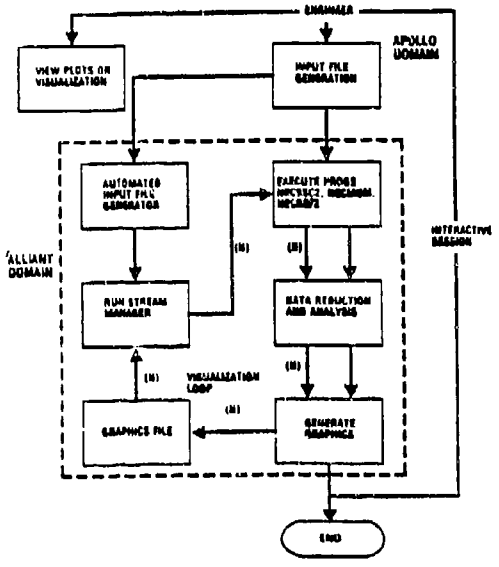

Figure 1. The Work Flow Diagram

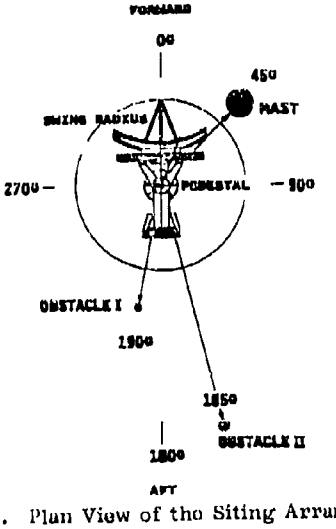

Figure 2. Plan View of the Siting Arrangement

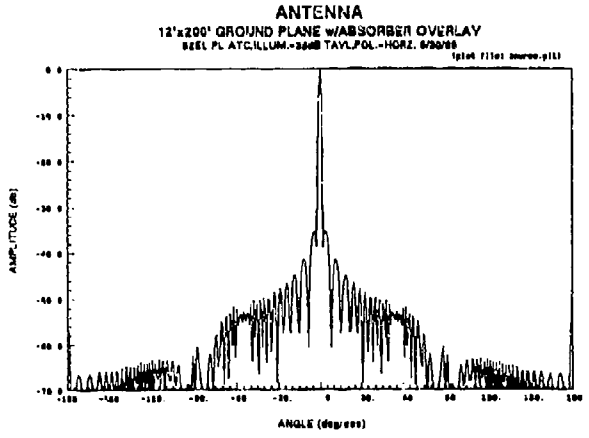

Figure 3. Ideal Far-Field Pattern for Antenna

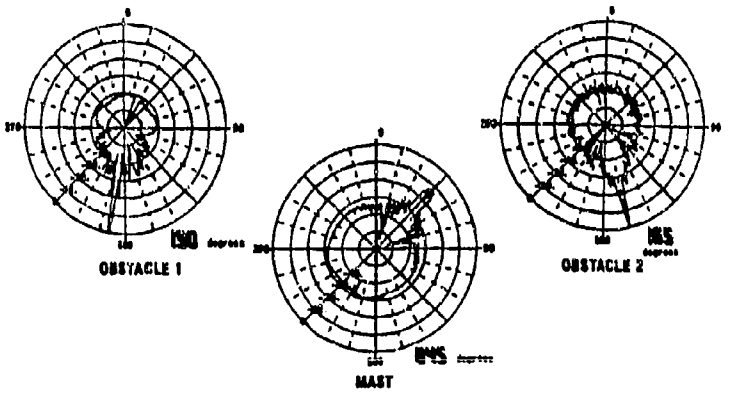

Figure 4. Realized Far-Field Patterns for Antenna Directed at Dominant Scatterers

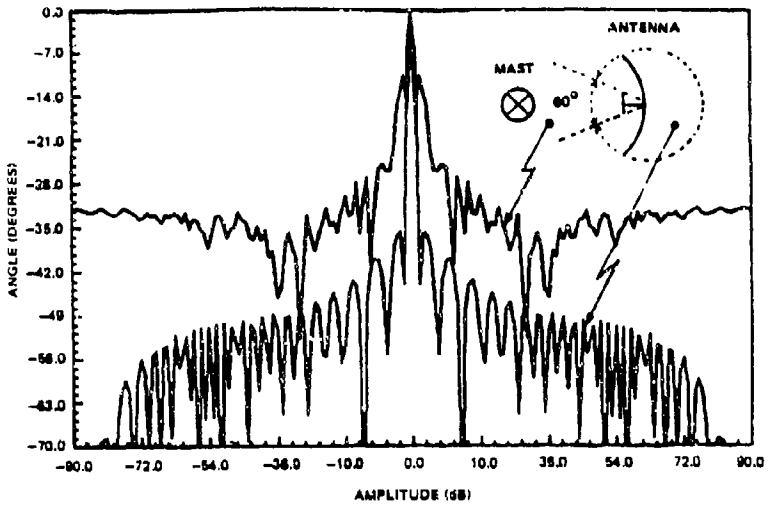

Figure 5.. High Sidelobes Result from Antenna Blockage and Scattering from Mast

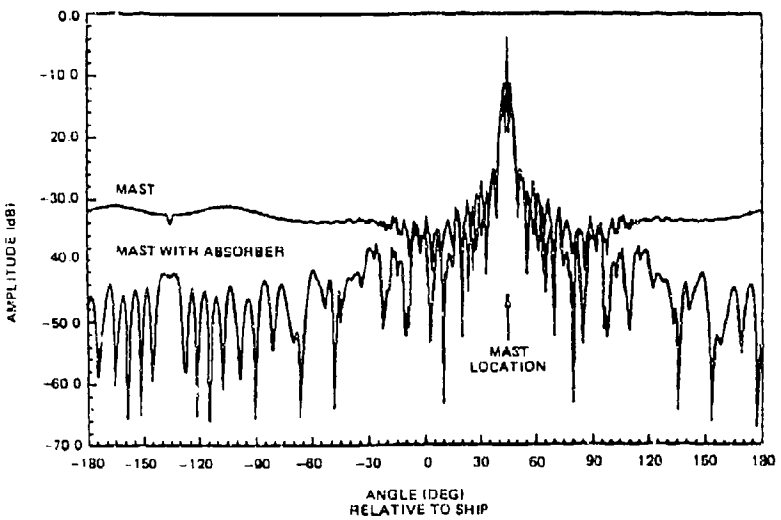

Figure 6. The Far-Field Pattern Shows Backscatter Reduction with Absorber

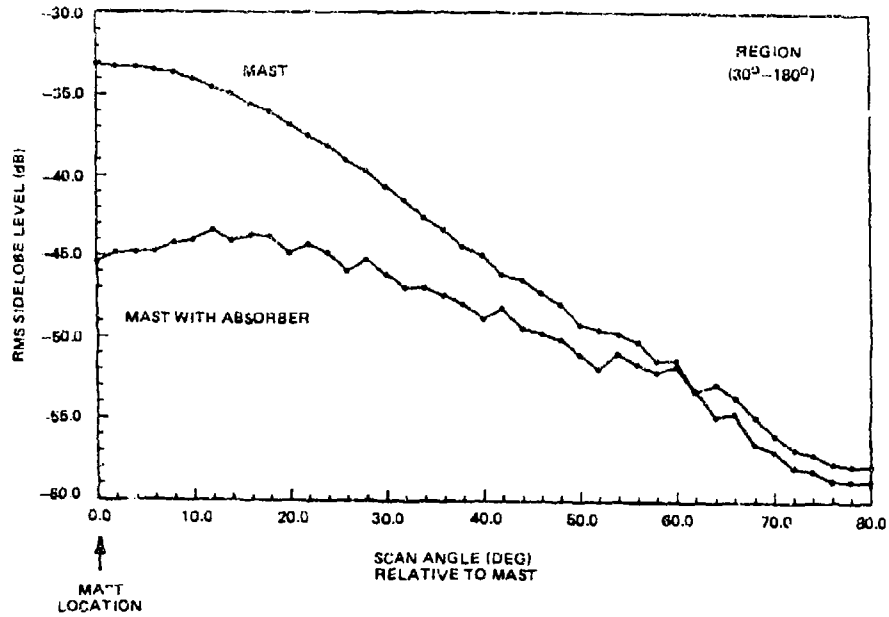

Figure 7. Antenna Performance for Mast With Absorber

Bistatic Physical Optics Scattering from a Surface Described by an Electromagnetic or Acoustic Impedance Boundary Condition

Robert T. Brown
Lockheed Advanced Development Company
Dept. 72-56, Bldg. 311, Plant B-6
P. O. Box 551
Burbank, California 91520

Abstract

The complete scattering matrix for bistatic scattering from an arbitrary planar surface in the physical optics approximation has been obtained for the case of a surface described by an impedance boundary condition. The analogous case of acoustic scattering at an impedance boundary in the local reaction approximation is shown to be identical in form to either one of the diagonal elements of the electromagnetic scattering matrix. The only differences between the acoustic and electromagnetic cases are in a factor depending on azimuth angle and in the form of the reflection coefficient obtained from the Fresnel equation relating impedance and reflectance. Although obtained under the assumption of validity of the impedance boundary condition, the results are functions only of the complex reflection coefficients, not the surface impedance.

1 Introduction

The most widely used computational method for predicting the scattering of electromagnetic radiation from targets of arbitrary shape is that of physical optics (PO), combined with the physical theory of diffraction (PTD). The physical optics approximation for electromagnetic scattering is obtained from the Stratton-Chu integral equation, an exact integral form of Maxwell's equations, by replacing the integral equation with an integral over the surface of the target. In the analogous acoustics case a high-frequency approximation can be obtained from the Helmholtz integral

This work was supported by the Defense Advanced Research Projects Agency under contract MDA972-89-C-0014.

equation [1]. This paper describes the results of an investigation of the similarities and differences between high-frequency acoustic and electromagnetic scattering, and in particular the possibility of adapting existing high-frequency electromagnetic scattering codes to the problem of predicting acoustic target strength.

2 Electromagnetic Bistatic Physical Optics Formulation

In the physical optics approximation, the E and H fields scattered by a surface S are given by

$$\mathbf{E}_s = \frac{-j\omega\mu_0}{4\pi R} e^{-jkR} \int_S [\hat{\mathbf{n}} \times \mathbf{H}^T - \sqrt{\frac{\epsilon_0}{\mu_0}} (\hat{\mathbf{n}} \times \mathbf{E}^T) \times \hat{\mathbf{k}}_s] e^{j\mathbf{k}_s \cdot \mathbf{r}'} ds' \tag{1}$$

and

$$\mathbf{H}_s = \frac{j\omega\epsilon_0}{4\pi R} e^{-jkR} \int_S [\hat{\mathbf{n}} \times \mathbf{E}^T + \sqrt{\frac{\mu_0}{\epsilon_0}} (\hat{\mathbf{n}} \times \mathbf{H}^T) \times \hat{\mathbf{k}}_s] e^{j\mathbf{k}_s \cdot \mathbf{r}'} ds' \tag{2}$$

Equations (1) and (2) are based on the far field approximation as well as the tangent plane approximation. The notation is the same as used by Ruck *et al.* [2], except for a time convention $e^{j\omega t}$. If the target surface can be described by an impedance boundary condition, with surface impedance Z, then the total fields at the surface $\mathbf{E}^T$ and $\mathbf{H}^T$ are related by

$$\hat{\mathbf{n}} \times (\hat{\mathbf{n}} \times \mathbf{E}^T) = -Z(\hat{\mathbf{n}} \times \mathbf{H}^T) \tag{3}$$

or

$$(\hat{\mathbf{n}} \times \mathbf{E}^T) = Z\hat{\mathbf{n}} \times (\hat{\mathbf{n}} \times \mathbf{H}^T) \tag{4}$$

so that (1, d (2) become

$$\mathbf{E}_s = \frac{j\omega\mu_0}{4\pi R} e^{-jkR} \int_S \left[\frac{1}{Z} \hat{\mathbf{n}} \times (\hat{\mathbf{n}} \times \mathbf{E}^T) + \frac{1}{Z_0} (\hat{\mathbf{n}} \times \mathbf{E}^T) \times \hat{\mathbf{k}}_s \right] e^{j\mathbf{k}_s \cdot \mathbf{r}'} ds' \tag{5}$$

and

$$\mathbf{H}_s = \frac{j\omega\mu_0}{4\pi R} e^{-jkR} \int_S [Z\hat{\mathbf{n}} \times (\hat{\mathbf{n}} \times \mathbf{H}^T) + Z_0 (\hat{\mathbf{n}} \times \mathbf{H}^T) \times \hat{\mathbf{k}}_s] e^{j\mathbf{k}_s \cdot \mathbf{r}'} ds' \tag{6}$$

where $Z_0 = \sqrt{\mu_0/\epsilon_0}$ is the impedance of free space. At the surface of the scatterer the total fields can be expressed in terms of the incident and scattered fields by means of the reflection coefficients $R_\perp$ and $R_\parallel$, which are related to the surface impedance Z by

$$R_\perp = \frac{Z\cos\theta_i - Z_0}{Z\cos\theta_i + Z_0} \tag{7}$$

and

$$R_\parallel = \frac{Z_0\cos\theta_i - Z}{Z_0\cos\theta_i + Z} \tag{8}$$

or

$$\begin{aligned}\frac{Z}{Z_0} &= \frac{1+R_\perp}{(1-R_\perp)}\frac{1}{\cos\theta_i} \\ &= \frac{(1-R_\parallel)\cos\theta_i}{1+R_\parallel}\end{aligned} \tag{9}$$

where θ_i is the angle of incidence measured from the normal to the surface.

If now a local coordinate system is defined such that the scattering surface is tangent to the (x, y) plane, with normal $\hat{n}$ in the z direction, the complete scattering matrix for radiation of arbitrary polarization takes a particularly simple form. The reflection coefficients $R_\perp$ and $R_\parallel$ of Eqs. (7) and (8) describe the scattering of radiation polarized with E field or H field tangent to the scattering plane, respectively. That is, in Eqs. (5) and (6) either $\mathbf{E}_i$ or $\mathbf{H}_i$ may be taken to be polarized in the $\hat{\phi}_i$ direction. Because of the free-space relationship between $\mathbf{E}$ and $\mathbf{H}$ this is equivalent to working with either $\mathbf{E}$ or $\mathbf{H}$ resolved into components in the $\hat{\theta}$ and $\hat{\phi}$ directions. With this convention, a plane wave incident on the surface may be described by

$$\mathbf{E}_i = E_0\hat{\phi}_i e^{-j\mathbf{k}_i\cdot\mathbf{r}'} \tag{10}$$

or

$$\mathbf{H}_i = H_0\hat{\phi}_i e^{-j\mathbf{k}_i\cdot\mathbf{r}'} \tag{11}$$

The relationship between incident and scattered fields is then

$$E^s_\phi = R_\perp E^i_\phi \tag{12}$$

and

$$H^s_\phi = R_\parallel H^i_\phi \tag{13}$$

so that (5) and (6) may be written

$$\begin{aligned}\mathbf{E}_s &= \frac{jk}{4\pi R}e^{-jkR}\int_S[(1-R_\perp)\cos\theta_i\hat{\mathbf{n}}\times(\hat{\mathbf{n}}\times\hat{\boldsymbol{\phi}}_i)\\ &+ (1+R_\perp)(\hat{\mathbf{n}}\times\hat{\boldsymbol{\phi}}_i)\times\hat{\mathbf{k}}_s]e^{jk(\hat{\mathbf{r}}_i+\hat{\mathbf{r}}_s)\cdot\mathbf{r}'}ds' \qquad (14)\end{aligned}$$

and

$$\begin{aligned}\mathbf{H}_s &= \frac{jk}{4\pi R}e^{-jkR}\int_S[(1-R_\parallel)\cos\theta_i\hat{\mathbf{n}}\times(\hat{\mathbf{n}}\times\hat{\boldsymbol{\phi}}_i)\\ &+ (1+R_\parallel)(\hat{\mathbf{n}}\times\hat{\boldsymbol{\phi}}_i)\times\hat{\mathbf{k}}_s]e^{jk(\hat{\mathbf{r}}_i+\hat{\mathbf{r}}_s)\cdot\mathbf{r}'}ds' \qquad (15)\end{aligned}$$

If the scattering surface is planar, the scattered fields become

$$\mathbf{E}_s = E_0[(1-R_\perp)\cos\theta_i\hat{\mathbf{n}}\times(\hat{\mathbf{n}}\times\hat{\boldsymbol{\phi}}_i)+(1+R_\perp)(\hat{\mathbf{n}}\times\hat{\boldsymbol{\phi}}_i)\times\hat{\mathbf{k}}_s]\mathcal{S} \qquad (16)$$

and

$$\mathbf{H}_s = H_0[(1-R_\parallel)\cos\theta_i\hat{\mathbf{n}}\times(\hat{\mathbf{n}}\times\hat{\boldsymbol{\phi}}_i)+(1+R_\parallel)(\hat{\mathbf{n}}\times\hat{\boldsymbol{\phi}}_i)\times\hat{\mathbf{k}}_s]\mathcal{S} \qquad (17)$$

where

$$\mathcal{S} = \frac{jk}{4\pi R}e^{-jkR}\int_S e^{jk(\hat{\mathbf{r}}_i+\hat{\mathbf{r}}_s)\cdot\mathbf{r}'}ds' \qquad (18)$$

It is now a straightforward but somewhat tedious exercise in vector algebra to show that

$$\begin{aligned}S_{\parallel\parallel} &= \mathbf{H}_s(\hat{\boldsymbol{\phi}}_i)\cdot\hat{\boldsymbol{\phi}}_s/H_0\\ &= [(R_\parallel-1)\cos\theta_i+(R_\parallel+1)\cos\theta_s]\cos(\phi_s-\phi_i)\mathcal{S} \qquad (19)\end{aligned}$$

$$\begin{aligned}S_{\parallel\perp} &= \mathbf{E}_s(\hat{\boldsymbol{\phi}}_i)\cdot\hat{\boldsymbol{\theta}}_s/E_0\\ &= [(R_\perp-1)\cos\theta_i\cos\theta_s+(R_\perp+1)]\sin(\phi_s-\phi_i)\mathcal{S} \qquad (20)\end{aligned}$$

$$\begin{aligned}S_{\perp\parallel} &= \mathbf{H}_s(\hat{\boldsymbol{\phi}}_i)\cdot\hat{\boldsymbol{\theta}}_s/H_0\\ &= [(R_\parallel-1)\cos\theta_i\cos\theta_s+(R_\parallel+1)]\sin(\phi_s-\phi_i)\mathcal{S} \qquad (21)\end{aligned}$$

$$S_{\perp\perp} = \mathbf{E}_s(\hat{\phi}_i)\cdot\hat{\phi}_s/E_0$$
$$= [(R_\perp - 1)\cos\theta_i + (R_\perp + 1)\cos\theta_s]\cos(\phi_s - \phi_i)S \quad (22)$$

are the elements of the scattering matrix S_{pq} such that

$$\sigma_{pq} = 4\pi|S_{pq}|^2 \quad (23)$$

gives the cross section for any combination of receiver and transmitter polarizations.

For a perfectly conducting surface, $R_\perp = -1$ and $R_\parallel = 1$, so that (19) through (22) become

$$S_{\parallel\parallel} = 2S\cos\theta_s\cos(\phi_s - \phi_i) \quad (24)$$

$$S_{\parallel\perp} = -2S\cos\theta_i\cos\theta_s\sin(\phi_s - \phi_i) \quad (25)$$

$$S_{\perp\parallel} = 2S\sin(\phi_s - \phi_i) \quad (26)$$

$$S_{\perp\perp} = -2S\cos\theta_i\cos(\phi_s - \phi_i) \quad (27)$$

in agreement with results previously obtained for bistatic scattering from planar perfectly conducting surfaces [3], [4].

As a further check, it can be noted that for the case of backscatter, $\theta_s = \theta_i$ and $\phi_s = \phi_i$, and Eqs (19) through (22) become

$$S_{\parallel\parallel} = 2R_\parallel\cos\theta_i \quad (28)$$
$$S_{\parallel\perp} = 0 \quad (29)$$
$$S_{\perp\parallel} = 0 \quad (30)$$
$$S_{\perp\perp} = 2R_\perp\cos\theta_i. \quad (31)$$

These results do not contradict those of Ruck *et al.*[2], Eqs. (2.2-87) and (2.2-88), which have non-vanishing off-diagonal scattering matrix elements. The results in [2] were obtained relative to a different coordinate system than that used in the present work, and do reduce to the form given by Eqs. (28) through (31) when expressed in the same coordinate system.

3 Acoustic Bistatic Physical Optics Scattering

In order to arrive at the acoustic analog of the above equations it is necessary to go back to the integral equation form of the scalar Helmholtz equation analogous to the Stratton-Chu equation for electromagnetics. In this equation the field quantity is the velocity potential $V(\mathbf{r})$; the scattered field at a point $\mathbf{r}$ is given by [6], [7]

$$V_s(\mathbf{r}) = \frac{1}{4\pi}\int_S \left[-V(\mathbf{r}')\frac{\partial}{\partial n}\left(\frac{e^{-jkR}}{R}\right) + \frac{e^{-jkR}}{R}\frac{\partial}{\partial n}V(\mathbf{r}')\right] ds' \tag{32}$$

The quantity R is the magnitude of the distance from a source point $\mathbf{r}'$ on the surface S to the observation point $\mathbf{r}$, and $\hat{\mathbf{n}}$ is the normal to the surface. For a harmonic wave with time dependence $e^{j\omega t}$ the impedance boundary condition analogous to Eqs. (3) and (4) for the electromagnetic case is [8]

$$\frac{\partial V}{\partial n} = -\frac{j\omega\rho V}{Z} \tag{33}$$

where Z is the acoustic impedance and ρ is the density of the fluid outside the boundary S. The normal derivative in the first term in Eq. (32) may be written [5]

$$\begin{aligned}\frac{\partial}{\partial n}\frac{e^{-jkR}}{R} &= \hat{\mathbf{n}}\cdot\nabla\frac{e^{-jkR}}{R} \\ &= -jk\hat{\mathbf{n}}\cdot\mathbf{R}\frac{e^{-jkR}}{R^2} \\ &= -jk\cos\theta_s\frac{e^{-jkR}}{R}\end{aligned} \tag{34}$$

so that (32) becomes

$$V_s(\mathbf{r}) = \frac{jk}{4\pi}\int_S \left[-\frac{\rho c}{Z} + \cos\theta_s\right] V(\mathbf{r}')\frac{e^{-jkR}}{R} ds' \tag{35}$$

where $k = \omega/c$ is the wavenumber and c the soundspeed in the fluid with density ρ. The quantity $V(\mathbf{r}')$ represents the total field at the surface. In the local reaction approximation, analogous to the tangent plane approximation of electromagnetic physical optics, the total field at a point on the surface may be written as the sum of incident and scattered fields $V(\mathbf{r}') = V_i + V_s = V_i(1 + R_a)$ related by the reflection coefficient [9]

$$R_a = \frac{Z\cos\theta_i - \rho c}{Z\cos\theta_i + \rho c} \tag{36}$$

where Z is the acoustic impedance defined by Eq. (33). This may be solved for Z to yield

$$Z = \frac{(1+R_a)}{(1-R_a)}\frac{\rho c}{\cos\theta_i} \tag{37}$$

which when substituted into (35) gives

$$V_s(\mathbf{r}) = \frac{jk}{4\pi}\int_S [(R_a-1)\cos\theta_i + (R_a+1)\cos\theta_s]\, V(r')\frac{e^{-jkR}}{R}ds' \tag{38}$$

Assuming the incident field to be the plane wave

$$V_i(\mathbf{r}') = V_0 e^{-j\mathbf{k}_i\cdot\mathbf{r}'} \tag{39}$$

where V_0 is the magnitude of the incident field, and making use of the far-field approximation used in deriving Eqs. (1) and (2), we have

$$V_s(\mathbf{r}) = \frac{jk}{4\pi R}e^{-jkR}V_0\int_S [(R_a-1)\cos\theta_i + (R_a+1)\cos\theta_s]\, e^{jk(\hat{\mathbf{r}}_i+\hat{\mathbf{r}}_s)\cdot\mathbf{r}'}ds' \tag{40}$$

or

$$V_s = V_0[(R_a-1)\cos\theta_i + (R_a+1)\cos\theta_s]\,S \tag{41}$$

where S is exactly the same as Eq. (18), the physical optics integral for the electromagnetic case. Except for the azimuthal factor $\cos(\phi_s - \phi_i)$, Eq. (41) is the same as either Eq. (19) or (22), the diagonal elements of the scattering matrix for the electromagnetic case.

For an acoustically soft body, $Z = 0$, $R_a = -1$, and (41) becomes

$$\left.\frac{V}{V_0}\right|_{soft} = -2S\cos\theta_i \tag{42}$$

while for an acoustically hard body, $Z \to \infty$, $R_a = +1$, and

$$\left.\frac{V}{V_0}\right|_{hard} = 2S\cos\theta_s \tag{43}$$

These results are completely analogous to the corresponding electromagnetic expressions (24) and (27). In the special case of backscatter, $\theta_s = \theta_i$, $\phi_s = \phi_i$, and

$$V_s = 2V_0 R_a S \cos\theta_i \tag{44}$$

again completely analogous to the corresponding electromagnetic expressions (28) or (31).

Figure 1 compares the physical optics electromagnetic and acoustic bistatic scattering patterns for a square plate two wavelengths on a side. The plate is in the (x, y) plane with with sides parallel to the x and y axes. Incidence is in the (x, z) plane at 45° elevation.

4 Numerical Examples and Conclusions

Figures 2 and 3 show comparisons of the results obtained with the methods presented above and method of moments calculations for bistatic scattering from $ka = 12$ perfectly conducting (acoustic hard and soft) circular cylinders. Figures 4 and 5 show similar comparisons for a $ka = 12$ circular cylinder with an impedance boundary condition with $Z = 1000\Omega/\Box$. In this case it is the TM polarization that is equivalent to the acoustic IBC. In three dimensions, comparisons were made between method of moments and physical optics results for a $ka = 10$ sphere. Computational models used are shown in Fig. 6, and Fig. 7 shows the principal plane cuts used for the bistatic patterns. Results are shown in Figs. 8 and 9. Although not presented here, all method of moments results were in essentially exact agreement with series solutions in both the two- and three-dimensional cases.

In view of the above results, it can be concluded that high frequency (physical optics) codes for bistatic electromagnetic scattering can be adapted to the acoustic case with only very minor changes. The changes required are actually simplifications, in that the acoustic analog of the electromagnetic bistatic scattering matrix is a single term, equivalent to and slightly simpler than either one of the diagonal elements of the electromagnetic matrix.

The acoustic scattering formulation should have the same range of validity as the electromagnetic, with two additional caveats. The Stratton-Chu electromagnetic integral equation, the starting point for the physical optics integrals (1) and (2) is in principle exact, as it is the integral form of Maxwell's equations. The acoustic Helmholtz equation, on the other hand, is based on a linear approximation to what is actually a nonlinear problem. In addition, both the electromagnetic and acoustic results are based on the validity of the impedance boundary condition. It is possible that this approximation has a different range of validity for the acoustic than for the electromagnetic case.

It is interesting to note that although both the acoustic and electromagnetic cases studied in the work reported here make use of the impedance boundary condition, in the final result it is not the surface impedance but the complex reflection coefficients that appear. It is possible that the results presented here have more general validity than would be expected from the starting conditions, although this is still to be determined.

References

[1] J. J. Bowman, T. B. A. Senior and P. L. E. Uslenghi, *Electromagnetic and Acoustic Scattering by Simple Shapes*, New York: Hemisphere Publishing Corporation, 1987, p. 29.

[2] G. T. Ruck, D. E. Barrick, W. D. Stuart, and C. K. Krichbaum, *Radar Cross Section Handbook*, New York: Plenum Press, 1970, pp. 50-54.

[3] S. K. Chaudhuri and W.-M. Boerner, "A Polarimetric Model for the Recovery of the High-Frequency Scattering Centers from Bistatic- Monostatic Scattering Matrix Data," *IEEE Trans. Antennas Propagat.* vol. AP-35, pp. 87-93, 1987.

[4] R. T. Brown, "Nonspecular Nature of Physical Optics Scattering," 1990 URSI National Radio Science Meeting, Dallas, Texas, May, 1990.

[5] P. Uslenghi, "Radar Cross Section of Imperfectly Conducting Bodies at Small Wavelengths," *Alta Frequenza*, vol. 33, pp. 541-46, 1964.

[6] P. M. Morse and H. Feshbach, *Methods of Theoretical Physics*, New York: McGraw Hill Book Company, 1953, p. 806.

[7] J. J. Bowman, T. B. A. Senior and P. L. E. Uslenghi, *op. cit.*, p. 15.

[8] P. M. Morse and H. Feshbach, *op. cit.*, p. 311.

[9] P. M. Morse and K. U. Ingard, *Theoretical Acoustics*, New York, McGraw-Hill Book Company, 1968, p. 259.

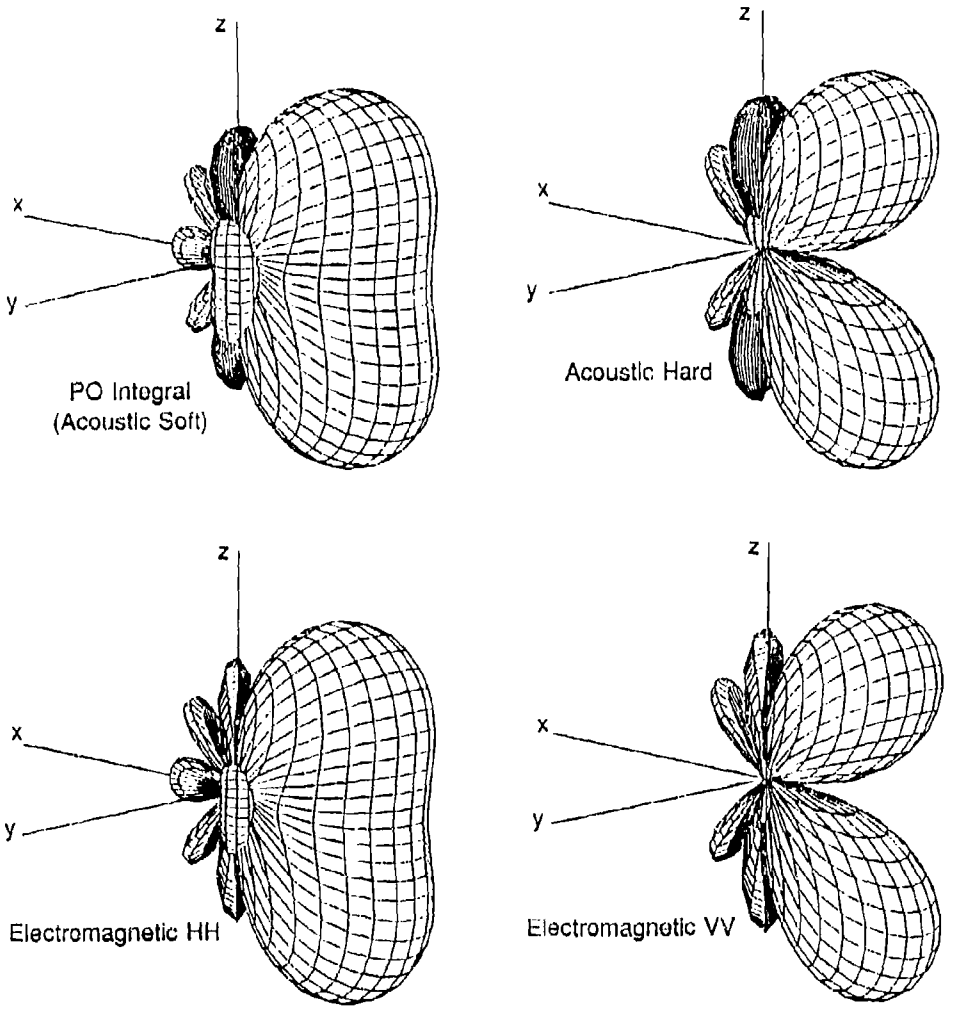

Figure 1: Comparison of bistatic electromagnetic and acoustic scattering patterns for a flat plate two wavelengths on a side. Edges are parallel to the x and y axes, with incidence in the (x, z) plane at 45°.

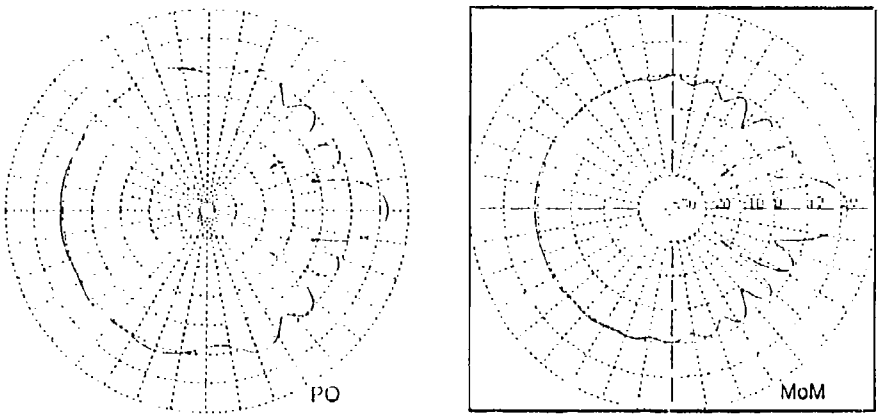

Figure 2: Bistatic scattering from a perfectly conducting circular cylinder, $ka = 12$, TE polarization (hard acoustic BC).

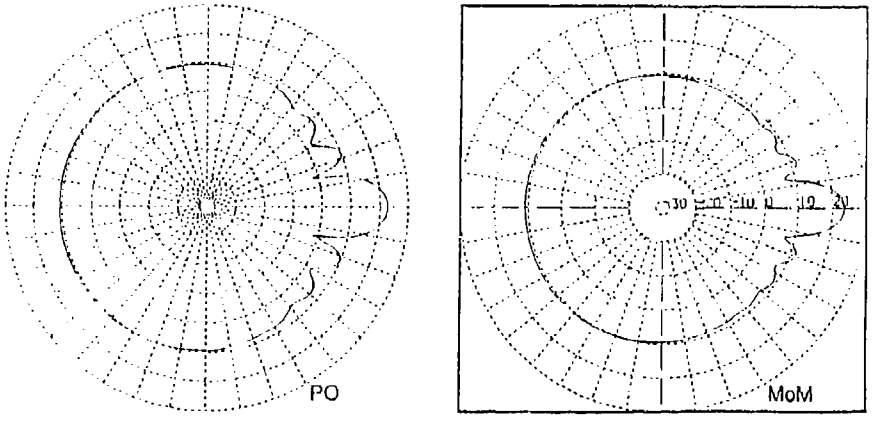

Figure 3: Bistatic scattering from a perfectly conducting circular cylinder, $ka = 12$, TM polarization (soft acoustic BC).

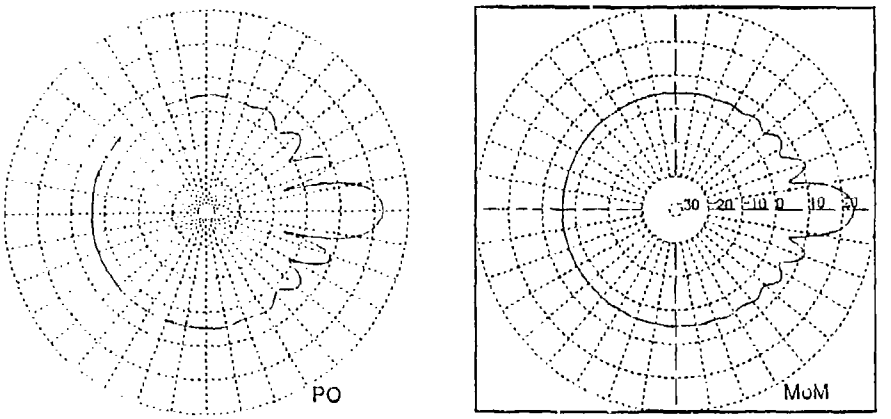

Figure 4: Bistatic scattering from a circular cylinder, $ka = 12$, TE polarization, IBC $Z = 1000\Omega/\square$.

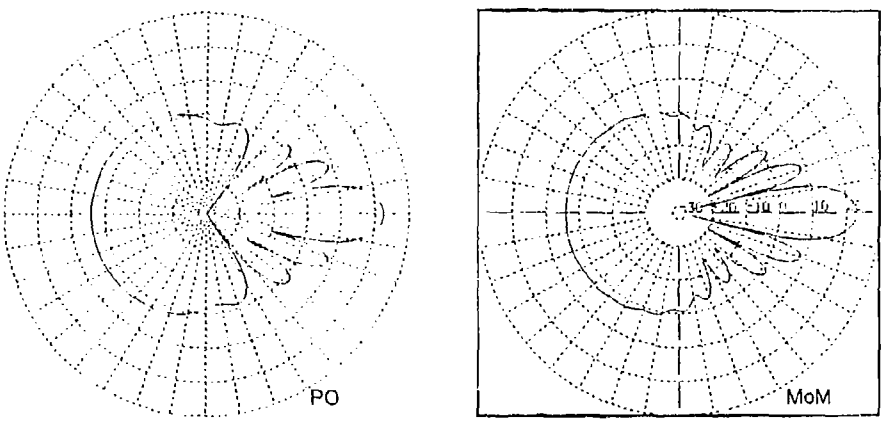

Figure 5: Bistatic scattering from a circular cylinder, $ka = 12$, TM polarization, IBC $Z = 1000\Omega/\square$, (equivalent to acoustic IBC).

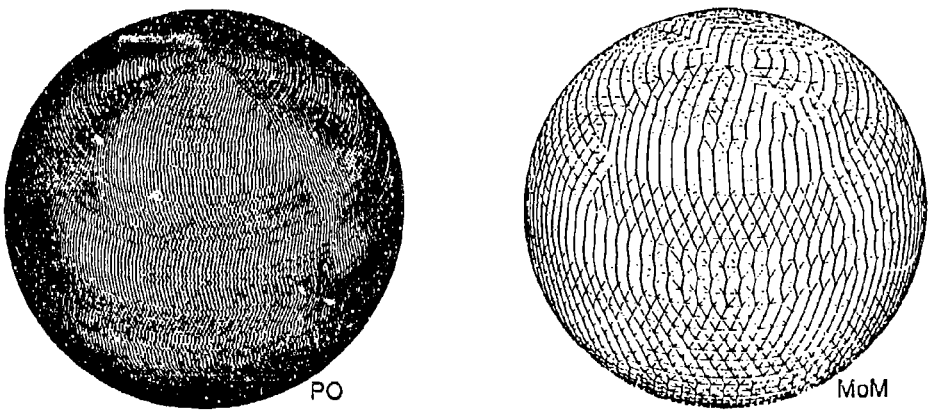

Figure 6: Computational targets for bistatic scattering from sphere. The PO sphere contains 71,876 facets, and the MoM sphere 5392 facets.

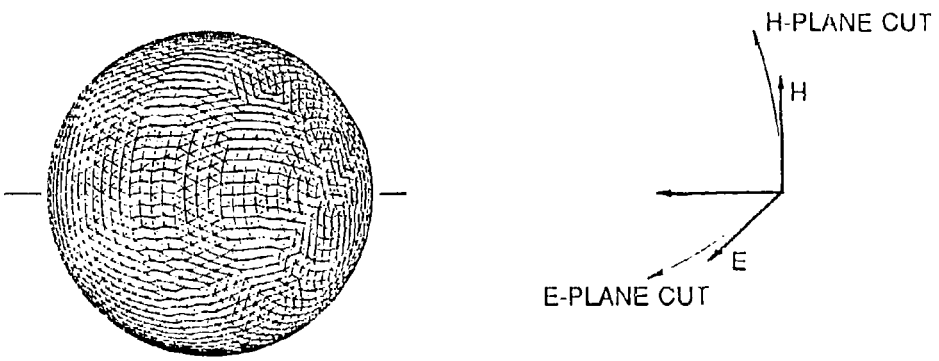

Figure 7: Conventional principal plane cuts for electromagnetic bistatic scattering.

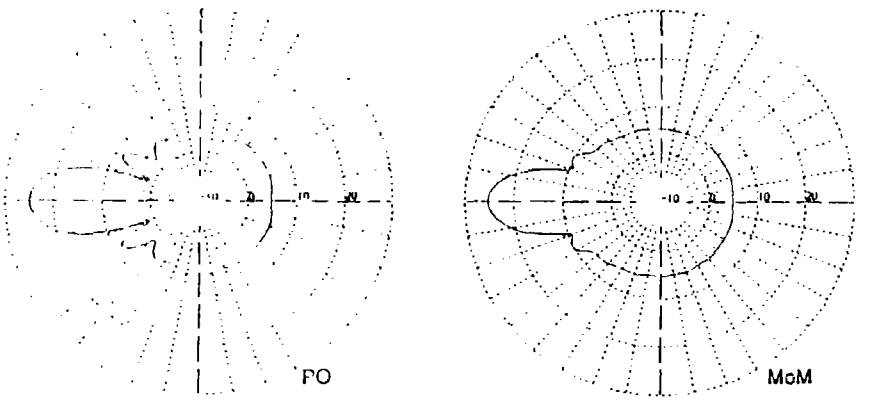

Figure 8: Bistatic scattering from perfectly conducting sphere, ka=10, E plane cut.

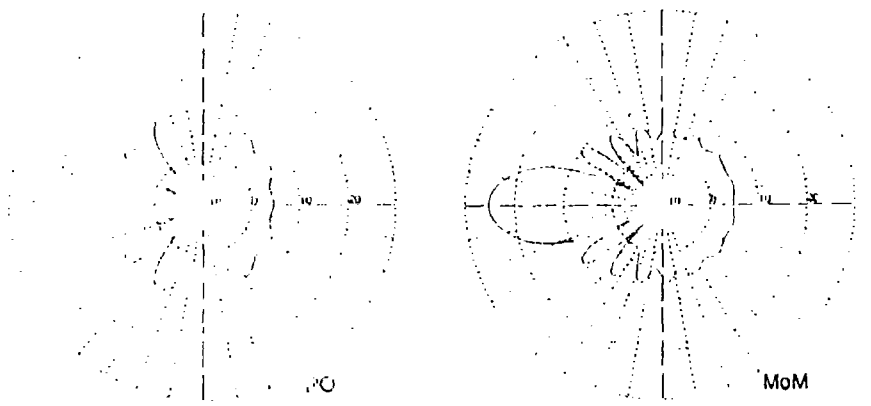

Figure 9: Bistatic scattering from perfectly conducting sphere, ka=10, H plane cut.

SESSION 5 - "NEW TECHNIQUES"

Moderator: Ronald Pogorzelski

A HYBRID FINITE ELEMENT AND MOMENT METHOD FOR ELECTROMAGNETIC SCATTERING FROM INHOMOGENEOUS OBJECTS

W. E. Boyse and A. A. Seidl
Lockheed Palo Alto Research Laboratories
O/91-60 B/256
3251 Hanover Street
Palo Alto, California 94304, USA

Abstract - A hybrid finite element formulation for three-dimensional electromagnetic scattering is given using an equivalent current approach. A new method, utilizing a body of revolution (BOR) formulation, is presented to terminate the finite element mesh and to implement the near field radiation condition. This BOR implementation utilizes Hermite cubic basis functions and a variable number of modes per basis function to achieve the greatest computational efficiency. The combined field integral equation formulation is employed to eliminate non-physical resonances of the mesh boundary. Examples are given showing such non-physical resonance behavior and its elimination as well as the accuracy of the solutions generated by this hybrid finite element method for bare and partially coated perfect electrical conductors.

INTRODUCTION

Finite element methods (FEM) are widely applicable to the solution of Maxwell's equations for electromagnetic scattering. Because of their differential nature, FEM can easily model combinations of penetrable and impenetrable materials and, in addition, these methods produce a sparse system matrix. However a difficulty, true for all differential methods, is in the treatment of the Sommerfeld radiation condition. Local boundary conditions which maintain sparsity of the system matrix work best when the mesh boundary is far from the scatterer [1]. Having the mesh boundary far from the scatterer greatly increase the number of finite element unknowns. This can generate large system matrices for problems involving even rather small scatterers. Hybrid finite element methods (HFEM) couple the differential method to another method, i.e. MOM [2, 3, 4] or modal expansion [5, 6, 7]. This coupling acts as a

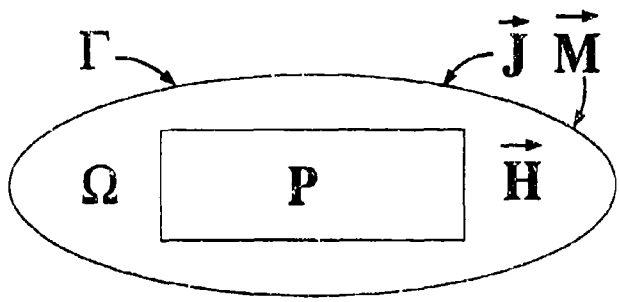

Figure 1: Geometrical configuration for mathematical formulation.

global boundary condition which implements the exact radiation condition in the near field. The details of coupling the FEM to another method on the boundary have a major effect on the computational efficiency.

A fully 3-dimensional HFEM in which the finite elements are coupled to a MOM on a BOR boundary is described in this paper. Since we are free to choose the exact shape of the terminating BOR boundary, we choose it to be smooth. Having a smooth boundary and modeling smooth fields allows us to use Hermite cubic basis functions. These basis functions have continuous first derivatives across elements and thus, when modeling smooth functions, can greatly reduce the number of unknowns on the boundary. This choice increases the computational efficiency of the method. Resonances of the mesh boundary encountered in some implementations [8] are eliminated by using a combined field formulation.

FORMULATION

The geometrical definitions used in formulating the scattering problem can be seen in Fig. 1 where we schematically show a perfectly conducting scatterer P, totally enclosed within a surface Γ, with the interstitial volume denoted by Ω.

For simplicity, in order to expedite the development, we consider at this point only scattering from perfectly conducting bodies. The magnetic field in Ω is denoted by $\vec{H}$, and the electric and magnetic currents on Γ are respectively labeled as $\vec{J}$ and $\vec{M}$. The scattering problem involves the solution of the

differential form of Maxwell's equations in Ω for the magnetic field $\vec{H}$, coupling this field to the equivalent currents $\vec{J}$ and $\vec{M}$ on Γ, and ensuring that $\vec{J}$, $\vec{M}$ and the incident field specify a radiating solution.

The fields $\vec{H}$, $\vec{J}$, and $\vec{M}$ satisfy

$$\nabla \times \frac{1}{\epsilon_r} \nabla \times \vec{H}(\vec{r}) - \mu_r k^2 \vec{H}(\vec{r}) = 0 \text{ for } \vec{r} \in \Omega \quad (1)$$

$$\frac{1}{\omega \epsilon_0} \hat{n} \times \nabla \times \vec{H}(\vec{r}) = 0 \text{ for } \vec{r} \in P \quad (2)$$

$$\vec{M}(\vec{r}) + \frac{1}{\omega \epsilon_0} \hat{n} \times \nabla \times \vec{H}(\vec{r}) = 0 \text{ for } \vec{r} \in \Gamma \quad (3)$$

$$\vec{J}(\vec{r}) - \hat{n} \times \vec{H}(\vec{r}) = 0 \text{ for } \vec{r} \in \Gamma \quad (4)$$

where ω is the angular frequency, a time dependence $e^{-\imath \omega t}$ is assumed, ϵ_0 and ϵ_r are the free space and relative permittivity respectively, μ_0 and μ_r are the free space and relative permeability respectively, k is the free space propagation constant, and $\hat{n}$ denotes the unit normal to the surfaces.

The boundary condition for a perfect electrical conductor on P (Eq. 2) and for coupling the magnetic current on Γ (Eq. 3) are conditions on the derivative of $\vec{H}$ and are imposed as natural boundary conditions. The boundary condition coupling the electric current on Γ (Eq. 4) is a condition on $\vec{H}$ itself, an essential boundary condition, and must be explicitly enforced. Letting $\vec{T}$ and $\vec{U}$ be test functions defined on Ω and Γ respectively we write the weak equations

$$\int_\Omega \left[\left(\nabla \times \vec{T}^* \right) \cdot \frac{1}{\epsilon_r} \left(\nabla \times \vec{H} \right) - k_0^2 \vec{T}^* \cdot \mu_r \vec{H} \right] dV + \imath \omega \epsilon_0 \int_\Gamma \vec{T}^* \cdot \vec{M} dS = 0 \quad (5)$$

and

$$-\imath \omega \epsilon_0 \int_\Gamma \hat{n} \times \vec{U}^* \cdot \left[\vec{J} - \hat{n} \times \vec{H} \right] dS = 0 \quad (6)$$

where the superscript * is complex conjugation. Integration of Eq. 5 by parts reveals that it is the weak form of Eq. 1 with natural boundary conditions Eq. 2 and Eq. 3, while inspection reveals that Eq. 6 is the weak enforcement of Eq. 4. A finite element discretization of these equations results in matrix equations which we denote by

$$\begin{aligned} [\,\mathbf{S}\,]\, H + [\,\mathbf{C}\,]\, M &= 0 \\ [\,\mathbf{C}\,]^*\, H + [\,\mathbf{N}\,]\, J &= 0 \end{aligned} \quad (7)$$

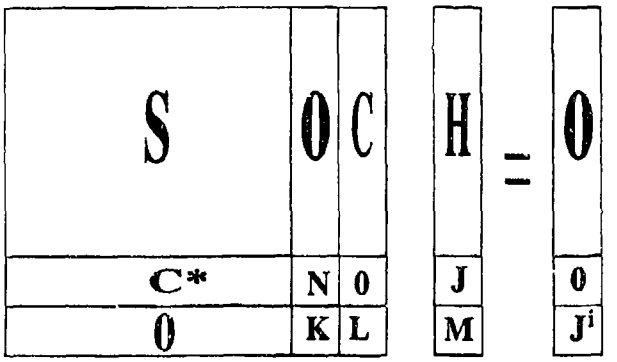

Figure 2: System matrix for generic hybrid finite element formulation.

where the superscript * on matrices refers to the adjoint, i.e. conjugate transpose.

To complete the specification of the scattering problem we introduce the incident field $\vec{H}^i$ and the induced current $\vec{J}^i = 2\hat{n} \times \vec{H}^i$ defined on Γ. The specification of a scattering solution is an equation relating $\vec{J}$, $\vec{M}$ and $\vec{J}^i$ on Γ, such as the magnetic, electric, or combined field integral equations. Discretization will produce a matrix equation which we denote by

$$[\,\mathbf{K}\,]\; J + [\,\mathbf{L}\,]\; M \;=\; J^i. \tag{8}$$

Collecting these into a single matrix equation we have the complete system matrix for the problem given schematically in Fig. 2.

SOLUTION

A computationally attractive solution of the matrix represented in Fig. 2 is facilitated by observing that the incident field couples only to $\vec{J}$ and $\vec{M}$, and that the knowledge of these quantities is sufficient for all scattering calculations. Therefore eliminating $\vec{H}$ first, we reduce this system to one involving only $\vec{J}$, $\vec{M}$, and $\vec{J}^i$. Performing this reduction we have

$$[\,\mathbf{N}\,]\; J + [\,\mathbf{D}\,]\; M \;=\; 0 \tag{9}$$

$$[\,\mathbf{K}\,]\; J + [\,\mathbf{L}\,]\; M \;=\; J^i \tag{10}$$

where

$$[\,\mathbf{D}\,] = \left[\,-\mathbf{C}^{*}\,\mathbf{S}^{-1}\,\mathbf{C}\,\right]. \tag{11}$$

For general three-dimensional scatterers, the matrix **D** is *always* a dense matrix, independent of the method of implementing the boundary integral on Γ.

It is worth noting at this point that Eq. 11 implies finding multiple sparse solutions of the matrix **S**. This is one of the places where limiting the number of unknowns on the boundary becomes important, since each unknown on the boundary contributes a column to the matrix **C**. Thus each unknown on the boundary necessitates another sparse solution

Next, given an incident field J^{i},

$$\left[\,\mathbf{L}+\mathbf{K}\,\mathbf{N}^{-1}\,\mathbf{D}\,\right]\,M \;=\; J^{i} \tag{12}$$

is solved for M and then

$$[\,\mathbf{K}\,]\,J \;=\; J^{i}-[\,\mathbf{L}\,]\,M \tag{13}$$

is solved for J, after which the scattering may be computed. For monostatic calculations, this is repeated for each monostatic point.

EXAMPLES

Resonance Case

Inspection of Eq. 13 reveals that it is of the same form as the equations found in an integral equation formulation of the scattering problem. The surface of integration is however not on any physical scatterer, but rather is a surface where $\vec{J}$ and $\vec{M}$ are defined and coupled to the interior solution for $\vec{H}$. Never the less, in cases where Eq. 13 has homogeneous solutions, resonance behavior is observed. This is illustrated in Fig. 3 where we plot a radar cross section (RCS), ϕ polarized, for a spherical conductor with a spherical mesh boundary with $ka_{\textit{mesh boundary}} = 2.744$. This corresponds to the lowest resonance of a perfectly conducting spherical cavity.

We plot the RCS computed using both the electric field and the magnetic field integral formulation on the mesh boundary. In comparison, we also plot the solution from the combined field integral formulation and a Mie series solution. It is clear that while the combined field formulation and the Mie series solution are virtually indistinguishable the purely electric or magnetic field formulations are wildly inaccurate. This resonant behavior is due to the

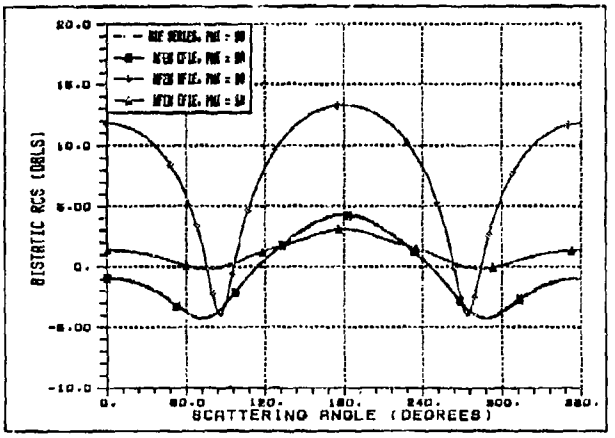

Figure 3: RCS at 109 MHz for a 1 m. radius conducting sphere with the mesh boundary terminating on a 1.2 m. sphere

manner in which we have chosen to solve the system matrix. A sub matrix of the system matrix is singular for this problem formulated with an electric or a magnetic integral equation, not the entire system matrix. The way we choose to solve the system unfortunately requires the inverse of this sub matrix. However the order in which we propose to solve the problem is so computationally attractive, that using a combined field approach to avoid resonant behavior is a small price to pay.

Conducting Non-BOR

In the next example we illustrate some aspects of the HFEM method in detail by computing monostatic scattering from a perfect conductor with a non-BOR geometry, a box of dimensions 2m by 1/2m by 1/ at 200 MHz. Figure 4 illustrates the geometry of part of the scatterer, part of the finite element mesh, and the generator for the BOR surface.

The surfaces representing one fourth of the conduction box can be seen on the left of the figure. The line just above the surfaces of the box is the generator of the BOR. The generator stays within a distance of about 1/20'th λ of the box all along its length. This generator is then revolved about the $\hat{z}$ axis, forming the BOR mesh boundary surface which is very close to the

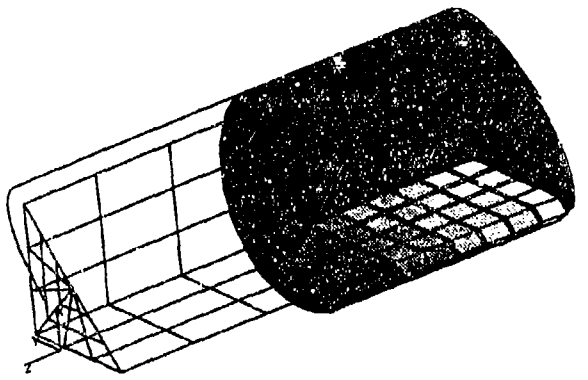

Figure 4: Part of mesh for PEC box example showing a fourth of the box, the generator of the BOR and a fourth of the subsequent mesh

scatterer. Figure 4 also shows one fourth of the mesh which occupies the volume between the scatterer and this BOR.

The sampling rates on the BOR surface are $5s/\lambda$ along the generator and modes $-3,\ldots,+3$, averaging a low $23s/\lambda^2$ over the $3\lambda^2$ surface area. The number of degrees of freedom of $\vec{J}$ (and $\vec{M}$) on Γ is $140 \approx 23s/\lambda^2 \cdot 3\lambda^2 \cdot 2$. There are 352 quadratic hexahedral finite elements providing a sampling rate of $10.5 \rightarrow 12.5s/\lambda$ in the interstitial volume.

The computational effort necessary to determine the monostatic cross sections involved first factoring a rank 12690 sparse matrix and back-substituting to generate 140 sparse solutions. The calculation of each monostatic point then involved a rank 140 dense matrix and an rank 140 block diagonal matrix (20 by 20 blocks). Figure 5 shows the monostatic cross section comparison between this hybrid finite element method code and a three-dimensional MOM code PATCH from Sandia National Laboratory.

Partially Coated Conductor

A perfect conductor, partially coated with a lossy dielectric and magnetic material, serves as the most stringent test of our implementation. Having loss means that the finite element matrix is complex. The magnetic component of

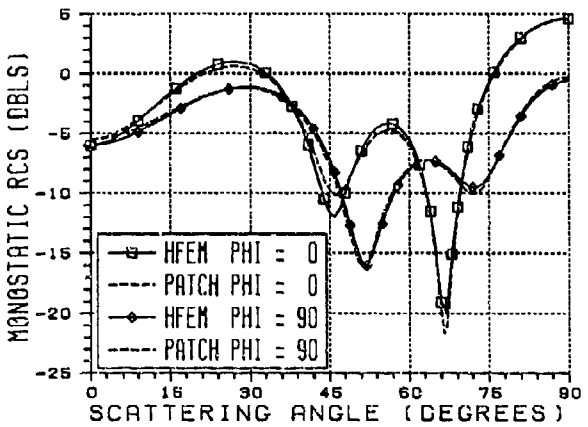

Figure 5: Monostatic scattering (dB/λ^2) from conducting box, 2m by 1/2m by 1/2m at 200 MHz.

the material causes a discontinuity in the solution, $\vec{H}$, at the material interface which must be specifically imposed by the code. In addition along a line on the scatterer we have three media in contact

A conducting prolate spheroid formed by revolving an ellipse, with major axis along $\hat{z}$ and length 1 meter and minor axis 1/4 meter, about the $\hat{z}$ axis with a 1/16 meter coating over half the surface was chosen as the scatterer. The coating is applied over one end of the conductor and preserves the BOR geometry. Electromagnetic properties of the coating are given by the relative permittivity and permeability constants

$$\epsilon_r = 2e^{i\frac{\pi}{6}} \sim 1.73 + 1.0i \text{ and } \mu_r = 4e^{i\frac{\pi}{3}} \sim 2.0 + 3.464i. \tag{14}$$

These parameters were chosen to yield an index of refraction of 2.

Figure 6 shows monostatic RCS comparisons betweem our HEFM implementation and one of the "CICERO" [9] family of codes. These results are in excellent agreement except for the $\phi = 90°$ plane around 120°. We would not necessarily assume that either code is more correct here and are not concerned at this 2 dB discrepancy 25 dB down from maximum monostatic scattering. The scattering from the bare metal end of the body is at $\theta = 0°$, while that from the coated end is at $\theta = 180°$.

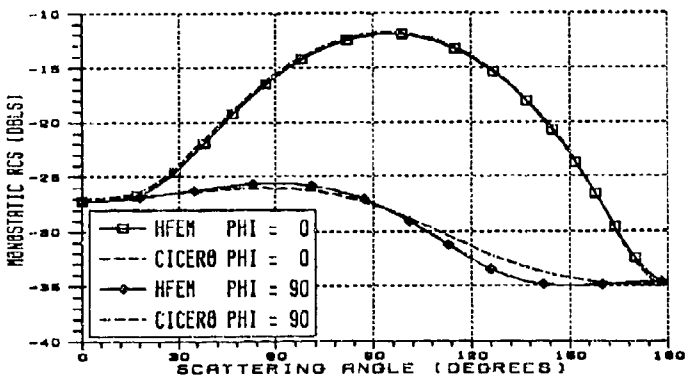

Figure 6: Monostatic RCS (dB/λ^2) from partially coated conducting prolate spheroid @ 100 MHz.

CONCLUSIONS

We have presented a new hybrid finite element method employing a unique BOR implementation utilizing Hermite cubic basis functions and the combined field integral equations. This formulation provides for efficient monostatic scattering calculations by combining the flexibility of a body of revolution mesh boundary, keeping the mesh boundary close to the scatterer, with a highly efficient BOR implementation, reducing the number of sparse solutions and the rank of the matrix used in scattering solutions. In addition, this method is not plagued by artificial resonances of the mesh boundary. This implementation has proven accurate and efficient on a large class of scatterers involving dielectric and magnetic materials, as well as the results shown here.

REFERENCES

[1] J. D'Angelo and I. D. Mayergoyz, "On the use of local absorbing boundary conditions for rf scattering problems," *IEEE Trans. Magnetics*, vol. 25, pp. 3040-3042, July 1989.

[2] K. D. Paulsen, D. R. Lynch, and J. W. Strobehn, "Three-dimensional finite, boundary, and hybrid element solutions of the maxwell equations

for lossy dielectric media," *IEEE Trans. Microwave Theory Tech.*, vol. 36, pp. 682–693, April 1988.

[3] J. Jin and V. V. Liepa, "Application of hybrid finite element method to electromagnetic scattering from coated cylinders," *IEEE Trans. Antennas Propagat.*, vol. 36, January 1988.

[4] W. E. Boyse and A. A. Seidl, "A hybrid finite element method for conductors with thin dense coatings," *Applied Computational Electromagnetics Society*, vol. 4, pp. 59–72, Fall 1989.

[5] K. K. Mei, "Unimoment method of solving antenna and scattering problems," *IEEE Trans. Antennas Propagat.*, vol. AP-22, pp. 760–766, November 1972.

[6] J. Lee and Z. J. Csendes, "Transfinite elements: A highly efficient procedure for modeling open field problems," *J. Appl. Phys.*, vol. 61, April 1987.

[7] J. B. Keller and D. Givoli, "Exact non-reflecting boundary conditions," *J. Comput. Phys.*, 1980.

[8] X. Yuan, D. R. Lynch, and J. W. Strohbehn, "Coupling of finite element and moment methods for electromagnetic scattering from inhomogeneous objects," *IEEE Trans. Antennas Propagat.*, vol. 38, pp. 386–393, March 1990.

[9] L. N. Medgyesi-Mitschang, P. L. Huddleston, and J. M. Putnam, "Radar scattering analysis: Mathematical formulations, Vol. I," Tech. Rep. MDCQ1230, McDonnell Douglas Research Laboratories, November 1984.

A New Expansion Function of GMT : the Ringpole

Jingliang Zheng
Institute of Fields and Waves, ETH Zürich
CH-8092 Zürich, Switzerland

Abstract - The Ringpole is a new expansion function of GMT (Generalized Multipole Technique) which has a strong analytical basic and a clear physical background. This Ringpole is suitable for calculating the fields in a domain, which has a part with a rotational symmetry. It has been programmed and may be used in MMP (Multiple MultiPole) programs. All the computed examples have shown, that the Ringpole can supply an excellent solution for the fields in the concerned domain with a massive reduction of the number of unknown parameters to be used and therefore the computation time in comparison with discrete Multipoles.

INTRODUCTION

The Generalized Multipole Technique (GMT) is a new method to solve electromagnetic problems, which has been developed in the past years. The MMP (Multiple MultiPole) programs are based on the GMT [1-3]. They offer fast and efficient computations of time harmonic electrodynamic problems with piecewise linear, homogeneous and isotropic materials. All kinds of examples have already proved, that the calculating results obtained by MMP programs have a good quality.

In GMT, the fields inside a domain are expanded as a superposition of the fields of several Multipoles. The unknown coefficients of these expansion functions are determined by matching the fields on the boundary of the various domains at discrete points. For complex geometrical form of a domain, many Multipoles are needed, so that the computation time, the memory requirements as well as the amount of work to create an Input file are not small. Introducing new expansion functions make it possible, to reduce the amount of all this work. Therefore, finding new expansion functions to increase the application's domain of GMT is a matter of particular interest.

MULTIPOLE - BASIC EXPANSION

MMP programs divide the total space into several domains, each of them is linear, homogeneous and isotropic. The fields inside a domain are expanded as a sum of several expansion functions.

$$F = \sum_{i=1}^{P} f_i$$

where each f_i is a Multipole expansion, which is the basic expansion function of MMP. These Multipole expansions are the exact solutions of the Helmholtz Equation in the concerned domain. In 3D problems they can be represented as

$$f_i = \sum_{n=1}^{N_i} \sum_{m=0}^{n} a_{nm} h_n(kr_i) P_n^m(\cos\theta_i) \begin{matrix}\cos \\ \sin\end{matrix}(m\phi_i)$$

where h_n are spherical Hankel (or Bessel) functions or their differentials, P_n^m are Legendre functions or their differentials, k is wavenumber in medium. The placement of the Multipoles must follow certain rules, so that the numerical linear dependencies among the expansion functions can be avoided. There are also other expansion functions in MMP programs, for example TEM expansions, plane waves and waveguide modes for rectangular and circular waveguides.

Let the expansions for the fields in various domains be matched in discrete matching points on the boundary between the domains. Generally, all 6 boundary conditions for the normal and transverse electric and magnetic fields are used. The coefficients a_{mn} are determined by solving the obtained equations. In the MMP programs, an overdetermined system of equations is used in order to improve the correct approximation of the fields solutions.

RINGPOLE

The expansion functions of a Multipole have an important character: they have a great influence upon the near region of origin and a small influence on the far region, which can often be neglected. Because of this behavior, the Multipoles should be placed around the domain, so that the whole boundary is covered by their neighborhoods. Therefore the locations of Multipoles are closely related to the domain form.

In order to reduce the amount of work, there is always the possibility of separating a complex geometry in many parts which are much simpler. Ringpole is suitable for calculating the fields in a domain, which has a part with a rotational symmetry. If the fields in such a domain are to be solved by GMT, many Multipoles have to be arranged on one ring. Their coefficients have a sinusoidal distribution. If these coefficients are transformed to Fourier series, then the experience shows that only the first few terms are dominant and the other terms can be neglected. Therefore, these discrete Multipoles can be replaced by a Ringpole with each of his orders corresponding to a term of the Fourier series above. The number of the unknown parameters in the problem may be massively reduced by this process.

The Ringpole is theoretical a line ring, which consists of many Multipoles. The expansion functions of Ringpole can be represented roughly as

$$f_i = \sum_{n=1}^{N_i} \sum_{m=0}^{n} \sum_{l=0}^{L_i} a_{lmn} \int_0^{2\pi} A(\zeta) h_n(kr(\zeta)) P_n^m(\cos\theta(\zeta)) \begin{matrix}\cos\\ \sin\end{matrix}(m\phi(\zeta)) \begin{matrix}\cos\\ \sin\end{matrix}(l\zeta) d\zeta$$

where each ζ corresponds a point on the ring, $(r(\zeta),\theta(\zeta),\phi(\zeta))$ are coordinates of field point in the local coordinate system with origin ζ, $\begin{matrix}\cos\\ \sin\end{matrix}(l\zeta)$ indicates the distribution of Multipoles on the ring, $A(\zeta)$ is a vector operator by which the corresponding components of the expansion function of Multipole should be obtained. If the orientations of the local coordinate system are chosen correctly, the modes for m>0 have only a very small contribution to the total fields, which can practically be neglected. If we set up a cylindrical coordinate system with the center of ring as origin and change all components into a new form corresponding to the cylindrical coordinate system, the integration above may be reduced on account of the symmetry by half. Therefore we have

$$f_i = \sum_{n=1}^{N_i} \sum_{l=0}^{L_i} a_{ln} \int_{\phi_0}^{\phi_0+\pi} B(\zeta) h_n(kr(\zeta)) P_n^m(\cos\theta(\zeta)) \begin{matrix}\cos\\ \sin\end{matrix}(l\zeta) d\zeta$$

where $B(\zeta)$ is a new vector operator, ϕ_0 is azimuthal coordinate of field point in the cylindrical coordinate system. Since $r(\zeta),\theta(\zeta)$ and $B(\zeta)$ all are the functions of ζ, it is at least very difficult, to find an analytical method, by which the integration above can be treated. The numerical integration, which is used in the program, is more practical.

In the physical sense, a Ringpole indicates the electric and magnetic currents along the circumferential ring and dipole-rings polarized in axial and radial orientations. Since this model can cause a much more accurate field in the corresponding domain than the discrete Multipoles, the original problem can be effectively simplified by the Ringpole.

EXAMPLE

A circular metallic plate is illuminated by a plane wave with a incidence of 45 degrees. The diameter and thickness of the plate are respectively 2.4 and 0.4 wavelength. Figure 1 shows the total near fields calculated by Ringpoles.

A circular horn antenna is excited by TE11 mode at the feedwaveguide. Both near and far fields are treated with Ringpoles. The E-field in the horn and the patterns of the horn in E- and H-plane are shown in Figure 2 separately.

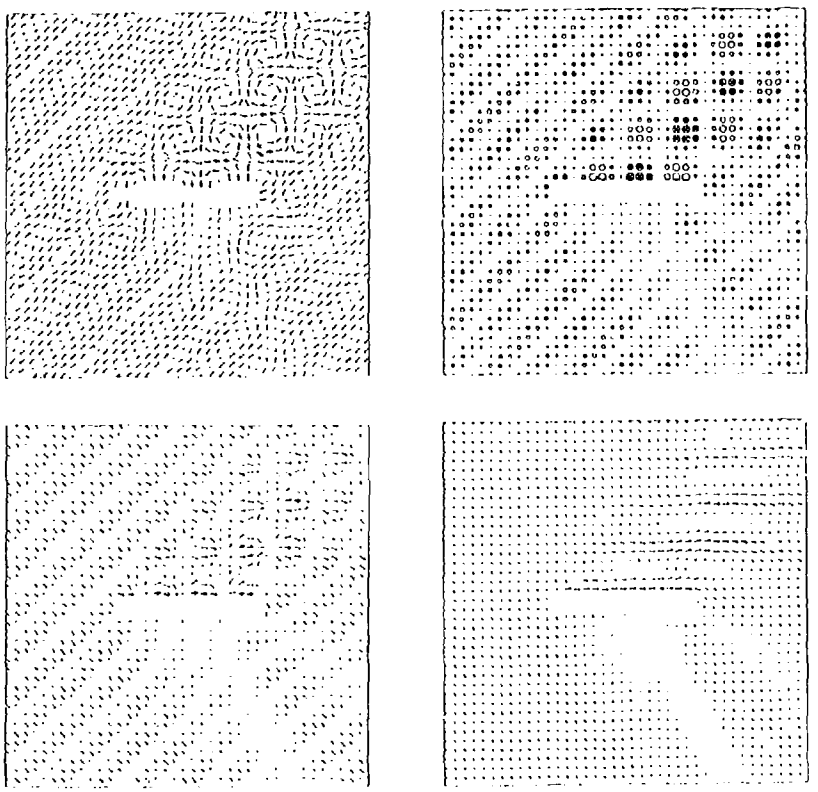

Fig.1 Fields near a metallic plate. *Left top:* E field. *Right top:* H field. *Left bottom:* Poynting vector. *Right bottom:* Poynting vector in time average.

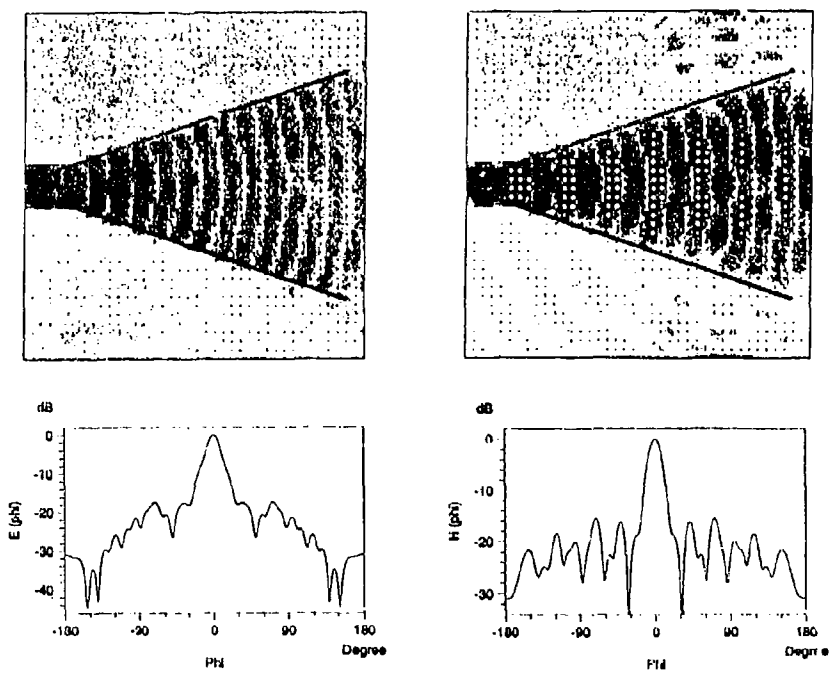

Fig.2 Fields of the horn. *On the top:* E field in the horn on E plane (*left*) and H-plane (*right*). *On the bottom:* Pattern of the horn on E-plane (*left*) and H-plane (*right*).

Conclusion

Ringpole can replace many discrete Multipoles for calculating the fields in the domain, which has a part with a rotational symmetry, or in the domain, which is rotational symmetrical (the latter one is a 3D problem for GMT). The placement of Multipoles and therefore the work to create a Input file can be simplified and the computation time can be massively reduced by this process. The quality of the solution of the fields in the concerned domain supplied by the Ringpole is excellent as good as by discrete Multipoles. With the help of Ringpole and all other new expansion functions, which we will treat, GMT will be even more comfortable.

References

[1] Ch. Hafner, The Generalized Multipole Technique for computational Electromagnetics, Artech House, London, 1990.

[2] L. Bomholt, MMP-3D -- A Computer Code for Electromagnetic Scattering Based on the GMT, Thesis ETH No. 9225, Zürich, 1990.

[3] L. Bomholt, Ch. Hafner, A MMP Program for Computations of 3D Electromagnetic Fields on PCs, 5th Annual Review of Progress in Applied Computational Electromagnetics (ACES), Conference Proceedings, March 1989.

AN APPLICATION OF SYMBOLIC MANIPULATION SOFTWARE IN COMPUTATIONAL ELECTROMAGNETICS

R. J. Pogorzelski†
General Research Corporation
5383 Hollister Avenue
Santa Barbara, CA 93160-6770

Abstract

Many of the expressions which arise in the formulations commonly used in computational electromagnetics are in the form of infinite series. Often these series are very slowly convergent and the resulting computational burden placed on a code which makes use of them can be prohibitive. A common series acceleration technique is the Kummer transformation which involves subtraction of a series of analytically known sum. Applying this technique with maximum effectivness often requires significant amounts of algebra prior to coding. This algebra can be carried out by means of symbolic manipulation software such as Mathematica with remarkable efficiency. Thus, by this means, one may greatly expand the effectiveness and breadth of applicability of such acceleration techniques in computational electromagnetics.

Introduction

Symbolic manipulation software performs algebraic and calculus operations in symbolic form rather than numerical computations although most such software is also able to calculate numerical results. Thus, it can function very effectively in support of computer code development in that the expressions leading to high level language statements can be derived using the symbolic capabilities and the resulting statements can be checkedfor coding accuracy using the numerical capabilities of the software.

As an example of the application suggested above, we consider the Green's function for helical structures derived by Pogorzelski [1] based on the work of Hill and Wait [2]. The elements of this dyadic Green's function are expressed in a Forminvolving several infinite series which are, for the range of arguments typically encountered in method of moments applications, very slowly convergent. The Kummer transformation can be employed to accelerate this convergence to an acceptable rate. In applying this technique, a series of analytically known sum is subtracted term by term from the

† Formerly with TRW Space & Technology Group, One Space Park, Redondo Beach, CA 90278 where this work was begun.

series to be accelerated. Then, the series of differences is summed and the analytically known sum is added to the result. The advantage of this procedure arises when the subtracted series is chosen so that its terms rapidly approach those of the series to be accelerated as the index of summation increases. That is, the terms of the known sum should be a large index asymptotic expansion of the terms of the desired sum. Derivation of the terms of this expansion can be extremely tedious. As will be demonstrated, it is here that symbolic manipulation software can be of very significantvalue to the electromagnetics programmer.

Analysis of Helical Structures

In carrying out the electromagnetic analysis of helical structures such as the twisted waveguide shown in Figure 1, the fields of currents disposed along helical trajectories around the symmetry axis are required. These fields become the elements of a dyadic Green's function appropriate to formulation of the problem in terms of an integral equation. Specifically, if the structure is perfectly conducting and one intends to use an electric field integral equation, one must obtain expressions for three independent vector components of the electric field due to three independent vector components of the current along a helix. The coordinate systems used to define these components is shown in Figure 2. As shown, the current is expressed in radial, longitudinal (along the helix), and transverse (across the helix) components while the electric field is expressed in the usual cylindrical coordinate system components, radial (ρ), azimuthal (ϕ), and axial (z). The three electric field components due to each of the three current components are the nine elements of the required dyadic Green's function. That is,

$$\begin{bmatrix} E_\rho \\ E_\phi \\ E_z \end{bmatrix} = \begin{bmatrix} G_{\rho\rho} & G_{\rho t} & G_{\rho\ell} \\ G_{\phi\rho} & G_{\phi t} & G_{\phi\ell} \\ G_{z\rho} & G_{zt} & G_{z\ell} \end{bmatrix} \begin{bmatrix} I_\rho \\ I_\phi \\ I_\ell \end{bmatrix}$$

$G_{z\ell}$ and $G_{\phi\ell}$ were previously obtained by Hill and Wait [2][3] and theremaining elements were provided by Pogorzelski [1]. For the present demonstration we select $G_{z\ell}$, the axial electric field of a longitudinal helical filamentary current, which may be expressed in the form,

$$G_{z\ell} = \frac{J}{2\pi k_o \rho_o} \sum_{n=-\infty}^{\infty} \frac{1}{k_o} \left(n\beta_n \sin\psi - w_n^2 \cos\psi\right) \times I_n(w_n\rho_o)\, K_n(w_n\rho)\, e^{-J\beta_n z}\, e^{Jn\phi}$$

where,

$w_n = \sqrt{\beta_n^2 - k_o^2}$, $\beta_n = \beta_o + \frac{2\pi n}{p}$, and p is the pitch of the helix measured along the axis of symmetry. When ρ is nearly equal to ρ_o, this series is very slowly convergent. To renderits use practical, it is necessary to accelerate the convergence.

Acceleration of the Series Convergence

As mentioned earlier, in order to accelerate the series convergence by means of the Kummer transformation, it is first necessary to form an analytically summable series whose terms are large index asymptotic approximations of the terms of the series to be accelerated. Fortunately, large index (order) expressions are available for the modified Bessel functions, I and K. [4] These are,

$$I_n(\zeta) \sim \frac{1}{\sqrt{2\pi}} \frac{e^{n\,\eta(\zeta/n)}}{\sqrt[4]{n^2+\zeta^2}}$$

$$K_n(\zeta) \sim \sqrt{\frac{\pi}{2}} \frac{e^{-n\,\eta(\zeta/n)}}{\sqrt[4]{n^2+\zeta^2}}$$

where,

$$\eta(\zeta/n) = \frac{1}{n}\left[\sqrt{n^2+\zeta^2} + n\,\ln\frac{\zeta}{n+\sqrt{n^2+\zeta^2}}\right]$$

With a minimal amount of algebra it is not difficult to show that for large n,

$$e^{n\,\eta(\zeta/n)} \sim \zeta^{n}\; n^{-n}\; e^{n\,[C - \ell n(1+C)]}\; e^{\left[\frac{C^2}{C+1}\right]\Delta}$$

where $C = \sqrt{1+Q^2}$, $\Delta = \left[\frac{Q}{1+Q^2}\right](\beta_o \rho)$, $Q = \frac{2\pi\rho}{p}$, and $\zeta = w_n \rho$.

Thus, the product of Bessel functions, IK, appearing in the series in question can be cast in the form,

$$I_n(w_n\rho_o)\, K_n(w_n\rho) \sim \frac{e^{-\alpha n - \gamma}}{\sqrt[4]{n^2 + (w_n\rho_o)^2}\;\sqrt[4]{n^2 + (w_n\rho)^2}}$$

where, $\alpha = [C - \ell n\,(1+C)] - [C_o - \ell n\,(1+C_o)] - \ell n\,[\rho_o/\rho]$, and

$$\gamma = \left[\frac{C^2}{C+1}\right]\Delta - \left[\frac{C_o^2}{C_o+1}\right]\Delta_o$$

and the subscript o indicates that ρ_o was used in place of ρ.

That is, the positive index part of the series expression for $G_{z\ell}$ has been cast in the form,

$$G_{z\ell} = \frac{J}{2\pi\, k_o\, \rho_o} \sum_{n=1}^{\infty} \frac{(n\,\beta_n \sin\psi - w_n^2\,\rho_o \cos\psi)}{k_o \sqrt[4]{n^2 + (w_n\rho_o)^2}\;\sqrt[4]{n^2 + (w_n\rho)^2}}$$

$$\times\; e^{-[\alpha - 2\pi J/p + J\phi]n - \gamma - J\beta_o z}$$

and the negative index part can be arranged similarly.

We now note that the series,

$$S = \sum_{n=1}^{\infty} \left[An + B + \frac{C}{n} + \frac{D}{n+1} \right] e^{-an}$$

possesses a closed form sum. That is,

$$\sum_{n=1}^{\infty} n\, e^{-an} = \frac{e^{-a}}{(1 - e^{-a})^2}$$

$$\sum_{n=1}^{\infty} e^{-an} = \frac{e^{-a}}{1 - e^{-a}}$$

$$\sum_{n=1}^{\infty} \frac{e^{-an}}{n} = \ln\left[\frac{1}{1 + e^{-a}}\right]$$

$$\sum_{n=1}^{\infty} \frac{e^{-an}}{n+1} = e^{a} \ln\left[\frac{1}{1 - e^{-a}}\right] - 1$$

We next note that the sum S above can be approximated to order n^{-2} by a series of the form,

$$\sum_{n=1}^{\infty} \left[\mathcal{A}n + \mathcal{B} + \frac{\mathcal{C}}{n} + \frac{\mathcal{D}}{n^2} \right] e^{-an}$$

Thus it becomes desirable to expand the asymptotic form of $G_{z\ell}$ given above in this form. That is, we wish to obtain $\mathcal{A}$, $\mathcal{B}$, $\mathcal{C}$, and $\mathcal{D}$ such that to order n^{-2},

$$\mathcal{A}n+\mathcal{B}+\frac{\mathcal{C}}{n}+\frac{\mathcal{D}}{n^2} = \frac{(n\beta_n \sin\psi - \omega_n^2 \rho_o \cos\psi)}{k_o \sqrt[4]{n^2 + (\omega_n \rho_o)^2}\ \sqrt[4]{n^2 + (\omega_n \rho)^2}}\, e^{-\gamma - j\beta_o z}$$

with $a = \alpha - 2\pi j/p + j\phi$. This is just the sort of operation at which symbolic manipulation software excels. In the case of Mathematica, one merely enters the above expression in BASIC format and issues the command,

```
Series[%,{n,Infinity,3}]
```

which instructs the software to expand the given expression in

powers of n about infinity; i.e., in inverse powers of n. The result is a set of algebraic expressions for $\mathcal{A}$, $\mathcal{B}$, $\mathcal{C}$, and $\mathcal{D}$. Figure 3 shows the expansion obtained by Mathematica upon applying a number of simplifying substitutions (variable definitions). One may also request that these results be placed in FORTRAN format for direct use in a FORTRAN program implementing this series acceleration (although the resulting FORTRAN appears to be somewhat inefficient).

It should be remarked at this point that the above approximation scheme can be generalized to any desired order of accuracy by generalizing the form of the approximating series to,

$$\sum_{n=1}^{\infty} An + B + \sum_{m=0}^{M} \frac{C_{mn}}{n+m} = \sum_{n=1}^{\infty} \mathcal{A}n + \mathcal{B} + \sum_{m=0}^{M+1} \frac{\mathcal{C}_{mn}}{n^m} + \mathcal{O}(n^{-(M+2)})$$

For large M, derivation of the algebraic expressions for the $\mathcal{C}_{mn}$'s by hand is prohibitively complicated. However, using symbolic manipulation software, one may carry it out with ease. One merely issues the command,

```
Series[%,{n,Infinity,M+2}]
```

An Example Result.

The above expressions for $\mathcal{A}$, $\mathcal{B}$, $\mathcal{C}$, and $\mathcal{D}$ permit the application of the Kummer transformation to the series for $G_{zz'}$. Since the asymptotic approximation very accurately approximates the terms of the G series in exactly the range of parameters where the series is most poorly convergent (where ρ is close to ρ_0), theresulting difference series converges very rapidly in all ranges of parameters. In particular, Figure 4 displays the partial sums of the original and accelerated series for a case where $\rho = 1.05\rho_0$. Note that the accelerated series converged in less than 10 terms while the original series has not yet converged after adding100 terms! Similar results have been observed for the other elements of the dyadic Green's function.

It is remarked in passing that the curves in Figure 4 also indicate why the Shanks transformation [5] would not be as effective as the present Kummer transformationin accelerating the series. Recall that the Shanks transformation makes use of the early partial sums to estimate the behavior of the

convergence curve viewed as a so-called "numerical transient". However, as is clear from Figure 4, in this case a very large number of partial sums would be required before one could accurately estimate the oscillation rate of the convergence transient. Thus, the Shanks transformation might require several tens of terms as opposed to the five or so terms required in the Kummer procedure.

Concluding Remarks.

The utility of symbolic manipulation software in programming acceleration of series has been demonstrated in the context of evaluation of a dyadic Green's function for helical structures. This nine component Green's function is suitable for the formulation of an electric field integral equation for perfectly conducting helical structures. A corresonding dyadic applicable to combined field formulations and helical dielectric structures would have thirtysix elements which are the electric and magnetic field components due to electric and magnetic currents. The algebra involved in accelerating all of these series would be truly staggering even though duality reduces thenumber by half. Nevertheless, such a task is well within the capacity of anyone having access to suitable symbolic manipulation software. It is concluded that such software can in many cases be an indispensible programming aid in computation electromagnetics.

References.

1. R. J. Pogorzelski, "On the Numerical Computation of a Green's Function for Helical Structures," National Radio Science Meeting, May 1990, Dallas, TX.

2. J. R. Wait, "Electromagnetic Theory of the Loosely Braided Coaxial Cable: Part I," IEEE Trans. MTT-24, 547-553, Sept. 1976.

3. D. A. Hill, "Propagation Along a Coaxial Cable with a Helical Shield," IEEE Trans. MTT-28, 84-89, Feb. 1980.

4. M. Abramowitz and I. A. Stegun, Handbook of Mathematical Functions, National Bureau of Standards Applied Mathematics Series 55, June 1964, pg. 378, Eqns 9.7.7, 9.7.8, and 9.7.11.

5. D. Shanks, "Non-linear Transformations of Divergent and Slowly Convergent Sequences," J. Math. and Physics, 34, 1955, pp. 1-42.

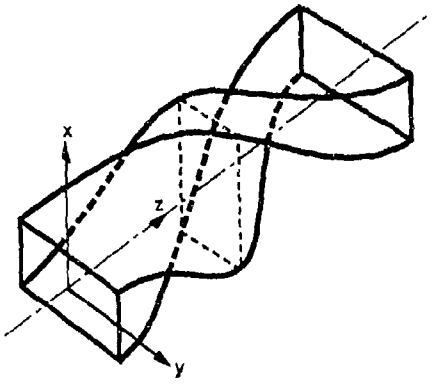

Figure 1. Twisted Waveguide.

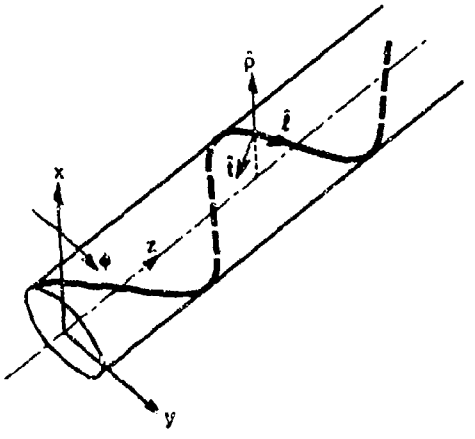

Figure 2. Helical Filamentary Source.

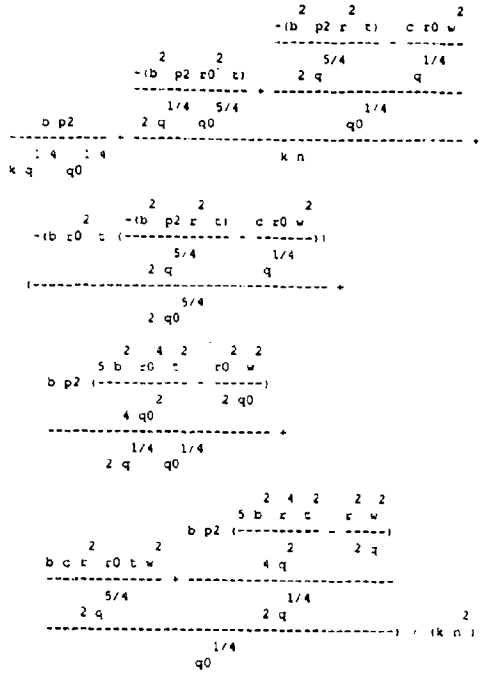

Figure 3. Mathematica Output.

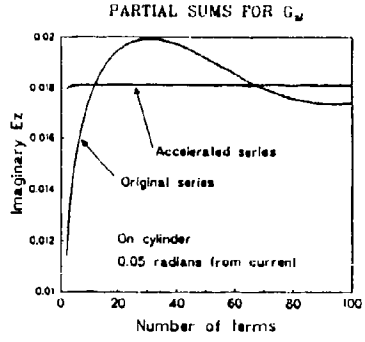

Figure 4. Series Convergence.

Efficient Solution of Matrix Equations in Finite Element Modeling of Eddy Current NDE

A. Mahmood, D.J. Lynch, Q.H. Nguyen, L.D. Philipp

* Washington State University at Tri-Cities, Richland WA 99352

ABSTRACT Finite element modeling (FEM) of eddy currents often involves large matrices. The efficiency of the algorithm used for solving matrix equations is extremely critical to the overall computation time. The purpose of this paper is to survey and analyze various approaches to solving matrix equations in main memory and to identify the most time efficient approach within the context of finite element formulation of two dimensional eddy current problems. A comparison of methods used to introduce boundary conditions shows the benefits of the "1's and 0's" substitution technique over the "blasting factor" method. Evaluation of matrix decomposition algorithms indicates that Cholesky decomposition yields the shortest run times of the methods considered. A modified Cholesky algorithm, eliminating back substitution for un-essential variables is developed. Minimum computation time is demonstrated using the modified Cholesky decomposition algorithm and the "1's and 0's" boundary condition technique.

1. Introduction

Finite element methods have been applied to many different engineering problems. In particular, they have been shown to be very useful in modeling eddy current NDE (non-destructive evaluation) phenomena.

In the finite element method, integral or differential equations are solved by dividing a problem region into subregions of simple form called finite elements. Nodes exist on boundaries of elements. By assembling the resulting equations involving the nodes and the elements, an equivalent problem in matrix algebra is formulated. The matrix equation to be solved has the general form, **Mx = b** where **M** is an nxn coefficient matrix, **x** is an nx1 vector of nodal unknowns, and **b** is a known nx1 vector. If **M** is a positive definite and/or non-singular matrix, then the problem is deterministic and has a unique vector solution x. In the case of finite element formulation of eddy current phenomena, the matrix equations involved have a positive definite coefficient matrix, since positive definiteness of **M** physically corresponds to stored energy being positive for all excitations [1].

For relatively large problems in finite element modeling, more than 95% of the computation time is consumed by the matrix equation solver subroutine. Thus the efficiency of the matrix solver algorithm is extremely critical to the overall computation time. In a two dimensional eddy current problem, matrix sizes of n =1000 to 5000 are typical and three dimensional fields may require matrix sizes in the range of 50,000 to 250,000 variables [1, 2]. Computation times of several minutes to a few hours can be encountered for such problems.

Finite element formulations generally produce sparse, banded and symmetric matrices, since each nodal variable is connected only to nodal variables which appear in the same finite element. Considerable savings in execution time and memory are achieved by taking advantage of these matrix properties.

* Sponsored by Electric Power Research Institute, EPRI, Contract RP 1570-26

2. Techniques for Introducing Boundary Conditions

There are two popular techniques for introducing boundary conditions in finite element problems. One is referred to as the "blasting factor" technique and the other as the "1's and 0's substitution" technique [3]. Both techniques preserve the symmetry and bandedness property of the original matrices and thus are convenient to use. We will briefly describe the two techniques and then compare their relative computational efficiencies.

In the blasting factor technique, a nodal variable, whose value is specified by boundary conditions, is multiplied by a large number, known as the blasting factor. The corresponding term in the vector **b** and the diagonal term in that row of **M** are also multiplied by the blasting factor. As an example, the following matrix shows how to effectively specify $x_1=c_1$, and $x_3=c_3$ assuming that the blasting factor is much larger than the largest element in **M**.

$$\begin{bmatrix} m_{11}\cdot 10^6 & m_{12} & m_{13} \\ m_{21} & m_{22} & m_{23} \\ m_{31} & m_{32} & m_{33}\cdot 10^6 \end{bmatrix} \begin{bmatrix} x_1 \\ x_2 \\ x_3 \end{bmatrix} = \begin{bmatrix} c_1 \, m_{11} \, 10^6 \\ b_2 \\ c_3 \, m_{33} \, 10^6 \end{bmatrix}$$

The result of using the blasting factor in row 1 of M and b is to effectively make $m_{12}=0$ and $m_{13}=0$, thus $x_1=c_1$. Similarly m_{31} and m_{32} are effectively reduced to 0 in row 3, making $x_3 = c_3$.

In the "1's and 0's substitution" technique, if the variable x_i is prescribed, the ith row and ith column entries in matrix **M** are set to 0 and m_{ii} is set to 1. The non-prescribed terms in b are modified to account for the prescribed variable values. A simple example is given below which shows how x_1 is set to a value c_1.

$$\begin{bmatrix} 1 & 0 & 0 \\ 0 & m_{22} & m_{23} \\ 0 & m_{32} & m_{33} \end{bmatrix} \begin{bmatrix} x_1 \\ x_2 \\ x_3 \end{bmatrix} = \begin{bmatrix} c_1 \\ b_2 - m_{21}\cdot c_1 \\ b_3 - m_{31} \, c_1 \end{bmatrix}$$

After boundary conditions have been introduced using either of these methods, the remaining step is to carry out the solution of the matrix equation.

2.1 Comparison of the "Blasting Factor" and "1's and 0's Substitution" Techniques.

Comparing the two techniques for setting boundary conditions, the "1's and 0's" substitution technique makes the matrix **M** more sparse because of additional zero entries within the banded portion. However, more operations are required on matrix **b** for the non-prescribed nodal variables. In general there will be n multiplications and n subtractions for every b corresponding to a non-prescribed variable. Fortunately, these extra operations are not required when the prescribed values are zero since the multiplication by zero and subsequent subtraction is not needed. This happens in the case of finite element formulation of the magnetic vector potential for eddy current problems [7]. Hence the coefficient matrix will have a large number of zero entries when using the "1's and 0's substitution" technique whereas for the blasting technique, the coefficient matrix will be less sparse although still banded.

Figure 1 shows timing curves for a sample eddy current finite element problem using the two techniques for applying boundary conditions. For each curve in the figure, the same algorithm, based on LU decomposition, is used to solve the matrix equations. For this case, the "1's and 0's" technique yields smaller execution times than the blasting factor technique. The smaller run time is due to the large number of zeros in the matrix generated from the "1's and 0's" technique as a floating point arithmetic operation takes significantly less time when one of the operands is zero as compared to when both are non-zero. Table 1 shows the differences in execution times of floating point operations on a PRIME 9755 computer when one operand is zero and when both operands are non-zero.

The size of the blasting factor has an effect on the accuracy and the overall execution time. A blasting factor less than 10^8 may not yield accurate results. A larger blasting factor may reduce the execution time by effectively creating more zero-valued entries to be used in the backward substitution phase but, a very large blasting factor may cause creation of more zeros because of floating point underflow. Handling of an underflow condition is more time consuming on certain computers and thus an improvement in execution time may not be observed.

3. Solution of the Matrix Equation

Since the matrices involved in the finite element formulation of eddy currents are positive-definite, banded and symmetric, we will focus on the efficient solution of matrices under these conditions. For eddy current testing of flaws in tubing, the probe coil is moved to various positions in the tube to be tested. The resulting eddy current response indicates the existence of a flaw. In terms of matrices, this corresponds to solving $\mathbf{M}\,\mathbf{x} = \mathbf{b}$ for different b vectors with no change in the coefficient matrix **M**. For efficient solution of the problem, it is very important that some sort of triangular decomposition scheme be used. Once **M** is decomposed into its triangular components by forward elimination, solutions for different b vectors can be quickly evaluated by repeatedly solving the two triangular equations. The latter step is known as back substitution. Thus, in the solution of finite element problems, forward elimination is carried out once only and back substitution is carried out for each of the different probe coil positions.

The Cholesky decomposition algorithm and two variations of LU decomposition are considered in this study in order to determine the best method for solving the matrix equation generated in the FEM of an eddy current problem. The algorithms discussed here differ mainly in the forward elimination phase since their back substitution phases are almost identical except for the modified Cholesky's algorithm. Theoretical time complexities are discussed for the forward elimination phase and the different approaches are compared for execution times on a sample problem.

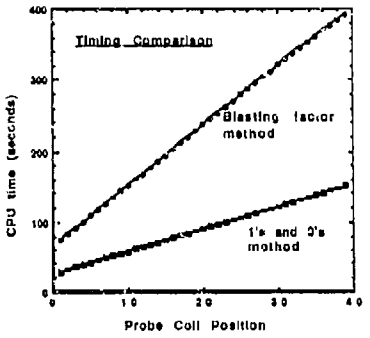

Figure 1. Comparison of matrix solution execution times for two methods of setting boundary conditions.

Operation	Non zero Operands (μs)	One Operand Zero (μs)
Complex Add	2.72	2.62
Real Add	1.05	0.80
Complex Sub.	2.88	2.78
Real Sub.	1.13	0.94
Complex Mult.	13.86	9.70
Real Mult.	1.82	0.72
Complex Div.	32.65	17.4
Real Div.	5.71	0.92
Complex Sqrt.	50.35	10.7
Real Sqrt.	15.83	2.17

Table 1. Comparison of Execution Times of Zero and Non-zero Operands

3.1 LU Decomposition Technique

In the LU decomposition technique, the coefficient matrix **M** is partitioned into its lower and upper triangular parts in the forward elimination phase as **M** = L U (where L is the lower triangular matrix and U is the upper triangular matrix). Then, two sets of triangular equations are solved in the back substitution phase.

$$\left.\begin{array}{ll} L\,y = b & \text{solve for } y \\ U\,x = y & \text{solve for } x \end{array}\right\} \text{back substitution}$$

The LU decomposition algorithm (forward elimination) for a symmetric matrix with semi-bandwidth B can be written as:

```
For k = 1,...,n - 1
    For i = k + 1,...,Min(k + B, n)
        m_ik = m_ik / m_kk
    For i = k + 1,...,Min(k + B, n)
        For j = k + 1,...,Min(k + B,n)
            m_ij = m_ij - m_ik m_kj
```

Upon completion of this algorithm, L and U replace the original matrix **M** such that $l_{ik} = m_{ik}$ for $k < i$, $l_{ij} = 1$, and $u_{kj} = m_{kj}$ for $k \le j$.

Two implementations of the LU decomposition technique were considered. The first version as used by Lord [5] is referred to as LUD1. It has exactly same number and type of operations as a standard LU decomposition program but the order of operations and the storage of the matrix is different. The second implementation is standard, referred to as LUD2.

In LU decomposition, Gauss elimination is used in the forward elimination phase. This process can be described by the following recurrence equations,

$$m_{ij}^{(k-1)} = m_{j,k-1}^{(k-1)} - \left(m_{ij}^{(k-1)} / m_{k-1,k-1}^{(k-1)} \right) \cdot m_{k-1,j}^{(k-1)} \quad (1)$$

and

$$b_i^{(k)} = b_i^{(k-1)} - \left(m_{i,k-1}^{(k-1)} / m_{k-1,k-1}^{(k-1)} \right) \cdot b_{k-1}^{(k-1)} \quad (2)$$

for $i, j = k, k+1, \ldots n$

where $b_i^{(1)} = b_i$ and $m_{ij}^{(1)} = m_{ij}$.

Considering a small matrix equation (n = 3) illustrates how different implementations of LU decomposition affect the execution time of the matrix solution task. Gauss elimination will transform matrices M (3x3) and b to give the following equation,

$$\begin{bmatrix} m_{11}^{(1)} & m_{12}^{(1)} & m_{13}^{(1)} \\ 0 & m_{22}^{(2)} & m_{23}^{(2)} \\ 0 & 0 & m_{33}^{(3)} \end{bmatrix} \begin{bmatrix} x_1 \\ x_2 \\ x_3 \end{bmatrix} = \begin{bmatrix} b_1^{(1)} \\ b_2^{(2)} \\ b_3^{(3)} \end{bmatrix} \quad (3)$$

Solving the above triangular matrix for the x's results in,

$$x_3 = b_3^{(3)} / m_{33}^{(3)}$$

$$x_2 = \left(b_2^{(2)} - m_{23}^{(2)} x_3 \right) / m_{22}^{(2)}$$

$$x_1 = \left(b_1^{(1)} - m_{12}^{(1)} x_2 - m_{13}^{(1)} x_3 \right) / m_{11}^{(1)} \quad (4)$$

Alternatively the above solution may be written:

$$x_3 = b_3^{(3)} / m_{33}^{(3)}$$

$$x_2 = b_2^{(2)} / m_{22}^{(2)} - \left(m_{23}^{(2)} / m_{22}^{(2)} \right) x_3$$

$$x_1 = b_1^{(1)} / m_{11}^{(1)} - \left(m_{12}^{(1)} / m_{11}^{(1)} \right) x_2 - \left(m_{13}^{(1)} / m_{11}^{(1)} \right) x_3 \quad (5)$$

In LUD1, the **M** matrix after forward elimination is stored as,

$$\begin{bmatrix} m_{11}^{(1)} & m_{12}^{(1)} / m_{11}^{(1)} & m_{13}^{(1)} / m_{11}^{(1)} \\ 0 & m_{22}^{(2)} & m_{23}^{(2)} / m_{22}^{(2)} \\ 0 & 0 & m_{33}^{(3)} \end{bmatrix} \begin{bmatrix} x_1 \\ x_2 \\ x_3 \end{bmatrix} = \begin{bmatrix} b_1^{(1)} \\ b_2^{(2)} \\ b_3^{(3)} \end{bmatrix} \quad (6)$$

Now for different sets of b's, we need to compute $b_2^{(2)}$, $b_3^{(3)}$ ... before solving the one triangular equation as shown above.

In contrast, using the alternative LU decomposition program (LUD2), the matrices after forward elimination appear as,

$$\begin{bmatrix} m_{11}^{(1)} & m_{12}^{(1)} & m_{13}^{(1)} \\ m_{12}^{(1)} / m_{11}^{(1)} & m_{22}^{(2)} & m_{23}^{(2)} \\ m_{13}^{(1)} / m_{11}^{(1)} & m_{23}^{(2)} / m_{22}^{(2)} & m_{33}^{(3)} \end{bmatrix} \begin{bmatrix} x_1 \\ x_2 \\ x_3 \end{bmatrix} = \begin{bmatrix} b_1^{(1)} \\ b_2 \\ b_3 \end{bmatrix} \quad (7)$$

Two triangular matrix equations will be obtained from equation (7) and solved in the back substitution phase as,

$$\begin{bmatrix} 1 & 0 & 0 \\ m_{12}^{(1)} / m_{11}^{(1)} & 1 & 0 \\ m_{13}^{(1)} / m_{11}^{(1)} & m_{23}^{(2)} / m_{22}^{(2)} & 1 \end{bmatrix} \begin{bmatrix} y_1 \\ y_2 \\ y_3 \end{bmatrix} = \begin{bmatrix} b_1 \\ b_2 \\ b_3 \end{bmatrix} \quad (8)$$

solve for y's

$$\begin{bmatrix} m_{11}^{(1)} & m_{12}^{(1)} & m_{13}^{(1)} \\ 0 & m_{22}^{(2)} & m_{23}^{(2)} \\ 0 & 0 & m_{33}^{(3)} \end{bmatrix} \begin{bmatrix} x_1 \\ x_2 \\ x_3 \end{bmatrix} = \begin{bmatrix} y_1 \\ y_2 \\ y_3 \end{bmatrix} \quad (9)$$

solve for x's

This yields,

$$x_3 = y_3 / m_{33}^{(3)}$$

$$x_2 = \left(y_2 - m_{23}^{(2)} x_3 \right) / m_{22}^{(2)}$$

$$x_1 = \left(y_1 - m_{12}^{(1)} x_2 - m_{13}^{(1)} x_3 \right) / m_{11}^{(1)} \qquad (10)$$

The y_1, y_2, and y_3 in above equations are similar to $b_1^{(1)}$ $b_2^{(2)}$, and $b_3^{(3)}$ respectively in case of LUD1. Thus the only important difference in LUD1 and LUD2 is the order of the operations. In LUD1, division by the diagonal elements m_{ii} had to be done first as shown in equation (5), whereas in LUD2, division is the last operation. This may have a significant effect in certain situations. For example, if m_{11} is a complex number with non-zero real and imaginary parts, and the rest of matrix is only real, then LUD1 will evaluate x_1 as,

$$x_1 = b_1 / m_{11} - (m_{12}/m_{11}) x_2 - (m_{13}/m_{11}) x_3$$

which indicates one complex division, two complex multiplications, and two complex additions. On the other hand, LUD2 will evaluate x_1 as,

$$x_1 = (b_1 \quad m_{12} x_2 - m_{13} x_3) / m_{11}$$

This will involve the same number of operations but now only one division is a complex operation and everything else is a real operation. Hence LUD2 will execute measurably faster in this case.

3.2 Cholesky Decomposition:

In Cholesky decomposition, **M** is decomposed such that $\mathbf{M} = LL^T$ where **L** is a lower triangular matrix. For this decomposition to exist, the matrix **M** must be positive definite, and this property is guaranteed in FEM. After performing the decomposition, the two triangular equations are solved as,

$M x = b$	starting matrix equation	
$LL^T x = b$	M is decomposed (forward elim.)	
$L y = b$	solve for y	(back substitution)
$L^T x = y$	solve for x	

For different sets of b's corresponding to different positions of the eddy current probe, it is necessary to solve only the last two triangular equations as L and L^T remain the same.

The Cholesky decomposition algorithm for a symmetric matrix with semi-bandwidth B is:

For $j = j_{min}, \ldots, i-1$

$$m_{ij} = \frac{m_{ij} - \sum_{k=j_{min}}^{j-1} m_{ik} m_{kj}}{m_{jj}}$$

$$m_{ii} = SQRT\left(m_{ii} - \sum_{k=j_{min}}^{i-1} m_{ik}^2 \right)$$

4. Comparison of Time Efficiencies of Algorithms

For most computers, floating point operations (flops) consume considerably more time than integer arithmetic operations. So in analyzing algorithms, all integer operations such as array indexing, loop overhead, etc. are ignored. All three triangular decomposition algorithms under consideration have a general time complexity of $O(n \cdot B^2)$ (where n is the length of coefficient matrix M and B is its semi-bandwidth). Although the time complexities are the same for the three algorithms discussed in this paper, they yield different execution times because the type of operations and the order of operations is different. For example, the Cholesky algorithm uses the square root operation whereas the LU decomposition does not.

In analyzing computational floating point complexity for the Cholesky algorithm, the number and type of operations in the forward elimination phase are:

Number of sqrt. = n
Number of div. = $B(n-1/2) - (1/2)B^2$
Number of mult. = $B(n/2 - 1/6) + B^2((n/2)-1/2) - (1/3)B^3$
Number of add. and sub. = $n + B((3/2)n - (2/3)) + B^2((n/2)-1) - (1/3)B^3$

The number of floating point operations in forward elimination phase of LU decomposition are:

Number of sqrt. = 0
Number of div. = $(n-1/2)B - (1/2)B^2$
Number of mult. = $(1/6)B + (n-1/2)B^2 - (2/3)B^3$
Number of add. and sub. = $(1/6)B + (n-1/2)B^2 - (2/3)B^3$

If the floating point operations are normalized with respect to "floating point add time", the time efficiencies can be more comprehensively described. Table 1 indicates that complex multiplication takes about 5 times more time than complex addition. Complex division takes 12 times longer and complex square root takes 19 times longer. Using these numbers as weighting factors in the flops count, the time efficiencies can be expressed as follows: for Cholesky's decomposition :

$20n + 16nB - 7.5B + 3nB^2 - 9.5B^2 - 2B^3$

for LU decomposition:

$12nB - 5B + 6nB^2 - 9B2 - 4B^3$

Figure 2 shows a comparison of the normalized floating point operation counts for Cholesky and LU decomposition for different n's and a fixed B. Figure 3 compares the two algorithms for a fixed n but different

B's. From figures 2 and 3, it is concluded that Cholesky decomposition yields a smaller execution time, hence, this algorithm is optimized for the finite element analysis of eddy current problems.

4.1 Modified Cholesky's Algorithm.

Typically, the eddy current probe impedance is the desired result for an FEM formulation of an eddy current NDE problem and this impedance can be calculated from the magnetic vector potential within the coils. The FEM code may calculate the magnetic vector potential in every element but when the desired potentials are available, the algorithm can be terminated. Using these properties, the Cholesky algorithm was modified. The forward elimination phase of the algorithm remains unchanged but in the back substitution phase, the sub-program is terminated as soon as the solution for the last desired field point is obtained.

4.2 Comparison of Execution Times for a Sample Problem.

Execution times for an axisymmetric eddy current problem are given in Figure 4, which shows a comparison of 5 algorithms i.e., LINPACK [6], LUD1, LUD2, Cholesky and modified Cholesky on a sample "differential coil in tube" problem. From this figure, it can be seen that LUD1, LUD2 and standard Cholesky have fairly close execution times. Forward elimination is carried out only in position 1. For the remaining probe coil positions, only back substitution is needed. The forward elimination phase of Cholesky is slightly better than LUD2 but the back substitution phase of Cholesky is almost exactly the same as LUD2. The slope of run time for different positions of the coil is thus the same for LUD2 and Cholesky decomposition. For the methods considered here, the modified Cholesky routine has the best performance since its back substitution phase is the shortest. Overall, an improvement of more than 25% was achieved by the modified Cholesky routine over standard Cholesky and LU decomposition programs.

It should also be noted that pivoting is not necessary in the forward elimination phase when dealing with positive definite matrices [4]. Since we are dealing with positive definite matrices, considerable saving in time is achieved in the triangular factorization phase. However, as a check on the accuracy of the non-pivoting methods, a standard LINPACK program (sub-routines CGBFA, CGBSL) [6], was used to compare the results since this routine uses pivoting. The execution time of the LINPACK routine is about three times larger compared to a customized Cholesky routine for decomposition and the solution of the matrix equation in this example, but all routines maintain the same accuracy in the solution.

5. Conclusions

This study began when lengthy CPU times were encountered while testing a two-dimensional finite element code for modeling eddy current NDE. In an attempt to improve the time-performance of the code, all aspects of the matrix solution problem were

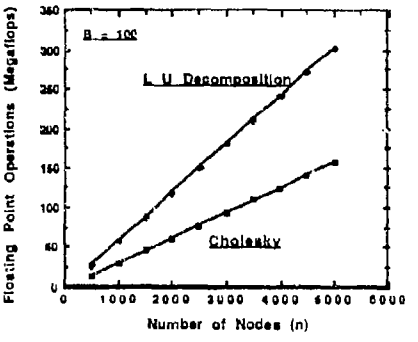

Figure 2. Comparison of LU and Cholesky decomposition floating point operation counts as a function of the number of nodes for fixed semi-bandwidth (B=100).

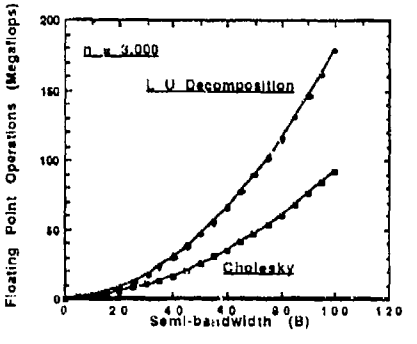

Figure 3. Comparison of LU and Cholesky decomposition floating point operation counts as a function of the semi-bandwidth for fixed number of nodes (n=3000)

considered in detail. Two popular methods of implementing boundary conditions were evaluated. Careful comparison of "blasting factor" and the "1's and 0's" methods showed that the latter technique produces a more sparse intermediate matrix and results in smaller execution times for all applications of this finite element model.

A comparison of different algorithms for triangular decomposition was also undertaken. Theoretical analysis and actual run time performance indicated that Cholesky decomposition yields better execution

times than LU decomposition for large problems. The Cholesky algorithm was modified for the special case of finite element formulation of eddy current NDE. The modified Cholesky algorithm , combined with the "1's and 0's" boundary condition technique, yields an overall improvement of a factor of three over the "blasting factor" boundary condition technique combined with LU decomposition used in earlier work in this field [5].

References

1. Sylvester, P.P. and R.L. Ferrari, "Finite Element for Electrical Engineers," Cambridge University Press, 1983.
2. Pissanetzky, S., "Sparse Matrix Technology," Academic Press, Inc., 1984.
3. Huebner, K. H. and E. A. Thornton, " The Finite Element Method for Engineers," John Wiley and Sons, 1982, pp. 50-53.
4. Forsythe, G. E. and C. B. Moler, "Computer Solutions of Linear Systems," Prentice-Hall Inc., 1967.
5. Lord, W., "Development of a Finite Element Model for Eddy-Current NDT Phenomena," EPRI NP2026, 1981.
6. Dongarra, J. J., C. B. Moler, J. R. Bunch, G. W. Stewart, "LINPACK user's guide," SIAM, 1985.
7. Palanisamy, R. and W. Lord, "Finite Element Analysis of Eddy Current Phenomena," Materials Evaluation, Oct. 1980

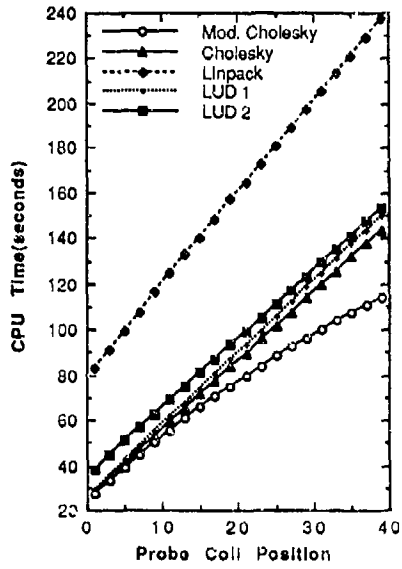

Figure 4. Comparison of execution times of matrix solution algorithms for a "differential coil in tube" problem (n=2400, B=30).

AN APPROXIMATE (SYMMETRIC) COMBINED FIELD INTEGRAL EQUATION FOR THE ANALYSIS OF SCATTERING BY CONDUCTING BODIES IN THE RESONANCE REGION

Luis M. Correia and Afonso M. Barbosa
Centro de Análise e Processamento de Sinais and
Departamento de Engenharia Electrotécnica e de Computadores,
Instituto Superior Técnico, Universidade Técnica de Lisboa
Av. Rovisco Pais, 1096 LISBOA CODEX, PORTUGAL

ABSTRACT

A new integral equation, the Approximate (Symmetric) Combined Field Integral Equation, is presented and used to analyze the scattering by conducting bodies in the resonance region. It results from a linear combination of the Electric Field Integral Equation with the Approximate (Symmetric) Magnetic Field Integral Equation. The matrix associated with this new equation is symmetric, reducing CPU time and computer memory. Condition numbers and scattering cross sections are presented for the sphere and the cube, and compared with those obtained using the exact integral equation. An analysis of CPU time and computer memory space is done.

I. INTRODUCTION

When dealing with the problem of scattering by conducting bodies in the resonance region, the Combined Field Integral Equation (CFIE) [1] (a linear combination of the Electric and the Magnetic Field Integral Equations - EFIE and MFIE) ensures a unique solution for the resonant frequencies. Usually, the Method of Moments [2] is used to solve the CFIE, but CPU time and/or computer memory may impose severe limitations on the dimensions of the bodies. To overcome these limitations, several approximations have been proposed (*e.g.* [3]). In order to reduce CPU time and memory, the authors have recently presented an Approximate (Symmetric) Magnetic Field Integral Equation (A(S)MFIE) [4], that generates a symmetric matrix when Galerkin's Method [2] is used. This matrix is generated by taking the average of the opposite coefficients (refering to the main diagonal) of the MFIE matrix. A symmetric matrix has two advantages: it needs less computer memory to be stored, and its factorization time is about half of the value for a general non-symmetric one.

In this communication, a new integral equation is presented, which will be refered as the Approximate (Symmetric) Combined Field Integral Equation - A(S)CFIE. As it

results from the linear combination of the EFIE with the A(S)MFIE, is has the advantage of generating a symmetric matrix, which is not the case for the CFIE. The triangular patch basis function [5] is used to solve the A(S)CFIE. The sphere and the cube are used as test scatterers. Results are shown for the condition number, and the back and forth scattering cross sections, and a comparison is made with identical results from the CFIE and others.

II. THE APPROXIMATE (SYMMETRIC) CFIE

The EFIE and the MFIE, which formulate the problem of scattering by a perfectly conducting body, are (in operator form) [1]

$$\mathcal{L}_E \mathbf{J}_S = \mathbf{F}^i_E \tag{1}$$

$$\mathcal{L}_M \mathbf{J}_S = \frac{1}{2}\mathbf{J}_S + \mathcal{L}_M{}'\mathbf{J}_S = \mathbf{F}^i_M \tag{2}$$

where

$$\mathcal{L}_E \mathbf{J}_S = \frac{1}{4\pi j\omega\varepsilon_0}\mathbf{n}\times\int_S \left[-\kappa^2 \mathbf{J}_S(\mathbf{r}')\,\Psi(\mathbf{r},\mathbf{r}') + \nabla'_S\cdot \mathbf{J}_S(\mathbf{r}')\,\nabla'\Psi(\mathbf{r},\mathbf{r}')\right] dS' \tag{3}$$

$$\mathcal{L}_M{}'\mathbf{J}_S = -\mathbf{n}\times\frac{1}{4\pi}\int_S \mathbf{J}_S(\mathbf{r}')\times\nabla'\Psi(\mathbf{r},\mathbf{r}')\,dS' \tag{4}$$

$$\mathbf{F}^i_E = \mathbf{n}\times\mathbf{E}^i(\mathbf{r}) \tag{5}$$

$$\mathbf{F}^i_M = \mathbf{n}\times\mathbf{H}^i(\mathbf{r}) \tag{6}$$

S is the (closed) surface of the object with exterior normal $\mathbf{n}$, $\mathbf{J}_S$ is the unknown surface electric current density, Ψ is the free-space Green's function, and $\mathbf{E}^i, \mathbf{H}^i$ are the incident electric and magnetic fields.

Using the Method of Moments to solve these equations, in its Galerkin formulation, matrices $\mathbf{M}^E, \mathbf{M}^M$ and vectors $\mathbf{V}^E, \mathbf{V}^M$ of dimension N are obtained, in terms of a surface patch basis function $\mathbf{b}_n$ and a inner product $< \mathbf{f}, \mathbf{g} >$. As the basis function is a tangential vector, all the components of the electric field can be considered in its integral equation and the coefficients of the matrix equation can be expressed by

$$M^E_{mn} = < \mathcal{L}_E \mathbf{b}_n, \mathbf{b}_m > \tag{7}$$

$$V^E_m = < \mathbf{E}^i, \mathbf{b}_m > \tag{8}$$

where the operator is rewritten as

$$\mathcal{L}_E \mathbf{J}_S = \frac{1}{4\pi j\omega\varepsilon_0}\int_S \left[-\kappa^2 \mathbf{J}_S(\mathbf{r}')\,\Psi(\mathbf{r},\mathbf{r}') + \nabla'_S\cdot \mathbf{J}_S(\mathbf{r}')\,\nabla'\Psi(\mathbf{r},\mathbf{r}')\right] dS' \tag{9}$$

The Reciprocity Theorem [6] guarantees that this operator is self-adjoint, therefore the associated matrix is a symmetric one. The coefficients related to the MFIE are given by

$$M_{mn}^{M} = < \mathbf{b}_n/2, \mathbf{b}_m > \; + \; < \mathcal{L}_{Mn}\mathbf{b}_n, \mathbf{b}_m > \tag{10}$$

$$V_m^M = \; < \mathbf{n} \times \mathbf{H}^i, \mathbf{b}_m > \tag{11}$$

The MFIE operator is not self-adjoint, consequently $\mathbf{M}^M$ is not symmetric.

The CFIE can then be written as

$$\mathcal{L}_C \mathbf{J}_S = \mathbf{F}_C^i \tag{12}$$

where

$$\mathcal{L}_C \mathbf{J}_S = \mathcal{L}_M \mathbf{J}_S + \frac{\alpha}{Z_0}\mathcal{L}_E \mathbf{J}_S \tag{13}$$

$$\mathbf{F}_C^i = \mathbf{n} \times \mathbf{H}^i + \frac{\alpha}{Z_0}\mathbf{E}^i \tag{14}$$

α being the parameter of the linear combination. The matrix and vector of the matrix equation are then given by

$$\mathbf{M}^C = \mathbf{M}^M + \frac{\alpha}{Z_0}\mathbf{M}^E \tag{15}$$

$$\mathbf{V}^C = \mathbf{V}^M + \frac{\alpha}{Z_0}\mathbf{V}^E \tag{16}$$

As in the case of the MFIE, $\mathbf{M}^C$ is not symmetric.

The A(S)MFIE has been proposed with the purpose of reducing the CPU time and computer memory related with the exact integral equation. This approximate equation does not change the vector of the MFIE, $\mathbf{V}^{SM} = \mathbf{V}^M$, but, as already stated, the matrix coefficients are taken as the average of the opposite coefficients of the MFIE matrix, i.e.,

$$\mathbf{M}^{SM} = \left(\mathbf{M}^M + \mathbf{M}^{M^T}\right)/2 \tag{17}$$

(the superscript ^{T} stands for transposed); this approximation does not have a significant error, because the contributions of the non-integral term of the MFIE operator are at least one order of magnitude greater than the others. The A(S)MFIE operator is given by

$$\begin{aligned}\mathcal{L}_{SM}\mathbf{J}_S \;=\; & \frac{1}{2}\mathbf{J}_S(\mathbf{r}) - \mathbf{n} \times \frac{1}{8\pi}\int_S \mathbf{J}_S(\mathbf{r}') \times \nabla'\Psi(\mathbf{r},\mathbf{r}')\, dS' \\ & + \frac{1}{8\pi}\int_S [\mathbf{n}' \times \mathbf{J}_S(\mathbf{r}')] \times \nabla'\Psi(\mathbf{r},\mathbf{r}')\, dS'\end{aligned} \tag{18}$$

where the adjoint operator of $\mathcal{L}_{Mn}$ has been introduced, and it has been assumed that the inner product is a symmetric one.

With the same purpose of the A(S)MFIE, an A(S)CFIE is proposed. It is obtained by taking the linear combination of the EFIE with the A(S)MFIE, instead of the MFIE, i.e.,

$$\mathcal{L}_{SC}\mathbf{J}_S = \mathcal{L}_{SM}\mathbf{J}_S + \frac{\alpha}{Z_0}\mathcal{L}_E\mathbf{J}_S \tag{19}$$

or

$$\mathbf{M}^{SC} = \mathbf{M}^{SM} + \frac{\alpha}{Z_0}\mathbf{M}^E \tag{20}$$

leaving the vector unchanged, $\mathbf{V}^{SC} = \mathbf{V}^C$. $\mathbf{M}^{SC}$ is symmetric (it is a linear combination of symmetric matrices), and that fact can and will be taken into consideration in the resolution of the matrix equation, in order to achieve the desired reductions.

It is known that the MFIE may experience some difficulties when the object does not have a smooth surface. This fact has been confirmed for a cube, mainly when the frequency of the incident wave is above the first resonance [7]; the solutions from the A(S)MFIE present also a significative error for the cube, in the same conditions, but for a smooth object like the sphere, the solutions from the MFIE and the A(S)MFIE are almost identical, even in the resonance region [7]. Thus, it is expected that this new A(S)CFIE may originate solutions with some error, if the object's surface presents edges.

III. NUMERICAL RESULTS

Rao's triangular patch basis function has been used to test the A(S)CFIE. The choice of the linear combination's parameter has been $\alpha = 1$.. The sphere (radius a) and the cube (side L) were used as scatterers: the sphere was modelled by 96 patches, corresponding to 144 unknowns; two models were made for the cube, a 96 patch and a 192 patch, corresponding respectively to 144 and 288 unknowns, and designated by `M144` and `M288`. An incident plane wave is considered, and its frequency ranges between values that contain the first two resonances of each object ($a/\lambda = .437, .616$, $L/\lambda = .707, .866$); two directions of incidence are considered for the cube, one normal to a face and another directed to a vertex, both with horizontal polarization, Fig.1. The adequate routines of *LINPACK* [8] were used to solve the matrix equations.

(a) *normal incidence* (b) *oblique incidence*

Figure 1: *Cube perspectives according to the direction of incidence.*

The condition numbers, CN, associated with the matrices of both the exact and the approximate CFIE, can be seen in Fig.2. It is confirmed that they are both stable

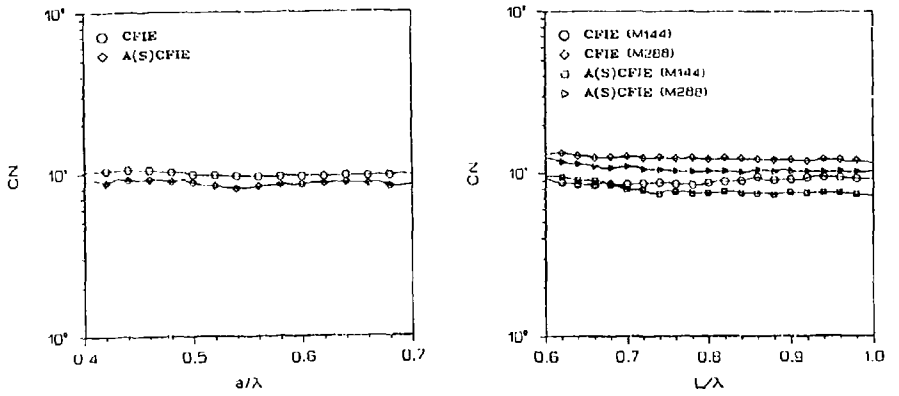

(a) *Cube* (b) *Sphere*

Figure 2: *Condition numbers associated with the CFIE and the A(S)CFIE.*

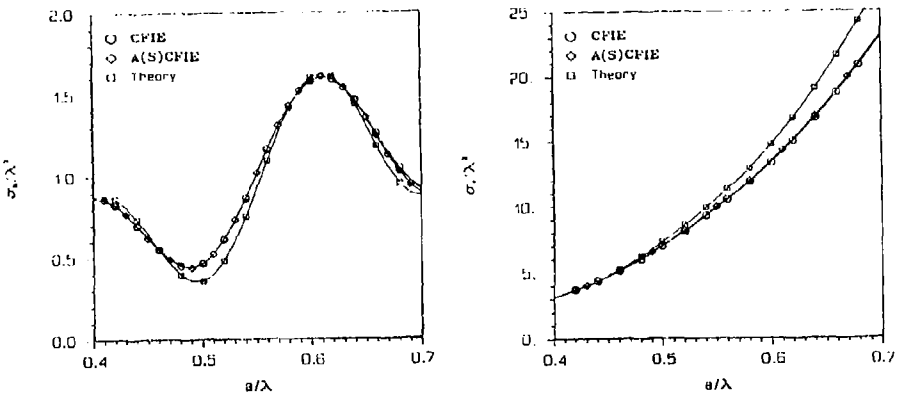

(i) σ_b/λ^2 (ii) σ_f/λ^2

Figure 3: *Scattering cross sections for the sphere.*

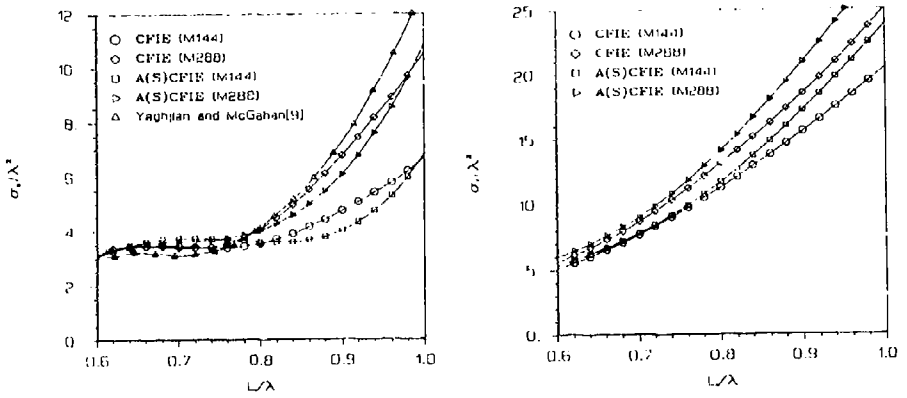

(i) σ_b/λ^2 (ii) σ_f/λ^2

(b) *normal incidence*

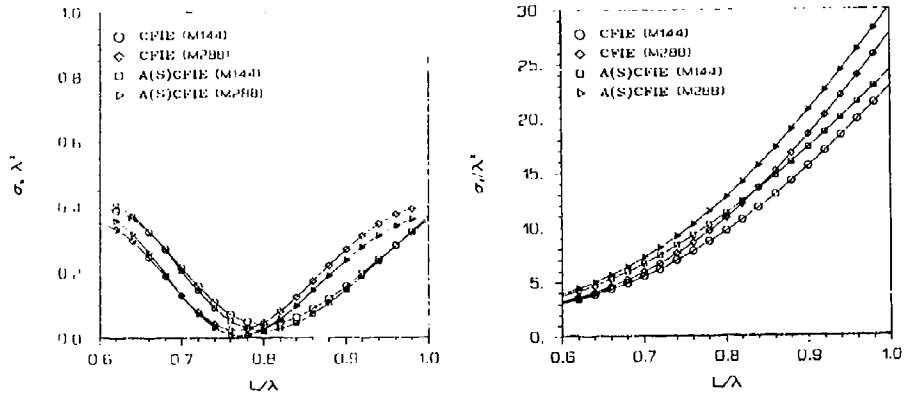

(i) σ_b/λ^2 (ii) σ_f/λ^2

(a) *oblique incidence*

Figure 4: *Scattering cross sections for the cube.*

in frequency: CN is almost constant, independently of the model. For each model, the condition number related to the A(S)CFIE is slightly lower than the one of the CFIE (a similar behavior has been noticed for the MFIE).

The back and forth scattering cross sections, σ_b, σ_f, have been calculated, Fig.3-4. The results for the sphere are compared with the theoretical ones; for the cube, a comparison is made for the backscatter for the normal incidence with results from [9] (the only available case in the literature, as far as we known). The scattering cross sections obtained for the sphere by the CFIE and A(S)CFIE are almost totally superimposed, although with discrepancies from the theoretical values. This means that the errors are due to the model, and its density, used for the sphere, and are not a consequence of the approximations made in the integral equation. For the cube there are some differences between the results from the approximate and the exact equations, but there are also differences between the two models. For each model, σ_b seems to be less sensitive to the approximations than σ_f.

As far as the codes are concerned, only the routines for matrix calculation and factorization differ in both equations; all the others remain unchanged, with its CPU time depending, at the most, with N^2. The time to calculate the A(S)CFIE matrix is about 90% of the corresponding time for the CFIE, both depending on N^2; this value is due to the fact that only the upper triangle of the symmetric matrix is stored. The matrix factorization time, which varies with N^3, suffers also a reduction of the order of 43% (the order of the number of operations lowers from $N^3/3$ to $N^3/6$). Hence the total CPU time for the A(S)CFIE, when compared with the CFIE, ranges from 75% to 50% when N varies between 100 and 1000, which is a significant reduction.

The computer memory necessary to solve both equations depends mainly on the storage of the matrix. Thus, its value is almost halved (from N^2 to $N(N+1)/2$) when one uses the A(S)CFIE intead of the CFIE. Although nowadays computer memory is not that important, this is also a significant reduction.

IV. CONCLUSIONS

An Approximate (Symmetric) Combined Field Integral Equation has been presented. This new equation is a linear combination of the EFIE with the A(S)MFIE, previously presented by the authors, originating a symmetric matrix. The triangular patch basis function was used to assess this equation, with the cube and the sphere. As expected, the approximate equation does not suffer the effects of the resonances, which can be confirmed by the condition number. Good results are obtained for the scattering cross sections, specially in the case of the sphere, for which the results for the CFIE and the A(S)CFIE are almost coincident; for the cube some discrepancies are found, but they tend to become

smaller when the patch density is increased. Therefore, one can say that the A(S)CFIE can be used instead of the CFIE, for objects with a smooth surface; for objects with edges in its surface, is appears that some precautions must be used in the application of the approximate equation. A reduction of about half is achieved in CPU time and computer memory.

REFERENCES

[1] Poggio,A.J. and Miller,E.K., *"Integral Equation Solutions of Three-Dimensional Scattering Problems"*, in Mittra,R. (ed.), *"Computer Techniques for Electromagnetics"*, Pergamon Press, New York, N.Y., 1973

[2] Harrington,R.F., *"Field Computation by Moment Method"*, MacMillan Comp., New York, N.Y., 1968

[3] Cheng,D.K. and Liang,C.-C., *"Thinning Technique for Moment-Method Solutions"*, Proc. IEEE, Vol. 71, No. 2, Feb. 1983, pp. 265-266

[4] Correia,L.M. and Barbosa,A.M., *"An Approximate (Symmetric) Magnetic Field Integral Equation for the Analysis of Scattering by Conducting Bodies"*, IEEE AP-S International Symposium, Dallas, Texas, May 1990

[5] Rao,S.M., Wilton,D.R. and Glisson,A.W., *"Electromagnetic Scattering by Surfaces of Arbitrary Shape"*, IEEE Trans. Antennas Propagat., Vol. AP-30, No. 3, May 1982, pp. 409-418

[6] Harrington,R.F., *"Time-Harmonic Electromagnetic Fields"*, McGraw-Hill, New York, N.Y., 1961

[7] Correia,L.M., *"Scattering by Arbitrary Shape Conducting Bodies in the Resonance Region"*, (in Portuguese) Ph.D. Thesis, Instituto Superior Técnico, Technical University of Lisbon, Lisbon, Dec. 1990

[8] Dongarra,J., Bunch,J.R., Moler,C.B. and Stewart,G.B., *"LINPACK Users' Guide"*, SIAM Publications, Philadelphia, 1978

[9] Yaghjian,A.D. and McGahan,R.V., *"Broadside Radar Cross Section of the Perfectly Conducting Cube"*, IEEE Trans. Antennas Propagat., Vol. AP-33, No. 3, Mar. 1985, pp. 321-329

New Expansion Functions for Long Structures in the MMP-Code

P. Leuchtmann
Electromagnetics group, ETH Zurich
CH-8092 Zurich, Switzerland
+41 1 256 51 38; FAX: +41 1 261 10 26

Summary

The MMP-code [1,2,3] uses a problem adapted expansion of the electromagnetic field (rather than an expansion of the sources). Hence, a "MMP-expansion-function" consists of six field components.

In the case of long structures (e.g. thin wires, edges etc.), the classical multipole expansions are not very efficient. The thin wire option [4] has been implemented and successfully applied to complicated situations [5]. In specific cases, namely when the field in the close vicinity around the wire does not have circular symmetry, the thin wire expansions are not sufficient. For those cases, new expansion functions have been developped. They have the following properties:

- Very simple *analytical* expressions for all field components:
- *Recursive calculation* of the 'higher order modes'.
- Satisfy Maxwell's equations in the domain analytically. (Singular only on a line of finite length)
- Weak variation of the field along a given line, but strong variation perpendicular to that line.

Mathematical expressions

All the field components of the new expansion functions may be written in the following general form: (for a straight line singularity of length l on the z-axis, starting at $z = 0$)

$$H_{rn} = \frac{n}{\pi 2^n (n-1)! r^n} \begin{matrix}\sin\\ \cos\end{matrix}(n\varphi)\left[G_0 z \cdot \alpha_n^{Hr} + G_l\left(\beta_n^{Hr} \cdot (z-l)\cos kl + \gamma_n^{Hr} k r^2 \sin kl\right)\right] \quad (1\text{-}1)$$

$$H_{\varphi n} = \frac{-1}{\pi 2^n (n-1)! r^n} \begin{matrix}\cos\\ \sin\end{matrix}(n\varphi)\left[G_0 z \cdot \alpha_n^{H\varphi} + G_l\left(\beta_n^{H\varphi} \cdot (z-l)\cos kl + \gamma_n^{H\varphi} k r^2 \sin kl\right)\right] \quad (1\text{-}2)$$

$$H_{zn} = 0 \quad (1\text{-}3)$$

$$E_{rn} = \frac{\mathrm{i}}{\pi\omega\varepsilon' 2^n (n-1)! r^n} \begin{matrix}\cos\\ \sin\end{matrix}(n\varphi)\left[G_0 \alpha_n^{Er} + G_l\left(\beta_n^{Er}\cos kl + \gamma_n^{Er} \cdot k(z-l)\sin kl\right)\right] \quad (1\text{-}4)$$

$$E_{\varphi n} = \frac{-n}{\pi\omega\varepsilon' 2^n (n-1)! r^n} \begin{matrix}\sin\\ \cos\end{matrix}(n\varphi)\left[G_0 \alpha_n^{E\varphi} + G_l\left(\beta_n^{E\varphi}\cos kl + \gamma_n^{E\varphi} \cdot k(z-l)\sin kl\right)\right] \quad (1\text{-}5)$$

$$E_{zn} = \frac{-\mathrm{i}}{\pi\omega\varepsilon' 2^n (n-1)! r^n} \begin{matrix}\cos\\ \sin\end{matrix}(n\varphi)\left[G_0 \frac{z}{r} \cdot \alpha_n^{Ez} + G_l\left(\beta_n^{Ez}\frac{z-l}{r}\cos kl + \gamma_n^{Ez} \cdot kr\sin kl\right)\right] \quad (1\text{-}6)$$

In the expressions above, the symbols have the following meanings:

- r, φ, z are the common cylindrical coordinates
- $H_r, \ldots$ and $E_r, \ldots$ are the components of the magnetic and the electric field respectively
- l is the length of the singularity on the z-axis
- $\mathrm{i} = \sqrt{-1}$; ω and ε' are the angular frequency and the complex permittivity respectively
- k is the wave number of the medium (complex or real)
- G_0, G_l are the functions $e^{\mathrm{i}k\sqrt{r^2+(z-z')^2}}/\sqrt{r^2+(z-z')^2}$ for z' equal $0, l$ respectively.
- n is an integer: the 'order' of the particular expansion function
- α_n, β_n and γ_n are complex parameters which will be defined below.

Note, that (1) describes *two* expansion functions with $\cos n\varphi$ or $\sin n\varphi$ dependency respectively. Similar formulae are true for another set of two expansions, interchanging $\sin kl$ and $\cos kl$ in the brackets. Finally, another four expansion functions are described by multiplying $\vec{H}$ by the negative square of the wave impedance and interchanging $\vec{E}$- and $\vec{H}$-components.

Recursions

For the calculation of the $\alpha_n^{Hr}, \ldots$ in (1), the following procedure is used. A more detailed description how these recursions have been found will be given in the full paper.

First of all, a basic series of terms is calculated:

$$\delta_0 = \frac{1}{k}; \quad \delta_1 = 1; \qquad \delta_{n+1} = \frac{2n-1}{\sqrt{r^2+(z-l)^2}}\delta_n - k^2\delta_{n-1} \tag{2}$$

$$v_0 = \frac{\sqrt{r^2+(z-l)^2}}{r^3}; \qquad v_{n+1} = \frac{r^2}{\sqrt{r^2+(z-l)^2}}v_n \tag{3}$$

from which we obtain the complex numbers $D_n := v_n\delta_n$. Setting $l = 0$ in (2) and (3) and changing the sign, the numbers A_n are obtained. Now, the following recursions are applied:

$$\alpha_0^{Hr} = 0; \qquad \alpha_{n+1}^{Hr} = 2n\alpha_n^{Hr} + A_{n+1} \tag{4-1}$$

$$\beta_0^{Hr} = 0; \qquad \beta_{n+1}^{Hr} = 2n\beta_n^{Hr} + D_{n+1} \tag{4-2}$$

$$\gamma_0^{Hr} = 0; \qquad \gamma_{n+1}^{Hr} = 2n\gamma_n^{Hr} + D_n \tag{4-3}$$

$$\alpha_n^{H\varphi} = \tilde{\alpha}_n^{H\varphi} + A_{n+1}; \qquad \tilde{\alpha}_0^{H\varphi} = 0; \qquad \tilde{\alpha}_{n+1}^{H\varphi} = (n+1)(\alpha_n^{H\varphi} + \tilde{\alpha}_n^{H\varphi}) \tag{5-1}$$

$$\beta_n^{H\varphi} = \tilde{\beta}_n^{H\varphi} + D_{n+1}; \qquad \tilde{\beta}_0^{H\varphi} = 0; \qquad \tilde{\beta}_{n+1}^{H\varphi} = (n+1)(\beta_n^{H\varphi} + \tilde{\beta}_n^{H\varphi}) \tag{5-2}$$

$$\gamma_n^{H\varphi} = \tilde{\gamma}_n^{H\varphi} + D_n; \qquad \tilde{\gamma}_0^{H\varphi} = 0; \qquad \tilde{\gamma}_{n+1}^{H\varphi} = (n+1)(\gamma_n^{H\varphi} + \tilde{\gamma}_n^{H\varphi}) \tag{5-3}$$

$$\alpha_n^{Hz} = 0 \tag{6-1}$$

$$\beta_n^{Hz} = 0 \tag{6-2}$$

$$\gamma_n^{Hz} = 0 \tag{6-3}$$

and for the parameters of the $\vec{E}$-components

$$\alpha_n^{Er} = \tilde{\alpha}_n^{Er} + nAn + 1 - A_{n+2} - k^2r^2A_n; \qquad \tilde{\alpha}_0^{Er} = 0; \qquad \tilde{\alpha}_{n+1}^{Er} = (n+1)(2\tilde{\alpha}_n^{Er} - k^2r^2A_n) \tag{7-1}$$

$$\beta_n^{Er} = \tilde{\beta}_n^{Er} + nD_{n+1} - D_{n+2} - k^2r^2D_n; \qquad \tilde{\beta}_0^{Er} = 0; \qquad \tilde{\beta}_{n+1}^{Er} = (n+1)(2\tilde{\beta}_n^{Er} - k^2r^2D_n) \tag{7-2}$$

$$\gamma_n^{Er} = \beta_n^{H\varphi} \tag{7-3}$$

$$\alpha_0^{E\varphi} = 0; \qquad \alpha_n^{E\varphi} = \tilde{\alpha}_n^{E\varphi} + k^2r^2A_{n-1} + A_{n+1}; \qquad \tilde{\alpha}_1^{E\varphi} = 0; \qquad \tilde{\alpha}_{n+1}^{E\varphi} = 2n(\tilde{\alpha}_n^{E\varphi} + k^2r^2A_{n-1}) \tag{8-1}$$

$$\beta_0^{E\varphi} = 0; \qquad \beta_n^{E\varphi} = \tilde{\beta}_n^{E\varphi} + k^2r^2D_{n-1} + D_{n+1}; \qquad \tilde{\beta}_1^{E\varphi} = 0; \qquad \tilde{\beta}_{n+1}^{E\varphi} = 2n(\tilde{\beta}_n^{E\varphi} + k^2r^2D_{n-1}) \tag{8-2}$$

$$\gamma_n^{E\varphi} = -\beta_n^{Hr} \tag{8-3}$$

$$\alpha_n^{Ez} = A_{n+2} \tag{9-1}$$

$$\beta_n^{Ez} = D_{n+2} \tag{9-2}$$

$$\gamma_n^{Ez} = D_{n+1} \tag{9-3}$$

Results

As a simple example, the field of a L-shaped structure is calculated. (See figs 1 and 2) The vertical branch has a length of half a wave length λ, the horizontal branch is one λ long, and both are $\lambda/20$ thick. The L is made of good conducting material, and the excitation is a plane wave, coming from top right at an angle of 30° to the vertical, linearly polarized in the L-plane.

More examples will be given in the full paper.

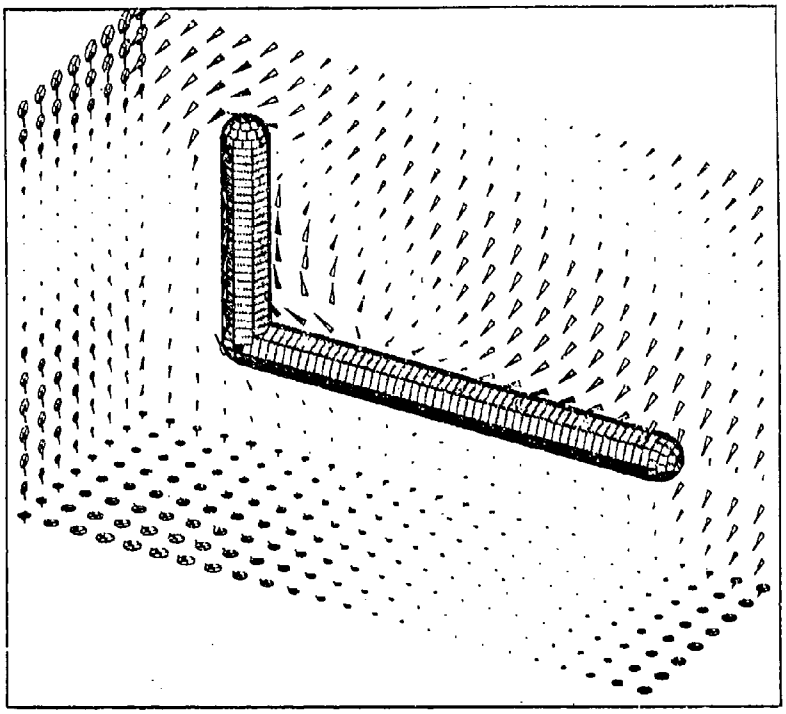

Figure 1 The field in the close vicinity of L-shaped structure. It is shown in three perpendicular planes. With respect to each plot-plane, the triangles give the tangential component and the circles the normal component of the instantaneous value of the Poynting vector.

References

[1] Ch. Hafner, *The generalized multipole technique for computational electromagnetics*, Artech House, London, 1990.

[2] L. Bomholt, *MMP-3D — A computer Code for electromagnetic scattering based on the GMT*, Diss. ETH No. 9225, Zurich, 1990.

[3] L. Bomholt, P. Regli, Ch. Hafner, P. Leuchtmann, "MMP-3D: A package for computation of 3D electromagnetic fields on PCs and Workstations," in *6th Annual Review of Progress in Applied Computational Electromagnetics (ACES), Conference Proceedings*, (Monterey), Mar. 1990.

[4] P. Leuchtmann and L. Bomholt, "Thin Wire Feature for the MMP-code," of functions in the MMP-method," in *6th Annual Review of Progress in Applied Computational Electromagnetics (ACES), Conference Proceedings*, (Monterey), Mar. 1990.

[5] P. Leuchtmann, "On the modelling of the electromagnetic field of EMC test arrangements with the MMP-code," in *Proceedings of the 5th Symposium on Electromagnetic Compatibility*, (Zürich), Mar. 1991.

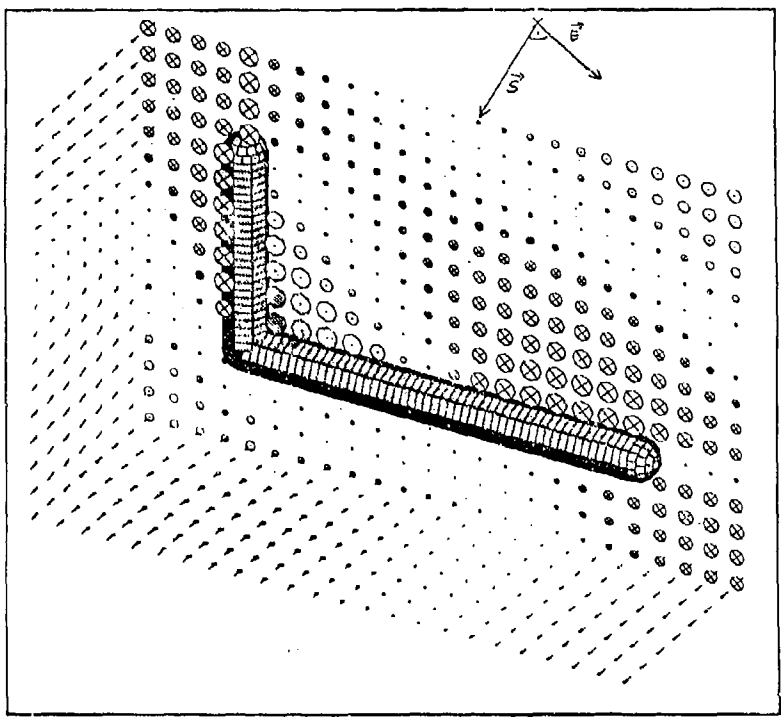

Figure 2 The magnetic field $\vec{H}$ of the same structure as shown in fig. 1.

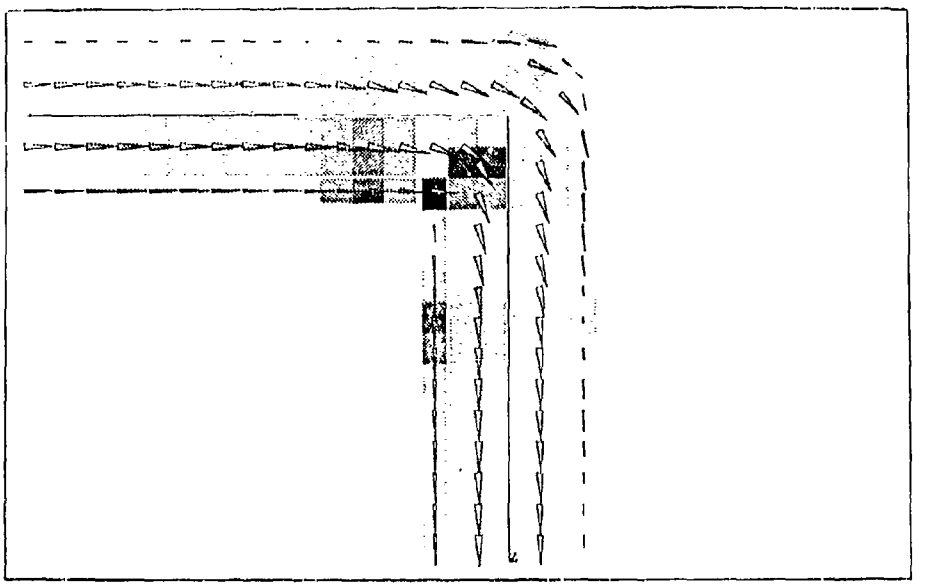

Figure 3 A detail of the same field: The time mean value of the Poynting vector on the surface of the conductor. The shading is proportional to the (erraneous) normal component. The latter is more than ten times smaller than the tangential component and is a indicator for the accuracy of the calculation.

DIRECT SOLUTION OF THE WAVE EQUATION USING PARALLEL COMPUTATIONAL TECHNIQUES

R.G. Hohlfeld[1], S.M. Sparagna[1,2], and G. v. H. Sandri[3]

Abstract

This research is concerned with the development of computational techniques utilizing parallel computer architectures which are appropriate to simulation of wave propagation from radiating elements in an antenna array. We have implemented numerical solutions of the wave equation in a parallel computer architecture to gain a computational speed advantage and to develop direct simulation techniques (based on a description dependent only on "local physics") which are an accurate representation of the physical system. Stable, energy conserving integration schemes for the wave equation represented in finite-difference form have been developed. By using using a nine-point finite-difference solution, developed by Vichnevetsky and Bowles, a two-dimensional scalar wave can be physically propagated through the processors of the Connection Machine, which correspond to spatial nodes of a computational mesh. The (2+1)D scalar wave equation was simulated since this is the simplest case which could be tested requiring solution of a multi-dimensional hyperbolic partial differential equation. Once this has been achieved, proceeding to the (3+1)D scalar wave equation and the full vector wave equation should be comparatively straightforward. These integration schemes have been extended to include terminating boundary conditions permitting the simulation of the free-space wave propagation on a finite computational mesh. The simulation is characterized by isotropic propagation whose spatial and temporal response is a function of the constitutive parameters of the medium in which the wave is propagating. Since each processor represents a point in space the physical constants (ϵ, μ, and σ) stored in each processor could be chosen to represent an arbitrary geometric distribution of these parameters. Therefore, the computational requirements of these simulation are only dependent on the the physical size of the computational mesh and are independent of the geometry of the simulation. This type of simulation can be used as an effective tool to simulate wave propagation in inhomogeneous media with an arbitrary spatial distribution of sources and reflectors. It is also appropriate as a method of evaluating antenna performance in both the far and near field.

[1] Elec. Comp. & Sys. Eng. Dept., College of Engineering, Boston University
[2] Equipment Division, Raytheon Company, Wayland, MA.
[3] Aerospace & Mech. Eng. Dept., College of Engineering, Boston University

I INTRODUCTION

Finite-difference solutions of hyperbolic differential equations in two or more dimensions pose a difficult computational problem owing to numerical instabilities exhibited by discretised versions of these equations (Hildebrand 1968; Smith 1965). A suitable approach for solving the wave equation on a spatial grid of two dimensions [i.e. the (2+1)D case] was developed by Vichnevetsky and Bowles (1982). In this approach the Laplacian operator is approximated by an appropriate convex combination of difference operators involving nearest neighbors and next-to-nearest neighbors on the computational grid. This algorithm was shown to exhibit isotropic wave propagation, in the limit of an infinitely long wave train, despite the underlying rectangular computational grid.

We have demonstrated that this algorithm is suitable for implementation on a massively parallel computer with processors arranged on a boolean hypercube, specifically on the Connection Machine-2 (Hillis 1985; Boghosian 1990). In this implementation each point in space is mapped to a particular processor (or virtual processor) and construction of the required finite difference operators of the Vichnevetsky and Bowles algorithm is readily accomplished by interprocessor communications on the boolean hypercube. In our development of this technique, we show that the wave propagation speed (effectively the square root of the "dielectric constant") may be assigned independently at each grid point (processor) and that sources and reflecting surfaces may be established in an arbitrary geometry with spatial resolution equivalent to the resolution of the computational grid. Thus geometrically complex simulations, which treat near field and far field on an equivalent basis, may be considered without computational penalty; execution times are effectively independent of these geometric issues. Computational rates in the GFlop range (1 GFlop = 10^9 floating point operations per second) are rountinely achieved.

In addition to our parallel implementations, we have also further investigated the numerical properties of the Vichnevetsky and Bowles algorithm. In particular, we have addressed the transient behavior of the algorithm by Z-transform techniques and also demonstrate that the algorithm is always energy-conserving at least in the mean, and for appropriate choices of parameters, conserves energy instanteously (i.e. at each time step).

II ANALYSIS OF THE FINITE DIFFERENCE SOLUTIONS OF THE HOMOGENEOUS (2+1)D WAVE EQUATION USING THE NINE POINT FINITE DIFFERENCE ALGORITHM

II.1 - Introduction

In this section we examine a discretised model of the (2+1)D wave equation which we have implemented on the Connection Machine. This work is an application and extension of the work of Vichnevetsky and Bowles (1982) which was directed towards the solution of the wave equation on a computational mesh. We outline here

the basic algorithm proposed by Vichnevetsky and Bowles and analyze briefly the ability of this method to support isotropic wave propagation despite the underlying rectangular computational mesh. We further analyse the algorithm's stability and the conservation of energy of the simulation. The stability analysis, in particular, includes new results on the transient response properties of the algorithm.

II.2 - Nine Point Algorithm for (2+1)D Simulations of Wave Propagation

The scalar wave equation in (2+1)D can be written

$$(1)\quad \frac{\partial^2 U(x,y,t)}{\partial x^2} + \frac{\partial^2 U(x,y,t)}{\partial x^2} = \frac{1}{c^2}\frac{\partial^2 U(x,y,t)}{\partial t^2}$$

The partial derivative can be represented in finite difference form as

$$f_{tt}(a) \simeq \frac{f(a+\Delta) - 2f(a) + f(a-\Delta)}{\Delta^2}$$

Here the time, t=nΔ and x=mh. The new variable, y, is defined equal to lh. Since we are using a square computational mesh, the spatial increment in the y direction is equal to the spatial increment in the x direction. Therefore,

$$(3)\quad h_y = h_x = h$$

When these definitions are used and equation (1) is put into finite difference form then

$$(4)\quad \frac{U(m+1,l,n)-2U(m,l,n)+U(m-1,l,n)}{h_x^2} + \frac{U(m,l+1,n)-2U(m,l,n)+U(m,l-1,n)}{h_y^2} = \frac{U(m,l,n+1)-2U(m,l,n)+U(m,l,n-1)}{c^2\Delta^2}$$

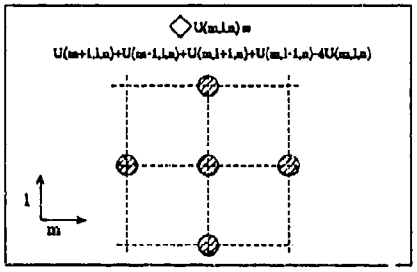

Figure: 1 Picture of a sample of the computational mesh showing how the processors are interconnected on a NEWS (north, east, west, and south) grid for the recursion formula in equation (5).

If equation (3) is substituted in equation (4) then

$$(5)\quad \frac{1}{h^2}\Big[U(m+1,l,n)+U(m-1,l,n)+U(m,l+1,n)+U(m,l-1,n)-4U(m,l,n)\Big] = \frac{U(m,l,n+1)-2U(m,l,n)+U(m,l,n-1)}{c^2\Delta^2}$$

If equation (5) is solved for U(m,l,n+1) the resulting recursion formula is

(6) $U(m,l,n+1) =$

$$2U(m,l,n) - U(m,l,n-1) + \frac{\gamma^2}{h^2}\Big[U(m+1,l,n)+U(m-1,l,n)+U(m,l+1,n)+U(m,l-1,n)-4U(m,l,n)\Big]$$

Figure 1 is a picture of a sample of the computational mesh showing how the processors are interconnected on a NEWS (north, east, west, and south) grid for the recursion formula in equation (6). The pattern formed by the information path required by each processor is called a stencil. To calculate the next value at processor P(m,l) requires information of the present state of all its nearest neighbors and its self at time n as well as its past state at time n-1. If a line is connected to all the points in the stencil like the dotted line in figure 1 they form a diamond. Vichnevetsky and Bowles dubbed the spatial operations in equation (6) as the diamond operator, $\Diamond U(n,l,n)$, which is defined as

(7) $\Diamond U(m,l,n) \equiv$

$$U(m+1,l,n)+U(m-1,l,n)+U(m,l+1,n)+U(m,l-1,n)-4U(m,l,n)$$

A closer look at figure 1 shows that the stencil can be rotated to form a different five point recursion relation where the information to calculate the value of processor P(m,l) at time n+1 comes from its next-to-nearest neighbors. The spatial distance distance between the processors is now $\sqrt{2}$. The finite difference form of the equation would then become

(8) $$\frac{1}{2h^2}\Big[U(m+1,l+1,n)+U(m+1,l-1,n)+U(m-1,l+1,n)+U(m-1,l-1,n)-4U(m,l,n)\Big] = \frac{U(m,l,n+1)-2U(m,l,n)+U(m,l,n-1)}{c^2\Delta^2}$$

and the recursion equation becomes

(9) $U(m,l,n+1) =$

$$2U(m,l,n) - U(m,l,n-1) + \frac{\gamma^2}{2h^2}\Big[U(m+1,l+1,n)+U(m+1,l-1,n)+U(m-1,l+1,n)+U(m-1,l-1,n)-4U(m,l,n)\Big]$$

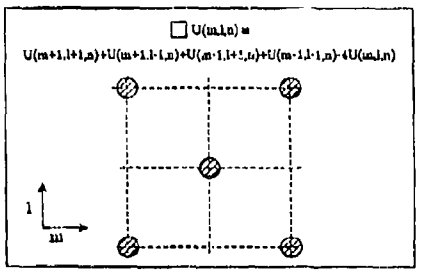

Figure: 2 Picture of a sample of the computational mesh showing how the processors are interconnected on a next-to-nearest neighbor (north-east, north-west, south-east, and south-west) grid for the recursion formula in equation (9).

Figure 2 is a sample of the computational mesh which shows how the stencil for this five point difference equation. If a line is connected to the ends of the stencil in this configuration they form a square. The square operator is the spatial operat-

ion in equation (9). The square operator, $\square U(m,l,n)$, is defined as

$$(10)\quad \square U(m,l,n) \equiv$$

$$\frac{1}{2}\Big[U(m+1,l+1,n)+U(m+1,l-1,n)+$$

$$U(m-1,l+1,n)+U(m-1,l-1,n)-4U(m,l,n)\Big]$$

Using either the diamond or square operator to represent the discretized form of the Laplacian leads to anisotropic wave propagation. Vichnevetsky and Bowles demonstrated that an appropriate convex combination of the diamond and square operators leads to a substantially isotropic propagation (to fourth order in the wave amplitude). The wave equation in full finite difference form with the weighting parameter β to define this convex combination becomes

$$(11)\quad U(m,l,n+1)-2U(m,l,n)+U(m,l,n-1)$$

$$= \frac{\chi^2}{2}\Big[\beta\square^{\bullet} + (1-\beta)\Diamond^{\bullet}\Big]U(m,l,n)$$

Isotropic propagation is obtained for β=0.5. This is the finite difference form used through the remainder of this research and which is simulated on the Connection Machine. The recursion formula from equation (11) is

$$(12)\quad U(m,l,n+1) =$$

$$\frac{\chi^2}{2}\Big[\beta\square^{\bullet} + (1-\beta)\Diamond^{\bullet}\Big]U(m,l,t)$$

$$+ 2U(m,l,n) - U(m,l,n-1)$$

Now that we have a finite difference form of the wave equation that is isotropic the regions of parameter space for stable operation can be evaluated.

II.3 - Stability Analysis

We shall consider the stability of these finite-difference equations using the von Neumann and Richtmyer method (1950).

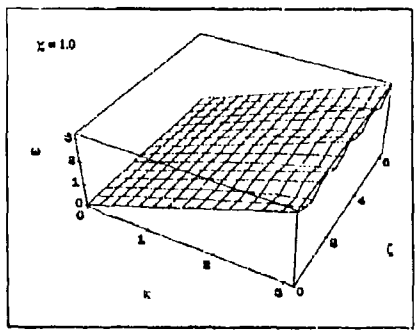

Figure: 3 Plot of ω versus κ as a function of ζ for the dispersion relation in equation (40). ω and κ have a range of (0-π) and ζ has a range of (0-2π). Δ and h equals one. c equals 1 (χ=1).

The dispersion relation obtained as a result of the stability analysis is:

$$(13)\quad \sin^2\left(\frac{\omega\chi h}{2c}\right) = \chi^2\left\{\frac{\sin^2\left[\frac{\cos(\zeta)\kappa h}{2}\right]}{2} + \frac{\sin^2\left[\frac{\sin(\zeta)\kappa h}{2}\right]}{2} + \frac{\sin^2\left[\frac{(\cos(\zeta)+\sin(\zeta))\kappa h}{2}\right]}{4} + \frac{\sin^2\left[\frac{(\cos(\zeta)-\sin(\zeta))\kappa h}{2}\right]}{4}\right\}$$

Figure 3 is a plot of the dispersion relation given in equation (13) where h and Δ are equal to one and c is

normalized to one (χ=1). From the stability analysis we know that the maximum stable value of θ is π. This plot shows the dispersion to be very weak. However varying χ by varying Δ, affects the peak value the angle θ can attain, while varying χ by varying c only affects only the rate at which θ will approach a maximum. Varying Δ will always return a smaller angle than varying c.

II.4 - Energy Conservation

For the (2+1)D wave equation we have shown that if the solution meets our criteria for stability, it is guaranteed to at least conserve the average energy, and possibly the instantaneous energy exactly if the free variables are chosen appropriately. We can write the general solution to the finite difference equation by taking the sum of all possible solutions as the general solution. Therefore for $\chi \leq 1$,

$$(14)\ \gamma(m,l,n) = U(m,l,n) + \iota I(m,l,n)$$
$$= a_1 e^{\iota(m\phi+l\psi+n\theta)} + a_2 e^{\iota(m\phi+l\psi-n\theta)}$$
$$+ a_3 e^{\iota(m\phi-l\psi+n\theta)} + a_4 e^{\iota(m\phi-l\psi-n\theta)}$$
$$+ a_5 e^{-\iota(m\phi+l\psi+n\theta)} + a_6 e^{-\iota(m\phi+l\psi-n\theta)}$$
$$+ a_7 e^{-\iota(m\phi-l\psi+n\theta)} + a_8 e^{-\iota(m\phi-l\psi-n\theta)}$$

where

$$a_j = a_j + \iota b_j \qquad \{1 \leq j \leq 8\}$$

For the (2+1)D complete wave equation there are eight possible solutions and sixteen free variables. From the definition of the Poynting Vector if the energy per meter squared is constant then the energy is conserved. The energy can be found by finding the modulus of the function $\gamma(m,l,n)$. An explicit expression for the energy in (2+1)D can be written (Sparagna 1990). It can be shown that in this expression, by choosing the free variables correctly all the sine and cosine terms will be zero and the energy density will be a constant.

II.5 - Analysis of the Finite Difference Solutions and Free Space Boundary Conditions

In the last section, we showed that the nine point algorithm proposed by Vichnevetsky and Bowles allows the direct solution of the complete wave equation in finite difference form. With the exception of the requirement imposed by the Nyquist limit on the computational mesh and frequencies, the only limitation is that for guaranteed stability the value of χ must be less than or equal to one. In this section the nine point algorithm will be treated analytically for an initial boundary condition, where at some pre-assigned position the value of the field will be bound to the function $\sin(\Omega n\Delta)$. The frequency Ω should be selected such that $\Omega\Delta$ is less than or equal to π. In this section the value of χ will be varied to see if the appropriate increase in the wave number κ is observed. The potential utility of these simulations lies in the ability to treat physical systems rigorously in a computationally expedient manner.

In this section we will analyse the nine point finite-difference algorithm by using the Z and discrete Fourier transforms to solve for

U(m,l,n) from the initial conditions U(m,l,0) and U(m,l,-1). We start by substituting the initial conditions into the nine point finite-difference equation below,

$$(15)\quad U(m,l,n+1)-2U(m,l,n)+U(m,l,n-1) = \frac{\chi^2}{4}\Big[U(m+1,l+1,n)+U(m+1,l-1,n)+U(m-1,l+1,n)+U(m-1,l-1,n)-4U(m,l,n)\Big] + \frac{\chi^2}{2}\Big[U(m+1,l,n)+U(m-1,l,n)+U(m,l+1,n)+U(m,l-1,n)-4U(m,l,n)\Big]$$

and find the particular form. The boundary condition is an infinite line source at the origin which is represented as a delta function in m and l and a sinusoid in n.

$$(16)\qquad U(0,0,n)= \sin(\Omega n\Delta)$$

The initial condition is specified as

$$(17)\qquad U(m,n,-1) = 0$$

We have shown that the nine point algorithm on the Connection Machine very accurately simulates wave propagation in (2+1)D, with some limitations. The analysis predicted and it was verified that the nine point algorithm exhibits a precursor or "superlight" propagation due to the discrete nature of the computational space. It was also demonstrated that the effect was a startup transient which propagates off the grid and does not effect the steady state solution for sinusoidal sources. We have also demonstrated that the Nyquist limits on the grid parameters and the compensation required due to the non-linear dispersion relation for the wave number or the propagation speed. Now that the utility of the simulation has been demonstrated, the problem of simulating a free space environment on a finite computational mesh must be considered. The next paragraphs discuss simulation of a free space (non-reflecting) boundary condition for the (1+1)D and (2+1)D complete wave equations in finite difference form on a finite mesh.

Many authors have treated the problem of free space boundary conditions for numerical wave propagation. Smith (1974) proposes a method of stopping reflections from the boundary by the superposition of solutions using Neumann and Dirichlet boundary conditions. This entails forcing the derivative of U(m,l,n) at the boundary equal to be zero along with the function U(m,l,n). The reflections at the boundaries will be equal in amplitude but out of phase by π. By superposing one solution on the other at the boundary, the reflection is eliminated. However, it can be shown that to calculate the derivative exactly requires twice as many data points and the propagation of two decoupled solutions. For large simulations this may become a limitation owing to memory space requirements. Another method of preventing reflections is to use the properties of the advection equation, a first-order hyperbolic equation which supports unidirectional wave propagation. Israeli and Orszag (1980) propose two methods of using these properties. One is termed the sponge boundary condition. By subtracting the proper advection equation to the wave equation with a proper weight the result in (1+1)D would be

$$(18)\quad \frac{\partial^2 U(x,t)}{\partial x^2} = \frac{1}{c^2}\frac{\partial^2 U(x,t)}{\partial t^2} - \epsilon\left\{\frac{\partial U(x,t)}{\partial x} + \frac{1}{c}\frac{Uf(x,t)}{\partial t}\right\}$$

Any solution of the form (x-ct) would force the term in parenthesis to zero and will have no effect on the propagation. However, any reflection will be on the other characteristic (x+ct) and add a first order damping term whose magnitude is controlled by ϵ. The other method is to change the solution from the full wave equation to the proper advection equation at some predetermined point interior to the boundary. Since, for χ equal to one, the complete wave equation and the advection equation are equivalent in the proper direction, there is no discontinuity at the crossover point, and when the wave hits the boundary it will not reflect. This last method is of the most utility. It will cancel the wave completely and does not need a dedicated finite region (or terminating zone) to cancel the wave, as compared to the first method of Israeli and Orszag which only damps the reflection and requires a dedicated region (which comes at the expense of the simulation space). The method of Smith cancels the wave exactly, but requires twice as many processors and causes some problems on the definition of the edge of a reflector or dielectric zone in the simulation.

The technique which is used here is a crossover scheme where the wave equation changes from the complete wave equation to the appropriate advection equation before the boundary. This only requires testing which one of the boundaries is being approached. In (1+1)D this method is natural and the easiest to implement. However, in (2+1)D the advection equation is not linear and cannot be used. This requires that the wave be decomposed into normal and parallel components. The normal components will pass through the crossover region and become a plane wave which is now a one-dimensional problem and the linear one-dimensional advection equation can then be applied. The parallel component will propagate along until it hits the other border, which by design it is normal to, and can thus be terminated in the same fashion.

To terminate the propagating wave in the (2+1)D, the wave must be decomposed into its normal and parallel components at the boundary. When the proper advection equation shown is applied at the four boundaries of the grid, this is essentially what happens. At the crossover point the wave can be represented by two orthogonal components. Since the advection equation can only take information from space and time which is behind it (or towards the source), it cannot corrupt its value from erroneous data in front of it. It automatically correctly calculates the value of the normal component. From this point on, the propagation is along normal lines which are completely decoupled from each other. The parallel component cannot propagate past the boundary, so it propagates along the boundary till it hits a perpendicular boundary. Since the boundaries are normal to each other the reflection which is parallel to one boundary will propagate normal to the other and be terminated. The only special condition is how to handle the corners

where the boundaries come together. For this research, they have been assigned arbitrarily to one of the boundaries. The error is small enough as to be unimportant except when very high dynamic ranges are required. For example, for nulls in a pattern which are down greater than 30dB this might have an effect. However, there is no absorption zone required for this method and the crossover point could be right at the boundary. Since any reflection from the boundary will decay as R^{-2} versus R^{-1} for the incident wave the effects will be greatly reduced. Also it takes a long time before the cumulative effects of four points along the whole surface can reflect enough energy into the system to be seen. The simulation only needs to run until all the wave fronts have reached the boundaries. This reduces the effect below the level of significance.

Figure 4 demonstrates the free space boundary condition. The frequency of the source is $\frac{\pi}{2}$. The parameters h, Δ, and c are all equal to one. The source is at processor P(63,63) and the grid is cold-booted to be 128x128. The time mark is taken at n equals 90. This is enough time for the wave to hit the boundary and to have propagated half way back. The crossover points are at m and l equal to 23 and 103. The corners are assigned to the m direction. A red line demarcates the crossover region in both plots. There are no reflections and no perceivable impact on the field in this linear display.

We have demonstrated the effectiveness and the advantages of the advection equations using Newton's forward and backward difference forms in terminating the complete wave equation in (2+1)D. The reflections are largely eliminated from the boundary and the interface from the complete to the advection equation only causes small perturbations at the corners, which are insignificant and could be eliminated if the corners are treated specially. Now that we have developed the tools to simulate the wave equation on a computational mesh more, complicated antennas can be examined.

III MULTIPLE ELEMENT SIMULATIONS

III.1 - Introduction

Up to this point we have only dealt with simulations of a single element to develop and validate the algorithms. The real utility of these simulation techniques will be in the modeling of complicated antenna geometries in inhomogeneous media. In this section we will simulate classical antenna arrays and verify that the beam steers and the sidelobes generated by the simulation are correct. Also we can demonstrate the ability of the simulation to model both the far and near field patterns which is analytically intractable.

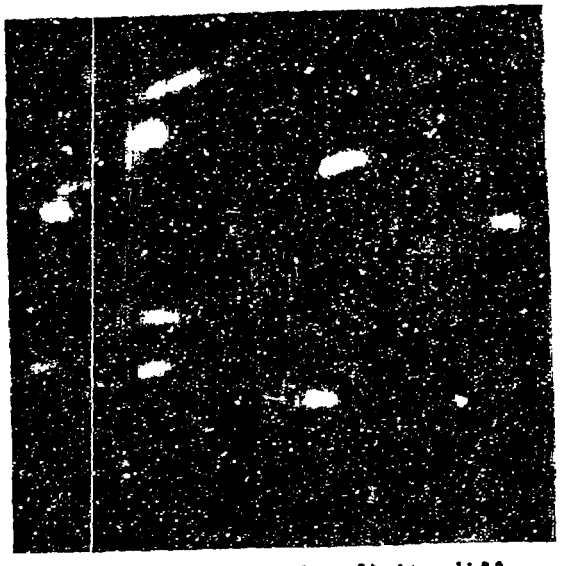

Figure: 4 Nine point finite difference algorithm with the absorbing boundary conditions. U(63,63,n) equals $\sin(\Omega\Delta n)$, $h=\Delta=c=1$. The time mark is at n equal to 90. The display is linear with the phase shown.

Figure: 5 Linear display of a two element array using the nine point finite difference algorithm on the Connection Machine. χ, h, and Δ are all one and the frequency of the source is $\frac{\pi}{2}$. The elements are $\frac{\lambda}{2}$ apart and driven in phase. The time mark is at n equal to 100.

III.2 - Phased Arrays in Homogeneous Media

The first antenna simulation is a two element array with elements spaced eight processors ($\frac{\lambda}{2}$) apart. The parameters are $\chi=c\Lambda/h=1$, $h=1$, and $\Delta=1$. The frequency of the source is (Ω) $\frac{\pi}{2}$ and the source is centered at processor P(63,63) on a 128x128 processor configuration. One source is at processor P(63,67) and the other is at processor P(63,59). Both sources are driven in phase with an amplitude of one. Figure 5 is the linear display of the two element array with a time mark at n equals 100.

The next simulation shown in figures 6[a,b] is with an eight element binomial array. All the elements are $\frac{\lambda}{2}$ apart and the C.M. is configured with a 256x256 processor dimension. The geometric center of the array is at processor P(127,127) and the elements are spaced eight processors apart and driven in phase with a frequency of $\frac{\pi}{2}$. The weights on the elements are (1-7-21-35-35-21-7-1) in order from one end of the array to the other. All the other parameters are the same as the last simulations except the time mark in figure (4) is at n equal to 200. The binomial array has the property of having no minor lobes in the continuum case as shown in Kraus and Carver (1973). This is also a case in the simulation to within 20dB of the main lobe which is a good verification of the algorithm.

The last simulation shown in figures 7[a,b] is a simple two element interferometer. The simple element will be built from two dipoles modeled in the first simulation. The center of the two, two-dipole elements are 10λ apart where all the elements are on a line. The C.M. is configured to a processor dimension of 512x512 and the geometric center is at processor P(255,255). The first dipole pair is at processors P(171,255) and P(179,255). The other pair is at processors P(331,255) and P(339,255). All the elements are driven in phase. The frequency and all the parameters are the same as in figure (5). If figure 7b is compared to the calculated antenna pattern for the two element interferometer in Kraus and Carver it is seen that the peaks and nulls in the pattern are identical and the calculated and simulation patterns are identical. The geometric pattern of cancellations in the field intensity obtained is a strong verification of the validity of this wave propagation simulation.

We have demonstrated with these simulations that the nine point algorithm accurately represents physical antenna in homogeneous media. The sidelobe predictions and the antenna gain patterns all agree with the classical theory. In addition, the structure in the near field is also shown where classical array theory approximations (treated in the limit of Fraunhofer diffraction) break down.

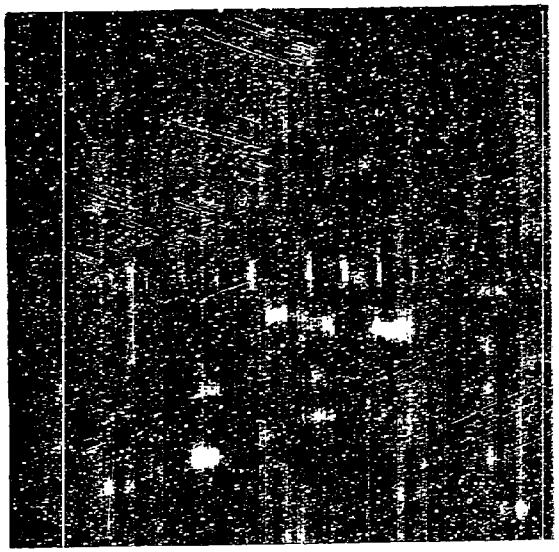

Figure: 6a Linear display of an eight element binomial array using the nine point finite difference algorithm on the Connection Machine. χ, h, and Δ are all one and the frequency of the source is $\frac{\pi}{2}$. The elements are $\frac{\lambda}{2}$ apart and driven in phase. The time mark is at n equal to 200. The weights on the elements are (1-7-21-35-35-21-7-1).

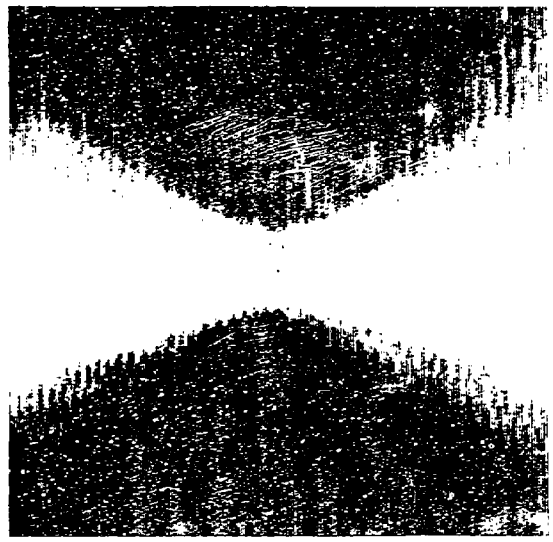

Figure: 6b Logarithmic display of an eight element binomial array using the nine point finite difference algorithm on the Connection Machine. χ, h, and Δ are all one and the frequency of the source is $\frac{\pi}{2}$. The elements are $\frac{\lambda}{2}$ apart and driven in phase. The dynamic range of the display is 20dB. The weights on the elements are (1-7-21-35-35-21-7-1).

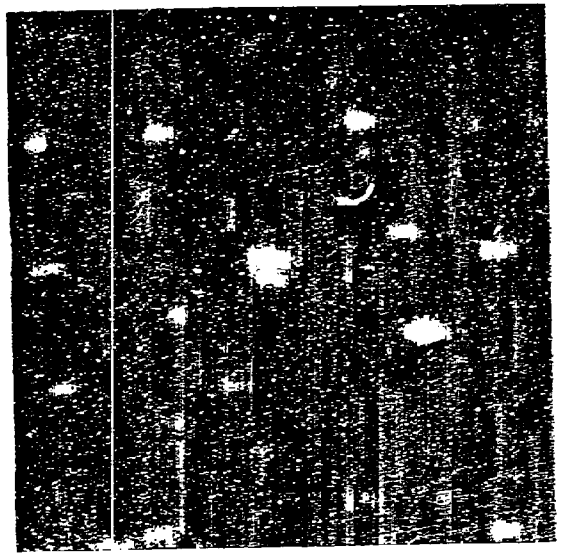

Figure: 7a Linear display of a simple two element interferometer using the nine point finite difference algorithm on the Connection Machine. χ, h, and Δ are all one and the frequency of the source is $\frac{\pi}{2}$. The elements are $\frac{\lambda}{2}$ apart and driven in phase. The time mark is at n equal to 400.

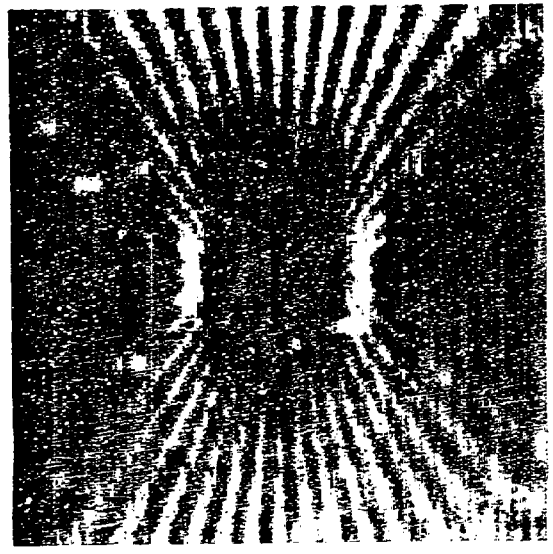

Figure: 7b Logarithmic display of a simple two element interferometer using the nine point finite difference algorithm on the Connection Machine. χ, h, and Δ are all one and the frequency of the source is $\frac{\pi}{2}$. The elements are $\frac{\lambda}{2}$ apart and driven in phase. The dynamic range of the display is 20dB.

Up to this point all the attention has been on the accuracy of the simulations and how well they represent the physical system. Not mentioned up to this point is the computational advantage and speed gained doing these simulations on a massively parallel architecture like the Connection Machine. One observation illustrating this advantage is the operation count required to do one time step of the simulation. Presently the (non-optimized) code requires 14 parallel operations to advance the simulation one time step. For a 512×512 grid this would require ≈ 3.7 million operations on a serial machine. The execution time for the simulation program is effectively independent of the distribution of sources and (as demonstrated in the next section) of the properties of the surrounding medium.

III.3 - Phased Arrays in Inhomogeneous Media

All of the work up to this point has been to develop a simulation tool that would allow complex antenna simulations in an inhomogeneous media. In this section the simulations have conducting cylinders, dielectric cylinders, and conducting planes separately and in combination. The absorbing boundary condition is applied in all the simulations and as in the last section the crossover point is always ten processors from the boundary. All the simulations will use an eight element array with $\frac{\lambda}{2}$ spacing and a frequency (Ω) of $\frac{\pi}{2}$. The grid dimensions for all the simulations are 512×512 and the array is centered at processor P(255,255).

Figure (8) shows the array with all the elements driven in phase and a conducting cylinder in the beam 128 processors from the source with a radius of 16 processors. The simulation shows the reflections off the cylinder and the diffraction of the wave around the object. The interference pattern set up by the object distorts the beam in the neighborhood of the reflector. The next simulation, shown in figure 9, has a dielectric cylinder in the beam which is steered at 45 degrees. The elements are all driven $\frac{\pi}{2}$ out of phase with each other for this beam steer. The center of the object is not directly in the beam to illustrate Snell's law as the beam is bent as it propagates across the dielectric boundary. The dielectric constant (ϵ) is set to 10 and is compensated using the program by the dispersion relation to get the continuum wave number. The continuum wave number is 3.16Ω. As the beam passes through the dielectric, the wave is focused due to the shape of the object. In figure 9 the field intensity is very high on the far side of the cylinder. Figures 10[a,b] show the simulation of a backed array. $\frac{\lambda}{2}$ behind the array is a ground plane where the field is forced to zero. The ground plane is a wavelength longer than the array on each end. By placing the reflector $\frac{\lambda}{2}$ behind the array the reflection will constructively, interfere with the signal propagating away from the reflector. All the elements are driven in phase in this simulation so that the beam will be oriented broadside to the array.

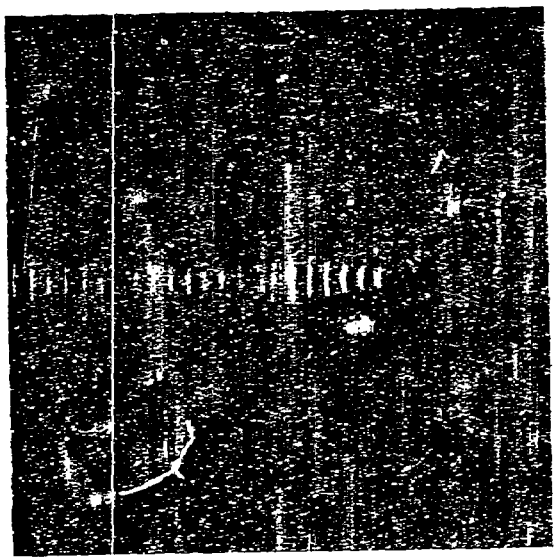

Figure: 8 Linear display of an eight element array using the nine point finite difference algorithm on the Connection Machine with a conducting cylinder in the beam. χ, h, and Δ are all one and the frequency of the source is $\frac{\pi}{2}$. The elements are $\frac{\lambda}{2}$ apart and driven in phase. The time mark is at n equal to 400.

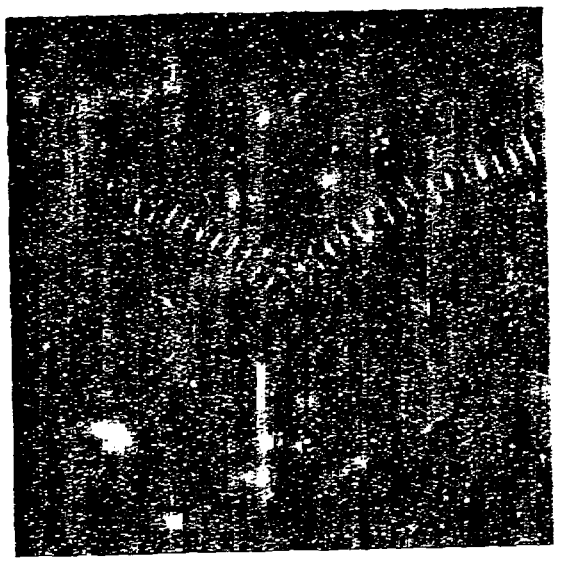

Figure: 9 Linear display of an eight element array using the nine point finite difference algorithm on the Connection Machine with a dielectric cylinder in the beam. χ, h, and Δ are all one and the frequency of the source is $\frac{\pi}{2}$. The elements are $\frac{\lambda}{2}$ apart and driven $\frac{\pi}{2}$ out of phase from each other. The time mark is at n equal to 400.

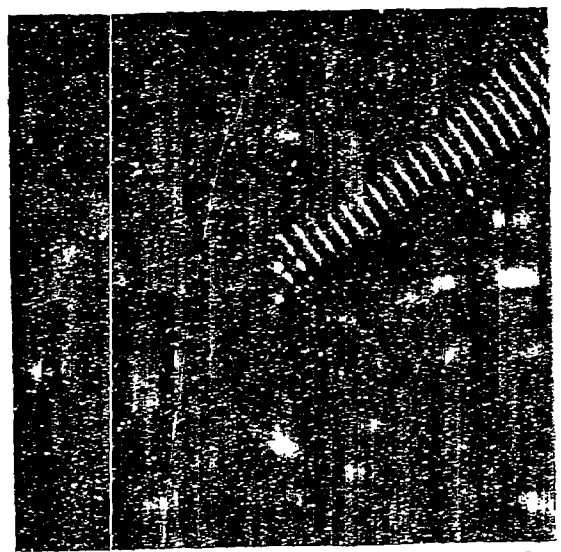

Figure: 10a Linear display of an eight element backed array using the nine point finite difference algorithm on the Connection Machine. χ, h, and Δ are all 1 and the frequency of the source is $\frac{\pi}{2}$. The elements are $\frac{\lambda}{2}$ apart and driven $\frac{\pi}{2}$ out of phase from each other. The time mark is at n equal to 400.

Figure: 10b Logarithmic display of an eight element backed array using the nine point finite difference algorithm on the Connection Machine. χ, h, and Δ are all one and the frequency of the source is $\frac{\pi}{2}$. The elements are $\frac{\lambda}{2}$ apart and driven $\frac{\pi}{2}$ out of phase from each other. The log display has 20dB dynamic range.

The last simulation shown in figure 11[a,b] is a combination of all three features of these simulations. The antenna is a backed array with a reflecting cylinder and a dielectric cylinder in the beam with a 45 degree beam steer. This simulation was performed to test the algorithm in a complicated medium in which both reflectors and dielectrics are present. This simulation represents a problem which is analytically intractable yet, it takes the same computational resources as the single element and is rigorous in the calculation of the field.

IV CONCLUSIONS

The objectives of this paper were to develop stable numerical solutions of the hyperbolic wave equation with radiating sources which take advantage of the large scale parallelism of the Connection Machine. These solutions must depend only on a local physical coordinate patch to take advantage of one of the natural modes of interprocessor communication in the Connection Machine, and more importantly to accurately represent the continuum wave equation which is local and treats all spatial locations equivalently. Also the algorithm must be insensitive to the simulation geometry and require minimal assumptions on the nature of the sources. A free space boundary solution was also required due to the physical memory bounds of the Connection Machine. This free space boundary condition permits us to simulate free space radiation problems in machines of finite size.

We have demonstrated the spatial isotropy, stability, and energy conservation of the solution. It was shown that the nine point algorithm proposed by Vichnevetsky and Bowles conserves energy always in the time average sense, and for some choices of parameters energy is conserved instantaneously. Waves propagate isotropically by this algorithm for $\chi \leq 1$ and for $\beta = \frac{1}{2}$, despite the underlying rectangular computational mesh. The implementation of this algorithm on the Connection Machine, along with the free space boundary termination developed from the advection equation, was shown to be a powerful and accurate computational tool for simulating wave propagation from a radiating element for very complicated geometries which could not be solved analytically.

We have also demonstrated that inhomogeneous media, i.e. varying "dielectric constant", and arbitrary distributions of reflectors may be accommodated in these wave propagation simulations. In particular the constitutive properties of the medium may be specified independently at each point of the simulation space (each virtual processor) without significantly increasing the run time of the simulation. This development is of great importance in view of the difficulty of obtaining exact, analytic solutions of wave propagation in inhomogeneous media and the limited ranges of validity of various approximation schemes (e.g. Born, WKBJ, Rayleigh approximation, etc.).

In closing, future research will be directed towards the four

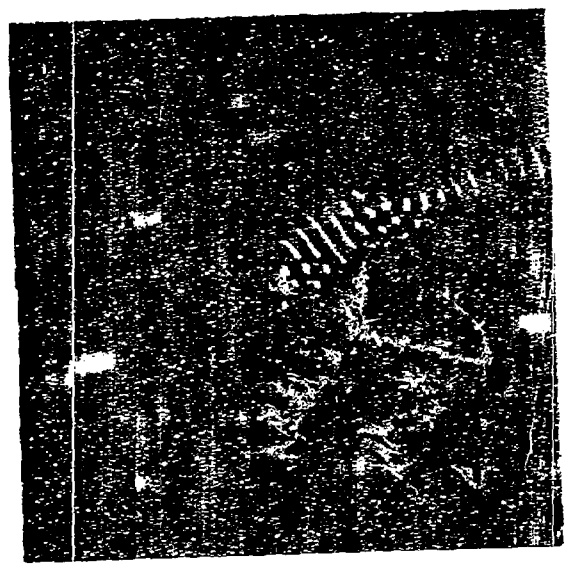

Figure: 11a Linear display of an eight element backed array using the nine point finite difference algorithm on the Connection Machine with a conducting and dielectric field in the beam. χ, h, and Δ are all one and the frequency of the source is $\frac{\pi}{2}$. The elements are $\frac{\lambda}{2}$ apart and driven $\frac{\pi}{2}$ out of phase from each other. The time mark is at n equal to 400.

Figure: 11b Logarithmic display of an eight element backed array using the nine point finite difference algorithm on the Connection Machine with a conducting and a dielectric region in the beam. χ, h, and Δ are all one and the frequency of the source is $\frac{\pi}{2}$. The elements are $\frac{\lambda}{2}$ apart and driven $\frac{\pi}{2}$ out of phase from each other. The log display has 20dB dynamic range.

dimensional [(3+1)D] problem and then to the vector wave equation, including tensor dielectric functions. We have developed the tools and have proven the algorithm so that the transition to the next step should not offer any insuperable conceptual problems.

ACKNOWLEDGMENTS

We would like to acknowledge the invaluable help supplied by Robert Putnam of Thinking Machine Inc. with the simulations done on the Connection Machine. We would also like to thank the Raytheon Corporation which funded the majority of this research through an Aldo E. Miccioli Scholarship.

REFERENCES

Boghosian, B.M. (1990); "Computational Physics on the Connection Machine"; Computers in Physics, Vol: 4, No: 1, ,pp. 14-33

Hildebrand, F.B.; "Finite-Difference Equations and Simulations"; Englewood Cliffs, New Jersey: Prentice-Hall, 1968

Hillis, D. C.,; "The Connection Machine"; Cambridge, Massachusetts: MIT Press, 1985

Israeli, M., Orszag, S.A. (1980); "Approximation of Radiation Boundary Conditions"; J. Comp. Phys., Vol: 41, pp. 115-135

Kraus, J.D., Carver, K.R.; "Electromagnetics"; New-York: McGraw-Hill Inc., 1973

Smith, G.D.; "Numerical Solutions of Partial Differential Equations"; New York: Oxford University Press, 1985

Smith, W.D. (1974); "A Nonreflecting Plane Boundary for Wave Propagation Problems"; Journal of Computational Physics, Vol: 15, pp. 492-503

Sparagna, S.M.; "Wave Propagation using Parallel Computational Techniques"; Boston, Massachusetts: Ph.D. Thesis, Boston University, 1990

Vichnevetsky, R., Bowles, J.B.; "Fourier Analysis of Numerical Approximations of Hyperbolic Equations"; Philadelphia: Society for Industrial and Applied Mathematics, 1982

von Neumann, J., Richtmyer, R.D. (1950); "A Method for the Numerical Calculation of Hydrodynamic Shocks"; J. Appl. Phys., Vol: 21, pp. 232-237

ON USING A CONCEPTUAL MODEL FOR DERIVING THE ELECTROMAGNETIC STATISTICS OF COMPLEX CAVITIES

T. H. Lehman* and E. K. Miller**

*Consultant, 3200 Carlisle NE, Albuquerque, NM, USA
**Los Alamos National Laboratory, USA

ABSTRACT

It is shown that the components of the electromagnetic field amplitudes in a perfectly conducting cavity with a complex shape are distributed according to a normal (Gaussian) distribution. The proof is obtained by invoking a virtual-cavity model which is used for expanding the field quantities in a complete set of orthogonal eigenvectors whose amplitudes are shown to have a normal distribution. This result is independent of the eigenvalue (mode number) and the shape of the cavity, requiring only that the shape of the cavity be complex. The proof that the components of the field amplitudes have a normal distribution follows immediately. Extensions of the theory to cavities with losses and sources is straightforward.

INTRODUCTION

For many years there has been considerable interest in the statistical properties of electromagnetic fields. This interest has been fostered not only by an inability of accurately predicting electromagnetic responses in complex environments, but also by the difficulty of interpreting and extracting usable information from experimental data. To date almost all attempts to characterize electromagnetic interactions statistically have been made using experimental data. The success of these efforts has been mixed. Without any a priori knowledge of distribution functions, analysts are forced to assume functional forms for the distributions using a limited number of data samples. Some of these assumed distributions seem to work well for certain types of problems but not for all, i.e., as they invariably have a limited range of validity.

If statistical techniques are to be useful for characterizing electromagnetic interactions, then one should be able to establish their range of validity using Maxwell's equations directly. If this is not possible, then statistical techniques will not have an important place in electromagnetics because the statistics of each problem would require independent determination. The number of samples required to do this is prohibitive from a measurement point of view.

To begin a discussion concerning the statistical nature of electromagnetic fields, it is appropriate to quote from Beran and Parrent [1]:

> "it should be made clear immediately that discussions of coherence or incoherence or partial coherence (statistics) need never enter a treatise on classical electromagnetic theory. In the classical electromagnetic theory governed by Maxwell's equations, one assumes that the electric field and magnetic field are measurable functions of position and time. In principle, one can, if one chooses, follow in detail the instantaneous variations of the electric or magnetic field, no matter how intricate the boundary conditions.

> In many cases, however, the procedure is extremely difficult and may, in fact, mask important physical effects . . . The situation is analogous to the one arising in classical statistical mechanics. Although in principle it is possible to follow in detail the dynamics of the system, it often proves much more useful to provide a statistical description."

It is clear that statistical electromagnetics can be nothing more than a theory which describes the behavior of the average values of appropriate functions of the electromagnetic field. These functions must in some sense be measurable and for example could include all powers of the three components of both the electric and magnetic field; all powers of the electromagnetic field power density; or all the powers of the differences of the above functions when they are measured at different locations or different times (spatial and temporal correlation functions).

The explicit purpose for constructing these average values is to provide the capability for extracting useful and usable information from measured data for those cases where the intricate and complex nature of the measured fields masks this information. An additional consideration includes those cases where small variations in the system topology or small changes in the excitation produce large changes in the response at specific locations within the system, or when small changes in the measurement location produce similarly large changes in the response. From a purely deterministic point of view, these situations give rise to a problem set which is currently not resolvable.

If information is to be extracted from the average values of the appropriate functions of the electromagnetic fields, it is immediately obvious that the amount of such information will in some sense be a strong function of the number of the average values that are determined. This fact will certainly limit the utility of an average-value theory since there is in principle an infinite number of average values; for example, all powers of the x-component of the electric filed. This limitation can be eliminated if it can be shown, *a priori* from the physics of the problem, that the average values of some of these functions are related to each other through well-defined relationships. This, of course, is found to be true in elementary statistical mechanics. We can imagine the state of statistical mechanics if the velocity distribution of molecules in a box was not Maxwellian and was instead a function of the shape of the box. Determining the relationships between different average values is an important step in any physics-based statistical theory. If these relationships exist and exhibit certain properties, then probability densities or distributions can be assigned to the field variables and the transition from an "average-value theory" to a "statistical theory" is complete.

For electromagnetics, no such average-value relationships had been demonstrated to exist. The derivation of these relationships and their range of validity are the subject of this paper. Our approach utilizes a conceptual, moment-method type model, from which the statistical properties of interest are derived, but without ever explicitly setting up or solving the moment-method model itself.

MATHEMATICAL PRELIMINARIES

Consider a cavity with volume V which is source free and is bounded by a perfectly conducting surface S of arbitrary shape. It is well known [Schiff (2)], that the electric field $\underline{E}(\underline{r},t)$ and the vector potential $\underline{A}(\underline{r},t)$ in the volume V, upon separating the space and time variations, can be expanded in a complete set of real vector functions $\underline{u}_k(\underline{r})$ or

$$E(\underline{r},t) = \sum_{k=-\infty}^{k=+\infty} \underline{u}_k(\underline{r})p_k(t), \quad (1)$$

$$A(\underline{r},t) = \sum_{k=-\infty}^{k=+\infty} \underline{u}_k(\underline{r})q_k(t) \quad (2)$$

The cartesian components of the vector functions must satisfy the second-order wave equation

$$\nabla^2 u_{k,s}(\underline{r}) + \frac{\omega_k^2}{c^2} u_{k,s}(\underline{r}) = 0, \quad (3)$$

where s denotes the cartesian coordinate, x,y,z. The vector function must also satisfy

$$\nabla \cdot \underline{u}_k(\underline{r}) = 0 \quad (4)$$

since there are no sources present. Also, the tangential components of the electric field and the vector potential must vanish on the surface S, so that

$$\mathbf{n} \times \underline{u}_k(\underline{r})|_{\underline{r},S} = 0 \quad (5)$$

where **n** is a unit vector normal to the surface. Using Eqs. (3-5) and with the help of Green's theorem it can be shown that the $\underline{u}_k$ and $\underline{u}_{k'}$ are orthogonal to each other or

$$\int_V \underline{u}_k \cdot \underline{u}_{k'} dv = \delta_{k;k'} \quad (6)$$

In the usual convention, k is an eigenvalue and $\underline{u}_k$ is an eigenvector.

Denoting spatial-average values by < >, then the average value of any function $W(\underline{r})$ over the volume V of the cavity is given by

$$\langle W \rangle = \frac{\int_V W(\underline{r})dv}{\int_V dv}$$

or

$$\langle W \rangle = V^{-1} \int_V W(\underline{r})dv \quad (8)$$

For the problem defined in this section, the quantities whose average values are of interest are functions of the electric field. These functions are the three electric field components E_x, E_y, E_z and all of their higher-order powers. These average values are defined by

$$\langle E_s^m \rangle = V^{-1} \int_V E_s^m(\underline{r})dv; \; s = x,y,z \text{ and } m = 0,1,2,\ldots \quad (9)$$

In order to evaluate the averages defined in Eq. (9), it is obvious from Eq. (1) that it will be necessary to evaluate the average values of all the powers $(u_{k,s})^m$ of the components of the eigenvector, or

$$\langle (u_{k,s})^m \rangle = V^{-1} \int_V (u_{k,s})^m dv \quad (10)$$

for all k and for all m. This is a monumental (essentially impossible) task, unless the integrals given by Eq. (10) are straightforward and can be shown to be simply related for various values of m. In the next sections, we outline an approach that shows this is indeed the case for complex cavities and in fact, it is shown that the integrals are independent of k and that they are just the moments of a normal probability density.

A CONCEPTUAL APPROACH FOR FINDING THE EIGENVECTORS

It is well known that exact solutions of the vector Helmholtz Eq. (3) are only possible for a

very few canonically-shaped cavities. Thus, for cavities of arbitrary shape, no attempt is made to find exact solutions. Instead, we seek approximate expressions for the eigenvectors. These approximate expressions are developed by expanding the eigenvectors in a set of entire-domain basis functions (EDBF). Although the choice of the EDBF is somewhat arbitrary, we choose basis functions that satisfy Eqs. (3) and (4), and select the expansion coefficients so that Eq. (5) is also satisfied.

Before outlining our approach for choosing the EDBF, we make the following observation. For cavities having canonical shapes, the cavity surfaces are defined by relationships of the form $\xi_\alpha = C_\alpha$ ($\alpha = 1,2,3$) where ξ_α is a generalized coordinate and C_α is a constant. For cavities of arbitrary shape, it will not be possible to define a surface by setting one or more of the generalized coordinates equal to a constant. Instead, we know that the eigenvector solutions must in some sense be a function of all of the dimensions of the cavity, i.e., the separation of variables that works for canonical geometries no longer holds. Our choice of basis functions must reflect this dependency.

We develop the EDBF by construction. To do this, we implement the following steps:

1) We specify a cartesian coordinate system for the space occupied by the volume V.

2) We assume that the eigenvalue k of a specific eigenvector $\underline{u}_k(\underline{r})$ is known.

3) We discretize the volume V into a large number N of cubes each having a volume $\Delta V = \Delta x \Delta y \Delta z = (\Delta x)^3$ such that $k\Delta x \ll 1$ and $V = N\Delta V$.

4) We project the six surface elements $\Delta S = (\Delta x)^2$ of each cube onto the walls of the cavity.

5) From the surface projections for each cube, we construct a rectangular cavity formed by the intersections of the six orthogonal planes containing each of the ΔS. The n'th rectangular cavity constructed from the n'th cube has dimensions X_n, Y_n, Z_n and the location of one of its corners with respect to the origin O of the coordinate system defined in step 1 is given by $\underline{r}_n$. We refer to these rectangular cavities as "virtual" cavities.

6) For each virtual cavity, we choose the set of three integers (l,m,p) which yields the best approximation to the expression

$$\frac{(\omega_k)^2}{c^2} = k^2 = \pi^2 \left[\frac{l^2}{X_n^2} + \frac{m^2}{Y_n^2} + \frac{p^2}{Z_n^2} \right] \qquad (11)$$

7) We write the eigenvector $\underline{U}_k(\underline{r};n)$ for the n'th virtual cavity assuming that each virtual cavity has perfectly conducting walls and that the components of the eigenvalues (i.e., the virtual cavity eigenvalue) are given by $k_x(n) = \pi l/X_n$, $k_y(n) = \pi m/Y_n$, $k_z(n) = \pi p/Z_n$.

8) We choose the resulting $\underline{U}_k(\underline{r};n)$ to be the EDBF and write the solution for the eigenvector $\underline{u}_k(\underline{r})$ as

$$\underline{u}_k(\underline{r}) = \sum_{n=1}^{N} \underline{U}_k(\underline{r};n). \qquad (12)$$

In the next section, we implement the above steps and show that an eigenvector can be written as a sum over a large number of standing waves. The wavevector $\underline{k}_n$ associated with the n'th standing wave is a function of X_n, Y_n, Z_n, i.e., the dimensions of the n'th virtual cavity. Thus, the eigenvector given by Eq. (12) not only satisfies the second-order wave equation (3), the constraint equation (4) and the boundary condition (5), but it is also a function of all of the dimensions that define the surface that bounds the volume V of space occupied by the cavity.

REPRESENTING THE EIGENVECTOR SOLUTIONS

We now proceed to develop the expressions for the eigenvector solutions using the approach as outlined in the previous section. We begin by defining a coordinate system having O as its origin and having an arbitrary orientation.

The eigenvalues k (i.e., the resonance frequencies) as well as the eigenvectors for an arbitrarily shaped cavity can be determined by using numerical techniques such as finite-element (FEM) or finite-difference (FDM) methods. A Hamiltonian approach, being based on energy relationships, would be a logical starting point for using FEM while a wave-equation formulation would be a natural starting point for using FDM. Either numerical solution method eventually would lead to matrix equations of the form

$$\begin{aligned} A_{xx}u_x + A_{yx}u_x + A_{zx}u_x + k^2u_x &= 0 \\ A_{xy}u_y + A_{yy}u_y + A_{zy}u_y + k^2u_y &= 0 \\ A_{xz}u_z + A_{yz}u_z + A_{zz}u_z + k^2u_z &= 0 \end{aligned} \qquad (13)$$

where the A's are NxN matrices, the u's are Nx1 vectors, and because of reciprocity, $A_{xy} = A_{yx}$, etc.

The eigenvalues k are solutions of

$$\begin{aligned} &\det|A_{xx} + A_{yx} + A_{zx} + k^2| = 0, \\ \text{or} \quad &\det|A_{xy} + A_{yy} + A_{zy} + k^2| = 0, \\ \text{or} \quad &\det|A_{xz} + A_{yz} + A_{zz} + k^2| = 0. \end{aligned} \qquad (14)$$

Similarly, the eigenvectors are solutions of Eq. (13) for specific values of k consistent with the constraint $\nabla\cdot\underline{u}_k = 0$. In this formulation, we are not interested in the exact, or for that matter explicit, values of k and $\underline{u}_k$. It suffices to know that they exist and, in principle, they could be determined, i.e., they are deterministic quantities. At this point, we assume that all of the k's are known although we do not care what their values are.

Proceeding with the prescription for determining the EDBF, we partition the volume V of the cavity into N cubes with each having a volume $\Delta V = (\Delta x)^3$ such that $V = N\Delta V$ and $k\Delta x \ll 1$. Next, we construct the N virtual cavities resulting from the intersections of the six planes defined by projecting each surface element ΔS of a cube onto the surface of the cavity. The parameters that define the n'th virtual cavity are the position vector $\underline{r}_n$ of one of the corners of the n'th virtual cavity with respect to the origin O of the coordinates of the cavity and the dimensions X_n, Y_n, Z_n of the virtual cavity. These parameters are deterministic although they are not unique since the orientation of the coordinate system is arbitrary. Note that the set of parameters that define the N virtual cavities define all of the dimensions of the cavity.

The next step in developing the EDBF is selecting the set of three integers l,m,p in Eq. (11) such that the best approximation is achieved. We proceed by assuming that the walls of each virtual cavity are perfectly conducting although, in fact, they are conducting only at the location of each ΔS_n. Consistent with the above assumption, then the eigenvector $\underline{U}_\Omega(\underline{r};n)$ for the n'th virtual cavity can be written as

$$\begin{aligned} \underline{U}_\Omega(\underline{r};n) = \underline{e}_x U_{xn}&\cos[\Omega_x(x - x_n)]\sin[\Omega_y(y - y_n)]\sin[\Omega_z(z - z_n)] \\ + \underline{e}_y U_{yn}&\sin[\Omega_x(x - x_n)]\cos[\Omega_y(y - y_n)]\sin[\Omega_z(z - z_n)] \end{aligned}$$

$$+ \mathbf{e}_z U_{yn} \sin[\Omega_x(x - x_n)]\sin[\Omega_y(y - y_n)]\cos[\Omega_z(z - z_n)] \quad (15)$$

where $\Omega_x = \pi l'/X_n$, $\Omega_y = \pi m'/Y_n$, $\Omega_z = \pi p'/Z_n$, $\Omega^2 = \pi^2[(l'/X_n)^2 + (m'/Y_n)^2 + (p'/Z_n)^2]$ and l', m', p' are integers of which at least two must be different from zero. The amplitudes of the eigenvector components are not independent, but are related by the divergence condition Eq. (4) which yields

$$U_{xn}\Omega_x + U_{yn}\Omega_y + U_{zn}\Omega_z = 0 \quad (16)$$

If we consider $\underline{\Omega}$ to be a vector with components Ω_x, Ω_y, Ω_z, Eq. (16) is the condition that $\underline{U}_n = (U_{xn}, U_{yn}, U_{zn})$ is perpendicular to $\underline{\Omega}$. There are, in general two linear independent vectors that satisfy this condition, corresponding to two possible polarizations. These vectors may be chosen arbitrarily as long as they are not coplanar. Therefore, there is another solution for the eigenvector which we denote by $\underline{W}_\Omega(\underline{r};n)$. It is identical in form to Eq. (15) with the U_{xn}, U_{yn}, U_{zn} replaced by W_{xn}, W_{yn}, W_{zn} such that $\underline{\Omega}\cdot\underline{U}_n = \underline{\Omega}\cdot\underline{W}_n = \underline{U}_n\cdot\underline{W}_n = 0$, i.e. they form an orthogonal set of vectors.

Now according to the prescription for constructing the EDBF outlined above, we set l' = l, m' = m, p' = p, so that $\Omega^2 = k^2$ and define $\underline{U}_k(\underline{r};n)$ and $\underline{W}_k(\underline{r};n)$ to be these functions. Thus, the eigenvector $\underline{u}_k(\underline{r})$ is given by

$$\begin{aligned}\underline{u}_k(r) = \sum_{n=1}^{N} \{ & \mathbf{e}_x u_{xn}\cos[k_{xn}(x - x_n)]\sin[k_{yn}(y - y_n)]\sin[k_{zn}(z - z_n)] \\ & + \mathbf{e}_y u_{yn}\sin[k_{xn}(x - x_n)]\cos[k_{yn}(y - y_n)]\sin[k_{zn}(z - z_n)] \\ & + \mathbf{e}_z u_{zn}\sin[k_{xn}(x - x_n)]\sin[k_{yn}(y - y_n)]\cos[k_{zn}(z - z_n)]\}\end{aligned} \quad (17)$$

with a similar expression for $\underline{w}_k(\underline{r})$, and where $k_{xn} = \pi l/X_n$, $k_{yn} = \pi m/Y_n$, $k_{zn} = \pi p/Z_n$, and $k^2 = \pi^2[(l/X_n)^2 + (m/Y_n)^2 + (p/Z_n)^2]$. We note that the three integers l,m,p that are used to define k_{xn}, k_{yn}, k_{zn} for the n'th EDBF are not necessarily the same set of three integers l',m',p' used to define the n-prime'th EDBF. Thus, although

$$\pi^2\left[\frac{l^2}{X_n^2} + \frac{m^2}{Y_n^2} + \frac{p^2}{Z_n^2}\right] = \pi^2\left[\frac{l'^2}{X_{n'}^2} + \frac{m'^2}{Y_{n'}^2} + \frac{p'^2}{Z_{n'}^2}\right],$$

and

$$k_n^2 = k_{n'}^2 = k^2$$

in general, $l' \neq l$, $m' \neq m$, $p' \neq p$, and $X_{n'} \neq X_n$, $Y_{n'} \neq Y_n$, $Z_{n'} \neq Z_n$, so that $\underline{k}_{n'} \neq \underline{k}_n$.

After further manipulation, the eigenvectors can be shown to have the form [Lehman and Miller (3)]

$$\underline{u}_k(\underline{r}) = \sum_{n=1}^{4N} \underline{U}_n \cos[\underline{k}_n\cdot(\underline{r} - \underline{r}_n)] \text{ and } \underline{w}_k(\underline{r}) = \sum_{n=1}^{4N} \underline{W}_n \cos[\underline{k}_n\cdot(\underline{r} - \underline{r}_n)] \quad (18)$$

where $\underline{k}_n\cdot\underline{W}_n = \underline{k}_n\cdot\underline{U}_n = \underline{W}_n\cdot\underline{U}_n = 0$ and $\underline{k}_n\cdot\underline{k}_n = k^2$ as before but in addition we have $\underline{U}_n\cdot\underline{U}_n = \underline{W}_n\cdot\underline{W}_n = V^2$ for all n. The summation is from n = 1 to 4N because each eigenvector can be written as the sum of eight plane waves or four standing waves, as

shown here.

The innerproduct $\underline{u}_k \cdot \underline{u}_k$ needed for evaluating the moments of the field components can now be put in the form

$$\begin{aligned}\underline{u}_k(\underline{r})\cdot\underline{u}_k(\underline{r}) &= \sum_{n=1}^{4N}\sum_{m=1}^{4N}\underline{U}_n\cdot\underline{U}_m\cos[\underline{k}_n\cdot(\underline{r}-\underline{r}_n)\cos[\underline{k}_m\cdot(\underline{r}-\underline{r}_m)] \\ &= \frac{1}{2}\left[\sum_{n=1}^{4N}\underline{U}_n\cdot\underline{U}_n + \sum_{n=1}^{4N}\sum_{m\neq n}^{4N}\underline{U}_n\cdot\underline{U}_m\cos[(\underline{k}_n-\underline{k}_m)\cdot\underline{r}+\underline{k}_m\cdot\underline{r}_m-\underline{k}_n\cdot\underline{r}_n]\right. \\ &\quad \left. + \sum_{n=1}^{4N}\sum_{m=1}^{4N}\underline{U}_n\cdot\underline{U}_m\cos[(\underline{k}_n+\underline{k}_m)\cdot\underline{r}-\underline{k}_m\cdot\underline{r}_m-\underline{k}_n\cdot\underline{r}_n]\right] \\ &= H_1(\underline{r}) + H_2(\underline{r}) + H_3(\underline{r})\end{aligned} \tag{19}$$

where the identity cosAcosB = (1/2)[cos(A - B) + cos(A + B)] has been used.

Integrating the first term H_1 over the volume V of the cavity yields

$$I_1 = \int_V H_1(\underline{r})dv = \frac{1}{2}\sum_{n=1}^{4N}\underline{U}_n\cdot\underline{U}_n dv = \frac{NV}{2}U^2 \tag{20}$$

which is dependent only on the volume of the cavity and independent of its shape. Because of Eq. (6), we also conclude that $U^2 = 2/NV$.

On the other hand, the values of the integral over both H_2 and H_3 will depend on the shape of the cavity, or

$$I_2 = \int_V H_2(\underline{r})dv = I_2(\text{SHAPE}), \tag{21}$$

$$I_3 = \int_V H_3(\underline{r})dv = I_3(\text{SHAPE}). \tag{22}$$

The only exceptions to Eqs. (21) and (22) will occur when the surface of the cavity has been generated by some random process, for example, a random walk. For this case, the phases given by $\underline{k}_n\cdot\underline{r}_n$ and $\underline{k}_m\cdot\underline{r}_m$ will be random variables and the standing waves will add incoherently so that both I_2 and I_3 vanish, i.e. $I_2 = I_3 = 0$.

In general, the magnitude of both I_2 and I_3 will be strong functions of the regularity of the shape of the cavity and will have maximum values for cavities with regular shapes. For example, for a right-circular rectangular cavity, the phases will be highly correlated and I_2 and I_3 will each be on the order of I_1. For cavities having very irregular shapes, for example the cockpit of an aircraft, the phases will be very weakly correlated and the values of both I_2 and I_3 will be very close to zero.

With this in mind, a complex cavity can be defined:

"A complex cavity is a cavity for which both $I_2 \ll I_1$ and $I_3 \ll I_1$ are true."

Of course there is no *a priori* way to test a cavity's complexity. The only way to proceed is to assume that a cavity is complex based on experience with other cavities and then use

experimental data to justify the assumption. Any other approach must address the details of each cavity separately.

Using the above results along with the definition of a complex cavity, it is now possible to estimate the average values of the amplitudes of the eigenvectors, the results of which are given next.

RESULTS FROM THE AVERAGE-VALUE EVALUATION

Performing the required integrations to obtain the average values defined by $\langle(\underline{u}_k\cdot\underline{u}_k)^n\rangle = \int_V(\underline{u}_k\cdot\underline{u}_k)^n dv$ is reasonably straightforward, but mathematically tedious. Therefore, we only summarize the results here, the derivation of which is described in more detail elsewhere [Lehman and Miller (3)].

$$\langle(u_{k,s})^n(u_{k,s'})^m\rangle = \langle(u_{k,s})^n\rangle\langle(u_{k,s'})^m\rangle \text{ for } s' \neq s;$$

$$\langle(w_{k,s})^n(w_{k,s'})^m\rangle = \langle(w_{k,s})^n\rangle\langle(w_{k,s'})^m\rangle \text{ for } s' \neq s;$$

$$\langle(u_{k,s})^n(w_{k,s'})^m\rangle = 0 \text{ for all } s, s', n \text{ and } m;$$

$$\langle(u_{k,s})^n\rangle = \langle(w_{k,s})^n\rangle$$

$$= 1\cdot3\cdot5\cdot7\cdots(n-1)\sigma^n \text{ for } n \text{ even},$$

$$= 0 \text{ for } n \text{ odd}; \; s = x,y,z;$$

$$\langle(\underline{u}_k\cdot\underline{u}_k)^n\rangle = \langle(\underline{w}_k\cdot\underline{w}_k)^n\rangle$$

$$= 1\cdot3\cdot5\cdot7\cdots(2n-1)(2n+1)\sigma^{2n};$$

and

$$\sigma = \sqrt{1/(3V)} \qquad (23)$$

DERIVATION OF THE NORMAL DISTRIBUTION

From elementary probability theory, it is well-known that the expectation value E{x} of the random variable x is given by

$$E\{x\} = \int x f_X(x)dx$$

where $f_X(x)$ is the density (function) of the random variable x. If one considers another random variable y which is a known function of the random variable x, $y = g(x)$, then the expectation value E{y} of the random variable y is given [Papoulis (4)] by either

$$E\{y\} = \int y f_Y(y)dy \qquad (24)$$

or

$$E\{y\} = \int g(x) f_X(x)dx \qquad (25)$$

where $f_Y(y)$ is the probability density of y. If it is assumed that position vector $\underline{r}$ is a random variable, then its probability density function $f_r(\underline{r})$ is given by

$f_r(\underline{r}) = 1/V$, if $\underline{r} \in V$ and

$f_r(\underline{r}) = 0$, otherwise.

Since the eigenvector $u_{k,s}$ is a function of $\underline{r}$, its expectation value $E\{u_{k,s}\}$ is given by [using Eq. (25)]

$$E\{u_{k,s}\} = \int u_{k,s}(\underline{r}) f_r(\underline{r})dv$$

where the integral extends over all space. Using the above value for $f_r(r)$, the expression for $E\{u_{k,s}\}$ simplifies to

$$E\{u_{k,s}\} = V^{-1}\int u_{k,s}(r)dv \qquad (26)$$

which is the same as the average value of $u_{k,s}(r)$ given by Eq. (10). Therefore, if the position vector r is considered to be random variable, then the expectation value of the amplitude of an eigenvector is identical to its average value or

$$E\{u_{k,s}\} = \langle u_{k,s}(r)\rangle. \qquad (27)$$

Similar arguments hold for all the higher moments of $u_{k,s}(r)$, so that in general, Eq. (27) may be written in the form

$$E\{(u_{k,s})^n\} = \langle (u_{k,s})^n\rangle = \begin{cases} 1\cdot 3\cdot 5\cdot 7\cdots(n-1)\sigma^n, \text{for } n \text{ even} \\ 0 \text{ for } n \text{ odd} \end{cases}; s = x,y,z \qquad (28)$$

But from Papoulis (4), Eq. (28) is the expression for the moments of a normal density. Therefore, with the help of Eq. (24), the probability density function $f_U(u_{k,s})$ for the amplitude of any eigenvector $u_{k,s}(r)$ can be written as

$$f_{US}(u) = (3V/2\pi)^{1/2}\exp[-(3V/2)(u)^2]. \qquad (29)$$

This is a one-parameter density function depending only on the cavity volume V.

From Eq. (1), the components of the electric field are seen to be given by expansions in terms of the eigenvectors, so that the three cartesian components of the electric field are also normal, independent, random variables with zero mean and variances σ^2 given by

$$\sigma^2 = \frac{1}{3V\sum_{k=-\infty}^{+\infty}[p_k(t)]^2} \qquad (30)$$

or

$$f_{E_s}(E_s) = \frac{1}{\sigma\sqrt{2\pi}}\exp\left|-\frac{E_s^2}{2\sigma^2}\right| \qquad (31)$$

Eq. (31) follows from the fact that the probability density of a random variable y = bx with b constant is given by

$$f_Y(y) = (1/|b|)f_X(y/b)$$

and that the sum of any number of normal independent random variables is also normal with a mean equal to the sum of the individual variances. Following the procedures outlined in this paper, it is possible to show that the distribution of the magnetic field components inside an ideal cavity with a complex shape are also normal with zero mean.

SOME REPRESENTATIVE RESULTS

Some results are presented in Fig. 1 of measurements made in a mode-stirred chamber (sometimes called a reverberation chamber) by Kaman Sciences [Smith (5)]. 200 measurements were made at a frequency of 6 GHz of the power coupled to a shielded cable, each one corresponding to a new position of the paddle, or mode stirrer, separated by 1.8 degrees in rotation. The measured data (the squares) are compared with the predicted probability density, shown as a solid line. The latter is based on the theory presented above, recognizing the fact that since there are two independent polarizations

for the electric field, the power then has a chi-squared distribution with two degrees of freedom. This is just an exponential distribution so that the probability density function for the power, $f_p(p)$, is given by

$$f_p(p) = (1/M_p)\exp(-p/M_p) \qquad (32)$$

where M_p is the average power. By matching the average of the theoretical and measured density distributions, and using the transformation of random variables $y = 10\log(x)$ to employ a dB scale for the power, we obtain the results shown. The corresponding cumulative distributions are shown in Fig. 2, where even better agreement can be observed.

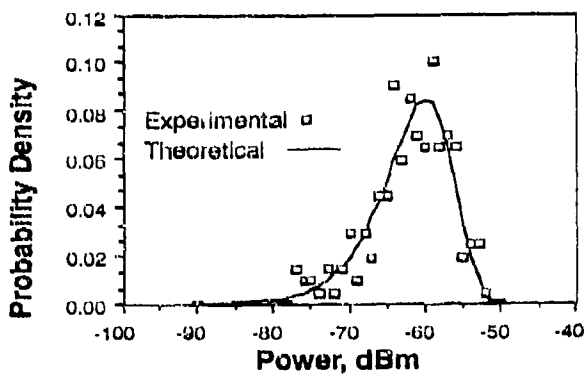

Figure 1. A comparison of the probability density for the power coupled to a shielded cable in a mode-stirred chamber measured by Kaman Sciences (1990) compared with the theory presented here.

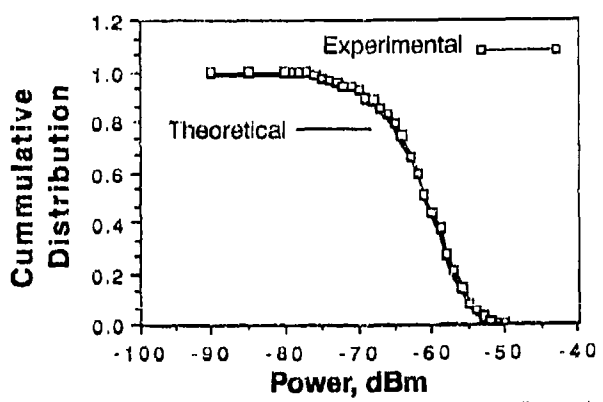

Figure 2. Cumulative distribution functions for results shown in Figure 1.

APPLICATIONS

The potential applications of statistical EM are varied and diverse. The most immediate

application would be to reverberation-chamber testing, which motivated the development presented here. Also a potential application is the characterization of far radiation and scattered fields. Both are discussed briefly below.

Reverberation-Chamber Testing

The most immediate utilization of the theory is to all aspects of reverberation-chamber testing, for which several benefits could be realized. Some areas of application could include: 1) chamber design, 2) data interpretation, 3) data storage, 4) characterizing the response of Equipment Under Test (EUT), and 5) test design. In addition, a rigorous theoretical description of a of reverberation chamber's EM response would certainly give such measurements a firmer analytical basis.

The capability to predict the field distributions inside a reverberation chamber would naturally lead to the optimum design for a given application. In particular, questions regarding source locations, chamber Q, source polarization, chamber dimensions, and numbers of sources needed can be addressed in the design phase.

Having access to the statistical properties of the EM fields would greatly simplify the interpretation of the measured data obtained from reverberation chamber tests. Rather than trying to force the interpretation of the data into deterministic descriptions, developing probabilistic statements about their nature would be easier and much more meaningful. For example, quantifying the probability that the field level in the test volume can exceed a certain level is then possible.

Since most of the distributions encountered in reverberation chamber tests will be functions of two parameters, the number of parameters needed to describe the results are four, at most. These are the expected value and standard deviation, the number of tuner positions, and the frequency.

Using statistical techniques to characterize EUT responses has many advantages. If the equipment is normally located in a complex cavity, for example an aircraft bay, reverberation chamber tests are a better simulation of the actual environment than are anechoic chamber tests. For this case, the only meaningful question is "given the average value of the field or power density inside the cavity, what is the probability that the EUT will experience a failure?" Using the statistical interpretation of data obtained from reverberation chamber tests, this question can be answered. This would not be possible using deterministic interpretations of data from either reverberation or anechoic chamber tests.

If the EUT is an entire small missile for example, normally located in free space, then the advantages of using statistical techniques are not as obvious. However, again the only meaningful question that can be asked is a probabilistic one, namely, "given a peak electric field value, what is the probability that the EUT will experience a failure?" The source of the uncertainty associated with this problem is the angle of incidence and polarization of the incident plane wave with respect to the orientation of the EUT. For many EUTs, the solid angle of interest will be 4π steradians; for others it will be much less, particularly when only near nose-on angles of incidence are important. For this problem, it is now feasible to adjust the reverberation chamber field levels to account for the external gain of the EUT. This procedure is possible because the functional form of the reverberation chamber fields are now known, and the external response of the EUT can be calculated for both plane wave and chamber fields. Since the two test methods can be

made equivalent, the reverberation tests are preferred, for obvious reasons.

The statistical description of reverberation chambers can also be used to optimize the test procedures. For example, the data quality is proportional to the number of tuner positions. Using statistical techniques, it is now possible to quantify the data quality (confidence) in terms of this number. As a result, for many tests, the number of tuner positions could be significantly reduced, with a corresponding reduction in the time required for the measurement and in the amount of data that needs to be collected and processed.

In summary, a statistical description of electromagnetic responses in complex cavities has many advantages over deterministic descriptions. Not only does it provide a simple yet rigorous theory, but also it provides results in a form that is easily related to system performance.

Far-Field Radiation and Scattering

The statistics of far fields are also of interest. In those cases where the radiation pattern of a large antenna or the monostatic or bistatic field scattered from a large body is needed, the numerical or experimental determination of the patterns can be expensive. This is especially so when a numerical model is solved using an iterative technique, in which case the solution must be repeated for each angle of incidence. The possibility of statistically characterizing the far field from a limited number of field samples using the theory presented here could substantially reduce the cost of determining needed parameters such as the expected value of the field, its variance, the most probable peak field, etc.

Because the current modes on the interior or exterior of a perfectly conducting, zero-thickness envelope have the same spatial variations, we expect that the analysis performed above for cavity fields should be applicable to the statistics of far radiated and scattered fields as well. Assuming this to be the case, it seems reasonable to expect that their statistics as a function of angle should be described by the same distributions. This possible application represents an area of future research.

REFERENCES

1. Beran, M. J. and G. B. Parrent, 1964, Theory of Partial Coherence, Prentice-Hall, Englewood Cliffs, NJ.
2. Schiff, Leonard I. (1955), Quantum Mechanics, McGraw-Hill Book Company, Inc., New York.
3. Lehman and Miller (1990), "The Statistics of Electromagnetic Fields in Complex Environments," to be submitted for publication.
4. Papoulis, A. (1965), Probability, Random Variables, and Stochastic Processes, McGraw-Hill Book Company, New York.
5. Smith, Robert (1990), Private Communication, Kaman Sciences, Colorado Springs, CO.

SESSION 6 – "FINITE ELEMENT AND FINITE DIFFERENCE FREQUENCY DOMAIN SOLUTIONS

Moderator: Glenn Crabtree

SOLUTION OF MULTI-MEDIA WAVE PROPAGATION AND SCATTERING PROBLEMS USING FINITE ELEMENTS

E. Thomas Moyer Jr.
Associate Professor of Engineering and Applied Science
The George Washington University, SEAS/CMEE
Washington, DC 20052
(202) 994-5970 ; E-Mail: moyer sparko.gwu.edu

Erwin Schroeder
Research Mathematician, Applied Mathematics Division
David Taylor Research Center
Bethesda, Maryland 20084
(301) 227-1660

ABSTRACT

Problems involving horizontal and vertical electric dipole sources in a stratified media environment with varying electrical conductivity and permitivity is studied. A curl-curl H field formulation is employed which imposes the correct continuity on the field components. The E field components are calculated using Legendre Polynomial smoothing without global averaging which gives rise to the correct discontinuities in the E field vector at material boundaries.

Specific problems are examined which focus on sources located in sea water with driving frequencies between 1 hz. and 100 hz. Solutions for both the sea water and air modeled as infinite half spaces are compared with available reference solutions. The effects of finite thickness layers of ice are considered. In addition, the configuration with a finite depth of sea water with a half space of sea bottom is also explored. Boundary conditions for the truncation of infinite domains are explored. Local expansion boundary conditions which manifest in high order dampers are compared with infinite elements.

Results of the analysis are compared with available analytic solutions and are in good agreement. In addition, the wave-guide characteristics due to media discontinuities and interface propagation are correctly predicted by the analyses. Having established the validity and accuracy of the formulation, extensions and difficulties associated with more complicated sources and scattering objects in the domain are explored.

Finite Element Solutions to the Mass-Tensor Form of the Ginzburg-Landau Equations

Kenneth G. Herd
GE Corporate Research and Development, P.O. Box 8
Schenectady, NY 12301

George Theodossiou
Rensselaer Polytechnic Institute, Department of Computer Science
Troy, NY 12180-3590

Abstract

The spatial variation of the magnetic field and supercurrents in anisotropic, type-II superconductors has been successfully described using a mass-tensor form of the phenomenological Ginzburg-Landau equations[1]. Closed-form solutions to these equations have been previously derived in a limited range near the upper critical field of a superconductor by using a linearized form[2,3]. General solutions to the nonlinear anisotropic problem require a numerical approach. A finite element solution to the mass-tensor form of the Ginzburg-Landau equations in two dimensions is presented herein. The Galerkin weighted residual approach is used to formulate the element matrices. The periodicity of the flux lattice in type II superconductors allows the solution domain to be limited to a single supercurrent vortex cell.

Introduction

The discovery of superconductivity in layered ceramic materials, such as Y-Ba-Cu-O, has led to a renewed interest in the phenomenology of superconductivity in anisotropic systems. All known copper-oxide superconductors are highly anisotropic; that is, their critical current density and critical field strength vary depending upon the direction of the transport current or the applied magnetic field with respect to the crystal axes. This characteristic is distinct from that of metallic superconductors, which generally behave isotropically.

Strongly anisotropic superconductors have been studied previously. The influence of the anisotropy on the superconducting properties has been successfully described by the introduction of a mass-tensor into the well known Ginzburg-Landau (G-L) equations. A general solution to the anisotropic G-L equations produces a complete characterization of the equilibrium free energy density, the reversible magnetization, the flux lattice structure,

and the lower critical field. Numerical results can be directly compared with experimental data on the magnetocaloric, magnetization, and critical field characteristics of anisotropic (and isotropic) superconductors.

This paper describes a finite element solution to the mass-tensor form of the G-L equations using a Galerkin weighted residual approach. The Euler-Lagrange equations for the two-dimensional solution domain are derived from the thermodynamic Gibbs free energy functional. The spatial variation of magnetic field and supercurrents are fully described by a scalar potential, f, and a vector potential, A. A transformation is introduced in which the vector potential, A, which has components A_x and A_y, is replaced in terms of the out-of-plane magnetic field component, h_z, using the relation $h=\nabla x A$. The number of degrees-of-freedom at any point in the solution domain is reduced from three to two.

Type-II behavior in superconductors is characterized by the penetration of discrete flux quanta, or fluxons, into the bulk superconductor in the presence of an applied magnetic field. These fluxons are sustained by the circulation of supercurrent vortices. Mutual repulsion of the vortices leads to an equilibrium condition wherein a vortex lattice is formed. The periodicity of this vortex lattice is such that the solution domain need only encompass a single vortex cell, with the appropriate periodic boundary conditions. The A to h_3 transformation permits the proper constraint of these boundary conditions.

Governing Equations

In 1937, Landau[4] proposed a general theory of second-order thermodynamic phase transitions which was based on the assumption that there exists an order parameter which goes to zero at the transition and that the free energy may be expanded in powers of this order parameter. In 1950, G-L[5] proposed an extension to Landau's original free energy expansion in order to describe a superconductor in the presence of a magnetic field. The isotropic form of the G-L free energy equation for superconductors may be stated as:

$$F_s = F_n + \alpha(T)|\psi|^2 + \frac{\beta(T)}{2}|\psi|^4 + \frac{1}{2m^*}\left|\left(-ih\nabla - \frac{e^*A}{c}\right)\psi\right|^2 + \frac{h^2}{8\pi} \qquad (1)$$

where F_s is the free energy of the superconducting state, F_n is the free energy of the normal state, ψ is a psuedo-wavefunction for a particle of effective charge e^* and mass m^*, α and β are temperature dependent coefficients, h is Planck's constant, c is the speed of light, $h^2/8\pi$ is the magnetic energy, and A is the vector potential for the magnetic field, h.

The free energy potential, Π_s, can be found by integrating the difference between the normal and superconducting free energies over the volume as:

$$\Pi_s = \int (F_s - F_n)\, dr \tag{2}$$

To find the thermodynamic equilibrium conditions, G-L minimized Π_s for variations of the order parameter ψ and the vector potential **A**. For Π_s to be a minimum, i.e. $\delta\Pi_s = 0$ for arbitrary nonzero variations $\delta\psi$ and δA, yields the two well known G-L equations:

$$\frac{1}{2m^*}\left[-ih\nabla - \frac{e^*A}{c}\right]^2\psi + \alpha\psi + \beta|\psi|^2\psi = 0 \tag{3}$$

$$\frac{\nabla \times h}{4\pi} = \frac{j}{c} = \frac{e^*h}{2im^*c}(\psi^*\nabla\psi - \psi\nabla\psi^*) - \frac{e^{*2}}{m^*c^2}\psi^*\psi A \tag{4}$$

where ψ^* implies the complex conjugate of ψ. A basic assumption of the original G-L theory described above is that the underlying normal metal Fermi surface is isotropic. This assumption was removed from the theory in 1952 by Ginzburg[1], who introduced a phenomenological mass-tensor to describe the Fermi surface anisotropy:

$$F_s - F_n = \alpha|\psi|^2 + \frac{\beta}{2}|\psi|^4 + \sum_{\mu=1}^{3}\frac{1}{2m_\mu}\left|\left(-ih\frac{\partial}{\partial x_\mu} + \frac{e^*A_\mu}{c}\right)\psi\right|^2 + \frac{h^2}{8\pi} \tag{5}$$

where m_μ (μ=1,2,3) are the principle values of the effective mass-tensor in the directions x_μ. Equation (5) reduces to the isotropic form (1) if each of the m_μ are equal. In the absence of a field and in equilibrium below the critical temperature, it can be seen from (3) that:

$$\psi = \psi_o = (-\alpha/\beta)^{1/2} \tag{6}$$

For the anisotropic formulation it is convenient to define a magnetic penetration depth, $\lambda(T)$, and a coherence length, $\xi(T)$, as:

$$\lambda(T) = \left[\frac{mc^2}{4\pi e^{*2}\psi_o^2}\right]^{1/2} \tag{7}$$

and:

$$\xi(T) = \left[\frac{-h^2}{2m\alpha}\right]^{1/2} \tag{8}$$

where:

$$m = (m_1 m_2 m_3)^{1/3} \tag{9}$$

All quantities in (5) may be expressed in a dimensionless form using a normalization in which length is measured in units of λ, magnetic field in units of $\sqrt{2}\, h_c=\phi_o/2\pi\xi\lambda$ (where h_c is the thermodynamic critical field and $\phi_o=hc/e^*$), the vector potential in units of $\lambda\sqrt{2}h_c=\phi_o/2\pi\xi$, and the energy density in units of $h_c^2/4\pi=\alpha^2/\beta$. The reduced free energy is then given by:

$$F_s - F_n = -|f|^2 + \frac{1}{2}|f|^4 + \sum_{\mu=1}^{3}\frac{m}{m_\mu}\left|\left(\frac{-i}{\kappa}\frac{\partial}{\partial x_\mu} + A_\mu\right)f\right|^2 + h^2 \qquad (10)$$

where $f=\psi/\psi_0$, and $\kappa=\lambda/\xi$ is known as the effective G-L parameter. It is possible to write f in terms of a magnitude and a phase:

$$f = f_o \exp(i\gamma) \qquad (11)$$

and to define the gauge–invariant quantity:

$$A_o = A + \frac{1}{\kappa}\nabla\gamma \qquad (12)$$

where A_G is usually referred to as the superfluid velocity. Note that A_o satisfies the relation $\nabla x A_o=\nabla x A=h$. Thus (10) becomes:

$$F_s - F_n = -f_o^2 + \frac{1}{2}f_o^4 + \sum_{\mu=1}^{3}\frac{m}{m_\mu}\left[\frac{1}{\kappa^2}\left(\frac{\partial f_o}{\partial x_\mu}\right)^2 + A_{o\mu}^2 f_o^2\right] + h^2 \qquad (13)$$

The Euler-Lagrange equations may be derived by integrating (13) over the volume of the solution domain and minimizing with respect to the unknowns A_μ and f (where the 'o' subscripts will be dropped hereafter), yielding the mass-tensor form of the G-L equations:

$$\sum_{\mu=1}^{3}\frac{m}{m_\mu}\left(-\frac{1}{\kappa^2}\frac{\partial^2 f}{\partial x_\mu^2} + A_\mu^2 f\right) = f(1-f^2) \qquad (14)$$

and:

$$-\frac{m}{m_\mu}A_\mu f^2 = \nabla \times (\nabla \times A)\cdot x_\mu = j_\mu \qquad (15)$$

In the present development, we will restrict the supercurrent domain to $\mu=1,2$. That is, the supercurrents are limited to the plane defined by x_1 and x_2 and the magnetic field has only components h_3. Invoking Maxwell's relation $\nabla x A=h$, (15) can be simplified as follows:

$$\frac{-m}{m_\mu}A_\mu f^2 = (\nabla \times h_3)\cdot x_\mu \qquad (16)$$

Using Maxwell's relation $\nabla x h = j$, then (16) becomes:

$$\frac{-m}{m_\mu} A_\mu f^2 = j \cdot x_\mu = j_\mu \tag{17}$$

Solving for A_μ:

$$A_\mu = \left(\frac{-m_\mu}{m}\right) f^{-2} j_\mu \tag{18}$$

Substitute (18) into (14):

$$\sum_\mu \frac{m}{m_\mu}\left(\frac{-1}{\kappa^2}\right)\frac{\partial^2 f}{\partial x_\mu^2} + \sum_\mu \frac{m_\mu}{m}\frac{j_\mu^2}{f^3} = f\,(1-f^2) \tag{19}$$

Again using Maxwell's relation $\nabla x h = j$, (15) finally becomes

$$\sum_\mu \frac{m}{m_\mu}\left(\frac{-1}{\kappa^2}\right)\frac{\partial^2 f}{\partial x_\mu^2} + \sum_\mu \frac{m_\mu}{m}\frac{1}{f^3}((\nabla \times h_3)\cdot x_\mu)^2 = f\,(1-f^2) \tag{20}$$

This is the first of the two modified Euler-Lagrange equations. Next we eliminate A_μ in terms of h_3 in (17) by taking the curl of both sides:

$$\frac{-m}{m_\mu}\left[\, f^2\,(\nabla \times A_\mu) + 2\,f\,(\nabla f \times A_\mu)\right] = \nabla \times j_\mu \tag{21}$$

Now substitute for A_μ from (18):

$$f^2\,(\nabla \times A_\mu) - \left(\frac{m_\mu}{m}\right)\frac{2}{f}\,(\nabla f \times j_\mu) = \frac{-m_\mu}{m}\,(\nabla \times j_\mu) \tag{22}$$

Invoking the relations $\sum(\nabla x A_\mu)=\nabla x A=h_3$, and $(\nabla x h_3)\cdot x_\mu=j_\mu$, then:

$$f^2\,h_3 = \sum_\mu \left(\frac{m_\mu}{m}\right)\left[\frac{2}{f}\,(\nabla f \times (\nabla \times h_3)\cdot x_\mu) - (\nabla \times (\nabla \times h_3)\cdot x_\mu)\right] \tag{23}$$

This is the second of the two modified Euler-Lagrange equations. It can be shown that equations (20) and (23) simplify to the isotropic form, equations (3) and (4), if $m_1=m_2$.

As discussed previously, the periodicity of the vortex lattice allows the solution domain to be restricted to a single supercurrent vortex cell. Vortex cell symmetry further allows the solution to be limited to a quadrant of the total cell. Figure 1 illustrates the solution domain of interest, with the appropriate boundary conditions for the two unknowns, f and h_3.

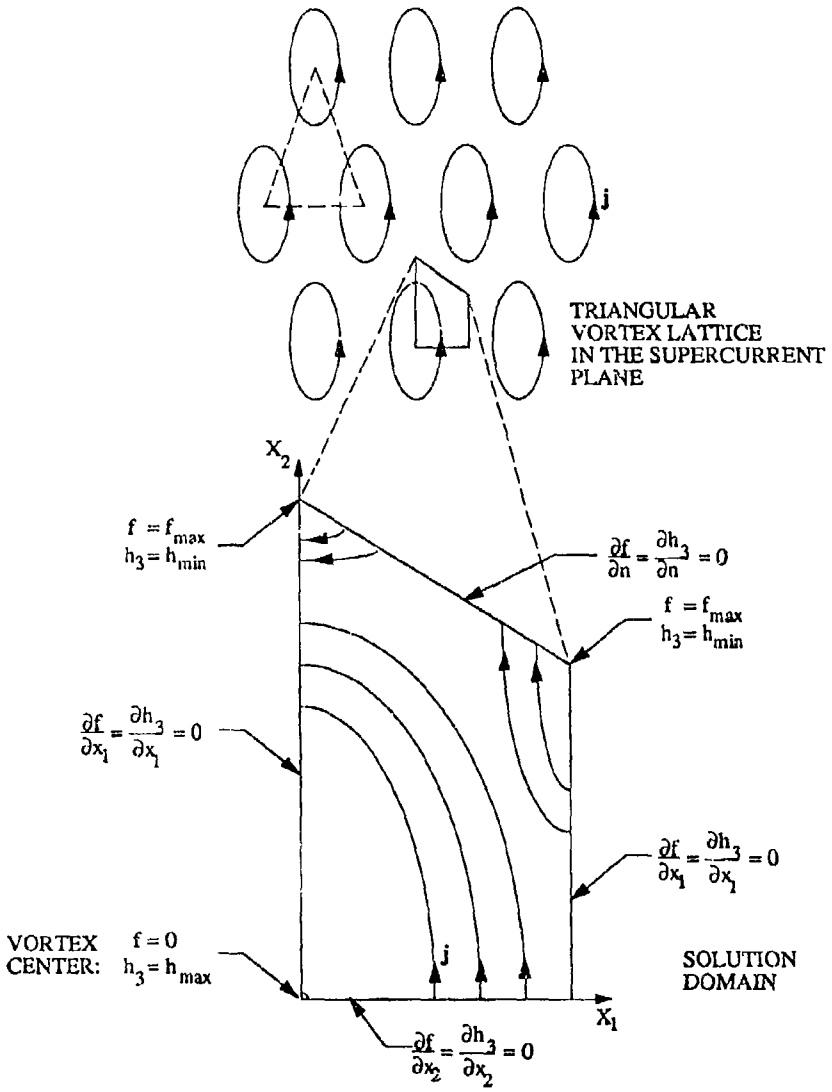

Figure 1: Solution domain in the supercurrent plane with boundary conditions,

Finite Element Formulation

Using the weighted residual approach, the Euler-Lagrange equations, (20) and (23), are multiplied by a weighting function and then integrated over the solution domain. The strong form of equation (20) is then:

$$\int_\Omega v\left\{\sum_{\mu=1}^{2}\left[\left(\frac{m}{m_\mu}\right)\left(\frac{-1}{\kappa^2}\right)\left(f\frac{\partial^2 f}{\partial x_\mu^2}\right)+\left(\frac{m_\mu}{m}\right)\left(\frac{1}{f^2}\right)\left(\frac{\partial h_3}{\partial x_\mu}\right)^2\right]-f^2(1-f^2)\right\}d\Omega=0 \qquad (24)$$

where v is the weighting function. Applying the divergence theorem to the second-order derivative terms produces the weak form of (24). We also introduce the substitution $u=f^2$ in order to reduce the order of the nonlinear terms:

$$\int_\Omega\left\{\sum_{\mu=1}^{2}\left[v\left(\frac{m}{m_\mu}\right)\left(\frac{1}{\kappa^2}\right)\left(\left(\frac{1}{4u}\right)\left(\frac{\partial u}{\partial x_\mu}\right)^2+\left(\frac{\partial v}{\partial x_\mu}\right)\left(\frac{1}{2}\frac{\partial u}{\partial x_\mu}\right)\right)+v\left(\frac{m_\mu}{m}\right)\left(\frac{1}{u}\right)\left(\frac{\partial h_3}{\partial x_\mu}\right)^2\right]\right.$$
$$\left.-v\,u\,(1-u)\right\}d\Omega-\int_\Gamma\frac{v}{2}\left[\sum_{\mu=1}^{2}\left(\frac{m}{m_\mu}\right)\left(\frac{\partial u}{\partial x_\mu}\right)n_\mu\right]d\Gamma \qquad (25)$$

where the n_μ terms are the direction cosines on the boundary Γ. Examining the boundary integral term, we see that it is in the form of the Neumann boundary condition for u, i.e. at the vortex cell boundary:

$$\left(\frac{m}{m_1}\right)\left(\frac{\partial u}{\partial x_1}\right)n_1+\left(\frac{m}{m_2}\right)\left(\frac{\partial u}{\partial x_2}\right)n_2=0 \qquad (26)$$

where the m/m_μ terms account for the material anisotropy. The boundary integral term in (25) is identically zero on the portion of the boundary where (26) must be satisified. On the remainder of the boundary, the weighting function, v, is identically zero in order to satisfy the Dirichlet conditions. The strong form of equation (23) can be written as follows, again substituting $u=f^2$:

$$\int_\Omega v\left\{\left(\frac{m_1}{m}\right)\left[\left(\frac{1}{u}\right)\left(\frac{\partial u}{\partial x_2}\right)\left(\frac{\partial h_3}{\partial x_2}\right)-\left(\frac{\partial^2 h_3}{\partial x_2^2}\right)\right]+\right.$$
$$\left.\left(\frac{m_2}{m}\right)\left[\left(\frac{1}{u}\right)\left(\frac{\partial u}{\partial x_1}\right)\left(\frac{\partial h_3}{\partial x_1}\right)-\left(\frac{\partial^2 h_3}{\partial x_1^2}\right)\right]-uh_3\right\}d\Omega \qquad (27)$$

As before, we apply the divergence theorem to the second-order derivative terms produces the weak form of (27):

$$\int_\Omega \left\{ \left(\frac{m_1}{m}\right)\left[\nu\left(\frac{1}{u}\right)\left(\frac{\partial u}{\partial x_2}\right)\left(\frac{\partial h_3}{\partial x_2}\right) + \left(\frac{\partial v}{\partial x_2}\right)\left(\frac{\partial h_3}{\partial x_2}\right)\right] + \left(\frac{m_2}{m}\right)\left[\nu\left(\frac{1}{u}\right)\left(\frac{\partial u}{\partial x_1}\right)\left(\frac{\partial h_3}{\partial x_1}\right) + \left(\frac{\partial v}{\partial x_1}\right)\left(\frac{\partial h_3}{\partial x_1}\right)\right] - \nu\, u\, h_3 \right\} d\Omega -$$

$$\int_\Gamma \nu \left[\left(\frac{m_1}{m}\right)\left(\frac{\partial h_3}{\partial x_2}\right) n_2 + \left(\frac{m_2}{m}\right)\left(\frac{\partial h_3}{\partial x_1}\right) n_1 \right] d\Gamma = 0 \qquad (28)$$

The boundary integral terms in (28) are in the form of the Neumann boundary condition for h_3 at the vortex cell boundary:

$$\left(\frac{m_1}{m}\right)\left(\frac{\partial h_3}{\partial x_2}\right) n_2 + \left(\frac{m_2}{m}\right)\left(\frac{\partial h_3}{\partial x_1}\right) n_1 = 0 \qquad (29)$$

The finite element method implies a subdivision of the domain into elements and the approximation of the unknowns within each element in terms element nodal values. The scalar potential u and the magnetic field h_3 may be approximated using a set of interpolation functions which relate the nodal point values to the distributions within each element:

$$u(x_\mu) = \mathbf{N}\,\mathbf{u} \qquad (30)$$

$$h_3(x_\mu) = \mathbf{M}\,\mathbf{h} \qquad (31)$$

where **u** and **h** are the vectors of the element nodal point unknowns and **N** and **M** are the vectors of interpolation, or shape functions. Using the Galerkin weighted residual approach, the weighting function, v, is of the same form as the interpolation function. Substituting into equations (26) and (28) yields, for each element:

$$\mathbf{S}_{11}\,\mathbf{h} + \mathbf{S}_{12}\,\mathbf{u} = 0 \qquad (32a)$$

$$\mathbf{S}_{21}\,\mathbf{h} + \mathbf{S}_{22}\,\mathbf{u} = 0 \qquad (32b)$$

where:

$$\mathbf{S}_{11} = \int_\Omega \left[(\mathbf{N}\bar{u})\mathbf{M}^T\mathbf{M} - \left(\frac{m_1}{m}\right)\left(\frac{\partial \mathbf{M}}{\partial x_2}\right)^T\left(\frac{\partial \mathbf{M}}{\partial x_2}\right) - \left(\frac{m_2}{m}\right)\left(\frac{\partial \mathbf{M}}{\partial x_1}\right)^T\left(\frac{\partial \mathbf{M}}{\partial x_1}\right)\right] d\Omega \qquad (35)$$

$$\mathbf{S}_{12} = \int_\Omega \left[\left(\frac{-m_1}{m}\right)\left(\frac{\partial \mathbf{N}}{\partial x_2}\bar{h}\right)(\mathbf{N}\bar{u})^{-1}\mathbf{N}^T\left(\frac{\partial \mathbf{N}}{\partial x_2}\right) - \left(\frac{m_2}{m}\right)\left(\frac{\partial \mathbf{N}}{\partial x_1}\bar{h}\right)(\mathbf{N}\bar{u})^{-1}\mathbf{N}^T\left(\frac{\partial \mathbf{N}}{\partial x_1}\right)\right] d\Omega \qquad (36)$$

$$S_{21} = -S_{12} \tag{37}$$

$$S_{22} = \int_{\Omega} \left\{ \left(\frac{1}{\kappa^2}\right)\left(\frac{m}{m_1}\right)\left(\frac{1}{2}\left(\frac{\partial N}{\partial x_1}\right)^T\left(\frac{\partial N}{\partial x_1}\right)+\frac{1}{4}\left(\frac{\partial N}{\partial x_1}\bar{u}\right)(N\bar{u})^{-1}N^T\left(\frac{\partial N}{\partial x_1}\right)\right) \right.$$

$$+ \left[\left(\frac{m}{m_2}\right)\left(\frac{1}{2}\left(\frac{\partial N}{\partial x_2}\right)^T\left(\frac{\partial N}{\partial x_2}\right)+\frac{1}{4}\left(\frac{\partial N}{\partial x_2}\bar{u}\right)(N\bar{u})^{-1}N^T\left(\frac{\partial N}{\partial x_2}\right)\right)\right.$$

$$\left. \left. - N^TN+(N\bar{u})N^TN \right\} d\Omega \right. \tag{38}$$

The overbar terms denote the primitive variables chosen for this set of nonlinear equations, which can be solved using a Newton-Raphson iteration. A non-symmetric matrix solver is required.

Equations (32) - (38) completely define the problem formulation. The solution of these equations for the distribution of u and h_3 produces a complete characterization of the equilibrium free energy density, the vortex core entropy, the reversible magnetization, the flux lattice structure, and the lower critical field.

Summary

A finite element solution to the two-dimensional anisotropic form of the G-L equations has been developed. The weak form of the integral equations have been formulated with the appropriate boundary terms. A transformation has been introduced in which the vector potential, A, has been replaced in terms of the out-of-plane magnetic field, h_3, thereby reducing the number of degrees-of-freedom at any point in the solution domain has been reduced from three to two. This substitution also enables the proper constraint of the vortex cell boundary conditions, which must be expressed in terms of h_3, rather than A.

References

1. V.L. Ginzburg, Zh. Eksp. Teor. Fiz. V23, 326 (1952).
2. D.R. Tilley, Proc. Phys. Soc. London, V85, 1177 (1965).
3. V.G. Kogan and J.R. Clem, Phys. Rev. B, V24, 2497 (1981).
4. L.D. Landau, Phys. Z. Sowjet U., V11, 11 (1937).
5. V.L. Ginzburg and L.D. Landau, Zh. Eksp. Teor. Fiz., V20, 1064 (1950).

Characterization of Anechoic Chambers by Finite Difference Method

Steffen Haffa*, Detlev Hollmann**, Werner Wiesbeck*

Abstract

A three-dimensional treatment of anechoic chamber problems by the finite difference method is presented. Maxwell's equations are solved in the frequency domain by solution of a boundary value problem. The presented method allows to compute the field distribution of the electromagnetic field inside a chamber. After a description of the general formulation, including the discretization, verifications are given for the two-dimensional and the three-dimensional calculations. Example structures show the capabilities of the method and demonstrate the applicapability to practical problems.

Introduction

Anechoic chambers are used in a large frequency range. At GHz-frequencies the properties of the chamber can be predicted, using the reflection coefficient of the absorbers. At lower frequencies the chamber has to be treated as a cavity with lossy dielectrics at the walls. The knowledge of the field configuration at MHz-frequencies allows optimization of measurement condition for EMC measurements. A finite difference method treatment in the frequency domain is presented for the lossy three-dimensional structure. The computation in the frequency domain gives fine frequency resolution and provides exact study of resonances.

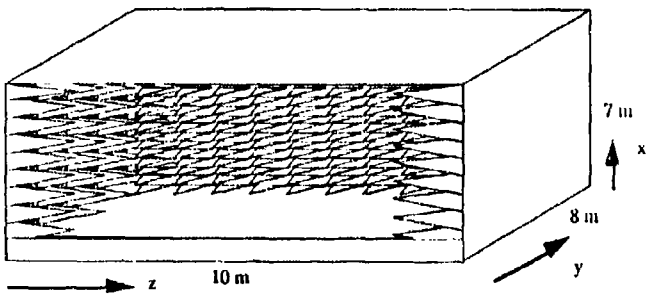

Fig.1 anechoic chamber and coordinate definition.

There are several methods for solving the three-dimensional problem of computing the field distribution. A number of authors work on field theoretical methods, which solve the problem in the

** Institut für Höchstfrequenztechnik und Elektronik, Universität Karlsruhe Kaiserstr.12, D-7500 Karlsruhe, Germany

* Standard Elektrik Lorenz AG Ostendstr. 3, D-7530 Pforzheim, Germany

time domain [1,2]. In our approach we present a more generalized version of a procedure, which has been introduced by [3] for eigenvalue problems and by [4,5] to model chip interconnections and lossy planar structures by [6].
The structure (Fig. 1) is modeled by a non-equidistant rectangular grid. Each elementary cell, formed by this grid, can consist of different lossy material. Both, dielectric and conductor losses are included. The non equidistant grid allows good approximation of geometric structures. The finite difference method is applied to discretisize Maxwell's equations in integral form. A system of equations is set up, which results in a sparse matrix. The system of equations is solved by the biconjugate gradient method on a supercomputer (2.7 GFLOPS). Using 230 Mbyte RAM a maximum matrix size of 330 000 is possible. This results in a structure of 55 000 elementary cells for a complex computation in the lossy case.

Discretization of Maxwell's equations

The three-dimensional structure is enclosed in a shielded rectangular box and contains arbitrary filling materials. The walls of the box are perfectly conducting. The whole box is divided into n elementary cells of arbitrary complex permittivity and permeability including ideal and non-ideal conductors. In order to reduce the computational efforts the elementary cells are of rectangular shape in a homogeneous but non necessarily equidistant grid. As shown in Fig. 2 the space components of the electric and the magnetic fields are defined upon each elementary cell. This kind of allocation has the advantage of implicitly fulfilling the continuity conditions between two neighbored cells of different material.

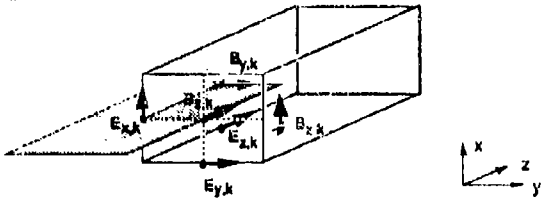

Fig. 2 Allocation of the electric and magnetic field components at the elementary cell k

In the following $\vec{E}$ and $\vec{H}$ are the electric and magnetic field strengths, $\vec{D}$ and $\vec{B}$ the flux densities and $\vec{J}_e$ the source current density. All field components and material related parameters are allowed to be complex. With a harmonic time dependence of the form exp(jωt), the first and second Maxwell's equation in integral form can be written:

$$\oint_c \vec{H} \cdot \vec{ds} = \int_A \left(j\omega\vec{D} + \kappa\vec{E}\right) \cdot \vec{dA} + \int_A \vec{J}_e \cdot \vec{dA} \qquad (1a)$$

$$\oint_c \vec{E} \cdot \vec{ds} = - \int_A j\omega\vec{B} \cdot \vec{dA} \qquad (1b)$$

with the relations $\vec{D} = \varepsilon \vec{E}$ $\vec{B} = \mu \vec{H}$.

A source free structure is assumed ($\vec{J}_e$=0). Polarization losses (tanδ) have been taken into account by the complex permittivity ε.

Applying these assumptions to eq. (1), Maxwell's equations can be discretisized for any cell k by a lowest order integration formula. The integration planes for the elementary cell k are shown in Fig. 2. Combining the resulting discretisized equations leads to a relation between each space component of cell k ($E_{x,k}$, $E_{y,k}$, $E_{z,k}$) and the neighboring components. This is visualized in Fig. 3 for the $E_{x,k}$ component.

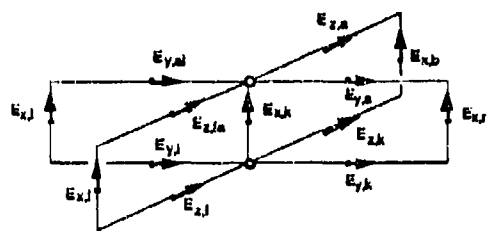

Fig. 3 $E_{x,k}$ component and dependent E components, defining a equation of the linear system of equations

Setting up the equations for all n cells of the whole structure leads to a linear system of equations (2). This matrix equation defines a boundary value problem for the unknown electric field.

$$[C]\begin{bmatrix}\vdots\\ \vec{E}_l\\ \vec{E}_k\\ \vec{E}_a\\ \vdots\end{bmatrix} = \begin{bmatrix}\vdots\\ \vec{E}_l\\ \vec{E}_k\\ \vec{E}_a\\ \vdots\end{bmatrix}_{\text{excited}} \qquad \vec{E}_k = \begin{bmatrix}E_{x,k}^{(Re)}\\ E_{x,k}^{(Im)}\\ E_{y,k}^{(Re)}\\ E_{y,k}^{(Im)}\\ E_{z,k}^{(Re)}\\ E_{z,k}^{(Im)}\end{bmatrix} \tag{2}$$

The right hand side is given by the exciting field. The complex values are splitted into real (Re) and imaginary (Im) parts, thus resulting a real system of equations.The coefficient matrix [C] is sparse and consists of 27 diagonals for lossy structures (μ real). The system of equations is solved iteratively by the biconjugate gradient method and leads to the electric field inside the structure.

Determination of the transverse electric modal fields inside the structure

For computation of the transverse electric field in any direction inside the structure the procedure of the three-dimensional case can be applied in a simplified version. The homogeneity of the field components in z-direction, depending on the propagation constant k_z, allows to eliminate the z-components by using the continuity equation.

$$\oiint_A j\omega \vec{D}\, d\vec{A} = 0 \tag{3}$$

After some rearrangements this leads to the following eigenvalue problem

$$([A] - \gamma [I])\, \vec{E} = 0 \qquad (4a)$$

with

$$\gamma = e^{-jk_z \Delta z} + e^{+jk_z \Delta z}, \qquad (4b)$$

that is to be solved for γ. The eigenvectors related to each of the propagation constant k_z can be computed by solving (4a) and give the transverse fields of each mode. The fields are orthogonal to each other.

Applying the orthogonality relation of the modal fields $\vec{E}_{ti}$, $\vec{H}_{ti}$ to the calculated field in a tangential z-plane $\vec{E}_t$ of the three-dimensional structure allows a modal decomposition [7,8].

Verification

At the frequencies under investigation the chamber behaves like a waveguide near cutoff. The two-dimensional computation have been checked against analytical solutions and results derived by other methods.

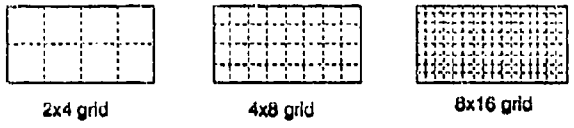

Fig. 4 Grid divisions of a waveguide filled with lossy dielectric material (ε_r=20 - j2); height h=5a, width w=10a; a: normalization constant.

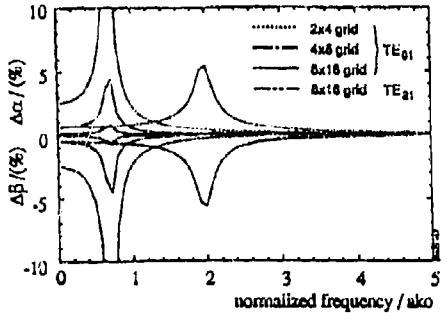

Fig. 5 Relative error of the propagation constant of the waveguide structures.

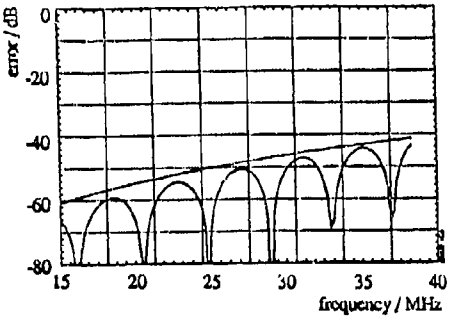

Fig. 6 Comparison of three-dimensional and two-dimensinal solution for z-homogeneous structure.

A waveguide filled with lossy dielectric material has been investigated in the frequency range below and above cut-off. The first 10 modes have been compared to the analytical solution for 3 different types of the grid, Fig. 4. The relative error of the propagation constants $\Delta\alpha$, $\Delta\beta$ is shown in Fig. 5 for the first (TE_{10}) and the seventh (TE_{21}) mode. The errors reach a maximum at cut-off, but they decrease in the region above cut-off to values below 1%. The distance of the two z-planes Δz, which is used in the calculation (see eq. (4b)), has been set to 0.01a. The geometry and frequency are normalized to the constant a.
The discretization error of the three-dimensional calculation can be checked for homogeneous structures by comparison to a two-dimensional solution [8]. As an example Fig. 6 shows a typical error and the envelope giving the minimum accuracy. The traces indicate the finite grid spacing in direction of propagation, which becomes larger with increasing frequency.

Application of the method

Fig. 1 shows the geometry of the investigated anechoic chamber. It is discretisized every 0.5m and by 0.3m in the absorber region. The pyramidal absorbers can not be discretisized in detail due to the limited number of elementary cells. They are modelled by sheets of dielectric material with an effectiv dielectric constant ε and a loss facter $\tan\delta$. This is an adequate simplification, because the dimensions of the pyramides are small compared to the wavelength in the used frequency range.Different materials were used for the tips of the absorbers and the ground sheet. The ground plane of the chamber and the walls consist of different absorbers. The values of ε are 1.7 and 1.2 and of $\tan\delta$ 1.0 and 0.3, respectively.

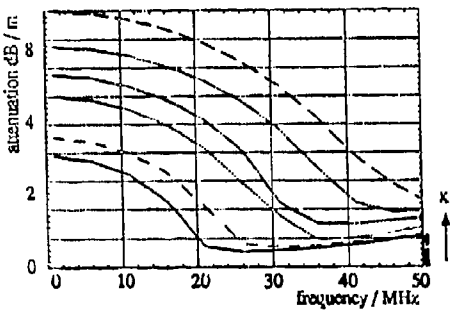

Fig. 7 Attenuation constant of the first modes in a chamber crossection.

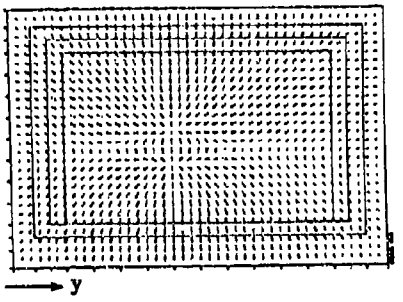

Fig. 8 Transverse electric field in a crossectional plane z=3.5m

An example for the two-dimensional solution for the chamber of Fig.1 in a plane z=const. is shown in Fig 7. The attenuation constant indicates the cutoff frequency for the first 6 modes. At a frequency of 20 MHz the first mode reaches its cutoff an will dominate the behavior of the whole structure. Even if there are some modes above cutoff frequency it is possible to excite only a few of them by an appropriate choice of the location of the exciting field.
For field excitation arbitrary components of the fieled inside the box can be given with arbitrary phase and amplitude. It allows to give any kind of polarization (linear, circular, elliptical) of the exciting field.

A vertical excitation at the plane z=1.5m in the location x=3m y=4m is for the following three-dimensional computations. This excitation corresponds to an electric dipole in x-direction. To show the influence of reflecting materials into the chamber a second example was computed. A metallic post is positioned in the chamber at the location z=8.25m y=3.5m with a size of 0.5m by 1m and a hight of 2m.

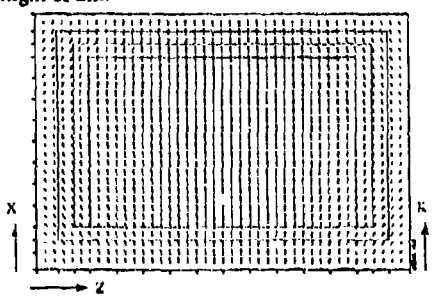

Fig. 9 Transverse electric field in a cross-sectional plane z=7m (frequency 30 MHz)

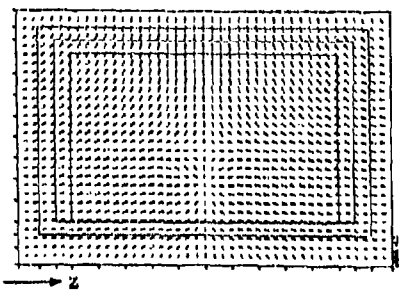

Fig. 10 Transverse electric field in a cross-sectional same as Fig. 9 with metallic post

A three-dimensional computation at 30 MHz shows the dominance of the first mode (like a TE_{10} waveguide mode). The electric field in two different planes near the excitation (plane z=2m) (Fig. 8) and away from it (plane z=7m) (Fig.9) show the attenuation of higher order modes. If the additional metallic post is included in the structure the field is changed near the post. Higher order modes are excited at the post (Fig. 10).

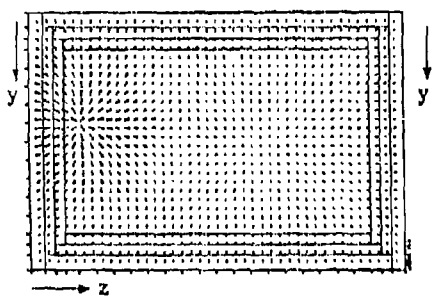

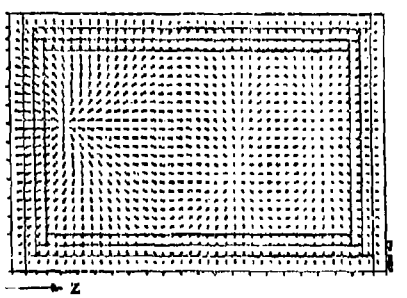

Fig. 11 a) 30 MHz b) 40 MHz
Transverse electric field in a cross-sectional plane x=2m (top view) in an empty chamber

Fig. 11 shows a top view of the electric field normal to the cross-section. Using a frequency of 40 MHz the field composition gets more complicated. Due to the asymmetric position of the exciting field there are a more modes excited than at 30 MHz.
The magnetic field of the same configuration is shown in Fig. 12 and Fig. 13 at two different times. A wavefront moving from the right side to the left can be seen especially if more time steps are used. The reflection from the metallic post can be noticed.

The magnetic energy Fig.14 indicates more reflections in presence of the metallic post and a higher energy content due to multiple reflections.

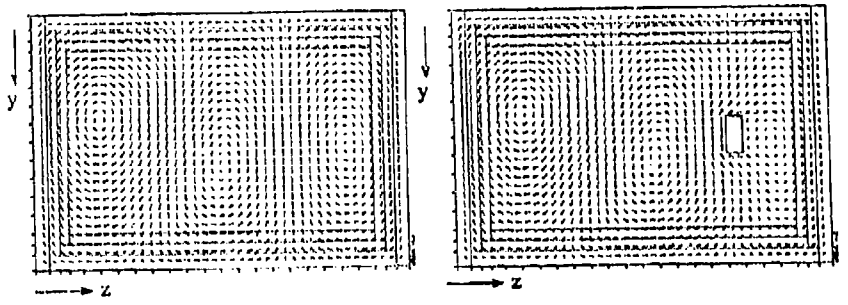

Fig. 12 a) empty chamber b) additional metallic post
Transverse magnetic field in a cross-sectional plane x=2m (top view) (frequency 40 MHz).

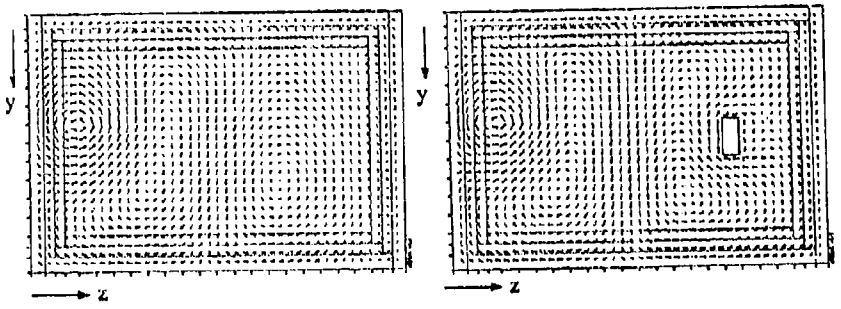

Fig. 13 a) empty chamber b) additional metallic post
Transverse magnetic field in a cross-sectional plane x=2m (top view) a quarter period later then Fig. 12 (frequency 40 MHz).

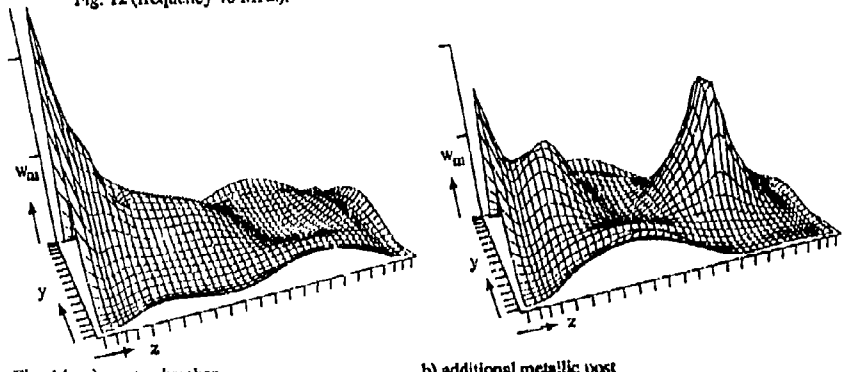

Fig. 14 a) empty chamber b) additional metallic post
Electric energy in a cross-sectional plane x=2m (top view)

Conclusion

The presented method is well suited for computation of anechoic chambers in the frequency range of 1 to 100 MHz. The flexibility of the geometry allows to include different absorbers, devices under test, and e.g. an antenna positioner in the computation. The plots of the computed three dimensional electric and magnetic fields and the electric and magnetic energy give informations on the behavior of the electromagnetic field. The large number of discretization elementary cells allows an excellent modelling of the investigated structures. Critical frequencies can be found by two-dimensional and three-dimensional computations. The position of an antenna and a device under test can be optimized for those frequencies.

References

[1] W. Hoefer, "The Transmission-line Matrix Method - Theory and Applications", *IEEE Trans on MTT*, vol. 33, pp. 882-893, Oct. 1985

[2] A. Taflove, M. E. Brodwin "Numerical Solution of Steady-State Electromagnetic Scattering Problems Using the Time-Dependent Maxwell's Equations", *IEEE Trans Microwave Theory Tech.*, vol. MTT-23, S. 623-630, Aug. 1975

[3] T. Weiland, "Die Diskretisierung der Maxwell-Gleichungen", *Physikalische Blätter*, Band 42, S. 191-201, July 1986

[4] A. Christ, H. Hartnagel, "Three-Dimensional Finite-Difference Method for the Analysis of Microwave-Device Embedding ", *IEEE Trans on MTT*, vol. 35, pp. 688-696, Aug. 1987

[5] A. Christ, "Streumatrixberechnung mit dreidimensionalen Finite-Differenzen für Mikrowellen-Chip-Verbindungen und deren CAD-Modelle", Ph.D. Thesis, *Fortschritt-Ber., VDI Reihe 21 Nr. 3* , VDI Verlag Düsseldorf, 1988

[6] S. Haffa, "*Statische und dynamische Verfahren zur Berechnung monolithisch integrierter Mikrowellen-Bauelemente*", PD-Thesis, Universität Karlsruhe, 1990

[7] D. Hollmann "*Feldtheoretische Verfahren zur Analyse dielektrischer Resonatoren in integrirten Mikrowellenschaltungen*", PD-Thesis, Universität Karlsruhe, 1991

[8] D. Hollmann, S. Haffa, W. Wiesbeck, "S-Parameter Calculation of Arbitrary Three-Dimensional Lossy Structures by Finite Difference Method", *Proc. of the Int. Conf. on Directions in Electromagnetic Wave Modeling*, Weber Research Institute of Polytechnic University, New York, Okt. 1990

Autors:

Steffen Haffa

Work mail address: Institut für Höchstfrequenztechnik und Elektronik, Universität Karlsruhe, Kaiserstraße 12, d-7500 Karlsruhe, Germany, Tel: 49-721-6082525, Fax: 29-721-691865
Home mail address: Offenburger Straße 29, D-7500 Karlsruhe 51, Germany, Tel: 49-721-888190

Steffen Haffa was born in Stuttgart, Germany, in 1956. He received the Dipl.-Ing. (M.S.) degree from the University of Karlsruhe in 1983.
From 1983 to 1986 he was employed at Richard Hirschmann Company, Stuttgart, Germany. He was responsible for the development of satellite receiving systems, with the main work on reflector antennas and feed systems.
From 1986 he is with the Institute for Microwaves and Electronics at the University Karlsruhe, where he received his Dr. Ing. (Ph. D.) in 1990. His research work was on field theoretical computation for device modeling and measurement at mm-wave frequencies. The main application of his work was on GaAs MMIC.

Detlev Hollmann
Work mail address: Institut für Höchstfrequenztechnik unf Elektronik, Universität Karlsruhe, Kaiserstraße 12, d-7500 Karlsruhe, Germany, Tel: 49-721-6082525, Fax: 29-721-691865
Home mail address: Scheibenhardter Weg 26, D-7500 Karlsruhe 51, Germany, Tel: 49-721-887936

Detlev Hollmann was born in Karlsruhe, Germany, in 1960. He received the Dipl.-Ing. (M.S.) degree from the University of Karlsruhe in 1987.
He then joined the GaAs mm-wave group at the Standard Elektrik Lorenz AG (SEL), Pforzheim, where he is responsible for network measurement and calibration. In a cooperation with the Institut for Microwaves and Electronics at the University of Karlsruhe he currently works towards the Dr.-Ing. (Ph.D.) degree. His main research interests include numerical computation of electromagnetic fields applied to dielectric resonator coupling on MMIC circuits, optimization methods and device modeling.

Werner Wiesbeck
Work mail address: Institut für Höchstfrequenztechnik unf Elektronik, Universität Karlsruhe, Kaiserstraße 12, d-7500 Karlsruhe, Germany, Tel: 49-721-6082525, Fax: 29-721-691865

Werner Wiesbeck (SM 87) was born near Munich, Germany in 1942. He received the Dipl. Ing (M.E.E.) and the Dr. Ing. (Ph. D.E.E.) degrees from the Technical University Munich in 1969 and 1972 respectively.

From 1972 to 1983 he was with AEG-Telefunken in various positions including head of R&D of the Microwave Division in Flensburg and marketing director Receiver and Direction Finder Division Ulm. During this time he had product responsibility for mm-wave radars, receivers, direction finders and electronic warfare systems. Since 1983 he has been director of the Institute for Microwaves and Electronics at the University Karlsruhe. Present research topics include radar, remote sensing, wave propagation and antennas. 1989 he spent a six month sabbatical at the Jet Propulsion Laboratory, Pasadena. He is engaged in several working groups in electrical engineering.

SESSION 7– "MOMENT METHOD THEORY"

Moderator: Allen Glisson

A Multilevel Enhancement of the Method of Moments

Khalil Kalbasi, *Kenneth R. Demarest

Radar Systems and Remote Sensing Laboratory
Department of Electrical and Computer Engineering
The University of Kansas
Lawrence, KS 66045

ABSTRACT : A multilevel formulation of the method of moments (MoM) for computing the fields scattered by electrically large conducting bodies is presented. This iterative method can handle very large MoM matrix equations efficiently, is particularly suitable for multiple excitations, and can be adapted as a "solve" module for almost any MoM code. We have formulated the method for a model problem (the EFIE applied to two-dimensional scatterers) successfully, and feel that it holds significant promise for other integral equations in two or three dimensions. Solutions are presented and are compared in efficiency performance with existing results.

INTRODUCTION

The method of moments continues to be an attractive technique for solving electromagnetic scattering problems. Its advantages are many and well known. In spite if its advantages, however, the MoM is for the most part relegated to resonance range frequencies for large scatterers. This limitation stems from the prohibitive computational cost associated with solving large systems of equations. As is well known, the computational cost of direct solvers grows as the cube the number of unknowns, making it unsuitable for very large problems.

Iterative methods have, for many years, been seen as attractive alternatives to direct solvers when matrix equations are very large. The computational cost per iteration of these solvers typically grows as the total number of nonzero entries of the matrix. This has prompted the use of iterative solvers in partial differential equation formulations where the resulting matrix is large and sparse.

Unfortunately, iterative methods, in general, have not been found particularly effective in MoM formulations. The reason is that the impedance matrices associated with electrically large scatterers tend to be huge, dense, non-hermitian, and non-symmetric. These negative features result in slowly converging, or worse yet, diverging solutions. Clearly, iterative procedures alone will not substantially increase the range of problems that MoM can address.

MULTILEVEL ITERATIONS

Classical linear iterations have the general characteristic that the local (i.e., fast, or high spatial frequency) solution behavior converges rapidly, but the global (i.e., slow, or low spatial frequency) behavior either diverges or converges slowly. The fast components of the solution are extracted quickly, while it takes many iterations to capture the slow modes. Therefore, the iteration process is selective in extracting some modes and "filtering" the others.

Multilevel based methods [1], capitalize on this selective property of the iteration process. The basic idea is as follows. A given geometry is first modeled with a fine level of discretization and an iterative solver is initiated. In just a few iterations, the high frequency modes of the solution will be quickly identified, but large low frequency errors will remain. At this point, the geometry is remodeled using a coarser level of discretization. At this coarser level, modes that appeared to be "slow" in the fine level now seem to be "fast". These modes can then be quickly identified with an iterative solver at this coarser level.

Multilevel techniques typically involve several levels of discretization. Solutions obtained by iteration at one level can be passed either "up" to a finer level or "down" to a coarser level to take advantage of the the mode selective characteristics exhibited by the iterative solvers at each level. Since the cost per iteration is far less at the coarser levels, the global characteristics of the solution can be identified at a fraction of the cost of either direct or classical iterative methods at a single level.

The key to a successful implementation of multilevel methodology to the MoM (hereafter called the *multilevel moment method*) is the development of basis functions that allow the remodeling of a given problem at different levels of discretization consistently and without the high cost of recalculating the impedance matrix elements. This is addressed in the next section. After sketching the main features of the technique, representative results for two-dimensional conducting objects using the Electric Field Integral Equation will be presented.

INTERLEVEL RELATIONS

To conceive a simple two-level moment method we start with the operator equation

$$L f = g, \qquad (1)$$

where $\mathbf{L}$ is a linear integral operator, g is a known excitation, and the function f is to be determined. Starting with the usual MoM procedure, let's assume that the unknown function is approximated via a pulse basis set of support (i.e.,length) h. Using a Galerkin scheme, the matrix equation $Z^h x^h = v^h$ is obtained. Next assume another matrix equation $Z^H x^H = v^H$ is generated, where H=2h is support associated with a coarser basis and weighting set of functions. Here, Z^h and Z^H correspond to fine and coarse representations of the operator $\mathbf{L}$, respectively . The same is true of the vector pairs g^h , g^H and x^h , x^H.

The vectors and matrices on fine level are related to their coarse counterparts through two transfer operators, [R] and [I], called restriction and interpolation operators, respectively. Mathematically, [R] maps a given vector from an N-dimensional space to some lower dimension (say N/2). The operator [I] does the opposite task.

It is possible to generalize the transfer operators associated with a given choice of basis and testing functions. For a Galerkin scheme, [R] and [I] are transposes of each other because of reciprocity. This suggests that the coarse level matrices and the right hand sides can be constructed using their representations at the fine level via the identities

$$[Z^H] = [\mathbf{R}]\,[Z^h]\,[\mathbf{I}], \tag{2}$$

and

$$g^H = [\mathbf{R}]\,g^h. \tag{3}$$

As an example, if subsectional pulse functions are used in a Galerkin scheme, [R] has the following structure:

$$[\mathbf{R}] = \frac{1}{2}\begin{bmatrix} 1 & 1 & 0 & 0 & 0 & 0 & \cdots & 0 & 0 \\ 0 & 0 & 1 & 1 & 0 & 0 & \cdots & 0 & 0 \\ 0 & 0 & 0 & 0 & 1 & 1 & \cdots & 0 & 0 \\ \vdots & & & & & & & & \vdots \\ 0 & 0 & \cdots & & 0 & 0 & 1 & 1 & 0 & 0 \\ 0 & 0 & \cdots & & 0 & 0 & 0 & 0 & 1 & 1 \end{bmatrix}_{\frac{N}{2} \times N} \tag{4}$$

Also, [I] is the transpose of [R] multiplied by a scale factor.

THE ALGORITHM

The multilevel algorithm starts at the finest level of discretization. Linear iteration schemes such as Gauss-Seidel or the Banded Matrix Iteration (BMI) [2] are used until the convergence has slowed. If we denote the iterative solution by x_k and the exact solution by x_*, the error after k iterations is

$$e_k = x_* - x_k . \tag{5}$$

This error is related to residual (i.e., boundary) error, $r_k = v - Z x_k$, via the residual equation

$$Z e_k = r_k . \tag{6}$$

The residual error contains the slow modes which are not easily reduced by the iteration process at the fine level of discretization.

Next we project r_k to the coarser level, H, via the operator $[R]$,

$$r^H = [R] r^h . \tag{7}$$

The residual equation (equation 6) is then solved at this coarser level. The solution at this level can be found by LU factorization if the number of unknowns is small, or by iteration if the number of unknowns is still relatively large. Once obtained, the coarse version of the error, e^H, is then interpolated via the interpolation operator, $[I]$, to the fine grid level. By interpolating the error to the fine level, we can construct an approximation to e^h and call it $\tilde{e}^h$:

$$\tilde{e}^h = [I] e^H . \tag{8}$$

A new estimate of the solution is thus obtained by adding $\tilde{e}^h$ to the previous estimate of the solution at the fine level

$$x_{k+1} = x_k + \tilde{e}^h . \tag{9}$$

This new estimate of the solution, x_{k+1}, can now be used as the starting point for a new multilevel cycle. This new estimate contains slow mode information that is not easily obtained at the fine level. It also contains fast mode errors since the coarse level can not adequately model these. These fast mode errors can, however, be

removed in just a few iterations at the fine level. The iterative procedure at the fine level once again is halted when the convergence starts to stall and the error is restricted for use in the coarse level.

OTHER CONSIDERATIONS

The scheme discussed above is a simple two-level design. It is the basis of almost all multilevel algorithms. Multilevel methods for specific problems can be devised by choosing the iteration, the number of levels, the directions of the jumps from one level to another (cycling), transfers between levels, . . . etc.

Among the linear iterative techniques, BMI [2] and Gauss-Seidel have proved to be the most appropriate for multilevel moment method. We have successfully implemented the multilevel moment method using both iterations. At the coarse levels, the iterations must be convergent. When the Gauss-Seidel iteration was employed at the fine level, the Kaczmarz iteration [3] was incorporated at coarse levels to guarantee convergence. Kaczmarz iteration is basically Gauss-Seidel applied to the hermitian form of the impedance matrix, i.e., Z^aZ, where Z^a is the complex transpose version of Z. When BMI is used as the iteration on the fine level, a guaranteed convergence at coarse levels may not be possible. This suggests that the combination of Gauss-Seidel and Kaczmarz iterations is superior to BMI.

LU factorization is commonly employed to solve the relatively small systems of equations at the coarsest level, although iterations could be used as well. If direct solvers are used, the factored form of the (coarsest) matrix is saved throughout the iteration. In cases of multiple excitations, the factored form of the coarsest matrix can be used advantageously for different excitations with considerable savings in computations.

For electromagnetic scattering problems, the coarsest discretization possible is limited by the characteristic wavenumber k_0. The order in which the solution process jumps between the levels is controlled by the *cycling* scheme chosen. The more commonly used cycling schemes, such as V and W [1], are inefficient with multilevel moment method . The V cycle, for example, starts by iterating on the fine level and then moves down p steps to the coarsest level, where the problem is usually solved exactly. This scheme progresses by then moving upward, one level at a time, until the results are carried over to the finest level. Therefore, one full V cycle requires visiting every level twice, once going down and once moving up.

For dense MoM matrix equations, sawtooth cycling appears to be more efficient than V or W cycling since it visits each level only once in a cycle. Sawtooth cycling starts at the coarsest level and moves upward until the finest level is reached, then jumps to the coarsest level.

The next section presents results and comparisons of the multilevel moment method for two-dimensional conducting bodies.

NUMERICAL RESULTS

Consider first the example of a thin, perfectly conducting corner reflector with equal and perpendicular sides. As shown in Figure 1*a*, the incident field is a TM plane wave, approaching at an angle of 40°. To model this geometry, we use the EFIE, with pulse basis functions and point matching on the plates [4]. The matrix equation is solved using the multilevel scheme discussed above. In all the numerical experiments presented here, a problem is considered "solved" when a residual error of less than 10^{-4} is obtained, corresponding to four digits of accuracy in the near field solution. The parameters of interest such as the sampling density, the number of levels, the type of iteration used, etc. . ., are given with the table and graphs.

The advantage of the multilevel scheme becomes apparent as the number of unknowns, N, increases. Table 1 includes some relevant information concerning the performance of the 3-level scheme applied to the corner reflector geometry, including number of unknowns, size of the reflector side in wavelength, fill time, factor time, iteration time, and number of required cycles for convergence. As this table shows, the number of cycles needed for convergence seems independent of the number of unknowns. (We have observed this same behavior on all geometries we have tried thus far.)

To investigate the performance of the multilevel moment method on a more complex scatterer, we next choose a modified NACA 0012 airfoil (Figure 1*b*). The tip to toe length (cord length) is changed to yield different values of N. In all cases, the starting discretization on the finest level was 16 points per wavelength.

Figure 2 compares the Gauss-Seidel multilevel technique with a standard conjugate gradient solver [5] for different tip to toe lengths of the NACA airfoil. Each curve shows the decrease in residual error of the fine level as a function of the number of Work Units (WU). (One WU is equal to the cost of one matrix vector multiplication at fine level, i.e., N^2 complex operations). For the conjugate gradient, the number of work units required for an acceptable solution grows linearly with N. Note that this is the

same total number of WUs as demanded by direct methods. For the multilevel moment method, the number of WUs is practically independent of N.

The performance of the multilevel scheme is clearly superior to conjugate gradient and direct methods. Furthermore, the advantage of the multilevel moment method becomes more pronounced as the number of unknowns increases. Similar results have been obtained using BMI variant of the multilevel scheme on different geometries, such as plates [6], and ogives.

CONCLUSIONS

In this paper we have shown the feasibility of the multilevel moment method for the EFIE in two dimensions. For this model problem, it was shown that the multilevel moment method is much faster than the conjugate gradient iteration applied to the discretized matrix equation, not to mention any direct method of solution. The multilevel moment method also does not suffer from the divergence problems associated with the application of linear iterations to MoM matrix equations. Appropriate iterations for multilevel treatment of method of moment problems were identified, as well as the transfer operators and cycling between adjacent levels of discretizations. In addition to these, very encouraging results were obtained where problems with a few thousands of unknowns are solved in less than 10 cycles of the method. Future extensions of the method are planned as solve modules for existing MoM codes.

REFERENCES

[1] W. Hackbusch *Multigrid Methods and Applications*, Springer-Verlag, 1985.

[2] T. R. Ferguson, "Efficient Solution of Large Moment Problems: Theory and Small Problem Results," *IEEE Trans. Antennas Propagat.*, March 1976, pp.230-235.

[3] K. Tanabe, "Projection Methods for Solving a Singular System of Linear Equations and Its Applications," Numer. Math., 17 (1971), pp. 203-214.

[4] R. F. Harrington *Field Computation by Moment Methods*, MacMillan Company, New York, 1968.

[5] A. F. Peterson, R. Mittra, "Convergence of the conjugate gradient method when applied to matrix equations representing electromagnetic scattering problems," *IEEE Trans. Antennas Propagat.*, vol. AP-34, pp.1447-1454, Dec. 1986.

[6] K. Kalbasi, K. R. Demarest, "Convergence Acceleration Techniques in the Iterative Solution of Integral Equation Problems," AP-S Symposium Digest, vol. 1, pp.64-68, May 1990, Dallas, Texas.

Figure 1

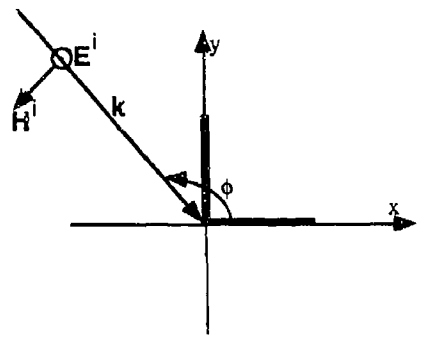

a) Uniform plane wave (TM^z) incident on a thin corner reflector of finite sides.

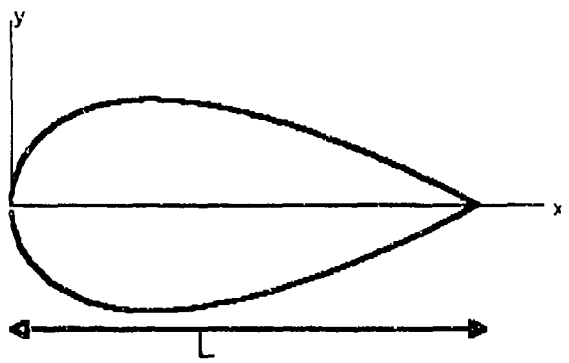

b) NACA0012 airfoil geometry with tip to toe length L. The coordinates convention is the same as part *a* above.

Table 1

Performance of 3-level scheme on a corner reflector with perpendicular sides. The incidence angle ϕ was 40°. Block Gauss-Seidel (BGS) was used as the iteration on the fine level and Kaczmarz iteration on coarser levels. The number m denotes the coefficients per block used in BGS. On the coarsest level LU factorization was employed to solve the system directly. The sampling density of 16 points per λ was chosen on fine level. Number of iterations at each stop on different levels was one.

N	Reflector Side (λ)	Matrix Generation Time (sec.)	Factor Time for Coarsest Level (sec.)	Total Iteration Time (sec.)	Cycles
200	6.25	0.23	0.03	0.68 (m=8)	6
400	12.5	0.94	0.24	2.94 (m=8)	7
600	18.75	2.11	0.8	5.54 (m=8)	6
800	25	4.0	1.86	12.14 (m=16)	6
1000	31.25	6.18	3.38	21.42 (m=8)	6
1200	37.5	9.2	5.69	28.75 (m=16)	7

Figure 2

Performance of multilevel moment method compared with the conjugate gradient (CG) iteration for different sizes of NACA airfoil. Block Gauss-Seidel on fine level and the Kaczmarz iteration on coarser levels was employed. Other relevant informations are : incident angle $\phi=165^0$, m=8, 3-level Scheme, 1 iteration per level. Tip to toe length of $L=12.2596\lambda$ (N=400), $L=24.51\lambda$ (N=800) and $L=36.77\lambda$ (N=1200) were used for airfoils.

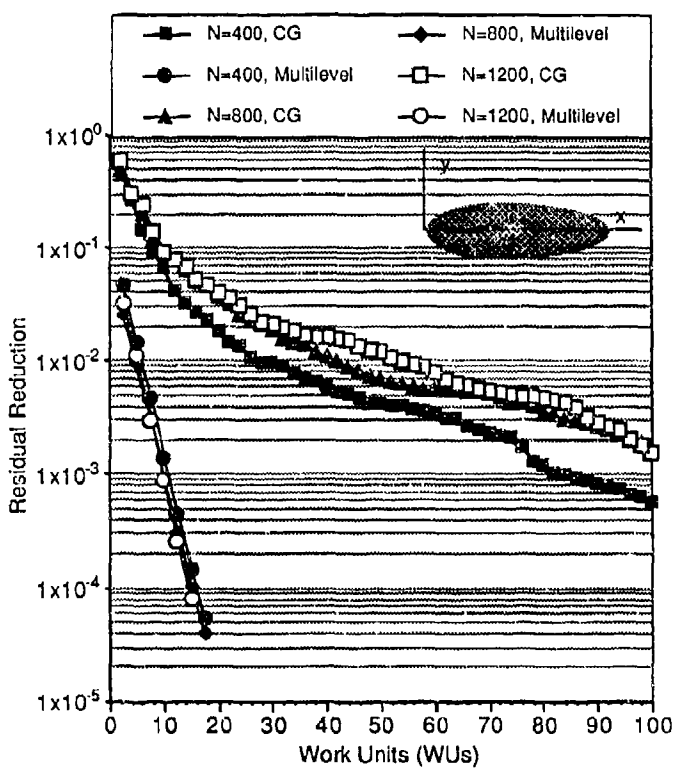

THIS PAGE IS
INTENTIONALLY
LEFT BLANK, ACCIDENTALLY.

On the Applicability of Pulse Expansion and Point Matching in the Moment Method Solution of Three-Dimensional Electromagnetic Boundary-Value Problems

Bierng C. Ahn, Karthikeyan Mahadevan, and Allen W. Glisson
Department of Electrical Engineering
University of Mississippi
University, MS 38677

Abstract

The use of a pulse expansion and point matching (PEPM) scheme in the electric field integral equation (EFIE) solution of three-dimensional, time-harmonic electromagnetic boundary-value problems is investigated. Problems of electromagnetic scattering by a few simple conducting bodies in free space are considered. A comparison of solutions obtained using the PEPM-EFIE scheme with those obtained using rooftop expansion functions and a line testing procedure indicates that the PEPM-EFIE scheme may not produce correct results for general three-dimensional geometries. An empirical explanation for the apparent failure of the PEPM-EFIE approach to EM scattering by arbitrarily shaped scatterers is suggested by studying the near field of a known pulse-approximated current.

I. Introduction

The integral equation technique is still a viable method for solving a large class of electromagnetic boundary-value problems, even though other approaches such as the finite-element method (FEM), and the conjugate gradient fast Fourier transform method (CG-FFT) are increasingly finding many applications in the solution of dynamic EM problems in recent years. Integral equations for EM problems are most often solved by the method of moments (MM), where the choice of the expansion and testing functions plays an important role in determining the accuracy and convergence rate of the solution. One of the most versatile and efficient expansion and testing schemes in the MM solution of surface integral equations for a special class of geometries is the rooftop expansion and line testing (RELT) approach proposed by Glisson and Wilton [1]. This approach was subsequently extended by Rao, Wilton, and Glisson for the treatment of arbitrarily shaped three-dimensional bodies [2].

The simpler pulse expansion and point matching (PEPM) approach has been widely used for static EM problems, and for specific formulations and polarizations in two-dimensional dynamic EM problems [3]. Recent work has shown that the PEPM approach can also be very effective for two-dimensional scattering problems modeled by the EFIE for both polarizations [4,5], but it has not been employed with any success in the electric field surface integral equations for three-dimensional dynamic EM problems to the best of the authors' knowledge. Yet compared to the RELT approach, the PEPM scheme generally requires fewer computations and may be more convenient in the segmentation of some boundary surfaces. Thus the PEPM approach would appear to be a preferable approach when it is applicable. The analytical methods recently proposed by Mahadevan and Auda [6,7] for evaluating accurately the singular surface integral involving the free-space Green's function allows one to efficiently use the PEPM

scheme in the surface integral equation.

In this paper, the applicability of the PEPM-EFIE for the solution of three-dimensional dynamic EM problems is investigated by solving scattering problems involving simple conducting bodies such as strips, thin wires, rectangular plates, and closed rectangular cylinders. In the following section, the PEPM-EFIE formulation and the numerical solution procedure are presented. In Section III, numerical results obtained with the PEPM and RELT schemes are compared and an empirical study is described which may explain the apparent failure of the PEPM-EFIE approach to model EM scattering by arbitrarily shaped scatterers.

II. PEPM-EFIE Formulation

Consider a perfectly conducting object illuminated by a prescribed incident field ($\mathbf{E}^i$, $\mathbf{H}^i$) in free space. To obtain an integral equation for the problem, one replaces the surface S of the object with the electric current density $\mathbf{J}$ induced on that surface, and enforces the boundary condition on the total field $\mathbf{E}^t$ or $\mathbf{H}^t$ to obtain

$$\hat{\mathbf{n}}\times\mathbf{E}^t(\mathbf{r}) = \hat{\mathbf{n}}\times[\mathbf{E}^s(\mathbf{r}) + \mathbf{E}^i(\mathbf{r})] = 0 \qquad \text{(EFIE)} \tag{1}$$

$$\hat{\mathbf{n}}\times\mathbf{H}^t(\mathbf{r}) = \hat{\mathbf{n}}\times[\mathbf{H}^s(\mathbf{r}) + \mathbf{H}^i(\mathbf{r})] = \mathbf{J}(\mathbf{r}) \qquad \text{(MFIE)} \tag{2}$$

where $\mathbf{r}$ is just outside S and $\hat{\mathbf{n}}$ is the outward normal to S. The PEPM procedure can be readily applied to (2), but it is well known that for objects with vanishing thickness (1) is still valid while (2) fails. Therefore, it is desirable to also be able to use (1) to obtain numerical solutions. The ability to solve (1) is also desirable because one approach to the avoidance of internal resonance problems is the use of the combined field integral equation (CFIE) [8], which may be formed as a linear combination of (1) and (2).

The scattered fields $\mathbf{E}^s$ and $\mathbf{H}^s$ are given by

$$\begin{aligned}\mathbf{E}^s(\mathbf{r}) &= \frac{1}{j\omega\epsilon}(k^2\mathbf{A} + \nabla\Phi) \\ &= \frac{1}{j\omega\epsilon}\left[k^2\int_S \mathbf{J}(\mathbf{r}')G(\mathbf{r},\mathbf{r}')dS' + \nabla\int_S [\nabla'\cdot\mathbf{J}(\mathbf{r}')]G(\mathbf{r},\mathbf{r}')dS'\right]\end{aligned} \tag{3}$$

$$\mathbf{H}^s(\mathbf{r}) = \nabla\times\mathbf{A} = \int_S \mathbf{J}(\mathbf{r}')\times\nabla G(\mathbf{r},\mathbf{r}')dS' \tag{4}$$

where $G(\mathbf{r},\mathbf{r}') = exp(-jkR)/4\pi R$, $R = |\mathbf{r} - \mathbf{r}'|$, and where the integral representation on the right side in (4) is valid for $\mathbf{r}$ outside S. The mixed potential expression (3) for the electric field is often preferred to other forms because it involves a less singular kernel. Implicit in this

statement, however, is the assumption that the gradient operator in (3) is evaluated only in a weighted average sense through the testing procedure. To solve (1) or (2) by the moment method, one next expresses the current density J in terms of an expansion function with unknown coefficients, i.e.,

$$\mathbf{J}(\mathbf{r}') = \sum_{i=1}^{N} I_i \mathbf{e}_i(\mathbf{r}') \tag{5}$$

A testing procedure is then chosen which leads to an appropriate system of linear equations. One factor in the choice of expansion functions and testing procedure is the form of the integral equation. It has long been known that the PEPM technique is well-suited for use with (2), where evaluation of the curl operation in (4) as the observation point approaches the surface along with (2) leads to a Fredholm integral equation of the second kind. It has been widely accepted that a smoother representation for the current density J is required for the EFIE, which is an integral equation of the first kind. Results obtained for two-dimensional geometries [4,5], however, have suggested that pulse basis functions may indeed be a viable alternative in the EFIE.

In this paper, only wires and a few simple conducting bodies whose surfaces can be subdivided into a set of rectangular patches are considered. The expansion functions $\mathbf{e}_i$ in (5) are chosen to be pulses on each of the rectangular subdomains in the PEPM approach. Thus we consider a rectangular patch subdomain with dimensions $2W_u \times 2W_v$ lying in the u-v plane with a uniform v-directed electric current density defined on it. With the origin of the coordinate system at the center of the patch and with (u,v,w) as the observation point, one obtains for the vector potential

$$\mathbf{A} = \hat{\mathbf{v}} \int_{-W_v}^{W_v} \int_{-W_u}^{W_u} \frac{e^{-jkR}}{4\pi R}\, du'dv' \quad ; \quad R = [(u'-u)^2 + (v'-v)^2 + w^2]^{1/2} \tag{6}$$

When the field point is within the source region, the kernel in (6) is singular and a direct numerical integration is impractical. In this case, the analytic expressions of Mahadevan and Auda [6] can be used, or for programming simplicity, one may extract only the singular portion of the vector potential to be evaluated analytically. In the latter case the vector potential may be represented as

$$\mathbf{A} = \hat{\mathbf{v}} \int_{-W_v}^{W_v} \int_{-W_u}^{W_u} \frac{e^{-jkR}-1}{4\pi R}\, du'dv' + \hat{\mathbf{v}} \frac{1}{4\pi} K_0(u,v,w;u'v') \Big|_{u'=-W_u}^{W_u} \Big|_{v'=-W_v}^{W_v} \tag{7}$$

where

$$K_0(u,v,w;u'v') = (u'-u)\,\ell n(v'-v+R) + (v'-v)\,\ell n(u'-u+R) - w\tan^{-1}\left[\frac{(u'-u)(v'-v)}{wR}\right] \tag{8}$$

The first term in (7) is then non-singular and is amenable to numerical integration. For the second term in (3), the divergence of the current may be represented as

$$\nabla' \cdot \mathbf{J}(\mathbf{r}') = \pm\delta(v' \pm W_v) \tag{9}$$

and one then obtains

$$\frac{\partial \Phi}{\partial p} = \int_{-W_u}^{W_u} \left[\frac{(p-p')(1+jkR)e^{-jkR}}{4\pi R^3} \right]_{v'=-W_v}^{v'=W_v} du' \tag{10}$$

where $p=u$, v, or w; $p'=u'$,v', or w'; $w'=0$. Since the match point is at the center of each rectangular element, the kernel in (10) is never singular and thus (10) can be evaluated accurately by numerical integration. It is worth noting that (10) can be obtained directly from $\nabla\nabla \cdot \mathbf{A}$ without reference to the divergence of the discontinuous pulse basis function for the current.

Results obtained in this work with the PEPM approach, which employs expressions of the form given by (6)-(10), are compared with results obtained via the RELT aproach. For comparison, the expansion and testing schemes used in the PEPM and RELT techniques are illustrated in Fig. 1.

Expressions similar to (7) and (10) can be obtained for the electric field due to the uniform u-directed current. The point matching of u and v components in (1) at the center of each segment leads to a coupled system of simultaneous equations which may be represented in matrix notation as

$$[Z_{uu}]\,[I_u] + [Z_{uv}]\,[I_v] = [V_u] \tag{11a}$$

$$[Z_{vu}]\,[I_u] + [Z_{vv}]\,[I_v] = [V_v] \tag{11b}$$

where elements of the impedance matrix can be computed using expressions presented in the preceding paragraphs. For example, expressions for $Z_{vv,mn}$ and $V_{v,m}$ are

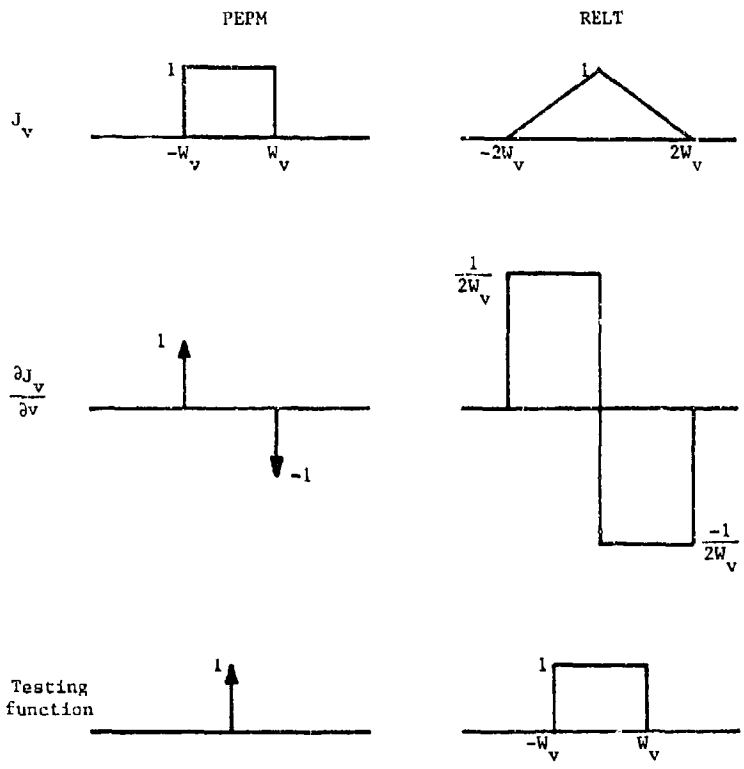

Figure 1. Cross-section representation of expansion and testing functions.

$$Z_{vv,mn} = \frac{1}{j\omega\epsilon}\left\{ k^2 \hat{v}_m \cdot \hat{v}_n \left[\int_{-W_{v,n}}^{W_{v,n}} \int_{-W_{u,n}}^{W_{u,n}} \frac{e^{-jkR_{mn}}-1}{4\pi R_{mn}}\, du'dv' \right.\right.$$

$$\left. + K_0(u_m, v_m, w_m; u_n+u', v_n+v') \Big|_{u'=-W_{u,n}}^{W_{u,n}} \Big|_{v'=-W_{v,n}}^{W_{v,n}} \right]$$

$$+ \hat{v}_m \cdot \int_{-W_{u,n}}^{W_{u,n}} [\hat{u}_n(u_m-u_n-u') + \hat{v}_n(v_m-v_n-v') + \hat{w}_n w_m]$$

$$\left. \times (1+jkR_{mn}) \frac{e^{-jkR_{mn}}}{4\pi R_{mn}^3} \Big|_{v'=-W_{v,n}}^{W_{v,n}} du' \right\} \tag{12}$$

$$V_{v,m} = \hat{v}_m \cdot \mathbf{E}^i(\mathbf{r}_m) \tag{13}$$

where m and n are indices which specify the observation and source patches, respectively, and where $R_{mn}=[(u_m-u_n-u')^2+(v_m-v_n-v')^2+w_m^2]^{1/2}$. The matrix equation for the PEPM-MFIE approach can be obtained using similar procedures once the limit in which the observation point approaches the surface has been taken to extract the principal value term. No extraction of a singular portion of the kernel is then necessary, although careful evaluation of the integral is often required for the nearby sources due to the rapid variation of the kernel.

III. PEPM-EFIE Applied to Simple Conducting Bodies

(A) Narrow Strips and Thin Wires

The PEPM-EFIE formulation presented in the previous section and the RELT-EFIE scheme [1] have been employed to solve electromagnetic scattering problems involving simple conducting bodies in free space. The current induced on a thin strip with width W that is situated parallel to the z-axis in the x-z plane and is illuminated by a normally incident plane wave $\mathbf{E}^i=\hat{x}\eta_0 e^{-jky}$ is solved by segmenting the strip into 1xN rectangular elements. Although the actual current has the $[1-(2x/W)^2]^{-1/2}$ variation, it can be shown that physical quantities such as the radar cross section and the driving point impedance can accurately be computed assuming a constant current across the strip width.

Extensive numerical experiments on the convergence of the solution for strip widths ranging 0.001λ-0.1λ show that in both schemes, for a fixed strip length, a larger number of unknowns is generally required for strips with smaller widths. For fairly long strips, a prohibitively large number of unknowns is required in the PEPM solution. As an example for

a $0.01\lambda \times 4\lambda$ strip, 480 unknowns was required in the PEPM, while 80 unknowns are enough in the RELT to achieve about the same percentage error in the current. The preceding comments also appear to hold true when multiple pulses are used to model the singular behavior of the current on the strip edge.

The thin-wire problem can also be solved by the PEPM-EFIE scheme. In this case for a straight wire radius a, the free-space Green's function is replaced by the thin-wire (reduced) kernel

$$G_a = \frac{e^{-jkR}}{4\pi R}$$
$$R = \sqrt{a^2 + (z-z')^2} \tag{14}$$

and the current density J_z is replaced by the total current $I_z = 2\pi a J_z$. The surface integral in (3) now becomes a line integral and point matching along the wire axis results in expressions corresponding to (12) and (13). The previous observations on narrow strips also appear to be appropriate for thin wires. Fig. 2 and Fig. 3 show the convergence of currents on $0.1\lambda \times 0.5\lambda$ strip and $0.01\lambda \times 0.5\lambda$ wire, respectively, solved using the PEPM and RELT schemes.

(B) Rectangular Plates

As one of the fundamental structures in electromagnetics, rectangular plates have received a fair amount of attention in recent years [9]-[13]. Fig. 4 shows the real and imaginary parts of the z-directed current on $1\lambda \times 1\lambda$ plate solved by the PEPM and RELT schemes using 10×10 segments. Even though the real part improves with more segments, the solution obtained with the PEPM shows significant error. The errors seem to be more pronounced for small plates.

(C) Closed Rectangular Cylinders

As an example of a closed rectangular cylinder, a $0.4\lambda \times 0.4\lambda \times 0.4\lambda$ closed perfectly conducting cube is considered. The back face of the object is on the x-z plane with the coordinate origin at its center. Fig. 5 shows the current on a path, from the center of the front face to the center of the back face along the line of symmetry, solved by various schemes. The excitation is same as before and the path length s is normalized. Again the solution by the PEPM-EFIE scheme is greatly in error.

(D) An Empirical Explanation for the Apparent Failure of the PEPM-EFIE Scheme

It is puzzling that the PEPM-EFIE seems to produce correct results only for two-dimensional geometries or for slender three-dimensional scatterers. For these two geometry types, however, the cross-polarized current component, which is excited only by the gradient of the scalar potential in (2), is either non-existent or negligible. The general success of the RELT scheme coupled with these results suggests that modeling the charge density in terms of impulse functions may be inappropriate. (It should be noted that the *effects* of impulse charges

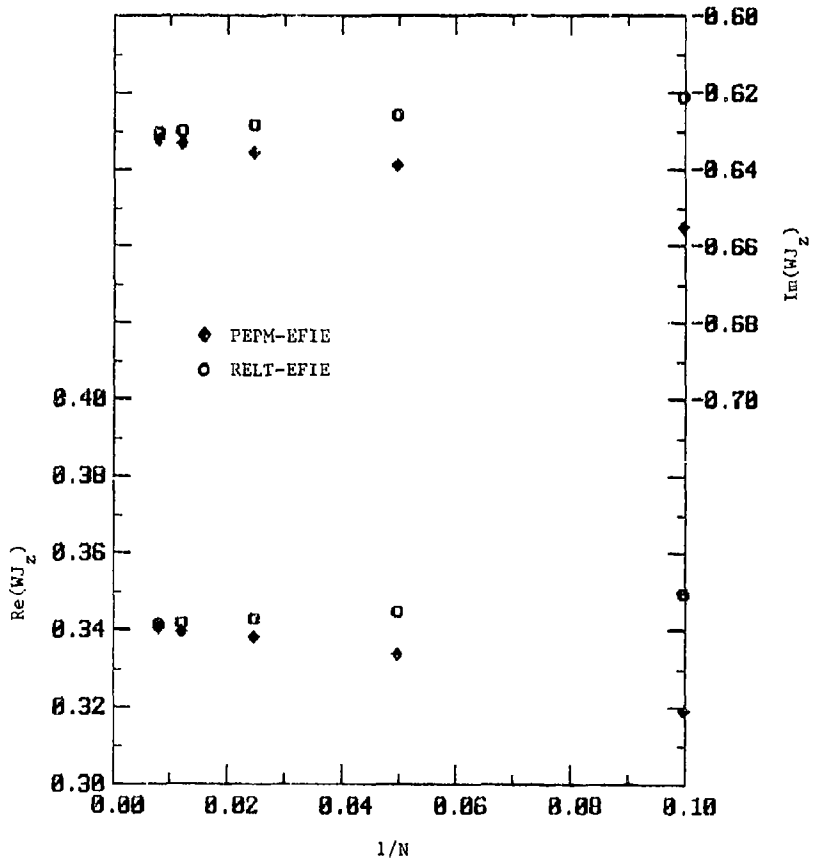

Figure 2. Convergence of the electric surface current density induced on a $0.01\lambda \times 0.5\lambda$ strip.

must appear in the PEPM scheme regardless of whether the equations are derived using impulse charges or not.) To check if a continuous distribution of current and a pulse-function approximation to the distribution generate the same field as the number of pulses used in the approximation increases, we first computed the field due to a z-directed rooftop current on a rectangular element on one of the corners of the $1\lambda \times 1\lambda$ plate, and the field due to the same current approximated by 14 pulses along the direction of current flow. Fig. 6 shows the difference between two fields. It should be noted that E_x arises entirely due to the $\nabla\Phi$ term, since $A_x=0$ for a z-directed current. One can easily see that the field component perpendicular

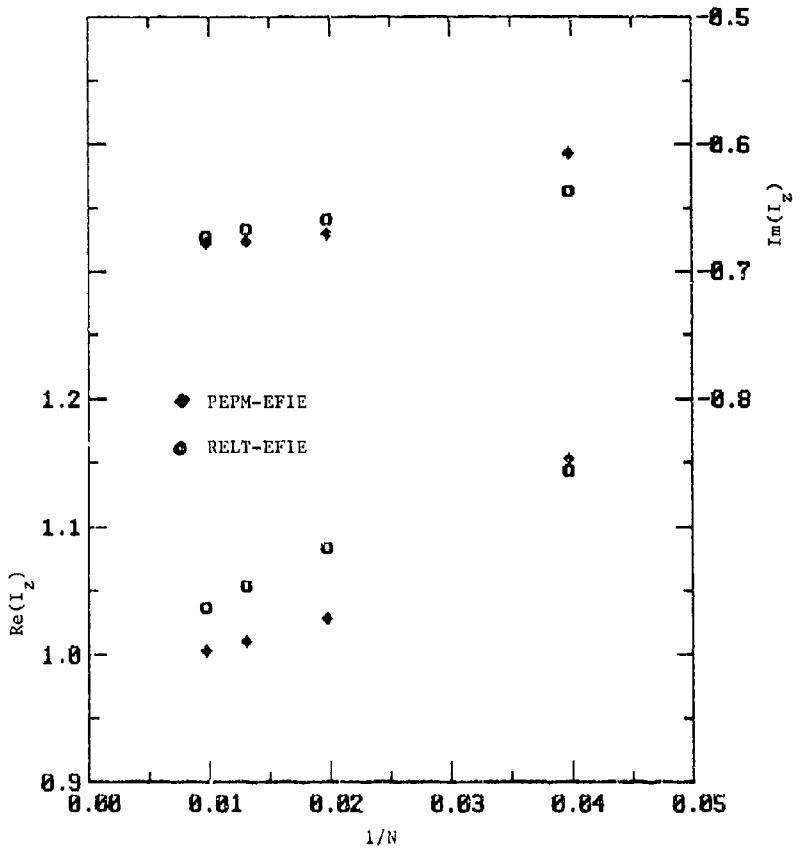

Figure 3. Convergence of the current induced on a 0.5λ long wire of radius 0.01λ.

to the current flow generated by the pulse-approximated current differs from that produced by the original continuous current and that the discrepancy is due to the impulse approximation to the charge density. For the field component parallel to the current flow, the pulse approximation of the current does not seem to cause a problem, which may be a clue to the success of the PEPM scheme for slender objects and in two-dimensional scattering problems.

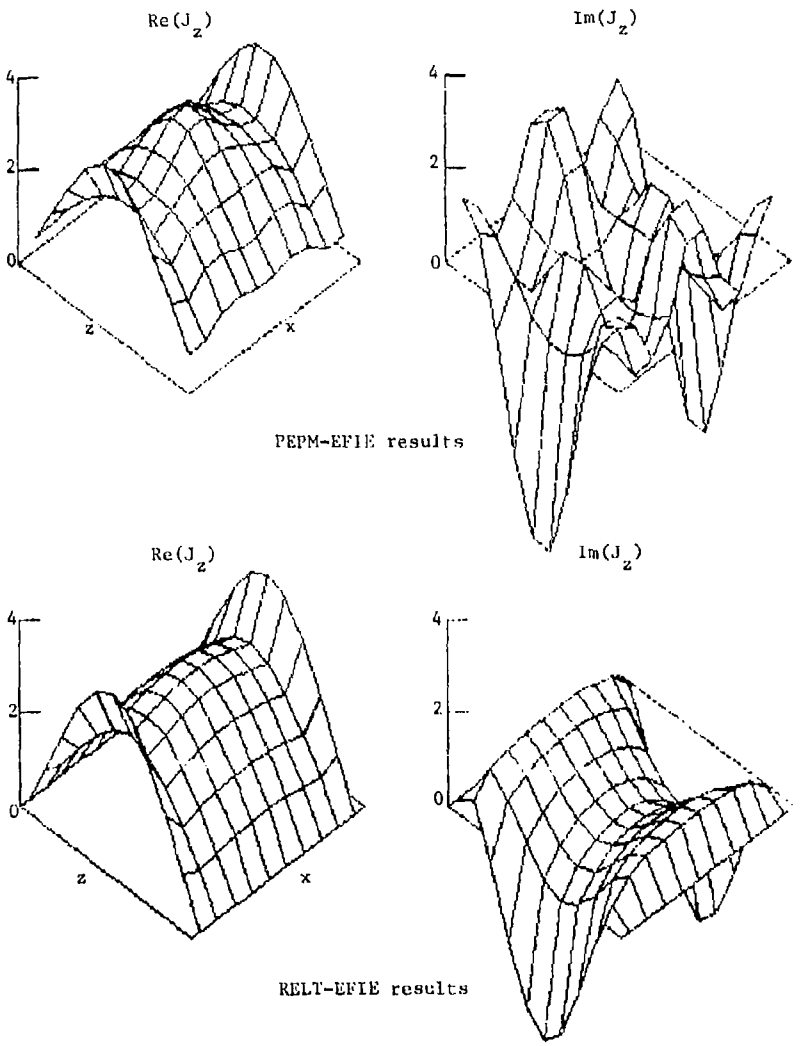

Figure 4. PEPM and RELT solutions for the dominant component of current induced on a 1λ by 1λ square plate excited by a normally incident plane wave.

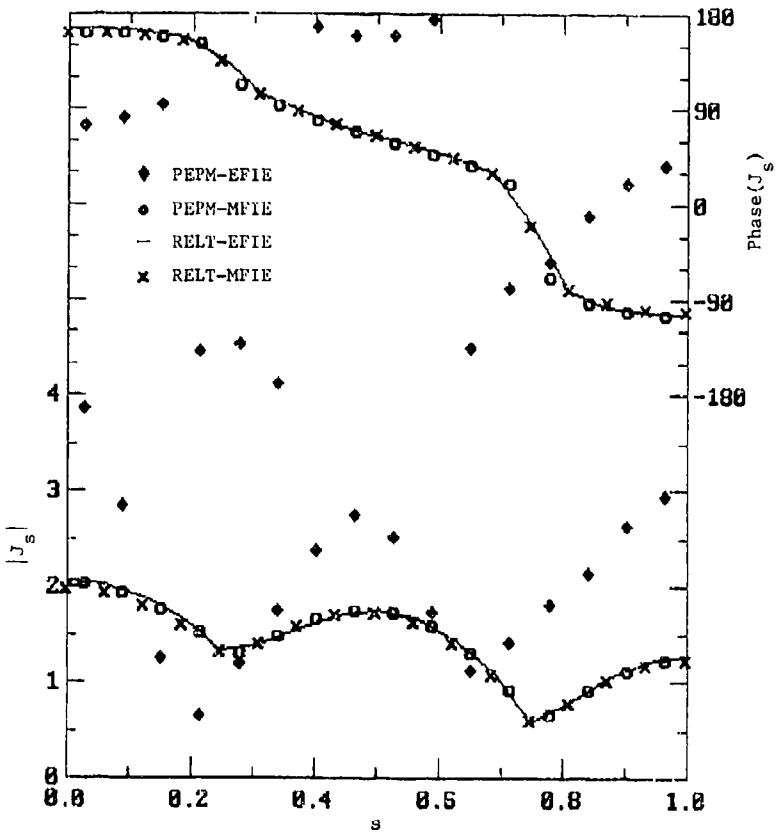

Figure 5. Comparison of solutions obtained by various approaches for the current induced on a 0.4λ wide cube.

IV. Summary

The use of a pulse expansion and point matching (PEPM) scheme in the electric field integral equation (EFIE) solution of three-dimensional, time-harmonic electromagnetic boundary-value problems has been studied. Problems of electromagnetic scattering by a few simple conducting bodies in free space have been considered and solutions obtained using the PEPM-

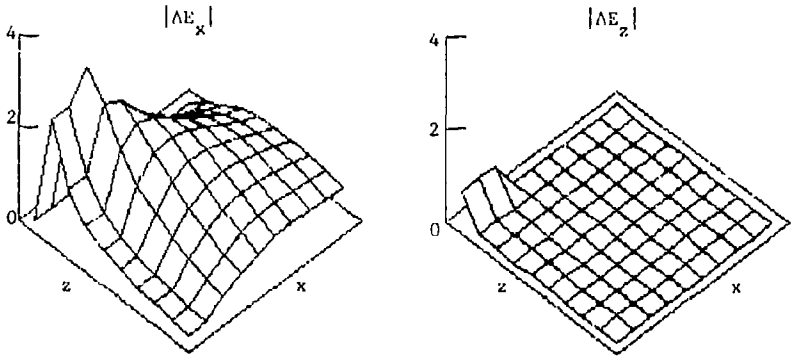

Figure 6. Plot of the difference between the field due to a rooftop current and that of the multiple-pulse-approximated rooftop current.

EFIE scheme have been compared with those obtained using rooftop expansion functions and a line testing procedure. The results indicate that the PEPM-EFIE scheme may not produce correct results for general three-dimensional geometries. An empirical explanation for the apparent failure of the PEPM-EFIE approach to EM scattering by arbitrarily shaped scatterers has been suggested by studying the near field of a known pulse-approximated current.

References

[1] A.W. Glisson and D.R. Wilton, "Simple and efficient numerical methods for problems of electromagnetic radiation and scattering from surfaces," *IEEE Trans. Antennas Propagat.*, Vol. AP-28, pp. 593-603, Sept. 1980.

[2] S.M. Rao, D.R. Wilton, and A.W. Glisson, "Electromagnetic scattering by surfaces of arbitrary shape," *IEEE Trans. Antennas Propagat.*, Vol. AP-30, pp. 409-418, May 1982.

[3] R.F. Harrington, *Field Computation by Moment Methods*. New York: MacMillan, 1968.

[4] A. W. Glisson and G. P. Junker, "A comparison of the dyadic Green's function approach and the mixed potential approach for the solution of surface integral equations," *IEEE Trans. Magnetics*, vol. MAG-25, pp. 3049-3051, July 1989.

[5] P. M. Goggans and T. H. Shumpert, "CFIE MM Solution for TE and TM Incidence on a 2-D conducting body with dielectric," *IEEE Trans. Antennas Propagat.*, Vol. AP-38, pp. 1645-1649, Oct. 1990.

[6] K. Mahadevan and H.A. Auda, "Electromagnetic field of a rectangular patch of uniform and linear distributions of current," *IEEE Trans. Antennas Propagat.*, Vol. AP-37, pp. 1503-1509, Dec. 1989.

[7] K. Mahadevan and H.A. Auda, "On the electromagnetic field of a rectangular patch of uniform and linear distributions of current in the source region," *IEEE Trans. Antennas Propagat.*, Vol. AP-38, pp. 1244-1248, Aug. 1990.

[8] J. R. Mautz and R. F. Harrington, "*H*-field, *E*-field, and combined-field solutions for conducting bodies of revolution," *AEÜ*, vol. 32, no. 4, pp. 157-164, Apr. 1978.

[9] T.K. Sarkar, E. Arvas, and S.M. Rao, "Application of FFT and the conjugate gradient method for the solution of electromagnetic radiation from electrically large and small conducting bodies," *IEEE Trans. Antennas Propagat.*, Vol. AP-34, pp. 635-640, May. 1986.

[10] T.J. Peters, and J.L. Volakis, "Application of a conjugate gradient FFT method to scattering from thin planar material plates," *IEEE Trans. Antennas Propagat.*, Vol. AP-36, pp. 518-526, Apr. 1988.

[11] M.F. Catedra, J.G. Cuevas, and L. Nuno, "A scheme to analyze conducting places of resonant size using the conjugate-gradient method and the fast Fourier transform," *IEEE Trans. Antennas Propagat.*, Vol. AP-36, pp. 1744-1752, Dec. 1988.

[12] W. Sun K.M. Chen, D.P. Nyquist, and E.J. Rothwell, "Determination of the natural modes for a rectangular plate," *IEEE Trans. Antennas Propagat.*, Vol. AP-38, pp. 643-652, May 1990.

[13] R. Kastner and N. Herscovici, "A concise conjugate gradient computation of plate problems with many excitations," *IEEE Trans. Antennas Propagat.*, Vol. AP-38, pp. 1239-1243, Aug. 1990.

Recursive Algorithms to Reduce the Computational Complexity of Scattering Problems

W. C. Chew, Y. M. Wang, L. Gurel, and J. H. Lin*

Abstract

It has been demonstrated recently that a recursive algorithm can reduce the computational complexity (of the full scattering solution of a scattering problem in two dimensions) to $O(N^2)$[5-10]. This is faster than the conjugate gradient method applied to the method of moments, and yet provides a scattering solution valid for all angles of incidence.

In this approach, a scatterer is divided into N subscatterers, and a recursive algorithm is used to construct the $n+n'$ subscatterer solution from the n subscatterer solution. Addition theorem is used to translate the field among the different coordinate systems of the subscatterers.

The algorithm has been applied to calculate scattering from a 10λ diameter object. Such an object requires about 12,000 unknowns to model, but it takes only about 30 secs on a CRAY-2 to solve with the fast recursive algorithm. It is estimated that it will take about 20 hours on the CRAY-2 to solve a similar problem with the method of moments.

We have also applied the algorithm to solve for scattering solutions from an array of metallic strips, and impenetrable scatterers. The solutions obtained are found to either agree well with closed form solutions, or solutions from the method of moments.

1. Introduction

A problem facing computational electromagnetics is the computational complexity of numerical methods used to solve for the scattering solution of a large inhomogeneous scatterer. The conventional method of moments requires a matrix inversion, and hence is of $O(N^3)$ complexity where N is the number of unknowns modeling the scatterer [1]. The conjugate gradient method can be used to reduce the computational complexity yielding an iterative algorithm with complexity $O(N^2P)$ where P is the number of steps in the iteration. However, the number of steps P required depends on the condition number of the matrix equation. For ill conditioned matrices, the method may not converge at all [2]. Fast Fourier transform method has also been used to exploit the convolutional nature of the scattering integral equation yielding a conjugate-gradient type algorithm with complexity $O(PN\log_2 N)$ [2,4]. However, conjugate gradient methods provide a solution for only one incident wave only at a time. The algorithm has to be restarted for each new incident wave.

Recently, we have developed a fast recursive algorithm using translation formulas [5-10]. The computational complexity of the fastest of such an al-

This work is supported by National Science Foundation under grant NSF ECS-85-25891, Office of Naval Research under grant N000-14-89-J1286. Computer time is partly provided by the National Center for Supercomputer Applications at the University of Illinois.

* Electromagnetics Laboratory, Department of Electrical and Computer Engineering, University of Illinois, Urbana, IL 6180.

gorithm is $O(N^2)$ where N is the number of unknowns used to model the problem. A program has been developed using this fast algorithm. Comparison with the method of moments shows that the fast algorithm is a lot more efficient. Moreover, the memory requirement of this algorithm is minimal. More importantly, this algorithm solves a $10\lambda \times 10\lambda$ scatterer with 12,000 unknowns in about 30 seconds on a CRAY-2. This time is much faster than that of solving a matrix equation with a similar number of unknowns. As opposed to the conjugate gradient method, the fast algorithm provides a full solution valid for an incident wave at all angles of incidence. We have also applied the algorithm to solve for scattering solutions from an array of metallic strips, and impenetrable scatterers. The solutions obtained are found to either agree well with closed form solutions, or solutions from the method of moments.

2. The Recursive Algorithm

In the fast recursive algorithm previously presented[5-10], an inhomogeneous scatterer is first divided into N subscatterers. The scattering solution from these N subscatterers is sought recursively so that the $(n+1)$-subscatterer solution is obtained from the n-subscatterer solution. The scattering by the subscatterers are expressed in terms of a transition matrix or $\overline{T}$ matrix. Furthermore, an aggregate $\overline{T}$ matrix is defined for the n subscatterers. Hence when the $(n+1)$-th subscatterer is added, only a two-body scattering problem need be considered. When the scattering solution is found for $(n+1)$ subscatterers, then an aggregate $\overline{T}$ matrix is defined for these scatterers. This procedure is repeated until all the N subscatterers are exhausted.

The previous algorithm works excellently for E_z polarized waves incident on an inhomogeneous cylinder. But for H_z polarized waves, the previously described algorithm is found not to work well because of the infraction of the addition theorem. As a generalization, instead of adding one subscatterer at each recursion, n' subscatterers could be added at each recursion when these n' subscatterers are equidistant from the origin (see Figure 1). By doing this, the infraction of the addition theorem could be avoided, and the resulting algorithm is found to work well even for H_z polarized waves. This generalized algorithm is described as follows.

Given n subscatterers, the total field could be written as (using the notation of references 5 to 10)

$$\phi(\mathbf{r}) = \Re g\psi^i(k_0, \mathbf{r}_0) \cdot \mathbf{a} + \psi^t(k_0, \mathbf{r}_0) \cdot \overline{\tau}_{(n)} \cdot \mathbf{a}. \tag{1}$$

When n' subscatterers are added to the previous n cluster, the total field could be written as

$$\phi(\mathbf{r}) = \Re g\psi^i(k_0, \mathbf{r}_0) \cdot \mathbf{a} + \psi^t(k_0, \mathbf{r}_0) \cdot \overline{\tau}_{n(n+n')} \cdot \mathbf{a} + \sum_{i=n+1}^{n+n'} \psi^t(k_0, \mathbf{r}_i) \cdot \overline{T}_{i(n+n')} \cdot \overline{\beta}_{io} \cdot \mathbf{a}, \tag{2}$$

where $\overline{\tau}_{n(n+n')}$ is the aggregate $\overline{T}$ matrix for n subscatterers in the presence of $n+n'$ subscatterers, and $\overline{T}_{i(n+n')}$ is the $(n+n')$-scatterer $\overline{T}$ matrix for the i-th subscatterer. The above constitutes a $n'+1$ unknown problem where the unknowns are $\overline{\tau}_{n(n+n')}$ and $\overline{T}_{i(n+n')}, i = n+1, \cdots, n+n'$. These $n'+1$ unknowns could be found as follows using the solution (1). First, we express the field from the n' subscatterers as incident field on the aggregated n subscatterers so that

$$\phi(\mathbf{r}) = \Re g\psi^t(k_0, \mathbf{r}_0) \cdot \mathbf{a} + \Re g\psi^t(k_0, \mathbf{r}_0) \cdot \sum_{i=n+1}^{n+n'} \overline{\alpha}_{oi} \cdot \overline{T}_{i(n+n')} \cdot \overline{\beta}_{io} \cdot \mathbf{a} + \psi^t(k_0, \mathbf{r}_0) \cdot \overline{\tau}_{n(n+n')}\mathbf{a}, \quad (3)$$

From Equation (1), we must have

$$\overline{\tau}_{n(n+n')} = \overline{\tau}_{(n)} \cdot \left(\overline{I} + \sum_{i=n+1}^{n+n'} \overline{\alpha}_{oi} \cdot \overline{T}_{i(n+n')} \cdot \overline{\beta}_{io} \right). \quad (4)$$

Next, we focus at the i-th subscatterer of the n' subscatterers and express the fields from all the other subscatterers as incident fields on the j-th subscatterer. By so doing, we have

$$\phi(\mathbf{r}) = \Re g\psi^t(k_0, \mathbf{r}_0) \cdot \overline{\beta}_{jo} \cdot \mathbf{a} + \Re g\psi^t(k_0, \mathbf{r}_j) \cdot \overline{\alpha}_{jo} \cdot \overline{\tau}_{n(n+n')} \cdot \mathbf{a} + \Re g\psi^t(k_0, \mathbf{r}_j) \cdot \sum_{i \neq j} \overline{\alpha}_{ji} \cdot \overline{T}_{i(n+n')} \overline{\beta}_{io} \cdot \mathbf{a} + \psi^t(k_0, \mathbf{r}_j) \cdot \overline{T}_{j(n+n')} \cdot \overline{\beta}_{jo} \cdot \mathbf{a}, \quad (5)$$

where the summation for $i \neq j$ is for $i = n+1, \cdots, n+n'$, for $i \neq j$. The scattered field off the j-th subscatterer must be related to the incident field via the isolated scatterer $\overline{T}$ matrix for the j-th subscatterer. Consequently, we have

$$\overline{T}_{j(n+n')} \cdot \overline{\beta}_{jo} = \overline{T}_{j(1)} \cdot \left(\overline{\beta}_{jo} + \overline{\alpha}_{jo} \cdot \overline{\tau}_{n(n+n')} + \sum_{i \neq j} \overline{\alpha}_{ji} \cdot \overline{\tau}_{n(n+n')} \cdot \overline{\beta}_{io} \right), \quad j = n+1, \cdots, n+n'. \quad (6)$$

Equation (4) can be used to substitute for $\overline{\tau}_{n(n+n')}$ in (6) to yield

$$\overline{T}_{j(n+n')} \cdot \overline{\beta}_{jo} = \overline{T}_{j(1)} \cdot \left[\overline{\beta}_{jo} + \overline{\alpha}_{jo} \cdot \overline{\tau}_{(n)} \cdot \left(\overline{I} + \sum_{i=n+1}^{n+n'} \overline{\alpha}_{oi} \cdot \overline{T}_{i(n+n')} \cdot \overline{\beta}_{io} \right) + \sum_{i \neq j} \overline{\alpha}_{ji} \cdot \overline{T}_{i(n+n')} \cdot \overline{\beta}_{io} \right], \quad j = n+1, \cdots, n+n'. \quad (7)$$

The above could be rearranged to yield

$$\overline{\boldsymbol{D}}_j \cdot \overline{\boldsymbol{T}}_{j(n+n')} \cdot \overline{\boldsymbol{\beta}}_{jo} = \overline{\boldsymbol{T}}_{j(1)} \cdot [\overline{\boldsymbol{\beta}}_{jo} + \overline{\boldsymbol{\alpha}}_{jo} \cdot \overline{\boldsymbol{\tau}}_{(n)} + \sum_{i \neq j} (\overline{\boldsymbol{\alpha}}_{jo} \cdot \overline{\boldsymbol{\tau}}_{(n)} \cdot \overline{\boldsymbol{\alpha}}_{oi} + \overline{\boldsymbol{\alpha}}_{ji}) \cdot \overline{\boldsymbol{T}}_{i(n+n')} \cdot \overline{\boldsymbol{\beta}}_{io}],$$

$$j = n+1, \cdots, n+n', \quad (8)$$

where $\overline{\boldsymbol{D}}_j = [\overline{\boldsymbol{I}} - \overline{\boldsymbol{T}}_{j(1)} \cdot \overline{\boldsymbol{\alpha}}_{jo} \cdot \overline{\boldsymbol{\tau}}_{(n)} \cdot \overline{\boldsymbol{\alpha}}_{oj}]$. The above constitutes n' equations for the n' unknows $\overline{\boldsymbol{T}}_{i(n+n')} \cdot \overline{\boldsymbol{\beta}}_{io}$. It can be written more succinctly as

$$\sum_{i=n+1}^{n+n'} \overline{\boldsymbol{A}}_{ji} \cdot \overline{\boldsymbol{T}}_{i(n+n')} \cdot \overline{\boldsymbol{\beta}}_{io} = -\overline{\boldsymbol{T}}_{j(1)} \cdot [\overline{\boldsymbol{\beta}}_{jo} + \overline{\boldsymbol{\alpha}}_{jo} \cdot \overline{\boldsymbol{\tau}}_{(n)}], \quad j = n+1, \cdots, n+n', \quad (9)$$

where

$$\overline{\boldsymbol{A}}_{ji} = \begin{cases} -\overline{\boldsymbol{D}}_j, & i = j, \\ \overline{\boldsymbol{T}}_{j(1)} \cdot \overline{\boldsymbol{\alpha}}_{jo} \cdot \overline{\boldsymbol{\tau}}_{(n)} \cdot \overline{\boldsymbol{\alpha}}_{oi} + \overline{\boldsymbol{T}}_{j(1)} \cdot \overline{\boldsymbol{\alpha}}_{ji}, & i \neq j. \end{cases} \quad (9a)$$

After having solved (9) for $\overline{\boldsymbol{T}}_{i(n+n')} \cdot \overline{\boldsymbol{\beta}}_{io}$, (4) could be used to find $\overline{\boldsymbol{\tau}}_{n(n+n')}$. Alternatively, (4) could be written as

$$\overline{\boldsymbol{\tau}}_{n(n+n')} = \overline{\boldsymbol{\tau}}_{(n)} + \sum_{i=n+1}^{n+n'} \overline{\boldsymbol{\tau}}_{(n)} \cdot \overline{\boldsymbol{\alpha}}_{oi} \cdot \overline{\boldsymbol{T}}_{i(n+n')} \cdot \overline{\boldsymbol{\beta}}_{io} \quad (11)$$

for more efficient computation.

When all the unknows in the $n+n'$ subscatterer problem is solved, then an aggregate $\overline{\boldsymbol{T}}$ matrix for $n+n'$ subscatterers can be defined as

$$\overline{\boldsymbol{\tau}}_{(n+n')} = \overline{\boldsymbol{\tau}}_{n(n+n')} + \sum_{i=n+1}^{n+n'} \overline{\boldsymbol{\beta}}_{oi} \cdot \overline{\boldsymbol{T}}_{i(n+n')} \cdot \overline{\boldsymbol{\beta}}_{io}. \quad (12)$$

Consequently, (11) could be substituted into (12) to yield

$$\overline{\boldsymbol{\tau}}_{(n+n')} = \overline{\boldsymbol{\tau}}_{(n)} + \sum_{i=n+1}^{n+n'} (\overline{\boldsymbol{\beta}}_{oi} + \overline{\boldsymbol{\tau}}_{(n)} \cdot \overline{\boldsymbol{\alpha}}_{oi}) \cdot \overline{\boldsymbol{T}}_{i(n+n')} \cdot \overline{\boldsymbol{\beta}}_{io} \quad (13)$$

Equations (9) and (13) permit us to find the $(n+n')$-subscatterer solution from the n-subscatterer solution. These equations could be used recursively to find the N subscatterer solution from a 0 subscatterer solution. The computational complexity of the above algorithm could be analyzed, and it is found that the computer time will grow as N^2 in two-dimensions, and as $N^{7/3}$ in three dimensions. When $n' = 1$ in the preceding algorithm, the above algorithm reduces to reduces to the algorithm described in [8,9]*.

* The computational complexity for three dimensional problem given in [9] is incorrect. It should also be $N^{7/3}$.

3. Numerical Simulation

A computer program has been developed using this recursive algorithm for computing the wave scattering solution of a large inhomogeneous object in two dimensions for both E_z and H_z polarized waves. This method gives the same solution as the method of moments for small scatterers of one or two wavelength in size. Hence, we have used the method of moments to validate the code for a general inhomogeneous scatterer. But for large scatterers, the method of moments is extremely inefficient due to its N^3 complexity.

The code has been used to calculate the scattering solution from a large cylinder which is about $10\lambda \times 10\lambda$, and comprising about 12,000 unknowns. Since the method of moments is extremely inefficient in this regime, we can only validate our solution by comparing it with the closed form solution of a circular, homogeneous cylinder, which is solvable by harmonic expansions.

In Figure 2(a), we show the comparison of the amplitude of the solution of scattering by an E_z polarized wave using the recursive algorithm and the closed form solution. In this case, n' need only be 1. As can be seen, the agreement is excellent.

In Figure 2(b), we show the comparison of the phase of the solution by recursive algorithm versus the closed form solution. We observe excellent agreements except for some angles of observation. However, for such a wavelength, note that if the diameter of the object is changed by 0.5%, a phase error of about 9^0 is possible, and hence, the phase solution is very sensitive to the size of the object.

In order to use the recursive algorithm, the subscatterers have to be ordered so that they are of increasing distance from the origin [7,8,9]. We have used the heapsort algorithm [11,12] to order the subscatterers with computer time proportional to $N \log_2 N$. If a naive sorting algorithm of $O(N^2)$ complexity is used, the sorting time could constitute as much as 40% of the total computer time.

On a CRAY-2 supercomputer, the 12,000 unknown problem is solved in about 30 seconds. In this simulation, we pick $M = 1$, and $P = 30$. The reason we have chosen $M = 1$ is because only the monopole term is important for the scattering from each subscatterer. Though the CRAY-2 has a peak performance of about 1.7 GFLOPS, this peak is in general not attainable for practical applications. For instance, for a simple fully vectorizable "DO" loop, the throughput of the CRAY-2 is about 100 MFLOPS unless special programming technique is used [13]. In general, the throughput is about 20 to 40 MFLOPS. Assuming a 30 MFLOPS throughput, and that it takes $N^3/3$ floating operations to invert an $N \times N$ matrix, and multiplying by a factor of 4 for complex floating point operations, we estimate that it will take about 20 hours to solve this problem by the method of moments. Figure 3 shows the comparison of the computer time of this method versus the number of unkowns on a CRAY-2 supercomputer. The 12,000-unknown point for the method of moments is extrapolated since it is too expensive to solve this problem by such a method.

In this program, the isolated scatterer $\overline{T}$ matrix and the translation formulas are calculated as they are needed. Hence, the dominant part of the memory is used to store the grid which is proportional to the number of unknowns N, whereas a matrix method like MOM would have required storage proportional to N^2.

Table I shows the breakdown of the computer time spent in various parts of the computer program. It is seen that about 16% of the time is spent in reading in the input for the program. This could be sped up by using binary data files for instance. Note that the memory used is about 0.385 MWord. A full matrix method as in the method of moments would have needed 290 MWords of memory.

In Figures 4(a) and 4(b), we show the comparison of the solution of scattering of H_z polarized waves by a circular dielectric cylinder using the recursive algorithm using method of moments, recursive algorithm, and analytic solution. As can be seen, the agreement between the method of moments and recursive algorithm is excellent while there is a small discrepancy with the analytic solution. The discrepancies come from imperfect modeling as the circular cylinder is divided into subscatterers which are squares. The resulting cylinder does not have the same surface area as the circular cylinder, even though they have the same cross sectional area. Since in the H_z polarized wave, the electric field polarizes surface charges on the surface of the cylinder, the discrepant surface area could give rise to the small error.

In Figures 5(a) and 5(b), we show the RCS of metallic strips for the E_z and H_z polarized waves respectively using such a recursive algorithm. The $\overline{T}$ matrices of the individual strips are found using the method of moments.

In Figures 6(a) and 6(b), we show the comparison of the scattering from an impenetrable metallic scatterer for the E_z polarized wave using the recursive algorithm. The metallic wall is modeled as z-directed wires tightly packed together. The case compared is a circular metallic cylinder where closed form solution exists.

IV. Conclusions

An efficient method for solving for the solution of wave scattering from a large scatterer has been developed. This method uses a minimal of computer memory, and is a lot more efficient than a full integral equation solver. Moreover, it provides a full scattering solution valid for all angles of incident. This method has been used to solve a $10\lambda \times 10\lambda$ problem with about 12,000 unknowns, in about 30 seconds on a CRAY-2 supercomputer with a typical throughput of about 30 MFLOPS. We have also applied the algorithm to H_z polarized waves showing excellent agreement with the method of moments. The algorithm could also be applied to scattering by an array of metallic strips, or impenetrable scatterers.

The method is faster than the method of moments applied to solving integral equations, and unlike the finite element method, it provides a solution that naturally satisfies the radiation condition at infinity. Moreover, the

subscatterers need not have to be close together: it works both for densely packed as well as sparsely packed subscatterers.

References

[1] R. Harrington, *Field Computation by Moment Method*, Malabar, FL, 1983.

[2] D. T. Borup, D. M. Sullivan, and O. P. Gandhi, "Comparison of two FFT conjugate gradient method and the finite-difference time-domain method for the 2-d absorption problem," *IEEE Trans. Microwave Theory Tech.*, vol. MTT-35, no. 4, pp. 383-395, April, 1987.

[3] C. C. Su, "Calculation of electromagnetic scattering from a dialectric cylinder using the conjugate gradient method and FFT," *IEEE Trans. Antennas Propag.*, vol. AP-35, no. 12, pp. 1418-1425, December, 1987.

[4] C. Y. Shen, K. J. Glover, M. I. Sancer, and A. D. Varvatsis, "The discrete Fourier transform method of solving differential-integral equations in scattering theory," *IEEE Trans. Ant. Propag.*, vol. AP-37, no. 8, pp. 1032-1041, August, 1989.

[5] W. C. Chew, "An N^2 algorithm for the multiple scattering solution of N scatterers," *Micro. Optical Tech. Letter*, vol. 2, no. 11, pp. 380-383, 1989.

[6] W. C. Chew, J. Friedrich, and R. Geiger, "A multiple scattering solution for the effective permittivity of a sphere mixture," *IEEE Geoscience and Remote Sensing*, vol. 28, no. 2, p. 207, 1990.

[7] Y. M. Wang and W. C. Chew, "An efficient algorithm for solution of a scattering problem," *Micro. Opt. Tech. Lett.*, vol. 3, no. 3, pp. 102-106, March, 1990.

[8] W. C. Chew and Y. M. Wang, "A fast algorithm for solution of a scattering problem using a recursive aggregate tau matrix method," *Microwave Optical Technology Letters*, vol. 3, no. 5, pp. 164-169, May 1990.

[9] W. C. Chew, *Waves and Fields in Inhomogeneous Media*, Van Nostrand Reinhold, New York, 1990.

[10] Y. M. Wang and W. C. Chew, "Application of the fast recursive algorithm to a large inhomogeneous scatterer for TM polarization," Micro. Opt. Tech. Lett., vol. 4, no. 3, March 1991.

[11] D. E. Knuth, *Sorting and Searching: The Art of Computer Programing*, vol. 3, Addison-Wesley, Reading, Mass, 1973.

[12] W. H. Press, B. P. Flannery, S. A. Teukolsky and W. T. Vetterling, *Numerical Recipes: The Art of Scientific Computing*, Cambridge University Press, New York, 1986.

[13] I. Dilber, "Matrix multiplication benchmarks on the CRAY-2 system," *Datalink* (NCSA, Univ. Illinois, Urbana-Champaign), vol. 4, no-5, pp. 15-18, May-June, 1990.

Table I. Breakdown of the CPU time spent for the 12,000 unknown problem using the fast recursive algorithm.

	Percentage of The Total CPU	CPU Time (second)	Times Been Called
Recursive Part	44.928	14.327	1
Translation Matrices	19.928	6.355	11,905
Input Data	16.176	5.158	1
Bessel Functions	16.013	5.106	35,862
$T_{\theta(1)}$ Matrices	2.062	0.657	11,905
Sorting	0.606	0.193	1
Main Program	0.287	0.092	1

Total CPU = 31.888 second
Total Memory = 0.385 MWord

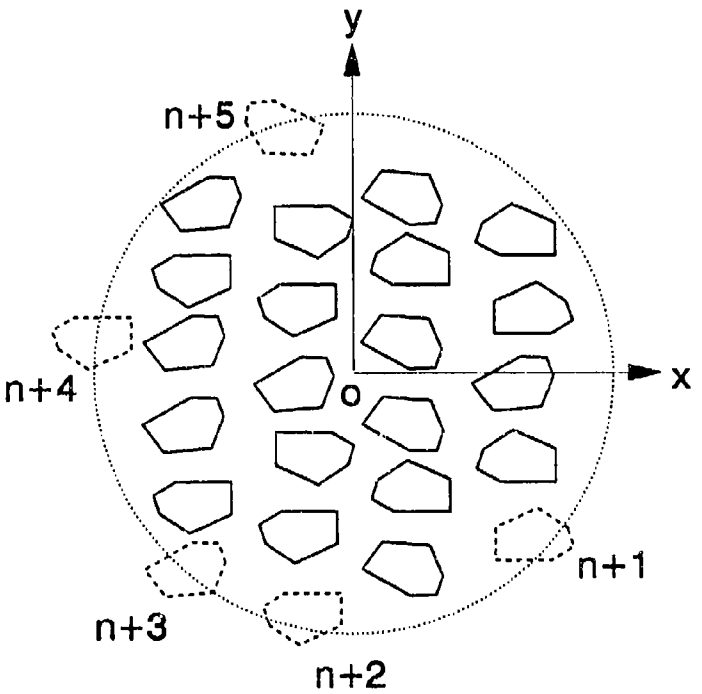

Figure 1. In the recursive algorithm, n-subscatterers solution is used to find the $n + n'$-subscatterer solution, where n' is the number of subscatterers equidistant from the origin. In this figure, $n' = 5$.

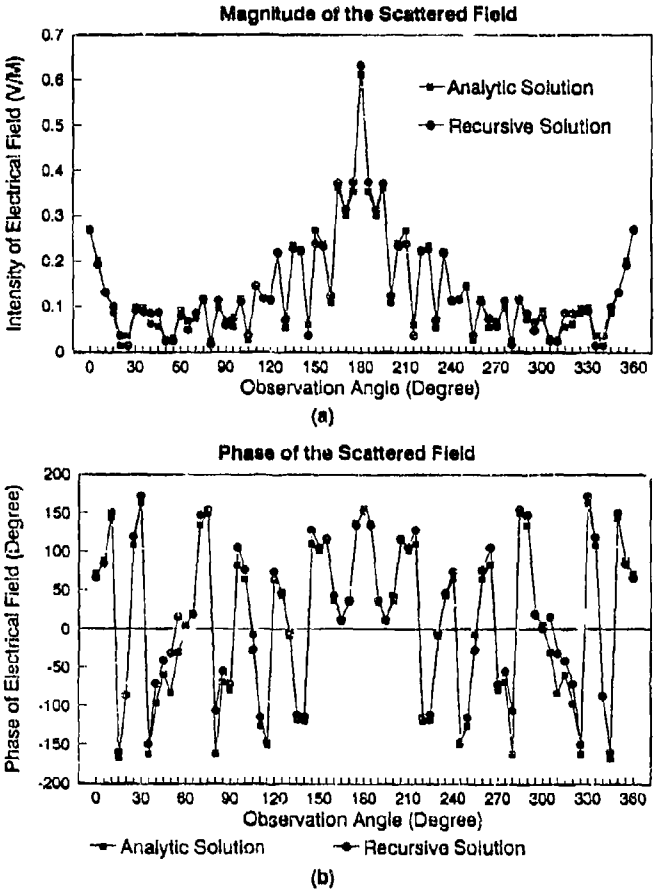

Figure 2. A 10λ diameter dielectric cylinder is solved with this recursive algorithm for an E_z polarized incident plane wave. In (a), a comparison of the field amplitude of the scattered field is made with analytic solution. In (b) a comparison is made of the phase. The dielectric cylinder is 2.6 meters in diameter with a relative permittivity of 4. The incident field is from 0° with a frequency of 300 MHz. The fields are measured 50 meters from the center of the cylinder.

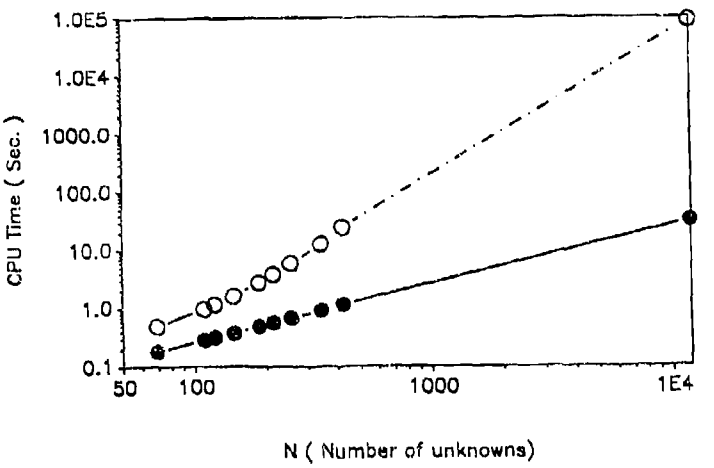

Figure 3. Comparison of the computer time as a function of the number of unknowns for the method of moments (open circles) and fast recursive algorithm (solid circles). At 12,000 unknowns, the method of moments is estimated to take 20 hours of CRAY-2 CPU time while the fast recursive algorithm takes only about 30 seconds of CRAY-2 CPU time.

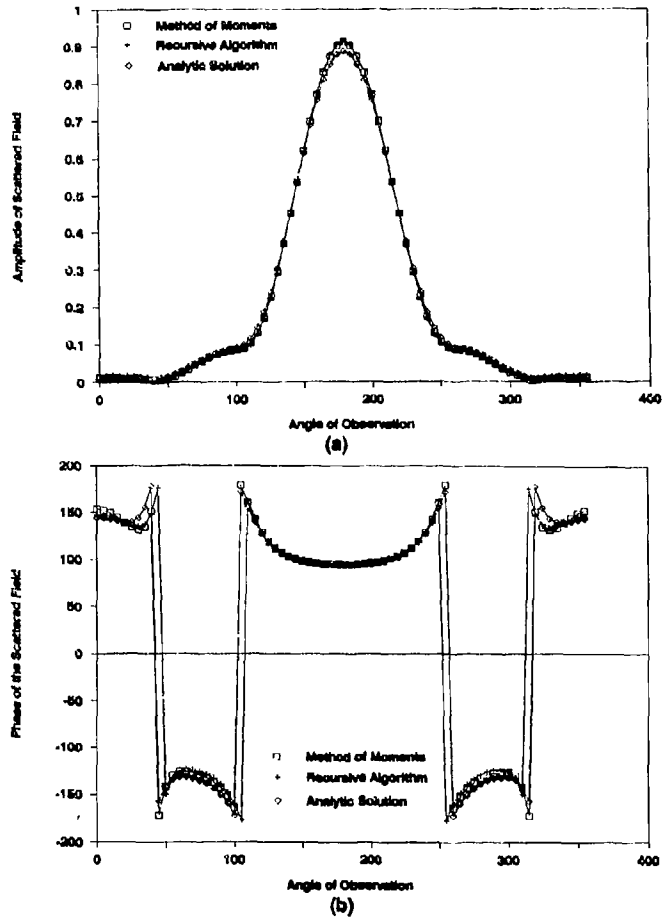

Figure 4. Scattering of H_z polarized incident plane wave using the fast recursive algorithm, the method of moments, and analytic solution. (a) compares the amplitude while (b) compares the phase. The frequency of the incident wave is 600 MHz. The dielectric cylinder has a diameter of 0.4 meters with a relative permittivity of 2. The field is measured at 1 meter from the center of the cylinder.

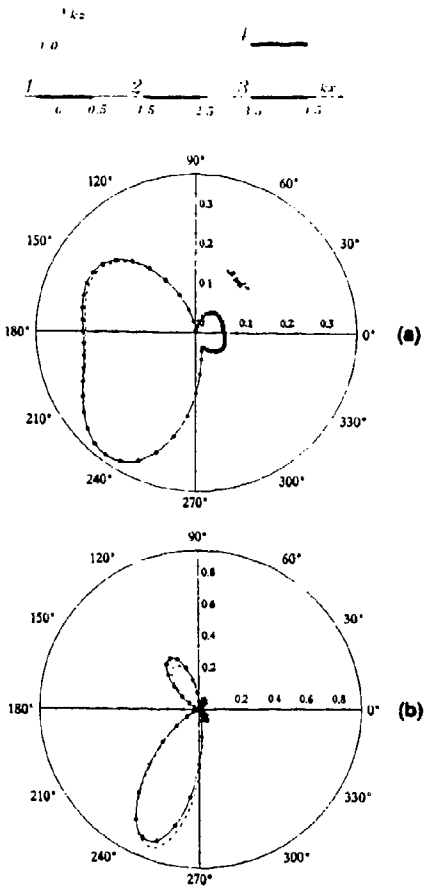

Figure 5. Comparison of the RCS of an array of strips computed using the generalized recursive algorithm (solid dots), method of moments (solid lines) and the recursive algorithm presented in references 7 (dotted lines). (a) is for E_z polarized wave while (b) is for H_z polarized wave. The error of using the old algorithm is larger for H_z polarized wave.

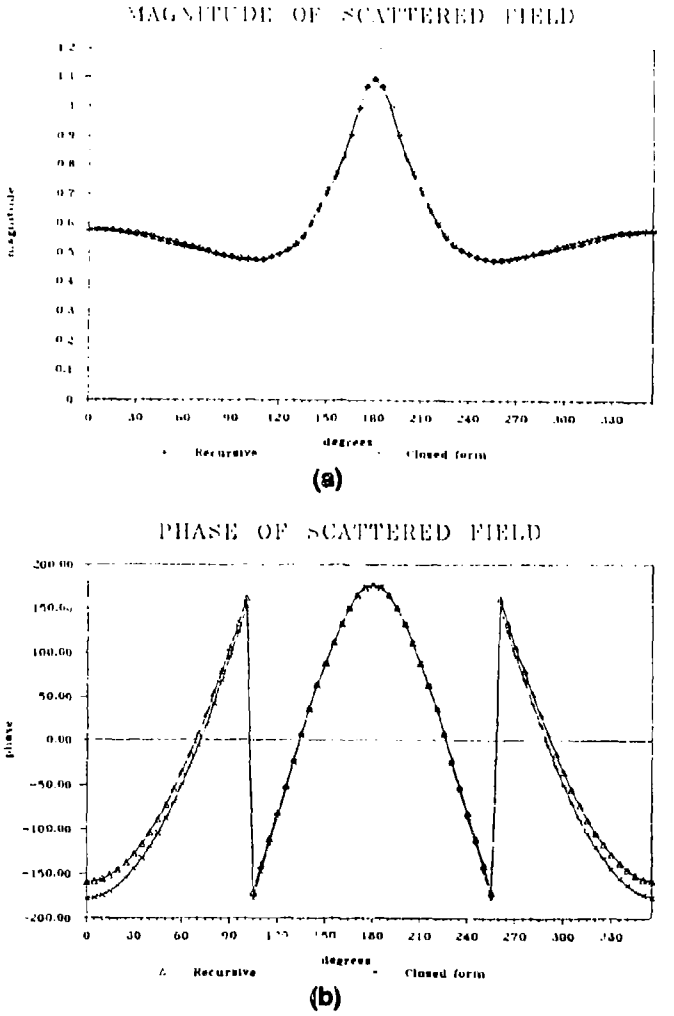

Figure 6. Comparison of the scattered field from a circular metallic cylinder using the recursive algorithm and the closed form solution. (a) is the case for the scattered field amplitude while (b) is the case for the scattered field phase.

Numerical Solution of the EFIE Using Arbitrarily-Shaped Quadrangular and Triangular Elements

T. Mader, H. Singer
Technical University Hamburg-Harburg
Hamburg, Germany

Abstract

For the numerical solution of the EFIE by the method of moments plane triangular patches are widely used because every three-dimensional structure can be approximated by plane triangles. In most cases the more convenient way of surface discretization is to compose the considered structure of quadrangular patches. If only basis function formulae for triangles are available, the quadrangles must be subdivided into triangles. Then the total number of elements increases and also the number of unknown currents. In general this splitting into triangles can be avoided only if nonplanar quadrangular patches of arbitrary shape are applied.

The goal of the paper is to present current basis functions suited for arbitrarily-shaped nonplanar quadrangular patches in parametric form. These basis functions can be combined with the commonly-used basis function [5] for plane triangles. Furthermore, it is shown how to extend the basis functions for plane triangles to any curved triangles given in a parametric formulation. Finally it is demonstrated that the developed basis functions can be used to perform the connection between wire-grid segments and surface patches.

Introduction

With the ever increasing computer power the application of the method of moments in electromagnetic field prediction became possible not only for thin-wire arrangements, but also for the treatment of arbitrarily-shaped three-dimensional bodies. At the beginning of the development the MFIE was used to handle thick-body problems, and for thin-wire structures the EFIE [2] was prefered. The combination between thin-wire structures and thick-body structures became possible with the introduction of a special basis function valid for the connection area [1].

The disadvantage concerning the MFIE is that it is only valid for closed bodies. In order to treat thin-shelled, open structures the researchers tried to apply the EFIE to this problem. Difficulties were arising, because the EFIE contains not only the unknown surface current itself, but also its first derivation. Therefore it is not sufficient to assume a uniform current distribution over a surface patch, as it is possible in the MFIE solution.

Special linear basis functions for plane rectangles, the so-called roof-top functions, were introduced by Glisson [3]. The resulting charge distribution is uniform over the whole surface patch, and it is assured that no point or line charges can occur. The important feature of this basis function is that it contains the possibility of zero surface

charge on the whole patch. This is necessary in the low frequency range, because there the current distribution must be solenoidal.

For the calculation of arbitrarily-shaped metallic bodies Rao [5] has devised a current basis function suited to plane triangular patches. Similar to the functions of Glisson [3], the current distribution is linear and the resulting charge is uniform all over the patch. But because of the reasons mentioned above, it is useful to have a further basis function valid for arbitrarily-shaped quadrangles. In the following it will be shown in which way the functions of Glisson and Rao can be enhanced so that they match to nonplanar, arbitrarily-shaped quadrangles or triangles.

A Short Review of the Basic Equations

For a better understanding of the paper at first a very short summary of the basic principles will be given. The EFIE, as it is applied here, has the following form:

$$\vec{E}_s = \int_S \left[\frac{-j\omega\mu}{4\pi} \vec{I} \frac{e^{-jkR}}{R} - \frac{j}{4\pi\omega\varepsilon} \operatorname{div} \vec{I} \operatorname{grad} \frac{e^{-jkR}}{R} \right] dS \,. \tag{1}$$

S = surface of the conducting bodies (including wires),
$\vec{I}$ = surface current or wire current, respectively,
R = distance between the field and the source points.

Eq. (1) represents the electric field produced by the currents induced on the structure. The total field is given by the addition of the incident field and the scattered field given in (1). For perfect conducting bodies, the tangential component of the total electric field must be zero all over the body. This condition is enforced here by using Galerkin's method with razor-blade functions as weighting functions. This results in the following equation for one matching section:

$$\int_S \vec{E}_s d\vec{s} = \int_S \vec{E}_{inc} d\vec{s} = U_{inc} \tag{2}$$

with $\vec{E}_s$ due to Eq. (1). The numerical evaluation of (2) leads to

$$U_{inc} = \int_S \left(\frac{-j\omega\mu}{4\pi} \cdot 0.5 \cdot (\vec{s}_2 - \vec{s}_1) \cdot \vec{I} \cdot [\, G(R_2) + G(R_1) \,] + \frac{j}{4\pi\omega\varepsilon} \cdot \operatorname{div} \vec{I} \cdot [\, G(R_2) - G(R_1) \,] \right) dS \tag{3}$$

with $G(R) = \frac{e^{-jkR}}{R}$.

The meaning of the indices is indicated in Fig. 1.

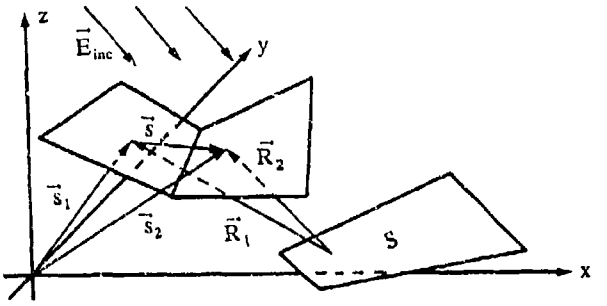

Fig. 1: Geometry concerning eq. (3)

As it can be seen in eq. (3), the line integral (2) of the first part of (1) is calculated by means of a 2-point trapezoidal rule, whereas for the second part, the integral is given exactly because of the grad operator. The fact that the second part can be integrated exactly is very important in the low frequency case, because this part is weighted by the factor $1/\omega$ and so gets very high values. But forming the line integral (2) around a closed path, that means to add certain equations in the eventually resulting equation system, the integral over the second part of (1) drops completely. Such an integration path is indicated in Fig. 2.

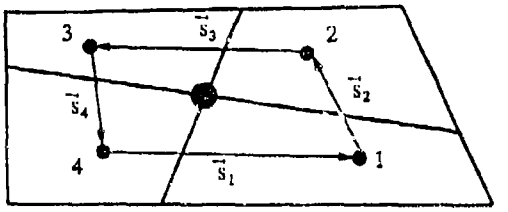

Fig. 2: Integration around a node of the structure

The addition of eq. (3) for a path due to Fig. 2 leads to the following equation for the nodes i = 1, ... 4:

$$U_{ind} = \sum_{i=1}^{4} \int_S \frac{-j\omega\mu}{4\pi} \cdot 0.5 \cdot (\vec{s}_{i+1} - \vec{s}_i) \cdot \vec{I} \cdot [\, G(R_{i+1}) + G(R_i) \,]\ dS\ ;$$

$$U_{ind} = \sum_{i=1}^{4} U_{inc,i}\ . \qquad (4)$$

Regarding eq. (4) more closely one can conclude that (4) means the line integral of the vector potential around a closed path, and thus eq. (4) represents also the surface integral of the magnetic induction, and so we have the law of induction due to

$$U_{ind} = j\omega \cdot \int_k \vec{A}\, d\vec{s} = j\omega \cdot \int_S \vec{B}\, d\vec{S} \qquad \text{with} \qquad \vec{B} = \text{curl}\,(\vec{A})\,. \tag{5}$$

Eq. (4) proves directly that the EFIE (1) contains the stationary case, but in this case the current must be solenoidal. Therefore it is necessary that the choosen basis functions allow a resulting current distribution without sources. Eq. (4) together with the basis functions described in the following section and the condition $\text{div}(\vec{I})=0$ can be used for the calculation of stationary eddy currents.

Current Basis Functions for Quadrangles

The current basis function that will be developed in this section shall be valid for every arbitrary quadrangle given in a parametric form according to

$$\vec{v} = \vec{v}(\eta,\xi)\,. \tag{6}$$

With such a parametric transformation any quadrangle given in the x,y,z coordinate system can be converted into a rectangle in the η,ξ system. Because of the high regularity of the obtained patch it is now easy to define a basis function. The position of the quadrangle in the η,ξ system and the choosen basis function are depicted in Fig. 3.

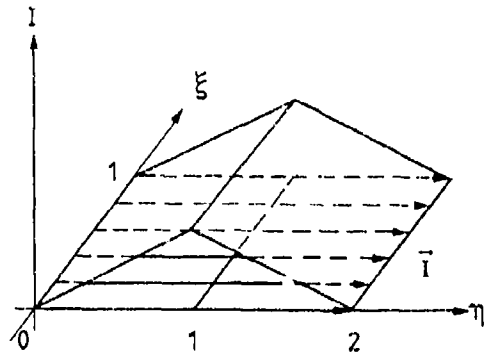

Fig. 3: Roof-top basis function in the η,ξ system

The essential step in the development of a current basis function is now to find a suitable transformation of the current vectors into the three-dimensional x,y,z coordinate system. After this task has been done, one finds for the left part of the roof-top according to Fig. 3:

$$\vec{I} = \frac{\vec{a}_\eta}{|\vec{a}_\eta \times \vec{a}_\xi|} \cdot \eta \cdot I_0 \tag{7}$$

with the metric coefficients

$$\vec{a}_\eta = \frac{\partial \vec{v}}{\partial \eta} \qquad \text{and} \qquad \vec{a}_\xi = \frac{\partial \vec{v}}{\partial \xi}$$

The reason for the vector product in (6) becomes quite clear by forming the divergence of the current. The divergence operator for general, non rectangular coordinates is given by [6]

$$\operatorname{div} \vec{f} = \frac{1}{|\vec{a}_\eta \times \vec{a}_\xi|} \cdot \left[\frac{\partial}{\partial \eta} \left(|\vec{a}_\eta \times \vec{a}_\xi| \cdot f_\eta(\eta,\xi) \right) + \frac{\partial}{\partial \xi} \left(|\vec{a}_\eta \times \vec{a}_\xi| \cdot f_\xi(\eta,\xi) \right) \right]$$

$$\text{with} \quad \vec{f} = f_\eta(\eta,\xi) \cdot \vec{a}_\eta + f_\xi(\eta,\xi) \cdot \vec{a}_\xi \; . \tag{8}$$

Eq. (8) applied to eq. (7) leads to

$$\operatorname{div} \vec{I} = \frac{I_0}{|\vec{a}_\eta \times \vec{a}_\xi|} \; . \tag{9}$$

The resulting current distribution on any patch is described by the superposition of 4 basis functions similar to eq. (7). Each of these 4 functions is associated with one edge of the quadrangle, and their charge distribution is given by eq. (9) with 4 different factors I_0. Thus the charge distribution is characterized by the addition of these 4 factors, and in the stationary case the sum of these factors tends to 0.

To assure that the current causes no line charge along the connection edge between two quadrangles, it is necessary to investigate the normal component along this edge. According to Fig. 4, for the normal component of the current the following formula can be derived:

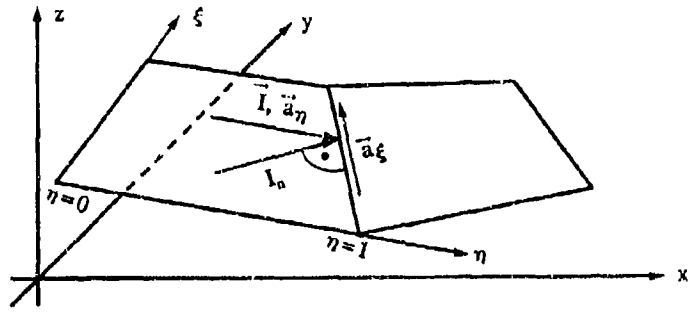

Fig. 4: Calculation of the normal component of the current along the connection edge of two quadrangles

$$I_n = \left| \frac{\vec{a}_\eta}{|\vec{a}_\eta \times \vec{a}_\xi|} \times \frac{\vec{a}_\xi}{|\vec{a}_\xi|} \right| = \frac{1}{|\vec{a}_\xi|} \; . \tag{10}$$

Because $\vec{a}_\xi$ depends only on parameters associated with the common edge it is obvious that the transition of the normal component is continuous along this edge.

In this paper, quadrangle patches are characterized by the following equations:

$$\vec{v} = \vec{v}_1 + (\vec{v}_2 - \vec{v}_1)\cdot\eta + (\vec{v}_4 - \vec{v}_1)\cdot\xi + (\vec{v}_1 - \vec{v}_2 + \vec{v}_3 - \vec{v}_4)\cdot\eta\xi \quad ; \tag{11}$$

$$\vec{a}_\eta = \frac{\partial\vec{v}}{\partial\eta} = \vec{v}_2 - \vec{v}_1 + (\vec{v}_1 - \vec{v}_2 + \vec{v}_3 - \vec{v}_4)\cdot\xi \quad ; \tag{12}$$

$$\vec{a}_\xi = \frac{\partial\vec{v}}{\partial\xi} = \vec{v}_4 - \vec{v}_1 + (\vec{v}_1 - \vec{v}_2 + \vec{v}_3 - \vec{v}_4)\cdot\eta \quad . \tag{13}$$

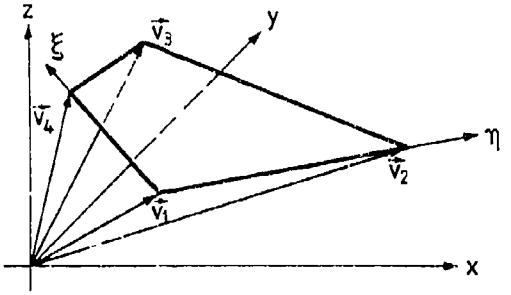

Fig. 5: Geometry of a quadrangular patch

As can be seen from eq. (13), $\vec{a}_\xi$ is constant for $\eta = 1$. This means that according to eq. (10) the normal component of the surface current along the connection edge is constant. Therefore the current function (7) together with the function (11) for the quadrangles can be combined directly with the triangle basis function suggested by Rao [5]. The legs of the quadrangles are straight lines, as can easily be seen from eq. (11).

Current Basis Functions for Triangles

In order to complete the subject described in the preceding section it should be mentioned that Rao's triangle basis function can also be expressed in a parametric formulation. The result is given by

$$\vec{I} = \frac{I_0}{|\vec{a}_\eta \times \vec{a}_\xi|}\,(\vec{a}_\eta\cdot\eta + \vec{a}_\xi\cdot\xi)\,. \tag{14}$$

The position of the triangle in the η,ξ coordinate system is indicated in Fig. 6. An obvious advantage of eq. (14) is that it is valid for arbitrarily-shaped triangles, that means there is no restriction to plane elements.

Connection between Wire Segments and Surface Elements

To investigate practical problems with the help of a moment-method code it is often necessary to consider thin wires in conjunction with surfaces. In order to account for this requirement, several techniques have been developed.

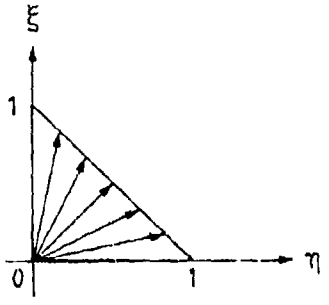

Fig. 6: Triangular patch with current filaments

The simplest technique to connect wires to surfaces is to fix them on one edge of a triangle or quadrangle. A detailed description of this method is given in [4].

Analyzing practical problems, it turned out that in some cases it is necessary to fix wires directly on a node of a discretized structure, for example because only the exact coordinates of the node are explicitly known in the input data, for reasons of symmetry or from other geometrical reasons. Therefore an appropriate function with reference to triangles which are connected to wires in one corner point, has to be created. For flat triangles, such a function can be expressd by the relation

$$\vec{I}\,(\vec{r}') = 0.5 \cdot \frac{I_0}{A} \cdot \left(x' \cdot \vec{e}_x + y' \cdot \vec{e}_y\right) \cdot \left[1 - \left(\frac{x_2' \cdot y_3' - y_2' \cdot x_3'}{x' \cdot (y_2' + y_3') - y' \cdot (x_2' + x_3')}\right)^2\right] \quad . \qquad (15)$$

The x',y',z' coordinate system is situated in the plane of the triangle. The geometrical quantities used in eq. (15) can be taken from Fig. 7.

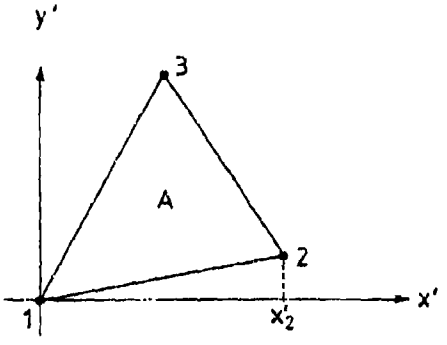

Fig. 7: Geometry for a triangle connected to a wire at corner 1

Taking the divergence of eq. (15) it can be seen that the surface charge distribution over the whole triangle is constant and thus the given function can be used together with the usual triangle basis function [5]. The surface current density tends to infinity at the junction point, but the value of the total current remains finite and is equal to I_0. It is evident that eq. (15) can be expressed in a form suitable for parametric triangles:

$$\vec{I} = \frac{I_0}{|\vec{a}_\eta \times \vec{a}_\xi|} (\vec{a}_\eta \cdot \eta + \vec{a}_\xi \cdot \xi) \cdot \left(1 - \frac{1}{(\eta+\xi)^2}\right) . \qquad (16)$$

Another possibility to create a basis function that correctly describes the connection between wires and triangle corners is to apply eq. (7) to a triangle. Performing this step, two corner points of a quadrangle must coincide, that is, the length of one edge of the quadrangle tends to zero, as indicated in Fig. 8. On the 2-3 edge the wire can be connected with the usual wire-edge connecting technique already described in [4]. The characteristic property of this method is that both the current density and the surface charge density tend to infinity at the junction point.

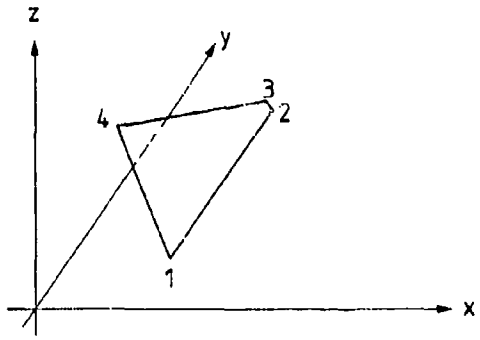

Fig. 8: Quadrangle degenerated to a triangle

Examples

To show that the described method works in the low as well as in the high frequency range, a test arrangement according to Fig. 9 was calculated by the code CONCEPT. The wire loop and the body are fixed on an ideal conducting ground plane of infinite extension. The figure shows the real part of the current distribution at a frequency of 150 MHz. At a frequency of 100 Hz the current in the wire behaves exactly according to Ohm's law.

To have a verification of the results, a top-loaded monopol antenna over an ideal conducting sheet according to Fig. 10 was calculated. The extensions of the sheet are large enough so that the fields near the antenna can be compared with an arrangement where the sheet is replaced by an unbounded plane. At first, the finite sheet was divided into triangles exclusively, and in a second computer run only quadrangles were used. The quadrangulation and the real part of the current distribution is shown in Fig. 11. The wave behaviour at 100 MHz can be seen very

well in this figure. Concerning the triangles, every quadrangle of Fig. 11 was subdivided into 2 triangles. The calculated x component of the electric field along the z' axis, indicated in Fig. 10, is given in Fig. 12. Fig. 12a shows the results for the arrangement with the triangular patches, and in Fig 12b the quadrangles are used. For sake of comparison the electric field produced by a top-loaded antenna over an infinite ground plane is also depicted in Fig. 12. The figure tells us that in both cases the agreement is very good, though in the triangle case 1100 unknowns are necessary, whereas in the quadrangle case only 740 unknown currents are used. But on this place it must be indicated that perhaps it is possible to attain a reduction of the unknowns in the triangle case by a more sophisticated triangulation. Therefore further investigations are necessary.

The power of the developed method is demonstrated by a greater example according to Fig. 13. In this figure, the imaginary part of the current distribution on an airplane is depicted. The arrangement is excited by a plane wave with its polarization vector in the symmetry plane. Utilizing this symmetry, the number of unknowns can be halved. For this example, about 1400 unknown currents occur. The amount of computation time on a HP-9000/825 is about 4 hours. The electric field distribution in the symmetry plane is given in Fig. 14. Inside the fuselage the field strength is almost zero except for the cockpit area. There the penetration of the field through the cockpit pane can be observed.

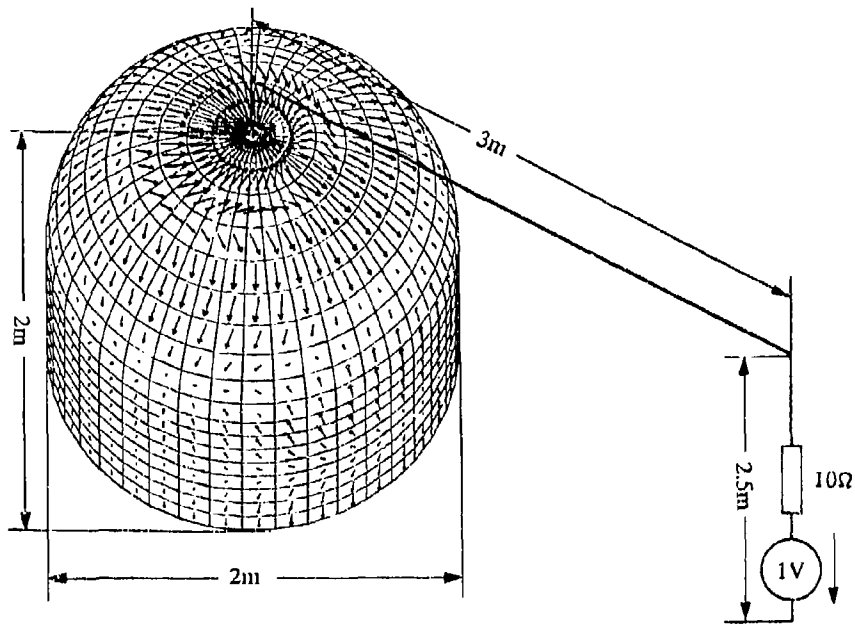

Fig. 9: Test arrangement of an halfsphere fed by a current loop in the HF range (f=150 MHz)

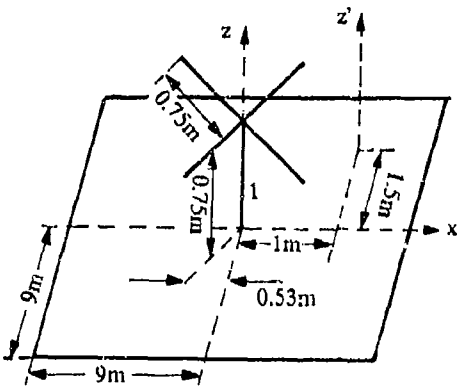

Fig. 10: Foot-point-fed monopol antenna excited at 100 MHz

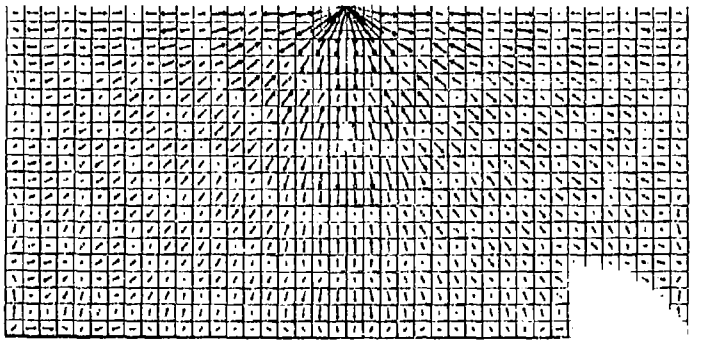

Fig. 11: Real part of the current distribution on the ground plan according to Fig. 10, front half of the plane

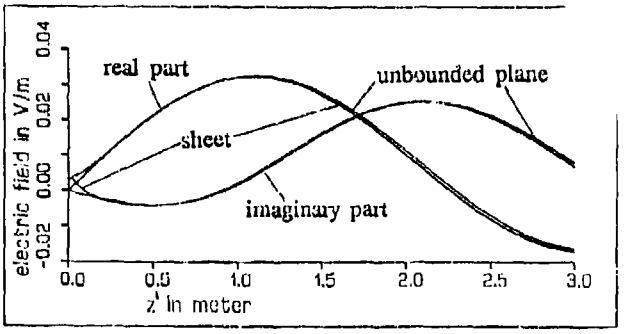

Fig. 12a: x component of the electric field using triangular patches

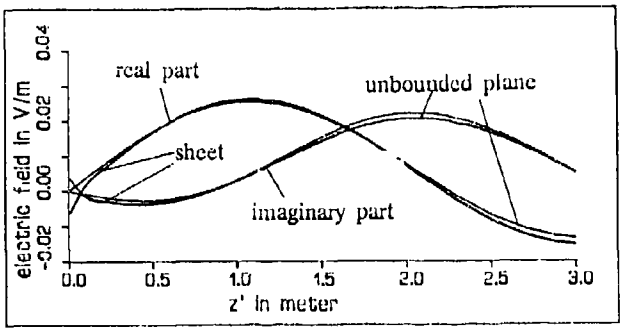

Fig. 12b: x component of the electric field using quadrangular patches

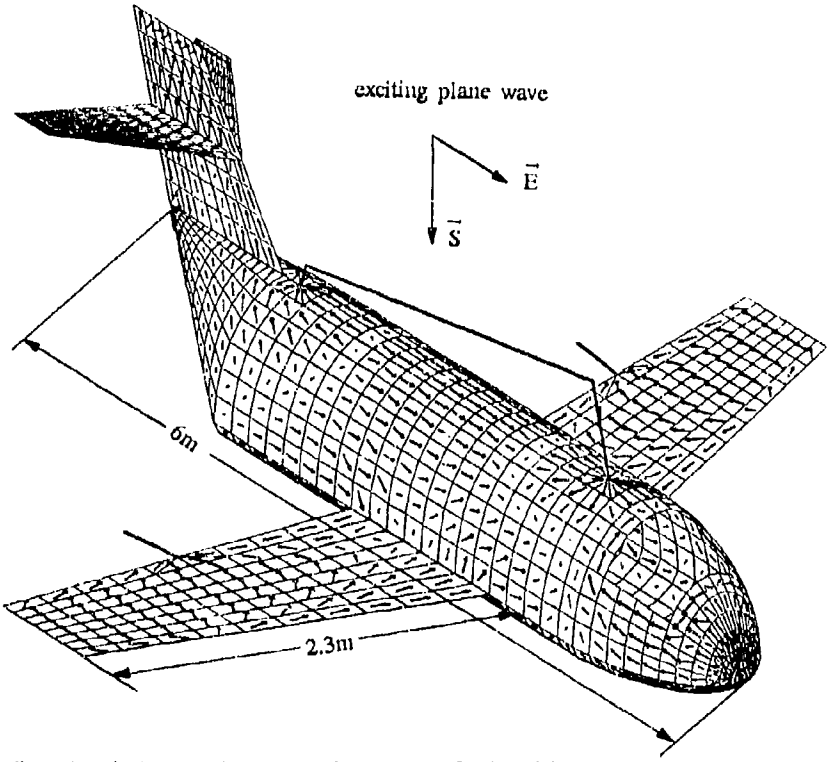

Fig. 13: Airplane excited by a plane wave of 100 MHz

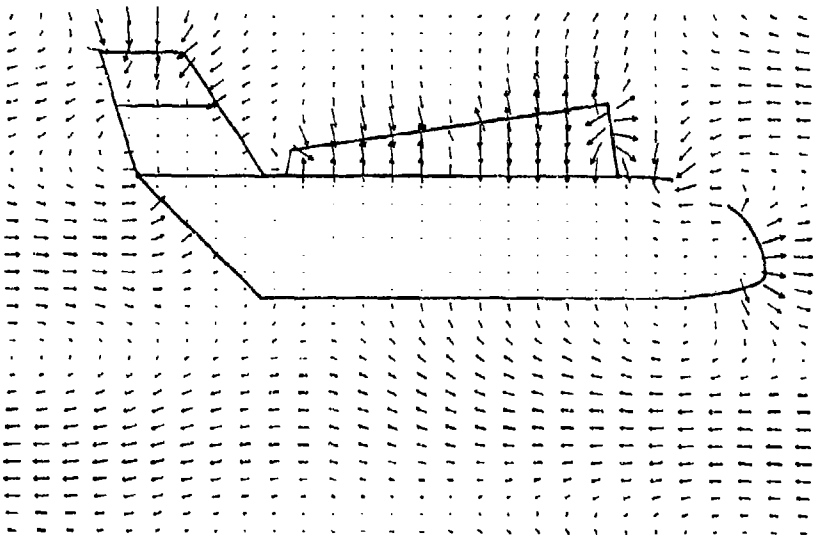

Fig. 14: Real part of the electric field around an airplane

References

[1] N. C. Albertsen, J. E. Hansen and N. E. Jensen, Computation of Radiation from Wire Antennas on Conducting Bodies, IEEE Trans. Ant. Prop., vol. AP-22 pp. 200-206, Mar. 1974

[2] H.-D. Brüns, Pulserregte elektromagnetische Vorgänge in dreidimensionalen Stabstrukturen, Thesis, Universität der Bundeswehr Hamburg, April 1985

[3] A. W. Glisson, On the Development of Numerical Techniques for Treating Arbitrarily-Shaped Surfaces, Thesis, University of Mississippi, 1978

[4] T. Mader, E-Field Solution for Scattering from Wires and Arbitrary Surfaces, IEEE Symp. on EMC, Washington D.C., 1990, pp. 657-661

[5] S. M. Rao, Electromagnetic Scattering and Radiation of Arbitrarily-Shaped Surfaces by Triangular Patch Modelling, Thesis, The University of Mississippi, August 1980

[6] J. A. Stratton, Electromagnetic Theory, McGraw-Hill Book Company, New York and London, 1941

SESSION 8- "MODELING EM INTERACTIONS IN MATERIALS"

Moderator: Kenneth Demarest

General Approach For Treating Boundary Conditions on Multi-Region Scatterers Using the Method of Moments*

J. M. Putnam

McDonnell Douglas Research Laboratories

Abstract

For complex geometries consisting of multiple regions with different types of boundary conditions imposed between the regions (i.e., conducting, dielectric, resistive, IBC, etc.), conventional method of moments (MM) procedures can become tedious and difficult to implement. Typically, MM based solutions to EM scattering and radiation problems proceed as follows:

- coupled integral equations are developed which represent the physics of the problem
- the boundary conditions are incorporated into the integral equations
- the MM technique is used to reduce the integral equations to a matrix equation.

In this paper, a simple technique will be presented for incorporating different types of boundary conditions and combinations of the field equations for scatterers with multiple homogeneous regions. Each interface between regions is considered separately. The Stratton-Chu integral equations representing the E and H fields on both sides of the interface are

*This research was conducted under the McDonnell Douglas Independent Research and Development program.

specified in terms of equivalent electric (J) and magnetic (M) currents on both sides of the interface. When the field point is located on the interface, there are four equations in eight unknowns ($E^{\pm}$, $H^{\pm}$, $J^{\pm}$, $M^{\pm}$). These eight unknowns are expanded in a series and the MM technique is applied, resulting in an overdetermined matrix equation. This matrix equation is independent of the boundary condition on the interface or the field equations which will be solved. The boundary condition and field equations to solve are specified by three matrices which operate on the overdetermined system, reducing it to a matrix equation of a determined system.

Examples will be given which illustrate how existing MM formulations in the literature can be recast using this technique. This technique has been implemented with Galerkin testing in a general purpose scattering code for 2D bodies, bodies of revolution, and arbitrary 3D bodies, consisting of multiple regions and boundary condition types. Numerical results will be presented which demonstrate the versatility of the method.

Introduction

The method of moments (MM) has been used extensively over the past two decades to solve a variety of scattering problems involving conducting and penetrable bodies. In [1] the electric field integral equation (EFIE) is solved for an arbitrary conducting body of revolution (BOR), and in [2] the magnetic and combined field integral equation (MFIE and CFIE) solutions are obtained. For arbitrary homogeneous BOR geometries, the PMCHW and Müller formulations are given in [3]. Impedance, resistive, and magnetically conducting boundary condition formulations are given in [4]. The above formulations are straightforward and easily implemented since only a single

surface is present. For geometries with multiple surfaces, where the number of surfaces and dielectric regions are fixed, the analysis is only slightly more complicated. For example, in [5] a CFIE formulation is given for a coated BOR, and in [6] five different formulations are presented for a partially coated BOR. In [7] a general formulation is presented for axially inhomogeneous BOR geometries consisting of multiple conducting and dielectric surfaces based on the EFIE and PMCHW formulations. The notation is complicated for the general case and the numerical implementation is not straightforward, and is further complicated when resistive and impedance boundary conditions are also allowed.

In this paper, a simple technique is presented for incorporating various types of boundary conditions and field solutions into a MM solution for a general body with multiple conducting and dielectric regions. The technique is directly applicable to all of the formulations cited above for BOR geometries, analogous two-dimensional geometries, and arbitrary three-dimensional geometries. Typically the MM is applied after the boundary conditions have been incorporated into a set of coupled integral equations. In the present approach, the MM is applied directly to a general set of coupled integral equations on each surface, and then the boundary conditions on the surface and field equations to test are incorporated. The technique facilitates the incorporation of different types of boundary conditions and field solutions into MM codes for general bodies.

Examples will be given which illustrate the technique for 2D and BOR geometries, using overlapping triangle function expansions and Galerkin testing. The Galerkin testing and orthogonal nature of the current expansions for 2D an BOR geometries results in special matrix properties which simplify the approach. The technique will be presented first for a

body consisting of a single surface, followed by some comments on how the technique extends to the case of multi-surface bodies.

General Integral Equations

Figure 1 depicts a scattering geometry with a single homogeneous interior region R_1. In the free-space region R_2, the total electric and magnetic fields are given by the Stratton-Chu integral equations

$$\theta_2 \vec{E}_2(\vec{r}) = \vec{E}^i(\vec{r}) - L_2\vec{J}^+(\vec{r}) + K_2\vec{M}^+(\vec{r}) \tag{1}$$

$$\theta_2 \vec{H}_2(\vec{r}) = \vec{H}^i(\vec{r}) - K_2\vec{J}^+(\vec{r}) - \frac{1}{\eta_2^2} L_2\vec{M}^+(\vec{r}) \tag{2}$$

where $\vec{E}^i$ and $\vec{H}^i$ are the incident electric and magnetic fields, $\vec{J}^+$ and $\vec{M}^+$ are the equivalent electric and magnetic currents, and the function $\theta_i(\vec{r})$ is defined as

$$\theta_i(\vec{r}) = \begin{cases} 1 & \text{for } \vec{r} \in R_i \\ 1/2 & \text{for } \vec{r} \in \partial R_i \\ 0 & \text{otherwise} \end{cases} \tag{3}$$

where ∂R_i is the boundary of region R_i.

The electric and magnetic surface currents on S in general are

$$\vec{J}^* = \hat{n}^* \times \vec{H}^*\Big|_S \tag{4a}$$

$$\vec{M}^* = -\hat{n}^* \times \vec{E}^*\Big|_S \tag{4b}$$

and

$$\eta_i = \eta_0 \sqrt{\frac{\mu_{ir}}{\epsilon_{ir}}}\ , \ \epsilon_i = \epsilon_0 \epsilon_{ir},\ \mu_i = \mu_0 \mu_{ir},\ \eta_0 = 377\ \Omega\ .$$

Time variation of $e^{j\omega t}$ is implied and suppressed in this discussion. The integro-differential operators L_i and K_i are defined as

$$L_i \vec{X}(\vec{r}) = j\omega\mu \int_{\partial R_i} \left(\vec{X}(\vec{r}') + \frac{1}{\omega^2 \mu \epsilon} \nabla\nabla' \cdot \vec{X}(\vec{r}') \right) \Phi(\vec{r} - \vec{r}')\, da' \tag{5}$$

and

$$K_i \vec{X}(\vec{r}) = \int_{\partial R_i} \vec{X}(\vec{r}') \times \nabla\Phi(\vec{r} - \vec{r}')\, da' \quad , \tag{6}$$

where for $\vec{r} = \vec{r}'$, the operators are interpreted as Cauchy principal-value integrals. The vector function $\vec{X}$ is in the domain of the operators L_i and K_i and is defined on ∂R_i. The Green's function is Φ, with Φ, ϵ, and μ defined in region R_i.

The total fields in region R_1 can be expressed likewise as

$$\theta_1 \vec{E}_1(\vec{r}) = - L_1 \vec{J}^-(\vec{r}) + K_1 \vec{M}^-(\vec{r}) \tag{7}$$

and

$$\theta_1 \vec{H}_1(\vec{r}) = - K_1 \vec{J}^-(\vec{r}) - \frac{1}{\eta_1^2} L_1 \vec{M}^-(\vec{r}) \quad . \tag{8}$$

General Matrix Equation

When the field point $\vec{r}$ is located on the surface S there are four equations (1, 2, 7, and 8) involving eight unknowns ($\vec{E}^*$, $\vec{H}^*$, $\vec{J}^*$, and $\vec{M}^*$), where $\vec{E}^+ = \vec{E}_2\big|_S$, $\vec{E}^- = \vec{E}_1\big|_S$, $\vec{H}^+ = \vec{H}_2\big|_S$, and $\vec{H}^- = \vec{H}_1\big|_S$. Once a set of expansion functions has been chosen for the eight unknowns and testing

functions have been selected, the four coupled integral equations can be reduced to an overdetermined system of linear equations using the method of moments. Written in matrix operator notation, the four integral equations reduce to

$$\begin{bmatrix} \mathcal{L}_2 & -\mathcal{K}_2 & 0 & 0 \\ \mathcal{K}_2 & \frac{\epsilon_2}{\mu_2}\mathcal{L}_2 & 0 & 0 \\ 0 & 0 & \mathcal{L}_1 & -\mathcal{K}_1 \\ 0 & 0 & \mathcal{K}_1 & \frac{\epsilon_1}{\mu_1}\mathcal{L}_1 \end{bmatrix} \begin{bmatrix} \tilde{\mathcal{K}} & 0 & 0 & 0 \\ 0 & \tilde{\mathcal{K}} & 0 & 0 \\ 0 & 0 & \tilde{\mathcal{K}} & 0 \\ 0 & 0 & 0 & \tilde{\mathcal{K}} \end{bmatrix} \begin{bmatrix} J^+ \\ M^+ \\ J^- \\ M^- \\ E^+ \\ H^+ \\ E^- \\ H^- \end{bmatrix} = \begin{bmatrix} \mathscr{E} \\ \mathscr{H} \\ 0 \\ 0 \end{bmatrix} \tag{9}$$

where $\mathcal{L}_i$ and $\mathcal{K}_i$ are the matrix operators which result from testing the integral operators L_i and K_i, respectively. The subscript specifies the region where the Green's functions is evaluated. The matrix operator $\tilde{\mathcal{K}}$ results from testing the total electric and magnetic fields on the surface, and $\mathscr{E}$ and $\mathscr{H}$ are the column vectors which result from testing the incident electric and magnetic fields, respectively. Note that the form of Eq. (9) assumes judicious placement of a factor η_0 in the current expansion and testing functions which will be detailed below. Equation (9) will be written in shorthand notation as $ZI + \tilde{Z}\tilde{I} = V$, where I represents the four current unknowns (J^*, M^*) and $\tilde{I}$ represent the four field unknowns (E^*, H^*).

Method of Moments Galerkin Technique

In general, Eq. (9) possess no special symmetry properties, however, when specialized expansion functions are used with Galerkin testing both the

Z and $\tilde{Z}$ method of moments matrices are symmetric. Explicit current and field expansions are given below for bodies of revolution (BOR) and two-dimensional bodies, using the same notation as in [7,8].

For BOR geometries, the unknown currents and fields are expanded as

$$\vec{J} = \sum_{n,k} \left(a^t_{nk} \vec{J}^t_{nk} - a^\phi_{nk} \vec{J}^\phi_{nk} \right) \tag{10a}$$

$$\vec{M} = \eta_0 \sum_{n,k} \left(b^t_{nk} \vec{J}^t_{nk} - b^\phi_{nk} \vec{J}^\phi_{nk} \right) \tag{10b}$$

$$\vec{E} = \eta_0 \sum_{n,k} \left(c^t_{nk} \vec{J}^t_{nk} - c^\phi_{nk} \vec{J}^\phi_{nk} \right) \tag{10c}$$

$$\vec{H} = \sum_{n,k} \left(d^t_{nk} \vec{J}^t_{nk} - d^\phi_{nk} \vec{J}^\phi_{nk} \right) \tag{10d}$$

where a, b, c, and d are the unknown expansion coefficients, and

$$\vec{J}^\alpha_{nk} = \vec{u}_\alpha \frac{T_k(t)}{\rho(t)} e^{jn\phi} , \qquad \alpha = t \text{ or } \phi \tag{11}$$

where $T_k(t)$ is the k-th overlapping triangle function on the surface S. With this expansion, the matrix operators can be written in partitioned form as

$$\mathscr{L} = \begin{pmatrix} \mathscr{L}^{tt} & \mathscr{L}^{t\phi} \\ \mathscr{L}^{\phi t} & \mathscr{L}^{\phi\phi} \end{pmatrix} \tag{12}$$

$$\mathscr{K} = \begin{pmatrix} \mathscr{K}^{tt} & \mathscr{K}^{t\phi} \\ \mathscr{K}^{\phi t} & \mathscr{K}^{\phi\phi} \end{pmatrix} \tag{13}$$

$$\tilde{\mathcal{K}} = \begin{pmatrix} \tilde{\mathcal{K}}^{tt} & \tilde{\mathcal{K}}^{t\phi} \\ \tilde{\mathcal{K}}^{\phi t} & \tilde{\mathcal{K}}^{\phi\phi} \end{pmatrix} = \begin{pmatrix} \bar{\mathcal{K}} & 0 \\ 0 & -\bar{\mathcal{K}} \end{pmatrix} \tag{14}$$

The matrix $\mathcal{L}'$ is symmetric, the matrix $\mathcal{K}$ is anti-symmetric, and the matrix $\bar{\mathcal{K}}$ is tridiagonal and symmetric.

Analogous matrices result for two-dimensional bodies, possessing the same symmetry properties. Assuming that the y-axis is the infinite axis of translation, the electric currents are expanded as

$$\vec{J} = \sum_k \left(a_k^t \hat{u}_t - a_k^y \hat{u}_y \right) T_k(t) \tag{15}$$

The other unknowns are expanded similarly as in Eq. (10). The matrix operators are written in partitioned form as

$$\mathcal{L}' = \begin{pmatrix} \mathcal{L}'^{tt} & 0 \\ 0 & \mathcal{L}'^{yy} \end{pmatrix} \tag{16}$$

$$\mathcal{K} = \begin{pmatrix} 0 & \mathcal{K}^{ty} \\ \mathcal{K}^{yt} & 0 \end{pmatrix} \tag{17}$$

$$\tilde{\mathcal{K}} = \begin{pmatrix} \tilde{\mathcal{K}}^{tt} & 0 \\ 0 & \tilde{\mathcal{K}}^{yy} \end{pmatrix} = \begin{pmatrix} \bar{\mathcal{K}} & 0 \\ 0 & -\bar{\mathcal{K}} \end{pmatrix} \tag{18}$$

Incorporation of Boundary Conditions

Equation (9) gives the general MM matrix solution. The boundary conditions are now incorporated into the overdetermined matrix equation by

specifying equivalent relationships between unknown current and field coefficients. These relationships are used to eliminate unknowns from the overdetermined system of equations $ZI + \tilde{Z}\,\tilde{I} = V$ as follows.

First, the unknown current coefficients in the vector I are rearranged so that $I = \begin{bmatrix} I_1 \\ I_2 \end{bmatrix}$, where I_1 represents the unknown current coefficients which will be retained in the final solution, and I_2 represents the coefficients which will be eliminated using the boundary conditions. Second, the boundary conditions are incorporated into a matrix A so that $I = AI_1$. The matrix A gives the relationships between the I_1 and I_2 unknowns which result from an application of the boundary conditions. Finally, the boundary conditions are used to eliminate the field unknowns $\tilde{I}$ by specifying a matrix B so that $\tilde{I} = BI_1$. The overdetermined system of equations in thus reduced to the system of equations

$$\left(ZA + \tilde{Z}B\right) I_1 = V \tag{19}$$

Combined Field Solution

At this point, there may be more equations than unknowns. The field equations are combined so as to reduce the system of equations to a determined system. The combined field solution is specified by a matrix operator C which is applied to Eq. (19) resulting in the matrix equation

$$C(ZA + \tilde{Z}B)\, I_1 = CV \tag{20}$$

The exact form of the matrix C will depend upon the boundary condition to be satisfied on the surface S, and the combined field formulation which is to

be solved. For a given boundary condition, certain choices for the matrices A, B, and C result in Eq. (20) being symmetric.

Some examples will be presented which illustrate the method for some typical boundary conditions. These examples apply to both BOR and 2D bodies using the MM Galerkin matrix operators previously defined.

Conducting Boundary

For a conducting boundary, the interior fields are zero and $\vec{E}_{tan} = 0$ on the surface S. This implies that $I_1 = J^+$, and $M^+ = J^- = M^- = 0$. The matrix A is given by

$$A = \begin{bmatrix} 1 \\ 0 \\ 0 \\ 0 \end{bmatrix} \tag{21}$$

since J^+ is the only nonzero current on the surface. The equivalent electric current is defined as $\vec{J}^+ = \hat{n}^+ \times \vec{H}^+$. Assuming $\hat{n} = \hat{\phi} \times \hat{t}$ for BOR geometries, this implies that the corresponding unknown coefficients are related by $J^+ = XH^+$ with $X = \begin{pmatrix} 0 & -1 \\ 1 & 0 \end{pmatrix}$ where the current and field coefficient are written in partitioned form as

$$J^+ = \begin{bmatrix} J^{+t} \\ J^{+\phi} \end{bmatrix} \quad , \qquad H^+ = \begin{bmatrix} H^{+t} \\ H^{+\phi} \end{bmatrix} \tag{22}$$

For 2D geometries with $\hat{n} = \hat{y} \times \hat{t}$, the same relationship holds if $\phi \to y$. Equivalently, $H^+ = -XJ^+$ and the B matrix is therefore given by

$$B = \begin{bmatrix} 0 \\ -X \\ 0 \\ 0 \end{bmatrix} \tag{23}$$

A combined field integral equation (CFIE) solution can be formed by taking $\alpha\vec{E}^+ + (1-\alpha)\ \hat{n}\times\vec{H}^+$ for $0 \le \alpha \le 1$. The C matrix which implements the CFIE formulation is given by

$$C = [\alpha \quad -(1-\alpha)X \quad 0 \quad 0] \tag{24}$$

Substituting the matrices A, B, and C into Eq. (20) yields the CFIE formulation for a conducting surface

$$\left[\alpha\,\mathcal{L}_2 - (1-\alpha)(X\cdot\mathcal{K}_2 - \tilde{\mathcal{K}})\right] J^+ = \alpha\,\mathcal{E} + (1-\alpha)\,X\cdot\mathcal{H} \tag{25}$$

which is equivalent to the CFIE solution in [2]. When $\alpha = 1$ the system of equations is symmetric and the EFIE is obtained. For 2D bodies the system of equations decouples into the TE and TM polarization cases.

Dielectric Boundary

For a dielectric boundary the tangential electric and magnetic fields are continuous across the interface S. The equivalent interior and exterior current coefficients are related by $J^- = -J^+$ and $M^- = -M^+$. The field coefficients are related to the equivalent current coefficients by $H^- = H^+ = -XJ^+$ and $E^- = E^+ = XM^+$. Using these relationships, the general combined field solution in [3] is obtained by setting

$$I_1 = \begin{bmatrix} J^+ \\ M^+ \end{bmatrix} \tag{26a}$$

$$A = \begin{bmatrix} 1 & 0 \\ 0 & 1 \\ -1 & 0 \\ 0 & -1 \end{bmatrix} \tag{26b}$$

$$B = \begin{bmatrix} 0 & X \\ -X & 0 \\ 0 & X \\ -X & 0 \end{bmatrix} \tag{26c}$$

$$C = \begin{bmatrix} 1 & 0 & -\alpha & 0 \\ 0 & 1 & 0 & -\beta \end{bmatrix} \tag{26d}$$

When $\alpha = \beta = 1$ the PMCHW formulation is obtained and is symmetric. Other choices for C will produce the E-field and H-field formulations in [6].

Impedance Boundary Condition

An impedance surface is characterized by the boundary condition $\vec{E}^+\big|_{tan} = \eta_s \eta_0 \hat{n}^+ \times \vec{H}^+$. This boundary condition can be expressed in terms of the unknown coefficients as $E^+ = \eta_s J^+$, $M^+ = -\eta_s X J^+$, and $H^+ = -XJ^+$. These relationships are incorporated by setting $I_1 = J^+$ and

$$A = \begin{bmatrix} 1 \\ -\eta_s X \\ 0 \\ 0 \end{bmatrix} \quad , \qquad B = \begin{bmatrix} \eta_s \\ -X \\ 0 \\ 0 \end{bmatrix} \tag{27}$$

The symmetric system of equations given in [4] is obtained if $C = {}^{t}A$ where t indicates the transpose. Other choices for C will produce different combined field IBC formulations.

Resistive Boundary Condition

A resistive surface is characterized by the boundary conditions $\vec{E}^{+}_{tan} = \vec{E}^{-}_{tan}$ and $\hat{n}^{+} \times (\vec{H}^{+} - \vec{H}^{-}) = \frac{1}{R_s \eta_0} \vec{E}^{+}_{tan}$. These conditions can be expressed in terms of the equivalent currents as $\vec{M}^{-} = -\vec{M}^{+}$ and $R_s \eta_0 (\vec{J}^{+} + \vec{J}^{-}) = \vec{E}^{+}_{tan}$. The A matrix is defined by setting

$$I_1 = \begin{bmatrix} J^{+} \\ M^{+} \\ J^{-} \end{bmatrix} \tag{28a}$$

$$A = \begin{bmatrix} 1 & 0 & 0 \\ 0 & 1 & 0 \\ 0 & 0 & 1 \\ 0 & -1 & 0 \end{bmatrix} \tag{28b}$$

The B matrix is obtained by noting that the boundary condition can also be written as $\vec{H}^{-}_{tan} = \frac{-1}{R_s \eta_0} \vec{M}^{+} + \vec{H}^{+}_{tan}$ where $\vec{H}^{+}_{tan} = -\hat{n}^{+} \times \vec{J}^{+}$.

$$B = \begin{bmatrix} R_s & 0 & R_s \\ -X & 0 & 0 \\ R_s & 0 & R_s \\ -X & -\frac{1}{R_s} & 0 \end{bmatrix} \tag{29}$$

A symmetric system of equations is obtained by letting $C = {}^{t}A$. The resulting system of equations reduces to the conducting case as $R_s \to 0$ and to the dielectric case as $R_s \to \infty$.

In a similar manner, the dual magnetically conducting boundary condition can be solved, and solutions can be obtained when both resistive and magnetically conducting boundary conditions are imposed.

Extension To Multiple Surfaces

This method can be easily extended to scattering geometries which contain multiple surfaces and homogeneous regions where each surface may be characterized by a different type of boundary condition. For each surface, the appropriate currents are specified by I_1, matrices A and B specify how the boundary condition on the surface is incorporated into the solution, and matrix C specifies the fields which are tested and combined. When the Stratton-Chu integral equations are tested, the $\mathscr{L}$ and $\mathscr{K}$ matrix operators must specify both the testing surface and the surface on which the equivalent currents reside. The C matrix on the test surface defines how the fields are combined while the A matrix on the source surface defines how the unknown currents are related.

Conclusions

A simple technique was presented for incorporating different types of boundary conditions and combined field solutions in conjunction with a method of moments solution. Examples were presented which illustrate that the technique can be used to write MM solutions for standard boundary conditions in a compact notational form. The method allows the efficient implementation of different boundary conditions and field formulations in MM

codes for multiple surfaces and regions. A formulation was presented for treating a resistive boundary condition between two different homogeneous dielectric regions. The dual magnetically conducting boundary condition solution is obtained in an analogous manner. Both solutions are numerically stable and are self consintent for limiting cases.

References

[1] J. R. Mautz and R. F. Harrington, "Radiation and scattering from bodies of revolution," Appl. Sci. Res., vol. 20, pp. 405-435, 1969.

[2] J. R. Mautz and R. F. Harrington, "H-field, E-field, and combined-field solutions for conducting bodies of revolution," Arch Elek. Übertragung., vol. 32, pp. 157-164, 1978.

[3] J. R. Mautz and R. F. Harrington, "Electromagnetic scattering from a homogeneous material body of revolution," Arch Elek. Übertragung., vol. 33, pp. 71-80, 1979.

[4] L. N. Medgyesi-Mitschang and J. M. Putnam, "Integral Equation Formulations for Imperfectly Conducting Scatterers," IEEE Trans. Antennas Propagat., vol. AP-33, pp. 206-214, 1985.

[5] P. L. Huddleston, L. N. Medgyesi-Mitschang, and J. M. Putnam, "Combined field integral equation formulation for scattering by dielectrically coated conducting bodies," IEEE Trans. Antennas Propagat., vol. AP-34, pp. 510-520, 1986.

[6] A. A. Kishk and L. Shafai, "Different formulations for numerical solution of single or multibodies of revolution with mixed boundary conditions," IEEE Trans. Antennas Propagat., vol. AP-34, pp. 666-673, 1986.

[7] L. N. Medgyesi-Mitschang and J. M. Putnam, "Electromagnetic scattering from axially inhomogeneous bodies of revolution," IEEE Trans. Antennas Propagat., vol. AP-32, pp. 797-806, 1984.

[8] J. M. Putnam and L. N. Medgyesi-Mitschang, "Combined Field Integral Equation Formulation for Inhomogeneous Two- and Three-Dimensional Bodies: The Junction Problem," IEEE Trans. Antenna Propagat. (accepted).

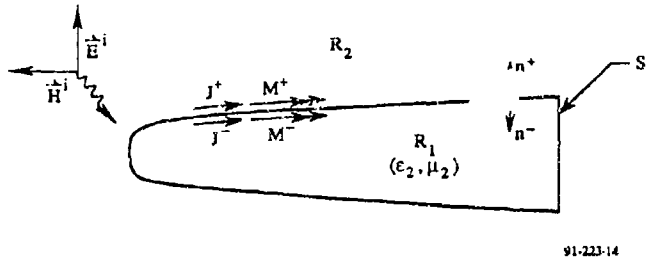

Figure 1. Scattering geometry.

Comparison of Computed and Measured Results for a Simple Man-with-Radio Model

Allen W. Glisson
Dept. of Electrical Engineering
University of Mississippi
University, MS 38677

Darko Kajfez
Dept. of Electrical Engineering
University of Mississippi
University, MS 38677

Perry Wheless
Dept. of Electrical Engineering
University of Alabama
Tuscaloosa, AL 35487

K. H. (Chuck) Agar
CM Engineering Co.
Las Cruces, NM 88047

Abstract

The radiation characteristics of a two-way radio in the presence of a simple model of the human body are investigated. The human-body model is a 14-inch PVC pipe filled with salt water. The triangular patch code PATCH is used to model the pipe as a simple impedance-sheet surface, while the radio body with its antenna is modeled as a perfectly conducting plate driven against a thin strip. Numerical results obtained with this model are compared with measured data in the 450-470 MHz range for the radio suspended beside the water cylinder.

Introduction

The radiation characteristics of a hand-held two-way radio are of interest for many applications. The effect of the human body on the radiation pattern and input impedance of the radio antenna are difficult to predict for realistic geometries. Various approaches to the modeling of similar problems have been considered, including the use of volume integral equation models and hybrid partial differential equation/integral equation models [1-5]. When the fields interior to the body are of interest, a volume formulation is necessary. However, if one is interested primarily in the input impedance and radiation characteristics of the antenna in the presence of the body, one might expect simpler models to be applicable. Surface integral equation (SIE) models which assume that the body is a homogeneous or layered homogeneous dielectric region [6] may prove satisfactory, particularly since the human body is lossy. Standard SIE formulations require the entire surface of the body to be modeled, however, and generally employ both electric and magnetic equivalent surface currents as unknowns in the numerical formulation. For a lossy dielectric the number of unknowns may be reduced by 50% in some situations by employing the impedance boundary condition (IBC) model [7]. The IBC model still requires the current distribution to be modeled over the entire surface of the dielectric body, but reduces the number of unknowns required in the model by enforcing a known relationship between the electric and magnetic equivalent surface current densities.

In this work we seek to employ a numerical model of intermediate complexity and to

compare the numerical results obtained using this model with measured data for a simple physical geometry representing the human body at frequencies in the 450 MHz range. The measured data for the radiation pattern of the radio are obtained using a vertical 14-inch O.D. PVC pipe filled to approximately six feet in height with salt water to represent the man. The radio is suspended from the top of the pipe with an adjustable plexiglass holder. The receiving antenna is fixed and the radiation pattern is obtained by varying the azimuthal position of the radio around the water-filled pipe.

The numerical model employed in this work is an impedance-sheet model for a thin dielectric shell [8]. This is a model of intermediate complexity in the sense that it is not a full volumetric model of a man or of the experimental water-column man. It requires fewer unknowns than does a full volume model, yet it is very flexible. The PATCH triangular patch code is capable of representing this type of model without modification. Thus, arbitrary surface shapes can be used to represent the man, and, in particular, appendages such arms can later be included in the model and oriented in an arbitrary manner. Of course, the use of this simple model ignores the internal structure of the human body, and may be expected to yield unsatisfactory results under some conditions. In principle, however, the impedance sheet model can be extended to represent a "volume" model by simply incorporating a set of interlocking impedance sheets to represent the interior region of the body. This procedure has been implemented successfully by Rubin and Daijavad [9] using rectangular source regions and rooftop basis functions [10]. A similar approach should be practical using triangular domains and the PATCH code. An advantage of this approach over standard volumetric models may be that the interlocking impedance-sheet volume model could be used only in the region of the body in close proximity to the radio, while the surface impedance-sheet model can be retained for the body region remote from the radio.

Formulation

To obtain the impedance sheet model for the body, we consider a thin, lossy dielectric shell centered around the actual body surface S_b. The radio body is modeled as a rectangular, perfectly conducting plate S_p, with an attached perfectly conducting thin strip S_s to model the wire antenna. The radio is excited by an impressed voltage source at the junction of the plate and the thin strip. An equivalent electric current $\mathbf{J}$ is assumed to be induced on the entire surface $S=S_b+S_p+S_s$. The current $\mathbf{J}$ induced on S_b is an equivalent surface current in the model, but it represents a volume polarization current $\mathbf{J}_v$ flowing within the impedance shell and tangential to the surface [8].

The scattered electric field produced by the current $\mathbf{J}$ may be expressed as

$$\mathbf{E}^s(\mathbf{r}) = -j\omega\mathbf{A}(\mathbf{r}) - \nabla\Phi(\mathbf{r}) \tag{1}$$

where

$$\mathbf{A}(\mathbf{r}) = \mu \int_S \mathbf{J}(\mathbf{r}')G(\mathbf{r},\mathbf{r}')dS' \tag{2}$$

$$\Phi(\mathbf{r}) = \frac{1}{\epsilon} \int_S \sigma(\mathbf{r}')G(\mathbf{r},\mathbf{r}')dS' \tag{3}$$

$$G(\mathbf{r},\mathbf{r}') = \frac{e^{-jk|\mathbf{r}-\mathbf{r}'|}}{4\pi|\mathbf{r}-\mathbf{r}'|} \tag{4}$$

ϵ and μ are the permittivity and permeability of free space, $k=\omega(\mu\epsilon)^{-1/2}$, $\mathbf{r}$ and $\mathbf{r}'$ represent observation and source coordinates, respectively, and the surface charge density σ is related to the surface current $\mathbf{J}$ through the equation of continuity

$$\nabla \cdot \mathbf{J} = -j\omega\sigma \tag{5}$$

The electric field integral equation for the thin dielectric shell portion of the multi-body geometry is then obtained by enforcing the volume polarization current definition

$$\mathbf{J}(\mathbf{r}) = j\omega(\epsilon-\epsilon_0)\tau\mathbf{E}_{tan}(\mathbf{r}), \quad \mathbf{r}\in S_b \tag{6}$$

where τ is the thickness of the shell, $\mathbf{E}_{tan}$ has been assumed to be constant across the thickness of the thin shell, and the volume polarization current $\mathbf{J}_v$ has been compressed into a surface current $\mathbf{J}$ residing on S_b. The component of $\mathbf{E}$ normal to the surface S_b is ignored. The EFIE for the shell may then be written as

$$[j\omega\mathbf{A}(\mathbf{r}) + \nabla\Phi(\mathbf{r})]_{tan} + Z_s(\mathbf{r})\mathbf{J}(\mathbf{r}) = \mathbf{E}^i_{tan}(\mathbf{r}) \tag{7}$$

where Z_s is the sheet impedance defined by

$$Z_s = [j\omega\epsilon_0(\epsilon_r-1)\tau]^{-1} \tag{8}$$

Dielectric loss is included by setting $\epsilon_r=\epsilon_r'-j\epsilon_r''$. When $Z_s=0$ Eq. (7) becomes the familiar EFIE for perfectly conducting bodies, and it can therefore be applied to both the lossy water cylinder and the conducting radio geometry when Z_s is appropriately chosen.

The PATCH moment method code [11] can be used to solve (7) for the induced electric surface current $\mathbf{J}$ and to compute the resulting radiation pattern. The code employs a triangular patch model of surfaces with basis functions defined on pairs of triangles [12].

Experiment

The PVC cylinder that is partially filled with salt water and the radio in its plexiglass holder are shown in Fig. 1. The cylinder is filled with water up to the measuring tape visible

Figure 1. PVC cylinder partially filled with salt water and radio in plexiglass holder used to obtain experimental data.

in the figure. Note that the monopole antenna is partially protruding above the top of the water level. The battery-operated radio is situated on a plexiglass arm, which can be manually shifted around the cylinder to obtain the azimuthal radiation pattern. The relative size of the cylinder in comparison with a person is shown in Fig. 2. For each measured point, the person had to hide behind the barrier of absorbing material. Although this method of measurement may be somewhat primitive, it nevertheless assures the absence of all feed cables, and it also provides for the stability and repeatability of the measurements. The measured points could be repeated with an accuracy of 1 dB. The receiving log-periodic antenna was located at a distance of 5.2m from the center of the cylinder.

The preliminary measurements were made with the cylinder filled with tap water, and the final measurements were made with a 0.2% solution of NaCl. The DC conductivity of the solution was measured to be 0.19 S/m. It is believed that the RF conductivity is about 0.5 S/m, but the exact RF measurement has not be conducted. It was found that there was very little

Figure 2. Water cylinder and radio with one of the authors.

difference between the radiation patterns obtained for tap water and salt water. The measured data, which are subsequently shown in Figs. 5 and 6, are for the salt water case.

Results

Numerical results have been obtained and compared with the measured data at 450, 460, and 470 MHz. As noted previously, the numerical model of the radio consists of a perfectly conducting flat plate attached to a thin strip representing the wire antenna. The triangular discretization of the radio model is shown along with the cylindrical model of the water column in Fig. 3. The water-filled pipe is modeled as a dielectric shell along the side and top of the water surface. The bottom face of the water column is not included in the model in Fig. 3. The dielectric shell is assumed to have a thickness τ of 0.07m, which is about a tenth of a wavelength, a relative dielectric constant ϵ_r of 80, and a conductivity σ of 0.3. All of these numbers are somewhat arbitrary since there is no true "shell" thickness, and the sheet impedance computed via (8) depends on the product of τ and the complex permittivity. The values chosen do not greatly affect the results over the range of frequency used in this work. In more critical situations, or if an interlocking sheet impedance model were to be used to represent a volume model, we expect that the sheet impedance should be chosen in the manner described in [9].

For the model shown in Fig. 3, the cylinder radius is 0.173m and the cylinder height is 1.82m. The PEC plate modeling the radio has dimensions of 0.195m high by 0.065m wide,

while the antenna (strip) has dimensions of 0.197m high by 0.01625m wide. The top center of the radio is positioned at (0.225425, 0.0, 1.73745) meters. Because the cylinder is almost three wavelengths long in the frequency range of interest, the model shown in Fig. 3 is actually a fairly crude model, particularly in the vertical dimension. The model shown uses 12 segments to model both the vertical and azimuthal directions and has 577 unknowns. Unfortunately, this was close to the limit of the model size which could conveniently be used and tests for numerical solution convergence were limited.

An effort was made to obtain a better numerical model in the vertical direction by truncating the cylinder while keeping the same number of unknowns. The truncated model, in which the bottom half of the cylindrical shell has been eliminated, is shown in Fig. 4. The cylinder is still model using 12 segments in both the vertical and azimuthal directions, so the triangle density is increased with respect to the model of Fig. 3. Truncation of the model was expected to be feasible due to the lossy nature of the body and the localized excitation. Results obtained using different truncation lengths showed only small variations, which is an indication that the truncation process was valid.

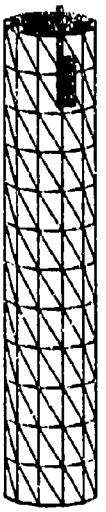

Figure 3. Full model of the water-filled PVC pipe and radio geometry.

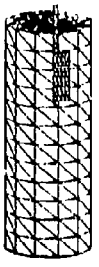

Figure 4. Truncated model of the water-filled pipe and radio geometry.

The comparisons of measured data with the numerical results for the full and truncated geometries are shown in Figs. 5 and 6, respectively. In the figures, the continuous lines represent the numerical data, while the measured data are represented by discrete symbols. The solid line represents data for 450 MHz, the dashed line for 460 MHz, and the dotted line for 470

MHz. For the measured data the plus (+) represents 450 MHz, the asterisk (*) 460 MHz, and the cross (x) and circle (o) represent two different 470 MHz trials. The agreement between the experimental and numerical data is fairly good for both geometries. However, the results obtained with the full-cylinder model show somewhat poorer agreement with the measured data and somewhat greater frequency sensitivity in the backward radiation direction ($\phi = 180°$). It seems likely that this is due to the rather crude numerical modeling of the cylinder in the vertical direction, since the maximum edge lengths in the model may exceed one-quarter wavelength for this case. The numerical results for the truncated cylinder geometry agree with measured data very well in the forward and backward directions, while some deviation is noted in the side radiation.

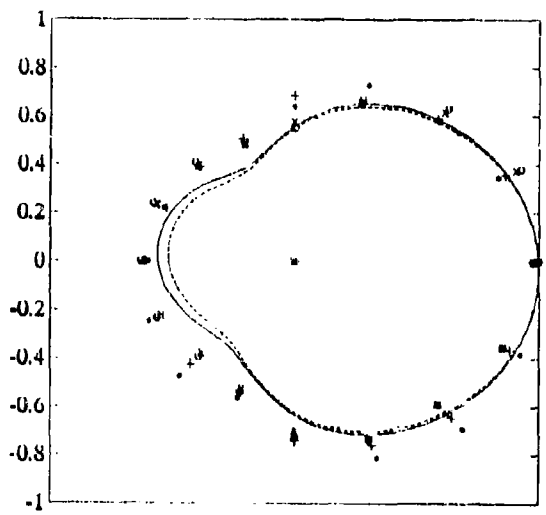

Figure 5. Comparison of results for full-cylinder model. Numerical results: 450 (solid line), 460 (dashed line), and 470 (dotted line) MHz. Measured data: 450 (+), 460 (*), and 470 (x,o) MHz.

Summary

The radiation characteristics of a two-way radio in the presence of a simple water-column model of the human body have been investigated. The human-body model used to obtain measured data was a 14-inch PVC pipe filled with salt water. The triangular patch code PATCH has been used to model the pipe as a simple impedance-sheet surface, while the radio body with its antenna is modeled as a perfectly conducting plate driven against a thin strip. Numerical results obtained with this model have been compared with measured data in the 450-470 MHz

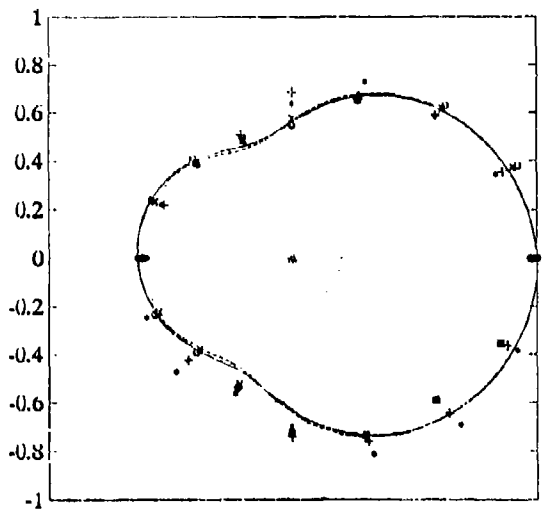

Figure 6. Comparison of results for truncated-cylinder model. Numerical results: 450 (solid line), 460 (dashed), and 470 (dotted) MHz. Measured data: 450 (+), 460 (*), and 470 (x, o) MHz.

range for the radio suspended beside the water column and have been found to be in good agreement. The PATCH triangular patch code used for the numerical solution is capable of representing arbitrary surface shapes and could be used in future work to represent a more complex model of a man, and, in particular, appendages such as arms could be included in the model and oriented in an arbitrary manner. With further work the impedance sheet model can be extended to represent a "volume" model by incorporating a set of interlocking impedance sheets to represent the interior region of the body, thus providing the ability to adjust the model complexity from a fairly simple model to a quite complex model with the same code as the need arises.

From the applications point of view, the results indicate that the radiation pattern for a 450-470 MHz portable radio in the presence of a human body shows a front-to-back ratio of about 4 dB, and side minima of up to 5-5.5 dB. These results are similar to the results reported in [2] for 165 and 250 MHz radios.

References

[1] D. E. Livesay and K.-M. Chen, "Electromagnetic fields induced inside arbitrarily shaped biological bodies," *IEEE Trans. Microwave Theory Tech.*, vol. MTT-22, pp. 1273-1280,

December 1974.

[2] J. B. Anderson and F. Hansen, "Antennas for VHF/UHF Personal Radio: A Theoretical and Experimental Study of Characteristics and Performance," *IEEE Trans. Vehicular Tech.*, vol. VT-26, pp. 349-357, Nov. 1977.

[3] D. H. Schaubert, D. R. Wilton, and A. W. Glisson, "A tetrahedral modeling method for electromagnetic scattering by arbitrarily shaped inhomogeneous dielectric bodies," *IEEE Trans. Antennas Propagat.*, vol. AP-32, pp. 77-85, January 1984.

[4] K. D. Paulsen, D. R. Lynch, and J. W. Strohbehn, "Three-dimensional finite, boundary, and hybrid element solutions of the Maxwell equations for lossy dielectric media," *IEEE Trans. Microwave Theory Tech.*, vol. MTT-36, pp. 682-693, April 1988.

[5] M. A. Morgan and B. E. Welch, "The field feedback formulation for electromagnetic scattering computations," *IEEE Trans. Antennas Propagat.*, vol. AP-34, pp. 1377-1382, December 1986.

[6] S. Govind, D. R. Wilton, and A. W. Glisson, "Scattering from inhomogeneous penetrable bodies of revolution," *IEEE Trans. Antennas Propagat.*, vol. AP-32, pp. 1163-1173, November 1984.

[7] L. N. Medgyesi-Mitschang and J. M. Putnam, "Integral equation formulations for imperfectly conducting scatterers," *IEEE Trans. Antennas Propagat.*, vol. AP-33, pp. 206-214, February 1985.

[8] R. F. Harrington and J. R. Mautz, "An impedance sheet approximation for thin dielectric shells," *IEEE Trans. Antennas Propagat.*, vol. AP-23, pp. 531-534, July 1975.

[9] B. J. Rubin and S. Daijavad, "Radiation and scattering from structures involving finite-size dielectric regions," *IEEE Trans. Antennas Propagat.*, vol. AP-38, pp. 1863-1873, Nov. 1990.

[10] A. W. Glisson and D. R. Wilton, "Simple and efficient numerical methods for problems of electromagnetic radiation and scattering from surfaces," *IEEE Trans. Antennas Propagat.*, vol. AP-28, pp. 593-603, Sept. 1980.

[11] W. A. Johnson, D. R. Wilton, and R. M. Sharpe, "Modeling scattering from and radiation by arbitrarily shaped objects with the electric field integral equation triangular surface patch code," *Electromagnetics*, vol. 10, pp. 41-63, January-June 1990.

[12] S. M. Rao, D. R. Wilton, and A. W. Glisson, "Electromagnetic scattering by surfaces of arbitrary shape," *IEEE Trans. Antennas Propagat.*, vol. AP-30, pp. 409-418, May 1982.

TOOLBOX FOR CHARACTERIZATION OF MATERIALS

b y
Joan R. Dornfest
Lockheed Missile & Space Company
Research and Development Division
Advanced Systems Technology
3251 Hanover Street
Palo Alto, California, 94304-1187

October 25, 1990

ABSTRACT

Designers need a handy tool to characterize materials for RCS (Radar Cross Section) scattering. This paper describes a three-step strategy for predicting the RCS scattering as a function of impedance for a given shape and frequency. This strategy has been generalized to be applicable to numerous codes.

The actions required to implement this strategy are specified in detail. A specific code, JRMBOR, is used to illustrate and give precise definition to the processes of implementation. (JRMBOR was written at Atlantic Aerospace Electronics Corporation in Greenbelt, Maryland.)

The software to generate multiple runs, and to compile the data needed for plotting, as well as performing the contour graphs, is presented. In summary, all the information for creating a "TOOL BOX FOR CHARACTERIZATION OF MATERIALS" in a minimum amount of time is included.

THREE-STEP STATEGY

1. Predict the RCS for a range of impedances by running the same RCS code multiple times. The size and shape of the body, the frequency of the wave, and all other input variables remain constant except the impedance. The output contains the amplitude and phase for Theta and Phi for one frequency and one impedance, but for a multiple of incident angles.

2. Compile the information for contour plotting by selecting from the multiple outputs only the amplitute and phase for a given incident angle.

3. Generate a contour plot for data selected to show both amplitude and phase for a range of impedances.

ACTIONS

CREATE NEW OUTPUT

To familiarize one with the input and output from the standard version of JRMBOR, in Fig. 1A, a sample input is shown. The input data, when placed in a DCL (Digital Control Language) command file, is used for running JRMBOR on a VAX computer.

In Fig. 1B, a partial output of JRMOUT.DAT, the one output from the standard version of JRMBOR is portrayed. The shape input is a 12" x 1" cyclinder. All output fields are shown. Since the information desired for the plot program is not readily available, JRMBOR required modification. To minimize the modification task and impact to other users,

an additional output was created, rather than modifying the existing one. In Fig. 1C the new output is illustrated.

ADMITTANCE

JRMBOR requires admittance, not impedance for input, but the final contour graphs used impedance. Therefore, a program, CHANGZ.FOR shown in Fig. 2A, was written to convert impedance to admittance, and enter admittance into the input stream at the appropriate point in the JRMBOR.COM command file. Also, the specific case of the impedance equal to zero needed to be defined, to avoid the non-defined case of dividing by zero.

Since JRMBOR is required to run one hundred and seventy-six times, a command file CHANGZ.COM depicted in FIG. 2B, is created. The new file, JRMBOR.COM, created by the CHANGZ program, is copied to another file JRMBOR1.COM (FIG. 2C), and is read by the CHANGZ program during the next run.

MULTIPLE RUNS

The command file RUNJRM.COM, displayed in Fig. 4, submits one hundred seventy-six runs, the desired number for this example. Each run is matched with an impedance; the output from each run later forms one point for the contour graph.

Impedance is a complex number, the real component is displayed along the x-axis, and the imaginary component along the y-axis. The variable, NUM1 when divided by ten is the smallest real component of impedance used. NUM2 when divided by ten is the largest imaginary component.

For one-hundred seventy-six runs, there are sixteen evenly-spaced points along the x-axis, ranging from zero to 1.5.and eleven along the y-axis, ranging from +.5 to -5. NUM2 and NUM2 are written out to ZLIST.DAT, read by CHANGZ and converted to an admittance.

COMPILE THE DATA

READDAT.FOR (Fig. 4A) is the interactive program written to read multiple JRMPLT.DAT files, each one created by one run of the modified JRMBOR program. The program compiles the appropiate data from one-hundred seventy-six runs into one file.

The program queries for the following two pieces of information: first, the number of data files to be searched, and then the size of the incident angle to be used. In Fig. 4B, the compiled data is shown.

CONTOUR GRAPH PROGRAM

After the data is compiled, the next step is to graph it. In Fig. 5, the code is portrayed. It uses routines from the DISSPLA Software Package from Integrated Software Systems Corporation of San Diego, California.

W is the matrix that contains the data for contour plotting. M equals 16 for the sixteen points along the x-axis. N is 11 for the eleven points along the y-axis. It is interactive and allows the user to choose one of four variables: Amplitude (Theta-Theta), Phase (Theta-Theta), Amplitude (Phi-Phi), or Phase(Phi-Phi), as well as to enter the number of points for the contour graph.

In addition, the program normalizes the values for the contour by the value at (0,0), which is 0,0 impedance.

CONTOUR GRAPHS

The contour graph for Amplitude (tt) is shown in Fig. 6A. In a similiar manner, the contour graph for Phase (tt) is portrayed in Fig. 6B. In Fig. 6C, the result is shown of the two graphs being overlayed, in order that the point of intersection is noted clearly.

```
$$$
```

```
CCCC
```

```
cccccccccccccccccccccccccccccccccccccccccccccccccccccccccccccccccccccccccccc

                    OUTPUT OF MODIFIED JRMBOR PROGRAM

                          FILENAME = JRMPLT.DAT

     THE FIRST LINE SHOWS THE FREQUENCY, THE SECOND THE IMPEDANCE Z AND
     THEN THE ADMITTANCE Y. THIS OUTPUT WAS OBTAINED FOR A 12 X 1 CYCLINDER.
     THE AMPLITUDE AND PHASE ARE LISTED FOR THETA AND PHI FOR SEVEN ANGLES.

cccccccccccccccccccccccccccccccccccccccccccccccccccccccccccccccccccccccccccc

WAVE#= 10.67667588 1/M
CONTOUR= 1  Z=(0.150000E+01,-.600000E+00)  [Y=(0.600000E+00,0.200000E+00)]
  7
   0.000       -0.971       41.486       -0.971       41.489
  30.000      -13.117       12.787      -11.861       67.158
  60.000      -17.750     -123.724      -13.456     -179.999
  90.000      -26.475      -87.606      -16.967     -171.296
 120.000      -24.787      -59.689      -19.111      137.005
 150.000      -23.151     -158.005      -15.830       95.818
 180.000      -19.956     -138.728      -19.956     -138.728

cccccccccccccccccccccccccccccccccccccccccccccccccccccccccccccccccccccccccccc
```

FIG. 1C. NEW OUTPUT FROM THE MODIFIED JRMBOR

```
!!!!!!!!!!!!!!!!!!!!!!!!!!!!!!!!!!!!!!!!!!!!!!!!!!!!!!!!!!!!!!!!!!!!!!!!!!!
C
C                          PROGRAM CHANGZ.FOR
C
C     THIS PROGRAM ACCEPTS A NEW COMPLEX # FOR THE IMPEDANCE (Z),
C     CONVERTS IT TO THE ADMITTANCE (Y) AND INSERTS IN INTO THE INPUT
C     DATA FILE FOR JRMBOR FOR THE CASE OF A SPECIAL CYLINDER.
C
C                    DO NOT USE IT FOR OTHER PURPOSES!!!!
C
C1111111111111111111111111111111111111111111111111111111111111111111111111111

      COMPLEX Z,Y,Y1
      DIMENSION A(80)
      OPEN (UNIT=9,NAME='ZLIST.DAT',STATUS='OLD')
      OPEN (UNIT=10,NAME='JRMBOR1.COM',STATUS='OLD')
      OPEN (UNIT=11,NAME='JRMBOR.COM',STATUS='NEW',CARRIAGECONTROL=
     *     'LIST')
      DO 1 I=1,17
         READ(10,100) (A(J),J=1,80)
         WRITE(11,100) (A(J),J=1,80)
100      FORMAT(80A1)
1     CONTINUE
      READ(10,*) Y1
      READ(9,*) N1
      READ(9,*) N2
      AN1 = FLOAT(N1)/10.
      AN2 = FLOAT(N2)/10.
      Z = CMPLX(AN1,AN2)
        IF(CABS(Z).EQ.0.) THEN
          Y = (1.E08,0.)
        ELSE
          Y = 1./Z
      END IF
      WRITE(11,*) Y
      DO 2 I=1,13
         READ(10,100) (A(J),J=1,80)
         WRITE(11,100) (A(J),J=1,80)
2     CONTINUE
      END
```

FIG. 2A. CODE TO CONVERT IMPEDANCE

```
$!!!
```

```
$$$
```

```
!!!
```

```
ccccccccccccccccccccccccccccccccccccccccccccccccccccccccccccccccccccccccccccccc

  THIS DATA HAS BEEN PREPARED FOR THE COUNTOUR PLOT PROGRAM. THE ANGLE USED
  IS PRINTED FIRST.  NEXT, APPEARS THE REAL AND IMAGINERY IMPEDANCE.  AFTER
  THAT IS THE AMPLITUDE AND PHASE FOR THETA AND PHI.  (THIS INFORMATION WOULD
  HAVE TO BE  STRIPPED, IF YOU WERE GOING TO THE DATA.

ccccccccccccccccccccccccccccccccccccccccccccccccccccccccccccccccccccccccccccccc

 100.000
   0.000    0.500   -7.117 -22.428   -7.117 -22.428
   0.100    0.500   -8.017 -23.521   -8.017 -23.521
   0.200    0.500   -8.895 -24.933   -8.895 -24.933
   0.300    0.500   -9.716 -26.647   -9.716 -26.647
   0.400    0.500  -10.509 -28.652  -10.509 -28.652
   0.500    0.500  -11.268 -30.941  -11.268 -30.941
   0.600    0.500  -11.988 -33.501  -11.988 -33.501
   0.700    0.500  -12.627 -36.319  -12.627 -36.319
   0.800    0.500  -13.233 -39.376  -13.233 -39.376
   0.900    0.500  -13.784 -42.647  -13.784 -42.647
   1.000    0.500  -14.275 -46.095  -14.275 -46.095
   1.100    0.500  -14.702 -49.698  -14.702 -49.698
   1.200    0.500  -15.065 -53.362  -15.065 -53.362
   1.300    0.500  -15.363 -57.059  -15.363 -57.059
   1.400    0.500  -15.599 -60.749  -15.599 -60.749
   1.500    0.500  -15.774 -64.372  -15.774 -64.372
   0.000    0.400   -7.275 -10.218   -7.275 -10.218
   0.100    0.400   -8.225 -17.529   -8.225 -17.529
   0.200    0.400   -9.140 -19.175   -9.140 -19.175
   0.300    0.400  -10.017 -21.138  -10.017 -21.138
   0.400    0.400  -10.855 -23.410  -10.855 -23.410
   0.500    0.400  -11.651 -25.985  -11.851 -25.985
   0.600    0.400  -12.400 -28.856  -12.400 -28.856
   0.700    0.400  -13.099 -32.014  -13.099 -32.014
   0.800    0.400  -13.743 -35.443  -13.743 -35.443
   0.900    0.400  -14.325 -39.116  -14.325 -39.116
   1.000    0.400  -14.842 -42.993  -14.842 -42.993
   1.100    0.400  -15.287 -47.028  -15.287 -47.028
   1.200    0.400  -15.658 -51.155  -15.658 -51.155
   1.300    0.400  -15.958 -55.314  -15.958 -55.314
   1.400    0.400  -16.185 -59.438  -16.185 -59.438
   1.500    0.400  -16.345 -63.465  -16.345 -63.465
   0.000    0.300   -7.468  -9.865   -7.468  -9.865
   0.100    0.300   -8.484 -11.289   -8.484 -11.289
   0.200    0.200   -9.433 -13.899   -9.433 -13.899
   0.300    0.300  -10.359 -16.321  -10.359 -16.321
   0.400    0.300  -11.244 -17.866  -11.244 -17.866
   0.500    0.300  -12.087 -20.732  -12.087 -20.732
   0.600    0.300  -12.883 -23.923  -12.883 -23.923
   0.700    0.300  -13.627 -27.438  -13.627 -27.438
   0.800    0.300  -14.313 -31.264  -14.313 -31.264
   0.900    0.200  -14.933 -35.377  -14.932 -35.377
   1.000    0.300  -15.479 -39.736  -15.479 -39.736
   1.100    0.300  -15.948 -44.276  -15.948 -44.276
   1.200    0.300  -16.328 -48.928  -16.328 -48.928
   1.300    0.300  -16.626 -53.665  -16.626 -53.665
   1.400    0.300  -16.840 -58.224  -16.840 -59.224
   1.500    0.300  -16.977 -62.708  -16.977 -62.708
   0.000    0.200   -7.698  -2.764   -7.698  -2.764
   0.100    0.200   -8.747  -4.642   -8.747  -4.642
   0.200    0.200   -9.785  -6.893   -9.785  -6.893
   0.300    0.200  -10.740  -9.183  -10.740  -9.183
   0.400    0.200  -11.675 -12.000  -11.675 -12.000
   0.500    0.200  -12.589 -15.155  -12.589 -15.155
   0.600    0.200  -13.417 -18.888  -13.417 -18.888
                      .                  .
                      .                  .
                      .                  .
   1.200   -0.400 -24.875 -32.516  -24.875 -32.516
   1.300   -0.400 -24.992 -46.695  -24.992 -46.695
   1.400   -0.400 -24.639 -59.485  -24.639 -59.485
   1.500   -0.400 -23.991 -70.072  -23.991 -70.072
   0.000   -0.500  -9.828  47.484   -9.828  47.484
   0.100   -0.500 -11.191  45.787  -11.191  45.787
   0.200   -0.500 -12.503  44.184  -12.503  44.184
   0.300   -0.500 -13.813  42.2 ~  -13.813  42.226
   0.400   -0.500 -15.167  39.8.   -15.167  39.823
```

FIG. 4B. THE COMPILED DATA

```
CCCC
```

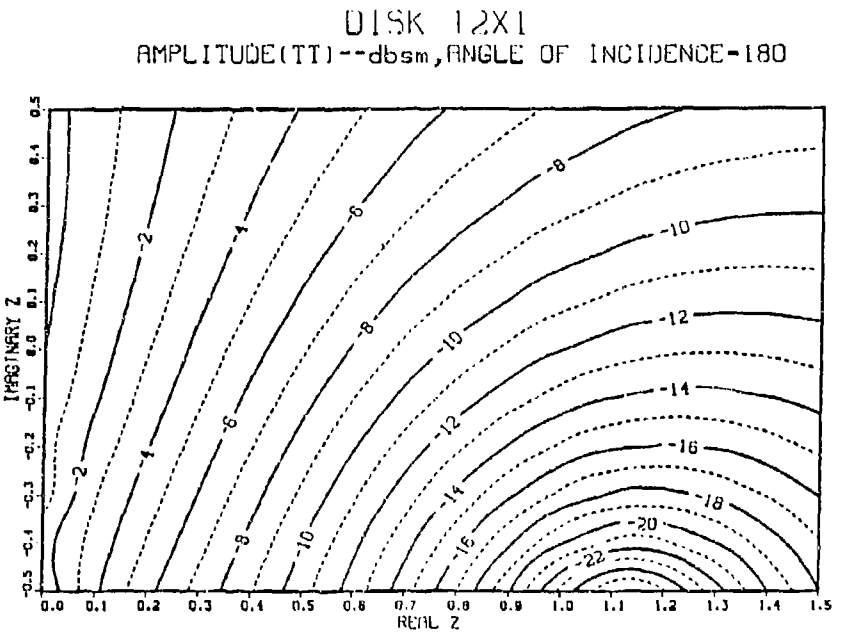

FIG. 6A. CONTOUR PLOT OF AMPLITUDE

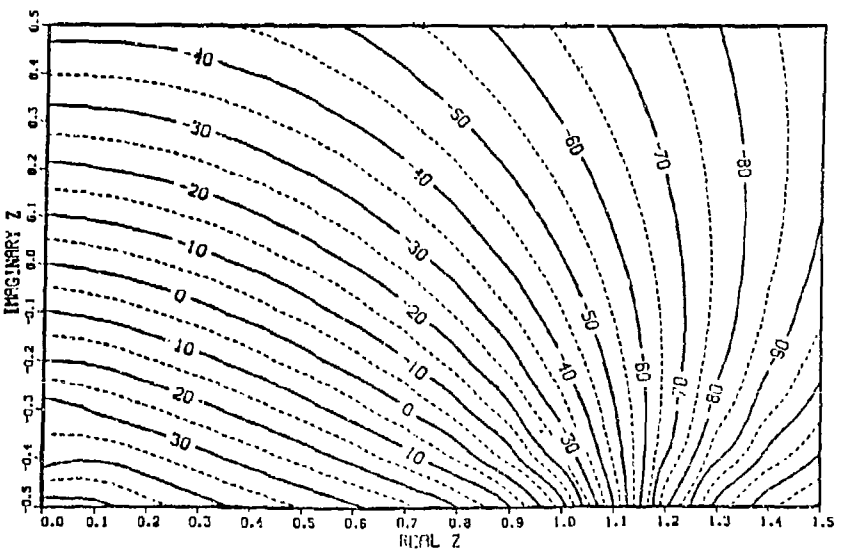

FIG. 6B. CONTOUR PLOT OF PHASE

DISK 12X1

OVERLAY CONTOUR PLOT OF AMPLITUDE & PHASE - INCIDENCE ANGLE = 180

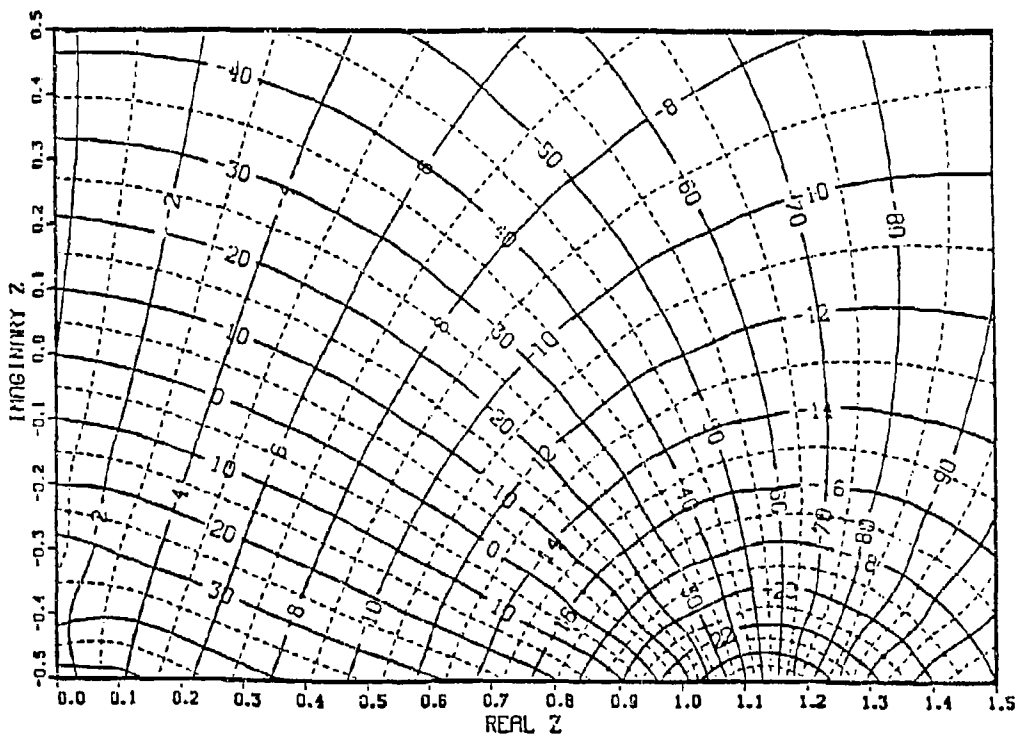

FIG. 6C. OVERLAY CONTOUR PLOT OF AMPLITUDE & PHASE

Polarimetric Scattering and Control of Radar Cross Section of Chiral Targets of Simple Geometries and Associated Code Development

Asoke K. Bhattacharyya
Tel: (505) 522–9468
Department of Electrical and Computer Engineering
New Mexico State University
Las Cruces, NM 88003–0002

I. ABSTRACT

This paper addresses the problem of electromagnetic scattering by chiral targets, namely, a sphere and a cylinder and the possibility of control of radar cross section (RCS) using chirality. It is found that by a proper choice of the radar and target parameters, one can most efficiently control target polarimetric scattering properties. It may be possible to design a chiral target invisible to radar with same transmitting and receiving polarizations since most of the energy would be transformed to the orthogonal polarization. Codes in Fortran for chiral sphere and chiral cylinder scattering have been developed. The chiral cylinder scattering problem has been extended to oblique incidence. The codes developed are handy and easy to use. The input parameters are radar and target parameters including chirality. The output quantities are co and cross pol cross sections with any combination of parameters.

The key conclusions of this study are: (1) the scattering properties of the chiral sphere are aspect dependent (2) the cross polarization component can be considerable for a chiral scatterer (3) there could be a significant difference in the copolar cross section (i.e. S_{11} and S_{22} are different) and also $S_{11} \neq S_{22}$ for a chiral sphere (4) with the chiral cylinder the normal or near normal scattering can be rich in cross–pol component and (5) these simple chiral structures can be used as polarization transformers.

II. INTRODUCTION

The subject of chiral research has attracted the attention of some workers for quite sometime. Chirality or 'handedness' stems from the lack of bilateral symmetry of an object. As a result the medium cannot support plane polarized wave but supports two oppositely rotating circularly polarized waves. An account of chiral research is given in [1,2,3]. It appears to the author that still the chiral research has not matured to conclude that the chiral medium can be successfully used in radar systems. Also, chiral codes are not readily available. The motivation of this work is to study EM scattering from chiral simple objects and develop codes for the same.

III. KEY EQUATIONS IN PROBLEM FORMULATION

We provide below the key mathematical equations for sphere and cylinder scattering.

The far zone scattering matrix $[S^c_{ij}]$ for the sphere [4,5] is–

$$\left[S^c_{ij}\right] = \begin{bmatrix} S^c_{11} & S^c_{12} \\ S^c_{21} & S^c_{22} \end{bmatrix} \tag{1}$$

where the coefficients are–

$$S^c_{11} = \sum_{n=1}^{\infty} \frac{2n+1}{n(n+1)} \left(-a_n \pi_n - b_n \tau_n\right) \quad ; \quad S^c_{12} = \sum_{n=1}^{\infty} \frac{2n+1}{n(n+1)} \left(c_n \pi_n - d_n \tau_n\right)$$

$$S^c_{12} = \sum_{n=1}^{\infty} \frac{2n+1}{n(n+1)} \left(d_n \pi_n - c_n \tau_n\right) \quad ; \quad S^c_{12} = \sum_{n=1}^{\infty} \frac{2n+1}{n(n+1)} \left(-a_n \tau_n - b_n \pi_n\right)$$

$$\pi_n = P_n^1(\cos\theta)/\sin\theta \qquad \tau_n = \frac{dP_n^1(\cos\theta)}{d\theta} \tag{2}$$

where the necessary parameters are available in [4].

The problem of chiral cylinder is discussed in [6,7,8]. In this presentation it is extended to a general case of oblique incidence. Assuming a z–directed incident wave and omitting the detailed steps the co and cross polarized scattered fields canbe shown to be given by–

$$E_z^s = \sum_{n=-\infty}^{\infty} a_n^s \, H_n^{(2)}(\kappa_2 \rho) \, F_n \qquad \text{for TM polarization.}$$

$$H_z^s = \sum_{n=-\infty}^{\infty} b_n^s \, H_n^{(2)}(\kappa_2 \rho) \, F_n \qquad \text{for TE polarization (3a–b)}$$

$k_2 = k_0 \cos\theta$; $F_n = \exp(-i(n\phi + k_2 z \sin\theta))\exp(i\omega t)$

The cross pol components are–

$$H_\phi^S = \sum_{n=-\infty}^{\infty} \left[-\frac{ik_2^2 a}{\mu_2 \omega} H_n^{(2)\prime}(k_2\rho) - \frac{nhb_n^s}{k_2^2 \rho} H_n^{(2)}(K_2\rho) \right] F_n \quad \text{for TE}$$

$$E_\phi^S = \sum_{n=-\infty}^{\infty} \left[-\frac{hn\, a_n^s}{\rho k_2^2} H_n^{(2)}(k_2\rho) + \frac{i\mu_2 \omega \, b_n^s}{k_n} H_n^{(2)\prime}(k_2\rho) \right] F_n$$

for TM polarization

where $N^2 = k_1^2 / k_2^2$; $K = \mu 1/\mu 2$; $\upsilon = k_2 a = k_0 a \cos\theta$; The coefficients a_n^s and b_n^s can be found from boundary conditions.

It can be noted here that in the case for oblique incidence the scattered fields are superposition of TE and TM even though the incident fields are pure TE or TM. This is true for achiral case also.

IV. CODE DEVELOPMENT, RESULTS, DISCUSSIONS AND CONCLUSIONS

Computer codes developed in Fortran are strightforward and handy. The input parameters are radar and target parameters. The target parameters include chirality of the material of which the target is composed of. The codes have been run for many combinations of parameters. Some results are presented. The author expects to project many more results during the session. Fig. 1(a) and 1(b) and Fig. 2(a)–(b) show the co– and cross–pol characteristics of a chiral sphere with different parameters. Fig. 3 through 5 show the properties of an isotropic infinite chiral cylinder under different constraints. The key observations can be summarized as follows. As regards chiral sphere, the scattering properties are aspect dependent. The cross pol components could be significant. There might be an appreciable difference in the copolar cross sections with i=j=1 and with i=j=2 in the [S] matrix. So a chiral sphere acts quite differently for copol case with transmitting and receiving polarizations interchanged. It is also observed that with other parameters remaining constant, the crosspol level can easily change by as much as 50 dB at certain aspects. The cross pol level also vary considerably with ka. For the same value of ka the cross–pol scattering can be con-

siderably stronger than copol scattering. As regards chiral cylinder scattering (Figs. 3 through 5) the following observations are made. The nature of variation of TE and TM cross sections are considerably different than an achiral case. The cross pol scattering may be considerably greater for normal incidence than copol scattering which never happens in the case of achiral cylinders.

It appears to the author from this limited study that even a simple chiral targets like sphere and cylinder can probably be used as a polarization transformer, a radar clutter simulator etc.

V. REFERENCES

[1] A. Lakhtakia, V. K. Varadan and V. V. Varadan–"Time–harmonic Electromagnetic Fields In a Chiral Medium", Springer–Verlag, 1989

[2] A. Lakhtakia (Ed.) –"Selected Papers On Natural Optical Activity", SPIE Milestone Series, SPIE Optical Eng. Press, 1990

[3] S. Bassiri–"Electromagnetic Waves In Chiral Media", in H. N. Kritikos and D. L. Jaggard (Ed)–"Recent Advances In Electromagnetic Theory", Springer–Verlag, 1990

[4] C. F. Bohren–"Light Scattering by an Optically Active Sphere", Chem. Phys. Lett., Vol. 29, 1974, pp. 458–462

[5] A. K. Bhattacharyya –"Control of Radar Cross Section and Cross–polarization Characteristics of an Isotropic Chiral Sphere", Electronics Letters, Vol. 26, No. 14, 5th July, 1990, pp. 1066–1067

[6] C. F. Bohren –"Scattering of Electromagnetic Waves by an Optically Active Cylinder", Jour. Colloid Interface Science, Vol. 66, No. 1, Aug. 1978, pp. 105–109

[7] J. R. Wait–"Scattering of a Plane Wave From a Circular Dielectric Cylinder at Oblique Incidence", Can J. Physics, Vol. 33, 1955, pp. 189–195

[8] A. K. Bhattacharyya–"Electromagnetic Scattering by an Isotropic Chiral Cylinder at Oblique Incidence: Control of RCS and Cross Polarization Characteristics", Under Review in IEEE Trans. AP–S

Legends to the Illustrations

Fig. 1: Variation of 20 Log_{10} ($|S^{c}_{ij}|$) with aspect angle for a chiral sphere

(a) a= λ; μ_r =1.0; ϵ_r =4.0; α =0.003; β = 0.002

(b) a= λ; μ_r =1.0; ϵ_r =4.0; α = β = 0.002

Fig. 2: Co and Cross–polarization Characteristics of the Chiral Sphere

(a) Cross Polarization Characteristics of Chiral Sphere Against Aspect Angle With Radius As a parameter; α =0.003; β =0.002

(b) Variation of Co– and Cross–polarization Levels at θ =0 with ka(α =0.003; β =0.002)

Fig. 3: Log_{10} ($|E^{s}_{ij}|$) Versus Aspect Angle for a Chiral Cylinder; f=10 GHz; β = 0.0045; $k_0 a$ = 6.28; ϵ_R =2.56; μ_R =1.0

Fig. 4: Log_{10} ($|E^{s}_{ij}|$) versus $k_0 a$ for a Chiral Cylinder for Normal Incidence; f= 10 GHz; β =0.0045; ϵ_R =2.56; μ_R =1.0

Fig. 5: Variation of Cross–pol Components With Chirality Parameters With θ =0 and 60 degrees; f=10 GHz; $k_0 a$=6.28;

(a) TE Polarization (b) TM Polarization

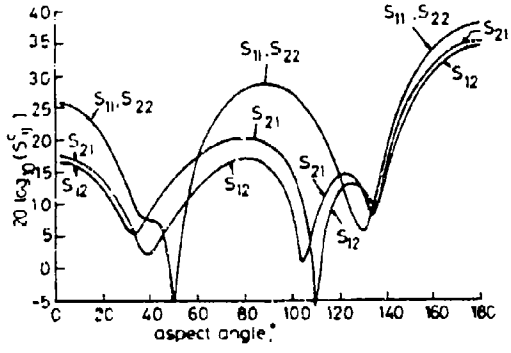

(a) a= λ; μ_r =1.0; ϵ_r =4.0; α =0.003; β = 0.002

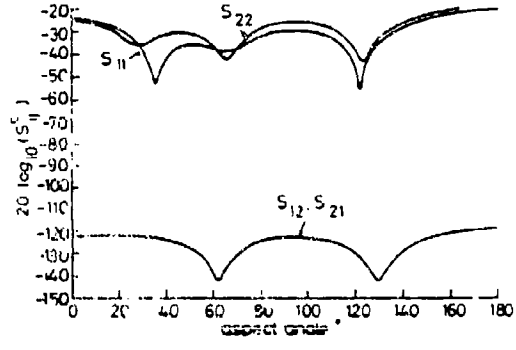

(b) a= λ; μ_r =1.0; ϵ_r =4.0; α = β = 0.002

Fig. 1: Variation of 20 Log $_{10}$ ($|S_{ij}^c|$) with aspect angle for a chiral sphere

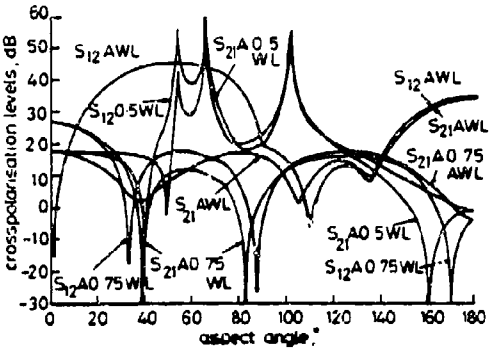

(a) Cross Polarization Characteristics of Chiral Sphere Against Aspect Angle With Radius As a parameter; α =0.003; β =0.002

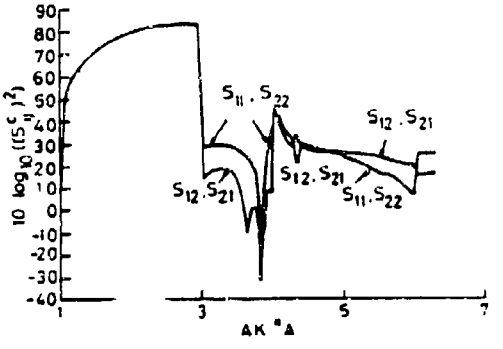

(b) Variation of Co- and Cross-polarization Levels at θ =0 with ka(α =0.003, β =0.002)

Fig. 2: Co and Cross-polarization Characteristics of the Chiral Sphere

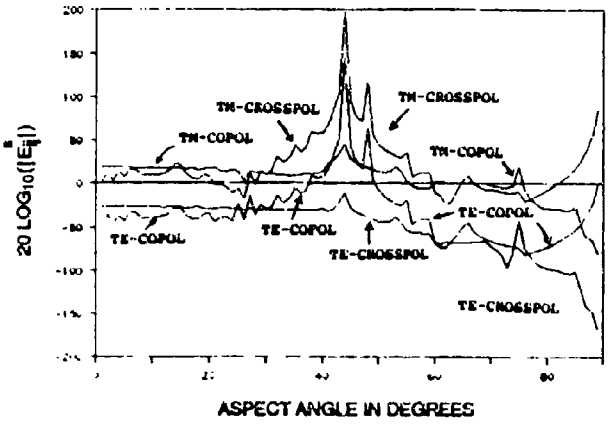

Fig 3: Log_{10} ($|\hat{E}_{ij}|$) Versus Aspect Angle for a Chiral Cylinder;
f=10 GHz; β = 0.0045; $k_0 a$ = 6.28; ϵ_R =2.56; μ_R =1.0

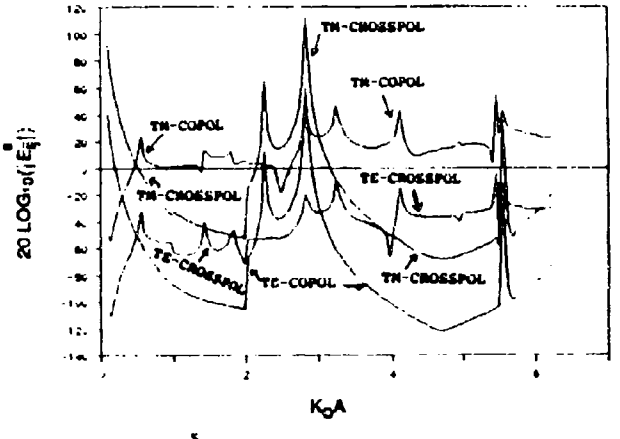

Fig. 4: Log_{10} ($|\hat{E}_{ij}|$) versus $k_0 a$ for a Chiral Cylinder for Normal Incidence;
f= 10 GHz; β =0.0045; ϵ_R =2.56; μ_R =1.0

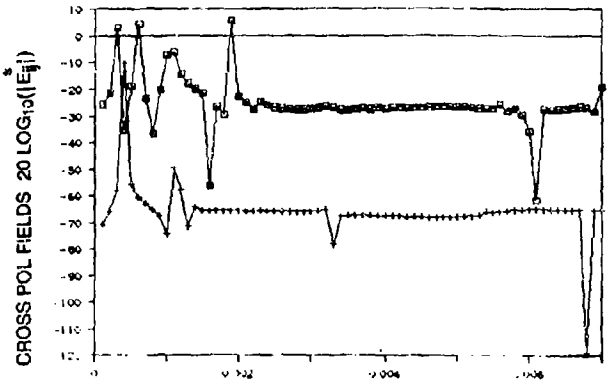

(a) TE Polarization

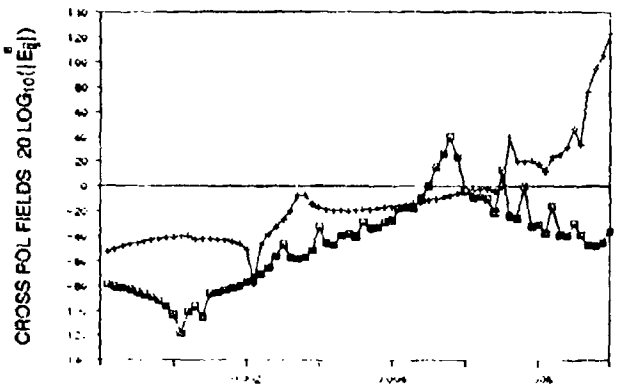

(b) TM Polarization

Fig. 5: Variation of Cross pol Components With Chirality Parameters With θ =0 and 60 degrees; f=10 GHz; k_0a=6.28;

SESSION 9– "HIGH FREQUENCY APPLICATIONS AND WIRE GRID MODELING TECHNIQUES"

Moderator: Christopher Trueman

SCATTERING BY SECTORED CYLINDERS

Benjamin Rulf, Grumman Corporate Research Center, Bethpage, NY 11714

Abstract:

Plane wave time harmonic electromagnetic scattering by a perfectly conducting sectored cylinder, shown in Figures 1(A) and (B), is analyzed for TE and TM polarizations. Mono and bi-static scattering cross sections are obtained for a variety of parameter combinations. The sectored cylinder is a simple model for a body with cavities.

The Problem:

The computation of scattering by large, complex and composite bodies relies on various techniques, such as high frequency asymptotics, finite difference approaches, and methods based on Galerkin's approach (Method of Moments). The need to validate the solutions obtained by these methods against some known "Canonical problems" is vital. For meaningful comparisons with scatterers that are non convex or have open cavities the canonical shapes should also posses such features. Solutions of canonical problems are also needed as benchmarks against which the speed (and other features) of various approximate methods can be compared.

Objectives:

We look for solutions of canonical problems that can model non convex bodies and bodies with cavities. Such solutions should not require physical or geometrical approximations or some a-priori knowledge (such as a clever "Ansatz"). The reason is that the physical and geometrical approximations that are required in various methods often give rise to errors that cannot be quantitatively estimated. Also, there are no systematic ways for guessing a good "Ansatz". On the other hand, it may be possible to find quantitative error bounds if only mathematical approximations are used, such as the summation of infinite series or the solution of infinite systems of linear equations. Also the speed and accuracy do not depend on how good an a-priori guess we found.

Approach:

The method we use is a generalized and somewhat simplified version of [1]. We shall outline the approach here, but omit many details which will appear in [2].

The time-harmonic $\left(e^{i\omega t}\right)$ electromagnetic field in two dimensions can be derived from a single scalar function $u(r,\phi)$. In the case of TM, or perpendicular, polarization we let

$$\underline{E}(r,\phi) = 1_z\, u(r,\phi), \tag{1}$$

$$H_r = \frac{i}{\omega\mu}\,\frac{1}{r}\,\frac{\partial u}{\partial \phi}, \quad H_\phi = \frac{-i}{\omega\mu}\,\frac{\partial u}{\partial r}, \tag{2}$$

and

$$\left(\nabla^2 + k^2\right)u = 0 \quad , k = \omega\sqrt{\varepsilon\mu} \tag{3}$$

On the scatterer's perfectly conducting surface we enforce the Dirichlet condition

$$u=0 \text{ on } S, \tag{4}$$

and on the arc r=a, $0 \le |\phi| < \psi$

$$u \text{ and } \frac{\partial u}{\partial r} \text{ are continuous.} \tag{5}$$

We assume a plane wave excitation in the form

$$u^{in} = \exp[ikr\cos(\phi - \phi')] = \sum_{n=-\infty}^{\infty} q_n\ (\phi')\, J_n(kr)\exp(in\,\phi), \tag{6}$$

$$q_n = [i\exp(-i\,\phi')]^n. \tag{7}$$

The case of TE, or parallel, polarization is analogous, with (4) replaced by a Neumann condition. The details will be given in [2].

We now write in Region 1

$$u=u^{in}+u^s \tag{8}$$

where u^{in} is given by (6) and

$$u^s = \sum_{n=-\infty}^{\infty} A_n H_n(kr) \exp(in\phi). \tag{9}$$

Here A_n are numerical coefficients that have to be computed, and $H_n(kr)$ is the Hankel function of the second kind (which assures that u^s satisfies the radiation condition at $r\to\infty$). For the Bessel and Hankel functions we use the excellent code developed by D. Amos of the Sandia National Laboratory [3]. For the asymmetric case of Figure 1(A) we write in Region 2

$$u = \sum_{j=1}^{\infty} B_j F_j(r,b) \sin[\upsilon_j(\phi+\psi)], \tag{10}$$

where B_j are numerical coefficients, and

$$\upsilon_j = j\xi, \quad \xi = \pi/2\psi, \quad j = 1,2,\ldots \tag{11}$$

We also choose

$$F_j(r,b) = J_{j\xi}(\rho) - J_{j\xi}(\beta)Y_{j\xi}(\rho)/Y_{j\xi}(\beta), \tag{12a}$$

$$F_j(r,0) = J_{j\xi}(\rho),$$

where $\rho=kr$ and $\beta=kb$. These choices assure that u satisfies (4) on the conducting boundaries of Region 2. On r=a we must satisfy (5) at the interface between the regions, and (4) on the conducting body. This implies

$$\sum_{n=-\infty}^{\infty}[A_n H_n(\alpha) + q_n J_n(\alpha)]\exp(in\phi) = \begin{cases} \sum_{j=1}^{\infty} B_j F_j(a,b)\sin[j\xi(\phi+\psi)] & \text{for } |\phi| < \psi, \\ 0 & \text{for } \psi < |\phi| \le \pi. \end{cases} \tag{13}$$

$$\sum_{n=-\infty}^{\infty}\left[A_n\, H_n^{'}(\alpha)+q_n\, J_n^{'}(\alpha)\right]exp(in\phi)=$$

$$=\sum_{j=1}^{\infty}B_j\, F_j(a,b)\,sin\left[j\xi(\phi+\psi)\right]\quad for\,|\phi|<\psi, \tag{14}$$

where α=ka and f'= $\frac{\partial f}{\partial r}|_{r=a}$

We use now the following notation for the orthogonality of the angular functions:

$$<< f_n, f_m >> = \int_{-\pi}^{\pi} f_n(\phi) f_m^{*}(\phi)d\phi, \tag{15}$$

$$< g_j, g_\ell > = \int_{-\psi}^{\psi} g_j(\phi) g_\ell^{*}(\phi)d\phi, \tag{16}$$

<exp(-imϕ), sin[j$\xi(\phi+\psi)$]>=<m,j>. (17)

Thus

<<exp(inϕ), exp(-imϕ)>>=$2\pi\delta_{n,m}$ (18)

<sin [j$\xi(\phi+\psi)$], sin [$\ell\xi(\phi+\psi)$]>= $\psi\delta_{j,\ell}$ (19)

$$< m,j > = \frac{\psi}{i}\ [i^{j}\,\frac{sin(j\xi-m)\psi}{(j\xi-m)\psi}\quad -i^{-j}\,\frac{sin(j\xi+m)\psi}{(j\xi+m)\psi}]. \tag{20}$$

Using these relations and notation we can eliminate the coefficients B_j from (13) and (14) and obtain an infinite system of linear equations for A_n in the form

$$A_m H_m(\alpha)+q_m J_m(\alpha) = \sum_{n=-\infty}^{\infty} [A_n H_n'(\alpha)+q_n J_n'(\alpha)]R_{m,n} \quad m=0,\pm1,\pm2. \qquad (21)$$

$$R_{m,n} = \frac{1}{2\pi\psi}\sum_{j=1}^{\infty}\frac{F_j(a,b)}{F_j'(a,b)} < m,j >< -n,j > \qquad (22)$$

If this infinite system is truncated at n=M, where M is appropriately chosen, then we have in (21) a set of 2M+1 equations which can be solved for A_n, -M≤n≤M. It can be shown that the coefficients A_n become very small when $|n| > ka$. Clearly we need to set M>ka, but we have not yet found out how to choose a minimal M for any combination of the parameters $(a, b, \lambda \text{ and } \psi)$. In all the cases we ran we saw that when M≈ $2ka$ the solutions do not change significantly anymore. This means that we solve $4ka$+1 equations to get good accuracy. More work is needed to quantify the dependence of errors on the choice of M. We also need to truncate the sum in (22) at a point j=L. It can be derived from (12), (20) and (22) that when $j\xi$ >>M the sum converges like $(j\xi)^{-3}$. Thus, for a given angle ψ we cab choose a truncation limit L and estimate the remainder of the series (22) quite accurately. We have obtained good results choosing $L\xi \geq 250$ In all the cases we ran. The choice of L is not critical in terms of the effect on computing time, but here too some additional experimentation is recommended.

When the scatterer is symmetric, as shown in Figure 1(B), the procedure is similar and the result is that $R_{m,n}$ is replaced by $R_{m,n}[1+(-1)^{m+n}]$. An analogous analysis for the TE case will not be shown here but can be found in [2].

The scattering width (SW) is given by

$$\sigma(\phi,\phi') = \lim_{r\to\infty}(2\pi r)\frac{\left|u^s\right|^2}{\left|u^{in}\right|^2} \equiv$$

$$\equiv \frac{4}{k}\left|\sum_{n=-M}^{M} A_n \exp\left[in(\phi+\pi/2)\right]\right|^2. \qquad (23)$$

When $\phi = \phi'$ this represents the mono-static SW, otherwise it is the bi-static SW.

Progress:

We have developed a computer program called SECTOR, based on the above analysis, which computes the mono or bi-static SW of sectored cylinders, symmetric or asymmetrics, for either TE or TM polarization.

To validate the results we have performed a number of tests. First, we have built in with each computation of the A_n coefficients of a sectored cylinder a computation of the coefficients C_n of the corresponding solid cylinder. These are given by

$$-C_n = \begin{cases} q_n J_n(\alpha)/H_n(\alpha), & \text{for TM polarization,} \\ q_n J_n'(\alpha)/H_n'(\alpha), & \text{for TE polarization.} \end{cases} \qquad (24)$$

Clearly, when ψ is very small, ka is large, and the incident wave does not illuminate the missing sector, we expect the numerical difference between A_n and C_n to be very small. This indeed was observed in all the tests that were run.

Another important test was the computation of the SW of a conducting strip, which is a special case of Figure 1(B) when b=0 and $\psi \to \pi/2$. Several cases of mono and bi-static SW of strips were compared with known solutions [4]. Agreements were usually within 1%.

Results and Conclusions:

Following are some figures that show computed results of the SW of large sectored cylinders with large cavities. Figures 2(A) and (B) show the monostatic SW of

a corner reflector that is embedded in a cylinder. The geometrical parameters are: a=1.0 m, b=0, psi=45° and the frequency is 1.67 GHz (ka=35). The typical wide lobes in the directions around ϕ=0° are apparent in both polarizations though the detailed structures of the lobes are slightly different due to the difference in the TE and TM diffraction phenomena. The projected aperature has a width of w =1.414 m at broadside. Physical optics (PO) predicts SW = kw^2 = 70 m at the peak for both polarizations. The actual values are slightly lower as a result of interference between the various field constituents i.e. reflection form the corner reflector and diffraction from the two edges and the smooth part of the cylinder. In both polarizations we notice a sharp spike about ϕ = 45°. Again, according to PO prediction these peaks should be 35 m for both polarizations but are in effect somewhat higher due to interference effects. The computed TM peak values are closer than the TE values to the PO predicted peaks at 0° and 45°. As the angle of incidence increases further, the structure appears more and more like a solid cylinder, especially in the TM case. When the incident wave comes from the back quarter (ϕ>135°) the missing sector is in the deep shadow and the structure is indistinguishable from a solid cylinder. Figure 3(A) shows the bistatic SW for the same corner reflector when the angle of incidence is ϕ = 0°. The sharp spike in the forward direction (ϕ' = 180°) is typical for a large solid cylinder and is not much affected by the presence of the corner reflector. In order to demonstrate this we show in Figure 3(B) the ratio between the bistatic SW of the structure and that of a solid cylinder. The corner reflector causes a large enhancement of the SW in the backward direction, but in the forward direction the ratio approaches unity, i.e. the structure is indistinguishable from a solid cylinder. Figures 4 and 5 show the monostatic SW of a sectored cylinder with a=1.0 m, b=0.4 m, and psi=12°. The frequency yields ka=26 in Figure 4 and ka=42 in Figure 5. Even though it is a fairly simple structure, the patterns are not easy to predict since they represent the combined effects of several wave phenomena such as diffraction by smooth bodies, edge diffraction and the effects of a large open cavity. In all these figures we show the ratio of the structure's SW to the SW of the corresponding solid cylinder for angles of incidence between 0° and 90°. We see that cross section enhancements of up to a factor of 5 may occur. Without this computer program it would be difficult to predict at what angles, frequencies or polarizations these peaks should be expected.

We conclude with the observation that the reported work, and its future generalizations, serve two important purposes. One is simply to serve as an accurate

and reliable benchmark for testing other numerical codes that analyze scattering by certain complex bodies. With some additional work the code SECTOR may become a useful benchmark code for large bodies with cavities, such as jet engines etc. The other purpose, which has not been exploited yet, may be the more interesting one: by doing an extensive parametric study of results that this program would yield we may broaden and deepen our understanding of the various interacting wave processes that occur in scattering by such bodies.

References:

[1] J.B. Billingsley and G. Sinclair: "Numerical Solutions to Electromagnetic Scattering from Strips, Finite Wedges and Notched Circular Cylinders", Can. J. Phys. 44. 3217-3225 (Dec. 1966).

[2] B. Rulf: "Scattering by Sectored Cylinders," submitted for publication

[3] D. Amos, ACM Trans. Math. Software 12 (3), 265-272 (1986)

[4] G.T. Ruck et al: "Radar Cross Section Handbook", Plenum Press, New York, 1970.

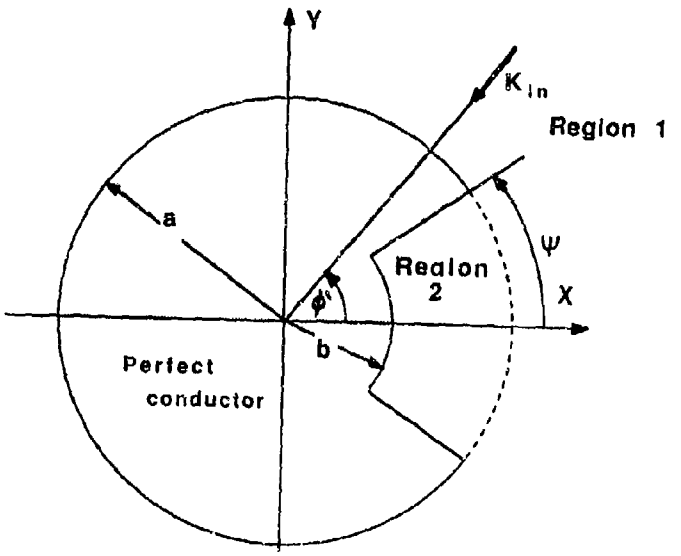

FIGURE 1 (A) THE SECTORED CYLINDER

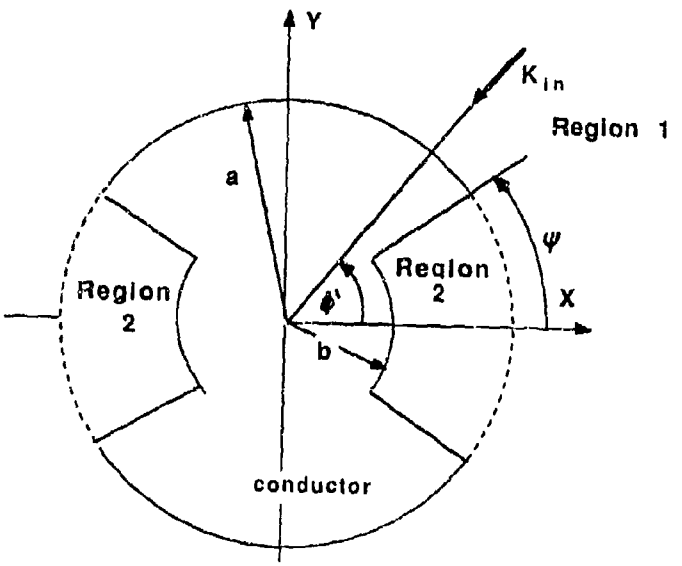

FIGURE 1 (B) THE SYMMETRICAL SECTORED CYLINDER

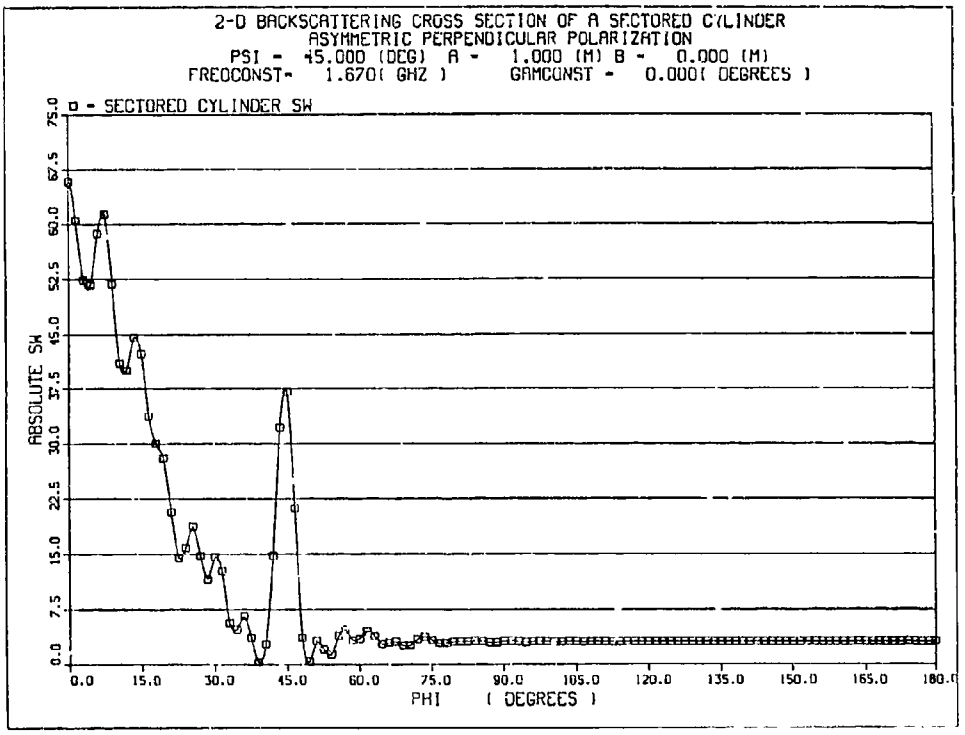

FIGURE 2 (A) CORNER REFLECTOR EMBEDDED IN A CYLINDER WITH A=1.0 M, B=0, PSI= 45 DEGREES KA=35. MONOSTATIC SW, TM POL.

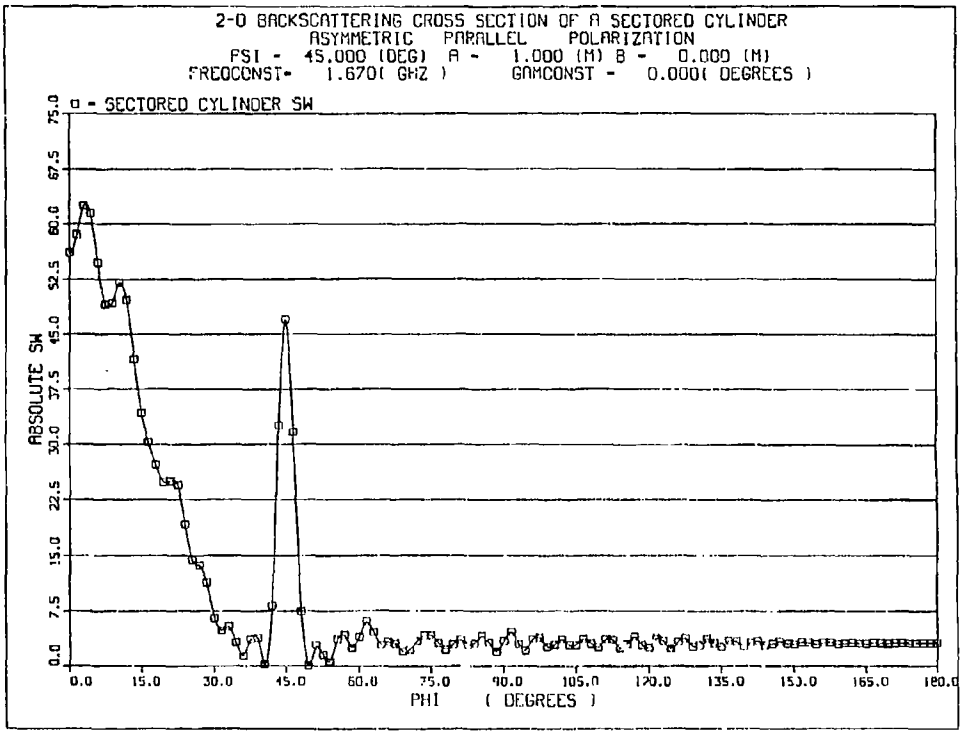

FIGURE 2 (B) SAME AS FIGURE 2 (A) BUT WITH MONOSTATIC SW, TE POL.

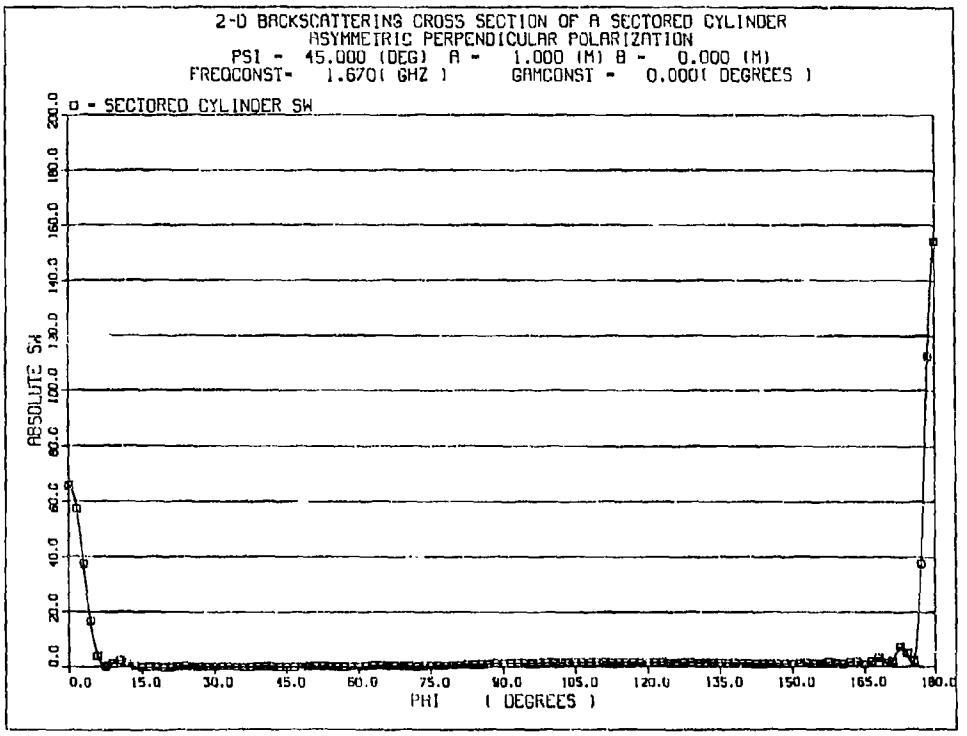

FIGURE 3 (A) SAME CORNER REFLECTOR AS IN FIG. 2 BISTATIC SW, TM POL.

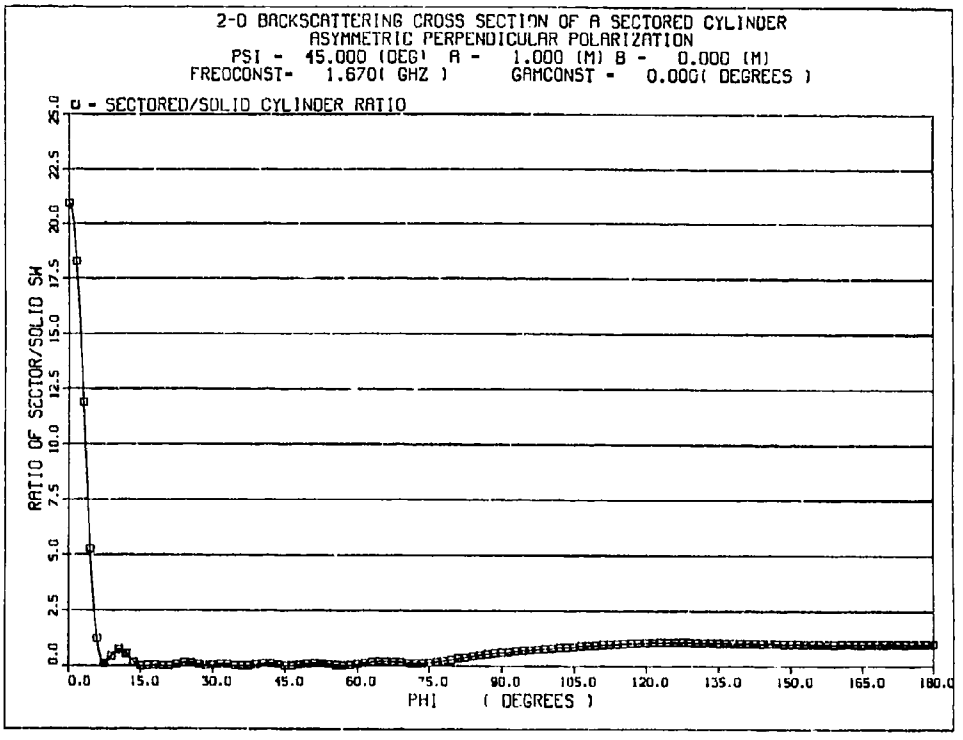

FIGURE 3 (B) RELATIVE BISTATIC SW, TM POL.

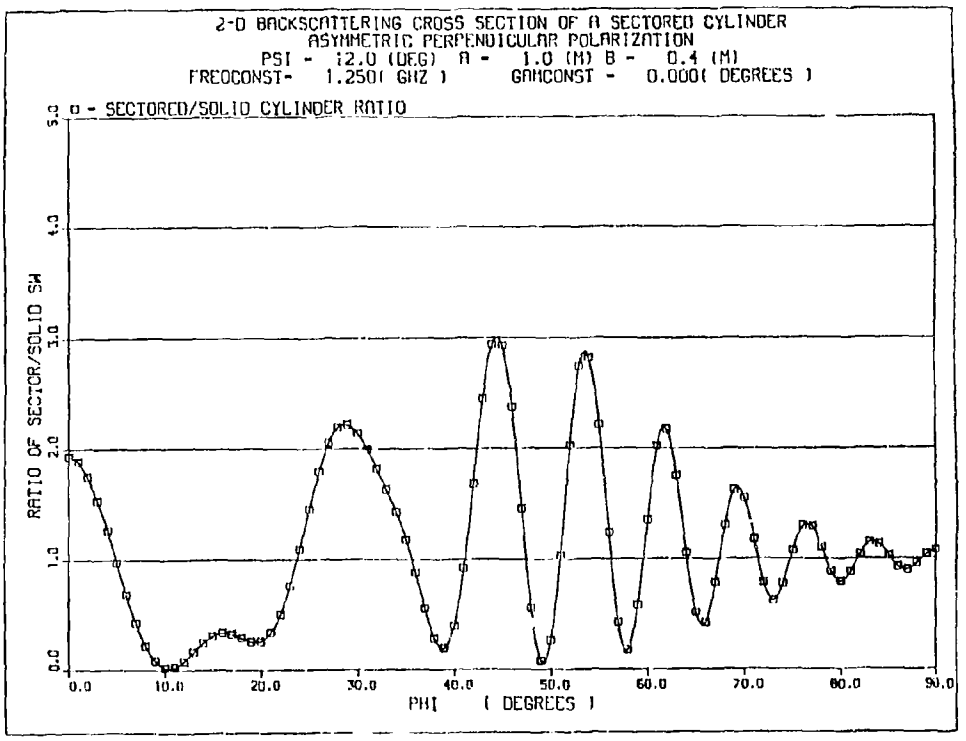

FIGURE 4 (A) SECTORED CYLINDER, A=1.0 M, 3=0.4 M, PSI=12 DEG., F=1.25 GHZ (KA=26), MONOSTATIC SW TM POL.

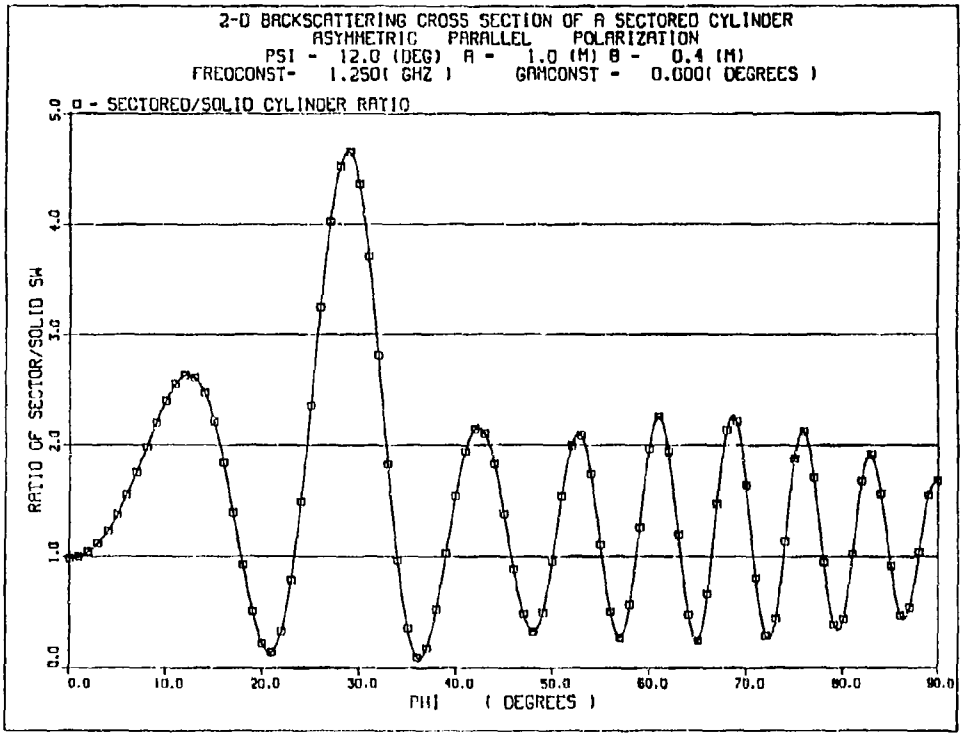

FIGURE 4 (B) SAME AS FIGURE 4 (A) WITH TE POL.

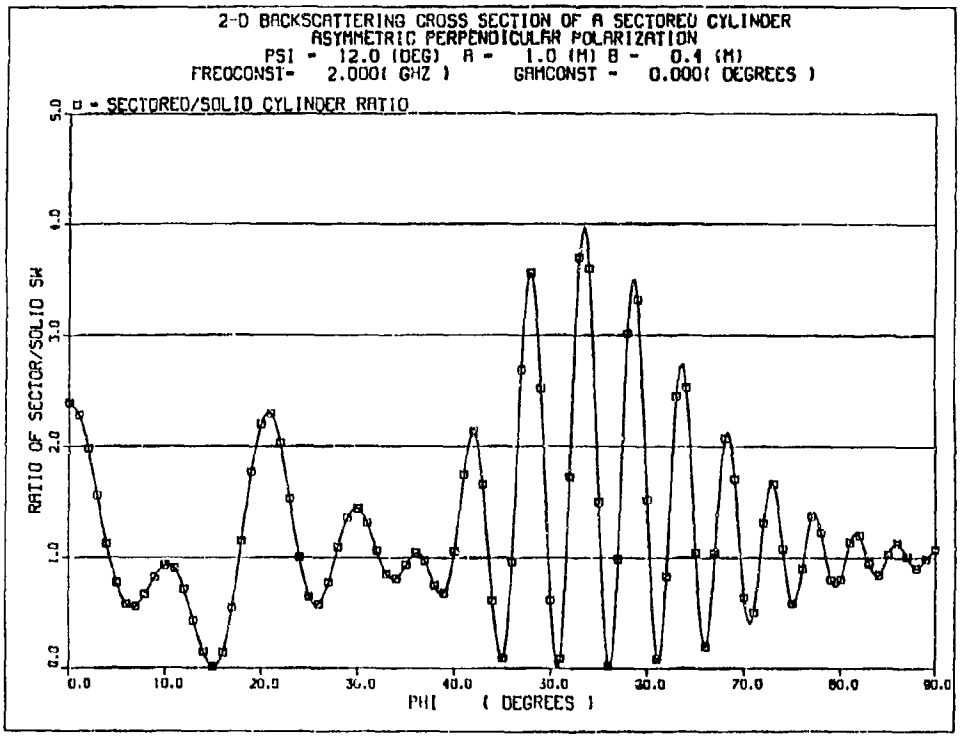

FIGURE 5 (A) SAME CONFIGURATION AS IN FIGURE 4 WITH F=2.0 GHZ (KA=42) TM POL.

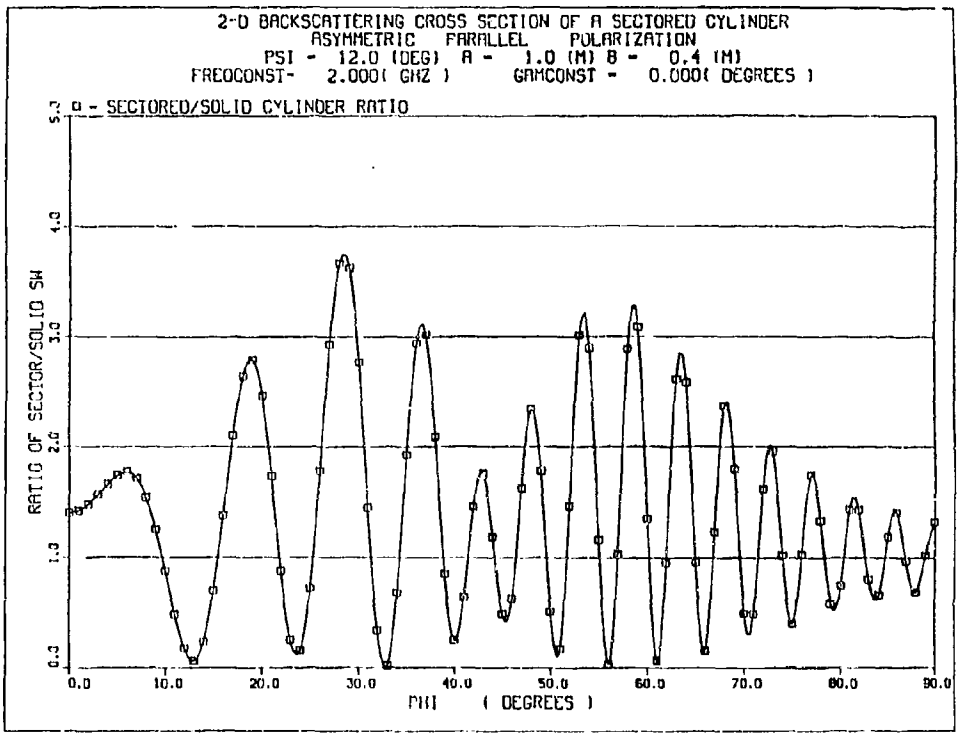

FIGURE 5 (B) SAME AS FIGURE 5 (A) WITH TE POL.

THIS PAGE IS
INTENTIONALLY
LEFT BLANK, ACCIDENTALLY.

RCS of Fundamental Scatterers in the HF Band

by C.W. Trueman*, S.R. Mishra**, and S.J. Kubina*

* Electromagnetic Compatibility Laboratory,
Concordia University,
7141 Sherbrooke Street West,
Montreal, Quebec,
Canada H4B 1R6.

** David Florida Laboratory,
Canadian Space Agency,
P.O. Box 11490, Station H,
Ottawa, Ontario,
Canada K2H 8S2.

Abstract-At HF frequencies a typical aircraft is comparable to the wavelength in size. Wire-grid modelling permits a detailed representation of the aircraft geometry. A moment-method code such as the Numerical Electromagnetics Code determines the currents flowing over the aircraft and its radar cross-section.

This paper proposes a set of "wire-grid guidelines" for constructing grids of complex surfaces such as aircraft. Estimates of the frequency range over which the grid is valid are provided. These guidelines are applied to model a cube, showing good agreement with the measured RCS, and demonstrating the validity of the bandwidth estimate.

Aircraft carry HF antennas for communication purposes. A strip scatterer and a cylinder scatterer are modelled without and with a wire "antenna" to determine the effect of the wire on the RCS. At frequencies making the wire odd multiples of the quarter-wavelength, the wire against the strip or cylinder as "ground" is resonant, and the wire has a large effect on the RCS. Good agreement between measurements and computations is shown.

Introduction

Coastal radar operating at HF frequencies has the potential of covering vast areas of ocean from a single station. The ground wave at HF adheres to the air-ocean interface and it may be possible to see aircraft and ships that are "beyond the horizon" with HF ground-wave radar. The aircraft of Fig. 1 is a complex target for the determination of radar cross-section. The aircraft is about 30 m long and so HF frequencies the aircraft dimensions are comparable to the wavelength. The computer model must represent the entire aircraft, allowing each part to interact with every other part. The aircraft carries wire antennas for HF communication. An objective of this work is to study the effect of the wire antennas on the radar cross-section of the aircraft.

Wire-grid modelling allows a detailed model of the entire aircraft to be constructed and solved. The surface is approximated by replacing it with a grid of thin wires. Ideally, the wires are positioned in two orthogonal directions, subdividing the surface into square cells or meshes. The wire radius is then related to the area of the adjacent meshes by the "equal-area rule"[1].

The currents on a grid of thin wires can be found by solving a thin-wire electric field integral equation(EFIE) by the moment metho '[2,3]. This project uses the well-known "Numerical Electromagnetics Code"(NEC)[4,5]. The derivation of the thin-wire EFIE and its solution by the moment-method lead to certain restrictions which the wire-grid must satisfy. Ref. [6] collects these restrictions as "NEC modelling guidelines" from references [4,5,7]. For the present purpose the essential restrictions are the following. In order that the wires be "thin", the wire radius should be less than $\lambda/30$. Each wire must be subdivided into "segments", which are comparable to $\lambda/10$, although sometimes segments as long as $\lambda/5$ are allowable. Burke[7] suggests that segments be maintained shorter than 0.14λ. Other restrictions on the ratio of the segment length to the wire radius, on wire junctions, and wire spacing are reviewed in reference[6].

This work was supported by the Defence Research Establishment, Ottawa under contract number W7714-9-9216/01-SZ, under the technical supervision of Dr. Tim Coyne.

Modelling Complex Surfaces

The wire-grid modelling guidelines of Table 1 are intended to aid in replacing a complex surface such as the aircraft by an "equivalent" grid of wires. Guidelines 1, 2 and 3 recommend that, ideally, the surface should be represented by an orthogonal grid of wires with square cells of *uniform area* throughout the grid. This is straightforward for regular objects such as plates, strips or cubes. An object of varying cross-sectional size, such as the aircraft fuselage or wings in Fig. 1, cannot use uniform, square cells. The number of cells must be increased as the cross-sectional size increases, to keep the segment length on the cross-sections close to the nominal value. This creates "transitions" from fewer to more cells in the tapered regions. Guideline 4 recommends "elegant transitions" which provide plausible paths for current flow at such a taper, by using some triangular cells. No axial wire is permitted to end abruptly at a circumferential wire. Instead, a diagonal wire must be provided to carry current to a nearby vertex.

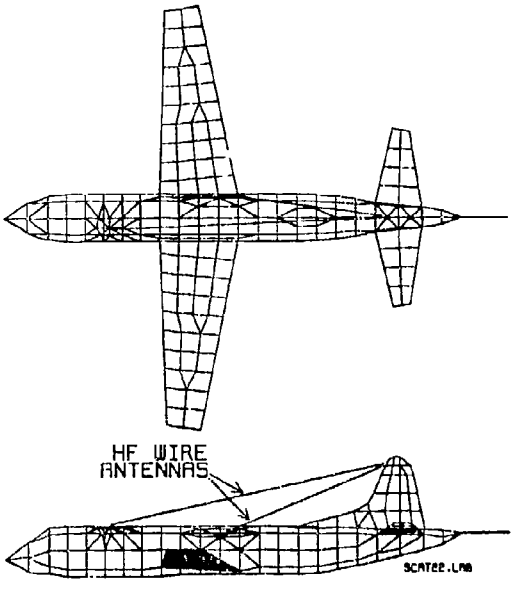

Fig. 1 A wire-grid representation of an aircraft.

Fig. 1 shows "elegant transitions" in the wings, from 4 cells across the wing, to 3 cells, then to 2 cells. These transitions are used to keep the cell area approximately constant over the entire wing surface. Each transition uses a triangular cell to combine currents flowing from the wing base toward the tip on two parallel wires into current on a single wire.

Guideline 5 recommends that wires be put where current is expected to flow. For example, around the "attachment point" of the wire antenna to the fuselage grid, current is expected to flow radially in the aircraft skin. This radial current flow has been supported with a set of 8 radial wires at the "attachment point" of each wire antenna.

A "match point error" occurs when the centre of a segment lies inside the volume of another wire[6]. Guideline 6 forbids wires that meet at shallow angles, with the associated "match point error". Guideline 7 explicitly forbids configurations including match point errors, and is there as a reminder of the restrictions on the wire geometry discussed in [6].

Once a grid has been arrived at, a radius must be specified for each wire, and Guideline 8 recommends that the "equal-area" radius rule be used. A version of the "equal-area rule" applicable to general grids is presented in a companion paper[8].

Guideline 9 addresses the problem of grid cells of small periphery in terms of the wavelength. Sometimes NEC-3 will compute large circulating currents on such cells[7]. The authors' experience is that, as a rule-of-thumb, cell peripheries longer than $\lambda/25$ are safe. Models with smaller cells should be examined carefully for circulating currents.

This paper examines wire-grid models that have been derived with the guidelines of Table 1 in mind, and which use the "equal-area" radius[8]. Models have been verified for "integrity" with program CHECK[6]. The currents and scattered fields are found with NEC-3[2,3].

Table 1
WIRE GRID GUIDELINES

1. Use a rectangular grid of wires oriented parallel to edges, with wires along edges.
2. Choose the segment length equal to $\lambda/10$ at the highest frequency of the band. Keep the area of the grid cells comparable to $(\lambda/10)^2$.
3. Keep grid cells square. Keep the cell area constant, hence segment length constant, throughout the grid.
4. Provide elegant transitions.
5. Put wires where current is expected to flow.
6. Avoid wires meeting at very shallow angles.
7. Keep the center of any segment outside the volume of any other segment.
8. Use the "equal-area rule" radius.
9. All meshes in the grid must have peripheries longer than $\lambda/25$.

Frequency Limitations

A wire-grid mesh is a valid representation of a solid object over a limited bandwidth. This section provides estimates of the lower and upper frequency limits.

If the shortest mesh periphery in the model is L_{min}, then the frequency where the mesh path of length L_{min} is $\lambda/25$ is given by

$$f_{min} = \frac{12}{L_{min}} \text{ MHz}$$

At frequencies less than f_{min}, the currents on the model should be inspected for large currents on individual small meshes.

Table 1 requires that the segments be shorter than $\lambda/10$, and thus the model has its best performance up to the frequency given by

$$f_{seg}^{(1)} = \frac{30}{\Delta_{max}} \text{ MHz}$$

where Δ_{max} is the longest segment length in the model. The model is often useful up to a frequency where the longest segment is $\lambda/5$, given by

$$f_{seg}^{(2)} = \frac{60}{\Delta_{max}} \text{ MHz}$$

However, Burke[7] suggests that NEC's solution not be used above the frequency where the longest segment is 0.14λ. For scattering purposes, wire-grid models often generate useful results at frequencies above $f_{seg}^{(1)}$, but few are useful above $f_{seg}^{(2)}$. In a well-designed wire grid, the longest segment, Δ_{max} is not very much longer than the average segment length, Δ_{av}. Then as the frequency increases all the segments in the model tend to become "too long" at a similar frequency.

If the longest mesh periphery in the model is L_{max}, then the model is limited to frequencies below f_{mesh}, given by

$$f_{mesh} = \frac{300}{L_{max}} \text{ MHz}$$

At this frequency the longest mesh periphery is equal to one wavelength. Above this frequency the long mesh path may be found to exhibit loop resonance. Then that mesh will be seen to carry a large current with a standing-wave pattern like that on a simple one-wavelength loop. In a well-designed wire-grid, f_{mesh} is larger than $f_{seg}^{(2)}$. But in a poorly designed grid which has a few exceptionally long mesh paths, f_{mesh} can be a significant limiting factor.

The thinness of the wires can be limit the bandwidth. If a_{max} is the largest wire radius in the model, then to keep this radius thinner than $\lambda/30$, the frequency must be less than

$$f_{thin} = \frac{10}{a_{max}} \text{ MHz}$$

If the equal-area radius is used on square grid cells of side length Δ, then the wire radius is $\Delta/2\pi$, and the thin-wire frequency limit is $f_{thin} = 62.8/\Delta$ and is approximately equal to the segment length frequency limit $f_{seg}^{(2)} = 60/\Delta$.

It is sometimes useful to estimate the bandwidth of a wire grid based on the average or "mean" segment length, rather than the longest segment. Thus to keep the mean segment length Δ_{av} shorter than $\lambda/5$, the frequency must be less than

$$f_{av}^{(2)} = \frac{60}{\Delta_{av}} \text{ MHz}$$

For scattering purposes, a wire-grid is expected to generate good results up to $f_{seg}^{(1)}$, poorer but useful results up to $f_{seg}^{(2)}$, and poorer but still useful results to $f_{av}^{(2)}$. However, above f_{mesh} the grid is certainly not useful. These limits will be illustrated by the wire-grid models presented below.

Face-on Incidence on a Cube

Fig. 2 shows the a grid model of a perfectly conducting, 15 m cube. The cube uses segments of length 2.14 m, for a total of 588 segments. The cube grid is expected to be useful up to $f_{seg}^{(2)} = 28$ MHz, for segments shorter than one-fifth of the wavelength. The meshes of the grid are one-wavelength long at $f_{mesh} = 35$ MHz. The grid is thus expected to be useful up to a cube size corresponding to $f_{seg}^{(2)}$ of about 1.4λ, but not beyond a cube size corresponding to f_{mesh} of 1.75λ.

Fig. 3 compares the computed cube RCS with measurements by Yaghjian and McGahan[9,10]. Fig. 3 shows surprisingly good agreement of the wire grid result well beyond f_{mesh}. Indeed the wire-grid model is seen to fail gracefully and generates reasonable results at double the f_{mesh} frequency. This is not generally true for wire-grid models.

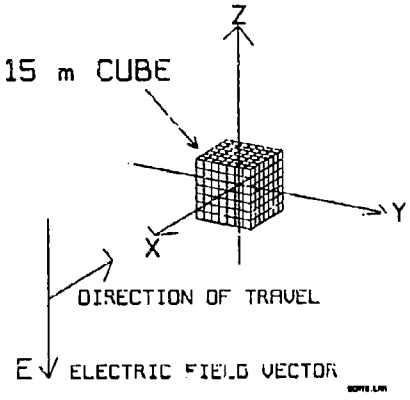

Fig. 2 A wire-grid of a cube with a plane wave incident on one face.

The cube cavity has a rich spectrum of internal resonances starting at size 0.707λ. The wire grid result is expected to fail at the internal resonant frequencies of the cube, but the data of Fig. 3 shows no sign of the dramatic failure often associated with the internal-resonance problem.

The Yaghjian and McGahan measured data of Fig. 3 was used to validate Mishra's measurement procedure at the David Florida Laboratory(DFL). The measurements are taken in a 20 foot anechoic chamber, with an HP 8510 network analyzer, using horn antennas for the 8 to 12 GHz frequency range. The target is mounted on a styrofoam column, and three measurements are taken: column alone, column with reference 7 cm sphere, column with target. The exact Mie series solution for the RCS of the sphere[3] is used to derive a correction factor accounting for the frequency response of the horns and cables. Then the room and column response are vector-subtracted from the target plus room plus column response, to determine the RCS of the target. The frequency range of the measurement will be extended with wider-bandwidth horn antennas.

In Fig. 3, cubes of sizes 1.24 cm, 2.466 cm and 7 cm were measured from 8 to 12 GHz to obtain the RCS in three size ranges. In all three cases the RCS lies close to Yaghjian and McGahan's measurement.

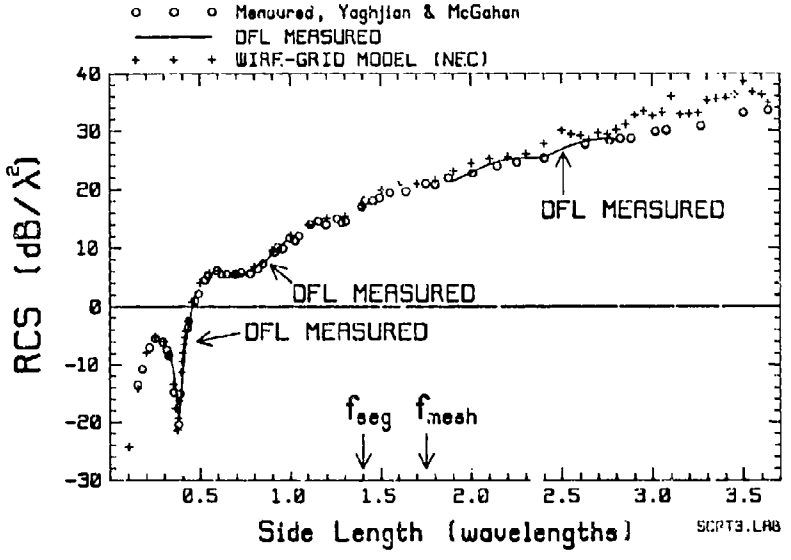

Fig. 3 Comparison of wire-grid results with measured data for the cube.

Vertex Incidence on a Cube

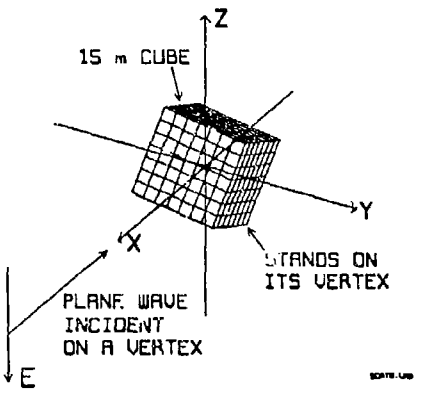

Fig. 4 A plane wave incident upon one vertex of a cube.

Ludwig[11] reports measurements by Flesher of the RCS of a cube with a plane wave incident upon one vertex, as shown in Fig. 4. The cube has vertices on the z-axis and the x-axis, with the plane wave incident upon a vertex of the cube. Fig. 5 compares the calculated cube RCS with Flesher's measurements. Up to the frequency $f_{seg}^{(1)}$ where the segments are one-tenth of the wavelength, the agreement is very good. Between that frequency and the frequency $f_{seg}^{(2)}$ where the segments are one-fifth wavelength, the agreement is poorer but the model is still useful. Above f_{mesh} where the meshes are longer than a wavelength, there is little agreement. Thus the comparison clearly demonstrates that wire-grid models should not be used above f_{mesh}.

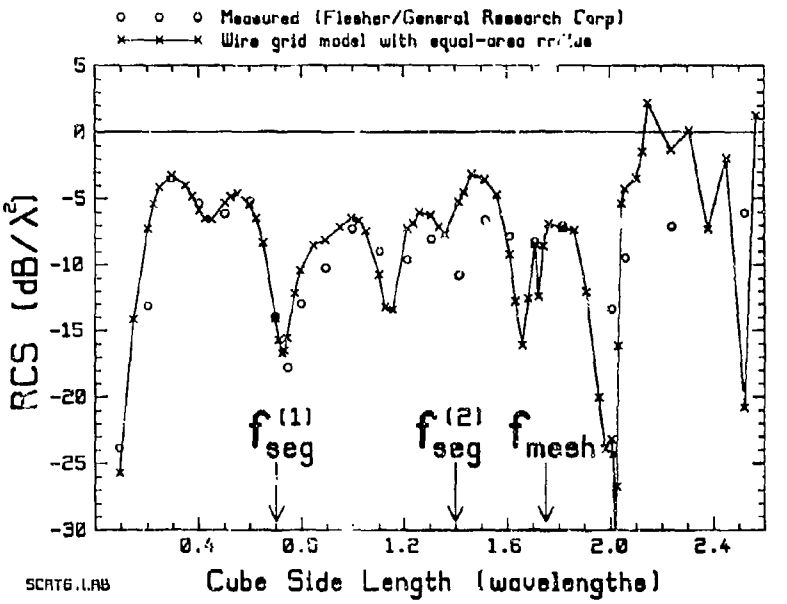

Fig. 5 Comparison of the wire-grid model's RCS with Flesher's measured result.

Strip-with-Wire

Fig. 6 shows a strip scatterer which was designed for measurement in the 1 to 16 GHz frequency range, such that it would be qualitatively similar to the behaviour of the aircraft with its wire antennas in the low HF range. The initial measurement of the RCS of the strip was limited by the available horn antennas to frequencies from 8 to 12 GHz, and it is intended to obtain wider-band horns so that a more complete measurement of the RCS may be made.

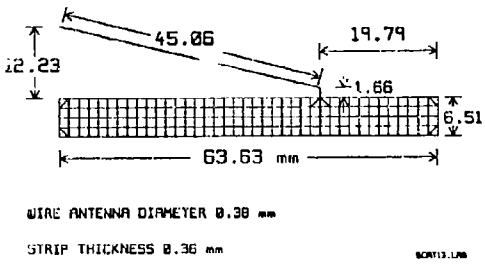

Fig. 6 A strip scatterer with a wire "antenna".

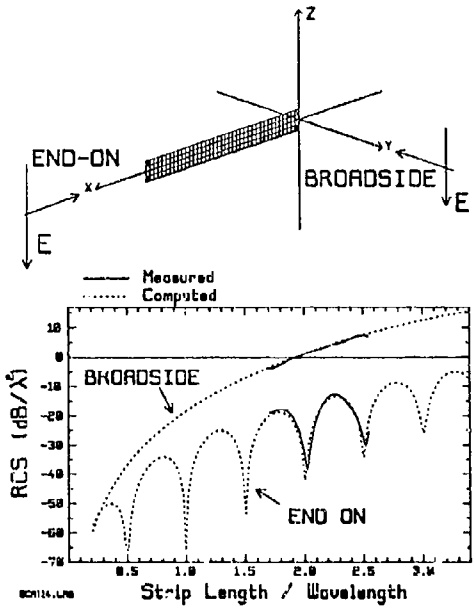

Fig. 7 Comparison of the RCS of the strip alone for broadside incidence with that for end-on incidence.

The strip provides a relatively simple target to model, for which a wire-grid model is expected to yield very accurate results. Fig. 6 shows the wire-grid model of the strip, which uses segments about 1.635 mm long. The frequency limit is $f_{seg}^{(0)}$=18 GHz for 0.1 wavelength segments, well above the 8 to 12 GHz frequency range where measured data was taken. The strip wire-grid includes two additional wires to serve as "radials" at the feed point, and "corner cutter" wires at each corner. The wire radii were derived as described in Ref. [8]. Thus the edge wires use about half the radius of the wires embedded in the grid. The radials and corner cutters use even thinner radii, related to the areas of the adjacent mesh cells.

Fig. 7 shows that for broadside incidence the strip RCS increases uniformly with strip length(frequency). The electric field induces current flow from the bottom edge to the top edge of the strip, which is fairly uniformly distributed across the width of the strip. At the low end of the frequency band of Fig. 7, the RCS increases at about 18 dB per octave of frequency, similar to the "Rayleigh" region of the sphere's RCS curve[3]. At the high end in Fig. 7, the RCS increases at about 6 dB per octave of frequency, similar to the "optical" region for the sphere.

For end-on incidence the strip RCS is quite similar to that found in Ref. [12]. The magnetic field is perpendicular to the strip surface hence it induces loop currents flowing on the strip surface. The regularly spaced series of peaks and sharp troughs arises because of interference of the fields scattered by current on the leading edge and on the trailing edge of the strip. The height of the peaks increases at about 6 dB per octave.

Fig. 7 compares the computed strip RCS with Mishra's measured data. The

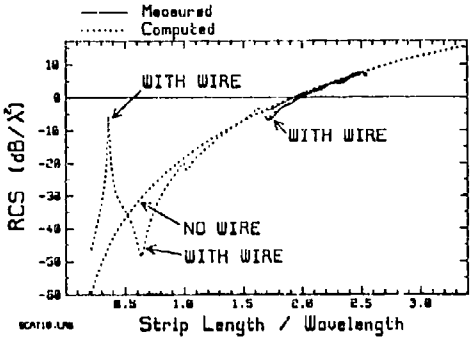

Fig. 8 Comparison of the RCS of the strip alone with that of the strip with the wire "antenna", for broadside incidence.

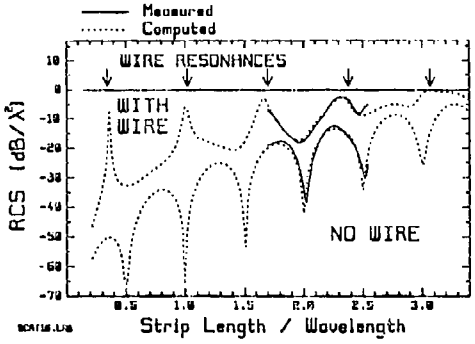

Fig. 9 Comparison of the RCS of the strip alone with that of the strip with the wire "antenna", for end-on incidence.

agreement with the measurement is quite good. There is a slight misalignment in the frequency at which the minima in the graph occur.

Fig. 8 compares the RCS of the strip with and without the wire, for broadside incidence. The wire antenna operated against the strip as a "ground" is expected to have resonances when its length is an odd multiple of the quarter-wavelength. Thus the 46.72 mm wire will have resonances at 1.61, 4.82, 8.03 and 11.24 GHz, corresponding to strip lengths of 0.341, 1.02, 1.70 and 2.38 wavelength, respectively. With the wire the strip RCS has a very sharp, narrow peak at a strip length(frequency) which makes the wire a quarter-wavelength long. There follows a sharp trough in the RCS. The strip with wire RCS shows small variations near the second and third resonant frequencies of the wire, where the wire is $3\lambda/4$ and $5\lambda/4$ in length. The wire does not have a dramatic effect on the broadside RCS at these frequencies, largely because the strip itself is such an effective scatterer for broadside incidence.

Fig. 9 compares the RCS of the strip with the wire "antenna" to that of the strip alone, with the plane wave incident end-on. The wire substantially enhances the RCS of the strip for end-on incidence, and that there are sharp peaks in the computed data at the frequencies expected for the resonances of the wire. There is good agreement with Mishra's measured data over the 8 to 12 GHz frequency range.

Fig. 10 compares the strip RCS for "nose-on" incidence and "tail-on" incidence. At low frequencies, there is little difference. Above the third resonant frequency of the wire, the "nose-on" and "end-on" curves differ by about 10 dB, and above the fifth resonant frequency the two curves deviate substantially. The measured data agrees well with the computations.

Cylinder-with-Wire

The aircraft fuselage is much more like a cylinder than a strip. A cylinder thus has substantial volume compared to a strip. Also, for end-on incidence the nature of the currents induced by the magnetic field on a cylinder might be thought to be different from those induced on a strip, hence an RCS like that of Fig. 7 for end-on incidence might not be expected. Fig. 11 shows a cylinder of dimensions similar to the strip of Fig. 6. The wire grid model has longest segment 2.37 mm, hence is limited in frequency to 23.3 GHz for segments shorter than $\lambda/5$. The longest mesh limits the frequency to f_{mesh} =29.91 MHz.

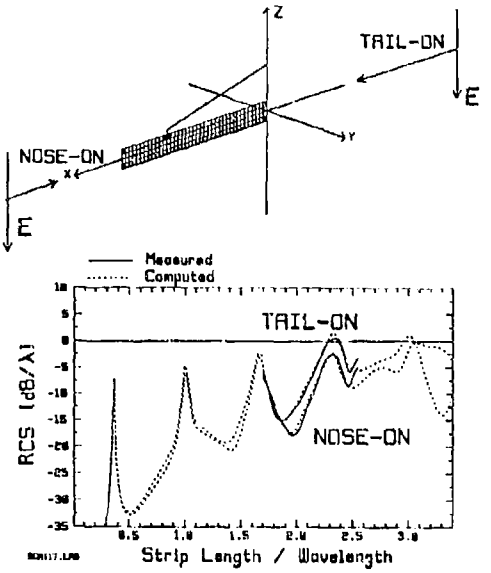

Fig. 10 Comparison of the RCS of the strip with the wire "antenna" for two directions of "end on" incidence.

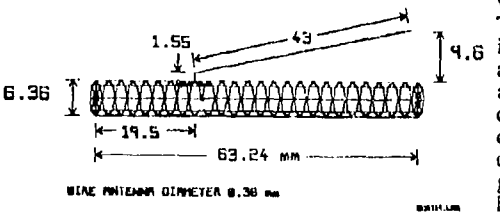

Fig. 11 A cylinder scatterer with a wire "antenna".

Fig. 12 shows the RCS of the cylinder without the wire. For broadside incidence the cylinder RCS rises monotonically, with slope about 18 dB per octave for small lengths(low frequencies), and so the cylinder is in the "Rayleigh" region of scattering. For long lengths(high frequencies) the slope is 6 dB per octave and the cylinder is in the "optical" region. For end-on incidence the cylinder does have the same set of regularly-spaced peaks and troughs that were seen in the strip RCS of Fig. 7. For end-on incidence the cylinder is in the resonance region over this whole range of cylinder lengths.

Fig. 12 compares the computations with the wire-grid model with the DFL measured data from 8 to 12 GHz. The agreement is quite good. As was found for the strip, there is some misalignment of the frequencies at which the sharp minima in the RCS curve fall.

The wire "antenna" length is 44.55 mm, and operating against the cylinder as "ground" has resonances at 1.68, 5.05, 8.42 and 11.78 GHz, when the cylinder is 0.354, 1.06, 1.77 and 3.19 wavelengths in length, respectively. Fig. 13 compares the cylinder RCS for end-on incidence without the wire to that with the wire. The wire greatly enhances the cylinder RCS. The wire introduces tall, narrow peaks at its resonant frequencies. There is reasonable agreement between the computations and Mishra's measurements. This cylinder was rather roughly made, and it was difficult to keep the wire straight and well centered, hence the agreement is not as good as that obtained for the strip. We hope to carry out a more precise cylinder RCS measurement over a wider bandwidth.

Conclusion

This paper proposes a set of guidelines for constructing wire-grid models, and applies them to model a cube, a strip and a cylinder. The wire radii are chosen by the "equal-area rule" discussed in references [1] and [8]. Estimates of the frequency limitations of a given wire-grid model are given and are shown to be reasonable for the cube.

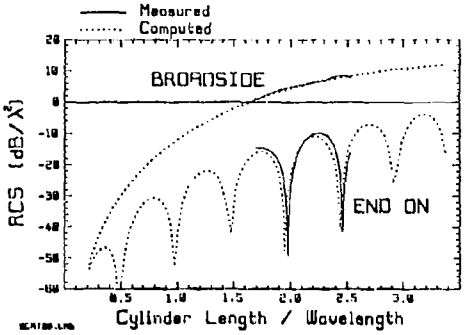

Fig. 12 Comparison of the RCS of the cylinder alone with that of the strip with the wire "antenna", for broadside incidence.

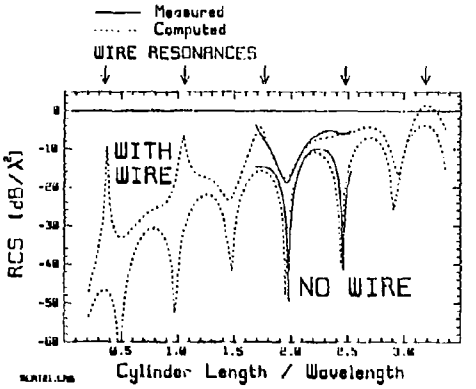

Fig. 13 Comparison of the RCS of the cylinder alone with that of the strip with the wire "antenna", for end-on incidence.

Scattering from a strip and a cylinder has been presented, showing similar RCS for targets of a similar size. The effect of a wire "antenna" on the RCS of the strip or cylinder was demonstrated. It was shown that, for the case of end-on incidence, the wire "antenna" dramatically changes the RCS. The wire against the strip or cylinder as "ground" is resonant at odd multiples of the quarter-wavelength. At those frequencies the wire carries a large current and its scattered field dominates.

Generally good agreement has been obtained between Mishra's measurements of RCS done at the David Florida Laboratory for cubes, strips and cylinders, and the wire-grid calculations. Some small misalignment of the frequency of the sharp troughs in the RCS has been found. In future the bandwidth of the measurement will be increased by using wider-band horn antennas.

The results shown here are directly applicable to the RCS expected of an aircraft carrying wire antennas. For nose-on incidence, the fuselage-alone scatters like the strip or the cylinder. The wire antennas contribute tall, sharp resonance peaks, and some troughs. For an aircraft such as that of Fig. 1, carrying a pair of wire antennas, there will be a dual set of wire resonances.

References

1. A. Ludwig, "Wire Grid Modelling of Surfaces", IEEE Trans. on Antennas and Propagation, Vol. AP-35, No. 9, pp. 1045-1057, September, 1987.
2. R. Mittra, Editor, "Numerical and Asymptotic Techniques in Electromagnetics", Springer-Verlag, New York, 1975.
3. C.A. Balanis, "Advanced Engineering Electromagnetics", Wiley, New York, 1989.
4. G.J. Burke and A.J. Poggio, "Numerical Electromagnetics Code - Method of Moments, Part I: Program Description-Theory", Technical Document 116, Naval Electronic Systems Command(ELEX 3041), July, 1977.

5. G.J. Burke and A.J. Poggio, "Numerical Electromagnetics Code - Method of Moments, Part III: User's Guide", Technical Document 116, Naval Electronic Systems Command(ELEX 3041), July, 1977.
6. C.W. Trueman and S.J. Kubina, "Verifying Wire-Grid Model Integrity with Program CHECK", Applied Computational Electromagnetics Society Journal, Vol. 5, No. 2, Winter, 1990.
7. G.J. Burke, "Recent Advances to NEC - Applications and Validation", Lawrence Livermore National Laboratory preprint number UCRL-100651, March 3, 1989.
8. C.W. Trueman and S.J. Kubina, "Automated Radius Calculation for Wire-Grid Models", 7th Annual Review of Progress in Applied Computational Electromagnetics, Monterey, March, 1991.
9. A.D. Yaghjian and R.V. McGahan, "Broadside Radar Cross-Section of the Perfectly-Conducting Cube", IEEE Trans. on Antennas and Propagation, Vol. AP-33, No. 3, March 1985.
10. M.C. Cote, M.B. Woodworth and A.D. Yaghjian, "Scattering from the Perfectly Conducting Cube", IEEE Trans. on Antennas and Propagation, Vol. 36, No. 9, pp. 1321-1329, Sept., 1988.
11. A. Ludwig, "Backscattering from a Cube", Applied Computational Electromagnetics Society Journal, Vol. 2, No. 2, pp. 55-74, Fall, 1987.
12. E.F. Knott, V.V. Liepa and T.B.A. Senior, "Plates and Edges", IEEE Trans. on Antennas and Propagation, Vol. AP-19, No. 6, pp. 788-789, November, 1971.

Automated Radius Calculation for Wire-Grid Models

by C.W. Trueman and S.J. Kubina

Electromagnetic Compatibility Laboratory,
Concordia University,
7141 Sherbrooke Street West,
Montreal, Quebec, Canada H4B 1R6.

Abstract-Ideally, a wire-grid model represents a solid surface with an orthogonal grid of wires, with square cells of a uniform size. But a grid of a complex surface such as an aircraft has many occurrences of irregular, non-square mesh cells, such as triangles, quadrilaterals, pentagons and so forth. The "equal-area rule" is often used to compute the wire radius for a uniform orthogonal grid, but it is difficult to apply to a general grid not conforming to the "orthogonal grid" ideal.

This paper postulates a modification of the "equal-area rule" which can be applied to grids of complex surfaces. The proposed "adapted equal-area rule" obtains the same radius as the "equal-area rule" for orthogonal grids of square cells. The "adapted" rule satisfies the criterion of subdivision: if a wire is sub-divided into two wires, the radius is unchanged. Also, if a short wire is a member of two large area grid cells, the "adapted" rule obtains a reasonable radius value. The "adapted equal-area rule" specifies a unique radius value for each wire of the grid depending on the geometry of the adjacent meshes.

The radius calculation process has been automated. Program "MESHES" reads a NEC geometry file and produces a mesh membership file "MESHES.MSH". Program "FNDRAD" uses MESHES.MSH to determine the radius of each wire, and outputs a revised NEC geometry file. The MESHES-FNDRAD sequence makes the re-calculation of radius quite straightforward, and readily repeated when small changes are made to the model.

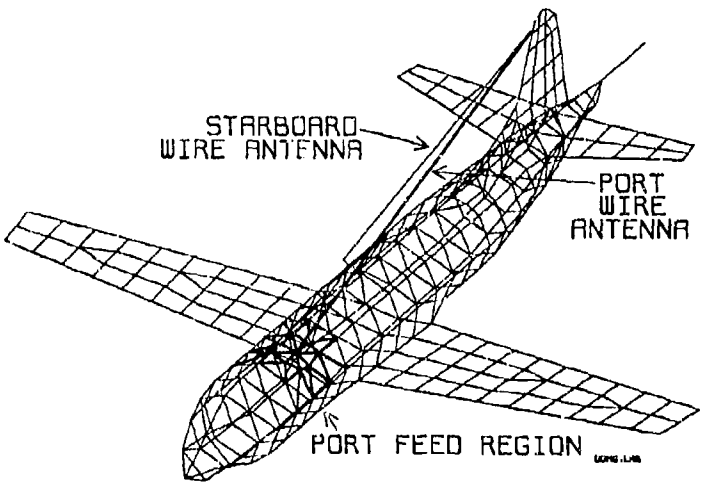

Fig. 1 A wire-grid model of an aircraft with two HF wire antennas.

Introduction

Wire-grid models are used to calculate radiation and scattering from solid objects such as cylinders, spheres, cubes, and less regular surfaces such as aircraft, at frequencies where the dimensions are comparable to the wavelength. Fig. 1 shows a wire-grid model of an aircraft, to be solved with the Numerical Electromagnetics Code(NEC)[1,2] for the antenna patterns or for the scattered fields. Ideally, the aircraft surfaces are to be modelled as an orthogonal grid of wires, with square cells of a uniform size. For the most part the fuselage and wings in Fig. 1 have been represented with a quasi-orthogonal grid of wires with nearly-square cells. But where the fuselage tapers, and where the wings taper, triangular mesh cells have been used. In the feed region of each HF wire antenna, illustrated in Fig. 2, radial wires have been used to support radial current flow near the attachment point. This subdivides the surface into triangular mesh cells. Further, the radials themselves consist of two wires in series, of unequal length, as shown by wires #1 and #2 in Fig. 2. Each wire of the grid must be assigned a wire-radius before the model can be "run" with NEC or another wire-grid analysis program. The objective of this paper is to define a "rule" for assigning a radius which can be applied to complex grids such as those shown in Figs. 1 and 2.

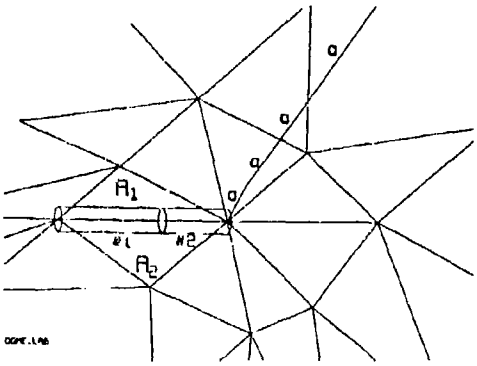

Fig. 2 The feed region of the port wire uses radial wires about the attachment point, and contains triangular mesh cells. Wires which are part of the wire antenna are marked "a".

The "equal-area rule"[3] is often used to compute the wire radius for a uniform orthogonal grid, but it is difficult to apply to a general grid not conforming to the "orthogonal grid" ideal. This paper postulates a modification of the "equal-area rule" which can be applied to grids of complex surfaces. The calculation of radius is then automated in programs called "MESHES" and "FNDRAD".

The "Equal-Area Rule"

Burke and Miller[4] summarize the literature on wire radius for wire-grid models of surfaces. For an orthogonal grid of wires representing a surface, as shown in Fig. 3, the "equal-area rule" states that the radius is chosen such that total surface area of the wires in one orthogonal direction is equal to the area of the surface. Lee, Marin and Castillo[5] show that the equal-area radius makes the inductance of the wires equal to the inductance of the surface. Ludwig[3] shows that, for an infinite cylinder modelled with a uniform array of infinite wires, the equal-area choice of radius is an exact solution. Paknys[6] shows that, for scattering from a cylinder, the "equal-area" radius is the value that minimizes the field in the interior of a wire-grid model of the cylinder. But the literature offers little explicit guidance for choosing the radii for a more general grid, such as that of Figs. 1 or 2.

In the orthogonal grid of Fig. 3 the cells are square if $\Delta_1 = \Delta_2 = \Delta$, of area $A_1 = A_2 = \Delta^2$. The "equal-area rule" radius can be interpreted to state that the wire of length Δ represents half the area of patch A_1 and half the area of A_2, so the radius is chosen according to

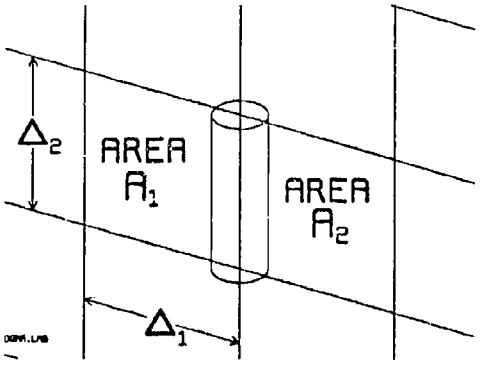

Fig. 3 A wire in an orthogonal wire grid. The grid has square meshes if $\Delta_1 = \Delta_2$.

$$2\pi a\Delta = \frac{A_1 + A_2}{2}$$

hence

$$a = \frac{A_1 + A_2}{4\pi\Delta} \qquad ..(1)$$

hence with square cells having $A_1 = A_2 = \Delta^2$ the wire radius is $\Delta/2\pi$. Fig. 4 applies the "equal-area rule" to an orthogonal grid wih rectangular cells, with $\Delta_1 > \Delta_2$. Then the surface area of wire #1 represents half the area of patch $A_1 = \Delta_1\Delta_2$ and half of $A_2 = \Delta_1\Delta_2$, so that the radius a_1 of wire #1 is chosen according to

$$2\pi a_1\Delta_1 = \frac{A_1 + A_2}{2} = \Delta_1\Delta_2$$

hence $a_1 = \Delta_2/2\pi$ and $a_2 = \Delta_1/2\pi$, and so the wire radii are different. The "equal-area rule" makes the wire radii proportional to the spacing of the parallel wires. This is unlike the equal radii actually shown in Fig. 4.

The "Adapted Equal-Area Rule"

In order to compute wire radii for a general grid such as the aircraft of Fig. 1, the "equal-area rule" has been adapted to be directly applicable to non-orthogonal geometries such as that of Fig. 2. Some important requirements of the "adapted rule" are as follows.

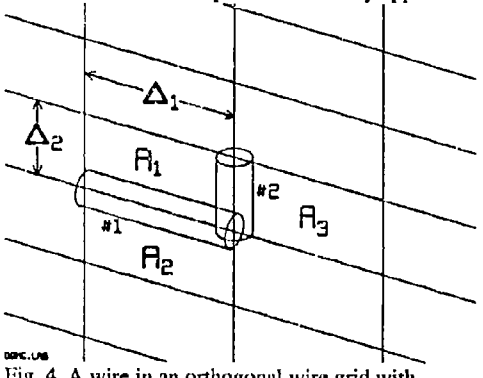

Fig. 4 A wire in an orthogonal wire grid with rectangular cells.

For an orthogonal grid of square cells, as in Fig. 3, the "adapted equal-area rule" should give the same radius, $a = \Delta/2\pi$, as the "equal-area rule".

Typically a wire in a grid subtends two mesh cells. The new radius rule should obtain a radius for a wire from a knowledge of the endpoint coordinates of the wires making up these two "mesh cells". The new radius rule should yield a radius for the wire no matter how many wires make up the adjacent mesh cells, or what shape the two mesh cells are. It is tempting to use Eqn. (1) directly for non-square mesh cells.

Consider the subdivision problem, in which wire #1 in Fig. 4 is subdivided into

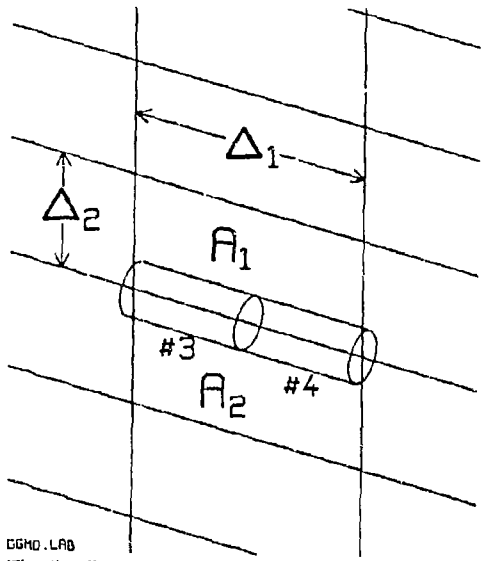

Fig. 5 Wire #1 in Fig. 4 is subdivided into two wires, but is expected to have the same radius as in Fig. 4.

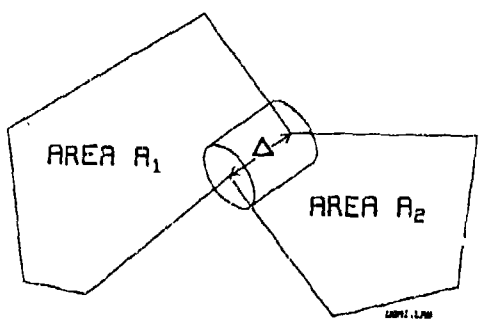

Fig. 6 A short wire which is a member of two large meshes.

two wires, illustrated by wires #3 and #4 in Fig. 5. For wire #1 in Fig. 4, Eqn. (1) obtains the radius $a = \Delta_2/2\pi$. If wire #3 of Fig. 5 has length $\Delta_1/2$, then applying Eqn. (1) obtains a radius of $a = \Delta_2/\pi$, twice the value for wire #1. But subdivision should not change the radius. The "adapted equal-area rule" must give the same radius for the single wire, #1 in Fig. 4, or the series connection of wires #3 and #4 in Fig. 5. Further, the radius must be the same if wires #3 and #4 are specified to NEC as one wire with two segments(one GW card) or two wires with one segment each(two GW cards). Thus for the feed region of Fig. 2, the "adapted equal-area rule" should get the same radius for the wires labelled "#1" and "#2".

Consider the problem of a very short wire which subtends two meshes made up of much longer wires, shown in Fig. 6. The radius of the short wire must not be made unreasonably large by the "adapted equal-area rule". Thus if Eqn. (1) were applied directly to this short wire, a large $(A_1 + A_2)$ is divided by a small Δ to obtain a huge radius. Eqn. (1) must be modified to account for the shortness of wire length Δ compared to the areas that the wire subtends.

An "adapted equal-area rule" is obtained by weighting each term in Eqn. (1) with a factor comparing the length of the wire segment, Δ, to the distance around the mesh periphery. Thus in Fig. 7 a wire segment of length Δ is a member of two meshes, of areas A_1 and A_2, and peripheries L_1 and L_2. The peripheries include Δ. If the adjacent meshes were square, then Δ should be one-quarter of the length of the periphery. Thus weight each term of Eqn. (1) with the ratio of the segment length, Δ, to its expected fraction of the periphery, $L/4$, to obtain

$$a = \frac{A_1}{4\pi\Delta}\frac{\Delta}{(L_1/4)} + \frac{A_2}{4\pi\Delta}\frac{\Delta}{(L_2/4)}$$

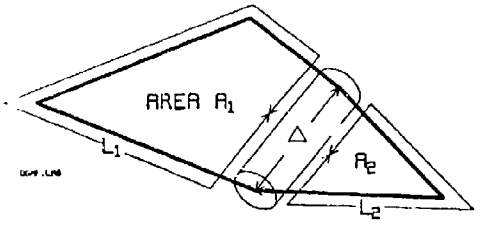

Fig. 7 The "adapted equal-area rule" uses the areas and the peripheries of the meshes that each wire subtends.

Then the "adapted equal-area rule" states that

$$a = \frac{A_1}{\pi L_1} + \frac{A_2}{\pi L_2} \qquad \ldots(2)$$

For an orthogonal grid of square cells, as in Fig. 3, $A_1 = A_2 = \Delta^2$, and the mesh peripheries are $L_1 = L_2 = 4\Delta$. Eqn. (2) gives $a = \Delta/2\pi$ as required. Note that this makes the total surface area of all the wires equal to twice the area of the surface.

Application of the Adapted Equal-Area Rule

The "adapted equal-area rule" of Eqn. (2) meets the requirement that it be readily applied to complex wire grids, such as Fig. 1 or 2, with many non-square cells. All that is needed is a knowledge of the wires making up the two meshes subtending the wire whose radius is to be found.

For the rectangular grid of Fig. 4, the "adapted" rule gets a somewhat different radius from the original "equal-area rule". Thus for either wire #1 or wire #2 in Fig. 4, $A_1 = A_2 = \Delta_1\Delta_2$, and $L_1 = L_2 = 2(\Delta_1 + \Delta_2)$, and with Eqn. (2) the radius of both wire #1 and wire #2 is

$$a = \frac{\Delta_1\Delta_2}{\pi(\Delta_1 + \Delta_2)} \qquad \ldots(3)$$

Thus wires #1 and #2 have the same radius, as shown in Fig. 4, which is different from the "equal-area rule" value of $a_1 = \Delta_2/2\pi$ or $a_2 = \Delta_1/2\pi$. It is readily shown that $a < a_1$ but $a > a_2$. The "adapted equal-area radius" is a compromise radius such that

$$\frac{1}{a_1} + \frac{1}{a_2} = \frac{1}{a} + \frac{1}{a}$$

The total surface area of *all the wires* is still equal to *twice the area of the surface*, but evidently this is different from making the total surface area of the wires *in one orthogonal direction* equal to the area of the surface. Thus for best results, keep the mesh cells of the wire grid square rather than rectangular.

The "adapted equal-area rule" handles the subdivision well. Thus for wire #1 in Fig. 4, the radius is that of Eqn. (3). For wire #3 or #4 of Fig. 5, the areas and peripheries used in Eqn. (2) are identical to those used to compute the radius of wire #1, hence lead to the same radius for wire #3 or #4 as for wire #1. The "adapted rule" radius does not depend directly on the length of the wire whose radius is being calculated. Instead, it uses the total peripheral length of each adjacent mesh, and the area of each adjacent mesh. Also, it does not matter whether the subdivision is done with one GW card specifying two segments, or two GW cards of one segment each.

Consider the short wire problem of Fig. 6. Eqn. (1) uses the ratio of the mesh area to the wire length, Δ, whereas Eqn. (2) uses the ratio of the mesh area to the mesh periphery, L, and thus obtains a smaller radius. In effect, the contribution of each area to the radius of Eqn. (1) has been reduced in Eqn. (2) by the factor $\Delta/(L/4)$ which is considerably less than one for geometries like Fig. 6. Fig. 6 is drawn to scale and shows that the "adapted equal-area radius" is a reasonable value. But a construction such as Fig. 6 embedded in a wire-grid is poor practice, grossly violating the principle that as many cells as possible in a grid should be "square", all with equal areas. If the short wire in Fig. 6 is absolutely required, then the adjacent large meshes should be subdivided into smaller mesh cells.

For wires at the edges of open surfaces, such as the wing edge wires in Fig. 1, there is only one mesh area to contribute to the radius. Hence the radius of edge wires is about half the value of the radius of wires embedded in the grid.

Automated Mesh Search and Radius Calculation

The "adapted equal-area rule" assigns a unique radius to each wire of a wire grid, from a knowledge of the wires making up the adjacent meshes. The calculation of the wire radius has been automated with the processing steps shown in Fig. 8. A NEC geometry file is input to the mesh-search program "MESHES", to obtain a "MESHES.MSH" file, which is a list of the wires making up meshes with each wire in the geometry file. The user can edit the MESHES.MSH file to delete meshes which he may not want to contribute to the radius of a given wire. The edit step gives the user full, detailed control over the radius calculation. The MESHES.MSH file is then input to the radius-finding program "FNDRAD", which reads which wires make meshes with each wire, and applies the "adapted equal-area rule" to find that wire's radius. The output is a new NEC geometry file called "OUTPUT.GW".

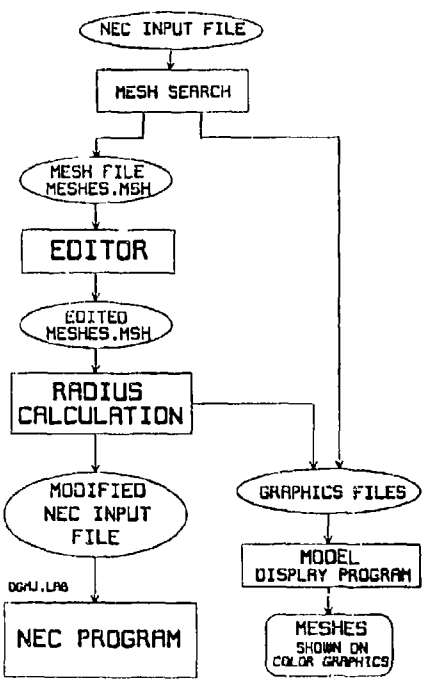

Fig. 8 Flow chart of processing steps in computing wire radii for a NEC geometry file. Data files are enclosed in ellipses, and rectangles are programs.

The present implementation of MESHES searches for loop paths of up to 8 wires. Then a loop is identified as a "mesh" by searching for "diagonal" paths across the loop. If any path across the loop is found which is shorter than the paths around the loop periphery then the loop is not a mesh. MESHES rejects cross-sections as meshes because all the vertices have the same x-coordinate. The current version does not reject 3-wire and 4-wire cross-sections, which must be manually edited out of the MESHES.MSH file. This was done to allow cylinder endcaps to be modelled with 3-wire and 4-wire meshes.

Program MESHES writes graphics files, for display with program "MODEL"[7], that are useful in spotting errors in the wire grid, and in identifying meshes requiring modification in "MESHES.MSH". MESHES writes a graphics file which identifies all the wires that are members of 3-wire meshes, and graphics files naming all the wires that are members of 4-wire

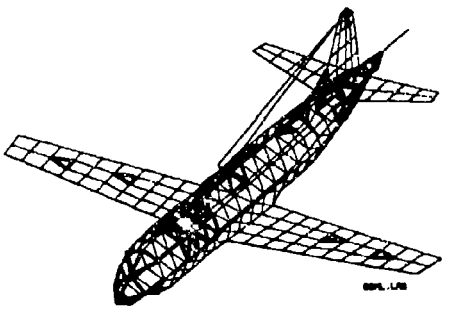

Fig. 9 Wires that are members of 3-wire meshes in the aircraft grid.

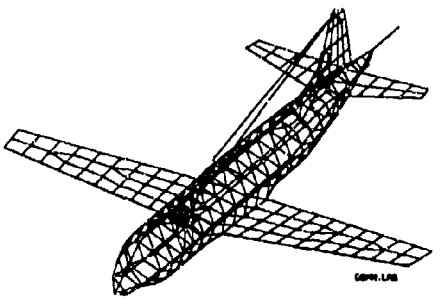

Fig. 10 Wires that are members of 5-wire meshes.

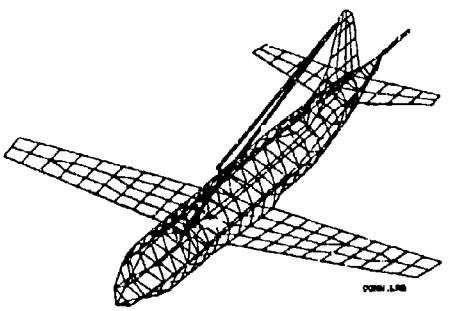

Fig. 11 Wires that are members of no meshes at all.

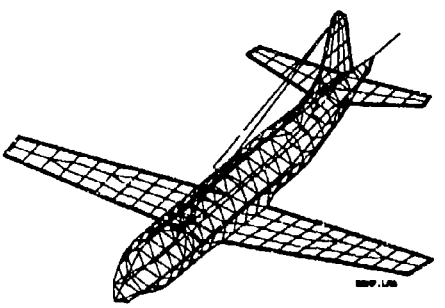

Fig. 12 Wires that are members of only one mesh.

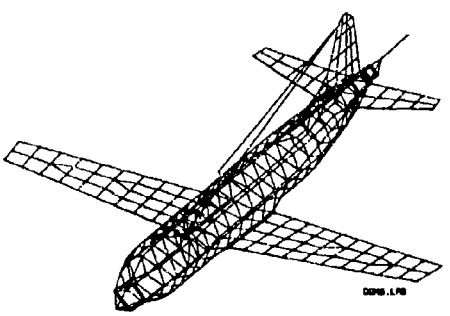

Fig. 13 Wires that are members of more than two meshes.

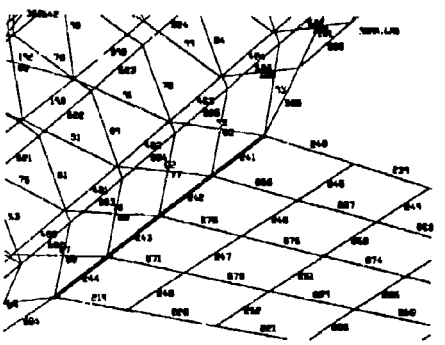

Fig. 14 Detail of a wing root showing the wing root wires and the tag numbers.

meshes, 5-wire, 6-wire, 7-wire and 8-wire meshes. Thus the aircraft grid of Fig. 1 has the 3-wire meshes shown in Fig. 9, the 5-wire meshes of Fig. 10, and no larger meshes. The user can inspect these displays from various viewing angles to look for wires that clearly should not be members of meshes with that number of wires. This can alert the user to errors in the model geometry.

To further increase the likelihood that errors in the model will be found, MESHES produces additional mesh-membership graphics files. Fig. 11 shows all the wires that are members of no meshes at all, clearly seen as the wire antennas and the wire modelling the magnetometer boom. If a wire in the grid were open-circuited at one end in error, it would be present in this display. Fig. 12 shows all wires that are members of only one mesh, readily seen to be the edges of the wings and the dorsal fin. Once again, errors in the grid can lead to wires being members of this group incorrectly. Fig. 13 shows wires that are members of more than two meshes. Wing roots and fin roots are members of two fuselage meshes and of one wing or fin mesh. The file also shows that there are three 4-wire cross-sections that need to be rejected manually.

The user edits the MESHES.MSH file to remove unwanted meshes. Each line of the file begins with a wire's tag number, followed by a zero(0), then the tag numbers of wires making meshes the first mesh, a zero, the wires making the second mesh, a zero, the third mesh, etc. For the wing-root wire #244 in Fig. 14, MESHES.MSH contains the line

244 0 59 67 479 0 60 68 503 0 219 248 671 0

The user simply deletes the tag numbers of unwanted meshes. For the wing root wires, such as those in Fig. 14, our convention is that the radius of these wires is calculated based on the two adjacent fuselage meshes, and that the wing mesh is ignored. The user must identify and delete from the mesh list the tag numbers of the wing mesh. This is done by modifying the line in MESHES.MSH to read

244 0 59 67 479 0 60 68 503 0

Then FNDRAD will use the fuselage meshes to compute the radius of wire #244.

Once the meshes have been identified and verified, it is straightforward to calculate the wire radii using the "adapted equal-area rule". Program FNDRAD repeats the decomposition into vertices and links(a fast step even for large models), and then for each wire reads the first two meshes from the MESHES.MSH file, and calculates a radius. If the wires specified to form a mesh in the MESHES.MSH file do not from a closed path, a fatal error results. This can happen if the MESHES.MSH file was modified incorrectly. FNDRAD generates its own graphics files of wires belonging to no meshes, to one mesh and to more than two meshes. At this stage, no wires should belong to more than two meshes. The user should display these wires to verify that no errors were introduced in editing MESHES.MSH.

Conclusions

This paper proposes a "adapted equal-area rule", Eqn. (2), which can be used to find a unique radius for each wire in a complex grid such as the aircraft in Fig. 1. For square mesh cells, the radius obtained is the same as that specified by the "equal-area rule". The "adapted" rule has been automated into a mesh search program, MESHES, and a radius-finding program, FNDRAD.

Display of the mesh content of a wire grid with computer graphics provides a valuable tool for checking the integrity of the grid. Certain common errors in grid geometry lead to obviously-wrong meshes, easily seen on the graphics screen. This has been an unexpected benefit of the mesh search. Some grids that had been extensively used over several years were found to contain errors!

For the 681 wire, 359 vertex aircraft of Fig. 1, MESHES takes 11 minutes 34 seconds on a 25 MHz 80386 computer, with an 80387 math coprocessor, running MS-DOS. The present implementation of MESHES program could be improved greatly in execution speed. The search method is crude and redundant-it tends to find the same meshes over and over again. The "diagonal search" approach to screening n-wire loops to find which are meshes is effective but tends to re-find all the smaller meshes. No advantage is taken of the knowledge that the fuselage grid models a closed surface.

Editing the MESHES.MSH file for the aircraft takes an experienced user about half an hour. To identify the tag numbers of meshes which must be "edited out", program MODEL is used to display the wire grid including tag numbers, in the format of Fig. 14. Some users would like to avoid the editing step. Perhaps FNDRAD could read a file of special cases, directing it to ignore certain meshes formed with the wing root wires. This would be convenient in making a series of small alterations to an aircraft geometry file.

After MESHES.MSH has been edited, running FNDRAD takes about 60 seconds for the aircraft, and produces a NEC geometry file with revised wire radii.

Automated radius calculation yields a unique radius for each wire, which depends on the local geometry of the wire grid. Wires subtending small meshes have thinner radii than wires subtending full-size "square" mesh cells. Where the mesh is deliberately made finer, such as the feed region of Fig. 2, the radius algorithm automatically tapers the radius in accordance with the cell areas. This refinement in wire-grid modelling appears to lead to more consistent computed results when models are analysed with the NEC program.

References

1. G.J. Burke and A.J. Poggio, "Numerical Electromagnetics Code - Method of Moments, Part III: User's Guide", Technical Document 116, Naval Electronic Systems Command(ELEX 3041), July, 1977.
2. G.J. Burke and A.J. Poggio, "Numerical Electromagnetics Code - Method of Moments, Part I: Program Description-Theory", Technical Document 116, Naval Electronic Systems Command(ELEX 3041), July, 1977.
3. A.C. Ludwig, "Wire Grid Modeling of Surfaces", IEEE Trans. on Antennas and Propagation, Vol. AP-35, No. 9, pp. 1045-1049, Sept. 1987.
4. G.J. Burke and E.K. Miller, "A Mesh Model of a Coaxial Transmission Line Using NEC", Sixth Applied Computational Electromagnetics Symposium, Monterey, California, March 19-22, 1990.
5. K.S.H. Lee, L. Marin and J.P. Castillo, "Limitations of Wire-Grid Modelling of a Closed Surface", IEEE Trans. on Electromagnetic Compatibility, Vol. EMC-18, No. 3, pp. 123-129, August, 1976.
6. R. Paknys, "The Near Field of a Wire Grid Model", to be published in the IEEE Trans. in Antennas and Propagation.
7. C.W. Trueman, "Program MODEL for the Display and Investigation of Wire Grid Model Geometries", Internal Report, Concordia University EMC Laboratory, in preparation.
8. C.W. Trueman and S.J. Kubina, "Verifying Wire-Grid Model Integrity with Program CHECK", Applied Computational Electromagnetics Society Journal, Vol. 5, No. 2, Winter, 1990.
9. G.J. Burke, "Recent Advances to NEC - Applications and Validation", Lawrence Livermore National Laboratory preprint number UCRL-100651, March 3, 1989.

SESSION 10- "MICROWAVE CIRCUITS AND MICROSTRIP ANTENNA ANALYSIS"

Moderator: Fabrice Huret

FULL-WAVE MODELING OF A MULTI-LAYER MICROSTRIP ARRAY WITH A SUPERCONDUCTING MICROSTRIP FEED NETWORK

Jeffrey S. Herd
Electromagnetics Directorate
Rome Laboratory
Hanscom AFB, MA 01731-5000
(617) 377-4214

ABSTRACT

Recent developments in high temperature superconductors have made it possible to fabricate microstrip feed lines with extremely low losses at liquid nitrogen temperatures. This technology is particularly applicable to high frequency arrays with microstrip feed networks, where ohmic losses severely limit the efficiency which can be obtained with conventional metals. This paper describes the analysis and design of a multi-layer microstrip antenna array with a superconducting microstrip feed network. A novel geometry will be described which integrates the array into a radome on the vacuum shield of a cryocooler for maximum thermal and RF radiation efficiency. A multi-layer spectral domain Green's function is used with the method of moments to design the microstrip feed network and proximity coupled microstrip elements for optimum impedance matching and operating bandwidth. Experimental measurements of the proximity-coupled microstrip elements in a waveguide simulator are used to validate the analysis.

1. INTRODUCTION

The primary advantage of using superconducting metals in antenna systems appears to be the reduction of ohmic losses in the power distribution and matching networks, particularly at millimeter wave frequencies [1], [2], [3], [4]. For example, the use of a superconducting feed network could increase the RF gain of a large microstrip-fed array by as much as 20 dB at 60 GHz, as shown in figure 1 from [4].

This paper describes the analysis and design of a multi-layer microstrip antenna array with a superconducting feed network. A novel geometry will be described which utilizes proximity-coupled microstrip patches integrated into a radome on the vacuum shield of a cryocooler as shown in figure 2 for maximum bandwidth, thermal efficiency and RF

pattern integrity. A multi-layer spectral domain Green's function is used with the method of moments to design the microstrip feed network and proximity-coupled elements. Experimental measurements of prototypical elements in a waveguide simulator confirm the validity of the analysis.

2. THEORY

To begin with, it should be pointed out that the analysis assumes the superconducting metal has infinite conductivity. This approximation works well for analyzing the impedance and radiation properties of the lines and patches as long as the metal is more than three penetration depths thick . For accurate predictions of ohmic losses, the model must be augmented to include surface resistivity effects.

The infinite array spectral dyadic Green's function is used in the analysis because it includes all effects caused by the dielectric layers and the mutual coupling between elements. These effects are likely to be important in a large scanning array printed on a high permittivity substrate. The method of moments is then used to solve an integral equation for the unknown current distributions on the feed lines and patches. The characteristic impedance and effective propagation constant of the microstrip feed lines is obtained by extending techniques developed in [5] to multiple dielectric layers.

Entire domain basis functions are used on the patches for both expansion and test because of their correspondence with the cavity-like behavior of the patches. For x-directed modes, the functions are given by;

$$\bar{J}_n^x(x,y) = \hat{x}\,\frac{1}{p_y}\,\sin\left[\frac{r\pi}{p_x}\left(x - \frac{p_x}{2}\right)\right] \tag{1}$$

For y-directed modes;

$$\bar{J}_n^y(x,y) = \hat{y}\,\frac{1}{p_x}\,\sin\left[\frac{s\pi}{p_y}\left(y - \frac{p_y}{2}\right)\right] \tag{2}$$

where p_x and p_y are the patch dimensions, and (r,s) are integer indices.

It has been found that the microstrip feed line excitation of the patch can be sufficiently modeled by a vertical electric current source at the inset point, provided that it is fairly close to the edge. For stacked, proximity-coupled patches, this is usually the case for 50 Ω input impedance [6].

The resultant matrix equation is given by;

$$\begin{bmatrix} Z_{11} & Z_{12} & \cdot & \cdot & \cdot & Z_{1N} \\ Z_{21} & Z_{22} & \cdot & \cdot & \cdot & Z_{2N} \\ \cdot & \cdot & & & & \cdot \\ \cdot & \cdot & & & & \cdot \\ \cdot & \cdot & & & & \cdot \\ Z_{N1} & Z_{N2} & \cdot & \cdot & \cdot & Z_{NN} \end{bmatrix}^{-1} \begin{bmatrix} V_1 \\ V_2 \\ \cdot \\ \cdot \\ \cdot \\ V_N \end{bmatrix} = \begin{bmatrix} I_1 \\ I_2 \\ \cdot \\ \cdot \\ \cdot \\ I_N \end{bmatrix} \tag{3}$$

where

$$Z_{mn} = \frac{1}{ab} \sum_{p=-\infty}^{\infty} \sum_{q=-\infty}^{\infty} \bar{F}_m(k_x,k_y) \cdot \bar{\bar{Q}}(k_x,k_y) \cdot \bar{F}_n(-k_x,-k_y) \tag{4}$$

$$V_n = \frac{-1}{ab} \sum_{p=-\infty}^{\infty} \sum_{q=-\infty}^{\infty} \bar{F}_m(k_x,k_y) \cdot \bar{\bar{Q}}(k_x,k_y) \cdot \bar{F}_{inc}(-k_x,-k_y) \tag{5}$$

$$k_x = \frac{2\pi p}{a} + k_0 u \tag{6}$$

$$k_y = \frac{2\pi q}{b} + k_0 v \tag{7}$$

$$u = \sin\theta_0 \cos\phi_0 \tag{8}$$

$$v = \sin\theta_0 \sin\phi_0 \tag{9}$$

where θ_0 and ϕ_0 are the beam pointing angles, k_0 is the free space wave number, the F_n's are the Fourier transforms of the entire domain basis functions, a and b are the unit cell dimensions, and Q is the Fourier transformed dyadic Green's function for a three layer grounded dielectric slab.

The input impedance is calculated from a reaction integral, which, for the infinite array, becomes:

$$Z_{in} = \frac{-1}{ab} \sum_{i=-\infty}^{\infty} \sum_{j=-\infty}^{\infty} \sum_{m=1}^{N} I_m \bar{F}_m(-k_x,-k_y) \cdot \bar{\bar{Q}}(k_x,k_y) \cdot \bar{F}_{inc}(k_x,k_y) \tag{10}$$

where

$$\bar{F}_{inc}(k_x,k_y) = \hat{z}\, e^{-jk_x x_p}\, e^{-jk_y y_p} \tag{11}$$

is the Fourier transform of a vertical current source at the feed inset point (x_p,y_p). All floquet series are truncated at $i=j=\pm 30$, and this is found to give sufficient convergence. With the input impedance known, the scanning reflection coefficient is computed by:

$$R(\theta,\phi) = \frac{Z_{in}(\theta,\phi) - Z_{in}(0^\circ,0^\circ)}{Z_{in}(\theta,\phi) + Z^*_{in}(0^\circ,0^\circ)} \tag{12}$$

where $Z_{in}(0^\circ,0^\circ)$ is the input impedance at broadside.

Several methods were used to check the numerical accuracy of the computer code. First, a comparison was made between the input power, P_{in}, and the power radiated from a unit cell, P_{rad}, where:

$$P_{in} = 1 - |R|^2 \tag{13}$$

and

$$P_{rad} = \int_{\text{unit cell}} \int \frac{1}{2}\, \mathrm{Re}(\bar{E} \times \bar{H}^*) \cdot \hat{z}\, dxdy \tag{14}$$

It was found that the values calculated from equations (13)and (14) were within one percent of one another for all scan angles except the blindness angle, and it is believed that the computational accuracy at that scan angle is affected by the singularity in the infinite array Green's function. As a second check of the code, it was confirmed that the boundary condition $E_{tan} = 0$ is being satisfied by the fields from the source and basis function expansion currents to within one part in a thousand.

3. EXPERIMENT

As a further validation of the theory, measurements from a waveguide simulator are used to replicate the environment seen by an element in an infinite scanning array. Figure 3

shows the measured and predicted reflection coefficient versus frequency for a three layer proximity-coupled element. This example shows a 2:1 VSWR bandwidth of approximately 20%. Good agreement between theory and experiment is obtained by using three x-directed modes (r=1,3,5) and two y-directed modes (s=1,2) on each patch.

4. SUMMARY

A full wave analysis has been applied to a three layer proximity-coupled microstrip antenna array. The unique geometry provides a wide bandwidth element for use with a high efficiency superconducting microstrip feed network. Future work will be done to add superconductor surface resistivity, substrate anisotropies, and alternative element designs for improved thermal shielding.

5. REFERENCES

1. R. C. Hansen, "Superconducting Antennas," IEEE Trans. Aero. and Elect. Sys. 26, no. 2, pp 345-355, 1990.

2. R. J. Dinger and D. J. White, " The Radiation Efficiency of a Small Dipole Antenna Made from a High Temperature Superconductor," IEEE Antenna and Prop. Int. Symp. Dig., Dallas, pp 724-727, 1990.

3. J. T. Williams and S. A. Long, "High Temperature Superconductors and their Application in Passive Antenna Systems," IEEE Antenna and Prop. Magazine, pp 7-18, Aug. 1990.

4. W. G. Lyons and R. S. Withers, "Passive Microwave Device Applications of High T_c Superconducting Thin Films," Microwave Journal, Vol. 33, pp. 85-102, Nov. 1990.

5. R. Jackson and D. M. Pozar, "Full-Wave Analysis of Microstrip Open-End and Gap Discontinuities," IEEE Trans. Microwave Theory and Tech., Vol. MTT-33, pp. 1036-1042, Oct. 1985.

6. J. S. Herd, "Scanning Impedance of Proximity Coupled Rectangular Microstrip Antenna Arrays," Ph.D. Diss., E.C.E. Dept., Univ. of Mass., Sept. 1989.

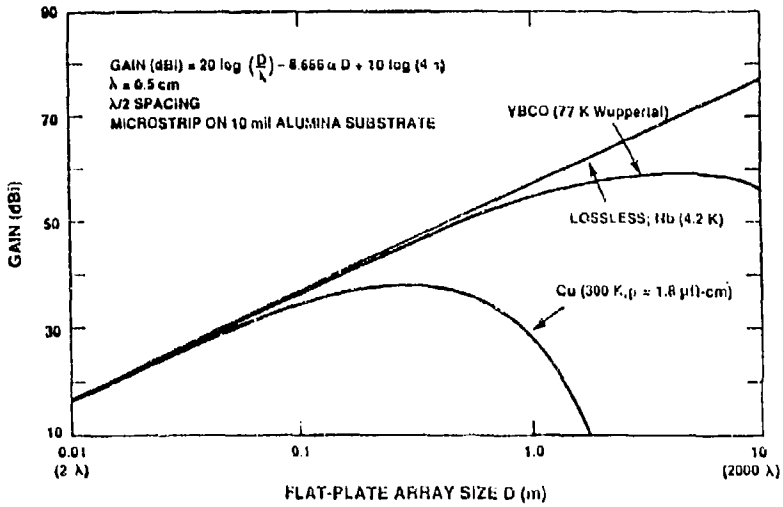

FIGURE 1. Effect of Distribution Loss on Antenna Array Gain, (from [4]).

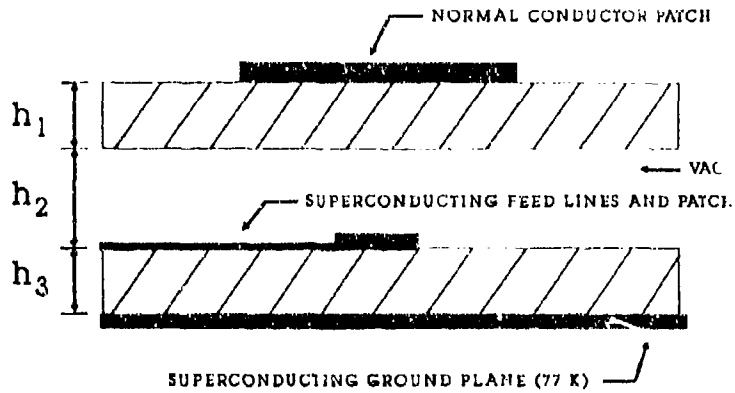

FIGURE 2. Superconducting Microstrip Array Geometry.

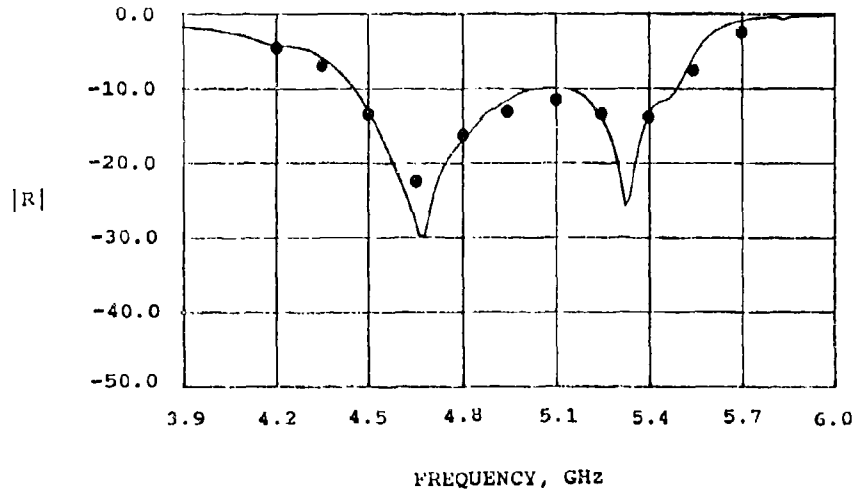

FIGURE 3. Reflection Coefficient Versus Frequency for Element in a Waveguide Simulator; $h_1=h_2=h_3=0.159$cm, $X_U=Y_U=1.87$cm, $X_L=Y_L=1.93$cm, $\varepsilon_1=\varepsilon_3=2.33$, $\varepsilon_2=1.0$, $a=3.35$cm, $b=3.60$cm, —— = measured, ● = predicted.

MODELING OF AN ANISOTROPIC STRIPLINE

M KAMAREI, N. DAOUD, R. SALAZAR, M. BOUTHINON

L.E.M.O.-I.N.P.G.-C.N.R.S. UAR 833, BP 257, Grenoble 38016, France

Indexing terms: anisotropic permeability, electromagnetic fields, propagation constant

A variety of substrate materials used in practice exhibit anisotropic behavior.The objective of this letter is to model the propagation properties of a stripline loaded with a dielectric material which has an isotropic permittivity and an anisotropic permeability.

I- Introduction

In recent years, a variety of anisotropic materials have increasingly found numerous and important applications at microwave frequencies. Anisotropy is either an inherent property of a substrate material or may be acquired during the manufacturing process. It has been established that when anisotropy is ignored in the development of design methods for single and coupled microstrip, an error is introduced which becomes significant for small linewidths and small line separation [1]. In certain applications of coupled line structures, anisotropy may prove beneficial in equalizing even and odd mode phase velocities and reducing the sensitivity of geometry tolerance [2]. An algorithm is developed which models structures such as microstrip on anisotropic substrates [3]. The characteristics of single and coupled microstrips on anisotropic substrates with a diagonal permittivity tensor have been analized by Alexopoulos and Krowne [4] by using a quasistatic-mode approach. Several other anisotropic dielectric substrate geometries have been treated in the literature [5], [6] by using the quasistatic method. Hybrid modes have been analysed for microstrip lines with anisotropic substrates [7]. T.Kitazawa and Y.Hayashi have also analysed the propagation characteristics of strip lines with multilayered anisotropic media [8].

This letter represents the modeling of a stripline loaded with a dielectric material which has an isotropic permittivity and an anisotropic permeability as is shown below:

$$\mu = \begin{bmatrix} \mu_{11} & \mu_{12} & 0 \\ -\mu_{12} & \mu_{22} & 0 \\ 0 & 0 & \mu_{33} \end{bmatrix} \qquad (1)$$

The relative permittivity (ε) and all the terms of the relative permeability matrix [μ] are complex.

We have already shown that the TEM modes which can exist in the bulk material, cannot propagate when this material is placed in the stripline structure. If any energy is transferred from input to output in the structure, there are hybrid modes which are the origin of this transfer. In fact, the anisotropic character of the material under study causes a coupling between the longitudinal components of the electric and magnetic fields.

The homogeneous property of the material and the assumption that the structure is unlimited along ox (figure 1) permit a decoupling of the longitudinal components (E_z and H_z) and a determination of the four transverse fields: E_x, E_y, H_x and H_y. Obtaining the characteristics of the hybrid modes with an analytical method is not possible. The numerical method which is adapted to this planar structure is the Spectral domain method which we have formulated and programmed. This programme, very general for the form of the anisotropic relative permeability matrix [μ], is validated for an isotropic material and also for a magnetic anisotropy.

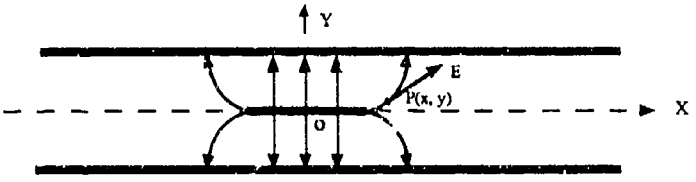

figure 1

II- Study of the coupling of the longitudinal components

We show that the anisotropic character of the material under study causes a coupling between the longitudinal components of the electric and magnetic fields. The possibility of determining the four transverse components depends on obtaining these longitudinal components. The homogeneous property of the material and the assumption that the structure is unlimited along ox (figure 1) permit a decoupling of the longitudinal components (E_z and H_z) and a determination of the four transverse fields E_x, E_y, H_x and H_y. We can then obtain the following:

$$\begin{cases} H_x = B_1\dfrac{\partial E_z}{\partial y} + B_2\dfrac{\partial E_z}{\partial x} + B_3\dfrac{\partial H_z}{\partial y} + B_4\dfrac{\partial H_z}{\partial x} \\ H_y = B_5\dfrac{\partial E_z}{\partial y} + B_6\dfrac{\partial E_z}{\partial x} + B_7\dfrac{\partial H_z}{\partial y} + B_8\dfrac{\partial H_z}{\partial x} \end{cases} \qquad (2)$$

$$\begin{cases} E_x = A_1\dfrac{\partial E_z}{\partial y} + A_2\dfrac{\partial E_z}{\partial x} + A_3\dfrac{\partial H_z}{\partial y} + A_4\dfrac{\partial H_z}{\partial x} \\ E_y = A_5\dfrac{\partial E_z}{\partial y} + A_6\dfrac{\partial E_z}{\partial x} + A_7\dfrac{\partial H_z}{\partial y} + A_8\dfrac{\partial H_z}{\partial x} \end{cases} \qquad (3)$$

where A_i and B_i (i=1, 2, . ., 8) are constants, functions of ω, ε and $[\mu]$. These constants are given in annex.

The Maxwell equations permit us to obtain:

$$A_1\left[\frac{\partial^2 E_z}{\partial x^2}+\frac{\partial^2 E_z}{\partial y^2}\right]+(A_2-A_5)\frac{\partial^2 E_z}{\partial x\,\partial y}=A_8\frac{\partial^2 H_z}{\partial x^2}-A_3\frac{\partial^2 H_z}{\partial y^2}+j\omega\mu_{33}H_z \qquad (4.1)$$

and :

$$(B_7-B_4)\frac{\partial^2 H_z}{\partial x\,\partial y}+B_8\left(\frac{\partial^2 H_z}{\partial x^2}+\frac{\partial^2 H_z}{\partial y^2}\right)=B_1\frac{\partial^2 E_z}{\partial y^2}-B_6\frac{\partial^2 E_z}{\partial x^2}+j\omega\varepsilon E_z \qquad (4.2)$$

These two equations show the coupling between the longitudinal components E_z and H_z. The anisotropic character of the material is the origin of the coupling.

III- Solution of the system of coupled equations

We suppose that the material is homogeneous and unlimited along ox and the Fourier Transformation is defined below:

$$\tilde{A}(\alpha,y)=\int_{-\infty}^{+\infty}A(x,y)\,e^{-j\alpha x}\,dx \quad , \quad A(x,y)=H_z(x,y) \text{ ou } E_z(x,y) \qquad (5)$$

With these conditions ($\partial/\partial x \rightarrow j\alpha$), the system of equations (4) gives the general solutions as shown below:

$$\begin{cases}\tilde{E}_z=c_1e^{\sigma_1 y}+c_2e^{\sigma_2 y}+c_3e^{\sigma_3 y}+c_4e^{\sigma_4 y}\\ \tilde{H}_z=c_1a_1e^{\sigma_1 y}+c_2a_2e^{\sigma_2 y}+c_3a_3e^{\sigma_3 y}+c_4a_4e^{\sigma_4 y}\end{cases} \qquad (6)$$

where σ_j and a_j (j=1, 2, ., 4) are functions of α, ω, ε and $[\mu]$. c_j are constants.

IV- Numerical treatment

The system of equqtions (2, 3, 6) give all the electromagnetic field components. The continuity condition of the electromagnetic field on the metalized interface (y=0), permits to obtain a relationship between the Fourier Transformation of the tangential components of the electric field and the current density on the metallic surface as is shown below:

$$\begin{bmatrix}\tilde{E}_x\\ \tilde{E}_z\end{bmatrix}=\begin{bmatrix}G_{11}G_{12}\\ G_{21}G_{22}\end{bmatrix}\begin{bmatrix}\tilde{J}_x\\ \tilde{J}_z\end{bmatrix} \qquad (7)$$

This equation is the fundamental equation of the Spectral domain method. The terms of [G] are the Green's coefficients of the Spectral domain method. Each of these is a function of the frequency, the complex propagation constant and the geometrical and physical characteristics of

the structure. In the perfect conductor, the electric field is null as is the current density in the dielectric. This particular property and the application of the Galerkin's Method, by a suitable choice of the basis functions for J_x and J_z, permit the solution of the fundamental equation of the Spectral domain method [9]. This enables us to obtain the complex propagation constant and afterwards the characteristic impedance and the distribution of the electromagnetic field of each of the higher order modes that propagate in the structure.

V-Results

We have programmed all the previous steps. Our analytical and numerical treatments are validated by using this general programme for an isotropic material ($\mu_{xx}=\mu_{yy}=\mu_{zz}=1+j0$, $\mu_{xy}=0+j0$, $\varepsilon_r=100+j0$) in a structure which has the same geometrical characteristics as the real structure under study (W/2h=0.17). The obtained results are in good agreement with the ones which are already well known.

By using the same programme, we have studied the variation of the propagation constant (calculated by our method) as the magnetic anisotropy increases progressively, in comparison with the propagation constant which is obtained from the following expression:

$$\beta_{expected} = \frac{2\pi\sqrt{\mu_r \varepsilon_r}}{\lambda_0} \qquad (8)$$

This is done for the several values of μ_{yy} (supposing that $\mu_{xx}=1$) and for the several values of μ_{xx} (supposing that $\mu_{yy}=1$) as shown in figures (2) and (3) respectively.

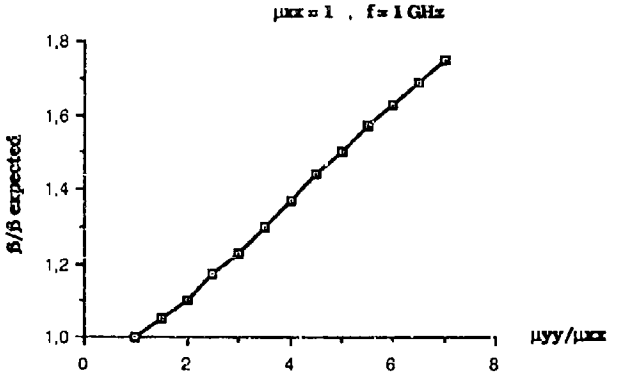

figure 2

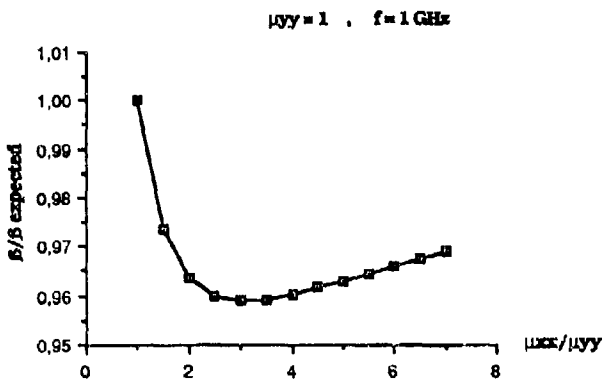

figure 3

Figures 2 and 3 show that $\beta_{calculated}$ goes linearly far from $\beta_{expected}$ when μ_{yy} increases but it remains close to $\beta_{expected}$ when μ_{xx} increases. This means that the propagation characteristics of the structure are more sensitive to the μ_{yy} variation than to that of μ_{xx}. This is also confirmed by the obtained results for the variations of the effective permittivity as a function of μ_{yy} and μ_{xx}.

Conclusion

A stripline structure loaded with a dielectric material which has an isotropic permittivity and an anisotropic permeability is studied and modeled. In the case of a magnetic anisotropy represented by the relative permeability matrix [μ], It is shown that the anisotropic character of the material causes a coupling between the longitudinal components of the electric and magnetic fields. The homegeneous property of the material and the assumption that the structure is unlimited along ox (figure 1) permit a decoupling of the longitudinal components (E_z and H_z) and a determination of the four transverse fields: E_x, E_y, H_x and H_y.

we have already shown that the TEM modes which can exist in the bulk material, cannot propagate when this material is placed in the stripline structure. If any energy is transferred from the input to the output of the structure, there are the hybrid modes which are the origin of this transfer. Obtaining the characteristics of the hybrid modes with an analytical method is not possible. The numerical method adapted to this planar structure is the Spectral domain method. This is formulated and programmed.

The realized programme, although very general for the form of the magnetic anisotropy, is validated for an isotropic material in a structure which has the same geometrical characteristics as the real structure under study. The obtained results are in good agreement with the ones which are already well known.

By using the same programme we have also studied the materials with an isotropic permittivity and anisotropic permeability. It is shown that the propagation characteristics of the structure are more sensitive to the μ_{yy} variation than that of μ_{xx} variation.

References

[1] N.G.ALEXOPOULOS:" Integrated circuit structures on anisotropic substrates."
IEEE Trans. Microwave Theory Tech., vol. MTT-33, pp. 847-881, oct 1985.

[2] N.G.ALEXOPOULOS, C.M.KROWNE:" Characteristics of single and coupled microstrips on anisotropic substrates."
IEEE Trans. Microwave Theory Tech., vol. MTT-26, pp.387-393, june 1978.

[3] A.NAKATANI, N.G.ALEXOPOULOS:" Toward a generalized algorithm for the modeling of tne dispersive properties of integratezd circuit structures on anisotropic substrates."
IEEE Trans. Microwave Theory Tech., vol. MTT-33, pp 1436-1441, december 1985.

[4] N.G.ALEXOPOULOS and C.M.KROWNE:" Characteristics of single and coupled microstrips on anisotropic substrates."
IEEE Trans. Microwave Theory Tech., vol. MTT-26, pp 387-393, june 1978.

[5] T.KITAZAWA and Y.HAYASHI:" Quasi-static characteristics of coplanar waveguide on a saphire substrate with its optical axis inclined."
IEEE Trans. Microwave Theory Tech., vol. MTT-30, pp 920-922, june 1982.

[6] M.HORNO" Quasi-static characteristics of microstrip on arbitrary anisotropic substrates."
Proc.IEEE vol.68, pp 1033-1034, 1980.

[7] A.M.A. EL-SHERBINY:" Hybrid mode analysis of microstrip lines on anisotropic substrates."
IEEE Trans. Microwave Theory Tech., vol. MTT-29, pp 1261-1265, descember 1981.

[8] T.KITAZAWA and Y.HAYASHI:" Propagation characteristics of strip lines with multilayered anisotropic media."
IEEE Trans. Microwave Theory Tech., vol. MTT-31, pp 429-433, june 1983.

[9] T.ITOH, R.MITTRA:" Spectral domain approch for calculating the dispersion characteristics of microstrip lines."
IEEE Trans. on Microwave Theory and Techniques, vol. MTT-21, July 1973.

Legends

Figure 1: Transverse section of the structure.

Figure 2: Variation of the relative propagation constant as a function of μ_{yy}.

Figure 3: Variation of the relative propagation constant as a function of μ_{xx}.

Annex

$$A_1 = \frac{\omega^2 \varepsilon \mu_{12} \gamma}{\Delta} \qquad A_2 = -\frac{\gamma\left(\omega^2 \varepsilon \mu_{11} + \gamma^2\right)}{\Delta}$$

$$A_3 = +\frac{(\omega^2 \varepsilon \mu_{12})^2 + \omega^2 \varepsilon \mu_{22}\left(\omega^2 \varepsilon \mu_{11} + \gamma^2\right)}{j\omega\varepsilon\Delta}$$

$$A_4 = -\frac{\omega^2 \varepsilon \mu_{12} \gamma^2}{j\omega\varepsilon\Delta} \qquad A_5 = -\frac{\gamma\left(\omega^2 \varepsilon \mu_{22} + \gamma^2\right)}{\Delta}$$

$$A_6 = -A_1 \qquad A_7 = A_4$$

$$A_8 = -\frac{(\omega^2 \varepsilon \mu_{12})^2 + \omega^2 \varepsilon \mu_{11}\left(\omega^2 \varepsilon \mu_{22} + \gamma^2\right)}{j\omega\varepsilon\Delta}$$

$$B_1 = -\frac{j\omega\varepsilon\left(\omega^2 \varepsilon \mu_{22} + \gamma^2\right)}{\Delta} \qquad B_2 = \frac{j\omega\varepsilon\,\omega^2 \varepsilon \mu_{12}}{\Delta}$$

$$B_3 = \frac{\gamma\,\omega^2 \varepsilon \mu_{12}}{\Delta} = A_1 \qquad B_4 = -\frac{\gamma\left(\omega^2 \varepsilon \mu_{22} + \gamma^2\right)}{\Delta} = A_5$$

$$B_5 = B_2 \qquad B_8 = -B_3$$

$$B_6 = -\frac{j\omega\varepsilon\left(\omega^2 \varepsilon \mu_{11} + \gamma^2\right)}{\Delta} \qquad B_7 = -\frac{\gamma\left(\omega^2 \varepsilon \mu_{11} + \gamma^2\right)}{\Delta} = A_2$$

$$\Delta = \left(\omega^2 \varepsilon \mu_{22} + \gamma^2\right)\left(\omega^2 \varepsilon \mu_{11} + \gamma^2\right) + \left(\omega^2 \varepsilon \mu_{12}\right)^2$$

ANALYSIS OF THE BEHAVIOUR OF QUASI COMPLEX MODES ON LOSSY SUBSTRATE BOXED MICROSTRIP LINES

F. HURET, P. PRIBETICH, P. KENNIS

Equipe Electromagnétisme des circuits
Centre Hyperfréquences et Semiconducteurs, U.A. CNRS N° 287
U.S.T.L. FLANDRES ARTOIS
59655 VILLENEUVE D'ASCQ FRANCE
Fax. number:20.43.49.95.

ABSTRACT:
In this communication, by using spectral domain approach improved by asymptotic expansions, we show by means of coupling integral values that the notion of quasi complex modes can be introduced for lightly lossy substrates. The quasi complex modes are particular modes with similar behaviour than lossless structure complex modes.

The analysis of discontinuities between planar transmission lines, particulary for microstrip lines, has received a great interest from many years.Accurate modeling of such discontinuities is of fundamental importance for successful monolithic integrated circuit design.In fact increasing circuit complexity needs very efficient numerical techniques in order to solve electromagnetism problems.In this mind when mode matching method in the discontinuity plane is used, it is necessary to determine the set of modes with as accuracy as possible.More ever for boxed losseless structure, it has been shown that complex modes can occur, so that ignoring those modes would lead to non accurate solutions [1] [2].

The properties of complex waves have been investigated in detail, both theoretically and experimentally for shielded circular dielectric rod [3],[4] and for boxed microstrip line[2].

Up to now, most of published works concern the possibility of propagation of complex modes in lossless structure and only a few works focuse on complex and backward-wave modes in lossy waveguides [5].So, when shielded microstrip lines laid on semi-insulating or doped semi-conductor substrates, are considered for MMIC applications, it is necessary to investigate the evolution of complex solutions for lossless structure, under the effect of bulk losses in the substrate.

In this communication, by using spectral domain approach improved by asymptotic expansions, we show by means of coupling integral values that the notion of quasi complex modes can be introduced for lightly lossy substrates. Naturally, for lossy structures all modes have complex propagation constant, so in our mind, the quasi complex modes are particular modes with similar behaviour

than lossless structure complex modes.

NUMERICAL RESULTS

The studied microstrip geometry is shown in figure 1. It has already been shown that complex modes can be supported by this lossless structure, using the Singular Integral Equation (S.I.E.) or the Spectral Domain Approach (S.D.A.) technics. This communication addresses the effect of a lossy substrate on complex modes. With this aim, as example we present fig. 2, 3 and 4 the freqential evolutions of the two propagation constants (γ_1, γ_2) for a pair of modes initialy complex on lossless structure, then we point out the evolutions of these modes, when we consider respectivly a substrate conductivity of $\sigma=3.10^{-3}$ S/cm, $\sigma=7.10^{-3}$ S/cm and finally $\sigma=2.10^{-2}$ S/cm.

For the lossless structure, in the complex frequancy range, we obtain:

$$\gamma_1 = \beta_1 - j\,\alpha_1 \; ; \; \gamma_2 = -\beta_2 - j\,\alpha_2 \text{ with } \beta_1 = \beta_2 > 0 \; , \; \alpha_1 = \alpha_2 > 0$$

Now let us investigate this pair of complex modes when losses are taking into account. As shown in fig. 3, 4 and 5, in the initialy complex frequency range γ_1 and γ_2 cannot yet be linking, so we are tempted to say that the pair of complex modes becomes two usual modes. Indeed, we obtain a continuous variation of γ_1 and γ_2 with α_1 never equals to α_2. However, when we take into account small values of the conductivity ($\sigma=3.10^{-3}$ S/cm, $\sigma=7.10^{-3}$ S/cm), we have to notice that if we consider frequencies smaller than the maximum of the complex frequency range, we obtain for the two modes (fig. 2 and 3):

$$\gamma_1 = \beta_1 - j\,\alpha_1 \; ; \; \gamma_2 = -\beta_2 - j\,\alpha_2 \text{ with } \beta_1 \neq \beta_2 > 0 \; , \; \alpha_1 \neq \alpha_2 > 0$$

This means that the mode 2 propagates in the -Z direction and it is attenuated in the opposite direction. This phenomenon is equally describing by the fig.5 which represents the evolution of the propagation constant for the two modes versus the substrate conductivity for a frequency equal to 19 GHz.
This apparent continuous energy gain on passive structure, can again be explained by strong coupling in energy sense [1] between the two considered modes (γ_1, γ_2) in the frequency and conductivity ranges when $\gamma_2 = -\beta_2 - j\,\alpha_2$ (β_2 and $\alpha_2 > 0$).This phenomenon is pointed out as example fig. 6; this curves show the evolution of the real part of the integrals (1) versus the substrate conductivity for a frequency equal to 19 GHz, while the fig. 7 represents the imaginary part of these integrals.

$$\int_S (e_1 \times h_2^*)\,dS = p \quad ; \quad \int_S (e_2 \times h_1^*)\,dS = p' \text{ with } p' \dashrightarrow -p^* \quad (1)$$

In this proposition of communication we have studied the evolution of the complex modes solutions initialy

obtained for a lossless microstrip line, due to bulk losses introduced in the substrate.

Naturally, all the propagation constants of the different modes become complex. In fact for the conductivity values considered ($\sigma<2.10^{-2}$ S/cm), the two initial complex modes are strongly coupled in the energy sense, and stay much more coupled around the initial complex frequency range, than outside; so that these two modes cannot exist alone inside this range ($\gamma_2 = -\beta_2 - j\,\alpha_2$, β_2 and $\alpha_2 > 0$).

As the frequency behaviour of these two modes are quite similar to the initial complex modes of lossless structure, we have called this pair of modes quasi complex modes.

At the conference , we propose to present in detail the notion of "quasi complex" modes on lossy substrate, and the improvements of the well known Spectral Domain Approach that we have used in this numerical simulation.

REFERENCES

[1] A.S. OMAR, K.F. SCHUNEMANN.
"The effect of complex modes at finline discontinuities".
IEEE Trans. on microwave theory and techniques, Vol. MMT 34, N° 12, December 1986, pp. 1508-1514.

[2] W.X. HUANG, T. ITOH.
"Complex modes in lossless shielded microstrip lines".
IEEE Trans. on microwave theory and techniques, Vol. 36, N° 31, pp. 163-165, January 1988.

[3] P.J.B. CLARRICOATS, K.R. SLINN.
"Complex modes of propagation in dielectric loaded circular waveguide".
Electronic Letters,1965, 1, pp. 145-146.

[4] V.A. KALMYK, S.B. RAYEVSKIY, V.P. YGVYUMOV.
"An experimental verification of existence of complex waves in a two layer circular shielded waveguide".
Radio Eng. & Electron. Phys., 1978, 26, pp. 16-19.

[5] K.N. WHITES, R. MITTRA.
"Complex an backward-wave modes in dielectrically loaded lossy circular waveguides".
Microwave and optical technology letters, Vol. 2, N°6, June 1989, pp.199-204.

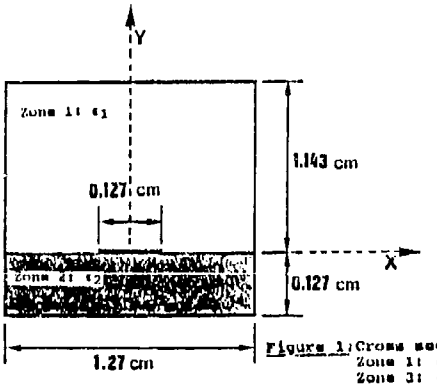

Figure 1: Cross section of the shielded microstrip line.
Zone 1: $\varepsilon_1 = \varepsilon_0$
Zone 3: $\varepsilon_2 = \varepsilon_0.(\varepsilon_r - j.\sigma/\varepsilon_0\omega)$; ε_r=8.875

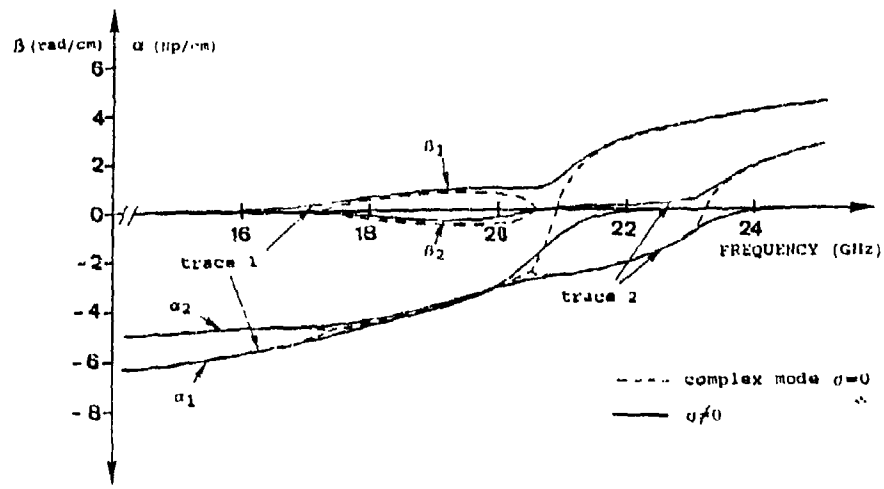

Figure 2: Propagation constant $\gamma = \beta + i.\alpha$ of the two modes versus the frequency for $\sigma = 3.10^{-3}$ S/cm.

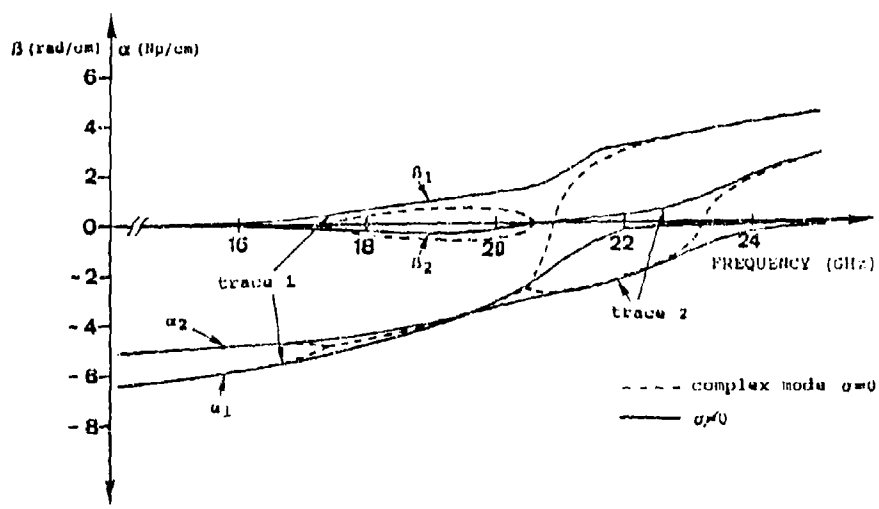

Figure 1: Propagation constant $\gamma = \beta + i.\alpha$ of the two modes versus the frequency for $\sigma = 7.10^{-3}$ S/cm.

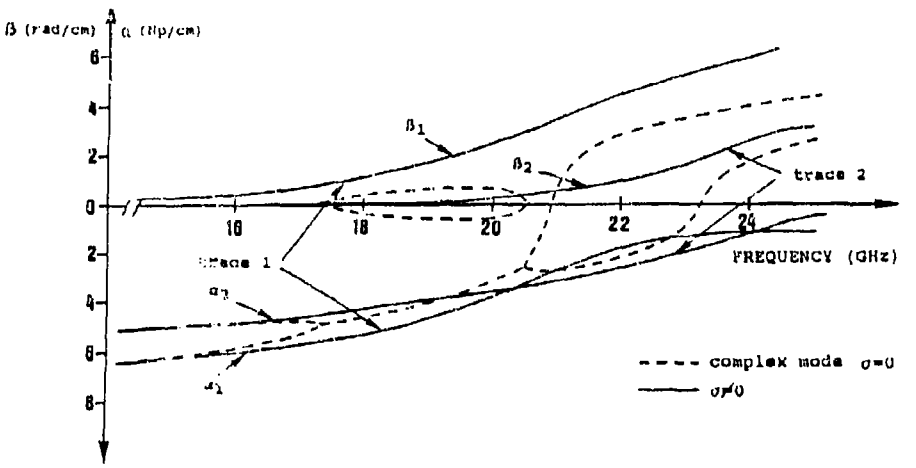

Figure 4: Propagation constant $\gamma = \beta + j\alpha$ of the two modes versus the frequency for $\sigma = 2.10^{-3}$ S/cm.

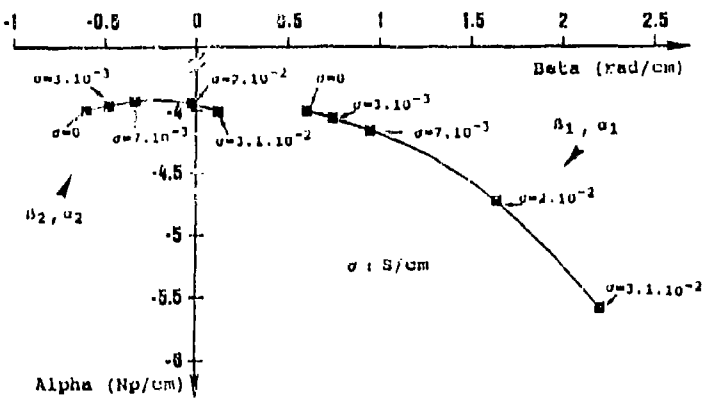

Figure 5: Propagation constant $\gamma = \beta + j\alpha$ of the two modes versus the conductivity for a frequency, F = 19 GHz.

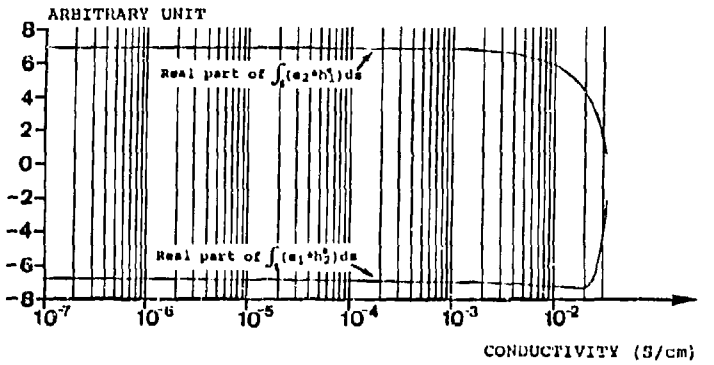

Figure 6: Evolution of the real part of the integrals $\int_s(e_1^* h_2^*)ds$ versus the conductivity for a frequency, F = 19 GHz.

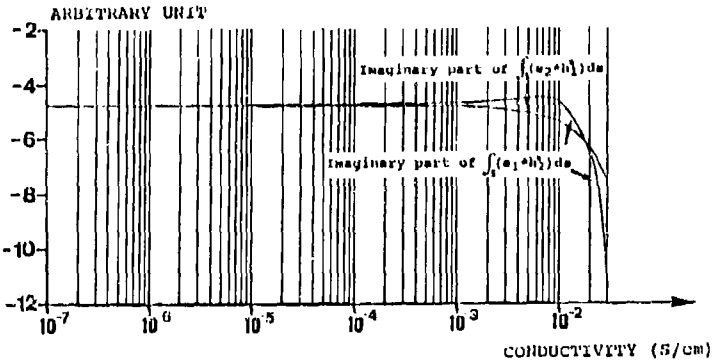

Figure 7: Evolution of the imaginary part of the integrals $\int_s(e_1^* h_2^*)ds$ versus the conductivity for a frequency, F = 19 GHz.

Computer Modelling of Helical Slow-Wave Structures for use in Travelling Wave Tubes

A.J.Marrison

AEA Technology, Culham Laboratory,
Abingdon, Oxon. OX14 3DB, England.

Abstract

This paper concerns the use of the Numerical Electromagnetics Code (NEC) to model helical slow-wave structures for use in Travelling Wave Tubes (TWT's). Properties such as coupling impedance and phase velocity can be obtained from such models. These results are of value in assessing the cold test properties of proposed TWT designs, and for providing calibration data for a 2-D axisymmetric time domain particle-mesh calculation of the self consistent interaction between an electron beam and the EM field supported by the TWT slow-wave structure.

NEC has been used to calculate EM fields, coupling impedance and phase velocity for an idealised slow-wave structure, the sheath helix (helically conducting cylinder), both with and without a coaxial conducting outer cylinder. The results of this numerical analysis are presented and shown to be in good agreement with analytic results.

1 INTRODUCTION

The object of the work described in this paper is to assess the possibility of using the Numerical Electromagnetics Code (NEC) [1] to model helical slow-wave structures in three dimensions. Results from such numerical models are of value in evaluating the cold test properties of helical Travelling Wave Tubes (TWT's).

This paper concerns the use of NEC to model an idealised slow-wave structure, the sheath helix. Analytic results for this structure are readily available [2] for comparison with numerical results.

Section 2 presents a brief description of the sheath helix. The construction of numerical thin wire models of the sheath helix for use in NEC is the subject of Section 3. Section 4 presents the results of NEC calculations using such models, and compares them with analytic results. Conclusions are drawn in Section 5.

2 THE SHEATH HELIX

The sheath helix is a helically conducting cylindrical sheet, where the direction of conduction makes an angle ψ with a plane normal to the cylinder axis; there is no conduction perpendicular to this direction.

Mathematical analysis of the electromagnetic fields supported by the sheath helix [2] shows that an electromagnetic wave can propagate parallel to the axis of the helix

with a phase velocity v_z given by

$$v_z = c \tan \psi, \tag{1}$$

where c is the speed of light *in vacuo*; this slow-wave has the form

$$\mathbf{E} = \mathbf{E}(r,\phi)e^{i(\omega t - \beta z)} \tag{2}$$

$$\mathbf{H} = \mathbf{H}(r,\phi)e^{i(\omega t - \beta z)} \tag{3}$$

in cylindrical polar coordinates (r,ϕ,z). The quantities of greatest interest are the wavenumber, β, and the coupling impedance Z_c, where

$$Z_c = \frac{E^2}{\beta^2 P}. \tag{4}$$

Here, E is the amplitude of the z-component of electric field, evaluated on the axis of the sheath helix, and P is the total power crossing a plane perpendicular to the helix axis.

3 THIN WIRE NUMERICAL MODELS OF THE SHEATH HELIX

The Numerical Electromagnetics Code (NEC) [1] is a method of moments code which uses straight wire segments and surface patches to model physical objects. When modelling a single helical wire with straight wire segments it is important that the number of segments per turn of wire is large enough to approximate a circular cross section; several helical wires modelled in this way were "screwed together" to form a thin wire approximation to the helically conducting sheath helix. The free ends of each helical wire were made resistive to ensure that reflections from the wire ends were damped out before reaching the central portion of the sheath helix. This resistive loading significantly reduced the standing wave ratio in the central portion of the thin wire model, so that conditions in this region closely resembled those in an infinitely long sheath helix; this enabled a direct comparison to be made between numerical results and those obtained from analytic treatments (e.g. Ref [2]) which apply to an infinitely long sheath helix.

Two numerical models were used for input to NEC, the first a thin wire model of a sheath helix, constructed in the manner described above, and the second comprising this same model of a sheath helix, plus a surrounding concentric cylindrical wire mesh simulating a perfectly conducting cylindrical outer surrounding the sheath helix. The wire mesh was constructed using the so-called "equal area rule" [4], which says that when modelling a solid surface with a wire mesh, the total surface area of the wires should equal the area of the solid surface.

Both thin wire models are illustrated schematically in Figs. 1 and 2, and their details are given in Table 1.

Figure 1: *Sheath helix (Model 1)*

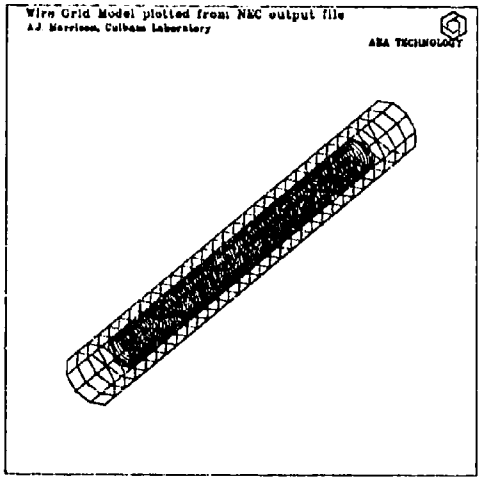

Figure 2: *Sheath helix with cylindrical outer (Model 2)*

	Model 1	Model 2
Length of sheath helix (m)	1.6	1.6
Pitch angle (ψ)	11.2°	11.2°
Radius of sheath helix (m)	0.064	0.064
Turn spacing (m)	0.08	0.08
Number of single helix copies	15	15
Number of wire segments per turn	20	20
Radius of conducting outer (m)	no outer	0.08
Length of conducting outer (m)	no outer	2.0
Total number of wire segments	6000	13230

Table 1: *Model parameters*

4 RESULTS AND INTERPRETATION

The thin wire model of the sheath helix was excited by applying a voltage excitation of frequency 300 MHz (with free space wavelength $\lambda_0 = 1$m) to each of the helical wires comprising the model. The resulting fields and currents were calculated by NEC, both in free space and in the presence of a cylindrical wire mesh surrounding the sheath helix. Figure 3 shows the amplitude of the current oscillation induced in one of the single helical wires plotted as a function of wire segment number (equivalent to distance along the wire). The large peak in this Figure indicates the position of the voltage excitation. As expected, the standing wave ratio in the central part of the wire is quite low at $\sim 1{\cdot}1$ due to the resistive loading described in Section 3.

The following Subsections present those numerical results of particular importance in TWT design: namely, the axial electric fields inside the sheath helix, the wavelength, λ, of the slow-wave propagating along the helix axis, and the coupling impedance Z_c. Throughout these subsections, cylindrical polar coordinates (r, ϕ, z) will be used, with the z-axis coinciding with the helix axis.

4.1 Model 1

Figure 4 compares the values of the axial electric field, E_z, computed by NEC with values obtained from analytic expressions [2]; the Figure shows the percentage difference between computed and analytic values of E_z plotted as a function of radial distance from the helix axis. The computed and analytic results are seen to be in good agreement until sampling points approach the surface of the thin wire model at

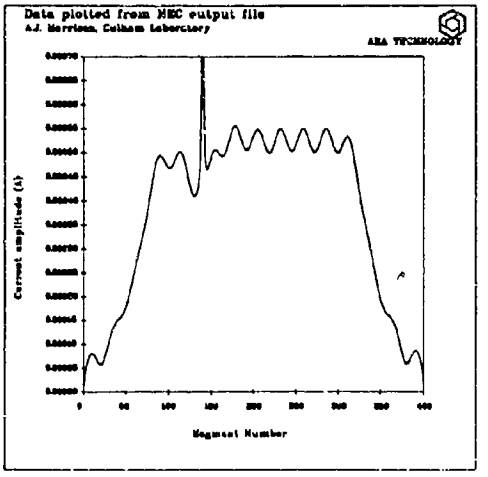

Figure 3: *Amplitude of current oscillation in single helix copy*

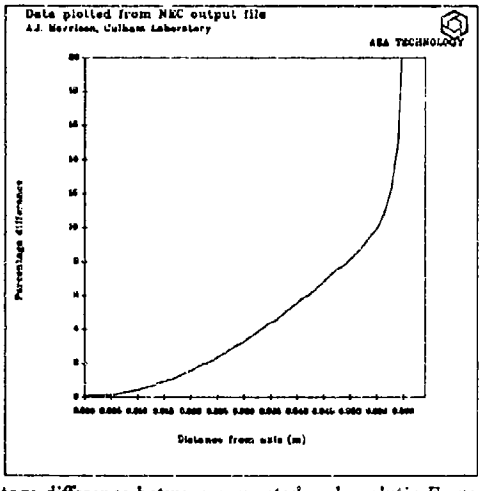

Figure 4: *Percentage difference between computed and analytic E_z vs. distance from axis*

the extreme right of Fig. 4; when this happens, the discrete nature of the thin wire model becomes important, and fields differ significantly from those near the perfectly smooth surface of the idealised sheath helix.

Figure 5 shows the amplitude of E_z, computed on the helix axis, plotted as a function of z. The small standing wave component evident in this figure has a wavelength of ~ 0.1m, so that the forward and reflected waves combining to produce it have a wavelength $\lambda \approx 0.2$m; this figure is in excellent agreement with that predicted by eq(1) of $\lambda_0 \tan\psi = 0.198$m, with $\lambda_0 = 1$m and $\psi = 11.2°$ (see Table 1).

A numerical integration of the Poynting vector over a plane perpendicular to the helix axis was performed in order to calculate the coupling impedance Z_c (eq(4)). This surface integration was reduced to an integration over a radial line segment by assuming azimuthal symmetry of all field quantities, in accordance with the assumptions made in analytic treatments [2]. This assumption is justified by Fig. 6, which shows the amplitude of E_r near the surface of the thin wire model plotted as a function of the azimuthal angle, ϕ. The amplitude of the variation in E_r is only 2% of the mean value of E_r – a good approximation to azimuthal symmetry.

The numerical integration of the Poynting power gave

$$P = 1.98 \times 10^{-3} \text{ W}.$$

From Fig. 5, the amplitude of the travelling wave component of E_z is 8.25 V/m, and with the wavenumber $\beta = \frac{2\pi}{\lambda} = 31.4\text{m}^{-1}$, eq(4) gives the coupling impedance:

$$Z_c = 34.8\ \Omega.$$

The analytic expression for Z_c [2] gives

$$Z_c = 31.9\ \Omega,$$

which is within 8% of the computed value.

4.2 Model 2

As stated in Section 3, this Model was identical to Model 1 apart from the presence of a cylindrical wire mesh of radius 0.08m surrounding the sheath helix, simulating a perfectly conducting cylindrical outer.

Figure 7 shows the variation of E_z with radial distance from the helix axis, out to a distance of four times the radius of the sheath helix. As expected, E_z vanishes outside the perfectly conducting outer at 0.08m.

In Fig. 8, the percentage difference between computed values of E_z and those obtained from an analytic expression [3] is plotted as a function of r out to the surface of the thin wire model of the sheath helix. Once more, computed and analytic results are in excellent agreement until sample points approach the surface of the thin wire model, where differences between computed and analytic results become significant for the reasons given in the previous Subsection.

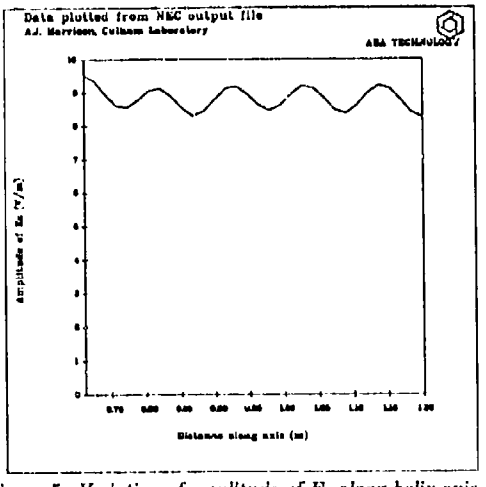

Figure 5: *Variation of amplitude of E_z along helix axis*

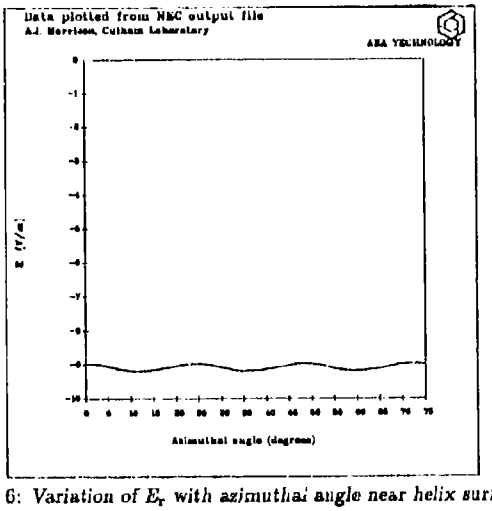

Figure 6: *Variation of E_r with azimuthal angle near helix surface*

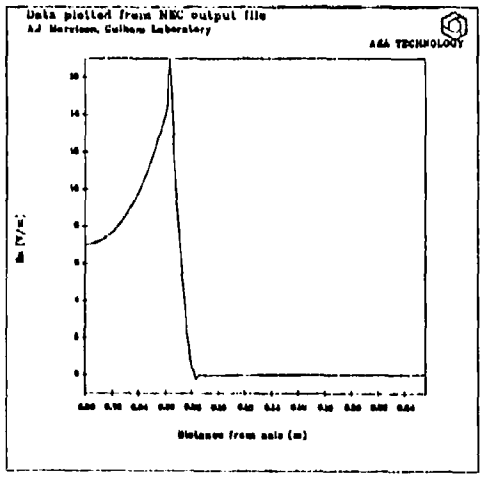

Figure 7: *Computed E_z vs. distance from axis*

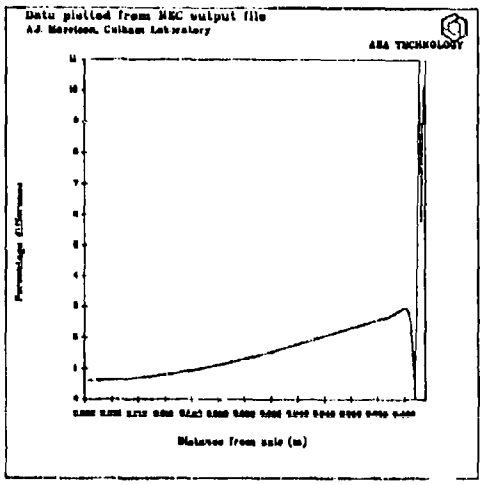

Figure 8: *Percentage difference between computed and analytic E_z vs. distance from axis*

Figure 9 shows the amplitude of E_z, computed on the helix axis, as a function of z. Again, there is a small standing wave component with wavelength ~ 0.1m giving a travelling wave wavelength of $\lambda \approx 0.2$m, in good agreement with the analytic value of 0.202m [3].

The power flowing through a plane perpendicular to the helix axis was calculated by a numerical integration of the Poynting vector in an identical manner to that described in the previous Subsection, giving

$$P = 2.94 \times 10^{-3} \text{ W}.$$

Figure 9 gives the amplitude of the travelling wave component of E_z as 7.4 V/m, and from eq(4), the coupling impedance is

$$Z_c = 18.9\ \Omega$$

This result is within 4% of the analytic result of 19.6 ohms [3].

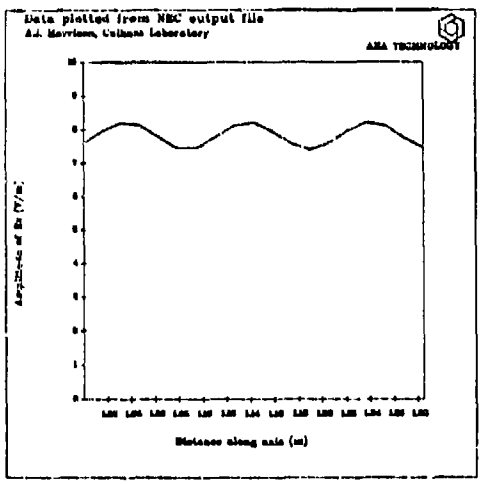

Figure 9: *Variation of amplitude of E_z along helix axis*

4.3 Summary of Results

The results presented in Subsections 4.1 and 4.2 are summarised in Table 2; there is excellent agreement between computed and analytic results.

5 CONCLUSIONS

Numerical models of the sheath helix, both with and without a conducting outer, have been constructed from a finite number of finite helical wires. Results from the numerical models are in good agreement with analytic results.

	Model 1	Model 2
Computed Wavelength(m)	0.2	0.2
Analytic Wavelength(m)	0.198	0.202
Error on computed wavelength	1%	1%
Computed coupling impedance (Ω)	34.8	18.9
Analytic coupling impedance (Ω)	31.9	19.6
Error on computed coupling impedance	8%	4%
Error on computed E_z in region of helix axis	< 8%	< 3%

Table 2: *Computed and analytic results*

Errors in the numerical results are due to the finite length of the numerical models, which gives rise to reflected waves, and to the discrete nature of the models, which leads to azimuthal field variations that do not appear in the idealised analytic model of the sheath helix.

It should be remembered, however, that in a TWT design application, NEC will be used to model real, finite helical structures, where reflected waves and azimuthal field variations are to be expected; the fact that finite numerical models have produced these features is encouraging.

The work reported here gives confidence that NEC is an appropriate code for modelling helical slow-wave structures, capable of predicting the electromagnetic fields within the structure with a typical error of less than 5%.

6 REFERENCES

[1] Burke, G.J. and Poggio, A.J., *Numerical Electromagnetics Code (NEC) - Method of Moments, Part III: User's Guide*, Lawrence Livermore National Laboratory Report UCID 18834, January 1981.

[2] Pierce, J.R., *Travelling Wave Tubes*, D.Van Nostrand, New York, 1950, pp 23–27, pp 229–232.

[3] Pöschl, K., *Wave propagation along a helix with a cylindrical outer conductor*, Arch. elek. Übertr. , 10, pp 195–208, 1956.

[4] Moore, J. and Pizer, R., *Moment Methods in Electromagnetism*, Research Studies Press Ltd., U.K., 1984, p 117.

ELECTRICALLY TRIMMED ARRAY SYNTHESIS FOR SOLID STATE RADAR APPLICATIONS

M.A. Hussain, B. Noble, and M. McKee
General Electric Research and Development Center
Schenectady, New York

1. INTRODUCTION

In this paper we briefly give results and outline a new approach to the synthesis of electrically trimmed arrays. We use a deterministic method to obtain a highly thinned space tapered array design (butterfly) for solid state radar applications.

For simplicity of design and implementation we consider only space tapered and highly thinned arrays with uniform current distribution for the elements. It is well known in the literature that for random as well as space tapered arrays, the control of sidelobes is extremely difficult and is predominantly determined by the number of elements in the array (Ref. [1,2]).

Low sidelobes close to the main beam together with low average sidelobes play a dominant part in the two-way beam utilization in radar systems in the presence of clutter. Our method allows for very strong control of the near-in sidelobes and soft control of the average sidelobes. Unequally spaced rows of elements discourages the presence of grating lobes, and the sidelobes away from the main beam follow the mathematical distribution studied in the theory of random arrays.

Our analysis is based on Taylor's analysis, with Woodward's method for one dimensional case and Dossier's representation for the circular case. In a previous paper (Ref. [3]) we have outlined the method for the circular aperture. In this paper we have extended the method to noncircular geometries. The trimming of the shape is done by a simple algorithm for the location of elements in the transverse direction. The algorithm for the determination of the number of elements in each row uses Taylor's theorem to avoid singularities of the illumination function; at the same time it also uses asymptotic Dolph-Tchebycheff theory for the control of the zeroes near the main beam.

The results are quite interesting in the sense that the algorithm gives the desired pattern and at the same time dictates the shape of the aperture. The results are given in the accompanying figures. Figure 1 gives the location of the elements; figures 2a and 2b show the pattern distribution for one set of parameters with the near-in sidelobe controlled to 40dB; figures 3a and 3b show the pattern distribution for another set of parameters with near-in sidelobe controlled to 50dB.

2. TWO DIMENSIONAL INTEGRAL EQUATION

The planar aperture integral equation for the illumination function leads to the following space factor equation (using spherical coordinate θ and ϕ),

$$\Pi(\theta,\phi) = \iint_A J(\xi,\eta) e^{-j\,k\,(\xi \sin\theta\cos\phi + \eta \sin\theta\sin\phi)} d\xi d\eta \qquad (1)$$

Where A represents area enclosed by a rectangle 2a by 2b. We assume a special current distribution represented as a product form $J(\xi,\eta) = g_1(\xi) g_2(\eta)$ over a rectangular area and further assume symmetric geometry. Equation (1) reduces to:

$$\Pi = 4 \int_0^a J_1(\xi)\, \cos(k\,u)\xi\, d\xi \int_0^b J_2(\eta)\, \cos(k\,v)\eta\, d\eta \qquad (2)$$

where $u = \sin\theta\cos\phi$, $v = \sin\theta\sin\phi$. Let
$\pi\xi = a\alpha$, $\pi\eta = b\beta$, $\frac{2a}{\lambda} = \frac{N}{2}$, $\frac{2b}{\lambda} = \frac{M}{2}$. Equation (2) can be written as:

$$\Pi(\theta,\phi) = \frac{ab}{\pi^2} F_1(u) F_2(v) \qquad (3)$$

Where

$$F_1(u) = 2\int_0^\pi g_1(\alpha)\cos(\alpha u)\, d\alpha \text{ and } F_2(u) = 2\int_0^\pi g_2(\beta)\cos(\beta u)\, d\beta$$

Above equation (3) are exactly the integral equation solved by Taylor [4].

3. NUMERICAL SOLUTION

In our approach we use numerical method rather than analytic method for the solution of the integral equation using Woodward's synthesis techniques. The result are identical to those of Taylor [4] . As in Taylor's result, however, the sidelobes are not of equal magnitude as was the case with Dolph-Tchebycheff analysis. To make them equal we iterate around the zeros and a convergent solution is obtained in a few iterations. The details are given in [5] and briefly outlined below: Let $g_1(p)$ have the following Fourier expansion:

$$g_1(p) = \frac{D_0}{2} + \sum_{m=1}^{\infty} D_m \cos(m\,p) \qquad (4)$$

for $0 < p \leq \pi$ otherwise $g_1(p) = 0$ for $p > \pi$. Substituting equation (4) into

equation (3) we have

$$F_1(u) = 2\pi \left(\frac{D_0 \sin(\pi u)}{\pi u} + \sum_{m=1}^{\infty} D_m \left(\frac{\sin(\pi (u+m))}{\pi (u+m)} + \frac{\sin(\pi (u-m))}{\pi (u-m)}\right)\right) \quad (5)$$

from (5) we have:

$$D_m = \frac{F_1(m)}{2\pi} \quad (6)$$

Denoting $F_1(m)$ $by F_m$, we have from equation (4) and (6):

$$g_1(p) = \frac{1}{4\pi}\left(F_0 + 2 \sum_{m=1}^{\infty} F_m \cos(m\ p)\right) \quad (7)$$

Suppose that we decide that our far field pattern should have zeroes at n=m for m>M, then .*

$$g_1(p) = \frac{1}{4\pi}\left(F_0 + 2 \sum_{m=1}^{M} F_m \cos(m\ p)\right) \quad (8)$$

This gives:

$$F_1(u) = a_0(u)\ F_0 + \sum_{m=1}^{M} F_m\ a_m(u) \quad (9)$$

where $a_0(u) = \sin(\pi u)/\pi u$

$$a_m(u) = \frac{\sin(\pi (u+m))}{\pi (u+m)} + \frac{\sin(\pi (u-m))}{\pi (u-m)} \quad (10)$$

From (9) and (10) we have F(n) =0 for n>M, and hence the Taylor's synthesis theorem is satisfied for finite value of the illumination function.**

We normalize so that F(0) $= F_0 = 1$. Then we have M unknowns, $F_1, F_2, \ldots, F_M$ at our disposal to control the size of the sidelobes and the null points. Also the knowledge of F_i gives $g_{1(p)}$ from equation (7). We now set up

---

* M corresponds to $\bar{n}$ - 1 in Taylor's paper.

** From here on our method differs considerably from that of T. T. Taylor. Taylor introduces a single stretching parameter for shifting M+1 zeroes. On the other hand, we use these M degrees of freedom to form the desired pattern.

M simultaneous linear algebraic equations for the determination of the F_i. The details of examples are given in ref. [5]. It should be noted that the product form of the illumination function leads to extremely small sidelobes in the u-v plane away from the axis and hence the success in rectangular designs for solid state radars.

4. ARBITRARY SHAPE OF AN APERTURE

In general the two dimensional integral equation may be very difficult to solve. In this section we outline another special case. We assume that $J(\xi,\eta)$ is a function of ξ only and the aperture can be described by $f_1(x)$.

Using the symmetry condition equation (1) can be simplified to:

$$\Pi(\theta,\phi) = 4\int_0^{\xi_1} (J(\xi)\frac{\sin(kf_1(\xi)v)}{kv}\cos(ku\xi)d\xi \tag{11}$$

or

$$\Pi(\theta,0) = 4\int_0^{\xi_1} J(\xi)f_1(\xi)\cos(ku\xi)d\xi \tag{12}$$

Comparing above equation with equation (3) we see that that the special case treated here gives a similar equation except the illumination function has much broader meaning e.g. for the case of uniform illumination we get an integral equation for the aperture distribution function. This will now be compared to space factor for a set of discrete elements.

5. DISCRETE DISTRIBUTION OF ELEMENTS

Consider a set of elements on the x-y plane located at $dx_{mn}dy_{mn}$. The usual element factor can be written as

$$E(\theta,\phi) = \sum_m\sum_n I_{mn}e^{jk(dx_{mn}u + dy_{mn}v)} \tag{13}$$

Considering a symmetric case let
$dx_{mn} = dx_m$, $dy_{mn} = -\frac{1}{2}L_m + \frac{1}{2}(n-1)$, for $m = 1,...R$, $m = 1,...N(m)$, and $I_{mn} = 1$.
Equation (13) then reduces to

$$E(\theta,\phi) = 2\sum_m N_m \left(\frac{\sin(\frac{kvN_m}{4})}{N_m \sin(\frac{kv}{4})}\right)\cos(kdx_m u) \qquad (14)$$

From above

$$E(\theta,0) = 2\sum_m N_m \cos(kdx_m u) \qquad (15)$$

and the comparison with the previous cases is straightforward.

In general for the design of discrete synthesis we have to locate both dx_m as well as the number of elements. The analysis has been carried out similar to given in reference[3]. Here for illustrative purpose, we take some quadratic distribution of the location of the rows and compute the number of elements from analysis of Taylor's synthesis as described in the previous section by forcing the illumination function to have zeros at the location given by Taylor theory. The detail analysis will be submitted soon. Some preliminary result are given in figure 1 showing the layout of elements and figure 2 giving element pattern for 744 elements and similar pattern for 1195 elements.

6. CONCLUSION

In this paper we have outlined our method for discretization of a non-circular aperture with a set of rows which are further discretized as a set of elements on a row. These elements have the same current magnitudes. For practical reason we have only concentrated on the near side lobes. To paraphrase Prof. Lo (ref. [2]), thinning as well as randomization of location has not been a success for reduction of side lobes. The difficulty of this problem may be attributed to the fact that the sidelobe level depends on the element spacing in a highly nonlinear manner, and that in general there is no analytical method to determine the highest sidelobe level nor the angle and direction in which the highest sidelobe may occur, even with all the element positions given. Except for smaller arrays, a numerical search with a modern computer is considered impractical. The reason is that the highest sidelobe position does not change continuously with the element position. With this understanding it is not surprising to find that so far all attempts for thinning and space tapering are not very successful. The dynamic programming technique has also been attempted (refs. [14] and [16]). Our method has concentrated only on the near sidelobes, with a fair degree of success. We are still in the process of refining our method and the results will be communicated soon. The array design algo-

rithm will have applications in many fields e.g. sonar and ultrasound.

7. REFERENCES

1. B.D. Steinberg, Principles of Aperture and Array System Design, New York: Wiley-Interscience Publication. ch. 8, p. 141, 1976.
2. Y.T. Lo and S.W. Lee, Antenna Handbook: Theory, Applications, and Design, New York: Van Nostrand Reinhold Company. ch. 14, pp. 4-5, 1988.
3. M.A Hussain, W-T. Lin, and M. McKee, "Representation of Continuous Circular Aperture as a Set of Discrete Rings for Prescribed Radiation Pattern", (submitted to Fourth Biennial IEEE Conference on Electromagnetic Field Computation), 1990.
4. Taylor, T. T.,"Design of Line-source Antennas for Narrow Beamwidth and Low Sidelobes", IRE Trans. on Antennas and Propagation Vol. Ap-3 pp 16-28 January 1955.
5. M.A Hussain,Ben Noble and W-T. Lin, "Numerical Solution of an Aperture Integral Equation " Transaction of the Seventh Army Conference on Applied Mathematics ans Computing. ARO Report 90-1. February 1990.

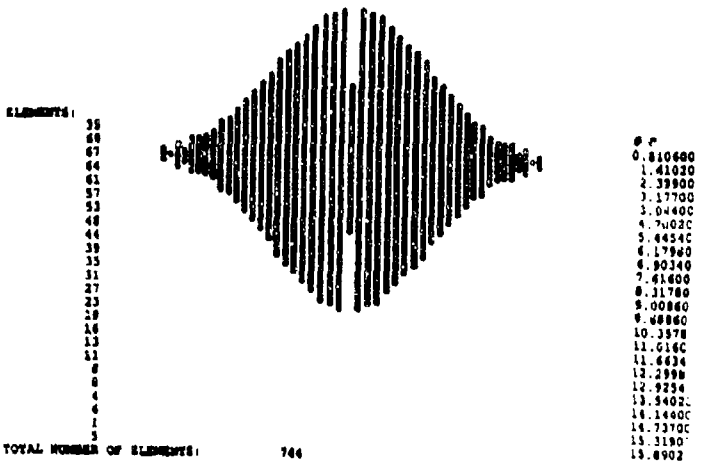

Figure 1: Layout and Location of Elements, Butterfly Design.

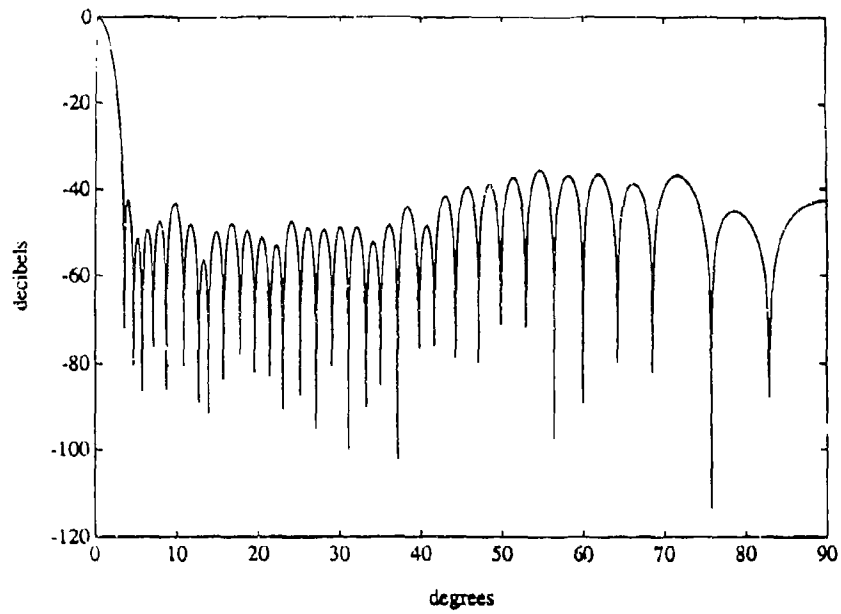

Figure 2a: 744 Elements, 40 dB Design

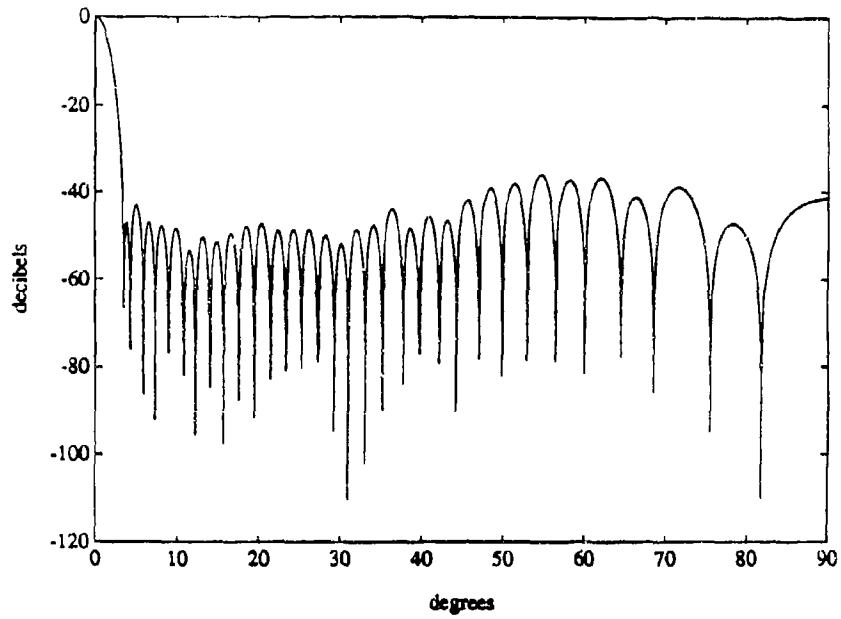

Figure 2b: Same configuration as Figure 2a, 1195 Elements

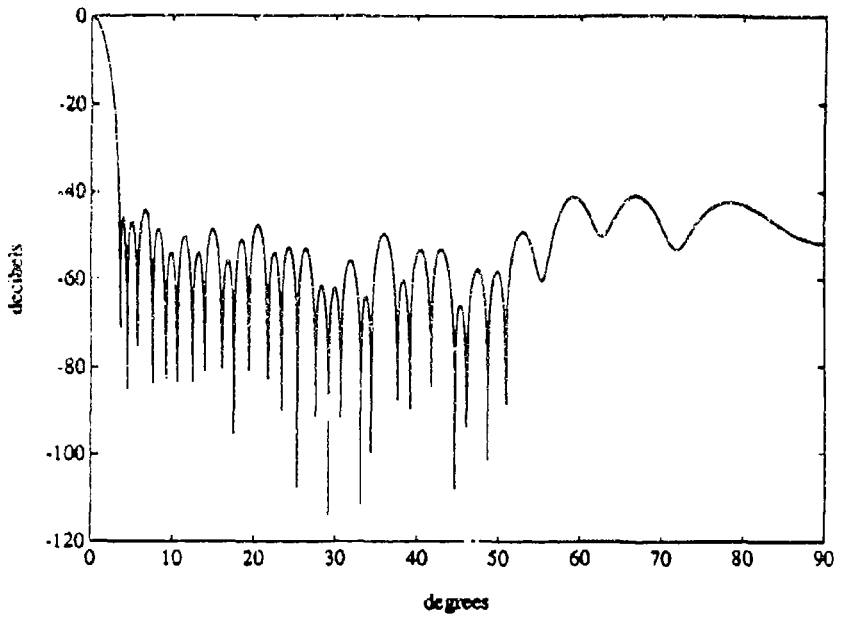

Figure 3a: 951 Elements, 50dB Design

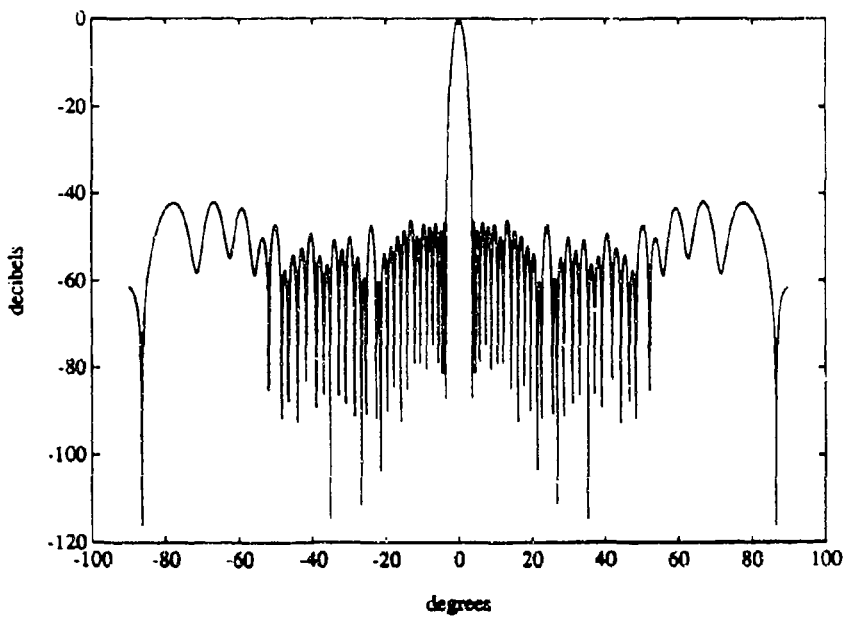

Figure 3b: Same configuation as Figure 3a. 1203 elements

GUIDED WAVE PROPAGATION ON TWO-DIMENSIONAL CLUSTERS OF DIRECTLY-COUPLED CAVITY RESONATORS

Ross A. Speciale

General Dynamics, Air Defense Systems

P.O. Box 50-800, MZ 601-71, Ontario, CA 91761-1885

ABSTRACT

We are attempting to determine the guided-wave propagation properties of electrically-large, two-dimensional delay structures, composed of clusters of directly-coupled, high-Q cavity resonators, ordered in either a square or in an hexagonal lattice.

The unit-cells of the delay structure with square lattice are four-port cavity resonators, with either square or circular cross-section, exhibiting C_{4v}-symmetry. This type of delay structure also has C_{4v}-symmetry, plus obvious translational symmetries in eight directions, spaced azimuthally by 45° from each other.

The unit-cells of the delay structure with hexagonal lattice are six-port cavity resonators, with either hexagonal or circular cross-section, exhibiting C_{6v}-symmetry. This second type of delay structure also has C_{6v}-symmetry, plus obvious translational symmetries in twelve directions, spaced azimuthally by 30° from each other.

Delay structures of either type are intrinsically image-matched, up to their outer edges or external boundaries, where an unconditional impedance match can be obtained by connecting appropriate multiport load-networks.

Our objective is to determine: a) The width of the propagation passbands, as function of the cavity-to-cavity coupling, b) The dispersion characteristics, or in other words the image-phase-

rotation dependence upon frequency, within any given passband and for any given value of the cavity-to-cavity coupling, c) The extent of azimuthal anisothropy of the wave dispersion characteristics, in a continuous 360° azimuth span through all translational symmetry axes, and d) The frequency dependence of the image-impedance matrix of the clustered delay structure, defined at any planar interface cutting edge-to-edge across the whole structure, at the discrete location between unit cells.

The used approach considers the unit-cells as linear, reciprocal, multiport networks, exhibiting either C_{4v}-symmetry or C_{6v}-symmetry, consistent with either the square-lattice or the hexagonal-lattice ordering of the unit cells. This approach applies the general theory discussed in a previous paper [Ref. 1], but specializes the treatment to the case of unit-cells constituted by high-Q cavity resonators, that are assumed to be characterized, analytically or experimentally, by a complex, multi-dimensional scattering matrix.

Because of the expected high-Q of the unit-cells, an initial analysis has been performed, by assuming losslessness, besides reciprocity and the appropriate type of symmetry. This combination of constraints largely reduces the complexity of the analysis, by drastically reducing the number of independent real parameters required to fully characterize a unit-cell. Indeed, already because of reciprocity and symmetry alone, only three complex quantities out of the 16 entries of the 4 x 4 scattering matrix of a four-port unit-cell have different values, and this introduces a single degeneracy among the four eigenvalues of the scattering matrix, that also reduce to only three different complex values. Further, if losslessness is also assumed, the three differing eigenvalues become unimodular (thus falling on the unit circle), so that the three real angular arguments of these eigenvalues may be conveniently assumed as the only free parameters of the reciprocal, symmetric, and lossless four-port unit-cell, and of a two-dimensional delay structure with square lattice.

Similarly, for six-port unit-cells, because of reciprocity and symmetry alone, only four complex quantities out of the 36 entries of the 6 x 6 scattering matrix have different values, and this introduces a double degeneracy among the six complex eigenvalues, that also reduce to only four different values. Finally, if losslessness of the six-port unit-cell is also assumed, the four different eigenvalues become unimodular, so that the four real angular arguments may be conveniently assumed as the only free parameters of the reciprocal, symmetric, and lossless six-port unit -cell, and of a two-dimensional delay structure with hexagonal lattice.

This drastic reduction in the dimensionality of the problem has made possible to derive closed-form expressions of the image-impedance matrices and of the image-transfer-function matrices of both the four-port and the six-port reciprocal, symmetric and lossless unit-cells, as direct functions of either analytically or experimentally obtained scattering parameters. Calibrated scattering parameters can be easily obtained, from a physical model of a single multiport cavity resonator, by means of an automated vector network analyzer.

The image-impedance matrix of a single unit-cell uniquely determines the image-impedance matrix of an electrically-large clustered delay structure, defined as stated above, at any planar interface cutting edge-to-edge across the whole structure, at the discrete location between unit cells. The image-impedance matrix of a single unit-cell also uniquely determines the appropriate multiport load-networks to be connected along the structure external boundaries to obtain an unconditional impedance match.

The image-transfer-function matrix of a single unit-cell uniquely determines: a) The dispersion characteristics of the delay structure within any given passband, b) The guided-wave attenuation, as function of frequency, within any given stop band, and c) The natural port-modes of the unit-cell (defined by the eigenvectors of the image-transfer-function matrix).

REFERENCES

[1] R. A. Speciale,"Wave Propagation on Infinite, Two-Dimensional Structures," 5th Annual Review of Progress in Applied Computational Electromagnetics, Naval Postgraduate School, Monterey, California, March 21-23, 1989, pp. 200-244.

[2] R. A. Speciale,"Projective Matrix Transformations in Microwave Network Theory," IEEE 1991 International Microwave Symposium Digest of Technical Papers, pp. 510-512.

[3] M. G. Andreasen and R. L. Tanner,"A Wire-Grid Lens Antenna of Wide Application - Part II: Wave-Propagation Properties of a Pair of Wire Grids with Square, Hexagonal or Triangular Mesh," IRE Trans. on Antennas and Propagation, July 1962, pp. 416-429.

SESSION 11- "ANTENNA ANALYSIS"

Moderator: Asoke Bhattacharyya

METHOD OF MOMENTS ANALYSIS OF CAVITY-BACKED WIRE ANTENNAS

David C. Jenn
Naval Postgraduate School
Monterey, CA 93943
and
Earl E. Barber
Hughes Aircraft Co.
Fullerton, CA 92634

Abstract

A method of moments solution is presented for the general case of a body of revolution in the presence of excited wires. Basis functions are used on all of the surfaces and wires, and consequently all contributions to the radiation field are included. For the special case of the wire feed point on the body axis of rotation, only the odd azimuthal modes are required. This fact along with symmetries between the positive and negative modes can be used to achieve a significant reduction in the largest matrix that must be inverted for a given antenna size. Calculated results are shown to be in good agreement with other calculated and measured data for cavity-backed dipoles and spirals.

I. Introduction

A large class of important practical antennas are comprised of two basic geometric structures: wires and surfaces of revolution. Primary examples are cavity or ground plane backed spirals and dipoles. However, electrically large rotationally symmetric reflectors fed by the above antennas also fall into this category.

High-frequency techniques are commonly used to predict the performance of these antennas [1,2]. For example, the presence of the bottom of a cylindrical cavity is approximated by a ground plane and the radiation from the wire and its image are calculated. The contribution from the rim is estimated using GTD. The primary deficiency in this approach is that the interactions between the wire and cavity are neglected, and these can be significant because of the small electrical size and closeness of the structures.

The method of moments (MM) is ideally suited for the analysis of these antennas. MM solutions for bodies of revolution (BORs) and wires are well known, and a combination of the two is straightforward. In the following sections the MM

solution for BORs and wires is outlined, and some interesting properties of the resulting matrix equation are discussed. The solution is implemented for planar wire structures such as dipoles and spirals, and the MM results are compared to other calculated and measured data.

II. Analysis

A. Method of Moments Solution

The antenna radiation problem considered here is a special case of the more general problem of radiation from wires in the presence of BORs. The solution of the E-field integral equation (EFIE) using MM has been presented by several authors, however the formulation due to Mitschang and Schafer in [3] applies directly, except for the junction basis functions which will not be needed for the antennas considered here. The details of the solution will not be repeated other than to introduce notation or point out exploitable features that apply to the specific geometry at hand.

The coordinate system for the antenna is shown in Figure 1. The cavity axis of symmetry is the z axis, and for practical antenna designs the wire will be centered on this axis. As described in [3], the surface is segmented into faceted rings and the wire into short segments. An arclength variable t is defined which is radially outward on the surface. In the case of the wire, a variable w is specified tangent to the axis. A second component of current is required on the surface; this is the azimuthal or ϕ component shown in Figure 1. The subsectional basis functions are as follows:

surface:

$$\vec{J}_{in}^{t} = \hat{t}\frac{T_i(t)}{\rho_i}e^{jn\phi} \tag{1}$$

$$\vec{J}_{in}^{\phi} = \hat{\phi}\frac{P_i(t)}{\rho}e^{jn\phi} \tag{2}$$

wire:

$$\vec{J}_i^{w} = \hat{w}\frac{T_i(w)}{2\pi a}. \tag{3}$$

$T_i(t)$ is the triangle function (which extends over two segments, i and $i+1$) and $P_i(t)$ is the pulse function. The azmuthal index n runs from $-\infty$ to ∞, but can be truncated at small values of n (say N) and still give excellent results for the antenna geometries considered here. The thin-wire approximation is assumed, and a is the radius of the wire. A discussion leading to the choice of these basis functions is given in [4]. Finally, the surface current is expressed as a weighted sum of all the basis functions

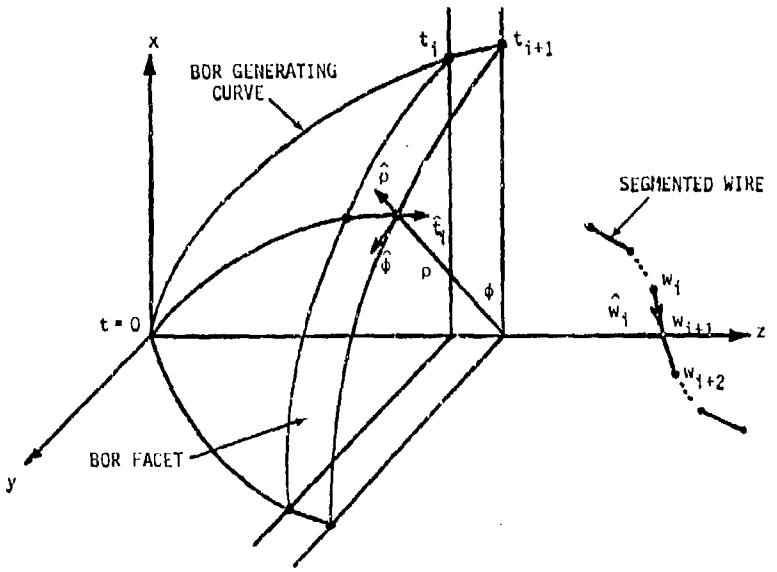

Figure 1: Cavity and wire geometry for the method of moments solution.

$$J = \sum_{n=-N}^{N} \left[\sum_{m=1}^{M} I_{mn}^{w} \vec{J}_{mn}^{w} + \sum_{p=1}^{P} I_{pn}^{t} \vec{J}_{pn}^{t} + \sum_{q=1}^{Q} I_{qn}^{\phi} \vec{J}_{qn}^{\phi} \right], \tag{4}$$

where M, P and Q are the number of wire, surface t-directed and surface ϕ-directed basis functions, respectively.

Testing functions are chosen according to Galerkin's method, and the standard MM procedure is used to reduce the EFIE to a set of simultaneous linear equations that can be written in the following block matrix form:

$$\begin{bmatrix} Z_{-N}^{ss} & & & & & Z_{-N}^{sw} \\ & \ddots & & & & \vdots \\ & & Z_0^{ss} & & & Z_0^{sw} \\ & & & \ddots & & \vdots \\ & & & & Z_N^{ss} & Z_N^{sw} \\ Z_{-N}^{ws} & \cdots & Z_0^{ws} & \cdots & Z_N^{ws} & Z^{ww} \end{bmatrix} \begin{bmatrix} I_{-N}^{s} \\ \vdots \\ I_0^{s} \\ \vdots \\ I_N^{s} \\ I^{w} \end{bmatrix} = \begin{bmatrix} V_{-N}^{s} \\ \vdots \\ V_0^{s} \\ \vdots \\ V_N^{s} \\ V^{w} \end{bmatrix}. \tag{5}$$

The vector I contains the current coefficients, $\vec{V}$ the excitation elements, and the superscripts s and w refer to surface and wire. The elements of the impedance matrix Z can be computed using the formulas in Table 2 of [3]. Each submatrix Z_n^{ss} in (5) can in turn be written in block form as

$$\begin{bmatrix} Z_n^{tt} & Z_n^{t\phi} \\ Z_n^{\phi t} & Z_n^{\phi\phi} \end{bmatrix}. \tag{6}$$

It can be shown from the explicit expressions for the elements that

$$\begin{aligned} Z_{-n}^{tt} &= Z_n^{tt} \\ Z_{-n}^{t\phi} &= -Z_n^{t\phi} \\ Z_{-n}^{\phi t} &= -Z_n^{\phi t} \\ Z_n^{\phi\phi} &= Z_n^{\phi\phi} \end{aligned} \tag{7}$$

and

$$Z_n^{ws} = (Z_{N-n+1}^{sw})^T \tag{8}$$

where T signifies transpose. The surface-wire terms are of two types: Z^{tw} and $Z^{\phi w}$, and have the following symmetry

$$\begin{aligned} Z_{-n}^{tw} &= Z_n^{tw} \\ Z_{-n}^{\phi w} &= -Z_n^{\phi w}. \end{aligned} \tag{9}$$

Note that the presence of the wire complicates the matrix problem; if the antenna were purely a BOR the impedance matrix would be block diagonal.

B. Matrix Reduction for Wire Excitation

When only the wire structure is excited it is possible to break the inversion in (5) into a series of smaller matrix inversions, and thereby reduce the computer memory requirements for a given antenna size. The simplification is accomplished via Woodbury's identity [5]

$$Z^{-1} = (A + UW)^{-1} = A^{-1} - A^{-1}U(\mathcal{I} + WA^{-1}U)^{-1}WA^{-1} \tag{10}$$

where $\mathcal{I}$ is the identity matrix and

$$A = \begin{bmatrix} Z^{ss}_{-N} & & & & \\ & \ddots & & & \\ & & Z^{ss}_{0} & & \\ & & & \ddots & \\ & & & & Z^{ss}_{N} \\ & & & & & Z^{ww} \end{bmatrix} = \begin{bmatrix} A_1 & & & & \\ & \ddots & & & \\ & & A_s & & \\ & & & \ddots & \\ & & & & A_S \\ & & & & & D \end{bmatrix} \tag{11}$$

$$U = \begin{bmatrix} Z^{sw}_{-N} & 0 \\ \vdots & \vdots \\ Z^{sw}_{0} & 0 \\ \vdots & \vdots \\ Z^{sw}_{N} & 0 \\ 0 & \mathcal{I} \end{bmatrix} = \begin{bmatrix} B_1 & 0 \\ \vdots & \vdots \\ B_s & 0 \\ \vdots & \vdots \\ B_S & 0 \\ 0 & \mathcal{I} \end{bmatrix}, \tag{12}$$

and

$$W = \begin{bmatrix} 0 & \cdots & 0 & \cdots & 0 & \mathcal{I} \\ Z^{ws}_{-N} & \cdots & Z^{ws}_{0} & \cdots & Z^{ws}_{N} & 0 \end{bmatrix} = \begin{bmatrix} 0 & \cdots & 0 & \cdots & 0 & \mathcal{I} \\ C_1 & \cdots & C_s & \cdots & C_S & 0 \end{bmatrix}. \tag{13}$$

For notational simplicity new matrices A, B and C have been defined corresponding to Z^{ss}, Z^{sw} and Z^{ws}, along with a new index

$$s = n + N + 1, \tag{14}$$

so that s takes on values from 1 to $S = 2N + 1$. From (8) it is apparent that

$$C_s = (B_{S-s+1})^T. \tag{15}$$

The inverse of A is easily computed since it is block diagonal

$$A^{-1} = \begin{bmatrix} A_1^{-1} & & & & \\ & \ddots & & & \\ & & A_s^{-1} & & \\ & & & \ddots & \\ & & & & A_S^{-1} \\ & & & & & D^{-1} \end{bmatrix}. \tag{16}$$

Using (12), (13) and (16) in (10) leads to

$$Z^{-1} = \begin{bmatrix} - & \cdots & - & A_1^{-1}B_1X_1D^{-1} \\ & \vdots & & \vdots \\ - & \cdots & - & A_s^{-1}B_sX_1D^{-1} \\ & \vdots & & \vdots \\ - & \cdots & - & A_S^{-1}B_SX_1D^{-1} \\ - & \cdots & - & D^{-1} - D^{-1}X_3D^{-1} \end{bmatrix} \tag{17}$$

where $-$ represents, in general, a non-zero submatrix, and the X_i are determined from the partitions of the inverted matrix

$$(\mathcal{I} + WA^{-1}U)^{-1} = \begin{bmatrix} \mathcal{I} & D^{-1} \\ \sum_{s=1}^{S} C_sA_s^{-1}B_s & T \end{bmatrix}^{-1} = \begin{bmatrix} X_1 & X_2 \\ X_3 & X_4 \end{bmatrix}. \tag{18}$$

When the antenna is transmitting, only the wire is excited and $\vec{V}$ will be of the form

$$\begin{bmatrix} 0 \\ \vdots \\ 0 \\ \vdots \\ 0 \\ V^w \end{bmatrix}. \tag{19}$$

Therefore only the last column of the inverse of Z in (17) is of consequence in the solution of $\vec{I}$. Finally, the vector of current coefficients can be written as

$$\vec{I} = \begin{bmatrix} A_1^{-1}B_1X_1D^{-1}V^w \\ \vdots \\ A_s^{-1}B_sX_1D^{-1}V^w \\ \vdots \\ A_S^{-1}B_SX_1D^{-1}V^w \\ D^{-1} - D^{-1}X_3D^{-1}V^w \end{bmatrix} = \begin{bmatrix} (Z_{-N}^{ss})^{-1}Z_{-N}^{sw}X_1(Z^{ww})^{-1}V^w \\ \vdots \\ (Z_0^{ss})^{-1}Z_0^{sw}X_1(Z^{ww})^{-1}V^w \\ \vdots \\ (Z_N^{ss})^{-1}Z_N^{sw}X_1(Z^{ww})^{-1}V^w \\ (Z^{ww})^{-1} - (Z^{ww})^{-1}X_3(Z^{ww})^{-1}V^w \end{bmatrix}. \tag{20}$$

Note that the matrices A_i and D are those that would have to be inverted if the surface and wire problems were solved independently. The only additional matrix inversion is imbedded in the determination of X_1 and X_3 through the use of (18). The A_i are $(P+Q)$ by $(P+Q)$, D is M by M and X is $2M$ by $2M$. Solving (5) directly would require inverting a matrix of dimension $S(P+Q)+M$ rather than the maximum of $(P+Q)$ or $2M$ as required by (20). The $2M$ limit could be reduced to M if X_1 and X_3 are inverted using partitioning. This is a significant reduction for antennas with long wires such as archimedian spirals, in which case M is much larger than $(P+Q)$.

C. Matrix Reduction for Center-Fed Wires

In the case of a pure BOR illuminated by a source located on the axis of symmetry, only the $n=\pm 1$ modes are required to determine the current coefficients. This is because the excitation elements, which are given by

$$V_n^s = \iint_S \vec{W}_{ni}^s \cdot \vec{E}_{inc} ds, \tag{21}$$

are zero unless $n=\pm 1$. It is true even if the source does not have rotational symmetry, e.g., if

$$\vec{E}_{inc} = (F_E cos\phi\,\hat{\theta} - F_H sin\phi\,\hat{\phi})\frac{e^{-jkR}}{R} \tag{22}$$

where F_E and F_H are not equal. This can be proved relatively easily by substituting $\vec{E}_{inc}$ and the testing functions $\vec{W}_{ni}^s$ (the complex conjugates of the corresponding basis functions) into (21) and performing the integration.

A similar result might be expected when the only nonzero wire excitation element is the triangle centered on the BOR axis of rotation. In fact there is a nulling of the even modes due to a combination of zero elements in the row of Z^{sw} that corresponds to the only non-zero element in V^w. A rigorous proof is difficult because it requires tracking the matrix symmetries while progressing through a series of inversions and multiplications. Therefore the following heuristic proof is offered in lieu of a formal one. The result has been verified computationally for dipoles and spirals.

The particular geometry of interest is shown in Figure 2. The feed point of the wire is located on the BOR axis of symmetry. The wire is assumed to be symmetric; that is, equal wire lengths on each side of the BOR axis. This simplifies the analysis but is not a requirement. If all of the segments have equal length Δ, then the number of wire segments will be even, and the number of basis functions

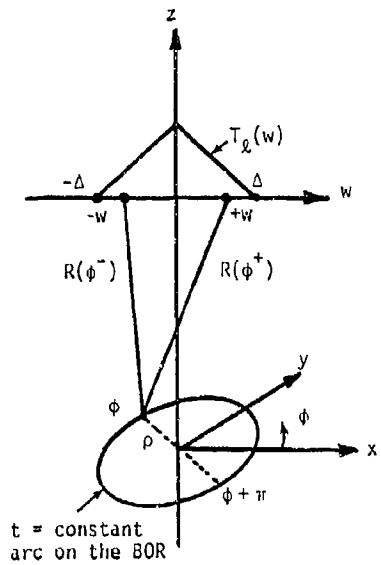

Figure 2: Symmetry conditions for on-axis excitation of the wire.

(M) odd. The interaction between the excited triangle and the surface is given by the surface-wire impedace elements in (9). For the first type

$$Z_{nil}^{tw} = \frac{jk\eta}{4\pi} \int_i dt \int_0^{2\pi} d\phi \int_\ell dw \left[T_i(t)T_\ell(w)\hat{t}_i \cdot \hat{w}_\ell - \frac{1}{k^2}T_i'(t)T_\ell'(w)\right]\psi(R)e^{-jn\phi} \tag{23}$$

where

$$\psi(R) = \frac{e^{-jkR}}{R} \tag{24}$$

$$\ell = \frac{M+1}{2} \tag{25}$$

and the primed quantities signify deriviatives. The circular curve in Figure 2 represents a t = constant arc. For two source points on the center triangle at $+w$ and $-w$, there is a symmetry in ϕ for test points on the arc

$$R^+(\phi) = R^-(\phi + \pi) \tag{26}$$

$$R^-(\phi) = R^+(\phi + \pi) \tag{27}$$

$$R^{\pm}(\phi) = \sqrt{(\rho \mp w)^2 + z^2 \pm 2\rho w \sin^2(\phi/2)}\,. \tag{28}$$

First, examine the last term in the square brackets in (23). The integration with respect to t and its associated quantities are omitted since it will be shown that the integrand goes to zero for each value of t. The integration can be performed over a single segment (half of the triangle) rather that two segments because of the symmetry in w

$$\int_0^{\Delta} dw \int_0^{2\pi} d\phi\, e^{-jn\phi}[\psi(R^+)T_\ell'(w) + \psi(R^-)T_\ell'(-w)]. \tag{29}$$

The slope of the triangle flips at $w = 0$

$$T_\ell'(w) = -T_\ell'(-w) \tag{30}$$

and because $\psi(R^{\pm})$ is periodic in 2π, the two terms in (29) cancel.

Likewise, breaking out the contributions from $+w$ and $-w$ for the first term in (23), using $\hat{t}_\ell \cdot \hat{w}_\ell \sim \cos\phi$ and dropping constants gives

$$\int_0^{\Delta} T_\ell(w)dw \int_0^{2\pi} d\phi \cos\phi\, e^{-jn\phi}[\psi(R^+) + \psi(R^-)]. \tag{31}$$

Using (26) and (27) in (31)

$$\int_0^{\Delta} T_\ell(w)dw \int_0^{\pi} d\phi\{\cos\phi\, e^{-jn\phi}[\psi(R^+) + \psi(R^-)] + \cos(\phi+\pi)\, e^{-jn(\phi+\pi)}[\psi(R^+) + \psi(R^-)]\} \tag{32}$$

which reduces to

$$\int_0^{\Delta} T_\ell(w)dw \int_0^{\pi} d\phi \cos\phi\, e^{-jn\phi}[\psi(R^+) + \psi(R^-)][1 - (-1)^n] \tag{33}$$

and thus vanishes for n even. A similar argument holds for the surface-wire impedance elements of the second type.

For the geometry described above, equations (28) and (33) imply the that center column in Z_n^{sw}, n even, will be zero. Because of the symmetries between the types of impedance elements and modes, the zero center column is present after each matrix operation in (20). The final matrix for the n^{th} mode is

$$[(Z_n^{ss})^{-1} Z_n^{sw} X_1 (Z^{ww})^{-1}] V^w \tag{34}$$

where the resultant matrix in the square brackets has M columns, the center one all zeros. Since M is the only nonzero row in the vector V^w, the final result is a column vector containing all zeros.

For the odd modes, equation (20) becomes

$$\vec{I} = \begin{bmatrix} I^s_{-N} \\ \vdots \\ I^s_{-1} \\ I^s_1 \\ \vdots \\ I^s_N \\ I^w \end{bmatrix} = \begin{bmatrix} (Z^{ss}_{-N})^{-1} Z^{sw}_{-N} X_1 (Z^{ww})^{-1} V^w \\ \vdots \\ (Z^{ss}_{-1})^{-1} Z^{sw}_{-1} X_1 (Z^{ww})^{-1} V^w \\ (Z^{ss}_1)^{-1} Z^{sw}_1 X_1 (Z^{ww})^{-1} V^w \\ \vdots \\ (Z^{ss}_N)^{-1} Z^{sw}_N X_1 (Z^{ww})^{-1} V^w \\ (Z^{ww})^{-1} - (Z^{ww})^{-1} X_3 (Z^{ww})^{-1} V^w \end{bmatrix} \tag{35}$$

with N odd. Making use of the symmetry between positive and negative modes, it is only necessary to calculate one of the two

$$I^s_{-n} = \begin{bmatrix} I^t_{-n} \\ I^\phi_{-n} \end{bmatrix} = \begin{bmatrix} I^t_n \\ -I^\phi_n \end{bmatrix}. \tag{36}$$

If the sum in (18) is accumulated using only positive (or negative) modes, then a factor of two must be added before the inversion is performed.

To summarize, if the wire feed point is located on the BOR axis of rotation, then it is not necessary to consider the even modes when solving for the current coefficients. Furthermore, because of symmetries due to the particular geometry and the azimuthal modes, the matrix equation need only be solved for either the positive or negative modes; the other set is simply obtained by multiplying the appropriate coefficients by -1.

III. Calculated Results

Once the current coefficients are known the radiated electric field is easily calculated [3]. The solution described above has been applied to several commonly used

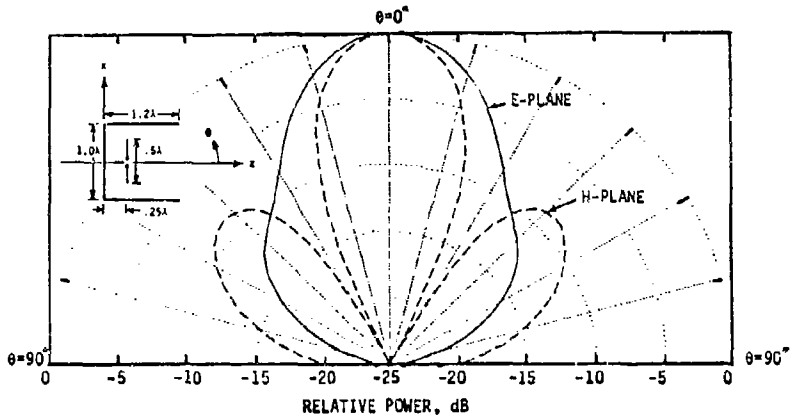

Figure 3: Principal plane patterns for a cavity-backed dipole. (The dimensions are taken from [6].)

cavity-backed wire antennas. The principal plane radiation patterns of a cavity-backed dipole are shown in Figure 3, and those for a cavity-backed dipole array with one element excited in Figure 4. The E-plane corresponds to $\phi = 0°$ and the H-plane to $\phi = 90°$. In both cases the dimensions are chosen to be the same as the designs in [6]. The results are essentially converged for $n = \pm 1$. When the $n = \pm 3$ modes were added the change in the pattern was about 1 dB at the -20 dB level and less at higher levels.

The radiation patterns for a 5.5 turn 6-inch two-arm archimedian sprial with a cavity and circular ground plane are shown in Figure 5 for a frequency of .75 GHz. The measured data was taken on a printed circuit spiral with line widths of .125 inch and an interline spacing of .125 inch. The gain of this spiral is plotted in Figure 6 for several frequencies along with data from [7]. Both the measured and calculated gain for the 5.5 turn sipral was consistently low compared to the curve from [7]. In the case of the measured data, some of this difference may be due to feed losses (estimated to be .4 dB). The remainder may be due to the inefficiency inherent in a small number of turns.

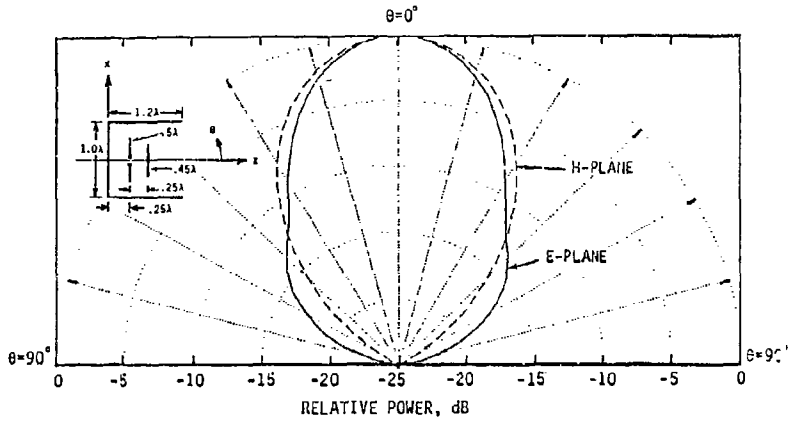

Figure 4: Principal plane patterns for a cavity-backed dipole array with one element excited. (The dimensions are taken from [6].)

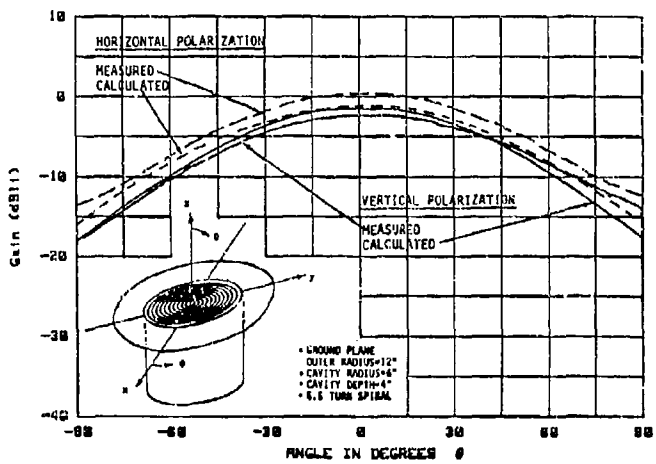

Figure 5: Comparison of calculated and measured principal plane patterns for a cavity-backed spiral.

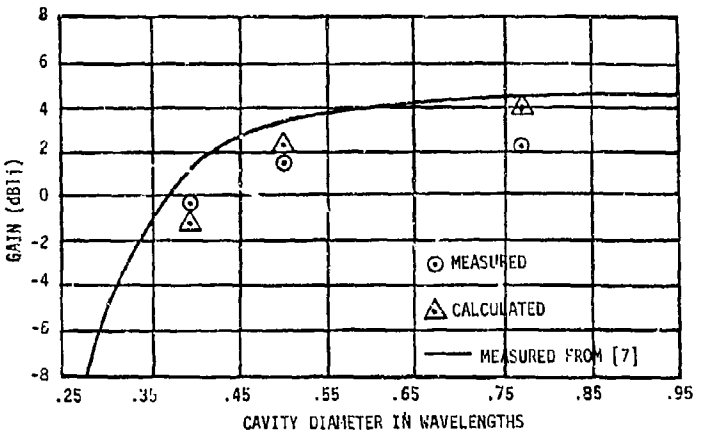

Figure 6: Comparison of calculated and measured cavity-backed spiral antenna gain.

IV. Summary

A method of moments solution for the general case of a body of revolution in the presence of excited wires has been described. MM is ideally suited for analyzing antennas of this type because it is a means of modeling both the wire and cavity that is sensitive to the detailed geometry. For the special case of the wire feed point on the body axis of rotation, only the odd azimuthal modes are required. This fact along with symmetries between the positive and negative modes can be used to achieve a significant reduction in the largest matrix that must be inverted for a given antenna size.

Calculated results are in good agreement with other calculated and measured data for several common cavity-backed wire antennas. Most of the available data is for simple cupped dipoles and spirals. However, more complicated mounting structures can be included in the MM solution. Thick cavity walls, circular ground planes, and chokes are some examples. Even a collection of disconnected wires in a single cavity can be treated with only a slight modification of the code [8], and extending the surfaces of revolution to include large reflectors and subreflectors is straightforward.

V. References

[1] A. Kumar and H. D. Hristov, Microwave Cavity Antennas, Artech House, 1989.

[2] H. Nakano, Helical and Spiral Antennas-A Numerical Approach, Research Studies Press, 1987.

[3] J. F. Shaeffer and L. N. Medgyesi-Mitschang, 'Radiation From Wire Antennas Attached to Bodies of Revolution: The Junction Problem,' IEEE Trans. on Antennas and Prop., vol. AP-29, no. 3, May 1981, p. 479.

[4] J. R. Mautz and R. F. Harrington, 'An Improved E-Field Solution for a Conducting Body of Revolution,' Syracuse University Technical Report TR-80-1.

[5] D. C. Jenn and W. V. T. Rusch, 'An E-Field Integral Equation Solution for the Radiation From Reflector Antennas With Struts,' IEEE Trans. on Antennas and Prop., vol. AP-37, no. 6, June 1989, p. 683.

[6] M. H. Hong, et. al., 'Radiation Fields of Open-Cavity Radiators and a Backfire Antenna,' IEEE Trans. on Antennas and Prop., vol. 18, no. 6, November 1970, p. 813.

[7] S. W. Lee, et. al., Antenna Handbook, Chapter 14.

[8] D. C. Jenn, 'Application of Integral Equation Theory to Reflector Antenna Analysis,' Ph.D. thesis, University of Southern California, December, 1987, Ch. 6.

MOMENT-METHOD MODELLING OF THE NORMAL-MODE HELICAL ANTENNA

Y J Guo and P S Excell
Department of Electrical Engineering, University of Bradford, West Yorkshire UK

Abstract

The normal-mode helical antenna is of interest as a convenient design for realization with high-temperature superconductors. Despite its simple structure, exact modelling of its behaviour is far from simple since it is essentially a hybrid loop-dipole antenna, a type known to cause instability with some moment-method representations. An investigation of the resonant frequency performance of such an antenna, excited by a separate loop, was undertaken using the moment method, with second-order B-spline functions as basis functions. Stable results were obtained and it was found that, for a fixed length of conductor, the resonant frequency of the antenna increased with the pitch and decreased when the radius of the helix was increased.

Introduction

The electrically-small helical antenna is a propitious design for realization with high-temperature superconductors, since it is of simple construction, and its efficiency is poor when realized with conventional conductors. Provided it is operated below the 'cross-over frequency' (above which the loss in the superconductor becomes worse than that in copper), superconductor offers the possibility of greatly improved efficiency, with a concomitant increase in Q-factor. This is, in principle, true for any electrically-small antenna but the standard electrically-small loop and dipole antennas have to be connected to tuning capacitors or inductors respectively, causing problems in manufacture from the ceramic high-temperature materials [1]. Tuning with transmission-line stubs is also possible [2] but the complete system is then no longer electrically small: it should also be noted that electrical connections between ceramic superconductors and conventional conductors have been found to be extremely unreliable.

The normal-mode helical antenna (NMHA) is a very attractive alternative design, since it can be manufactured using existing processes for production of superconducting 'wire', and it can be parasitically connected to the external circuit via a copper coupling coil, thus avoiding the need for electrical connections to the superconductor. There are three convenient approximate ways of viewing its behaviour: (i) as a multi-turn loop antenna without a lumped tuning capacitor, but tuned by stray inter-turn capacitance; (ii) as a short dipole antenna with integral central loading inductor, in which the 'arms' of the dipole have vanished, their function being performed by the turns toward the ends of the helix (a natural evolution of the earlier 'fat dipole' design [1]); (iii) as a coiled-up self-resonant half wavelength transmission line. The loop and dipole viewpoints are particularly useful as they indicate that the NMHA inherently radiates in both modes simultaneously and its radiation is always elliptically polarized. By appropriate choice of the dimensions, the polarization can be made circular, or nearly linear in either the θ or ϕ direction. The parasitic feed arrangement is also advantageous in that it provides

good thermal isolation between the helix and the loop and no additional matching network is required. Since the antenna operates at the first resonant mode it is particularly important to predict its resonant frequency precisely.

A moment-method study of multi-turn polygonal loop antennas was first proposed by Richards [3]. Later, Taylor and Harrison presented work on helical antennas [4]. Since they both considered antennas with only a few turns, which were not electrically small, few general rules about the relationship between the resonance and the helix parameters were given. Besides, in their physical models the helices were directly excited at the middle or the ends and the helices, together with the sources, formed closed structures. In the work reported here, the helix was isolated and consisted of many turns. The circumference of each turn was extremely small compared with the operating wavelength, so care had to be taken to ensure the validity of the moment method [5] since electrically-small loops and structures combining these with highly-charged open-circuit stubs are known to be particular sources of instability (an attempt to model the antenna with the NEC program [6] was unsuccessful). The second-order B-spline function was chosen as a basis function, since it has better continuity than, for instance, the piecewise sinusoidal function.

Theory

The integral equation used was that given by Taylor and Harrison [4]: it is of the form:

$$\int ds'G(s,s')[d^2/ds'^2+k^2(\hat{s}.\hat{s}')]\ I(s')-d/ds'I(s')G(s,s')|_0^l = -j4\pi k/\eta(E^i(s)-Z_iI(s)) \quad (1)$$

where E^i represents the impressed field, k represents the wave number, η is the wave impedance in the environmental medium and Z_i the internal impedance per unit length of the wire. The Green's function G(s,s') is given by:

$$G(s,s') = \exp(-jkR)/R$$

where R is the linear distance between two points denoted by s and s'. The application of Eq. (1) demands that the pitch of the helix should be at least four times as large as the wire radius. Otherwise, the proximity effect must be taken into consideration [7].

Since a second-order differentiation is required in Eq. (1), the following second-order B-spline function was used as the basis function to replace the piecewise sinusoidal function adopted in [4]:

$$f(x) = \begin{cases} -4/3|x|^2+1 & |x|<1/2 \\ 2/3|x|^2-2|x|+3/2 & 1/2\le|x|<3/2 \\ 0 & |x|\ge 3/2 \end{cases} \quad (2)$$

It is easily shown that the first order derivative of f(x) is continuous. Following the standard point-matching procedures of the moment method, the current on the helix can be found from Eq. (1) once E^i is given.

As the circumference of the coupling loop is electrically very small, it is reasonable to assume a uniform current I_0 on it, and the radiated field from the loop can be taken as the impressed field on the helix. This treatment also avoids the problem of modelling the source region.

The impedance at the input of the coupling loop is:

$$Z_i = Z_{11} + Z_{12} \tag{3}$$

where Z_{11} is the self-impedance of the loop, and Z_{12} represents the mutual impedance between the helix and the loop, given by:

$$Z_{12} = (j\omega/I_0) \int A \, ds \tag{4}$$

where A is the vector potential of the current on the helix induced by I_0 and the integration is over the coupling loop [8]. The resonant frequency of the antenna f_r can be obtained by solving the equation:

$$\mathrm{Im}\,(Z_i) = 0 \tag{5}$$

Numerical Results

Using the equations given above, a Fortran computer program was written: calculated results are presented in Table 1. As the model was electrically small, a convergence test when increasing the number of segments N was first undertaken (Fig. 1). For low N, the resonant frequency varies greatly as N is increased. It is observed, however, that when N is greater than 30, f_r fluctuates with a relative error less than 0.8%. Since the pitches of adjacent turns varied somewhat in the experimental helix, which seemed to have the effect of reducing the resonant frequency, a relative error of 2.8% between the numerical and experimental results is quite reasonable.

After a helix is constructed, its resonant frequency can only be adjusted by changing the length of conductor or the helix parameters, pitch P and radius R. Due to the nature of ceramic superconductor, the options for such adjustment are very limited: the length can only be adjusted downwards, coarsely and irreversibly, by snapping pieces off; only minute adjustments in the radius are possible, but variation of the pitch over a substantial range is possible. Richards stated [3] that the resonant frequency is mainly determined by the wire length of the helix. However, the results from the program discussed above indicate that, for the electrically-small helix with constant wire length, there is a close relationship between the resonant frequency and the helix parameters. For a fixed wire length, increasing the pitch will increase the resonant frequency significantly, while increasing the radius will decrease it. The resonant length can be longer or shorter than a half wavelength depending on the parameters P and R; this

does not appear to have been noticed by the previous investigators.

Conclusions

The resonant performance of the loop-excited normal-mode helical antenna has been investigated by the moment method with the second-order B-spline function as the basis function. Although the antennas studied were electrically very small, the program provided convergent results which agreed well with those of an experiment. It was shown that the resonant frequency of the antenna is closely related to the helix parameters. When the wire length is held constant, the resonant frequency increases with the pitch and decreases when the radius of the helix is increased. With a fixed helix diameter, a critical turn spacing exists which determines whether the resonant length is greater or less than one half wavelength. By adjusting the turn spacing of the helix, a specific resonant frequency can be obtained.

Computation of the radiated field and radiation resistance should be straightforward using a similar program, although this has not yet been attempted. Computation of losses and the Q-factor is much more complex as it is known that there is a non-uniform current distribution around the wire perimeter [7] and currents will also flow transversely to the wire axis due to the inter-turn capacitance. These matters are the subject of ongoing work.

References

1. Excell, P S & Alford N Mc N: 'Superconducting Electrically-Small Dipole Antenna', IEE Int. Conf. on Antennas & Propagation, York, Vol. 1, 1991.

2. Khamas, S K et al: 'High-T_c Superconducting Short Dipole Antenna', Electronics Letters, Vol. 24, No. 8, 1988, pp. 460-461.

3. Richards, G A: 'Reaction Formulation and Numerical Results for Multiturn Loop Antennas and Arrays', PhD Dissertation, The Ohio State University, 1970.

4. Taylor, C D & Harrison, C W: 'On Thin-Wire Multiturn Loop Antennas', IEEE Trans. Antennas & Prop., Vol. AP-22, No. 3, 1974, p. 407-413.

5. Burke, G J: 'Enhancements and Limitations of the Code NEC for Modelling Electrically-Small Antennas', Lawrence Livermore National Laboratory, Report No. UCID-20970, 1987.

6. Burke, G J & Poggio, A J: 'Numerical Electromagnetics Code (NEC) - Method of Moments', Lawrence Livermore National Lab., Report No. UCID-18834, 1981.

7. Smith, G S: 'Proximity Effect in Systems of Parallel Conductors', J. Appl. Phys., Vol. 43, No. 5, 1972, pp. 2196-2203.

8. King, R W P & Prasad, S: 'Fundamental Electromagnetic Theory and Applications', Prentice-Hall, Englewood Cliffs, 1986.

Acknowledgements

Y J Guo was funded by a visiting scholarship provided by the British Council. Superconducting samples were provided by ICI Advanced Materials. Other hardware was funded by the UK Science & Engineering Research Council.

Table 1 Resonant frequency of a helical antenna with varying pitch and radius and fixed wire length L = 4.88m (= λ/2 at 30.7MHz)

(a) Fixed pitch = 0.004m					
radius (m)	0.03	0.04	0.05	0.06	0.07
f_r (MHz)	32.1	26.9	23.4	21.5	20.5
(b) Fixed radius = 0.0318m					
pitch (m)	0.0032	0.0038	0.004	0.0059	0.007
f_r (MHz)	28.6	30.3	30.8	35.2	37.8

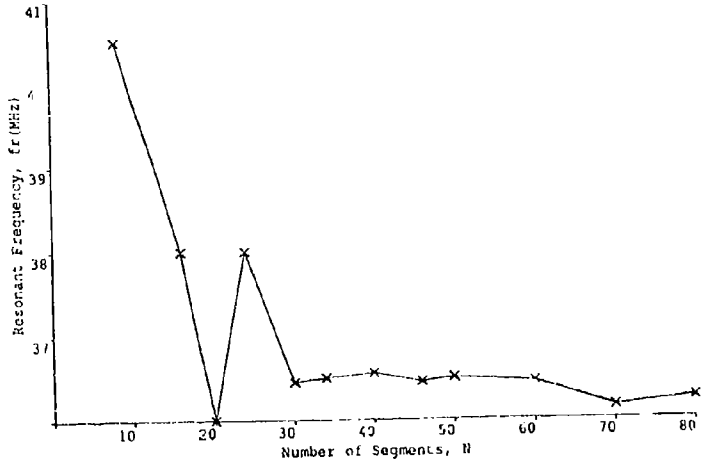

Fig. 1 Computed resonant frequency of a helical antenna with varying number of segments. Helix parameters: pitch = 0.0038m, radius = 0.023m, wire length = 5.06m. Experimental result: f_r = 35.5MHz

INTERCOMPARISON OF SEVERAL MOMENT-METHOD MODELS OF DIPOLES AND FOLDED DIPOLES

P S Excell & A F Armanious*
Electrical Engineering Department, University of Bradford, West Yorkshire, UK
*now at Sultan Qaboos University, Oman

Abstract

A simple 0.47λ dipole was modelled using ten different moment-method formulations: six simple versions employing the magnetic frill generator, and four well-established published versions. The terminal impedance was the main parameter examined. It was found that convergence to a stable solution was poor in all of the six simple formulations, which may be a consequence of the choice of generator model. Results for the resistance were all similar, but reactance results showed substantial variation. Some well-established analytical solutions showed substantial disagreement in both resistance and reactance, but a measurement agreed well with the mean of the moment-method predictions.

In a separate study, the impedance of folded dipoles operated below resonance were investigated. The pattern behaviour was similar to the electrically-small loop antenna. The impedance was found to be prone to extreme instability, including negative resistance, especially when capacitive end-loading was added.

1. Introduction

It is well known that the results from moment-method computer programs show variations (which may or may not be significant) when the segmentation or the formulation are changed. An investigation of this effect using a very simple test object (a 0.47λ dipole) was undertaken using a wide raugte of formulations and the results are presented below. Such a simple dipole is clearly a useful test object for intercomparison of the predictions of different approaches, not least because it is amenable to analytical solutions as well.

Another potentially useful test object is the electrically-small folded dipole. The demands that this places on modelling strategies were discovered in the course of an exercise to compute the behaviour of such antennas, as they are an important canonical type for 'unintended receiving antennas', useful in EMC analyses. The problems that were encountered in this exercise are outlined below.

2. Modelling the 0.47λ Dipole

A simple 'half-wavelength' dipole was modelled using ten different moment-method formulations. The actual length used was 0.47λ, to accommodate the well-known phenomenon of resonance just below λ/2: the conductor diameter chosen was 0.01λ. The formulations tested were as follows:

1. Rectangular pulse basis functions and point-matching
2. Piecewise-linear basis functions and point-matching
3. Piecewise-sinusoidal basis functions and point-matching
4. Rectangular pulse basis functions with Galerkin's method
5. Piecewise-linear basis functions with Galerkin's method
6. Piecewise-sinusoidal basis functions with Galerkin's method
7. Rectangular pulse basis functions with a modified Galerkin method: separate treatment of charge and current (the MININEC method [1])
8. Three-term trigonometrical-function basis functions with point-matching (the NEC method [2])
9. Approximated piecewise-linear basis functions with a modified Galerkin method (Chao and Strait's method [3])
10. Reaction integral equation solved by piecewise-sinusoidal basis functions with Galerkin's method (Richmond's method [4])

A magnetic frill generator was used in the first six methods and delta-gap voltage generators in the other methods.

The results of convergence tests are shown in Table 1. The field pattern results converged to a realistic value with very few segments and were not considered to be an onerous test: impedance results were thus concentrated upon.

It was found that convergence was poor in all of the first six methods, especially in the reactance results: this may be due to the use of the delta-function generator. The best results were achieved with Galerkin's method and either of the piecewise basis functions.

The version of the Chao and Strait program used became unstable before complete convergence had been achieved. The other "published" programs (methods 7, 8 and 10) achieved more rapid convergence than methods 1 to 6, possibly due to the avoidance of the magnetic frill source.

The reactance results in methods 1 to 6 were all in the region of 14 ohms. The results from MININEC and the Richmond code (and also from the Chao and Strait code before it became unstable) were around 5 ohms, and the result from NEC was 9 ohms. For comparison, a computer implementation of T T Wu's analytical long-dipole model [5] (still claimed to be valid at a half wavelength) gave a reactance of 10 ohms, but a value of resistance (90 ohms) substantially different from that predicted by the numerical models. Further analytical predictions are given in tabular form in Ref [6], together with some experimental results. Relevant results (interpolated to correspond to the dipole modelled here) are given in Table 2. It is rather extraordinary to note that the experimental result agrees more closely with the numerical predictions (especially MININEC and Richmond) than with the analytical predictions. Given that an experiment exactly simulating the conditions modelled is extremely difficult, and that analytical models still involve certain approximations, these results beg the question of just what may be taken as the "true" value of impedance and they also serve to re-emphasise the criticality of reactance in antenna modelling. This criticality is particularly marked for a resonant antenna of this type, since the rate of change of reactance with increasing antenna length is extremely high.

3. The Electrically-Small Folded Dipole

In a separate study, the properties of folded dipoles operated below their resonant frequency were investigated. The behaviour was found to be rather like an electrically-small loop antenna, but with additional subtleties apparently caused by the close proximity of some of the conductors. Four moment-method codes were tried: NEC; Chao and Strait; Richmond; and TWC (a Bradford code using the MININEC solution procedure) [7]. With NEC there was a curious instability in the reactance results in that, as the number of segments was increased, the result converged to a stable value, then went unstable and then converged again. With the Chao-Strait code the results appeared to converge rapidly but the number of segments was limited by the implementation used. The Richmond code was very unstable, showing negative resistance. TWC gave rapid convergence to realistic, stable results (see Table 3).

The object of the exercise was the modelling of shapes likely to be significant in radiative electromagnetic compatibility, and to this end, capacitive stubs were attached to the ends of the folded dipole to see whether this could cause a reduction in the reactance. This caused serious instabilities (negative resistance) with NEC, although the problem could be cured with care. TWC appeared to give rapid convergence to reliable, stable results. The problems with NEC are known to be related to well-known problems with electrically-small loops [8].

References

1. Rockway, J W et al: 'The MININEC System: Microcomputer Analysis of Wire Antennas', Boston: Artech House, 1988.

2. Burke, G J & Poggio, A J: 'Numerical Electromagnetics Code (NEC)', Lawrence Livermore Nat. Lab., Report No. UCID-18834, 1981.

3. Chao, H H & Strait, B J: 'Computer Programs for Radiation and Scattering by Arbitrary Configurations of Bent Wires', Air Force Cambridge Research Labs., Report No. AFCRL-70-0374, 1970.

4. Richmond, J H: 'Computer Program for Thin Wire Structures in a Homogeneous Conducting Medium', NASA Report No. CR-2399, 1974.

5. Wu, T T: 'Theory of the Dipole Antenna and the Two-Wire Transmission Line', J. Math. Phys., Vol. 2, No. 4, pp. 550-574, 1961.

6. King, R W P: 'Tables of Antenna Characteristics', New York: IFI/Plenum, 1971.

7. Armanious, A F & Excell, P S: 'Enhancements to Moment-Method Field Computation Packages', IERE Conf. on EMC, York University, 1986, pp. 191-196.

8. Burke, G: 'EM Modeling Notes', ACES Jnl. & Newsletter, Vol. 2, No. 2, pp. 30-44, 1987.

Acknowledgements

This work was funded by a studentship grant from the University of Bradford Research Committee. Some software and hardware was provided by the UK Science & Engineering Research Council.

Table 1: Impedance and Convergence Results: 0.47λ Dipole

Method	Resistance R (Ω)	Reactance X (Ω)	No. of Segments for Convergence, N
1	79	14	~100(R) ~100*(X)
2	79	14	80(R) ~90*(X)
3	79	14	80(R) ~80*(X)
4	79	14	80(R) ~90*(X)
5	80	15	30(R) ~60*(X)
6	79	15	30(R) ~60*(X)
7	76	4.2	30(R) 50(X)
8	78	9	15(R) >60(X)
9	75	4	25(R) >44(X)†
10	77	5.5	20(R) 35(X)

*Figures for knee of curve, where dX/dN falls to a relatively small value: in all cases X is still increasing slowly at N=200 (maximum value tried).
Values of X given are for N=200.
†Not fully convergent, but goes unstable with more segments.

Table 2: Analytical and Experimental Results: 0.47λ x 0.01λ Dipole

Source	Impedance (Ω)
Wu's long-dipole treatment [5]	89.7+j10.0
King & Wu tubular monopole* [6,p.11]	89.5-j10.7
King & Harrison thin dipole* [6,p.41]	70.8+j0.3
Hartig monopole experiment* [6,pp.137-8]	77.3+j5.1

*Interpolated from tabulated results (monopole impedances doubled)

Table3 Input impedance of an electrically-small folded dipole antenna using the NEC2 (with extended thin-wire kernel option), TWC, Chao & Strait and Richmond programs.

Codes	No. of segments Major	Minor wires	d*	d/a**	Input Impedance
NEC2	3	1	0.004	4	0.0052 + j87.3
	5	1	0.004	4	0.0049 + j83.6
	7	1	0.004	4	0.0053 + j89.0
	11	1	0.004	4	0.0077 - j129.8
	17	1	0.004	4	0.0053 + j86.9
	23	2	0.002	2	0.0053 + j78.6
	23	4	0.001	1	0.0046 + j88.2
TWC	8	2	0.002	2	0.0027 - j0.67
	12	2	0.002	2	0.0051 + j84.8
	18	2	0.002	2	0.0054 + j87.1
	24	2	0.002	2	0.0054 + j88.8
	24	4	0.001	1	0.0054 + j89.0
Chao & Strait	8	2	0.002	2	0.0053 + j86.4
	12	2	0.002	2	0.0053 + j86.3
	16	2	0.002	2	0.0053 + j86.2
	24	2	0.002	2	***
	24	4	0.001	1	***
Richmond	6	1	0.004	4	0.0081 + j83.3
	8	1	0.004	4	0.0043 + j83.5
	10	1	0.004	4	-0.0027 + j83.8
	12	1	0.004	4	0.0120 + j84.0
	14	1	0.004	4	0.0041 + j84.2
	16	1	0.004	4	0.0210 + j84.6
	18	1	0.004	4	-0.0350 + j84.9

* d is the minimum segment length in terms of wavelength.
** d/a is the ratio of the minimum segment length to the wire radius.
*** Outside program limitations.

SIMPLIFIED HORN ANTENNA PARAMETER ESTIMATION USING SELECTIVE CRITERIA*

Paul D. Ewing

Instrumentation and Controls Division
Oak Ridge National Laboratory,† P.O. Box 2008,
Oak Ridge, Tennessee 37831-6007

Paper to be Presented at

7th Annual Review of Progress in Applied
Computational Electromagnetics

March 19-21, 1991
Monterey California

*Research sponsored by Department of the Navy, Naval Air Systems Command AIR-5161, under Interagency Agreement 1501-1501-A1 with the U.S. Department of Energy.

†Managed by Martin Marietta Energy Systems, Inc., for the U.S. Department of Energy under Contract No. DE-AC05-84OR21400.

SIMPLIFIED HORN ANTENNA PARAMETER ESTIMATION USING SELECTIVE CRITERIA*

"The submitted manuscript has been authored by a contractor of the U.S. Government under contract No. DE-AC05-84OR21400. Accordingly, the U.S. Government retains a nonexclusive, royalty-free license to publish or reproduce the published form of this contribution, or allow others to do so, for U.S. Government purposes."

Paul D. Ewing
Instrumentation and Controls Division
Oak Ridge National Laboratory,† Oak Ridge, Tennessee

Abstract

An approximation can be used to avoid the complex mathematics and computation methods typically required for calculating the gain and radiation pattern of the electromagnetic horn antenna. Because of the curvature of the antenna wave front, calculations using conventional techniques involve solving the Fresnel integrals and using computer-aided numerical integration. With this model, linear approximations give a reasonable estimate of the gain and radiation pattern using simple trigonometric functions, thereby allowing a hand calculator to replace the computer. Applying selected criteria, the case of the E-plane horn antenna was used to evaluate this technique. Results showed that the gain approximation holds for an antenna flare angle of less than 10° for typical antenna dimensions, and the E field radiation pattern approximation holds until the antenna's phase error approaches 60°, both within typical design parameters. This technique is a useful engineering tool.

INTRODUCTION

In general, the electromagnetic horn antenna is a simple aperture antenna used to provide a smooth transition for a wave traveling from a waveguide into free space. The dimensions of the waveguide are usually chosen to allow the propagation of one dominant mode, and the horn antenna will support only that mode by acting as a filter for other modes that might be excited in the transition. The horn antenna has the advantages of high gain, relatively wide bandwidth, and easy construction. However, a disadvantage is that the calculations for determining gain and radiation patterns are mathematically rigorous and involve solving the Fresnel integral and performing numerical integration that may require using a computer. To avoid the complex mathematics and computation methods, approximations for the gain and radiation pattern can be used. As with other engineering approximations, values derived from the calculations are useful only within the limited constraints of the approximation.

*Research sponsored by Department of the Navy, Naval Air Systems Command AIR-5161, under Interagency Agreement 1501-1501-A1 with the U.S. Department of Energy.

†Managed by Martin Marietta Energy Systems, Inc., for the U.S. Department of Energy under Contract No. DE-AC05-84OR21400.

The case of the E-plane horn antenna was used to evaluate the feasibility of the approximation technique. The E-plane horn antenna, shown in Fig. 1, is formed by flaring the waveguide in the y-z plane, the E-plane of the antenna's aperture. The horizontal dimension of the aperture is the same as the width of the original waveguide, and the vertical dimension is much greater than the height of the original waveguide.

GAIN AND RADIATION PATTERNS

Knowledge of electromagnetic horn antenna theory has been around since the 1930s, and derivations of the gain and radiation patterns of the E-plane horn antenna are well documented.[1-3] The geometry of the E-plane horn antenna in the direction of the vertical flare is shown in Fig. 2. With the flare, the waves do not arrive at all points in the aperture at the same time; therefore, they form a cylindrical wave front with a phase error.

In Fig. 2, the length of the antenna flare and the angle of the flare are represented by $\mathcal{L}$ and α, respectively. The phase error is represented by $\delta(Y_a)$, since it varies along the y axis, and can be expressed as

$$\delta(Y_a) = \frac{KY_a^2}{2\mathcal{L}} \quad , \tag{1}$$

where the phase constant as a function of wavelength λ is expressed as

$$K = \frac{2\pi}{\lambda} \quad . \tag{2}$$

The aperture distribution for the E-plane horn antenna is

$$E_a(Y_a) = E_o e^{j\delta(Y_a)} \quad , \tag{3}$$

and, by substituting Eq. (1) into Eq. (3), can be expressed as

$$E_a(Y_a) = E_o e^{-jKY_a^2/2\mathcal{L}} \quad , \tag{4}$$

where E_o is the distribution across a uniformly illuminated aperture.

Antenna gain is the ratio of the maximum power density and the average power density in an antenna; that is,

$$G = P_{max}/P_{ave} \quad . \tag{5}$$

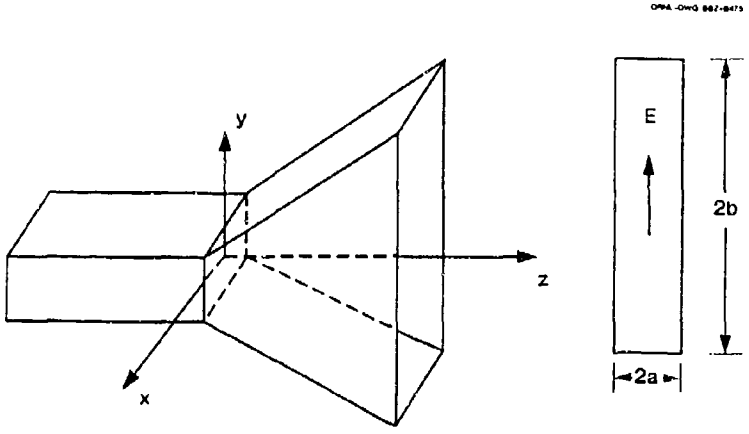

Figure 1. The E-plane horn antenna.

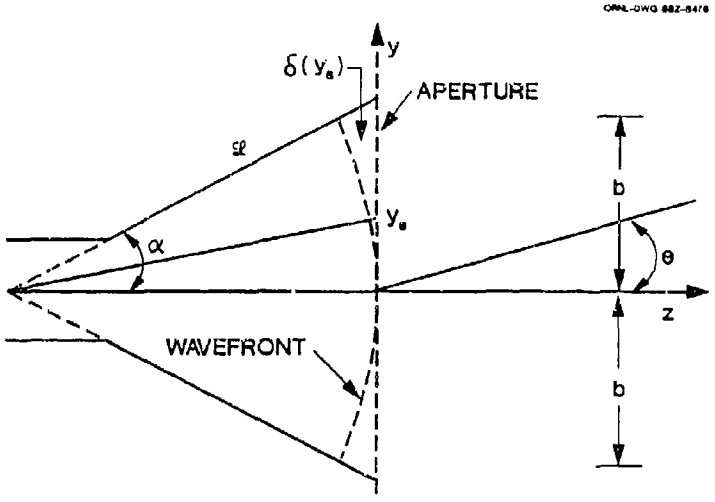

Figure 2. Geometry of E-plane horn antenna.

The maximum power density is

$$P_{max} = \frac{1}{\eta r^2 \lambda^2} \left| \iint_s E_s(X_s, Y_s) dS \right|^2 \quad , \tag{6}$$

where

S = area of the aperture,
dS = differential area element,
η = intrinsic impedance of the medium,
r = spherical coordinate indicating the distance to the point of observation.

The average power density is the total radiated power for the area of a sphere, $4\pi r^2$. Therefore, the average power density can be expressed as

$$P_{ave} = \iint_s \frac{|E_s(X_s, Y_s)|^2}{\eta \ 4\pi r^2} \ dS \quad . \tag{7}$$

The terms in Eq. (5) can be replaced by Eqs. (6) and (7) so that the gain becomes

$$G = \frac{4\pi}{\lambda^2} \ \frac{\left| \iint_s E_s(X_s, Y_s) \ dS \right|^2}{\iint_s |E_s(X_s, Y_s)|^2} \ dS \quad . \tag{8}$$

For the aperture distribution of the E-plane horn antenna given in Eq. (4) and the phase constant in Eq. (2), the gain is calculated to be

$$G = 8\pi \ \frac{a/\lambda \ \ell/\lambda}{b/\lambda} \ [C^2(\mu) + S^2(\mu)] \quad , \tag{9}$$

where

$$\mu = \sqrt{\frac{2}{\lambda \ell}} \ b \quad , \tag{10}$$

and $C(\mu)$ and $S(\mu)$ are Fresnel integrals.

The radiation patterns represent the radiating properties in the far field of an antenna and are a function of the direction from the antenna. They are the relative intensities of the E and H fields normalized to their maximum intensities. The E-field in the E-plane of a rectangular aperture is

$$E_E = j \ \frac{e^{-jkr}}{\lambda r} \cos^2 \frac{\theta}{2} \iint_s E_s(X_s, Y_s) \ e^{jkY_s \sin\theta} \ dS \quad . \tag{11}$$

For the aperture distribution given in Eq. (4), Eq. (11) can be expressed as

$$E_E = jE_o \frac{e^{-jKr}}{\lambda r} \cos^2 \frac{\theta}{2}\, 2a \int_{-b}^{b} e^{jK(\sin\theta Y_s - Y_s^2/2f)}\, dY_s \quad . \tag{12}$$

The integral in Eq. (12) has no closed form and must be evaluated by numerical means. Using numerical integration, the integral will take the form of

$$\int_{-b}^{b} e^{jK(\sin\theta Y_s - Y_s^2/2f)}\, dY_s = 2b\, F(Kb\sin\theta,\delta) \quad , \tag{13}$$

where $F(Kb\sin\theta,\delta)$ is the relative E-field radiation pattern for the E-plane horn antenna. A graphical representation of $F(Kb\sin\theta,\delta)$ is shown in Fig. 3.

The H-field in the E-plane of a rectangular aperture is

$$H_E = j \frac{e^{-jKr}}{\lambda r} \cos^2 \frac{\theta}{2} \iint_s E_a(X_s,Y_s)\, e^{jK\sin\theta X_s}\, dS \quad . \tag{14}$$

By substituting the aperture distribution in Eq. (4), the H-field can be expressed as

$$H_E = j \frac{2}{\pi} E_o \frac{e^{-jKr}}{\lambda r} \cos^2 \frac{\theta}{2}\, 4ab\, \frac{C(\mu) - jS(\mu)}{\mu}\, \frac{\cos(Ka\sin\theta)}{1 - \left(\frac{2}{\pi} Ka\sin\theta\right)^2} \quad . \tag{15}$$

Thus, the relative H-field pattern is

$$F(Ka\sin\theta) = \frac{\cos(Ka\sin\theta)}{1 - \left(\frac{2}{\pi} Ka\sin\theta\right)^2} \quad . \tag{16}$$

Figure 4 is a graphical representation of the relative H-field radiation pattern as a function of the direction from the antenna.

GAIN APPROXIMATION

An approach to approximating the gain can be the ratio of the power radiated by the E-plane horn antenna (P_E) to the power radiated by a lossless isotropic antenna (P_I); that is,

$$G' = \frac{P_I}{P_E} \quad , \tag{17}$$

with a linear approximation of the E-plane horn antenna wave front being used to estimate P_E. The ratio of P_I and P_E can be derived by letting the magnitude of the E-field strength from the isotropic antenna (E_I) equal the magnitude of the E-field strength from the E-plane horn antenna (E_E); that is,

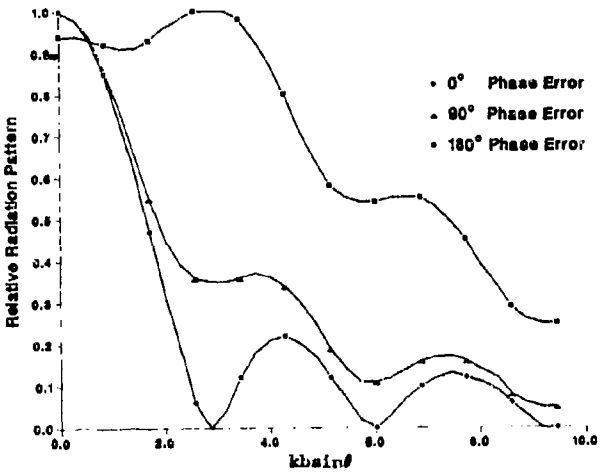

Figure 3. Relative E-field radiation pattern.

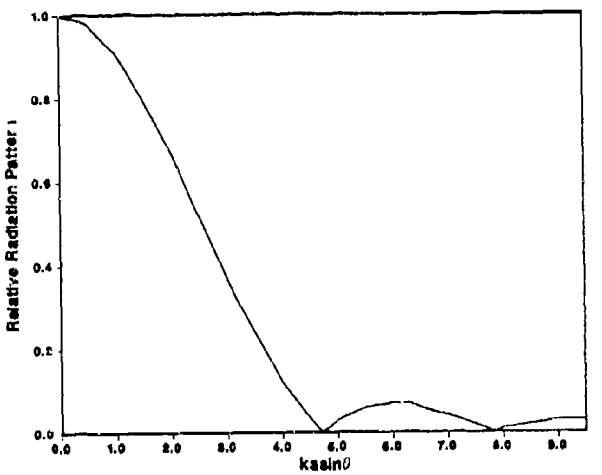

Figure 4. Relative H-field radiation pattern.

$$|E_I| = |E_E| \quad . \tag{18}$$

For the isotropic antenna, the power density (P_{DI}) can be used to relate P_I and E_I since

$$P_{DI} = \frac{E_I^2}{\eta} \tag{19}$$

and

$$P_{DI} = \frac{P_I}{4\pi r^2} \quad . \tag{20}$$

By setting the power density terms equal, E_I can be expressed as

$$E_I = \sqrt{\frac{\eta\ P_I}{4\pi r^2}} \quad . \tag{21}$$

If the intrinsic impedance is replaced by $\eta = 120\pi = 377$ for the far field and consideration is given to the isotropic nature of the antenna, the magnitude of the E field strength is

$$|E_I| = \frac{\sqrt{30\ P_I}}{r} \quad . \tag{22}$$

Figure 5 shows a linear approximation of the E-plane horn antenna wave front that will divide the wave front and the antenna into two sections, each acting as an independent horn antenna. With the linear approximation, the vertical dimension b can be replaced by

$$d = \frac{b}{\cos\alpha} \quad . \tag{23}$$

The phase error is zero, and the angular direction away from the antenna is approximately the angle of the antenna flare.

With the linear approximation, the aperture distribution is

$$E_s(X_s, Y_s) = E_o \quad , \tag{24}$$

and from Eq. (11), the E-field is

$$E_E = 2j\ \frac{e^{-jKr}}{\lambda r}\ \cos^2\frac{\alpha}{2}\ E_o \int_{-a}^{a} dX_s \int_{-d/2}^{d/2} e^{jX\sin\alpha Y_s}\ dY_s \quad . \tag{25}$$

By solving the integrals in Eq. (25), the E-field can be expressed as

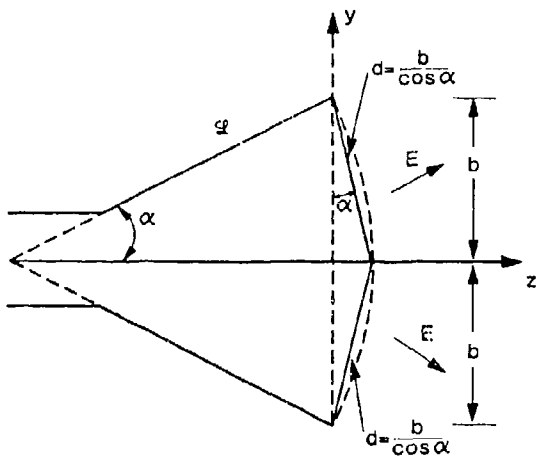

Figure 5. Geometry of linear approximation.

$$E_E = 2j \frac{e^{-jKr}}{\lambda r} \cos^2 \frac{\alpha}{2} E_o \, 2a \left[\frac{d \sin(K\, d/2 \sin\alpha)}{K\, d/2 \sin\alpha} \right] . \tag{26}$$

Also, if the d term is replaced by its value in Eq. (23), the E-field becomes

$$E_E = 2j \frac{e^{-jKr}}{\lambda r} \cos^2 \frac{\alpha}{2} E_o \frac{2ab}{\cos\alpha} \left[\frac{\sin(K\, b/2 \tan\alpha)}{K\, b/2 \tan\alpha} \right] . \tag{27}$$

So, from the E-field in Eq. (27), its magnitude can be expressed as

$$|E_E| = \frac{4ab}{\lambda r \cos\alpha} E_o \cos^2 \frac{\alpha}{2} \left[\frac{\sin(K\, b/2 \tan\alpha)}{K\, b/2 \tan\alpha} \right] . \tag{28}$$

However, the magnitude of E_E is not expressed in terms of P_E, and the power density of one section of the antenna (P_{DE}) will have to be used to relate E_E and P_E; that is,

$$P_{DE} = \frac{E_o^2}{\eta} , \tag{29}$$

and

$$P_{DE} = \frac{P_E/2}{2ab/\cos\alpha} \quad . \tag{30}$$

By setting the power density terms equal, E_o can be expressed as

$$E_o = \sqrt{\frac{\eta\ P_E/2\ \cos\alpha}{2ab}} \quad . \tag{31}$$

By substituting the intrinsic impedance $\eta = 120\pi = 377$ and Eq. (31) into Eq. (28), the magnitude can be expressed as

$$|E_E| = \frac{4ab}{\lambda r\ \cos\alpha}\ \frac{60\pi\ P_E\ \cos\alpha}{2ab}\ \cos^2\frac{\alpha}{2}\left[\frac{\sin(K\ b/2\ \tan\alpha)}{K\ b/2\ \tan\alpha}\right] \quad . \tag{32}$$

With the magnitude of the E-field from the E-plane horn antenna in Eq. (32) and the magnitude of the E-field from the lossless isotropic antenna in Eq. (22), the equality set forth in Eq. (18) can be completed and will yield

$$\frac{30\ P_I}{r} = \frac{4ab}{\lambda r\ \cos\alpha}\ \frac{60\pi\ P_E\ \cos\alpha}{2ab}\ \cos^2\frac{\alpha}{2}\left[\frac{\sin(K\ b/2\ \tan\alpha)}{K\ b/2\ \tan\alpha}\right] \quad . \tag{33}$$

By squaring both sides of Eq. (33), manipulating the terms, and substituting the value of the phase constant K, the ratio of P_I and P_E and in turn the approximated gain becomes

$$G' = \frac{P_I}{P_E} = 16\pi\ a/\lambda\ b/\lambda\ \frac{\cos^4 a/2}{\cos\alpha}\left[\frac{\sin(\pi\ b/\lambda\ \tan\alpha)}{\pi\ b/\lambda\ \tan\alpha}\right]^2 \quad . \tag{34}$$

Graphical representations of the actual gain and derived gain approximation results are shown in Figs. 6 and 7, where the vertical aperture dimension b/λ varies with the horizontal aperture dimension of $a/\lambda = 0.5$ and an angle flare of $\alpha = 5°$ and $\alpha = 10°$ respectively. Using the criterion that the approximated values fall within 3 dB of the calculated values, the results show that the gain approximation holds for an antenna flare angle of less than 10°.

RADIATION PATTERN APPROXIMATION

As shown in Eq. (16), the H-field radiation pattern in the E-plane is rather simple to calculate, making it unnecessary to use an approximation to derive it. However, the E-field radiation pattern in the E-plane is more complex and requires the use of numerical integration for its evaluation. From Eq. (13), the actual E-field radiation pattern can be expressed as

$$F(Kb\sin\theta,\delta) = \frac{1}{2b}\int_{-b}^{b} e^{jK(r_o\sin\theta Y_s - Y_s^2/2r_o)}\ dY_s \quad . \tag{35}$$

The pattern of the E-plane horn antenna is shown in Fig. 8, and the relative E-field radiation pattern, as a function of direction and phase error, has been shown in Fig. 3.

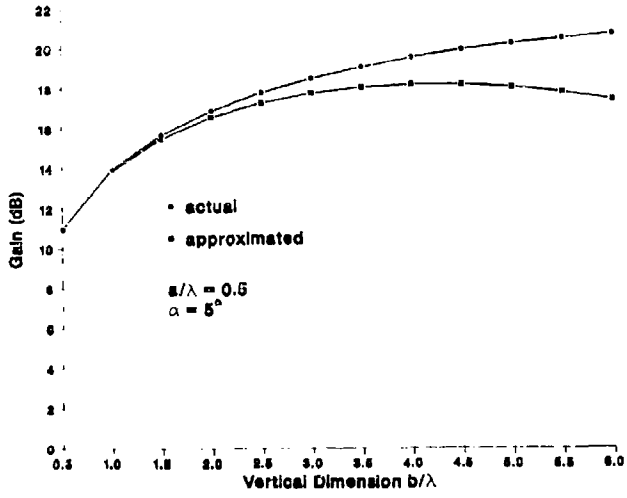

Figure 6. Actual gain vs approximated gain--
$a/\lambda = 0.5$, $\alpha = 5°$, $b/\lambda = 0.5$ to 6.0.

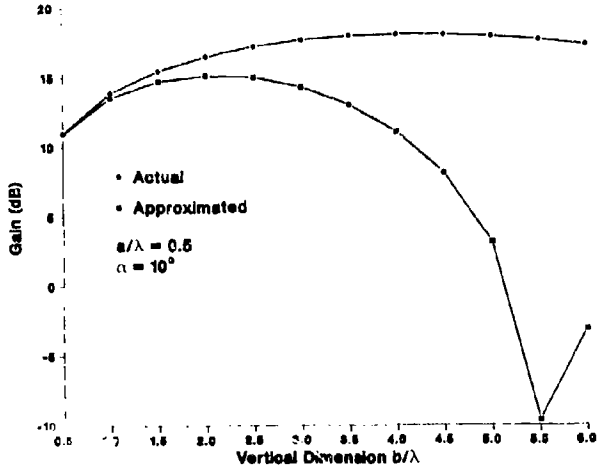

Figure 7. Actual gain vs approximated gain--
$a/\lambda = 0.5$, $\alpha = 10°$, $b/\lambda = 0.5$ to 6.0.

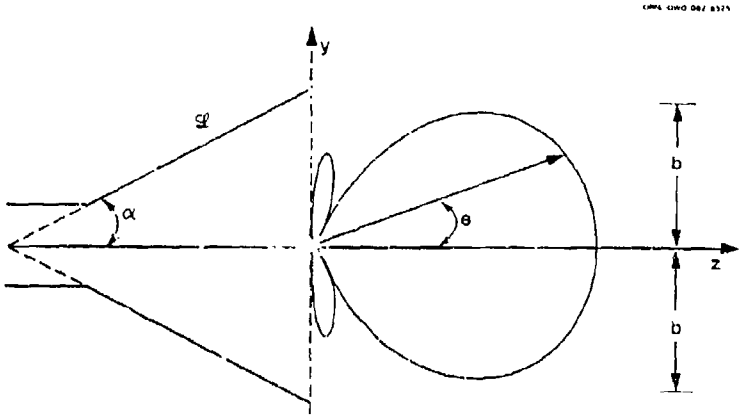

Figure 8. E-plane horn antenna pattern.

An approach to approximating the E-field radiation pattern can be similar to the one used for the gain approximation in the sense that the antenna will again be divided into two sections, with each acting as an independent antenna. Figure 9 shows the geometry of each section and its associated pattern. An estimate of the total radiation pattern will encompass a combination of the individual radiation patterns related by the angles of direction θ' and θ''.

An approximation of the E-plane radiation pattern will involve the radiation patterns of the individual sections, which can be expressed as

$$F(Kb\sin\theta') = \frac{\sin\,(kb\sin\theta')}{Kb\sin\theta'} \tag{36}$$

and

$$F(Kb\sin\theta'') = \frac{\sin\,(Kb\sin\theta'')}{Kb\sin\theta''} \quad . \tag{37}$$

The radiation patterns in Eqs. (36) and (37) are the patterns for the E-plane radiation from a rectangular aperture. From Fig. 9, the angles θ' and θ'' are related to the original angle of direction θ and the flare angle α of the E-plane horn antenna by

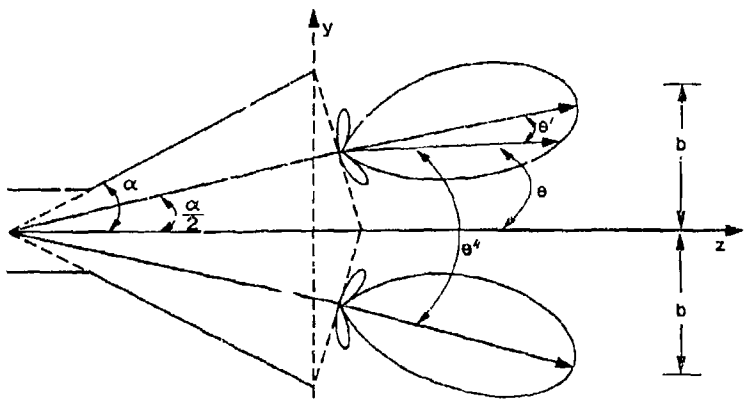

Figure 9. Geometry of E-plane radiation pattern approximation

$$\theta' = \frac{\alpha}{2} - \theta \tag{38}$$

and

$$\theta'' = \frac{\alpha}{2} + \theta \ . \tag{39}$$

The E-plane radiation pattern approximation will combine Eqs. (36) and (37) and can be expressed as

$$F'(Kb\sin\theta) = \frac{1}{2}\left[\frac{\sin(Kb\sin\theta')}{Kb\sin\theta'} + \frac{\sin(Kb\sin\theta'')}{Kb\sin\theta''}\right] \ . \tag{40}$$

The final expression in Eq. (40) is actually only half of the sum of the radiation patterns of the two sections because of the overlap between them.

Graphical representations of the actual E-field radiation pattern and the approximated radiation pattern are shown in Figs. 10 and 11 for maximum phase error values of 15°and 60° respectively. Using the criterion that the approximated values fall within 3 dB of the calculated values, the E-field radiation pattern approximation holds until the antenna's phase error approaches 60°.

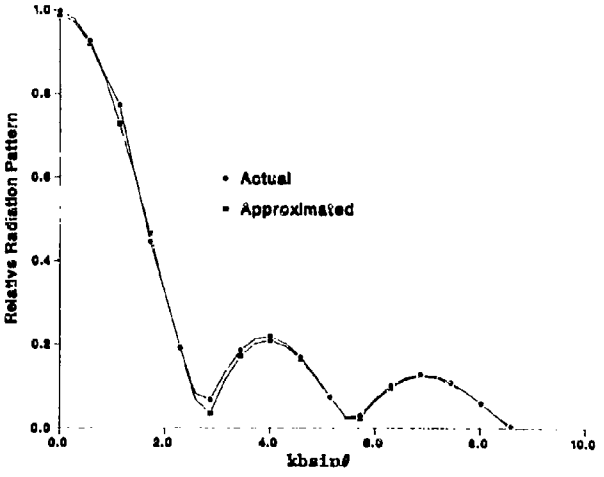

Figure 10. Actual vs approximated radiation pattern--maximum phase error = 15°.

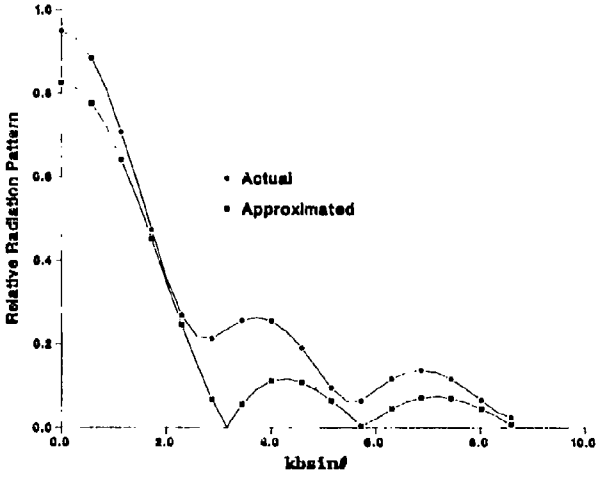

Fig: e 11. Actual vs approximated radiation pattern--maximum phase error = 60°.

CONCLUSIONS

A gain and radiation pattern approximation can be used to avoid the complex mathematics and computation methods typically involved in calculating the gain and radiation pattern. A hand-held calculator can be used to solve the trigonometric terms in the approximations, while a computer may be required to calculate the Fresnel integrals in the actual gain equation and perform numerical integration to determine the actual radiation pattern.

When the flare angle of the E-plane horn antenna is less than 10° for typical antenna dimensions, the 3-dB criterion for the approximation is met. However, the correlation between the actual and approximated gain falls off quickly when the angle flare is 10° or greater. When the phase error is 15° or less for the antenna, the approximation criterion for the radiation pattern is met. Except for the regions around the multiples of π, the approximated radiation pattern holds up well until the phase error is over 60°.

References

1. Edward A. Wolff, *Antenna Analysis*, Wiley, New York, 1966.

2. Warren L. Stutzman, and Gary A. Thiele, *Antenna Theory and Design*, Wiley, New York, 1981.

3. Richard C. Johnson and Henry Jasik, eds., *Antenna Engineering Handbook*, 2d ed, McGraw Hill, New York, 1984.

4. Paul D. Ewing, *Gain and Electric Field Radiation Pattern Approximations for the E-Plane Horn Antenna*, ORNL/TM-10983, Oak Ridge National Laboratory, December 1988.

FAR-FIELD PATTERNS OF ULTRA HIGH GAIN ANTENNA ARRAYS OF FINITE SIZE

Ross A. Speciale

General Dynamics, Air Defense Systems

P.O. Box 50-800, MZ 601-71, Ontario, CA 91761-1885

ABSTRACT

We are attempting to establish, by rigorous formal and numerical analysis, the validity of recent claims purporting the practical feasibility of so-called 'non-diffracting' beams, at essentially any frequency across the electromagnetic spectrum, including microwaves, millimeter waves, infrared and visible light [Ref. 1-4].

Our objective is to determine whether any physically realizable, finite-size planar-aperture distribution can be defined that can be proved to even only approximate, within some acceptable tolerance, the radiation characteristics of a non-diffracting beam.

Our approach has been to synthesize such a planar aperture distribution in terms of a vectorial expansion in cylindrical modes, while imposing the constraint of zero average radial energy flow everywhere in the half space facing the aperture. We showed in a previous paper [Ref. 5] that this condition can be met by properly choosing the coefficients of the TE and TM components of the cylindrical wave spectrum with any given common azimuthal index m, and that for every such set of cylindrical modes optimum values of the radial and axial wave numbers k_ρ and k_z exist, that maximize the average axial energy flow within any given radius from the center of the circular aperture. The planar aperture distribution so synthesized is very much different from the simple plane-wave, flat-phase distribution that would be suggested by the conventional wisdom. It is characterized by radial phase alternations,

superimposed upon a linear azimuthal phase evolution, and by a position-dependent axial ratio and ellipticity across the aperture.

So far, however, our analysis has assumed an essentially infinite planar aperture, and the feasibility of generating any reasonable approximation to a non-diffracting beam has been strictly a matter of conjecture, based on the computed high concentration of radiated axial energy flow within relatively small radii from the aperture center, especially for cylindrical modes with low azimuthal index m .

We are now attempting to determine the effects on the far-field pattern of truncating the circular aperture to some optimum finite radius. Our objective is to determine whether an optimum radius exists, and whether some edge-field taper can be defined that minimize the effects of the truncation of the circular aperture to a finite radius.

The approach followed in this attempt is to compute, both formally and numerically, an equivalent plane-wave expansion representing the radiated field in the half space facing the truncated aperture. The main problem to be solved is the determination of the radiated field on the plane of the aperture, at larger radii than its physical outer radius. This fringing field is obviously non-zero, and may depend on the particular shape of the edge, as well as on the assumed edge-field taper. Planar wave spectra are computed numerically through a 2D-FFT, as in planar near-field scanning, without probe pattern correction. Planar wave spectra can also be computed analytically, by using Sommerfeld's integral representation of Bessel functions [Ref. 6].

The obtained far-field patterns are being evaluated against comparable Hansen's 'one parameter' circular aperture distributions [Ref. 7], that have been proposed as the best compromise between directivity and sidelobe level.

REFERENCES

[1] C. W. Oseen,"Die Einsteinsche Nadelstichstrahlung und die Maxwellschen Gleichungen," Ann. Phys., Vol. 69, pp. 202-204.

[2] J. E. Durnin,"Exact Solutions for Nondiffracting Beams. - I The Scalar Theory," J. Opt. Soc. Am. A, Vol. 4, No. 4, April 1987, pp. 651 - 654.

[3] J. E. Durnin and J. H. Eberly,"Diffraction Free Arrangement," US Patent No. 4,852,973, August 1, 1989.

[4] J E. Durnin, J. J. Miceli, and J. H. Eberly,"Diffraction Free Beams," J. Opt. Soc. Am. A, Vol. 3, March 1986, p. 128.

[5] R. A. Speciale and Paul F. Wacker,"Ultra High Gain Antenna Arrays," 6th Annual Review of Progress in Applied Computational Electromagnetics, Naval Postgraduate School, Monterey, California, March 19-22, 1990, pp. 241-252.

[6] J. Stratton,"Electromagnetic Theory," McGraw-Hill, New York, 1941, pp. 364-369.

[7] R. C. Hansen,"A One-Parameter Circular Aperture Distribution with Narrow Beamwidth and Low Sidelobes," IEEE Trans. on Antenna and Propagation, July 1976, pp. 477-480.

SESSION 12- "NEC ANTENNA ANALYSIS"

Moderator: Peter Excell

MODELING A SHIPBOARD FAN ANTENNA

Lance Koyama
Code 824
Naval Ocean Systems Center
San Diego, CA 92152

Abstract

In the frequency range for which US Navy shipboard fan antennas are designed, 2-6 MHz, the whole ship is in fact the antenna. This makes for a very large and complex numerical modeling problem. This paper describes an effort concentrated on a destroyer, the Spruance (DD-963), for which NOSC has a 1/48 scale brass model to make measurements on for comparison with the calculations. The antenna characteristics used for judging the accuracy of the numerical model with regards to measured data were the feedpoint impedance and the voltage across the insulator at the apex of the fan.

NEC-3-VLF was used on a 719 segment model. To make a good comparison between measured and calculated data, the code was run for 51 frequencies between 1.5 and 6.5 MHz. The computer used was a Convex C210 which has close to the performance of a single processor on the Cray X/MP-48. The code was compiled to take advantage of the vector architecture of the Convex and its 64 bit word size.

There was a very good match between the antenna characteristics of the numerical model and the measurements from the brass model, showing NEC to be a viable tool for modeling a complex structure with reasonable engineering effort and use of computer resources.

Introduction

At the NOSC Model Range, the capability exists to build both computer and physical models to duplicate the electromagnetic behavior of full scale ships. The models provide a relatively convenient, economical, and timely means of evaluating various antenna configurations. When practical, the model data is validated against measurements on board the actual ship.

Presently NEC-3-VLF is used on the NOSC Convex C210 computer for the numerical models. The Convex has close to the performance of a single processor on the Cray X/MP-48. The code was compiled to take advantage of the vector architecture of the Convex and its 64 bit word size.

The physical models are 1/48 scale brass models. NOSC has a model for every ship class in the US Navy. Measurements were taken two different ways for the purposes of this study: (1) in the frequency domain, using a network analyzer and (2) in the time domain, using a pulser to get the impulse response which is subsequently converted to the frequency domain. The signal above noise ratio is about the same for the two methods. The frequency domain measurements have superior frequency resolution in the present NOSC equipment. The time domain measurements are inherently more immune to background transients but these are usually readily recognizable in the frequency domain measurements so that data can be retaken if

necessary.

The object of this modeling study was the fan antenna on the destroyer, USS Spruance (DD-963), pictured in figure 1 below.

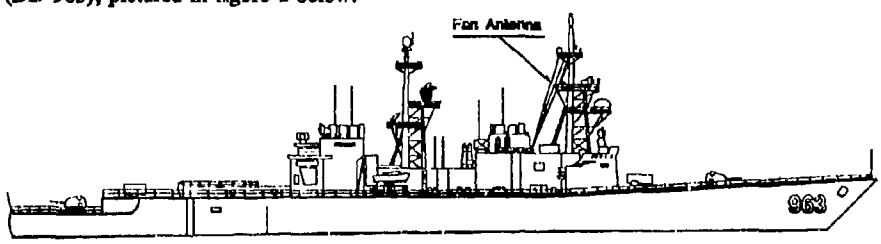

Figure 1 DD-963, USS Spruance

As seen in the figure, the fan extends from the forward mast aftward. A typical configuration of a fan antenna is shown in figure 2. The fan as used on the DD-963 is shown in figure 3. This configuration is called a twin fan. There is a single feed at the top feeding two fans that terminate down into the two apex insulators. Because of the frequency range for which this antenna is used, 2-6 MHz, essentially the whole ship becomes the radiator; making the modeling task very large and complex.

The antenna characteristics used for judging the accuracy of the numerical model with regards to the physical model were the feedpoint impedance and the voltage across the insulator at the apex of the fan. Plans are under way to also conduct these measurements on board the actual ship.

NEC Model

As a matter of course, the brass models are constructed to very fine detail. Because of the complexity of a ship and computer run time and cost constraints, a numerical model cannot hope to achieve the same detail. Keeping in mind the areas of the ship that would make the most electrical difference and the electrical length of all objects, an optimized model can be constructed that would not severely tax computer time and costs.

A long term goal of this project was to hone the skills needed to create an optimized model of a complex ship so that in the future, should measurement data not be so easily available, the numerical modeling effort can be done with more confidence. For this project, reliable impedance data was obtained from the brass model so the object of the NEC model construction was to match this data.

Although the superstructure of the ship modeled contains large amounts of plate steel conducive to modeling with patches, the topside of the ship is full of poles and wires conducive to modeling with wires. An all-wire model approach was chosen for the better accuracy and ease of modeling.

Because of the complex topside, creating a regular grid to represent surfaces would lead to using more wires than necessary. It is more efficient to use the junctions of "wire" type structures to surfaces as the intersection points of a grid. Additional intersection points within the surface can be added to make the cell sizes as desired. A disadvantage of the irregular

gridding is the difficulty in complying with the "diameter of wire equal to separation of wires" rule for representing surfaces with wires.

38 versions of the model were run in seeking to optimize the model, the later versions run at 51 different frequencies between 1.5 and 6.5 MHz. The final model contains 719 segments and took 143 minutes of CPU time to run the 51 frequencies. Figure 4 shows the model and figure 5 shows two views of the fan antenna with parts of the supporting mast structure.

Some of the lessons learned in the optimization process are as follows:

- For the frequency range of interest, 1.5-6 MHz, 0.1 meter accuracy in specifying wire length was sufficient.

- The distance between the top part of the fan (where it is fed) and the yardarm from which it is hung did not make much of a difference.

- The excitation segment joins the top part of the mast structure to the four feed wires of the fan. Its length is critical. Making it shorter made the antenna impedance more capacitive.

- Slight changes in the length of the apex insulators did not result in significant changes in the feedpoint impedance although the voltage across the insulators did change noticeably.

- With the vertical and horizontal members of the mast structure defined, adding cross members made little difference.

- To find out what parts of the ship were most important in attaining a correct impedance for the fan antenna, a test was run. The wire radii of the model was reduced to about 1/50 of the actual value for each part of the ship. Then singly and in combinations, the wire radius of various parts of the ship were increased up to the actual value. Although the impedance of the reduced radii model was way off the correct impedance, no single part of the ship proved to be the major contributor to attaining the correct impedance. Listed below is the approximate decreasing order of importance of various parts of the ship to the fan antenna impedance.

Part of Ship	Area of Smith Chart Impedance Improved by Correcting Wire Radius
Fan feed	Highest frequencies
Forward mast	Lower frequencies
Superstructure and deckhouses	Lower frequencies
Fan wires	Higher frequencies
Aft mast	Little difference
All whips	Little difference

Results

1. Impedance

The Smith chart comparison of the frequency domain measurement data and the NEC data are shown in figure 6. The resistances and reactances for these two data sources plus the time domain measurement data are shown in figure 7. There is good agreement except at approximately 3.2 and 3.6 MHz where the peaks are of different magnitude. This is the area of first anti-resonance.

2. Apex insulator voltage

Since NEC does not give voltage information except for the voltage across a source, the voltage across an insulator is obtained by substituting a very high resistance for the insulator and measuring the current through it, then applying Ohm's law. From brass model measurements, the maximum magnitude of the impedance measured at the apex insulators is approximately 4,000 ohms, so a resistance of 1 Gigohm was used for the insulator. This was judged high enough so as not to disturb any other electrical parameter.

The NEC calculated voltage across the insulators was highly sensitive to the length used for the insulators even though the feedpoint impedance showed little change. The length used on the brass model was the equivalent of about 1 m. Three lengths were tried with NEC: 1.0 m, 1.5 m, and an insulator length of 0.15 m attached to a conductive length of 0.85 m. The NEC voltages of all three lengths are shown in figures 8 (port apex) and 9 (starboard apex). As can be seen, the voltage for an insulator length of 1.5 meters falls between that for insulator lengths of 1 meter and 0.15 meters on the port side but the 1.5 meter data is close to the 0.15 meter data for the starboard insulator.

To try to get a better feel of the effect of the insulator length on the fan antenna, a test fan was constructed, pictured in figure 10 to the right. It is just a simple structure to simulate a mast (segments 1-10), a feedpoint (segment 11), a single wire "fan" (segments 12-20), and an insulator (segments 21, 22). The dimensions approximate the fan under study. The following insulator lengths were tried:

1. 2 m insulator to ground
2. 1.5 m insulator to ground
3. 1 m insulator to ground
4. 0.5 m insulator to ground
5. 0.5 m insulator to a 0.5 m post to ground
6. 0.15 m insulator to a .85 m post to ground

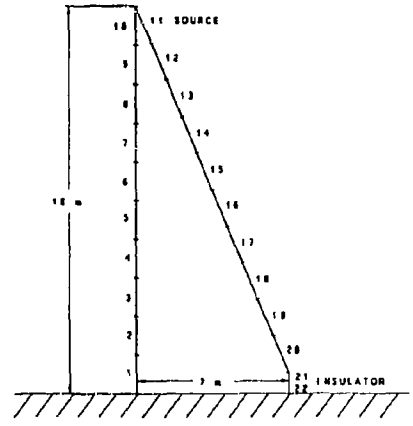

Figure 10 Test Model

The feedpoint resistances and reactances, and the insulator voltages are shown in figure 11. The currents for the various segments for various frequencies are shown in figure 12. As can be seen, the feedpoint impedance is rather insensitive to the insulator lengths. The voltage across the insulator is very dependent on the length but not in a very predictable way.

The determination of the effective length of an insulator on a scale model is difficult due to the relative size of the test leads involved in making a voltage measurement. Thus, an arbitrary length was chosen for the NEC model and just the shapes of the frequency responses were compared between the NEC model and the brass model. This is a reasonable method of comparison since in the NEC calculations for both the DD-963 model and the test model, the shape of the frequency response did not change with insulator length.

The voltages from the brass model time domain and frequency domain data, and the NEC model data are shown in figures 13 (port apex) and 14 (starboard apex). The time domain data, due to equipment limitations, has coarser frequency increments than the other two, and because of the greater amount of processing involved to present data in the frequency domain, is more uneven. The frequency domain data though, matches quite nicely with the NEC prediction except for some constant factor which could probably be attributed to differences in the length of the insulator. What was especially gratifying though, was the similarity in shapes even in the 3.2 to 3.6 MHz region (the anti-resonance region) where the impedance data differed greatly between NEC and the frequency domain measurements. Apparently the voltage at the apex insulator is insensitive to the feedpoint impedance, at least in the anti-resonance region.

Conclusions

- The very complex geometry of a fan antenna on board a destroyer type ship can be accurately represented by a numerical model with a reasonable use of computer resources.

- Comparing data with a very accurate 1/48 scale brass model, the NEC model showed a very close match in feedpoint impedance except for first anti-resonance.

- Although the magnitude of the voltage across the apex insulators differed between the two models, the shape of the frequency response was close.

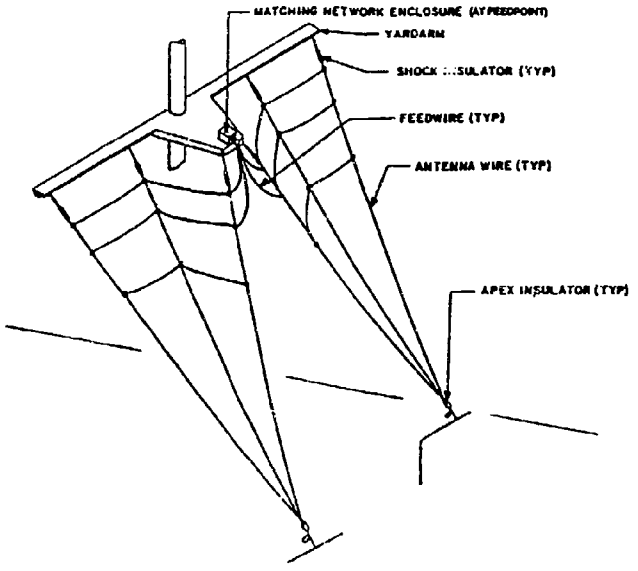

Figure 2. Fan Antenna, Typical Configuration

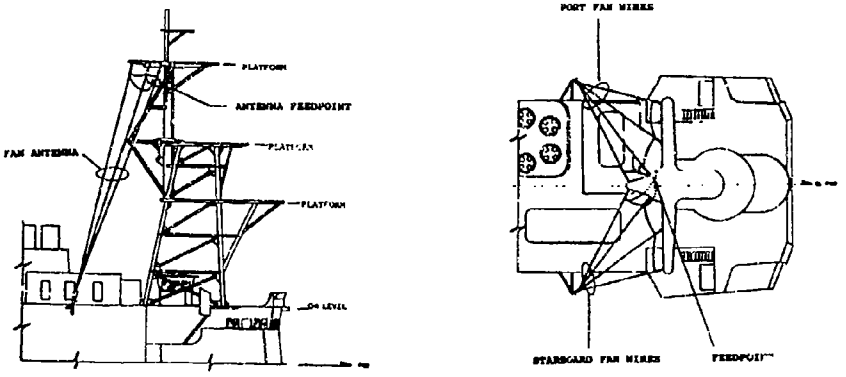

Figure 3. Fan Antenna on the DD-963, Starboard and Top Views

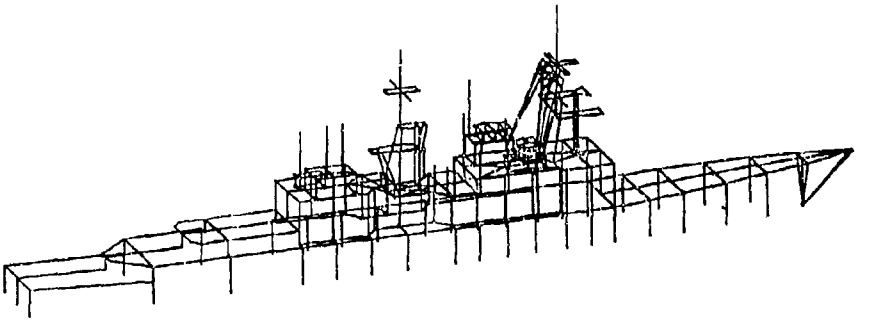

Figure 4. NEC Model of the DD-963

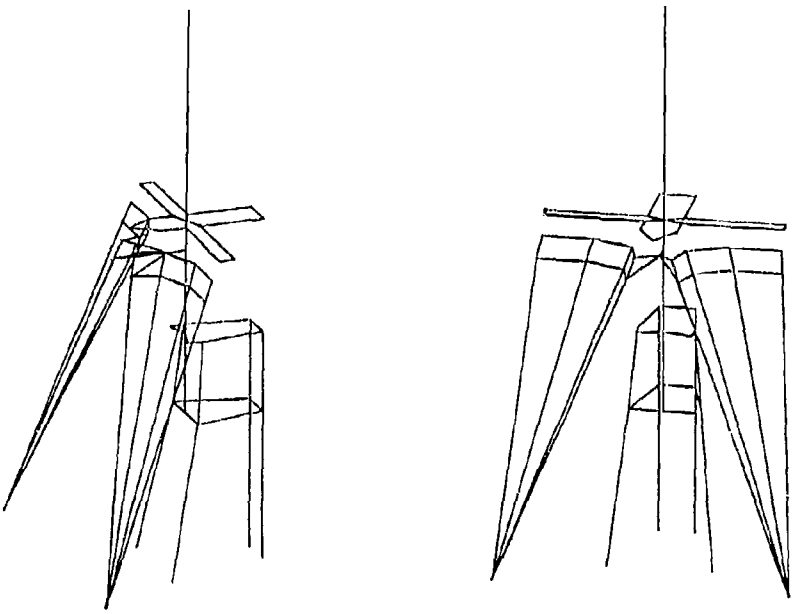

Figure 5. Fan Antenna, two views, NEC Model of the DD-963

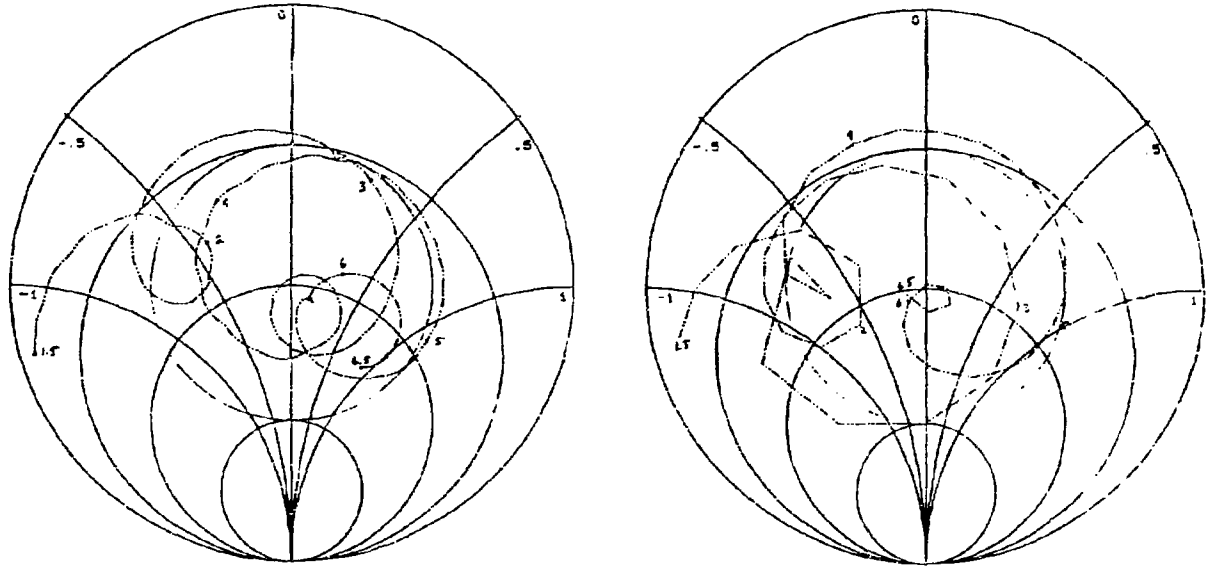

Figure 6. Impedance: (a) Brass Model, Frequency Domain Range, (b) NEC Model

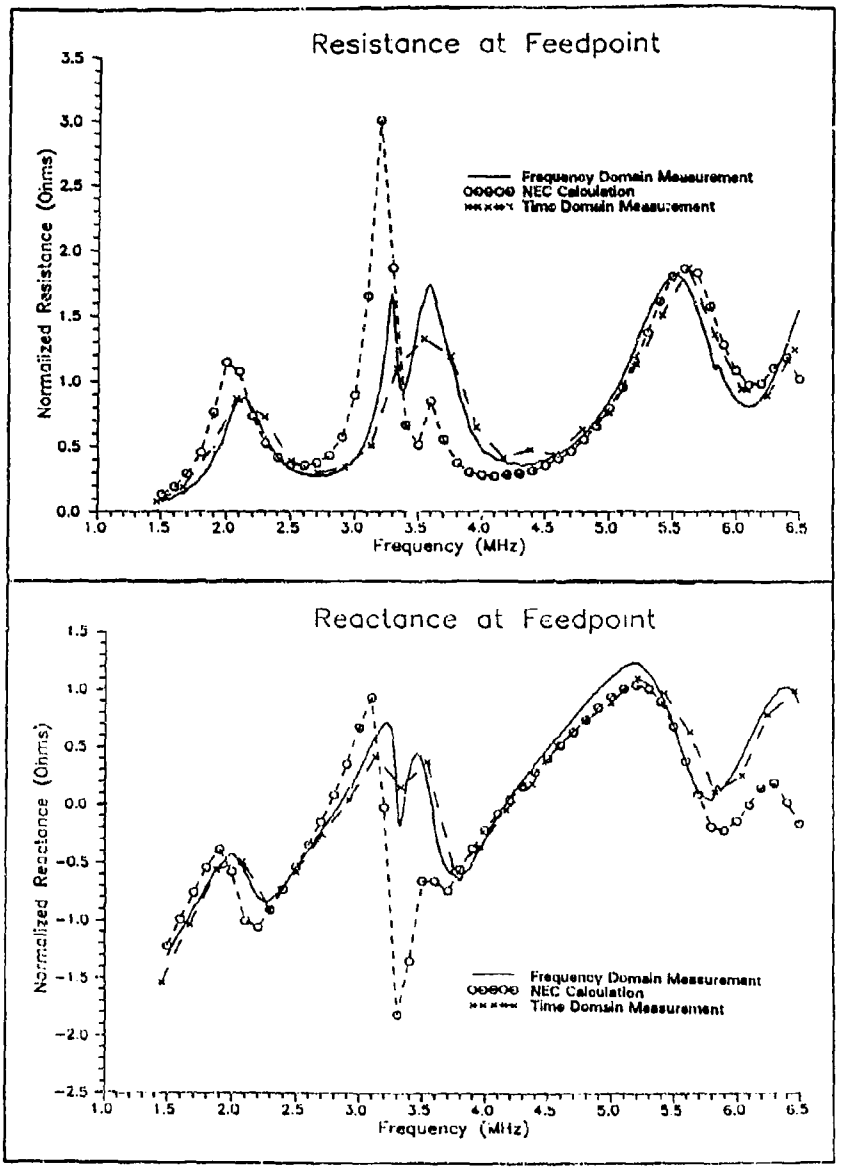

Figure 7. Model Impedance Summary, Resistance and Reactance

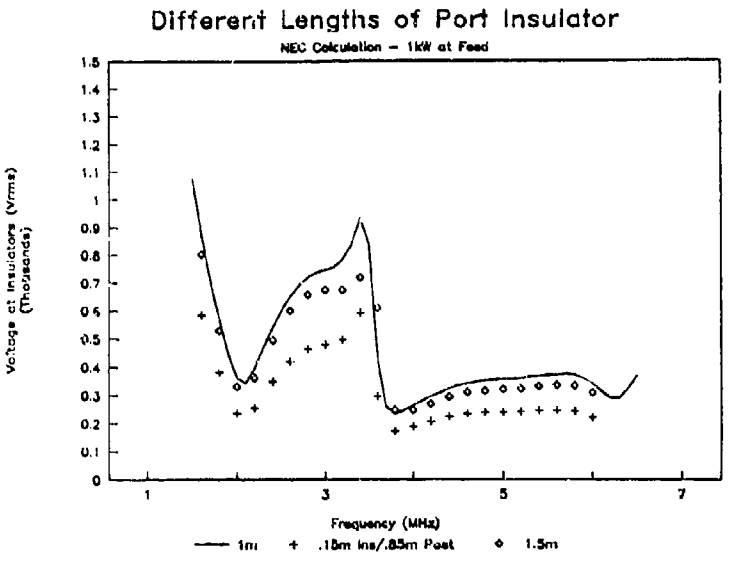

Figure 8. Voltage Across Different Lengths of Port Insulator

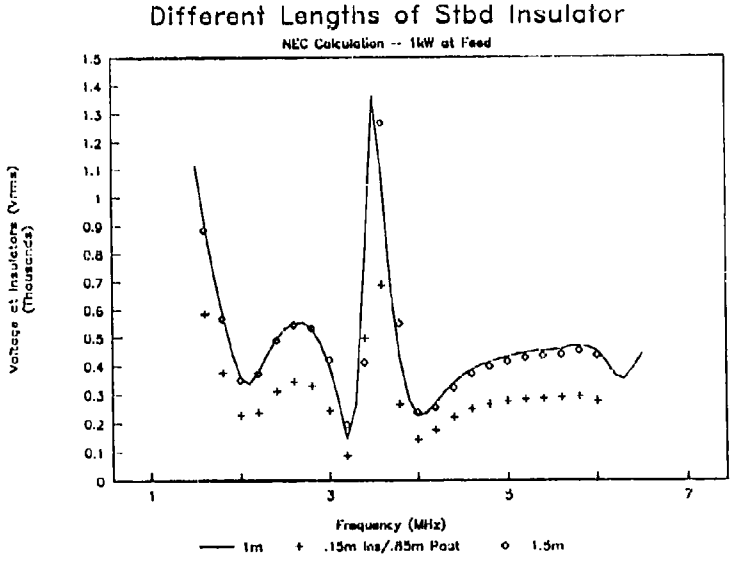

Figure 9. Voltage Across Different Lengths of Starboard Insulator

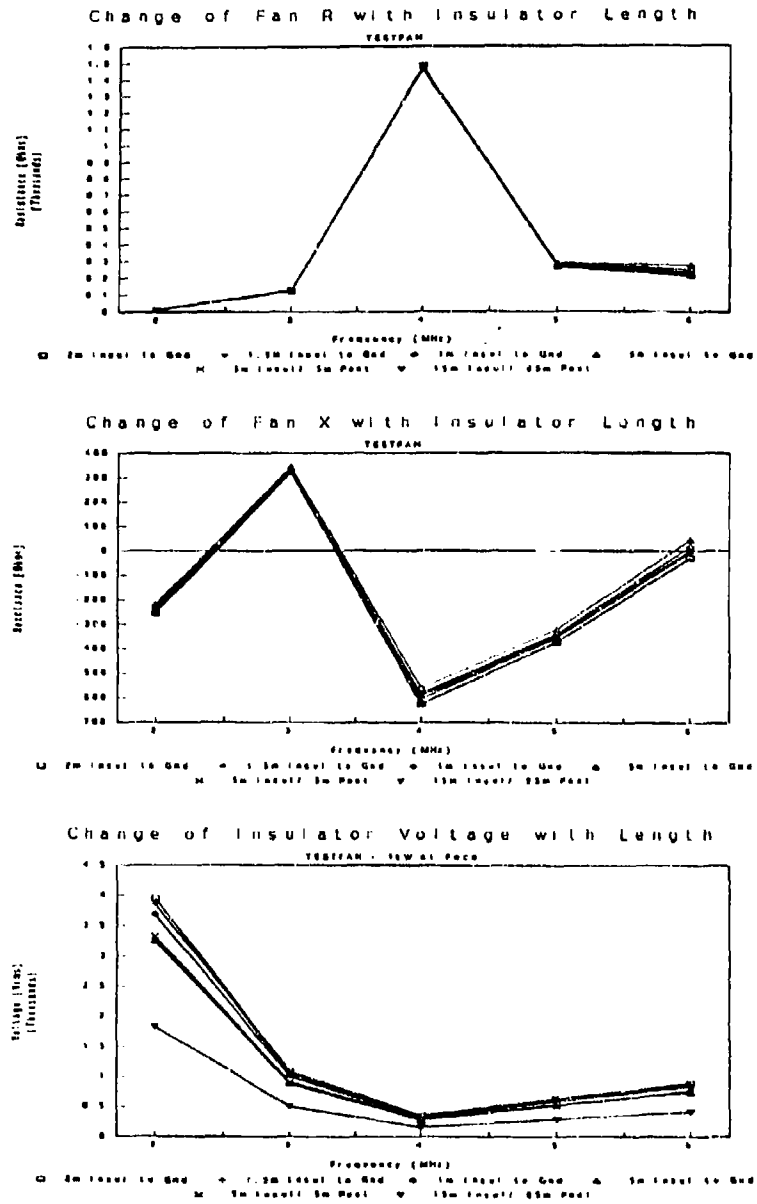

Figure 11. Test Model: Resistances, Reactances, and Voltages

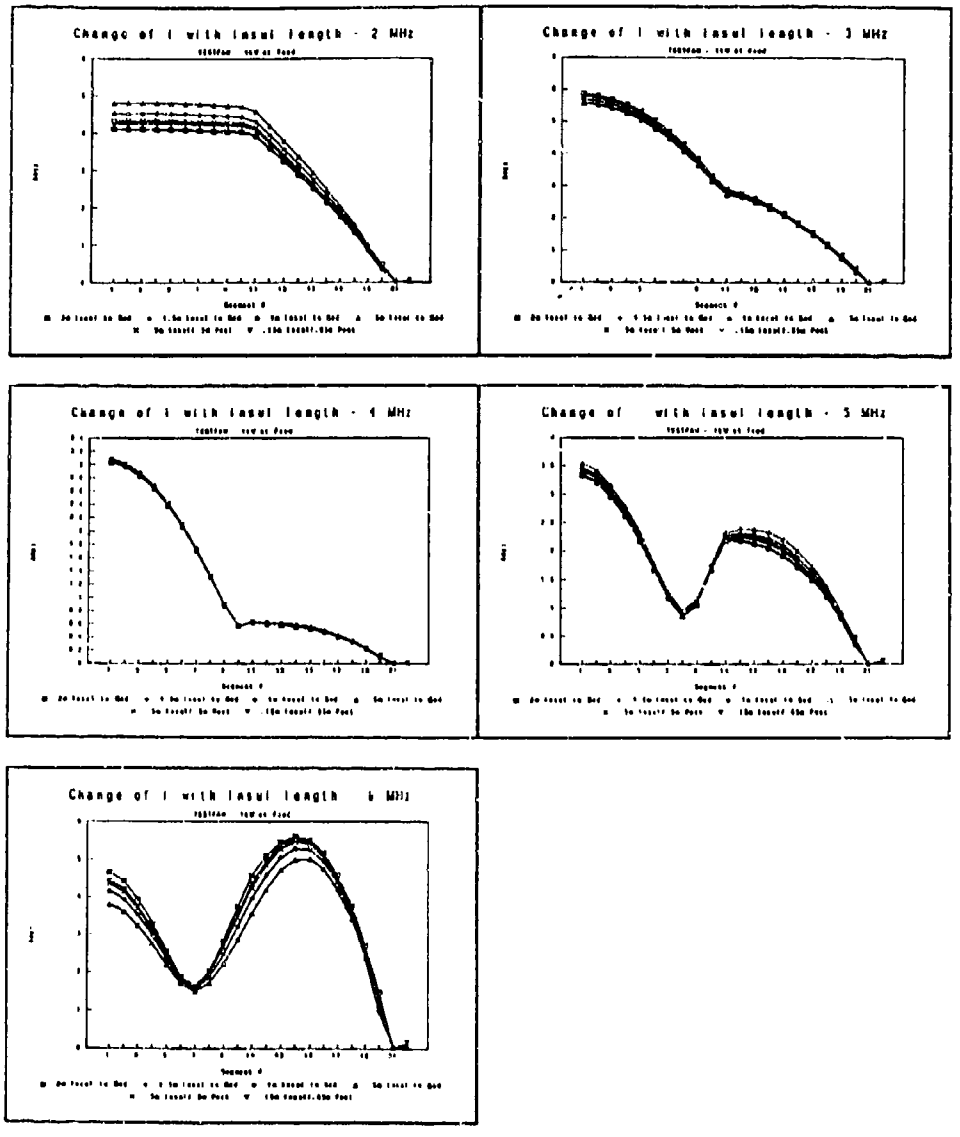

Figure 12. Test Model: Segment Currents

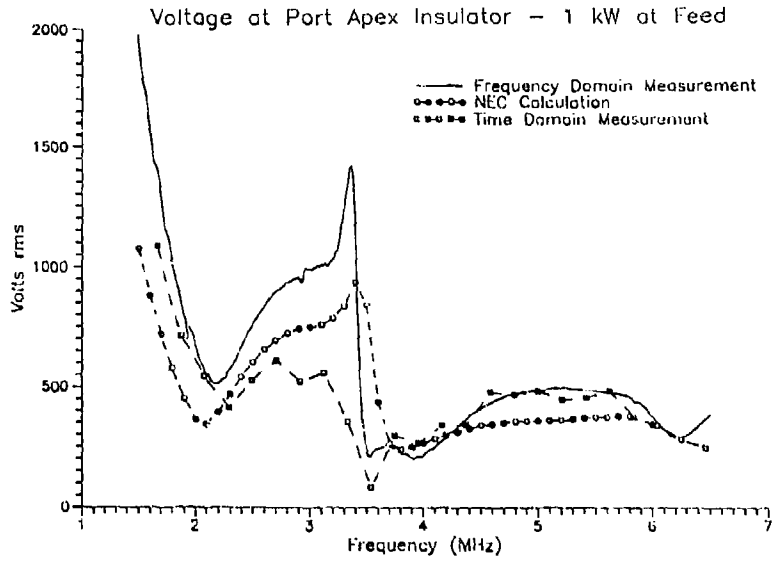

Figure 13. Port Insulator Voltages: Time Domain Range, Frequency Domain Range, NEC

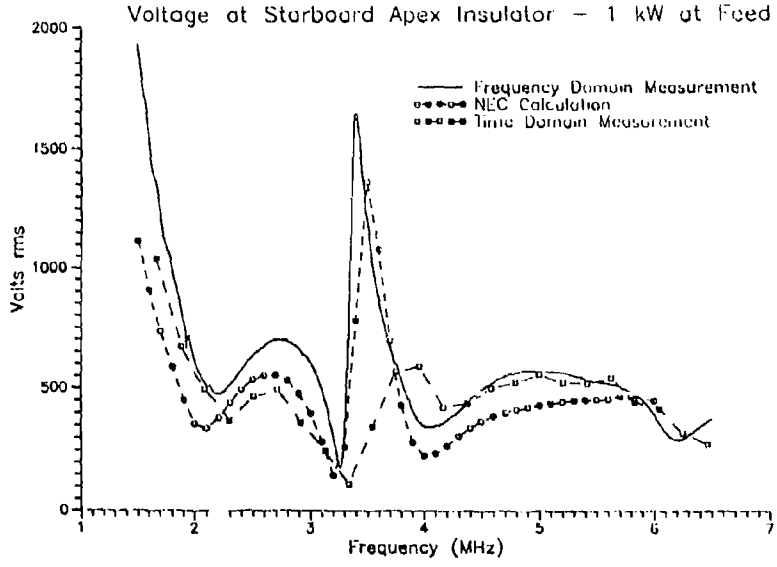

Figure 14. Starboard Insulator Voltages: Time Domain Range, Frequency Domain Range, NEC

Optimizing Sidelobe Levels of an Array Using NEC

Randy L. Haupt and Christopher J. McCormack
Department of Electrical Engineering
United States Air Force Academy, CO 80840

Warren F. Brandow III
82nd FTW 98 FTS
Williams AFB, AZ 85240

Abstract.

This paper describes how to use NEC (Numerical Electromagnetics Code) to optimize the sidelobe levels of an array with uniformly spaced center elements and nonuniformly spaced edge elements.

Introduction.

Low sidelobe array synthesis generates a current taper through analytical or numerical optimization of the array factor. Applying the synthesized taper (e.g. Chebychev, binomial, etc.) to an antenna array does not produce the desired result, because mutual coupling is not accounted for in the theory. It is possible to optimize the array pattern by including mutual coupling at the expense of dramatically increasing the computation time needed in the synthesis process.

We set out to investigate the possibility of optimizing the sidelobe levels of small arrays of dipoles using NEC (Numerical Electromagnetics Code) [1]. Our primary interest is in partial amplitude tapering and partial nonuniform spacing of the array elements. This paper describes how we use NEC in conjunction with an optimization method to optimize the spacing of the edge elements of small arrays of colinear dipoles to obtain the lowest possible sidelobe levels.

Optimization Using NEC on a VAX Computer.

Our plan of attack for synthesizing a low sidelobe array is to begin with an array of equally spaced collinear dipoles, then nonuniformly space the outer elements, while keeping the inner elements uniformly spaced (Figure 1). The array lies along the x-axis and is symmetric about its physical center. There are $2N$ uniformly spaced elements in the center and M elements on either edge of the array. The goal of the optimization process is to adjust the spacing of the outer 2M elements to produce the lowest possible sidelobe level.

The first step in the problem is to change the constrained optimization problem into an unconstrained problem. Rather than optimizing on the element spacing with constraints (such as $x(i+1)>x(i)$, an outer element is farther from the center array than an inner element), the program optimizes on an unconstrained parameter, γ, where

$$\gamma = \arccos\left[\frac{2(x(i)+d)}{x(i+1)} - 1\right]$$

where

$x(i)$, $x(i+1)$ = distance of elements i and i+1 from the center of the array
d = distance between uniformly spaced elements

The next step is to choose an optimization subroutine. We used the downhill simplex and Powell's method from **Numerical Recipes** [2]. Both routines produced satisfactory results.

Finally, a cost function is needed. The cost function used for the results in this paper is the minimum relative sidelobe level of the array. NEC calculates the relative far field pattern of the array of dipoles, then a search routine finds the maximum sidelobe level from the output generated by NEC.

A block diagram of the program appears in Figure 2. The main program prompts the user for the number of elements in the array, the number of elements that are nonuniformly spaced, the length of the dipole, the initial element spacing, and the number of segments per wire length. It also changes the constrained spacing problem into an unconstrained angle problem before calling the optimization subroutine. The optimization subroutine calls the function MAXSLL which returns the maximum sidelobe level of the array as calculated by NEC. The optimization routine continues until a specified tolerance is met or the maximum number of iterations is exceeded. All the output data from NEC resides in a file called FIELD.OUT and the relative far field pattern, the array spacing, and value of the maximum sidelobe level resides in another file called FLD.TBL.

The three problems we had to overcome were running NEC from within the optimization routine, passing input data to NEC, and dealing with all the output data files NEC creates. The first problem is resolved by creating an auxiliary file to control NEC when the process is spawned. This file (called ABC.XYZ) contains the input and output file names to be used by NEC and is created with the following FORTRAN statements:

```
open (unit=1,file='ABC.XYZ;1',status='new')
write(1,*) 'FIELD.INN;1'
write(1,*) 'FIELD.OUT;1'
close(unit=1)
```

After creating the control file (ABC.XYZ) and the input file (FIELD.INN), the program calls NEC as a sub-process with the following lines of code:

```
fnam = 'nec2s'
inam = 'ABC.XYZ;1'
onam = 'nl:'
rstat = lib$spawn(%descr(fnam),%descr(inam),%descr(onam))
```

The second problem of passing input data to NEC is solved by opening a new input file each time the element spacing changes and writing the new spacing to the file. The following statements accomplish this task:

```
      open (unit=4,file='FIELD.INN;1',status='new')
      write (2,39) <etc>
39    format <etc>
      close(4)
```

Finally, to avoid disk quota problems, the old files are deleted before creating the new files using the commands:

```
fnam = 'FIELD.OUT;1'
rstat = lib$delete_file(%descr(fnam))
fnam = 'FIELD.INN;1'
rstat = lib$delete_file(%descr(fnam))
```

In order to use the above commands, place the following variable definitions at the beginning of the program:

```
integer rstat
character*12 fnam, inam, onam
```

Results.

We first investigated optimizing an array factor of 8 isotropic elements with N=2 and M=2 (4 uniformly spaced elements in the center and 2 nonuniformly spaced on each end of the array). This model does not include mutual coupling and results in a -5.37 dB decrease in the maximum sidelobe level with center elements spaced .5λ apart while the two edge elements are spaced .69λ and .72λ apart. Optimizing a NEC λ/4 colinear dipole array model that does include mutual coupling results in a -3.9 dB decrease in the maximum sidelobe level with center elements spaced .5λ apart while the two edge elements are spaced .54λ and .57λ apart. Thus, a small perturbation to two edge elements on each end of the array results in an almost 4 dB decrease in the sidelobe level. The NEC results are considerably different from the array factor results. Figure 3 shows the resulting far field pattern calculated by NEC for the nonuniformly spaced array.

The next examples are for 12 element arrays of .474λ colinear dipoles. Figure 4 is the far field pattern resulting from an array with the center 10 elements spaced .6λ apart and the edge element separated from the next element by 1.11λ. The maximum relative sidelobe level is -15.42, which is 2.32 dB less than the maximum sidelobe level of a 12 element array with a spacing between elements of .6λ. Figure 5 is the far field pattern resulting from an array with the center 10 elements spaced .7λ apart and the edge element separated from the next element by 1.21λ. The maximum relative sidelobe level is -15.42, which is 2.65 dB less than the maximum sidelobe level of a 12 element array with a spacing between elements of .7λ. Increasing the uniform spacing from .6λ to .7λ decreases the relative sidelobe level a small amount.

Figure 6 shows the optimized far field pattern for a 12 element array of colinear .474λ dipoles with a uniform spacing of .7λ. In this case, N=3 and M=3. Increasing the number of nonuniformly spaced elements does not necessarily help reduce the maximum sidelobe level of the array.

Conclusions.

NEC provides a useful tool for the investigation of array optimization. We have shown that the sidelobes of small arrays of colinear dipoles may be lowered by nonuniformly spacing the edge elements. Mutual coupling plays an important role in determining the spacing of the elements and the lowest possible sidelobe level.

References.

[1] G. J. Burke and A. J. Poggio, "Numerical Electromagnetics Code (NEC) - Method of Moments," Lawrence Livermore National Laboratory, Document UCRL-90560.

[2] W. H. Press, et.al., *Numerical Recipes*. New York: Cambridge University Press, 1986.

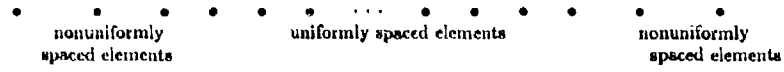

Figure 1. A linear array having the center 2N elements uniformly spaced and the outer M elements on either end of the array nonuniformly spaced.

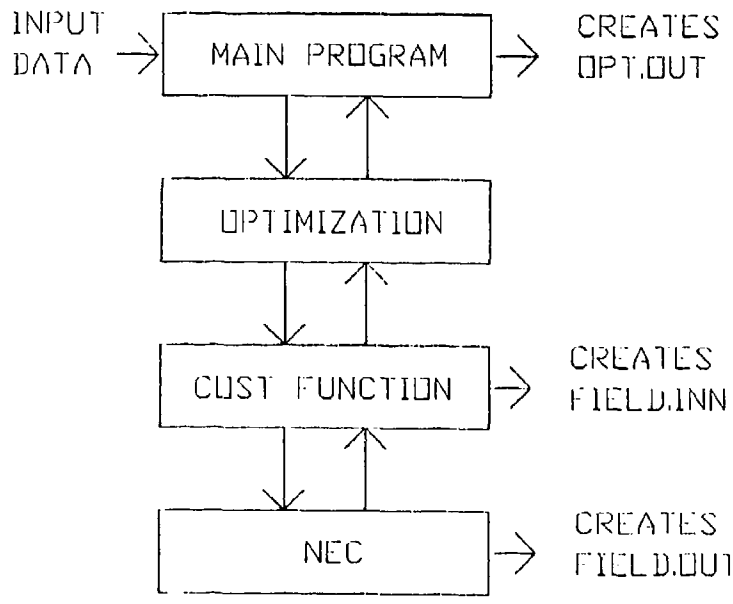

Figure 2. Flow chart of the computer program that uses NEC and an optimization routine to find the lowest possible sidelobe level from nonuniformly spacing the edge elements.

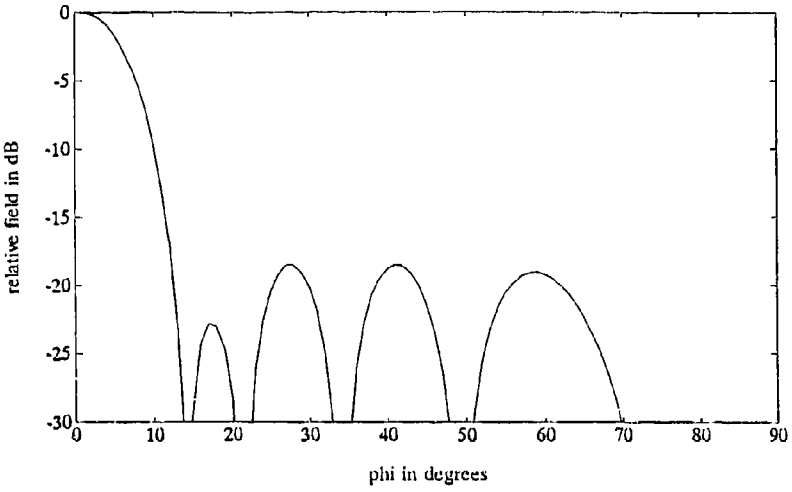

Figure 3. Relative far field pattern of an array of 8 $\lambda/4$ colinear dipoles. The center 4 elements are equally spaced ($.5\lambda$) and the two edge elements on each end are nonuniformly spaced.

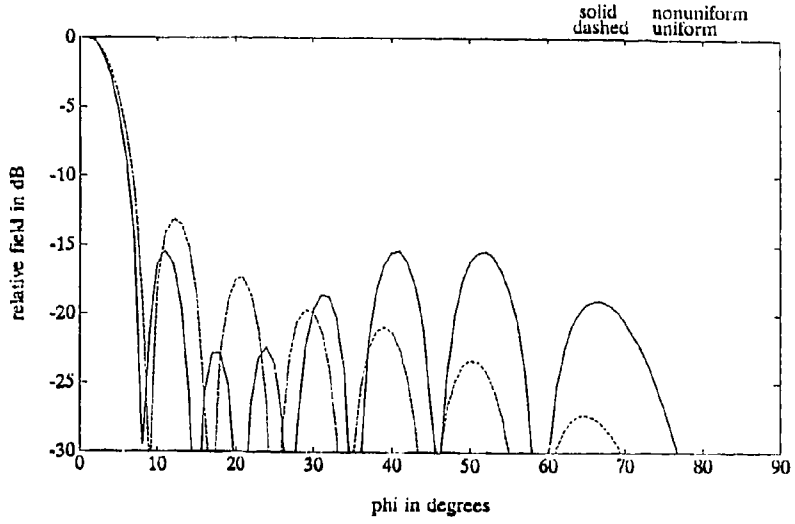

Figure 4. Relative far field pattern of an array of 12, $.474\lambda$ colinear dipoles. The center 10 elements are equally spaced ($.6\lambda$) and the edge elements are nonuniformly spaced.

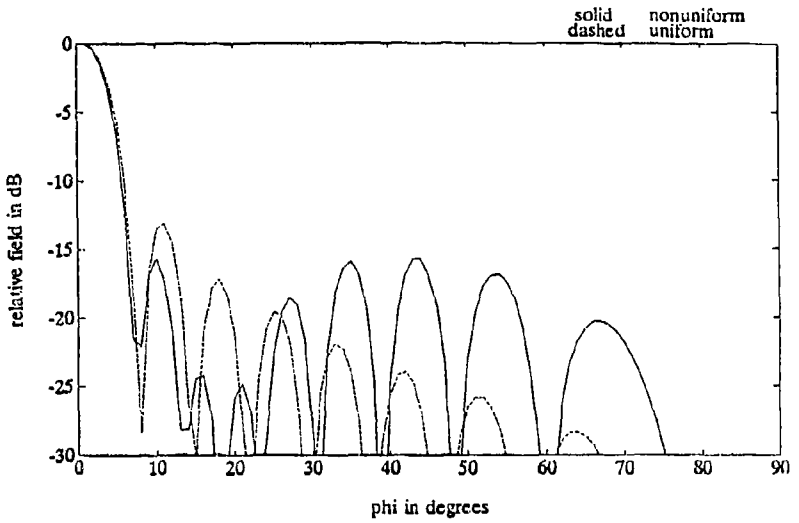

Figure 5. Relative far field pattern of an array of 12, .474λ colinear dipoles. The center 10 elements are equally spaced (.7λ) and the edge elements are nonuniformly spaced.

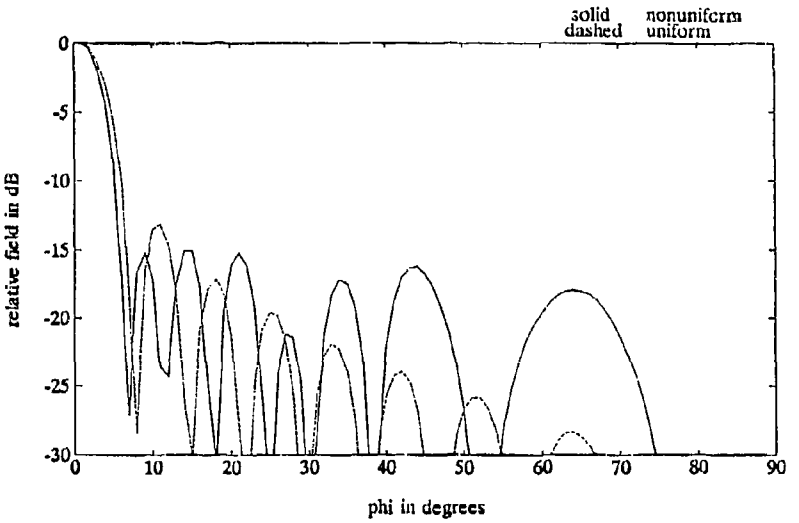

Figure 6. Relative far field pattern of an array of 12, .474λ colinear dipoles. The center 6 elements are equally spaced (.7λ) and the edge elements are nonuniformly spaced.

USING THE NUMERICAL ELECTROMAGNETICS CODE (NEC) TO CALCULATE MAGNETIC FIELD STRENGTH CLOSE TO A SOMMERFELD GROUND

G.R. Haack

Microwave Radar Division
Surveillance Research Laboratory
Defence Science and
Technology Organisation
PO Box 1650
Salisbury
South Australia 5108
AUSTRALIA

A H.J. Fleming

Electromagnetic Compatibility Section
Telecom Australia
Research Laboratories
770 Blackburn Road
Clayton
Victoria 3168
AUSTRALIA

ABSTRACT

This paper presents the results of calculations using the Numerical Electromagnetics Codes (NEC) for problems involving horizontal dipoles near the interface between two semi-infinite half spaces. The examples chosen demonstrate difficulties which may occur in the calculation of magnetic fields in the near field region. The reasons for these difficulties are discussed and m thods for correcting them are suggested.

1. INTRODUCTION

In a previous paper, [1], problems in calculating the near magnetic fields of a horizontal dipole above a lossy ground and in free space, were investigated. Three distinct types of errors were discovered by comparing numerical results obtained using NEC-2 and NEC-3 with experimental results for the centre-fed dipole shown in Figure 1, operating at frequencies of 1.2, 10 and 20 MHz. These frequencies were chosen to demonstrate effects ranging from near resonance to electrically small.

The errors found for this problem were,

(1) At all frequencies NEC-3 over estimated the H-fields very close to the interface by a very large factor, while NEC-2 gave more reasonable results;

(2) Both NEC-2 and NEC-3 gave erroneous results at 1.2 MHz over the entire range of heights above ground examined in that the measured results varied almost linearly with height while the computed results resembled an S-bend, Figure 2;

(3) NEC-3, and upon closer examination NEC-2 also, gave a 'saw-tooth' type ripple at certain discrete heights; this effect was greatest at 10 MHz, while the results also indicated at least one single saw-tooth at 1.2 MHz. (see Figures 2 and 3).

The reason for the erroneous results close to the interface when using NEC-3 is explained in [2]. When the Sommerfeld integral option is used, NEC calculates the near-magnetic field by numerically evaluating the curl of the electric field by a six-point central difference formula. The increment size used in the finite difference evaluation is $10^{-3}|\lambda\pm|$ to each side of the specified point for evaluation of the field in the upper (+) or lower (-) medium. Hence the magnetic field will generally be inaccurate within this distance from the interface since the vertical component of the electric field is discontinuous across the interface. The same method is used in NEC-2, however it has been found that the calculated vertical component of the electric field is continuous across the interface and the resulting magnetic field near the interface is approximately correct. It should be noted that NEC-2 does not calculate the correct electric fields below the air-ground interface. A modified finite difference scheme which corrects the problem when using NEC-3 will be presented elsewhere.

Accounting for error types (2) and (3) requires examination of both the truncation errors associated with the 6-point finite difference (FD) scheme employed in subroutine NHFLD, and the errors, includind round-off, in both the overall moment method calculation of the E-fields and the differencing of these E-fields to form the curl from which the H-fields are then derived.

In principle it should be possible to reduce the errors of type (2) by using a smaller increment size Δ, for the FD calculations as outlined in [1]. The success of this approach will depend on the accuracy of the calculated E-fields and round-off errorrs in computing the FD components. An example where this approach has been used successfully is the horizontal dipole problem in Figure 1, where an increment size of $10^{-4}\lambda$ was required to obtain accurate results at a frequency of 1.2 MHz. In other more recent problems it has been found that even smaller increments of the order of $10^{-8}\lambda$ must be used to obtain accurate results. This was the case for a horizontal dipole in a medium such as sea water at very low frequencies where it is found that the near fields decay rapidly with height above the interface.

Rather than simply reducing Δ to minimize the type (2) errors, higher order FD schemes that have smaller truncation errors may also be used. Perhaps an even better solution would be an adaptive algorithm which automatically selects the appropriate increment size for any given problem by examining the convergence of the H-field solution as Δ and the order of the FD scheme are changed.

Trying to understand the reasons for the saw-tooth (type (3)) errors, and additionally ways to overcome them was a difficult task which involved a detailed examination of the sources of errors in numerically computing H-fields by FD approximations to the curl of the E-field, and alternative methods of formulating the H-field solution.

It will be shown in the following that for the horizontal dipole problem of Figure 1, errors due to the FD curl approximation used in NEC are primarily due to the components of the E-fields which mathematically should have a zero curl component, while the numerical approximation is non-zero.

2. CALCULATION OF NEAR-MAGNETIC FIELDS BY FINITE-DIFFERENCE APPROXIMATION

It is well known that in a uniform homogeneous medium the magnetic field is related to the electric field by the following,

$$\vec{H}=\frac{j}{\omega\mu}\nabla x\vec{E} \qquad (1)$$

For problems involving wire antennas in the presence of an imperfect ground, NEC calculates the Electric fields by numerically solving the Sommerfeld integrals. However, as discussed above, the near magnetic fields are obtained by using a finite-difference approximation of the curl of the electric field. Hence the accuracy of the magnetic fields calculated by this method will generally be one order of magnitude worse than the electric field since the former requires differences of quantities which themselves are

not exact.

Under certain conditions it has been found that the calculation of the magnetic fields by this method can be an ill-conditioned problem. This is illustrated by the case of a horizontal dipole shown in Figure 1. It was found that NEC-2 and NEC-3 gave similar, but not identical results. The main differences are that NEC-3 predicts a magnetic field which oscillates in magnitude as a function of height up to about 6.0 m, whereas NEC-2 produced a smooth curve, This is particlarly evident in Figures 3 which is for a frequency of 10MHz, although it is also present in Figure 2, but not as pronounced.

When [1] was prepared, the reasons for this behaviour were not understood, however, subsequent investigations by the present authors have revealed the nature of the problem. While NEC-2 and NEC-3 do not use identical methods for numerical evaluating the electric fields via the Sommerfeld integrals, [3], [4], comparison of the calculated E- fields over the range of heights shown in Figures 2 and 3 show that the two codes give values which generally agree to within about 3 significant figures. The differences between the calculated H- fields however is obviously much greater. At some points the differences are of the order of several dB. While in practical terms errors of this magnitude may not be significant, the purist demands an explanation.

On closer examination of the results in Figure 2, it was found that if smaller increment sizes are used in the finite-difference curl approximation with NEC-3, that the smooth ripple at a height of approximately 2.3 m changes to a sudden step over a distance comparable to the increment size. This effect was not noticeable using NEC-2, although for smaller increment sizes the results become inaccurate as demonstrated by random variations in the computed H-fields. (Note that both NEC-2 and NEC-3 used here use double precision as single precision was found to be inadequate for these problems).

Closer examination of the finite-difference components of the H-field in the region of interest revealed that the contributions due to the E_x and E_z fields were similar in magnitude, but the phase difference was very close to 180°. Hence in this region, even though the E-fields from NEC-2 and NEC-3 are very similar the differences in the computed H-fields are magnified by the near cancellation of the curl components of E_x and E_z. (Note that for points in the vertical plane containing the dipole, E_y is zero and its derivative is also zero as this is a plane symmetry for E_y, and hence this component of the E-field does not contribute to the H_y field).

A further difficulty in the region near x = 6.0 m and z = 2.3 m is that the magnitudes of both E_x and E_z are near a maximum and the derivatives in the curl expression are small.

In an attempt to alleviate the numerical problem of cancellation in the curl approximation, instead of using finite-differences in the x and z directions, differences in plane rotated 45° about the y-axis were tried, however, the problem with NEC-3 is not changed significantly. An analysis of the reasons for the difficulties encountered for this dipole problem follows.

3. ERROR ANALYSIS OF FINITE-DIFFERENCE APPROXIMATION

To understand the nature of problems which may arise in approximating the curl function by finite differences, alternative formulations of the H- field solution of Maxwell's equation are examined. One method commonly used to obtain the electric and magnetic fields due to currents and charges is in terms of vector and scalar potential line $\vec{A}$ and $\emptyset$ [5]. The solutions are of the form

$$\vec{E} = \nabla\phi - j\omega\vec{A} \tag{2}$$

$$\vec{H} = \frac{\vec{B}}{\mu} = \frac{\nabla x\vec{A}}{\mu} \tag{3}$$

From the vector identity $\nabla x\nabla\phi = 0$, [4] it is readily shown that (3) is mathematically identical to (1). The success or otherwise of finite difference methods for obtaining the H-field from the E-field via the curl relationship will depend on the relative magnitudes of the two terms on the RHS of (2) and the magnitudes of the curl of these terms. For example, if the magnitude of $\nabla\phi$ is much larger than $j\omega\vec{A}$ or the sum of the terms is much smaller than either of the two terms we might expect that finite difference techniques would be inaccurate, particularly when the E-fields are not exact as in the case of NEC calculations. Indeed the latter is the situation in the vicinity of the troublesome region referred to in the previous section!

While there is no simple method of separating the $\nabla\phi$ and $j\omega\vec{A}$ in the E-field calculated by NEC, the previous statement can be verified by examining an alternative solution for the fields of a horizontal dipole above a conducting ground. Bannister, [6], has given image-theory expressions for the quasi-static fields of infinitesimal and finite-length dipoles at or above the earth's surface. This image theory approximation is strictly valid for field points somewhat greater than the skin depth from the ordinary mirror image of the source, although in many cases the approximation is valid throughout the quasi-static range, i.e. distances much less than the wavelength in air. In Bannister's expressions it is also assumed that displacement currents in the ground are negligible compared with the conduction currents. i.e. for the ground:
For the horizontal dipole problem considered previously, with $\epsilon_r = 10$, $\sigma = 0.011 S/m$, at 1.2 MHz we find $\mu\sigma/\omega \sim 165$, so

$$\epsilon_r < \mu\sigma/\omega \qquad (4)$$

that (4) is reasonably well satisfied. Bannister's analytical solution for the E- and H- fields are given in terms of the Hertzian Vector Potential $\vec{\pi}$, as

$$\vec{E} = -\gamma_0^2\vec{\pi} + \nabla(\nabla.\vec{\pi}) \qquad (5)$$

$$\vec{H} = i\omega\epsilon_0\nabla\times\vec{\pi} \qquad (6)$$

Using (5) it is a relatively simple matter to separate the two terms on the RHS of (5). Note that the second term in (5) contributes nothing to $\vec{H}$ in (6) since $\nabla.\vec{\pi}$ is a scalar, analogous to ϕ in (2), and as noted previously, $\nabla\times\nabla\phi=0$. Separating the two terms on the RHS of (5) and comparing their relative magnitudes at a height near 2.3 m for the horizontal dipole at 1.2 MHz, we find that both terms are of comparable magnitude, in the troublesome region, however the sum of these two terms is of the order of 20 dB smaller than either term.

Comparison of the calculated E-fields using NEC and Bannister's image theory expressions show that they generally agree to within about 3 dB. This difference is most likely due to Bannister's formula being for an infinitesimal dipole whereas the dipole model used with NEC is finite in length and the points at which the fields are evaluated are at a distance comparable to the dipole length. We note that both methods show a maximum in the magnitudes of E_x and E_z respectively near z = 2.3 m and x = 6.0 m as shown in Figure 4. As previously noted, in this region the derivatives of E_x and E_z in this region are similar in magnitude but are almost in anti-phase in the curl expression for the H-field. We also note that Bannister's expression for the H-field does not show the anomalous behaviour predicted by NEC-3 near z = 2.3 m which tends to support the argument that the latter is inaccurate.

Unfortunately, Bannister's expressions cannot be applied to the horizontal dipole problem at 10 MHz since the inequality (4) is not satisfied and also because the distances are becoming comparable with the free-space wavelength and the quasi-static assumption is invalid. We can however make the following observations. At a height of approximately 0.7m where the first sawtooth appears in Figure 4, we again find that the derivatives of E_x and E_z in the curl expression for the H-field are of similar magnitudes and almost in anti-phase. Thus the saw-tooth effect is almost certainly due to loss of precision due to the subtraction of two quantities of similar magnitudes.

One possible solution to the difficulties experience may be to calculate the H-field from the Hertzian Vector potential $\vec{\pi}$ as in (6), instead of (1). This would presumable require considerable modifications to NEC and

the auxiliary program SOMNEC. In order to test this approach we could try using Bannister's image theory expression to compute the H-field of a horizontal dipole by using finite difference approximations to both (1) and (6) since solutions for $\vec{\pi}$, $\vec{E}$ and $\vec{H}$ are available [6].

The basic problem with calculating the H-fields by finite-difference approximation of the curl of the E-field for horizontal dipoles at a small height above ground can be better understood by examination of Bannister's image theory formulae [6]. For a dipole parallel to the x-axis we find that the E_x-field due to the first term on the RHS of (5) is of the form.

$$E_{x_1} \alpha -\gamma_0^2\left(\frac{1}{R_0}-\frac{1}{R_2}\right) \tag{7}$$

where R_0 is the distance from the dipole to the field point and R_2 is the distance from an image dipole at a complex depth below ground which depends on the conductivity of the ground [6].

The contribution of the second term on the RHS of (5) to the E_x-field is of the form.

$$E_{x_2} \alpha \frac{1}{R_0^3}\left(\frac{3\rho^2}{R_0^2}-1\right)-\beta\frac{1}{R_1^3}\left(\frac{3\rho^2}{R_1^2}-1\right) \tag{8}$$

where ρ is the radial distance from the dipole to the field point, R_1 is the distance from the ordinary mirror-image of the dipole to the field point, and β is a constant depending on the wave numbers in air and in the ground.[1]

Similarly, the E_z-field components due to the first and second terms on the RHS of (5) are of the form

$$E_{z_1} \alpha -\frac{\gamma_0^2}{\rho}\left[\frac{(d+z+h)}{R_2}-\frac{z+h}{R_1}\right] \tag{9}$$

and

$$E_{z_2} \alpha \rho\left[\frac{z-h}{R_0^5}-\beta\frac{(z+h)}{R_1^5}\right] \tag{10}$$

We see that the components of E_x and E_z which contribute to $\vec{H}$ are varying with distance as $1/R$, (7) and (9), while the components which do not contribute are varying as $1/R^3$, (8)

[1] It should be noted that in Bannister's paper the second term in his equivalent to (8) here is incorrect; the "3" is missing in the "$3\rho^2$" term in the second part of this expression.

and (10). It is not surprising that inaccurate results may be obtained when the H-fields are calculated from partial derivatives of the E-fields and finite-differences are used to approximate these derivatives; if the magnitudes of the derivatives of (8) and (10) are large compared with those of (7) and (9) such difficulties may be expected since ideally the larger derivatives should cancel one another, but in practice the residual error may be comparable to the desired result.

4. CONCLUSION

We have identified three types of error conditions in using NEC to calculate the near magnetic fields of a horizontal dipole close to an imperfect ground. The main difficulty with using the FD curl approximation to obtain the H-fields and E-fields is that the latter may include components whose curl is mathematically zero but when this operation is carried out numerically errors may be introduced due to slight inaccuracies in the E-fields.

For the problem considered here the errors appear as saw-tooth discontinuities in the calculated H-field which are associated with the curl of two orthogonal E-field components almost cancelling one another.

We believe that the difficulty can be overcome by re-formulating the H-field solution in NEC in terms of the Hertzian vector potential or an alternative vector potential function.

REFERENCES

[1] I P Macfarlane, A H J Flemming, S Iskra and G R Haack "Pilgrims Progress - Learning to Use the Numerical Electromagnetics Code (NEC) to Calculate Magnetic Field Strength Close to a Sommerfeld Ground" ACES Journal, Winter 1990, pp58-75

[2] G J Burke "Numerical Electromagnetics Code - Method of Moments, User's Guide Supplement for NEC-3 for Modelling Buried Wires" Lawrence Livermore Laboratory, Report UCI9-19918, October 1983

[3] G J Burke, E K Miller, J N Brittingham, D L Lager, R J Lytle and T J Okada "Computer Modelling of Antennas Near the Ground" Electromagnetics, Vol 1, 1981, pp29-49

[4] G J Burke and E K Miller "Modelling Antennas Near to and Penetrating a Lossy Interface" IEEE Trans Vol AP-32, No 10, October 1984, pp1040-1049

[5] S Ramo and J R Whinnery "Fields and Waves in Modern Radio" John Wiley & Sons, New York, 2nd Edition, 1962, Chapter 4

[6] P R Bannister "Summary of Image Theory Expressions for the Quasi-Static Fields of Antennas at or Above the Earth's Surface" Proc IEEE, Vol 67, No 7, July 1979, pp1001-1008

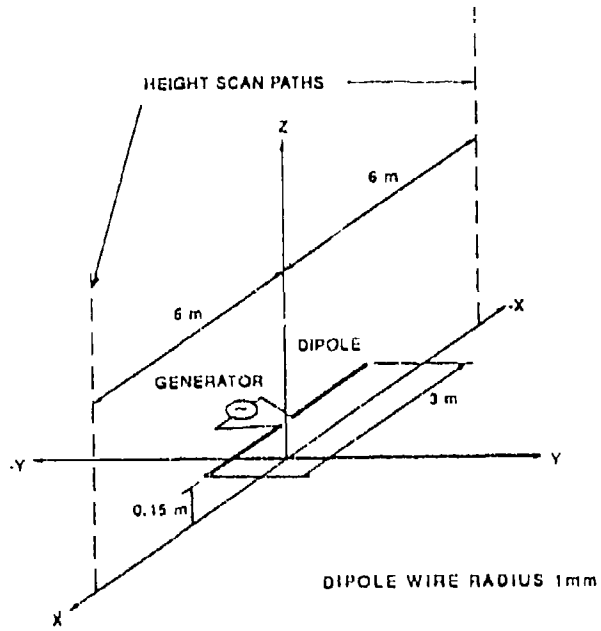

FIGURE 1. GEOMETRY OF THE EXPERIMENTAL MEASUREMENTS AND OF THE MODEL USED IN THE NEC2D AND NEC3D CALCULATIONS

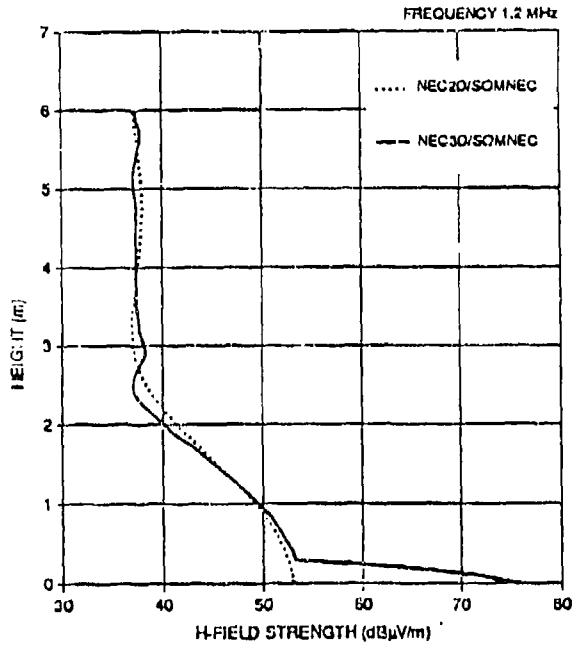

FIGURE 2. 1.2 MHz

COMPARISON OF THE H-FIELD STRENGTHS CALCULATED BY NEC3D AND BY NEC2D - HORIZONTAL 3 METRE DIPOLE OVER A SOMMERFELD GROUND WITH CONSTANTS σ = 11 X 10^{-3} S/m AND ε_r = 10

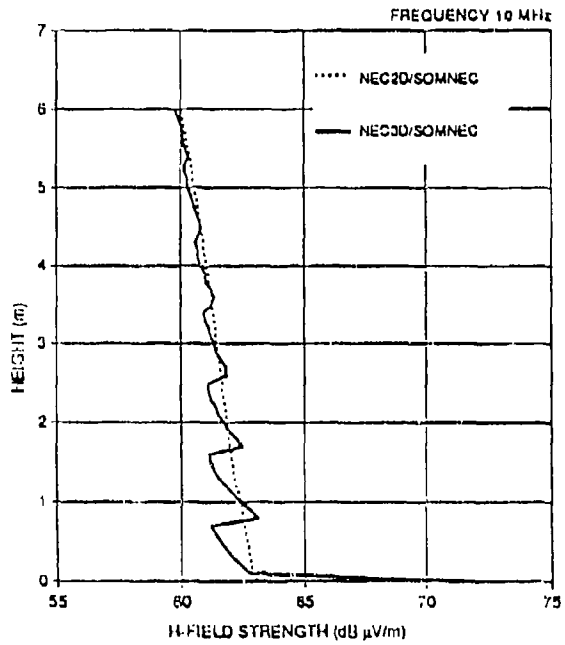

FIGURE 3. 10 MHz

COMPARISON OF THE H-FIELD STRENGTHS CALCULATED BY NEC3D AND BY NEC2D - HORIZONTAL 3 METRE DIPOLE OVER A SOMMERFELD GROUND WITH CONSTANTS σ = 11 X 10^{-3} S/m AND $\varepsilon_r = 10$

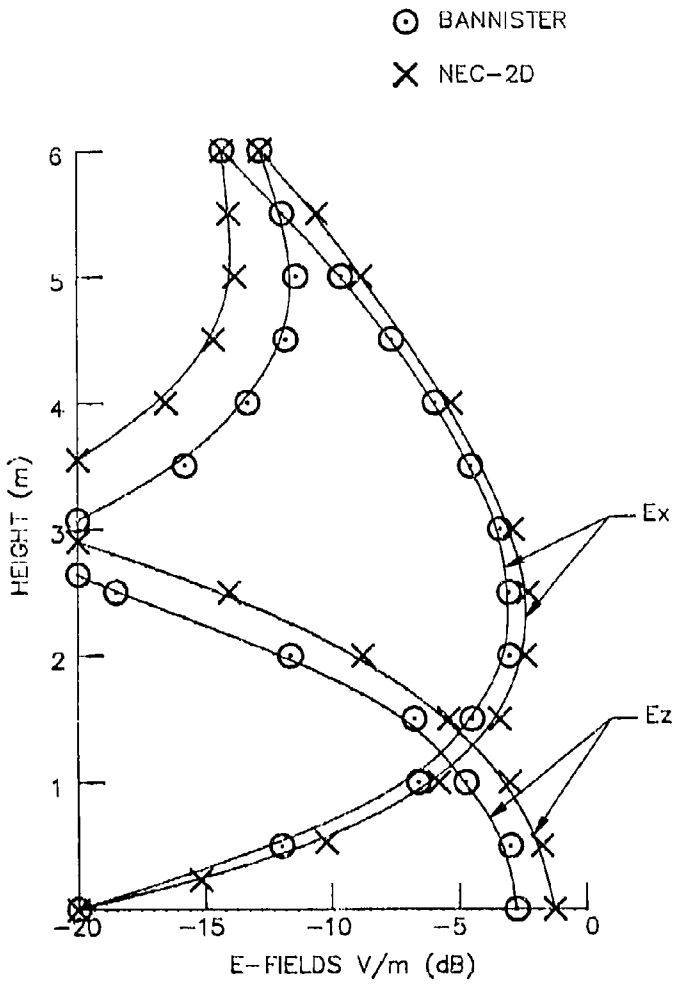

FIGURE 4A 1.2 MHz

COMPARISON OF E-FIELD STRENGTHS CALCULATED BY NEC-2D AND BANNISTER'S FORMULAE AS A FUNCTION OF HEIGHT AT A HORIZONTAL DISTANCE OF 6.0m FROM DIPOLE CENTRE

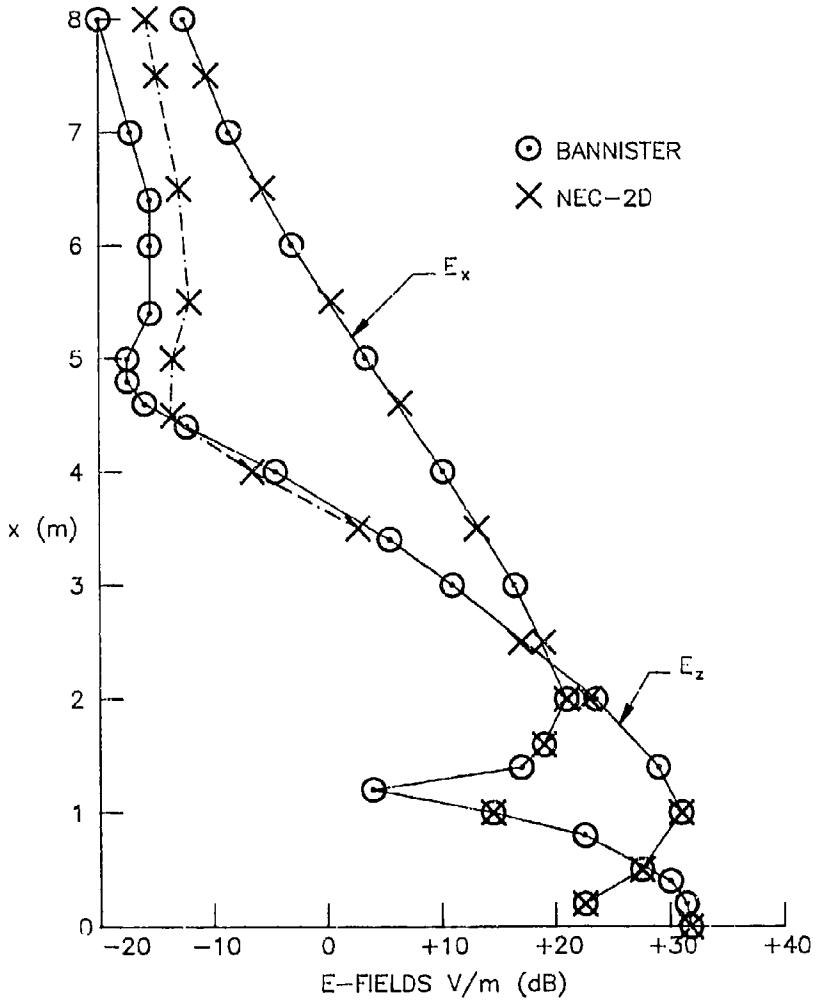

FIGURE 4B 1.2 MHz

COMPARISON OF E–FIELD STRENGTHS CALCULATED BY NEC–2D AND BANNISTER'S FORMULAE AS A FUNCTION OF HORIZONTAL DISTANCE FROM DIPOLE CENTRE AT A HEIGHT OF 2.3m

REFINEMENT OF HF VERTICAL HALF RHOMBIC CHARACTERIZATION

W.P. Wheless, Jr.
University of Alabama Electrical Engineering Department
Tuscaloosa, Alabama 35487

M.D. Fanning
UDS Motorola
Huntsville, Alabama 35805

D.L. Faust and M.B. King
Eyring, Inc. Communication Systems Division
Provo, Utah 84601

Abstract – Numerous radiation pattern profiles for the commercially available Barker & Williamson AC–1.8–30 antenna were presented in an earlier paper [1], where the computed patterns were obtained with the code NEC2 executed on a personal computer, assuming a purely real antenna termination of 804 Ω. This paper improves the earlier results by use of measured complex impedance values for the antenna termination, and then extends the comparison of computed to measured values to include patterns calculated by the code NEC3 executed on an IBM 3090 mainframe computer.

INTRODUCTION

The Barker & Williamson model AC–1.8–30 hf antenna used in this study is depicted in Figure 1. This configuration could be called a (balanced–feed, loaded) pyramid. The antenna of Figure 1 is referred to as a vertical half rhombic (VHR), however, because the VHR descriptor is more widely known and evokes an essentially accurate mental visualization of the geometry.

An earlier paper [1] presented graphical comparisons of several measured and computed radiation patterns for this antenna, with the computed patterns obtained from the personal computer (pc) code NEC2 (specifically, NEC–81, version 2.2). In [1], the antenna termination was taken as 804 Ω, purely resistive, over the 3–30 MHz hf spectrum. Subsequent measurements on the termination have revealed that its value is complex and depends significantly on frequency, as shown by the experimental data contained in Table 1. The resultant changes in computed patterns obtained from NEC2 with the refined termination parameters are minor, but perceptible.

The initial motivation for the work reported in [1] was to assess the accuracy and reliability of a pc–based analysis code in the case of a typical wire antenna near real ground. The convenience of using a personal computer is attractive, and it appears that NEC2 is acceptable for many applications. However, because the subject antenna has two ground stakes penetrating the earth's surface in addition to a single counterpoise wire very close to the surface, the potential improvement in numerical pattern predictions accuring from the utilization of the (mainframe) computer code NEC3 merits investigation. This paper reports new predicted patterns which have been computed with double–precision NEC3 code on an IBM 3090 mainframe. Graphical comparisons are made of the NEC2 personal computer and NEC3 mainframe results to the original experimental pattern data.

The pattern measurements were carried out using Eyring's Broadband Antenna Test System (BATS) at its Cedar Valley, Utah, test range. Details regarding the BATS

configuration and methodology are available in references [2] and [3], and the antenna measurement beacon is discussed in [4]. Test site ground parameters ϵ_r (dielectric constant) and σ (conductivity) are measured for each pattern profile as described in reference [5]. The measured data here are unchanged from that in [1].

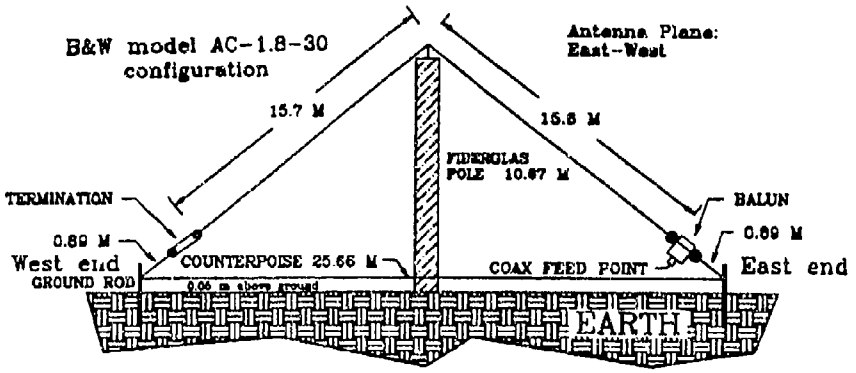

Figure 1. Antenna geometry.

TABLE 1
Measured Termination Impedance

Freq. (MHz)	Impedance (Ω)	Freq. (MHz)	Impedance (Ω)
1.0	798 – j 35	16.0	585 – j333
2.0	794 – j 62	17.0	567 – j342
3.0	786 – j 94	18.0	550 – j348
4.0	777 – j118	19.0	532 – j358
5.0	766 – j146	20.0	510 – j370
6.0	753 – j171	21.0	487 – j371
7.0	739 – j190	22.0	466 – j371
8.0	727 – j211	23.0	449 – j369
9.0	713 – j232	24.0	435 – j368
10.0	695 – j253	25.0	419 – j368
11.0	678 – j271	26.0	405 – j370
12.0	660 – j286	27.0	388 – j368
13.0	642 – j299	28.0	372 – j365
14.0	623 – j311	29.0	358 – j362
15.0	603 – j325	30.0	341 – j358

COMPARISON OF COMPUTED AND MEASURED PATTERNS

Measured radiation pattern profiles were acquired at the Eyring facility at frequencies of 3.195, 10.12, 19.0475, and 22.9015 MHz. Corresponding NEC2 patterns were subsequently computed on an IBM pc, and NEC3 patterns were computed (double precision) on an IBM 3090 mainframe. BATS software, running on the pc, was used to overlay the NEC2 and downloaded NEC3 computed patterns, compensated for efficiency, on the measured data plots.

Figures 2–4 are gain versus elevation pattern profiles at respective frequencies of 3.1925, 10.12, and 19.0475 MHz. The measured data was derived from airborne flyovers along a North–South course (perpendicular to the axis of the antenna). The polarization attitude was horizontal, with the measurement beacon radiator aligned parallel to the VHR axis. Manifestations of high winds aloft are evident in the flyover patterns of figures 3 and 4, which were measured four days earlier than the figure 2 pattern. While the NEC2 pc predicted patterns exhibit satisfactory shape characteristics for figures 2–4, the pattern size predictions are substantially in error (≈ 5 dB) at 3.1925 and 19.0475 MHz. The NEC3 predicted patterns emulate the measured data in all three instances.

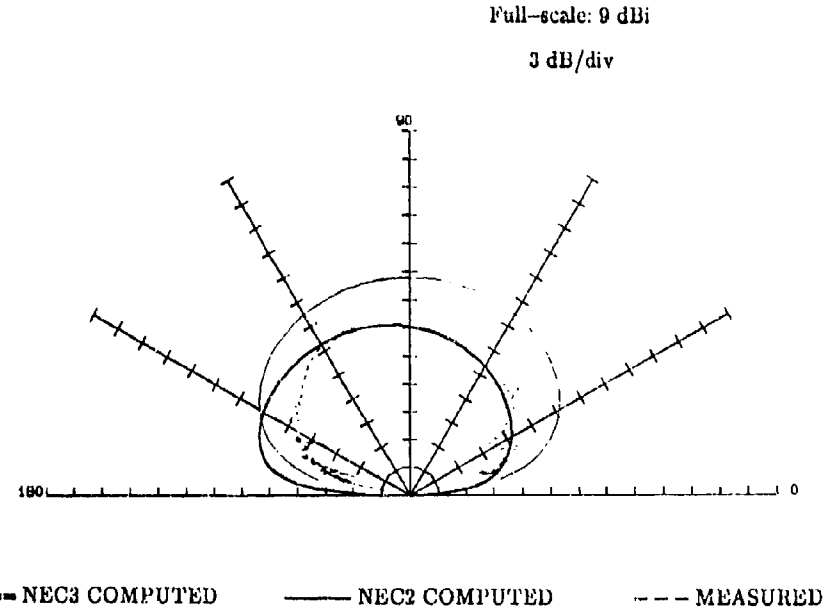

Figure 2. Gain versus elevation for horizontal polarization at 3.1925 MHz, compass azimuth = 0° ($\epsilon_r = 18.5$, $\sigma = 4.3$ mS/m).

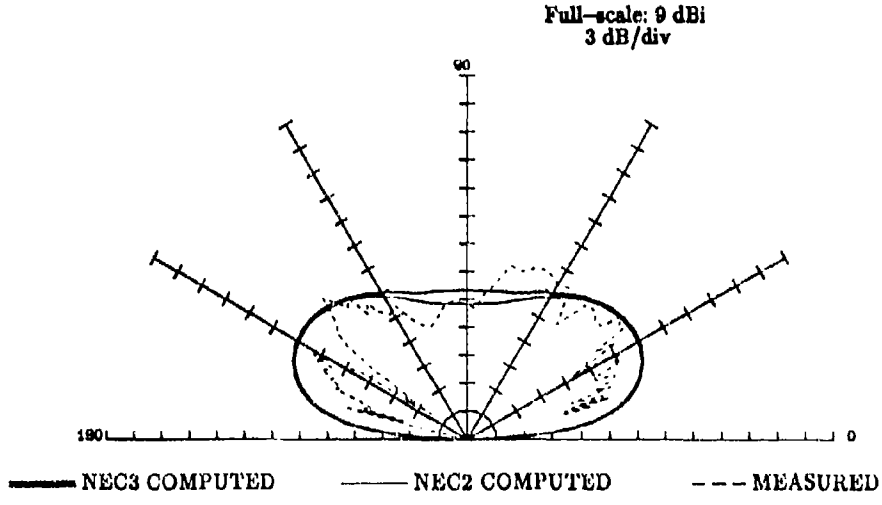

Figure 3. Gain versus elevation for horizontal polarization at 10.12 MHz, compass azimuth = 0° ($\epsilon_r = 8.7$, $\sigma = 6.7$ mS/m).

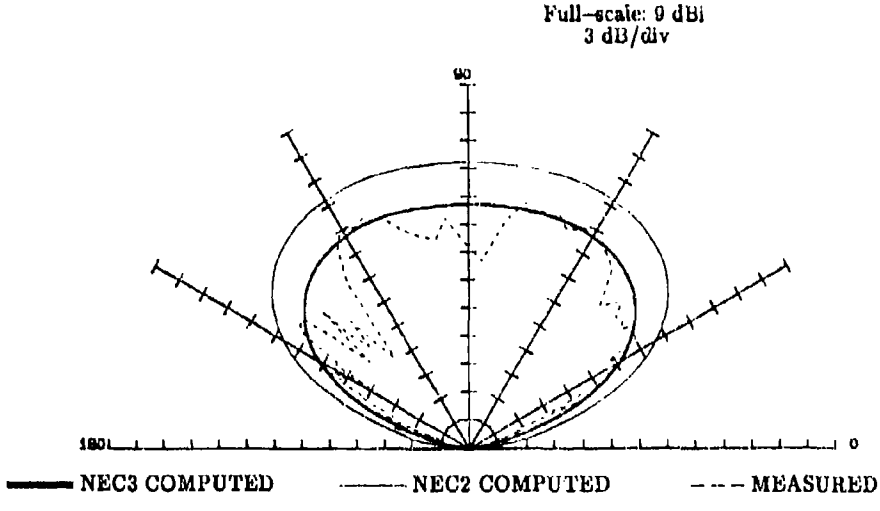

Figure 4. Gain versus elevation for horizontal polarization at 19.0475 MHz, compass azimuth = 0° ($\epsilon_r = 7.8$, $\sigma = 8.9$ mS/m).

Figures 5–11 present seven gain versus azimuth pattern profiles (involving various values of elevation angle θ above the horizon). Figures 5–9 are vertical polarization cases, while the polarization is horizontal in figures 10 and 11. The NEC3 predicted patterns for figures 5–7 are notably more successful than NEC2 in the minor lobe regions. Also, figure 7 depicts a case where the overall pattern size from NEC2 is unacceptable while the NEC3 results correlate well against measurements. Although neither code predicts the back lobe in figure 8, the NEC3 pattern size is far superior to the NEC2 analysis. In the case study of figure 9, NEC3 afforded only modest improvement over the NEC2 results in the minor lobe region.

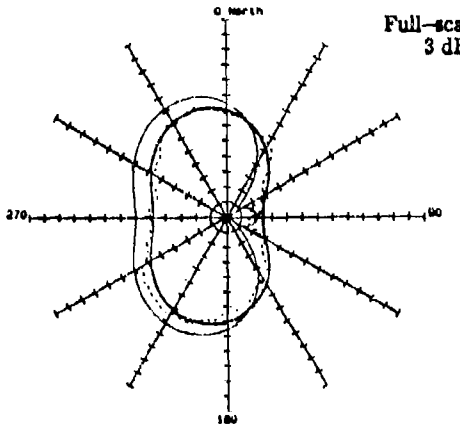

NEC3 COMPUTED ——— NEC2 COMPUTED – – – MEASURED

Figure 5. Gain versus azimuth for vertical polarization at 10.12 MHz, 5° elevation ($\epsilon_r = 10.0$, $\sigma = 8.0$ mS/m).

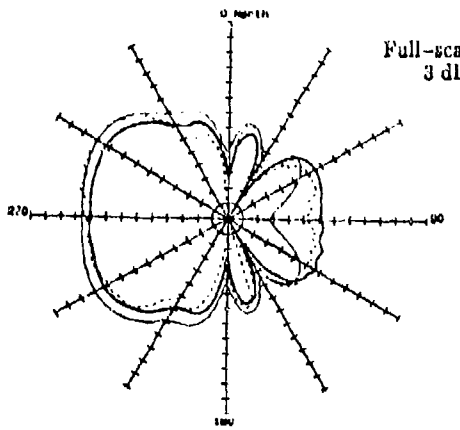

NEC3 COMPUTED ——— NEC2 COMPUTED – – – MEASURED

Figure 6. Gain versus azimuth for vertical polarization at 22.9015 MHz, 10° elevation ($\epsilon_r = 6.3$, $\sigma = 8.5$ mS/m).

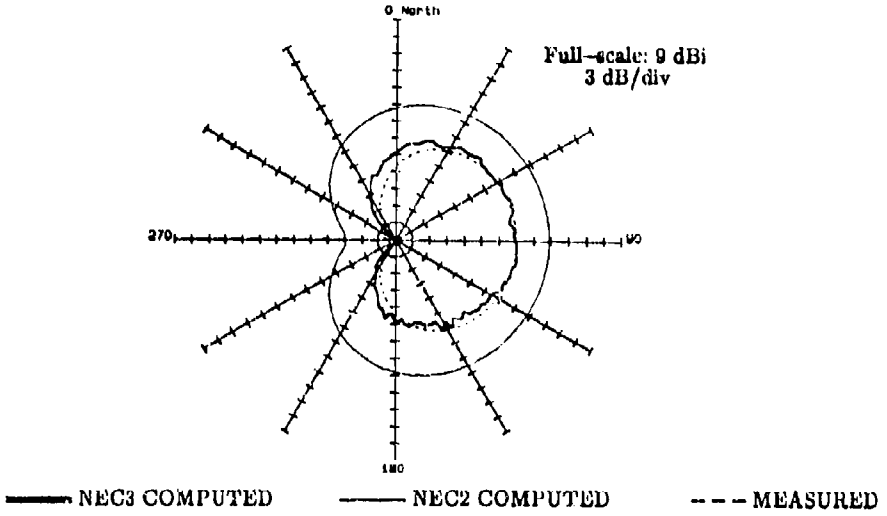

Figure 7. Gain versus azimuth for vertical polarization at 3.1925 MHz, 20° elevation ($\epsilon_r = 18.5$, $\sigma = 4.3$ mS/m).

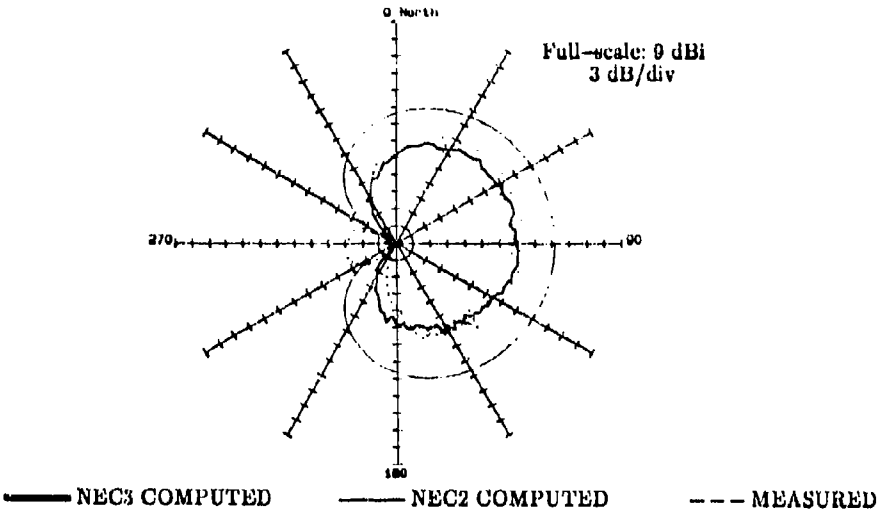

Figure 8. Gain versus azimuth for vertical polarization at 3.1925 MHz, 40° elevation ($\epsilon_r = 18.5$, $\sigma = 4.3$ mS/m).

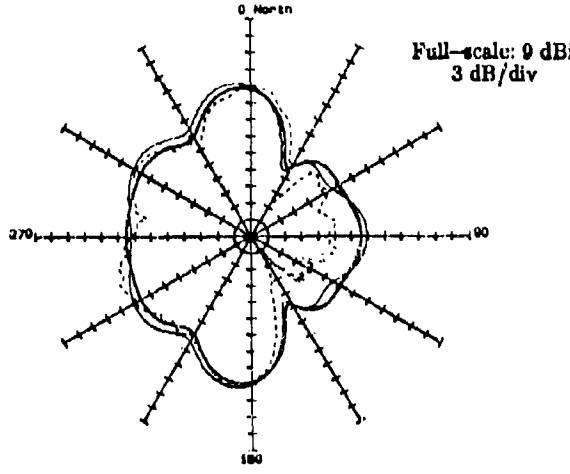

NEC3 COMPUTED ——— NEC2 COMPUTED – – – MEASURED

Figure 9. Gain versus azimuth for vertical polarization at 19.0475 MHz, 30° elevation ($\epsilon_r = 8.9$, $\sigma = 10.8$ mS/m).

Figures 10 and 11 show more intricate horizontal-component patterns at 10.12 and 19.0475 MHz, respectively. NEC2 and NEC3 predictions are of comparable quality in these cases.

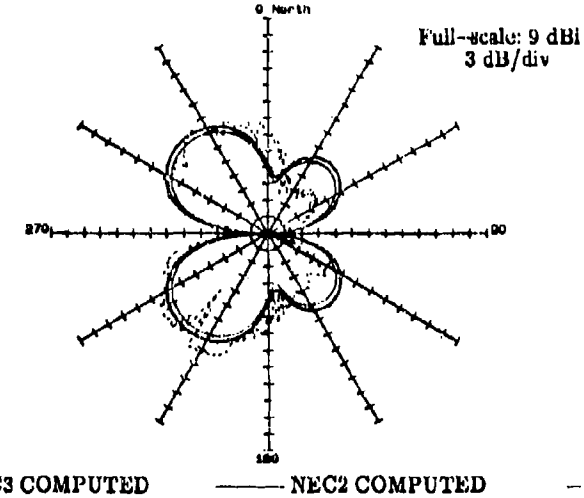

NEC3 COMPUTED ——— NEC2 COMPUTED – – – MEASURED

Figure 10. Gain versus azimuth for horizontal polarization at 10.12 MHz, 30° elevation ($\epsilon_r = 8.7$, $\sigma = 6.7$ mS/m).

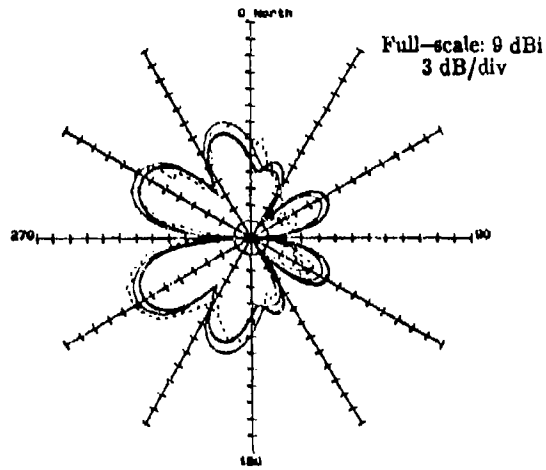

Figure 11. Gain versus azimuth for horizontal polarization at 19.0475 MHz, 30° elevation ($\epsilon_r = 8.9$, $\sigma = 10.8$ mS/m).

CONCLUSIONS

This work has sampled, through a specific case study, the accuracy and reliability of NEC2 and NEC3 radiation pattern predictions for hf wire antennas in close proximity to finite ground. Significant improvement accrued from the use of NEC3, which consistently outperformed NEC2 in predictions concerning pattern size and minor lobe structure. Once the NEC3 model is sufficiently inclusive to give good agreement with the results of a modest pattern measurement series at a few discrete frequencies, patterns at new intermediate frequencies may be predicted by use of NEC3 with a high degree of confidence.

REFERENCES

1. M.D. Fanning, W.P. Wheless, Jr., D.L. Faust, and M.B. King, "Characterization of a high–frequency vertical half rhombic," *Proc. 6th Annual Rev. of Progress in Applied Computational Electromagnetics*, pp. 300–307, Monterey, CA, March 1990.
2. D.L. Faust and M.B. King, "Broadband HF antenna testing," *Proc. of RF Technology Expo '86*, pp. 625–631, Anaheim, CA, January 1986 (Eyring Document No. 800–0758).
3. D.L. Faust, "The low profile antenna/rollout hf antenna: a new tactical communications option," *HF Radio Clinic*, St. Louis, MO, September 1986 (Eyring Document No. 900–0013).
4. _____, "Antenna measurement beacon," January 1989, Eyring Document No. 900–0034.
5. _____, "Ground measurement probe," March 1990, Eyring Document No. 900–0036B.

BIOGRAPHY

W. Perry Wheless, Jr. (205) 348–1757
University of Alabama
Electrical Engineering Department
Box 870286
Tuscaloosa, AL 35487–0286

Perry Wheless is an Associate Professor of Electrical Engineering at the University of Alabama. He has continuous engineering experience since 1968 with rf, microwave, millimeter wave, and ionizing–radiation devices and systems.

Mike D. Fanning (205) 430–7032
UDS Motorola
5000 Bradford Drive
Huntsville, AL 35805–1993

Mike Fanning is a Design Engineer with UDS Motorola. He attended the University of Alabama, where he received both the B.S. and M.S. degrees in Electrical Engineering, and he is quite active in various facets of amateur radio.

David L. Faust (801) 375–2434
Eyring, Inc.
Communications Systems Division
1455 West 820 North
Provo, UT 84601

David Faust has been associated with Eyring, Inc., for twelve years. He is now Program Manager and Test Engineer in Eyring's Communication Systems Division. He has extensive experience with hf antenna systems and rf measurement techniques.

Moray B. King (801) 375–2434
Eyring, Inc.
Communications Systems Division
1455 West 820 North
Provo, UT 84601

Moray King has been with Eyring, Inc., for eleven years and he is a Systems Engineer in Eyring's Communication Systems Division. His prior professional experience includes the Valley Forge Research Center and the University of Pennsylvania, and the BATS software utilized in this study is among his many credits.

SESSION 13- "ELECTROMAGNETIC COMPATIBILITY (EMC)"

Moderator: David P. Millard

A Survey of Numerical Techniques for Modeling Sources of Electromagnetic Interference

Todd H. Hubing
University of Missouri-Rolla
Rolla, MO 65401

Abstract

This paper describes the preliminary results of a study to identify ways of using numerical modeling techniques to analyze sources of electromagnetic interference (EMI). First, two canonical EMI sources were developed that represent the type of configurations that need to me modeled. Then a number of numerical electromagnetic modeling techniques were evaluated to determine their suitability for analyzing these configurations. None of the currently available techniques appears to be a very practical approach, however hybrid techniques that combine a surface integral method with a finite method show considerable promise.

Introduction

Manufacturers of electronic equipment are taking more of an interest in the amount of electromagnetic radiation that emanates from their products. This is due to strict laws regulating electromagnetic interference (EMI) and the potentially high cost of shields, filters, and other EMI fixes required to make an otherwise noisy product meet these requirements. Many companies employ full-time EMI engineers who view every electronic system as an electromagnetic radiation source. By understanding how and why different configurations radiate, these engineers work at developing designs that meet the radiation requirements at the lowest possible cost.

Traditionally, EMI engineers have relied primarily on their measurement experiences, rules-of-thumb, and simple intuitive models to guide them in making design choices. Unfortunately, EMI rules-of-thumb that apply in some situations may not apply in others. Simple modeling techniques such as circuit, transmission line, or basic antenna models only work well when the source and all relevant current paths can be readily identified. Most EMI problems today however are not obvious enough to be predicted or analyzed using these simple techniques. Therefore, the only tools remaining for EMI engineers in most cases are measurements of the system or its components. Unfortunately, practical measurements can not be made without existing hardware and this is not usually available early in a product's development when critical design decisions are being made. Also, measured results in the absence of a theoretical model can be misleading and do not necessarily suggest how a design should be modified to minimize radiated emissions.

Numerical modeling techniques, which have revolutionized the fields of antenna and microwave system analysis, have had relatively little impact on EMI source analysis. Some work involving the modeling of components and cables has been done, but the scope of this work is limited and these techniques are not widely used by EMI engineers. The primary reason for this is that the types of problems that EMI engineers would like to model cannot be analyzed by available numerical techniques. In the following section, two configurations representing the type of problems EMI

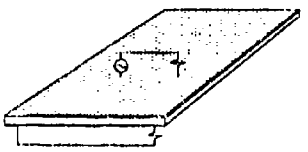

Figure 1: Canonical Printed Circuit Board Model

engineers need to be able to model are described and the extent to which numerical techniques can be used to model these configurations is discussed.

Canonical EMI Sources

Consider the configuration illustrated in Figure 1. It consists of two circuits mounted on opposite sides of a thin, dielectric-coated metal plate. This configuration is similar to a printed circuit board environment with components on one side of the board and traces on the other. A model like this might be used by EMI engineers to answer questions about possible problems with crosstalk between circuits. Prominent features of this configuration include its electrically small-to-resonant size, the presence of a dielectric, the thin metal plate with wires attached to both sides, the unbounded geometry, and the close proximity of the circuit leads to the plate.

Surface integral techniques based on the method-of-moments can be very efficient at analyzing electrically small-to-resonant radiation problems. However, they are not well-suited to modeling arbitrary configurations containing dielectrics or wires attached to opposite sides of a thin plate.

Finite techniques such as the finite element method, finite difference time domain, finite volume time domain and transmission line matrix techniques excel at analyzing complex, inhomogeneous configurations with both conductors and dielectrics. However, these techniques require that a 3-dimensional grid be constructed throughout the entire volume to be analyzed. For unbounded radiation problems, this grid quickly grows very large. A great deal of computation may be required even for relatively simple geometries.

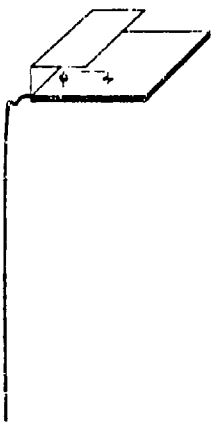

Figure 2: Canonical EMI Source Model

The configuration in Figure 1 is not large, but it is unbounded. It also requires a detailed grid in the vicinity of the wires because of their proximity to the plate. Because of these constraints, the author has not been able to locate a readily available computer code capable of analyzing this type of configuration efficiently. However finite techniques such as the finite volume time domain and finite element methods could theoretically be applied to this problem given sufficient computer resources.

Although the configuration in Figure 1 represents an important class of EMI problems, printed circuit cards rarely exist isolated from other sources or conductors. The configuration in Figure 2 is more typical of an EMI source configuration [1]. It consists of a printed circuit board configuration with a partial metal enclosure and an attached cable. Assuming that the cable is shielded, all of the currents contributing to the EMI can be assumed to flow on the outer surface and in most cases, the cable can be modeled with a solid wire. Like the model in Figure 1, this configuration contains dielectrics and thin plates with multiple wire attachments making surface integral techniques impractical. However, because of the presence of the relatively long thin wire, finite techniques are also impractical. This is because creating a grid throughout a volume large enough to contain the card, shield, wire, and the entire near field of the source results in a problem that is unmanageable from a computational standpoint. Although the model in Figure 2 represents a relatively simple EMI source, it cannot be analyzed effectively by any existing numerical techniques. This illustrates why numerical modeling techniques are not commonly used to model EMI sources.

Hybrid Techniques

Surface integral techniques such as most moment method techniques and the boundary element method are very efficient at analyzing long, thin wires and large conductive surfaces. Finite techniques are best at modeling complex, inhomogeneous regions. Therefore, it makes sense to combine a surface integral technique with a finite technique in order to take advantage of the best properties of each. A number of hybrid methods have been proposed that combine two existing techniques [2-6]. Generally, the configuration is divided into two or more regions. The numerical technique best suited to each region is applied in that region and boundary conditions are enforced at the interface between regions. For example, a hybrid moment method finite element technique might apply a finite element analysis within the small volume containing the card and inside surface of the shield in Figure 2. A moment method technique would simultaneously be applied to the surface defined by the wire, shield, and the boundary with the finite element region.

So far, no one has implemented a hybrid technique capable of analyzing the configuration in Figure 2 or most types of configurations of interest to EMI engineers. However progress continues to be made in this area. While most numerical methods appear to have fundamental limitations that will prevent them from ever being efficiently applied to most EMI sources, hybrid techniques have the potential to overcome these limitations.

Summary

EMI engineers have not yet benefitted significantly from the numerical techniques that have revolutionized the antenna and microwave engineering fields. The two simple configurations presented here illustrate some of the difficulties involved with applying numerical techniques to EMI source models. Hybrid techniques that combine a surface integral method with a finite method

appear to be the best long-term approach, however more development of these techniques is required.

Hopefully, given the rate at which progress in this area is being achieved, an algorithm capable of accurately analyzing the configurations presented here is not far off. Once such an algorithm is implemented, it will likely become one of the most powerful tools available to EMI engineers.

Acknowledgement

This work was supported by a grant from Intel Corporation.

References

[1] T. H. Hubing and J. F. Kauffman, Modeling the Electromagnetic Radiation from Electrically Small Table-Top Products, *IEEE Transactions on Electromagnetic Compatibility*, vol. 31, Feb 1989, pp. 74-84.

[2] A. Taflove and K. Umashankar, "A Hybrid Moment Method/Finite-Difference Time-Domain Approach to Electromagnetic Coupling and Aperture Penetration into Complex Geometries," *IEEE Transactions on Antennas and Propagation*, vol. 30, no. 4, July 1982, pp. 617-627.

[3] M. A. Morgan, C. H. Chen, S. C. Hill, and P. W. Barber, "Finite Element-Boundary Integral Formulation for Electromagnetic Scattering," *Wave Motion*, vol. 6, 1984, pp. 91-103.

[4] J. M. Jin and J. L. Volakis, "A Finite Element-Boundary Integral Formulation for Scattering by Three-Dimensional Cavity-Backed Apertures," *IEEE Transactions on Antennas and Propagation*, vol. 39, no. 1, January 1991, pp. 97-104.

[5] X. C. Yuan, D. R. Lynch, and J. W. Strohbehn, Coupling of Finite Element and Moment Methods for Electromagnetic Scattering from Inhomogeneous Objects, *IEEE Transactions on Antennas and Propagation*, vol. 38, no. 3, March 1990. pp. 386-393.

[6] X. C. Yuan, Three-Dimensional Electromagnetic Scattering from Inhomogeneous Objects by the Hybrid Moment and Finite Element Method, *IEEE Transactions on Microwave Theory and Techniques*, vol. 38, no. 8, August 1990, pp.1053-1058.

COMPUTER AIDED ELECTROMAGNETIC COMPATIBILITY ANALYSIS

D.P. Millard, J.K. Daher, R.M. Herkert, and J.A. Woody
Electromagnetic Environmental Effects (E^3) Laboratory
Georgia Tech Research Institute
Georgia Institute of Technology
Atlanta, Georgia 30332

ABSTRACT

Electromagnetic Compatibility (EMC) analysis is essential during all stages of system design, from concept to deployment. However, EMC analyses of systems are very complex, requiring inputs which may not be known to the EMC analysts. Also not all of the computer aided engineering (CAE) tools available to perform the analyses are appropriate for performing EMC analyses at each stage of the design. Care must be exercised when using these CAE tools such that the garbage-in-garbage-out syndrome does not prevail. What is required is a front-end CAE tool which will: (1) assist the EMC analysts to better define the problem to be analyzed; (2) allow the analyses to be performed optimally for the input data available; (3) select the appropriate analytical tool (existing EMC CAE program); and (4) produce uniform outputs which the EMC analysts can understand.

An EMC CAE tool which meets these requirements is under development at Georgia Tech and is called the Georgia Tech Configuration Analysis Program (GTCAP[1]) [1-3]. GTCAP is a modular EMC CAE tool with a relational database based on a framework concept and a "lessons learned" capability. It is menu and list directed, has a graphical user interface (GUI), and contains default input values based on specifications. GTCAP guides the EMC analysts through the process of performing EMC analyses at each stage in the design, acting as the EMC expert, based on the input data available at the time. GTCAP is designed to operate on PC-based machines under several operating systems.

INTRODUCTION

Modern platforms (e.g., military vehicles) are designed to employ complex systems and electronic devices which utilize much of the electromagnetic spectrum. Also, the electromagnetic environment (EME) to which these platforms will be subjected is very complex and can contain emitters which generate field strengths capable of causing adverse electromagnetic environmental effects (E^3). Therefore, E^3 analyses must be performed during each phase of the platform's life cycle from concept to deployment. The type, degree, and reliability of the available input data for these E^3 analyses varies as the platform progresses through its life-cycle phases. To perform E^3 evaluations of configured platforms in a timely, cost effective manner, a computer-based tool is required which utilizes the available input data and which allows the engineer/operator to configure the platform with avionics and electronic systems, including boxes, cables and antennas;

---

[1] Copyright GTRC, 1988.

perform an analysis (evaluation); and report the results. Also, the operator must be permitted to save the results, to re-configure the platform's systems, and to re-do the analysis as needed.

The CAE tool which can perform this analysis in an integrated fashion is GTCAP. GTCAP is highly modular in design, menu and database driven, and contains a "lessons learned" feature which allows the operator (and the program) to learn during each analysis.

CONFIGURATION ANALYSIS PROGRAM

The general structure of the GTCAP CAE software is shown in Figure 1. A modular software structure is used which includes all required inputs and outputs for module-to-module communication, and the software is programmed to DOD-STD-2167 [2]. The major modules include the User Interface Module (UIM), the Platform Evaluation Module (PEM), and the various measures of performance (MOP) modules.

The UIM is the program "executive" which provides the interface between the GTCAP operator and the PEM. The logic for the UIM and GTCAP analysis process is shown in Figure 2. The UIM allows the operator to (1) select the platform and the work order (WO) being implemented; (2) position the equipment on the platform; (3) compute and store the equipment position and orientation in a database; and (4) set-up the evaluation scenario by selecting the mode (baseline without interference, intersystem, or platform with external EME), the equipment and the platform operation/mission. After the E^3 evaluation is complete, the UIM generates the analysis reports. It then permits the operator to reiterate the configuration/analysis process[2].

The PEM is called by the UIM to perform the E^3 evaluation of the platform configuration defined in the platform configuration database. The PEM uses the electromagnetic interference (EMI) module to compute the intra-platform coupling and perform E^3 analyses of the configuration. The PEM also uses the mission module to compute the coupling of external emitters to on-board antennas and perform electromagnetic vulnerability (EMV) predictions.

The MOP evaluation modules utilize intersystem and inter-platform E^3 analysis results from the PEM to determine the degradation in the MOP's on the platform. Each system (Flight Control, Communications, Navigation, Electronic Warfare, Radar, Electro/Optic) has its own MOP evaluation module, EMI database and MOP database.

GTCAP utilizes large databases generated off-line. These databases include: the platform structure descriptors, the electromagnetic MOP, platform graphics based on NASTRAN finite element models (FEM), equipment EMI parameters, and platform operations/mission descriptors. The equipment EMI and MOP databases, which are critical to the E^3 evaluation of the platform, must be constructed from EMI and EMV test results or generated through analyses. The MOP databases are generated by the various system specialists in collaboration with E^3 engineers. Where actual EMI test data or analysis results are not available, MIL-STD-461 [3] emission and

---

[2] (NOTE: other analyses, e.g., weight and balance, could be performed if the appropriate modules are added).

susceptibility limits are assumed to apply and are used as default data. All database entry and update screens are designed to accommodate off-line database management.

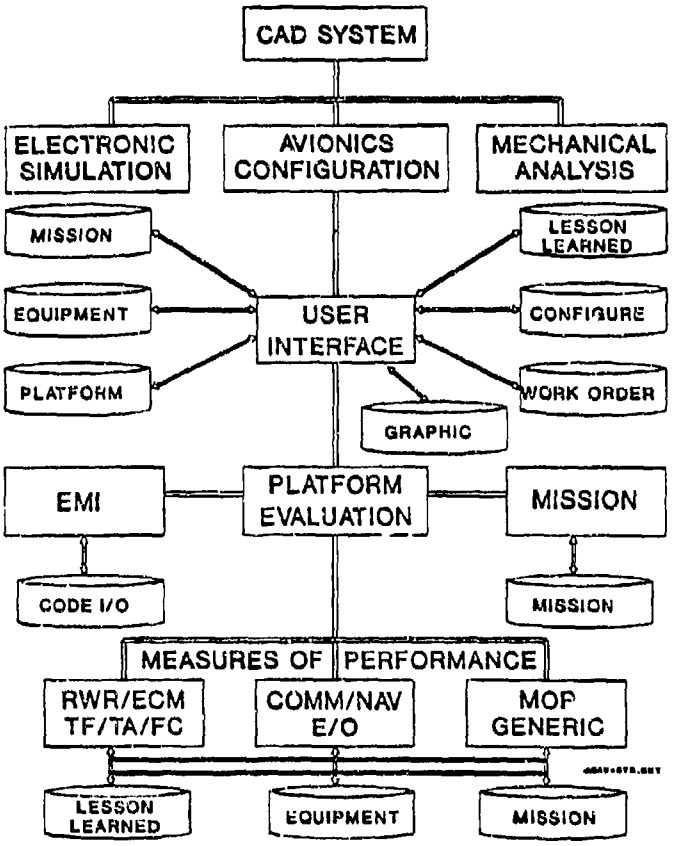

Figure 1 GTCAP Software Structure.

PLATFORM EVALUATION MODULE

The PEM is the E^3 engineering core of GTCAP. Its purpose is to direct the E^3 evaluation of the electronics for various platform configurations in a defined EME. The PEM saves the E^3 results for each evaluated equipment and provides a matrix of intersystem EMI interaction between equipment. A typical EMI matrix is shown in Figure 3.

The PEM obtains, from the appropriate databases: (1) the platform configuration, (2) the selected analysis mode, and (3) the created equipment list. The PEM uses the EMI module to perform the EMI analysis and uses the mission module to define the EME produced by external emitters and to determine the active equipment list for specific mission segments. The PEM relies on each of the equipment MOP modules to determine the amount of degradation (adverse E^3) caused by on-board and external emitters.

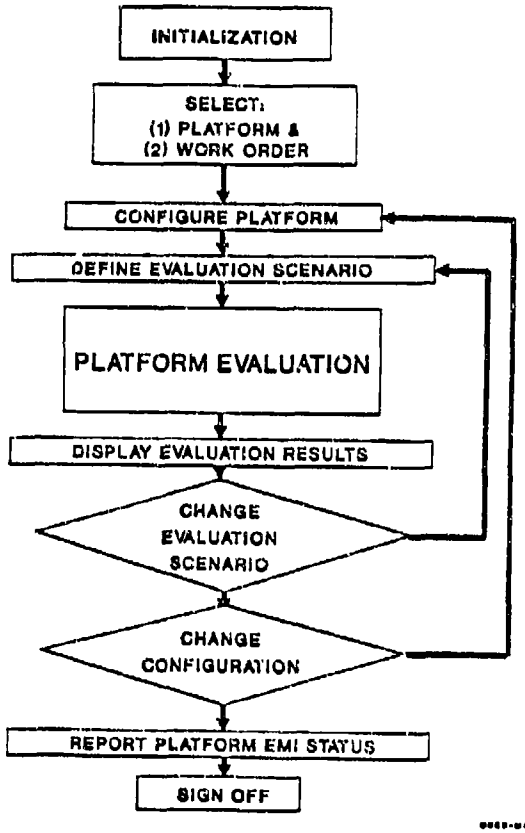

Figure 2 GTCAP Analysis Process Flow Diagram.

EMI MODULE

The EMI Module is used to compute the intersystem coupling, "quick look" EMI margins, and the EM susceptibility assessment for the platform. The on-board, intersystem EME is defined by the radiated and conducted emissions of the equipment on the platform. The external inter-platform EME is defined by emitters external to the platform. The primary EMI assessment codes utilized in the EMI module include:

AACIM - Antenna-to-Antenna Coupling Interference Model (GTRI Intrasystem EMI Analysis Program)
GEMACS - Generalized Electromagnetic Model for the Analysis of Complex Systems
IEMCAP - Intrasystem Electromagnetic Compatibility Analysis Program
BSC - Basic Scattering Code
AAPG - Aircraft inter-Antenna Propagation with Graphics

GTCAP uses these codes, unmodified, to compute antenna-to-antenna coupling, antenna patterns of on-board antennas, and box-to-box, box-to-cable and cable-to-cable coupling internal to the

platform. In addition GTCAP utilizes AACIM for quick look antenna-to-antenna coupling analyses and frequency culls.

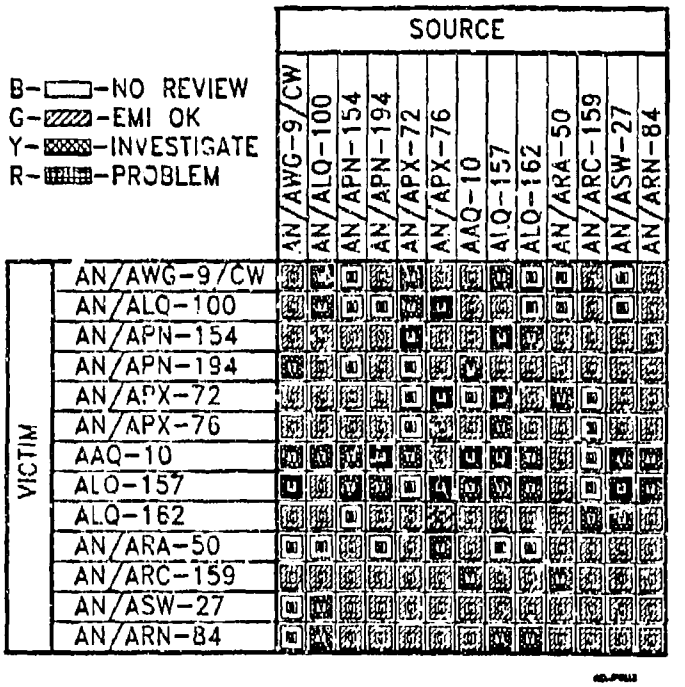

Figure 3 EMI Status Report Matrix.

ANALYSIS APPROACH

Equipment/system EMI parameters and MOP data together with EM coupling data form the basis for E^3 analyses and EMI margin calculations. The EMI Module accesses the EMI and MOP databases and calculates the EM coupling. First-order approximations of the effects of frequency, pulse width, and pulse repetition frequency (PRF) are assumed.

EM energy can couple to a system through one or more system ports of entry (POE's) [6]. POE's are grouped into two separate categories: front-door and back-door. From an analysis perspective, front-door paths are better characterized in terms of coupling to the POE. Front-door coupling is further subdivided into in-band and out-of-band cases. In-band coupling tends to be more straightforward to analyze than out-of-band coupling both in terms of the interaction of the

incident EM radiation with the antenna or sensor and the propagation of the coupled energy to a potentially susceptible component.

Solving EM coupling problems and performing an EMI analysis using computer codes can be an overwhelming task. The front-door EMI coupling problem consist of the parts illustrated in Figure 4. To compute the coupling from a source (transmitter) to a receptor (receiver) the output level of the transmitter must be known. Then the cable loss between the transmitter and its antenna; the antenna gain; the coupling path loss; the receive antenna gain; and the cable loss to the receiver must be calculated. These factors must then be appropriately combined to calculate the EM coupling. Both in-band and out-of-band effects must be included.

The EMI module permits frequency and/or amplitude culls such that baseline "quick look" E^3 analyses may be initially performed. It also has the ability to perform trade-off analyses by comparing the EMI margins of the current configuration with that of a previously evaluated system. Finally, the EMI module permits tailoring of EMI limits to increase or decrease MIL-STD-461 limits to reflect the expected operational EME.

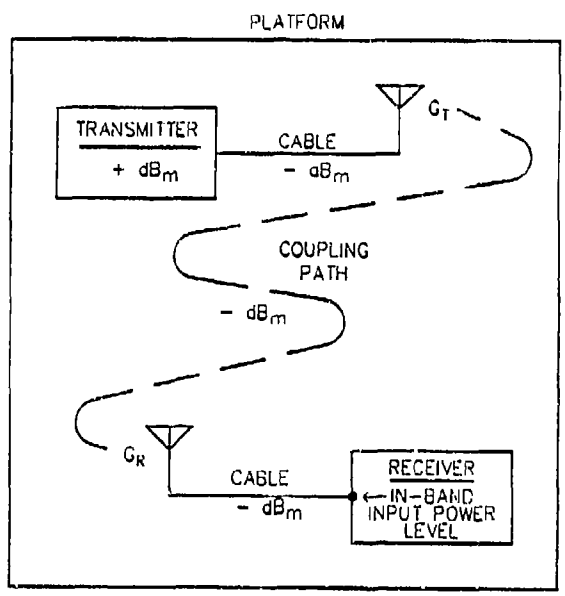

Figure 4 EM Coupling Paths.

EMI CODE SELECTION

The various EM codes utilized in the EMI module can calculate various parts of the E^3 analysis problem. Since there are multiple codes to choose from, selection criteria must be established so that the correct EMI code for the particular problem is used. This selection criteria must reflect the input data available depending on the life-cycle phase, the transmit and receive frequencies of the equipment, the relative size of the platform in wave lengths, and whether the coupling is internal or external to the platform. Also the required input data to each of these codes is different and the amount of data is large. The data must provide an EM platform structural description, the equipment configuration, and the equipment EMI parameters. GTCAP utilizes an expert system process to select the appropriate EMI code and structures the input data in a proper format to accurately execute the code. The logic of the code selection process is based on the parametrics of each EM code and information contained in the "lessons learned" database. Several of these

parameters are shown in Table 1 and GTCAP's EM Codes Parameter Matrix contains a complete set of parameters for each of the EM codes in GTCAP. Typical input data vectors are shown in Table 2 and are mapped into the GTCAP database.

Table 1 GTCAP Typical EM Code Parameter Matrix.

Property	IEMCAP	AAPG	BSC	GEMACS	UTRI-AACIM
Stated frequency range	Wire analysis: 30Hz-10GHz. Antenna analysis: 14KHz-100Hz.	150 MHz - 15 GHz	>300 MHz	MOM: <100 MHz GTD: >300 MHz	GTD: >300 MHz Prilic: Freq/3d^2
Usable frequency range	Antenna analysis: 150MHz-10GHz.	100 MHz - 15 GHz	>300 MHz		GTD: >300 MHz Prilic: Freq/3d^2
Lambda/d or Lambda/l restrictions	Frequency > 1.0/90618 per radian (inches) for curved surfaces. Separation > 3*d^2/Lambda (far-field).	Not Applicable	Each plate edge >= 1 lambda; sources >1 lambda from dielectrics; antennas >1 lambda from all edges; radii of cylinders >= 1 lambda; distance from antenna to rec. > 1 lambda.	GTD - plates >1 lambda. PO - grid dimension <1 lambda, default size .1 lambda. MOM - wire segments <.14 lambda long. Scattering center >= 1 lambda apart. Min patch area = .01 lambda^2.	Separation > 3*d^2/lambda (far-field), and characteristic dimensions > 1 (Lambda 10%).
Analytic method	Coupling analysis: Friis equation.	GTD - uniform theory of diffraction. Accurate to within 3 dB.	Geometric theory of diffraction (Actually UTD - which is a modified GTD).	Method of moments (MOM). Geometric theory of diffraction (GTD). Finite difference (FD). Hybrids of the above.	GTD shadding loss and Friis formula.
Geometric structure used	a) Aircraft: cylinder with cone fuselage, flat plate wings. b) spacecraft: aircraft without wings. c) ground station: antenna-antenna coupling only over conducting ground plane, no shading.	Cylinder with cone fuselage. Wings and stabilizers are flat, 3 or 4 sided plates.	Flat plates (multi-sided), ellipsis cylinders, thin dielectrics, layered dielectrics.	MOM: thin wires, patches. GTD: plates, ellipsis cylinders, and cone. PO: boundries specified by GTD plates.	Free space or elevated cylindrical surfaces.

CONCLUSIONS

GTCAP, a new EMC analysis CAE tool, has been described. This tool allows the engineer to configure and analyze complex systems through any phase of the system life-cycle. The tool contains databases of default and system EM characteristics which serve as input data in conjunction with specific test or design data, if available, for the analyses. GTCAP utilizes existing EM codes to minimize the development effort, thereby, developing a standard product which utilizes EM codes endorsed by the military research establishment. By parameterizing the EM

codes and their associated input and output vectors, GTCAP can select the optimum EM code for the evaluation of specific EM problems. It provides an "expert system" to select the correct EM code based on various factors such as the availability of input data. The results of the E^3 analyses are compared to the MOP's and displayed, reported, and stored as "lessons learned."

Table 2 EM Code Typical Input Data Vector.

ITEM	PARAMETER DESCRIPTION	UNITS	SOURCE	TYPE	FORMAT	EMCAP	AACIM	WIRE	ESC
1	aircraft model designation	none	DBASE	CONTROL	AIR	X			
2	ground station designation	none	DBASE	CONTROL	GROUND	X			
3	space vehicle designation	none	DBASE	CONTROL	SPACE	X			
4	ground station longitude	degrees	GTCAP	INPUT	*	X	X		X
5	ground station latitude	degrees	GTCAP	INPUT	*	X	X		X
6	ground station altitude	feet	GTCAP	INPUT	*	X	X		X
7	adjustment safety margin	dB	DBASE	INPUT	*	X			
8	EMI margin print limit	dB	DBASE	INPUT	*	X			
9	wire-to-wire common impedance	ohms/meter	DBASE	INPUT	*	X		X	
10	fuselage model designation	none	DBASE	CONTROL	FUSLGE	X			
11	nosecone length	inches	DBASE	INPUT	*	X			
12	fuselage radius	inches	DBASE	INPUT	*	X			
13	nosecone minimum radius	inches	DBASE	INPUT	*	X			
14	vertical zero reference	inches	DBASE	INPUT	*	X			
15	flat-bottom cylinder 0 ref	inches	DBASE	INPUT	*	X			
16	round cylinder designation	none	DBASE	CONTROL	ROUND	X			
17	flat cylinder designation	none	DBASE	CONTROL	FLAT	X			
18	wingroot designation	none	DBASE	CONTROL	WNGRT	X			
19	butt line of wing root	inches	DBASE	INPUT	*	X			
20	water line of wing root	inches	DBASE	INPUT	*	X			
21	fuselage station, forward root	inches	DBASE	INPUT	*	X			
22	fuselage station, aft root	inches	DBASE	INPUT	*	X			
23	wingtip designation	none	DBASE	CONTROL	WGTIP	X			
24	butt line of wingtip	inches	DBASE	INPUT	*	X			
25	water line of wingtip	inches	DBASE	INPUT	*	X			
26	fuselage station, forward tip	inches	DBASE	INPUT	*	X			
27	fuselage station, aft tip	inches	DBASE	INPUT	*	X			
28	ambient field frequencies desig	none	DBASE	CONTROL	LIFQ	X			
29	ambient field frequencies	Hz	DBASE	INPUT	*	X			

ACKNOWLEDGEMENTS

The authors wishes to thank the following people for their contributions to this work: T.A. Torres for the initial concept and funding, H.W. Denny, R.J. Levin, D.W. Acree, G.E. Beebe, M.L. Wheeler and Dr. J.A. Mahaffey for their enlightened discussions, assistance with the EM code evaluations, and providing the EM code input vectors and ideas on the user interfaces.

REFERENCES

1. Millard, David P., "Helicopter and Avionics Systems Electromagnetic Environmental Effects," Digital Avionics Systems Conference, 16-18 October 1990, Virginia Beach, Virginia
2. Millard, David P. and Woody, Jimmy A., "System E3 Platform Evaluation," 1990 International Symposium on Electromagnetic Compatibility - Symposium Re d, Washington, D.C., pp. 607-611, 21-23 August 1990.

3. Millard, David P., "System E^3 Analysis and Prediction Program," EMC EXPO 89, Washington, D.C.
4. DOD-STD-2167A, "Defensive System Software Development," 27 October 1987.
5. MIL-STD-461C, "Electromagnetic Emission and Susceptibility Requirements for Control of Electromagnetic Interference," 4 August 1986.
6. Denny, H.W., Daher, J.K. and Beebe, G.E., "E^3 Analysis Guidelines,"Technical Report No. 2, Gtri Project No. A-4892 for Rome Air Development Center, Air Force System Command, Griffiss AFB, New York, Contract No. F30602-87-C-0134, December 1990.

SESSION 14-- "LOW FREQUENCY APPLICATIONS"

Moderator: Perry Wheless, Jr.

Transler. Leakage Field in Transformers with Saturable Magnetic Core

Mihaela I.Morega ^, Alexandru.M.I.Morega^^

Abstract

The problem of the magnetic leakage field distribution arround windings with saturable magnetic core is solved with a method which couples the numerical magnetic field calculus and the solution of the magnetic circuit, equivalent to the electric and magnetic structure.

1. Introduc_lon.

Leakage field computation in transformer structures is aimed to determine the shortcircuit parameters, electromagnetic forces and stry losses in windings and framework. The computation is usually made according to the classical core model with infinite magnetic permeability, in other words, the assumption of the windings with compensated amperturns [1]-[6].

There are experimental researches [5] which evidence the increase of the magnetic flux values in transformer cores in some particular shortcircuit working conditions, as compared to the values reached in nonload service. In such conditions, the distribution of the leakage flux is influenced as well. This is why this paper presents a computational method for the leakage field, which allows to consider any working conditions of the transformer as well as the influence of its iron-core magnetisation curve.

In this paper, a hybrid representation of a three-phased transformer is proposed. The magnetic core nonlinearity and the specific working conditions are studied on an electro-magnetic equivalent network; the solution of this circuit problem provides for nonhomogeneous boundary conditions as well as the amperturns values of the field sources, in the magnetic field problem. A finite difference or finite element method is used to obtain the distribution of the leakage field.

The method is presented with reference to a three-phased transformer, but it can be used to study any other similar devices: transformers, induction field coils, eetromagnets, etc.

2. The Electro-Magnetic Circuit.

For the representation of the transformer, an electro-magnetic network is proposed (fig.1), which is composed both of the equivalent electric circuits of the primary and secondary windings as well as the equivalent magnetic circuit with the magnetic reluctances and the windings amperturns.

^ Dept.of Electrical Eng., Chair of Electrical Machines, Poly.Inst of Bucharest, ROMANIA
^^Dept.of Electrical Eng., Chair of Electrotechnics, Poly.Inst of Bucharest, ROMANIA

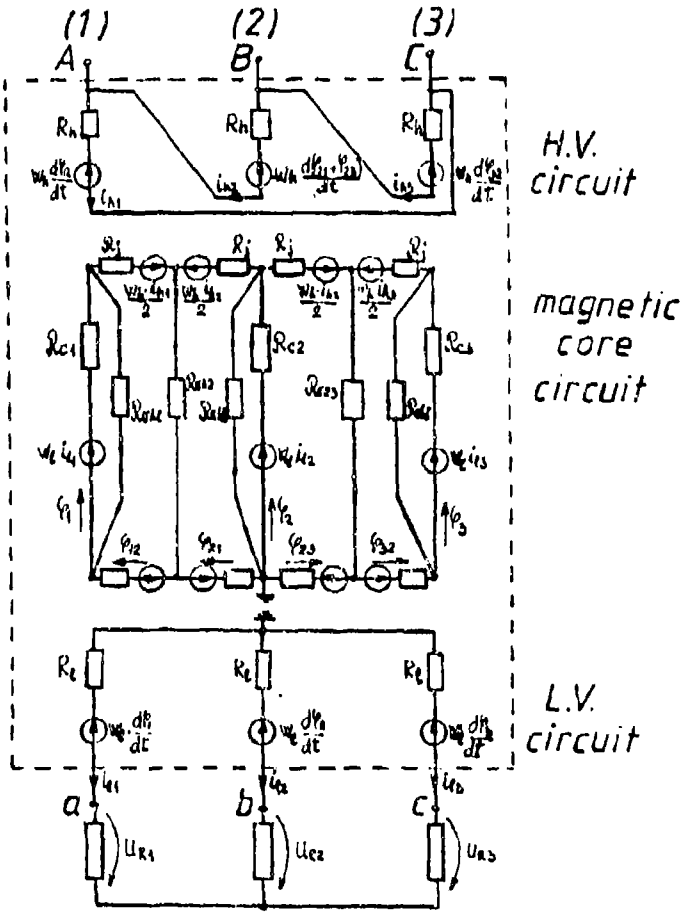

Figure 1

The representation is based on the following assumptions:

1. The nominalisation of the windings as primary or secondary as well as the connection of the phase coils are arbitrarly made. The voltage three-phase source is (u_1, u_2, u_3) and the load is represented through the voltage system (u_{R1}, u_{R2}, u_{R3}). The circuits of the windings contain: the electric resistances (R) and the induced voltages ($wd\phi/dt$); the "h" and "L" indexes are for high voltage (HV), respectively low voltage (LV), windings.

2. The magnetic circuit is represented by nonlinear magnetic reluctances (R_j - for the jok[illegible] and R_c - for the columns) as well as linear magnetic

reluctances for the leakage field domains (R). The amperturns of the windings are the current sources (wi).

3. The representation takes into account the symmetry of the transformer, which simplifies the solution process, without beeing a mandatory condition.

The set of equations which describe the transformer, with the formerly specifications, for any for time variation, or charge symmetry, is the following:

$$u_1(t) = R_h i_{h1}(t) + w_h d\phi_{12}(t)/dt \quad (1)$$

$$u_2(t) = R_h i_{h2}(t) - w_h d(\phi_{12}(t) + \phi_{23}(t))/dt \quad (2)$$

$$u_3(t) = R_h i_{h3}(t) + w_h d\phi_{32}(t)/dt \quad (3)$$

$$i_{L1}(t) + i_{L2}(t) + i_{L3}(t) = 0 \quad (4)$$

$$R_L i_{L1}(t) + w_L d\phi_1(t)/dt + u_{R1}(t) = R_L i_{L2}(t) + w_L d\phi_2(t)/dt + u_{R2}(t) \quad (5)$$

$$R_L i_{L2}(t) + w_L d\phi_1(t)/dt + u_{R2}(t) = R_L i_{L3}(t) + w_L d\phi_3(t)/dt + u_{R3}(t) \quad (6)$$

$$\phi_k(t) = f_k(w_h i_{h1};\ w_h i_{h2};\ w_h i_{h3};\ w_L i_{L1};\ w_L i_{L2};\ w_L i_{L3}) \quad (7)$$

The equations (1) - (6) result by applying the Kirchhoff's laws for the circuits "a" and "c" (fig.1); the equation (7) represents the nonlinear dependences in the magnetic circuit "b". The index "k" stands for: k = 1; 2; 3; 12; 23; 31.

Remarks:

* Naturally, the equivalent network could be less simple, for a better approach to the real structure, but the improvement of the results does not justify the complication of the computation.

** The values of the leakage reluctances (R_σ) could be determined after the field calculus and depends on the magnetisation level of the core as well, but they are 2 to 3 times greater than the reluctances of the iron regions, in the sense of magnitude order; that is why it is not necessary, for the moment, to have more accurate values than those obtained as a result of field estimation based on a simplified model.

It is not possible to solve the system of nonlinear equations (1) - (7), by analytic methods, and as such, **RESEL**, the well known computer code [8] was used to simulate the coupled circuits in fig.1.

The outputs of the simulation provides for the values of the magnetic flux density in different zones of the transformer magnetic core as well as for the values of the windings amperturns, at each simulation time step.

3. The Magnetic Field Problem.

The leakage field is computed in the longitudinal cross-section plane of the transformer window, which includes the windings of two phases and is limited by the magnetic core. The field equations in the domain are in agreement with Maxwell's laws in terms of the magnetic vector potential [1]-[4], [6]; the boundary conditions, of Neumann type, the values of the field sources, the amperturns of the windings, are imposed by the "working point" of the above formulated electro-magnetic circuit.

The finite element or finite differences method may be used to determine the momentaneous magnetic field distribution. Our model, as compared with those formulated in [1]-[4], [6], eventualy admits more general, nonhomogeneous boundary conditions as well as uncompensated amperturns for the sources.

4. Application.

This hybrid computational method has been applied in order to simulate a three-phased transformer, under transient working conditions, during the net shortcircuit regime. The numerical data belong to a 630kVA; 20/0.4kV transformer with cylindrical windings.

The paper presents the magnetic field distribution, for the same time moment, during the shortcircuit, in two situations:

1. the magnetic core has infinite magnetic permeability (fig.2a);

2. the magnetic core has a nonlinear magnetisation curve (fig.2b). In this case the unbalance of the equivalent amperturns in the domain is 95,700A (the average values of the magnetic flux density at the boundaries are marked on the figure).

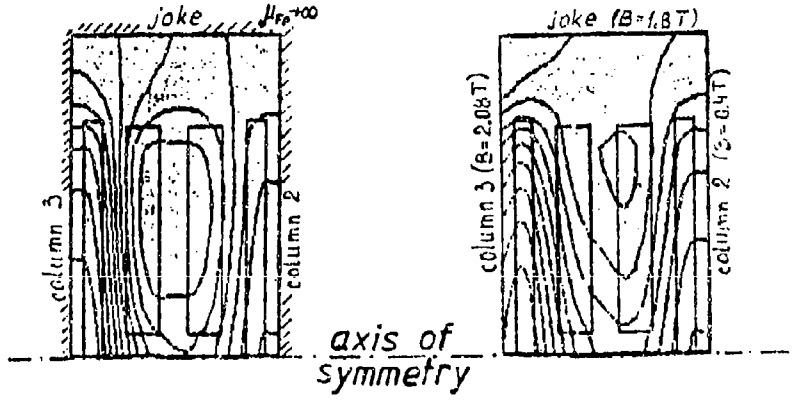

a. b.

Figure 2

5. Conclusions.

The purpose of this research program was to estimate the distribution of the electrodyna stresses during the net shortcircuit process. The combined circuit-field mod above formulated, has proved to be a conceptualy flexible and quantitatively sufficient accurate approach to rather complex electromagnetic structures, such as transformers, under less restrictive assumptions.

The results have proved that our hybrid model which implements, without special difficulties the magnetic core nonlinearity as well as uncompensated windings amperturns, allows a better approach to and in good agreement (in modelling sense) with the published experimental data [5], [7].

Its applicability to other equivalent electromagnetic devices models is natural.

The basic concept of our model is the *combined* use of global (voltages, currents, fluxes) quantities (the actualy measurable ones) and local (magnetic vector-potential) quantities (obtained through field analysis) and, as such, the combined use of an electric-circuit simulator and a field-analyser.

6. Acknowledgements.

Special thanks to prof.A.Moraru and C.Fluierasu for the very usefull discutions.

References

1. Andersen,O.W., - *Transformer Leakage Flux Program based on the FEM* - IEEE Transactions on PAS-92, nr.2/1973.
2. Silvester,P.,Konrad,A., - *Analysis of Transformer Leakage Phenomena by Higher Order Finite Elements* - IEEE Transactions on PAS-92 nr.4/1973.
3. Polonjadoff,M.,a.o. - *The Dimensional Flux Calculation on a Three Phase Transformer* - IEEE Transactions on PD, nr.3/1986.
4. Mihalache M., - *Numerical Study of the Transformer Leakage Magnetic Field* - ISEF, Lodz, Poland, 1989.
5. Circea,D., - *Doctoral Dissertation* - Poly.Inst.of Bucharest, Romania, 1978.
6. Morega,M., - *Magnetic Leakage Flux Distribution in the Three Phase Transformers* - ISEF, Lodz, Poland, 1989.
7. Morega,M., - *Doctoral Dissertation* - Poly.Inst.of Bucharest, Romania, 1988.
8. Fluierasu C., - RESEL - *Numeric Computational Package for Nonlinear Electric Circuits* - Polyt.Inst.of Bucharest, Romania, 1987. (rev.1989).

FINITE ELEMENT ANALYSIS OF MAGNETIC FIELD DISTRIBUTION IN FERROMAGNETIC SHIELDS

Constantin V. Bălă , Ovidiu C. Craiu , Mihaela I. Morega
Polytechnic Institute of Bucharest
Depatment of Electrical Engineering
Splaiul Independentei 313, Bucharest, Romania

ABSTRACT

A model for the analysis of the magnetic field distribution and the computation of eddy currents losses in laminated ferromagnetic shields is proposed in this paper. The magnetic field normal penetration into the laminated shield, coupled with the reaction of the eddy-currents leads to a three-dimensional magnetic field problem in a nonlinear medium. The numerical treatment involves the FEM in conjuction with the Newton-Raphson technique.

INTRODUCTION

The ferromagnetic and electromagnetic shields are placed in the vecinity of the electrical machines solid parts, in order to reduce the eddy-currents losses due to the time varying leakage fields [1,2,3,4]. The computation method of the magnetic field distribution and the eddy-currents losses, presented in this paper, are applied on a three-dimensional structure of a power transformer, with the tank wall protected to the normal leakage flux penetration, by many saturabile iron shields (fig.1.)

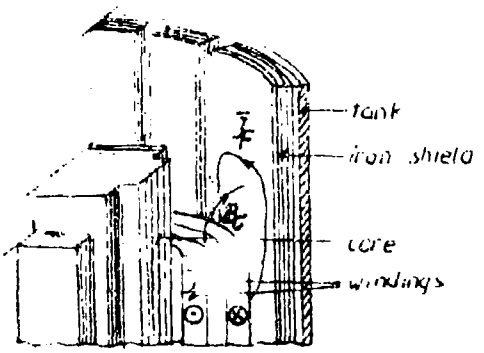

Fig. 1

The governing electromagnetic field equation is

$$\mathrm{curl}(\nu\ \mathrm{curl}\ \underline{A}) = \underline{J} - \sigma\frac{d\underline{A}}{dt} \qquad (1)$$

where σ and ν are the material properties: conductivity and reluctivity, $\underline{A}$ is the magnetic vector potential, $\underline{J}$ is the current density in the transformer coils (the source of leakage field) and $-\sigma \cdot \frac{\partial \underline{A}}{\partial t} = \underline{J}_F$ is the eddy-cuurent density in the iron shield (with its two components — on the azimuthal and on the axial direction). The primary source of the magnetic field is the prescribed alternating electric current density $\underline{J}$ in the coils of the transformer.

The laminated structure of the shield allows to neglect, without loss in accuracy, the reaction magnetic field of the eddy-current density $\underline{J}_F$. This assumtion leads to an easier magnetic problem formulation and provides a higher computation efficiency.

THE COMPUTATION METHOD

The numerical model for the eddy-currents losses computation in the ferromagnetic shield follows a step by step algorithm:

1) The first problem is to solve the Poisson type equation.

$$\text{curl}(\nu \text{curl} \underline{A}) = \underline{J} \tag{2}$$

in a plane domain, selected by cylindrical symmetry (fig.2), which includes: the windings with magnetic core, the shield, the tank and the surrounding air. Some usual simplifying assumptions are made:

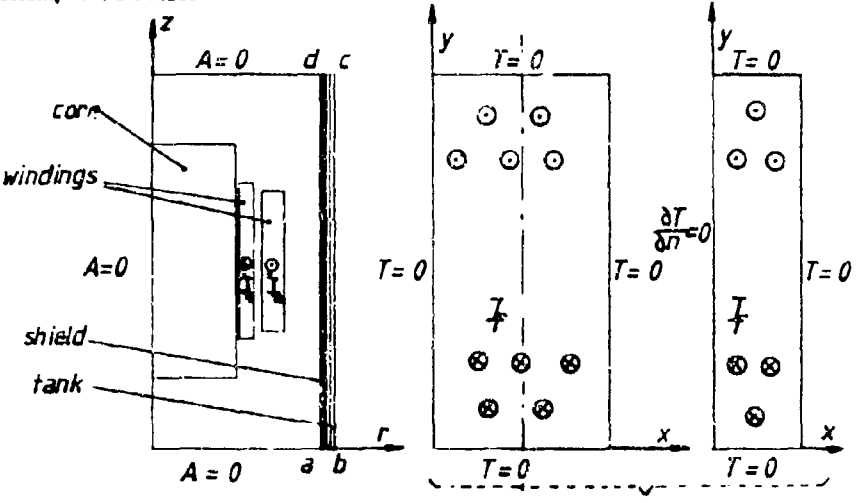

Fig. 2

Fig. 3

* $\underline{J}$ has a sinusoidal time shape and only an azimuthal component, similar to $\underline{A}$;
* for the moment, the quasi-steady state is assumed and the eddy-currents are neglected.

The boundary conditions are of Dirichlet type, as the figure shows.

The solution of equation (2) is obtained by the FEM, coupled with a Newton-Raphson technique if the nonlinear magnetisation curves of the shield and tank are considered. The FEM formulation leads to the standard equation:

$$[GK] \cdot \{A\} = [R] \cdot \{J\} \tag{3}$$

and, according to the Newton-Raphson iteration procedure, the increment of the unknown variable $\{\delta A\}_{k+1} = \{A\}_{k+1} - \{A\}_k$ for the „$k+1$"-th iteration step is given by:

$$\{\delta A\}_{k+1} = -\left\{\frac{\partial^2 F}{\partial A_i \, \partial A_j}\right\}^{-1} \cdot \frac{\partial \{F\}}{\partial A_i} \tag{4}$$

where the energy functional, F is expressed by:

$$F = \int_{(D)} \left(\int_0^B H \, dB - JA \right) dv \tag{5}$$

The discretisation mesh is not a very refined one, for exemple the depth of the shield is covered by a single row of triangular elements. The solution of eq.(3) allows to compute the values of the normal flux density on the surface of the shield.

2) The values of $\underline{A}$, obtained as the solution of the first step, are used to generate (by polinomial interpolation) the boundary conditions for a detailed computational domain: the shield-the air space-the tank (the domain $abcd$ in fig.2).

The problem is similar to the first, only a Laplace type equation is to be solved:

$$\text{curl}(\nu \ \text{curl} \ \underline{A}) = 0 \tag{6}$$

3) The solution of the second step allows to compute the values of the magnetic flux density in the shield, especially the normal (radial) component:

$$B_r = -\frac{\partial A}{\partial z} \tag{7}$$

at the level of each triangular element of the mesh.

4) For the computation of the eddy-currents distribution, each sheet of the laminated ferromagnetic shield is considered with a plan-parallel symmetry (fig 3). The governing equations are :

$$\begin{aligned} \text{curl} \ \underline{J_f} &= -\sigma \cdot \frac{\partial \underline{B}_r}{\partial t} \\ \text{div} \ \underline{J_f} &= 0 \end{aligned} \tag{8}$$

if a current vect :r potential $\underline{T}$ is introduced by the equation.

$$\begin{aligned} \text{curl} \ \underline{T} &= \underline{J_f} \\ \text{div} \ \underline{T} &= 0 \end{aligned} \tag{9}$$

it is possible to reduce the problem at the standard FEM equation :

$$[CK] \cdot \{T\} = \{J_S\} \tag{10}$$

where the eddy-currents field source $\{J_S\}$ is given by:

$$\{J_S\} = -\sigma \cdot \frac{\partial \{B_r\}}{\partial t} \tag{11}$$

The boundary conditions are settled by natural considerations, as fig.3 shows.

5) The eddy-currents losses in every sheet could be evaluated by :

$$P_F = \int_{(D)} \frac{1}{\sigma} \cdot J_F^2 \, dv = \frac{\Delta_\epsilon}{\sigma_\epsilon} \sum_{k=1}^{n} J_{F,k}^2 \cdot \Delta_k \tag{12}$$

The sum combines the contributions of the n triangular elements of the sheet, each having a Δ_k surface and $J_{F,k}$ current density. The sheet has the Δ_ϵ thickness (depth) and the σ_ϵ conductivity.

Remarks:

i) At this step it is possible to do a control of the above procedure. The problem from the first step is completed with the distribution of the eddy-currents density $\underline{J}_F$ (the azimuthal component) in the sheet. With the same procedure is calculated the magnetic flux density, produced both by the conduction current density ($\underline{J}$ — through the coils) and the eddy-currents density ($\underline{J}_F$ — through the sheet).
The distribution of the flux density in this situation, evaluated on the surface of the sheet, is compared with the similar distribution, computed at the first step. If the differences do not exceed a prescribed error value, then the method is satisfactorily; in other case, the procedure needs a corection. However, the applications of the computational method prooved the coherence and the correcness of the algorithm.

ii) The process described above by the steps 1–5 corresponds to a value of the initial current density $\underline{J}$ in the windings. If the nonlinearity of the ferromagnetic regions is taken into account, the time variation of the magnetic flux density ($\underline{B}_f$) has another form than the current density ($\underline{J}$) and the procedure previous described must be repeted at each time step.

NUMERICAL RESULTS

Fig. 4.a. shows the geometry of the model used for a numerical application of the previous algorithm. A plan axial section through a two winding transformer with magnetic core, in the vecinity of a ferromagnetic shield and the tank of the transformer is the computational domain for the first step. Because of the longitudinal symmetry, only the superior half of the domain is considered. The geometrical dimensions and the boundary conditions are specified in fig.4.a.

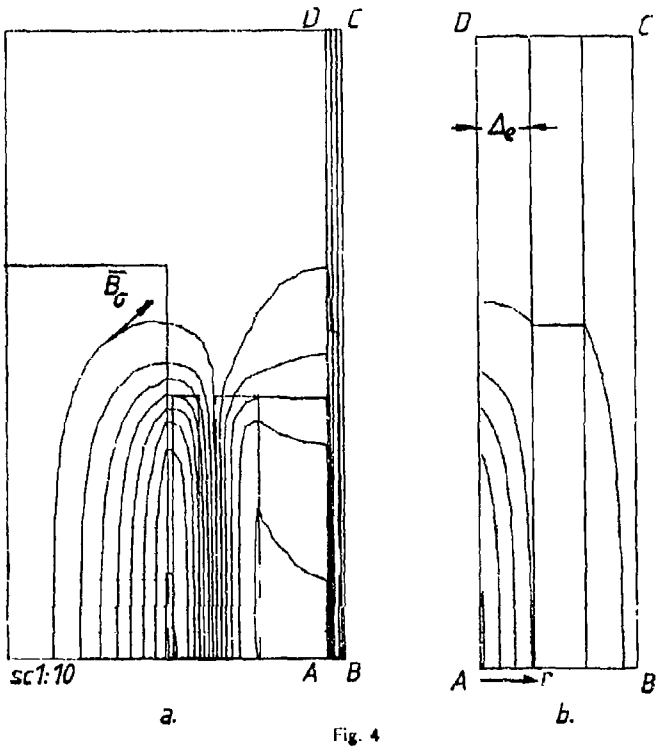

Fig. 4

The magnetic field distribution estimate at the first step considering the nonlinearyties of the domain is also presented.

For the second step of the algorithm, only the domain ABCD is considered; the boundary condition on AD is settled with the results of the first step. The mesh is much refined, for exemple the depth of the shield and of the tank are covered with ten time more elements than at the first step. Fig.4.b. shows the distribution of the magnetic field lines in the shield-air-tank region ABCD.

At the fourth step, the computational domain is a segment of the divided shield (fig.3). The depth of the shield is composed by ten sheets. The distribution of the current density is different from a sheet to another (see fig. 5), being visible the protecting effect of the shield toward the tank wall.

CONCLUSIONS

The use of the ferromagnetic shields is a necessity in the design of the high power electrical machines. It does not exist a general method to dimension such constructions. The algorithm, which was presented before, allows to select the most favourable configuration of the shield (its geometry and emplacement) in order to obtain minimum supplementary losses.

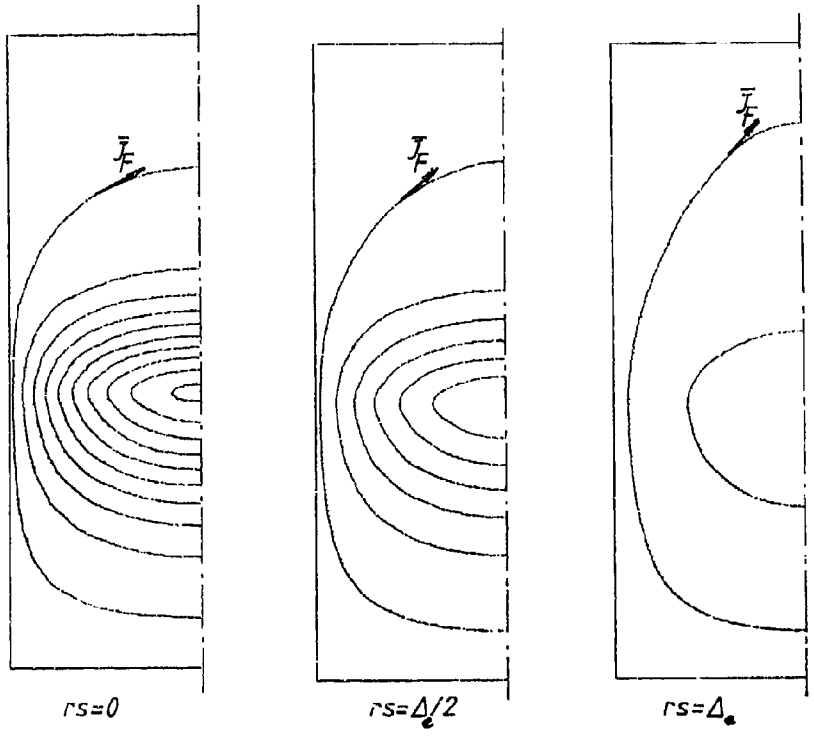

Fig. 5

The method is usefull because it solves a difficult three dimensional magnetic field problem, through a sequence of easier two-dimensional ones, based on the same classical finite element computational method. The gradual display of the algorithm follows the physical phenomena and allows the estimate of the intermediary results.

REFERENCES

[1] Moullineux, N., Reed, J.R.: *Eddy current shielding of transformer tanks.* Proc.IEE vol.113, no.5/1966

[2] Chiampi, M., Negro, A., Tartaglia, M.: *Alternating Electromagnetic Field Computation in Laminated Cores.* IEEE Trans. on Magnetics, vol MAG-19, no.4/1983

[3] Bălă, C.V., Badea, E., Teodorescu, R.: *The 3D FEM to estimate the transient parameters of coils with non-ferromag ietic core.* European TEAM Workshop, Oxford, UK, April 1990

[4] Bălă, C.V., Badea, E., Teodorescu, R.: *The transient parameters estimation of coils with ferromagnetic core by 3D FEM.* ICEM-90 (august 1990), MIT Cambridge, USA.

A MODEL FOR DYNAMIC ANALYSIS OF AC CONTACTOR

by Paulo I. Koltermann, J. P. Assumpção Bastos, Sérgio R. Arruda

GRUCAD / EEL / CTC CP. 476 UFSC 88049 Florianópolis Brazil

ABSTRACT

This paper presents a methodology for dynamic analysis of AC contactors. In these devices, mechanical and electrical parts are coupled and it is necessary to evaluate with good precision the electrical parameters, specially the indutances. The device is voltage fed through a sinusoidal source, the dynamic force equation is considered, and a method for numerical integration is adopted. A Finite Element method is used to determinate the parameters used in an equivalent circuit. The comparison between theoretical and experimental results shows that the methodology is consistent.

INTRODUCTION

Contactors are devices composed by a set of springs and a magnetic circuit. When a voltage is applied to the coil, electromagnetic force attracts the mobile part toward the fixed part in order to close the external contacts of the device. Although these structures are well known, an accurate calculation of their movement is difficult, because it is necessary to evaluate the variable reluctances. Notice that AC contactors have copper short-circuit rings, and its magnetic effects have to be composed with the action of the principal coil. In this work a FE system determines, for several positions of the mobile part, the inductances of the contactor. Currents are calculated in the equivalent circuit, enabling fluxes to be obtained, therefore the magnetic forces are determined; finally the forces are used in the dynamic equation which is then solved by the forth order Runge-Kutta method.

CONTACTOR DESCRIPTION AND EQUATIONS

Figure 1 presents the contactor used. It is composed by the coil, the magnetic circuit, a short circuit ring, a spring set and the contacts.

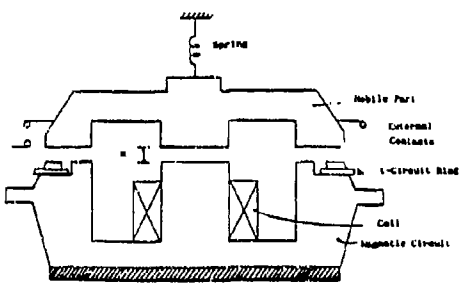

Fig. 1 AC Contactor Elements

The main equation for the FE method is:

$$\text{Curl } \nu \text{ curl } A = Je \qquad (1)$$

where A is the vector potential, Je is the external current and ν is the reluctivity [1],[2],[3].

Figure 2a presents the magnetic circuit, and the equivalent circuit is shown in figure 2b.

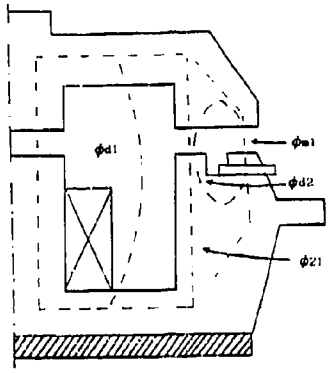

Fig 2a Magnetic Circuit

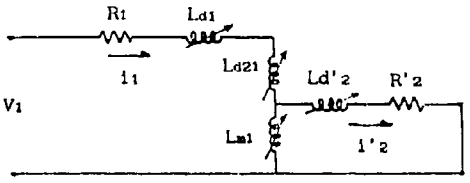

Fig 2b Equivalent Circuit

here R_1 and R'_2 are the coil and the short-circuit ring resistances
L_{d1}, L_{d21} and L'_{d2} are coil and ring leakage inductances
L_{m1} is the mutual inductance

All these inductances are found by FE method for several values of distance and they are refered to the primary. The equivalent circuit of fig. 2b is used by both, transient and permanent regimes. During the first step, the inductances change and they are obtained from the curves previously determined from FE results (and aproximated by the square minima method). When the contactor is closed (permanent regime) the values of indutances are fixed, since there is no movement any more. The example under study show no appreciable saturation. Thus the analysis by phasor diagram is possible; this diagram permits an easy visualisation of the angles between the currents (fluxes) in the coil and in the ring. The final result of currents and fluxes is a resultant force with a non null value, avoiding an undesirable vibration.

The mechanical equation is:

$$M.d^2x/dt^2 = Fe - K.x - B.dx/dt \qquad (2)$$

which is solved by time step integration. Where Fe is the electromagnetic force, K is the spring elasticity coefficient, B is the friction coefficient, M is the mass and x the displacement.

The general form of the force, given by Maxwell Tensor, is:

$F = (Bm.\sin wt)^2 . S/2.\mu o$ N/pole

where Bm is the magnetic induction in the airgap

In pole 1 the force is $F_1 = \frac{\phi_1^2 \sin^2 wt}{2.\mu o.S_1}$ (3)

The force produced in the ring pole is:

$$F_2 = \frac{\phi_{21}^2 . \sin^2 wt}{2.\mu o.S_{21}} + \frac{\phi_{m1}^2 . \sin^2 (wt-\alpha)}{2.\mu o.S_{22}}$$

Expanding $\sin^2 wt$ and assembling the terms, the expression becomes:

$$F_2 = \frac{\phi_{21}^2}{2.\mu o.S_{21}} + \frac{\phi_{m1}^2}{2.\mu o.S_{22}} - \frac{\phi_{21}^2 . \cos 2wt}{2.\mu o.S_{21}} - \frac{\phi_{m1} . \cos(2wt-2\alpha)}{2.\mu o.S_{22}} \quad (4)$$

where ϕ_{21} and ϕ_{m1} are the fluxes in the external and internal surfaces (S_{21} and S_{22}) of the ring, respectively; α is the angle between the fluxes [4].

The resultant force in the ring face is made of two components which individually pass through zero value, although the resultant has non null minimum value . The first two terms correspond to the average component and the two last ones represent the alternate component of the force.

The resulting force (Fe) is: $Fe = F_1 + F_2$

The fluxes of equations (3) and (4) are obtainned from the currents i1 e i2, calculated in the equivalent circuit. With the voltage law of Kirchoff, the following equation system is obtainned:

$$\begin{bmatrix} \bar{V}_1 \\ 0 \end{bmatrix} = \begin{bmatrix} R_1 + jw.Ld & -jw.L_{m1} \\ -jw.L_{m1} & R'_2 + jw.Ld'_2 \end{bmatrix} . \begin{bmatrix} \bar{I}_1 \\ \bar{I}'_2 \end{bmatrix} \quad (5)$$

where $Ld = Ld_1 + Ld_{21}$

Making some algebric transformations in equations (5), the state equations of current i1 e i2 ($\dot{x}_1$ e $\dot{x}_2$ respectively) are:

$$\begin{bmatrix} L_{m1} + Ld & -L_{m1} \\ -L_{m1} & L_{m1} + L'd_2 \end{bmatrix} . \begin{bmatrix} \dot{x}_1 \\ \dot{x}_2 \end{bmatrix} = \begin{bmatrix} -R_1 & 0 \\ 0 & -R'_2 \end{bmatrix} . \begin{bmatrix} x_1 \\ x_2 \end{bmatrix} + \begin{bmatrix} V_1 \\ 0 \end{bmatrix}$$

and:

$$\begin{bmatrix} \dot{x}_1 \\ \dot{x}_2 \end{bmatrix} = \begin{bmatrix} A_{11} & A_{12} \\ A_{21} & A_{22} \end{bmatrix} . \begin{bmatrix} x_1 \\ x_2 \end{bmatrix} + \begin{bmatrix} B_{11} \\ B_{21} \end{bmatrix} . \begin{bmatrix} V_1 \\ 0 \end{bmatrix} \quad (6)$$

where the matrix "A" is the inverse inductances matrix multiplied by the resistences matrix.

From the mechanical equation (2), the state equations of displacement ($\dot{x}_3$) and speed ($\dot{x}_4$) are obtainned as:

$$\begin{cases} \dot{x}_3 = x_4 \\ \dot{x}_4 = 1/M \,.\,(Fe - Fm - B.x_4) \end{cases} \qquad (7)$$

The mechanical force (Fm) is given by the sum of all forces due to springs. In order to solve the state equations, the 4th order Runge-Kutta method is adopted for the numerical integration. When the state variables are obtainned by this method, all the others variables of the structure are easily avaluated, defining completely the devices' dynamic behaviour.

RESULTS

The methodology is applied to a test case. Figure 3b shows the flux distribution when the ring is current fed , in order to obtain the inductances Ld2 and Lm2. Fig. 3a shows the flux distribution when the coil is fed, and the inductances L_{d1}, L_{d21} and L_{m1} are evaluated. In figure 4, the transient current is shown. Figure 5 presents the resultant force for steady state showing without doubt that it has never a null value. The experimental results have a good agreement with the theoretical ones, as far as closing time, transient and permanent current and finally, forces are concerned. It is interesting to note that this process is an important tool, as far as design of contactors is concerned.

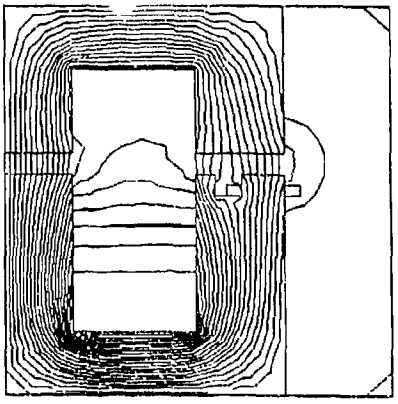

Fig. 3a Flux Distribution

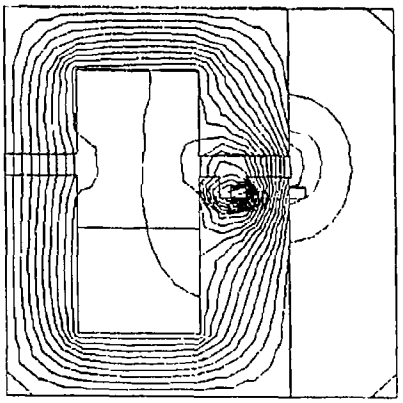

Fig. 3b Flux Distribution

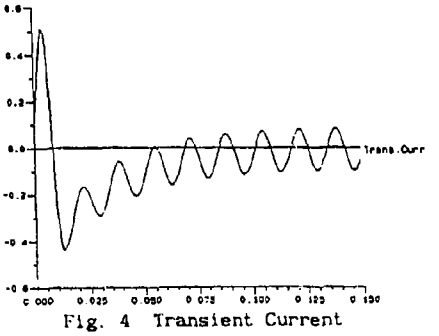

Fig. 4 Transient Current

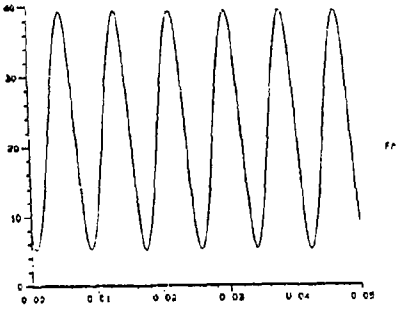

Fig. 5 Resultant Force

CONCLUSION

Although AC contactors are well known and widely used devices, their analysis is complex, because electrical and magnetic phenomena are coupled and few papers deal with this subjec. In this work a dynamic analysis method for AC contactor is presented. To achieve this goal, FE method, mechanical equations and phasor analysis are used. The results are consistent with a test case. We estimate that this method can be usefull for performance evaluation of this kind of equipment.

REFERENCES

[1] T. Nakata, N. Takahashi "Direct Finite Element Analysis of Flux and Current Distributions under specified conditions", 1982 IEEE Transaction on Magnetics, USA

[2] B. Davat, Z. Ren, M. Lajoie-Mazenc "The Movement in Field Modeling", 1985, Compumag, Fort Collins, USA

[3] J.P. Assumpção Bastos "Eletromagnetismo e Cálculo de Campos", 1989, Editora da UFSC, Florianópolis, Brazil

[4] H.C. Roters "Electromagnetic Devices", 1970, John Wiley & Sons, Inc, New York, USA

EDDY CURRENT ANALYSES OF THE CORE PLATE IN A LARGE POWER TRANSFORMER

Yuanren Chiu Wei Wang Qinke Zhang Guochun Xiao
Xianghua Li*

Electrical Engineering Dept., Xi'an, Shaanxi, 710049 P.R.C.
*Xi'an Tranformer & Electric Furnace Works, Xi'an, 710077 PRC

ABSTRACT

In this paper, the eddy current distribution and losses in the core plate of non-magnetic steel material of a large power transformer have been analysed. This paper also discuss how the strength of the eddy current demagnetizing effect and the magnitude of the resistance of the eddy current path both influence the eddy current loss of the non-magnetic conducting plate. The problem to limit the local overheating caused by these losses has been touched on. Experiments have been performed on small model plates to examine the analyses.

INTRODUCTION

Leakage flux problem becomes more and more serious as the rating of power transformer increased. Leakage flux induces eddy current in metal structural components, thus generates additional losses. Although eddy current losses sometimes are of insignificant magnitude as compared with the total losses, but in severe cases, it may cause excessive overheating and lead to performance failure. In this paper, eddy current loss on core plate due to winding leakage flux has been taken into consideration.

Papers from different investigators /1, 2, 3, 4, 5, 6, 7/ are helpful in showing different ways of mathematical formulation, using magnetic vector potential A or electric vector potential T to describe eddy current phenomena at power frequency. As well known, A is defined as a flux describing function, and T is defined as a current describing function. As magnetic flux passes through not only ferromagnetic part but also non-magnetic part of the space, while conducting current flows only in conductor. Evidently, to describe eddy current problems, T formulation has the advantage of limited area over A formulation and is also more convenient to specify boundary condition in certain situation.

For these eddy current problems, potential functions and field quantities are time variables, but at power frequency and in sinusoidal steady-state circumstances, the displacement current can be ignored, while time variables can be expressed by phasors to eliminate the time factors.

In this paper, the distribution of winding leakage flux over the core plate has been calculated with magnetic vector potential A in the axisymmetric system, and the eddy current distribution and loss in the core plate have been calculated with current vector potential T in the rectangular coordinates system.

WINDIND LEAKAGE FLUX DISTRIBUTION

Calculation Model and Formulation

To calculate the winding leakage flux distribution over the core plate of a three-phase transformer, only a single phase winding is taken into consideration, with the interference among phases neglected. The current flowing in the phase winding is assumed to be in the θ direction, then the winding current density:

$$\vec{J}s = Js\phi\vec{\theta}^{\circ}, \quad Jsr = Jsz = 0$$

and the magnetic vector potential A:

$$\vec{A} = A_{\phi}\vec{\theta}^{\circ}, \quad Ar = Az = 0$$

The calculation domain may be simplified as axisymmetric. (see Fig.1)

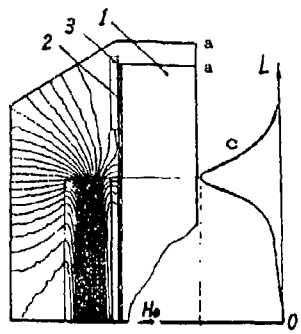

1. Core 2. Core plate
3. Clamping element

Fig.1. Distribution of the Winding Leakage Flux

In the steady state alternating field, the complex potential $\dot{A}_{\phi}$ satisfies the diffusion equation, it is expressed as:

$$\frac{\partial}{\partial r}\left[\frac{1}{\mu r}\frac{\partial(r\dot{A}_{\phi})}{\partial r}\right] + \frac{\partial}{\partial z}\left(\frac{1}{\mu}\frac{\partial\dot{A}_{\phi}}{\partial z}\right) = j\omega\sigma\dot{A}_{\phi} - \dot{J}_{s\phi} \tag{1}$$

where μ and σ represent the permeability and the conductivity respectively.

Let $\dot{A}_{\phi} = 1/r(r\dot{A}_{\phi}) = 1/r\,\dot{U}$, $\mu r = \mu'$ and $\sigma/r = \sigma'$
Equation (1) turns into:

$$\frac{\partial}{\partial r}\left[\frac{1}{\mu'}\frac{\partial\dot{U}}{\partial r}\right] + \frac{\partial}{\partial z}\left[\frac{1}{\mu'}\frac{\partial\dot{U}}{\partial z}\right] = j\omega\sigma'\dot{U} - \dot{J}_{s\phi} \tag{2}$$

Equation (2) is used to analyse the eddy current problems in the axisymmetric coordinates system.

The boundary conditions of the calculation domain are: (see Fig.1)

$$\begin{aligned} &\dot{U} = \dot{U}_0 && \text{on the boundary line of } \overline{ab} \\ &\partial\dot{U}/\partial n = 0 && \text{on the other parts of the boundary} \end{aligned} \tag{3}$$

It is known that the boundary value problem of equation (2) and (3) are equivalent to the variational problem:

$$\begin{cases} \iint_{\Omega}\frac{1}{2\mu}\left\{\left[\left(\frac{\partial\dot{U}}{\partial r}\right)^2 + \left(\frac{\partial\dot{U}}{\partial z}\right)^2\right]\frac{1}{r} - f\dot{U} + \frac{1}{2}j\omega\frac{\sigma}{r}\dot{U}^2\right\}drdz - \int_{s2}qds = \min \\ S1:\ \dot{U} = \dot{U}_0 \end{cases} \tag{4}$$

By finite element method, the domain Ω under investigation is subdivided into a set of triangular elements. Within each element, the potential $\dot{U}$ is approximated by linear interpolation function. The approximate solution to equation (4) is a set of nodal potential values, and in each element, potential $\dot{U}$ is taken by linear

interpolation from the vertex potential values.

The magnetic field strength H of each elements can be calculated by:

$$\dot{\vec{H}} = \dot{H}_z\vec{z}^\circ + \dot{H}_r\vec{r}^\circ = \frac{1}{\mu r}\left[\frac{\partial \dot{U}}{\partial r}\vec{z}^\circ - \frac{\partial \dot{U}}{\partial z}\vec{r}^\circ\right] \tag{5}$$

H will be uniform in each elemnnt for the linear interpolation.

The Distribution of Winding Leakage Flux Over the Core Plate

According to the specific situation of the core plate, winding leakage flux exert normally on the core plate, its tangential components are negligible. The curve 'c' on Fig. 1 shows the magnetic field strength Ho of the winding leakage flux distributing normally along the height of the core plate. It is seen that the Ho has a maximum value corresponding to the height of the winding terminal. This is agreeable with the theoretical analysis.

EDDY CURRENT AND LOSS IN THE CORE PLATE

Application of Current Vector Potential T

The magnetic field strength Ho of the winding leakage flux distributes normally over the surface of the core plate. Take this normal direction as the z direction of a rectangular coordinate system, then we have Ho $\vec{z}^\circ$=Hz $\vec{z}^\circ$. Furthermore, put the plane of the core plate in parallel with the x-y plane of that rectangular coordinate system. As the thickness of the core plate compared with its plane dimensions is rather small. The induced eddy current density Je has only two components: $\vec{J}e = Jex\,\vec{i}^\circ + Jey\,\vec{j}^\circ$. The eddy current flows parallelly to the plane of the plate. This is a two dimension eddy current problem, only single component Tz is needed for the calculation purpose.

Phasor $\dot{T}z$ satisfies the boundary value problem expressed as follows:

$$\begin{cases} \dfrac{\partial}{\partial x}\left(\dfrac{1}{\sigma}\dfrac{\partial \dot{T}}{\partial x}\right) + \dfrac{\partial}{\partial z}\left(\dfrac{1}{\sigma}\dfrac{\partial \dot{T}}{\partial z}\right) = j\omega\mu\dot{T} + j\omega\mu\dot{H}o & (6) \\ S1: \quad \dot{T} = 0. & (7) \end{cases}$$

where subscript z omitted, and the boundary condition S1 is according to the fact that the equipotential line of Tz represents the eddy current line in the x-y plane. Since there will be eddy current flowing along the perimeter of the plate, the perimeter of the plate is an equipotential line of Tz.

Equ.(6) has the same form as that of equation (2), it can be calculated in the same manner as equation (2), with the general computer program completed.

Analyses of Eddy Current Loss on Model Plate

The loss in the conductor per unit volume caused by eddy current density Je may be expressed as :

$$p = |J|^2 \cdot \rho = \frac{|\vec{E}|^2}{\rho}$$

Evidently, only when E maintains constant, the loss of the conductor decreases

with the increase in the resistivity. But, practically, when the applied field strength Ho maintains constant, E will be changed as eddy current changes, since the demagnetizing effect of eddy current may counteract the applied field strength to a certain extent. Therefore, the eddy current loss in conductor is influenced by both the resistance of the eddy current path and the demagnetizing effect of the eddy current when applied magnetic field strengh Ho remains stable.

For example, there are three plate conductors with the same length of 480 mm and the different width of 200, 100 and 20 mm respectively. They have the same permeability of μ_0 and their resistivities are varying according to the label of the horizontal axis. Calculation has been performed by assuming that they are under the same stable and uniform magnetic field of Bo = 490 GS which penetrating normally towards those conducting plates.

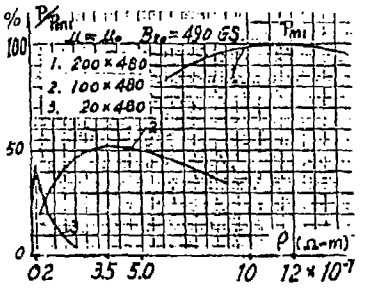

Fig. 2. Losses against resistivity ρ

The curves of the eddy current losses against the resistivities from calculation results are shown in Figue 2 . Every curve has a maximum loss Pm and a corresponding resistivity ρ_0 . Each curve can be divided into two parts at the point Pm. The left part of the curve may be considered as the region affected mainly by demagnetizing effect of the eddy current, named 'L region'. The right part of the curve may be considered as the region affected mainly by the resistivity of the eddy current path named 'R region'. These curves show that the smaller the width of the plate is, the greater R region and the smaller L region will be.

To decrease the eddy current loss of a plate conductor , we can make slots on the plate. As the slots are longer and the distance between slots is shorter, it is more possible to transfer the characteristic from L region to R region, and also to decrease the eddy current loss.

Local Over-Heating Problem

According to the former discussion, it is seen that we can reduce the eddy current loss by making slots on the plate. At the same time we should pay attention to avoiding local overheating on the plate.

By calculation, we find that when slots has been made to transfer the characteristic from L region to R region, the decreasing rates of the loss are not simultaneous with the decreasing rate of the maximum current density. The eddy current loss and the maximum eddy current density against the length of the slot on a plate conductor working at R region are plotted in Fig.3, in which Po

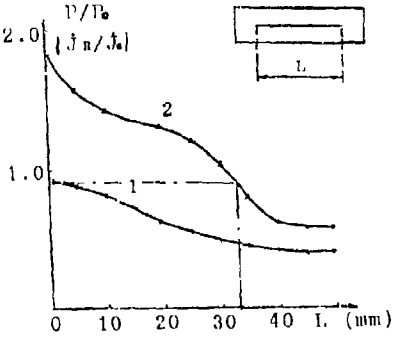

Fig.3. 1---Eddy current loss
2---Maximum eddy current

and Jo indicate the eddy current loss and the maximum eddy current density, respectively, of the plate without slot. Fig.3 shows that only when the length of the slot is greater than 33 mm, the maximum eddy current density will be lower than Jo. This is the case caused by the uniform applied external field. When the applied field is not uniform, the slot should be made passing through the spot where maximum applied field exists.

Eddy Current Distribution and Loss on the Core Plate

The non-magnetic steel core plate has the permeability of $\mu=(1\sim3)\mu_0$ and the resistivity $\rho=7.2$ E-7 Ω-m. The winding leakage flux distribution along the height(length) of the core plate has been shown in Fig.1 by curve 'c'. This leakage flux causes eddy current induced in the core plate. The distribution of eddy current over one-fourth of each plate is shown in Fig.4. The core plate shown in Fig.4 (a) has two slots, (b) has one slot and (c) without slot. The eddy current loss of plate (a) is 207 w., plate (b) is 332 w. and plate (c) is 424 w. It shows that these plates are all working in the L region. It implies that there should be have more slots on the plate, so as to shift the plate working from L region to R region and to reduce the eddy current loss effectively.

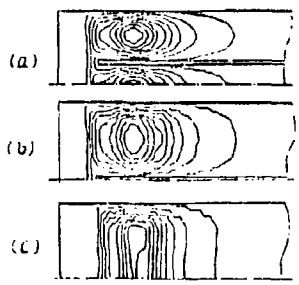

Fig. 4. Distribution of eddy currents in core plates

MODEL EXPERIMENTS FOR IDENTIFICATION

The principle diagram of the experiment is shown in Fig.5. The symbol 'a' refers to an installation for producing magnetic field. When the current passes through the winding, an uniform magnetic field will be produced in the gap. A plate conductor sample 'b' is placed in the gap. By this, the eddy current loss of the plate conductor can be tested.

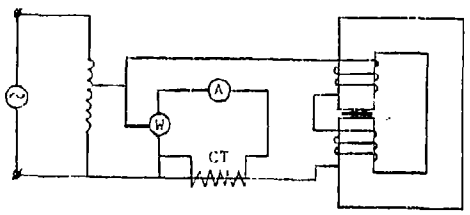

Fig.5. Principle diagram for experiment

The Experimental and Calculated Results

The experimental results and the calculated results of the eddy current losses of two 480x20x11 mm aluminum plates match quite well as shown in Fig.6. The plate (a) is without slit, and the plate (b) is with one slit. The loss in plate (b) decrease evidently since there's a slit on it. It shows that the characteristics of these plates are under the R region.

Another experiment has been performed on three pieces of aluminum plate which have the same dimensions of 480x44x11 mm. The first plate is without slot, the second one with one slot and the third one with three slots. The losses of these three plates against the uniform magnetic flux density are plotted in Fig.5. It shows the loss of the second one is greater than that of the first one, and

the loss of the third one is less than that of the first one. It is shown that the first one is under the L region, and the second one still working under L region. The characteristics of the third one have been transferred from L region to R region, and the loss is reduced. The experimental results coincide with the analytical results discussed formerly.

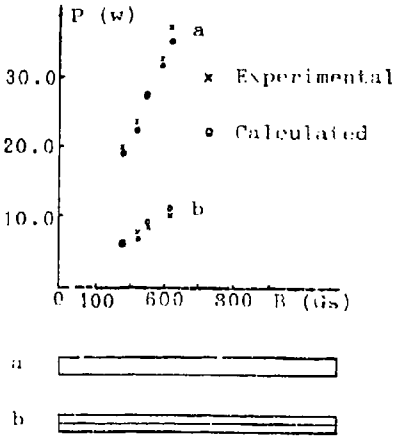

Fig. 6. a---Plate without slit
b--- Plate with slit

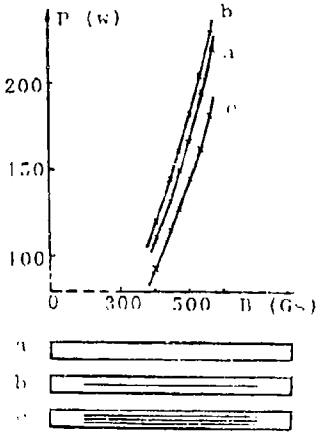

Fig. 7. Eddy current losses in plate conductors

CONCLUSIONS

Adopting non-magnetic steel material for core plate of a large power transformer can limit the eddy current losses and avoid local over-heating to a great extent.

In case of the applied magnetic field source remain unchanged. When neglecting the demagnetizing effect of the the eddy current, losses are inversely proportional to the resistance of the current path. But through practical calculation, the results show that even for non-magnetic steel material, the demagnetizing effect of the eddy current could not be neglected. So, how the variation of resistance influences on the losses should be known from calculation results.

REFERENCES

1. C.J. Carpenter, Proc. IEE. Vol.124, No.11, November 1977.
2. T. Sato and Y. Inui, Paper No. A 77 029-2, IEEE PES Winter Meeting, NY, Jan. 30-Feb. 4, 1977.
3. S.J. Salon and J.M. Schneider, Paper No. A 79 545-5, IEEE PES Summer Meeting, Canada, July, 1979.
4. T.W. Preston and A.B.J. Reece, IEEE Trans. MAG-18, No.2, March 1982.
5. L. Brown, Proc. IEE Vol. 129, Pt.A, No.1, January 1982.
6. A. Konrad, IEEE Trans. MAG-21, No.5, Sep. 1985.
7. T. Tokumasa, S. Doi, K. Ito and M. Yammamoto, IEEE Trans. on PAS, vol. PAS 103, No.6, June 1984.

ENGINEERING RESOLVABILITY OF ENGINEERING EDDY CURRENT PROBLEMS

Z.Cheng,S.Gao,D.Zhang,J.Wang and C.Ye
Baoding Transformer Works,Baoding 071056, China

ABSTRACT

This paper proposes some ideas of engineering resolvability technique of large engineering 3D eddy current problems through solving a simple electrical engineering model[1] for evaluation of power loss in steel. The engineering application of TEAMed (tested by TEAM) codes Will be specially emphasized.

1. ENGINEERING FIELD PROBLEMS AND ENGINEERING SOLUTION

In electrical engineering engineers often encounter various kinds of engineering field problems, especially, including electromagnetic field problems, the major difficult points of those problems are that: very large size and complex geometry of solved region with multi-materials. The maximum size of solved region may be more than 10 metres, but the penetration depth is very small in steel parts of electric machinery, in general,it may be less than 3 mm, the finite elements should be enough fine, thus the application of 3D electromagnetic softwares will be stemmed from too large computer storage and CPU time.

In engineering design a series of performance parameters of products will be determined by aided field analysis. Unfortunately, engineers can not find out exact solutions of complex 3D nonlinear eddy current problems.

We have proposed an idea of engineering solution of engineering problems[9].The main characteristics of engineering solution may be described as follows: the confirmable and stable error extent, the lower computing cost, and the favorable usability.

2. ENGINEERING TEAM AND BENCHMARK TEAM

Recent years,TEAM workshops have proposed and solved successfully 13 benchmark problems[2-10], many excellent 3D codes have been made[2-9]. All these effectively push forward the development of 3D eddy current analysis. However, the benchmark problems are far from large engineering eddy current problems. Authors propose an idea of engineering TEAM for the sake of showing the differences with TEAM workshop of solving benchmark problems.

As we know, the aim of benchmark TEAM is to test electromagnetic analysis methods, beyond doubt, doing those tests in simple models is a best way. TEAMed codes provide useful tools, while engineering TEAM ingeniously uses those tools to solve large engineering problems, and develops various practical analysis techniques, including making usable 3D eddy current codes, and checks their engineering usability.

In engineering TEAM the proposed test problems will be based on typical engineering background, the developed resolvability techniques will be directly used in aided analysis of products. It will aim at the engineering application of electromagnetic analysis softwares.

3. REVIEW OF ENGINEERING RESOLVABILITY TECHNIQUES

As above,to solve a large engineering field problem, the first thing is to do the reasonable assumptions to make the problem resolvable[8], and to choose the most practi-

cal approach. The brief review of engineering resovability techniques is as follows:

1) Simplification from 3D to 2D

Most of electrical engineering field problems are real three dimensional, nonlinear and transient. In some cases,3D engineering field problems have apparent 2D field characteristics,thus one can make some reasonable assumptions and define a solvable 2D model. For example, the leakage flux field of large power tranformer, obviously, is a 3D nonlinear eddy current problem, but if you only want impedance parameters of transformers then 2D software can provide good results, in this case, 3D field analysis is not necessary.

Moreover, Engineer's experiences have shown that using 3D finite element software with coarse meshes the computing results usually may be not better than that of 2D codes. Nowadays, any 2D engineering electromagnetic field problem can be solved without any difficulties.

It does not imply that 2D code can solve any engineering field problems.3D softwares have to be used to solve those special 3D field problems.

2) Local solvability processing of 3D field problems

The local solvability processing of 3D field problems means that delimitting a subregion from the whole solved region, it can be called as resolvable domain solving by TEAMed codes, the requirments of computer storage and CPU time can be substantially reduced.

The influnce from the regions outside the resolvable regarded domain can be determined by some simplified analysis techniques, this part can be regarded as influnce domain. The external influnce on resolvable domain can be applied in different ways. An applied term appearing in governing equations is the most simple way.

3) Thin penetration modeliing

In electrical engineeering the evaluation of power losses and its distribution in steel parts is an important problem to design lower loss products without local overheating.

The difficult points of those problems are that the planar size of the steel parts is very large, however, the penetration depth is very small. For instance, the thickness of steel tank of transformers is 10 mm, it is near 5 times of penetration depth, if the whole solved region are analysed by any 3D eddy current code based on FEM then the steel tank region have to be divided into 4 to 5 layers for getting accurate results of eddy current, so the computing cost will be very large. Fortunately, engineers have found some practical approach or use some modified experiment formulas after getting magnetic flux density outside the steel plate. The researchers have developed some feasible approach, for example, using the surface impedance element methods[7] to modelling the thin penetration problems.

4) Coupled field-circuit approach

A large power transformer and generator is an element of electrical system, determining a resolvable field problem of electric machinery will relate to electric and magnetic parameters obtained from electric and magnetic circuit theory, especially, for reverse problems.

For example,the overfluxing problem of large power transformers, connecting to a.c

voltage source,is difficut to solve exactlly by only field analysis because the exciting current is not known beforehand,the coupled field-circuit approch shuld be used. For more complicated enginering problems the coupled experiment-analysis methods have to be used, i.e., simulation test or product test provide necessitated data for doing further field analysis.

4. AN EDDY CURRENT LOSS MODEL

The design of the 3D eddy current model is based on typical power loss problems in transformers. It consists of two air-core coils with the same number of turns and the same dimensions in which the a.c exciting currents flow in opposite directions, the role of exciting coils is to provide an applied field only. A steel plate of 10 mm thick is placed parallelly to the coils as shown in Fig.1.

The aim of this modelling is to calculate the distribution of 3D eddy current and eddy current losses in steel plate, to check the engineering usefulness of 3D eddy current codes made by authors, finally, to attempt to find out practical engineering computing methods used in aided analysis of products, This will be demonstrated through solving the simple problem.

1) 3D eddy current analysis

This is a 3D, nonlinear, single connected eddy current problem. It can be solved by varied kinds of TEAMed codes, this model provides a possibility that the distribution of 3D eddy current in steel plate can be analysed in detail. The initial analysis results using 3D eddy current code based on T-Ψ approach with coarse meshes have been shown in Fig.2(a). Fig.2(b) shows another distribution of eddy current to verify the 3D code, in that test example the same applied magnetic fields are perpendicular to the steel plate anywhere.

The different schemes of the solvable models have been shown in Fig.3 (a) and (b) to indicate the dealing with the external influnce in different ways. In Fig.3(a) the solved region includes the exciting coil, but Fig.3(b) shows that the influnce of exciting coils was replaced by an applied term.

2) Simplified 2D analysis

In this model the regular coils and the thin steel plate placed parallelly to the coils show the evident characteristics of 2D field, so it can be approximately calculated using 2D software,the 2D model has been shown in Fig.4.

To confirm the accuracy of field analysis in different ways authors have done 2D analysis using both 2D FEM code and Image modelling program, those 2D analysis results have been shown in Fig.5.

3) Experiments of flux density

The testing model has been made, the measurement of power loss in steel plate is difficult, because the total power losses stored in both exciting coils and steel plate,determination of the losses generated only in steel plate and the local power losses should use some special experiment technique which will be further developed.

The measurement results of magnetic flux density at specified points have been shown in Fig.6.

5. CONCLUSIVE REMARK

The engineering resolvability technique of large eddy current problem will be further developed, an idea of engineering TEAM has been proposed by authors, it is expected that engineering-oriented analysis technique will be effectively used in electrical engineering.

REFERENCES

[1] Z.Cheng,S.Gao and D.Zhang,"An electrical engineering model for Loss evaluation", submitted to Asian TEAM workshop-Sendai,1991

[2] T.Nakata,N.Takahashi,K.Fujiwara and Y.Okata:"Improvements of T-Ω method for 3-D eddy current analysis", IEEE Trans. on magnetics, Vol.Mag-24,(1988),pp.94-97

[3] O.Biro and K.Preis: "Finite element analysis of 3-D eddy currents", IEEE Trans. on magnetics,Vol.Mag-26,(1990),pp.418-423

[4] D.Rodger and J.F.Eastham: " A formulation for low frequency eddy current solutions", IEEE Trans. on magnetics,Vol.Mag-19,(1983),pp.2443-2446

[5] C.R.I.Emson and J.Simkin: "An optimal method for 3D eddy currents", IEEE Trns. on Magnetics, Vol.Mag-19,(1983), pp.2450-2452

[6] J.Zhou: "Integrated finite element modelling of electromagnetic fields and leakage field computation of large power transformers", Ph.D.Dissertation, March 1990

[7] E.M.Deeley:"Improved surface models for 2D and 3D problems",IEEE Trans.on magnetics, Vol. Mag-24,(1988),pp.209-211

[8] P.Chen,L.Yan and R.Yao: "The theory and computation of electromagnetic fields in electric machinery", Science press,1986

[9] Z.Cheng, S.Gao and J.Wang: " Engineering solution of engineering field problems in transformers", 3-D Electromagnetic Field Analysis, (edited by T.Nakata), Sep. 1989, pp.151-154

[10] T.Nakata, N.Takahashi, K.Fujiwara, P.Olszewski and K.Muramatsu: "Analysis of magnetic fields of 3-D non-linear magnetostatic model (problem 13)", Proceedings of European TEAM workshop and international seminar on electromagnetic field analysis, Edited by Y.Crutzen, N.J.Diserens, C.R.I.Emson, D.Roger, Oxford, England, 23-25 April 1990

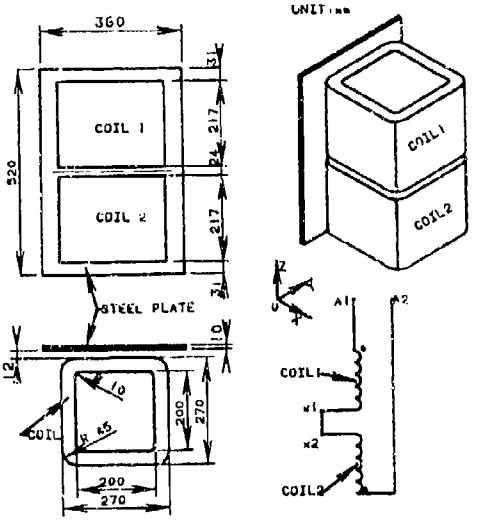

Fig.1 Engineering model

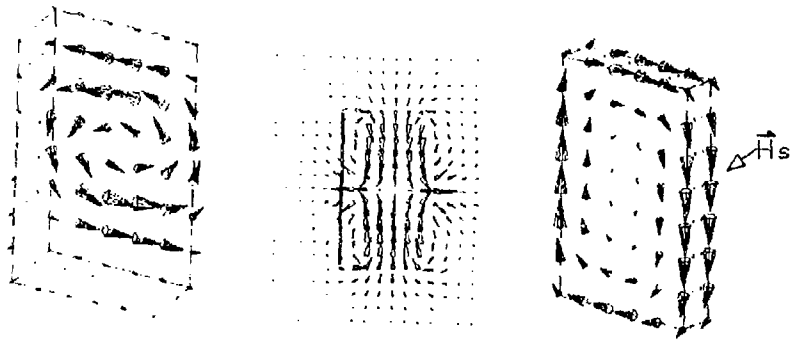

(a)Engineering model Applied field by coils (b) Test model

Fig.2 Distribution of 3D eddy current in the steel plate (The thickness of steel plate was enlarged)

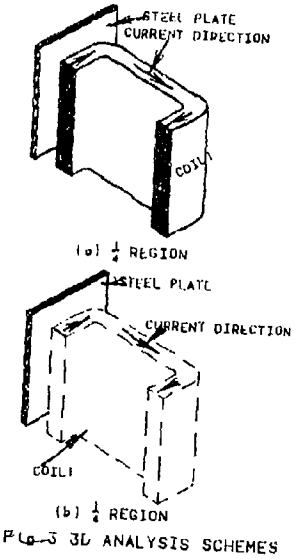

Fig.3 3D ANALYSIS SCHEMES

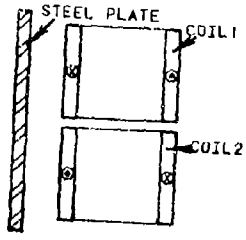

Fig.4 2D MODEL

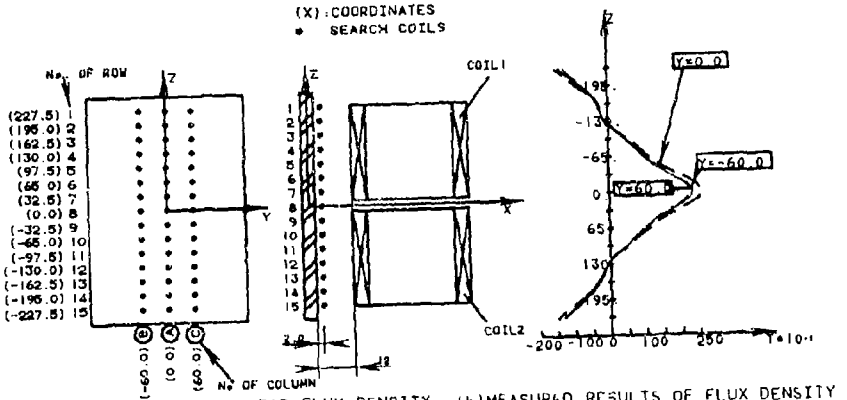

(a)SPECIFIED POSTIONS FOR FLUX DENSITY (b)MEASURED RESULTS OF FLUX DENSITY

Fig.5 MEASUREMENT OF FLUX DENSITY

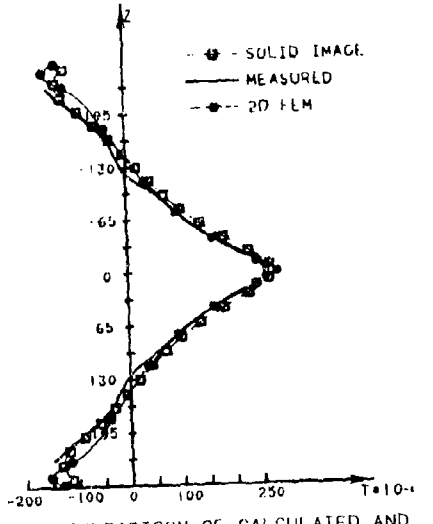

Fig 6 COMPARISON OF CALCULATED AND MEASURED FLUX DENSITY

SESSION 15- "TIME DOMAIN METHODS"

Moderator: Gerald Burke

COMPARISON OF GTD AND MOM SCATTERING COMPUTATIONS AND TRANSFORMATION TO THE TIME DOMAIN

by

Paul G. Elliot
ARCO Power Technologies, Inc.
1250 24th St. NW, Suite 850
Washington, DC 20037
(202) 223-8808

Ira Kohlberg, President
Kohlberg Associates
PO Box 23077, Alexandria, VA 22304
(703) 751-5637

ABSTRACT

Frequency domain scattered fields are computed using the Method of Moments (MOM) and the Geometrical Theory of Diffraction (GTD). An inverse Fourier transform is used to obtain the time domain field.

The NEC code from Lawrence Livermore Labs was used for the MOM computation, and the Basic Scattering Code (NEC-BSC) from Ohio State University was used for the GTD computation. A comparison of these frequency domain results shows agreement when typical guidelines for the use of these two approaches are met.

The radiating source is a horizontally polarized infinitesimal dipole source over ground. A fence in front of the source backscatters electromagnetic energy to an observer. The fence is modeled somewhat differently in the two models. The MOM fence model consists of three horizontal wires, and the GTD fence model is a single flat plate. The models were designed for a switch from the MOM to the GTD method at a radian frequency of $\omega=10^8$, corresponding to the smallest dimensions of interest. The GTD model thus provides accurate scattering results for frequencies higher than $\omega=10^8$ while the MOM fence model is designed to be accurate below $\omega=10^8$.

The near field options of the codes were used to compute backscattered energy reaching the observer. Both models should be accurate close to $\omega=10^8$, and in fact the magnitude plot shows the best agreement from $\omega=1\times10^8$ to 1.5×10^8. The phase plot shows good agreement from about 0.8×10^8 to 1.8×10^8. At low frequencies the GTD results deteriorate and show erratic spikes.

An inverse Fourier transform is used to convert the wide bandwidth frequency domain scattering transfer function into the time domain with weighting of the frequency domain components by the incident pulse spectrum. The resulting time domain response shows the resolution obtained using this approach.

INTRODUCTION

Electromagnetic fields generated by EMP simulators that reach the suburban communities have recently attracted much attention. One method for limiting these fields is by the use of reflecting and diffracting fences. This study deals with the use of computer models to determine the EMP fields in the presence of simple configurations of fences.

This paper demonstrates the use of frequency domain computer codes for solving this time domain pulse scattering problem. Scattered fields including diffraction are computed using the Method of Moments (MOM) and the Geometrical Theory of Diffraction (GTD). The NEC-MOM code (Version 2) from Lawrence Livermore Labs[1] was used for the MOM computation and the Basic Scattering Code (NEC-BSC) from Ohio State University[2] was used for the GTD computation.

Our investigation describes the time domain solution for a particular geometry, and also compares the NEC-MOM with the NEC-BSC results in the frequency domain. A number of other fence geometries and observer positions have also been modeled using the NEC-MOM and NEC-BSC codes[3]. Time domain measurements made on a scale model of a fence[4] compared well with computer calculations using an algorithm[5] similar to the one described in this paper.

GEOMETRY

One major asset of the NEC-MOM and NEC-BSC codes is the wide variety of 3D geometries that can be modeled. The geometry selected for this presentation is shown in Figure 1. The purpose of the fence is to reduce the magnitude of the electromagnetic field in the suburban region, designated as the "far field" in Figure 1, while minimizing the effect of the fence on the waveform in the region labeled "test point". This paper describes the field at the test point in both the time and frequency domains. Reference 3 describes additional time domain results at numerous field points on both sides of the fence and for several fence geometries.

The geometry consists of a horizontally polarized infinitesimal dipole source placed 20 m over a ground plane at the point labeled "simulator". The fields are computed at the observer position labeled "test point" which is 50 meters behind the source and 5 meters above the ground. A 45 degree conducting inclined fence is placed in front of the source as shown. The fence crossection is shown in Figure 1 since the fence lies parallel to the dimension into the paper. The test point and simulator both lie in the vertical plane of the drawing. A ground conductivity of $\sigma = 0.02$ mhos and ground relative dielectric constant of $\varepsilon_r = 15$ are used in the computations.

COMPUTER MODEL DESCRIPTION

The NEC-MOM code was used for the lower frequencies of the pulse spectrum and the NEC-BSC code provided the GTD solution for the

FIGURE 1. GEOMETRY OF FENCE, SOURCE, AND OBSERVER

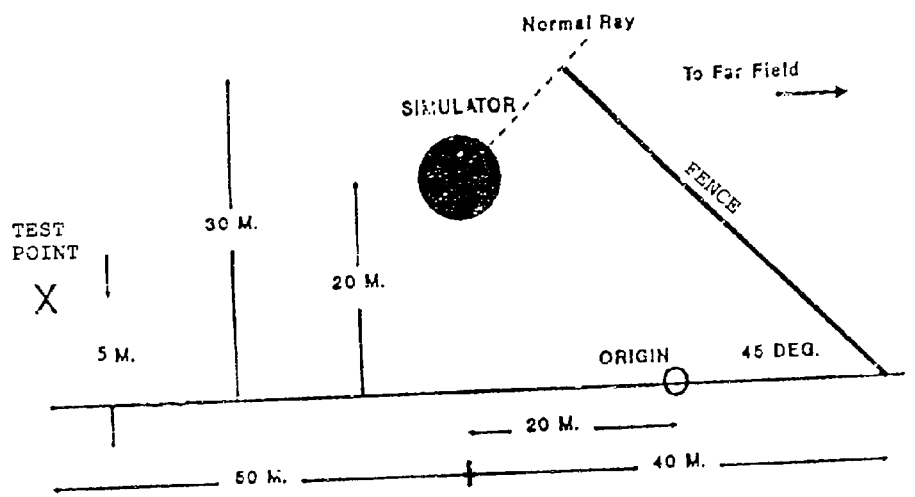

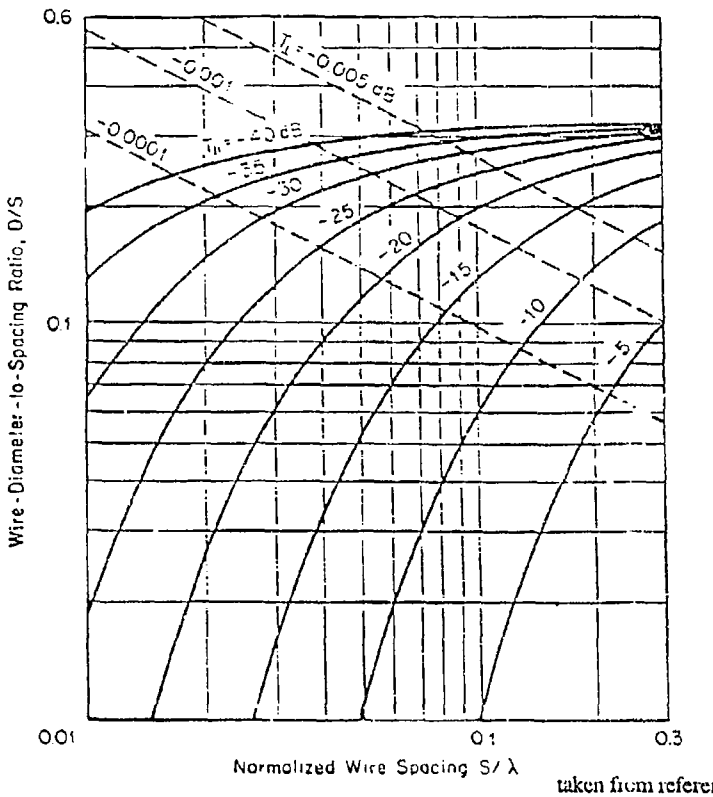

taken from reference 6

Figure 2. Transmission coefficient for parallel and perpendicular polarization for a grid of round wires of diameter D and center-to-center spacing S

higher frequencies. Two different computer models of the same geometry were therefore used for different frequency ranges.

The radiating source in both computer models is a horizontally polarized infinitesimal dipole source over ground. The fence is modeled differently in the two models. The GTD fence model is a single flat conducting plate of the height and inclination shown in Figure 1, and 600 meters long (direction into paper). Plates were not used in the MOM model since that code requires plates to be used only for closed surfaces. For MOM, horizontal wires are used to model the fence. This MOM fence consists of 16 horizontal wires of diameter 0.6 meters spaced 2.83 meters apart. Each of these horizontal wires is 40 meters long (direction into paper) and is segmented into 2 meter long segments.

An angular frequency of $\omega=10^8$ is selected as the transition frequency from MOM to GTD for this geometry, based on the physical dimensions shown in Figure 1, and on computer run time considerations. Since the high frequency GTD computer model runs 350 to 600 times faster than the low frequency MOM model, it is desirable to use GTD for the broadest possible frequency band over which it yields accurate results.

The guidelines for the use of the two codes as follows. The GTD code is most accurate when all dimensions of the structure are longer than approximately one wavelength. The distance from the source to the fence should also be approximately one wavelength or more. The distance of the source to the ground is less critical and may be less than a wavelength. The smallest dimension of the fence is the slant length of 42 meters, and the source is 14 meters from the fence at the closest point. These constraints are approximate so GTD was used to a maximum wavelength of 20 meters, which corresponds to frequencies of $\omega=10^8$ and higher. This should provide good accuracy combined with minimum computer run time.

The MOM fence model is intended to be accurate below about $\omega=10^8$. The 2 meter segments used for the MOM model are 0.1 wavelengths at $\omega=10^8$. As can be determined from Figure 2[6], the MOM fence dimensions given above should limit transmission through the fence to -18 Db of the incident field at $\omega = 10^8$ and to less than -18 Db at lower frequencies. Thus, for all practical purposes the wire model of the fence provides an excellent representation of a perfectly reflecting surface for parallel polarization.

COMPARISON OF MOM AND GTD RESULTS

The near field options of the codes were used for a frequency domain computation of the direct and scattered energy reaching the observer. Figures 3a and 3b show the magnitude and phase of the MOM and GTD results in the frequency domain. These curves are normalized to the field that would be present at the observer position if the same source were radiating into free space (no ground or fence). Due to this normalization the results shown in Figures 3a and 3b will be referred to as the frequency domain

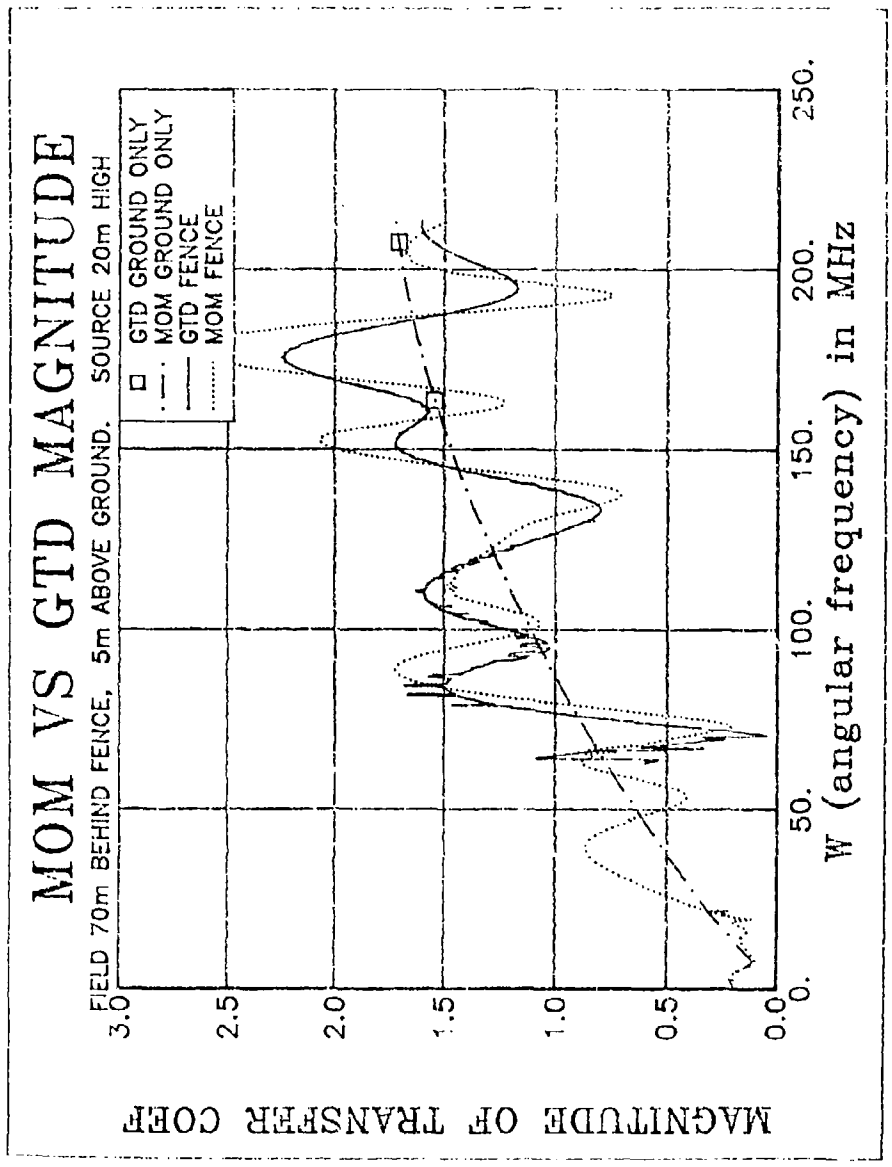
MOM VS GTD MAGNITUDE
FIELD 70m BEHIND FENCE, 5m ABOVE GROUND. SOURCE 20m HIGH
GTD GROUND ONLY
MOM GROUND ONLY
GTD FENCE
MOM FENCE
MAGNITUDE OF TRANSFER COEF
3.0
2.5
2.0
1.5
1.0
0.5
0.0
0.
50.
100.
150.
200.
250.
W (angular frequency) in MHz

FIGURE 3a

FIGURE 3b

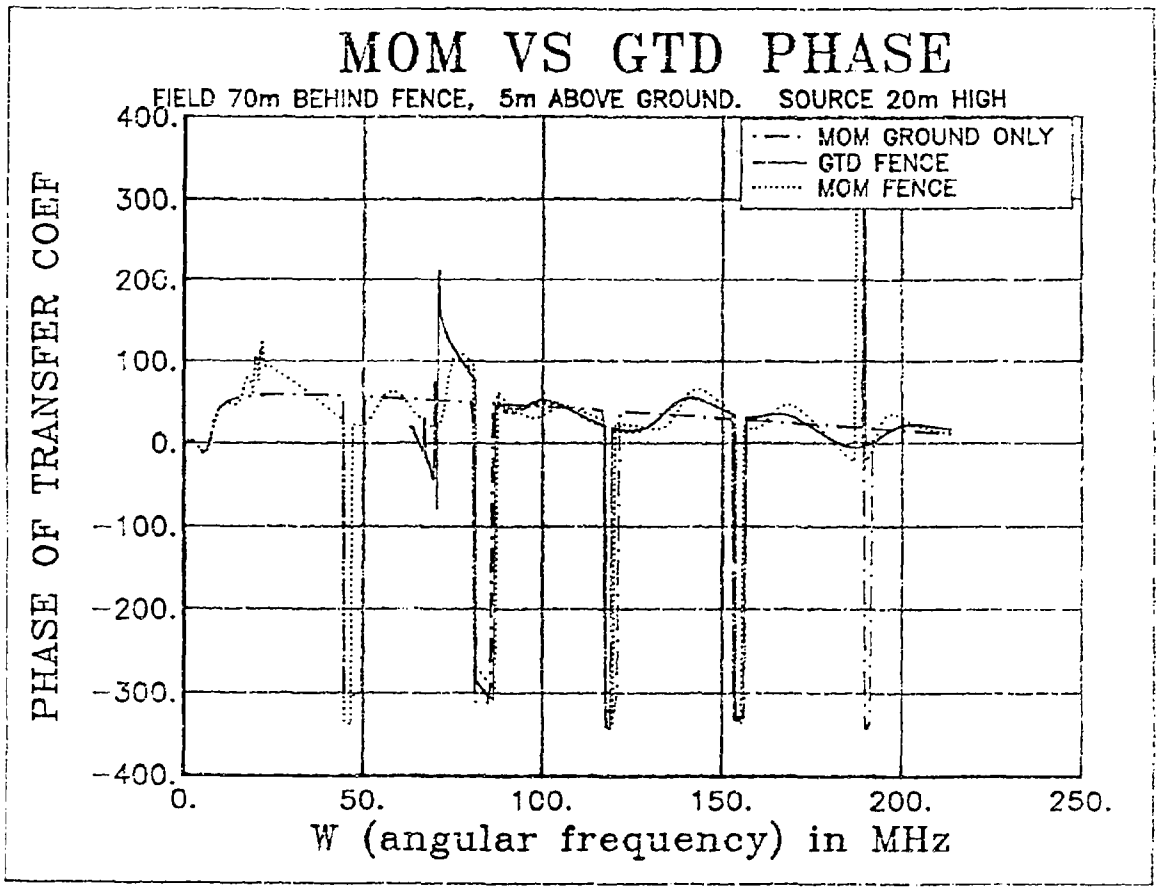
MOM VS GTD PHASE
FIELD 70m BEHIND FENCE, 5m ABOVE GROUND. SOURCE 20m HIGH
MOM GROUND ONLY
GTD FENCE
MOM FENCE
PHASE OF TRANSFER COEF
400.
300.
200.
100.
0.
-100.
-200.
-300.
-400.
0.
50.
100.
150.
200.
250.
W (angular frequency) in MHz

transfer function $T(\omega)$ for the particular geometry and observer position. Also shown in Figure 3a is the magnitude with the ground present but no fence, which is the same result using either of the two computer codes.

The MOM and GTD models should both be accurate close to $\omega=10^8$ as explained above. In fact the magnitude plot shows the best agreement from $\omega=1\times10^8$ to 1.5×10^8. The phase plot shows good agreement from about 0.8×10^8 to 1.8×10^8. At low frequencies the GTD results deteriorate and show erratic spikes.

CONVERSION TO TIME DOMAIN

The time domain response to a pulse was calculated by inverse Fourier transforming the weighted frequency domain transfer function $T(\omega)$. $T(\omega)$ was weighted in the frequency domain by the frequency spectrum of the incident pulse using a formula typically used to describe EMP pulses[7]:

$$E(t) = E_o\,[\exp(-\beta t) - \exp(-\alpha t)]$$

where $\alpha = 4 \times 10^8$ and $\beta = 6 \times 10^6$. 1500 values for the frequency domain transfer function $T(\omega)$ shown in Figures 3a and 3b were computed between DC and $\omega = 10^{10}$. 500 of these points were below $\omega = 10^8$ and so were obtained using MOM. The remaining 1000 points were above $\omega = 10^8$ and so were calculated using GTD.

Curve A of Figure 4 shows the time domain field for the geometry of Figure 1. Curve B is the incident waveform which is the field which would exist in the absence of the ground or fence, and all the curves are normalized to the peak value of this incident waveform. Curve D is the field with no fence but with the ground. Curve D therefore does not show peaks and minima which are produced by reflection and diffraction from the fence. Curve C is the field with the fence and ground except that only the higher frequency components were used; the lower frequency (MOM) results have been omitted from the inverse Fourier transform.

The time of arrival of each ray reflected or diffracted from the fence is shown by the onset of each large ripple in curve A. These results are in excellent agreement with the theoretical predictions using ray theory. A comparison of curves A and C shows that in curve C (only high frequencies used, no MOM results) the onset of the large ripples produced by diffraction occurs before the ray actually arrives at the observer. It is clear that when the full spectrum is not used the time domain results are not correct.

This work was supported by the Harry Diamond Labs under Contract # DAAL002-87-C-0052 with Kohlberg Associates, Inc. Mr. Elliot was a consultant to Kohlberg Associates.

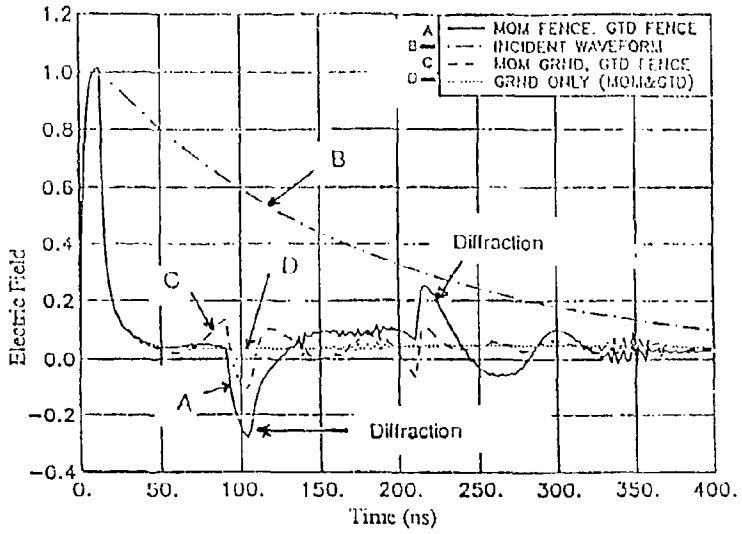

Figure 4. Electric field for point in test volume 50 m from simulator at a height of 5 m for inward inclined fence

1. G.J. Burke and A.J.Poggio, "Numerical Electromagnetics Code (NEC) -- Method of Moments", Lawrence Livermore National Laboratory, Report UCID-18834, January 1981.

2. R.J. Marhefka and W.D.Burnside, "Numerical Electromagnetics Code - Basic Scattering Code, NEC-BSC (Version 2) Part 1: Users Manual," Technical Report ESL7122-4214, Ohio State University Electroscience Laboratory, Columbus, OH, December 1982.

3. I.Kohlberg, P.Elliot, and T.Waltemyer, "Diffraction Techniques for Reducing the Electromagnetic Fields of EMP Simulators Beyond the Test Volume," presented at the 1990 IEEE International Conference on Nuclear and Space Radiation Effects, Reno, NV 16-20 July, 1990.

4. J. Loftus, V.Fronczak, and I. Kohlberg, "A Comparison of the Diffracted Fields as Measured and Predicted for a Totally Reflecting Fence in a Scale Model Test for and EMP Simulator," Harry Diamond Laboratories Report HDL-TR-2173, February 1990.

5. I. Kohlberg, "Diffraction of Far Fields Produced by EMP Simulators Due to a Wire Mesh Fence," Harry Diamond Laboratories Report HDL-CR-90-052-2, Kohlberg Associates, Inc., Contract DAAL02-87-C-0052, September 1990.

6. R. Johnson and H. Jasik, Antenna Engineering Handbook, McGraw-Hill, NY, 1984. pg. 46-6.

7. Y. Lo and S. Lee, Antenna Handbook, Van Nostrand Reinhold, NY, 1988. pg.30-3.

EVALUATION OF MODIFIED LOG-PERIODIC ANTENNAS FOR TRANSMISSION OF WIDE-BAND PULSES *

G. J. Burke
Lawrence Livermore National Laboratory
P.O. Box 5504, L-156, Livermore, CA 94550

Abstract

Modified forms of the log-periodic dipole antenna have been proposed in the literature for radiating a short pulse with minimum distortion and also for a phase response tailored to compress a linear FM pulse. These designs are reviewed, and the antennas are evaluated by numerical modeling with the frequency domain code NEC. Responses for transient input signals are obtained from the NEC solution by inverse transforming and convolution. Antennas modified to obtain a linear phase characteristic are seen to be effective in transmitting an input pulse with minimum distortion. The antennas for compressing a linear FM pulse are somewhat effective but do not appear to work as well as might be expected.

Introduction

The log-periodic dipole (LPD) antenna can operate over a very wide frequency band, limited only by mechanical constraints. However, the antenna introduces significant distortion when radiating a transient signal, due to its nonlinear phase-versus-frequency response. A modified design has been proposed by Yatskevich and Fedosenko in [1] to reduce distortion of a pulse by making the phase response linear or, more generally, to develop a filter characteristic for compressing a signal such as a linear FM pulse. Some results from numerical modeling of these linear-phase and FM-compression antennas are presented here to evaluate their effectiveness.

Standard LPD antennas are constructed as an array of parallel dipoles arranged so that their ends subtend a constant angle α, as shown in Figure 1. The lengths of successive dipole elements form a geometric progression with scaling factor $\tau < 1$, so that

$$\frac{\ell_n}{\ell_{n-1}} = \frac{r_n}{r_{n-1}} = \frac{d_n}{d_{n-1}} = \tau. \tag{1}$$

The dipoles are fed with a transmission line that reverses phase between each pair of dipoles. Another parameter often used to describe a LPD antenna is

$$\sigma = \frac{d_n}{2\ell_n} = \left(\frac{1-\tau}{4}\right)\cot\alpha.$$

Thus σ is the distance in wavelengths from a $\lambda/2$ resonant element to the next smaller dipole in front of it. Values of σ are typically in the range 0.06 to 0.22, with τ in the range 0.78 to 0.98. Carrel [2] determined that the optimum gain for a given τ occurs with

$$\sigma \approx 0.22\tau - 0.0335. \tag{2}$$

* Work performed under the auspices of the U. S. Department of Energy by the Lawrence Livermore National Laboratory under Contract W-7405-Eng-48.

The transient responses of LPD antennas shown here have been obtained by running the frequency domain Moment-Method code NEC [3] and then inverse transforming and convolving the result with an input pulse function. In the NEC model, the radiating elements are broken into small segments, and the mutual interactions of all segments are computed to form an interaction matrix. The ideal transmission line equations are applied to establish a relation between voltage and current at the transmission line connection points (using TL commands.) The combined system of transmission line and electromagnetic interaction equations is then solved by NEC to obtain the current on the radiating elements. Yatskevich and Fedosenko employed an equivalent method described in [4].

LPD antennas can also be modeled directly in the time domain using the code TWTD [5]. Since TWTD does not include a model for ideal transmission lines, it is necessary to model the transmission line wires with segments. The transmission line is placed in a plane normal to the plane of the radiating elements, and the elements on either side of the antenna connect alternately to the top or bottom transmission line wire to obtain the required phase reversal. This explicit transmission line model more closely resembles the way that LPD antennas are typically built than does the implicit transmission line model in which the dipoles lie in a plane. However, both models give essentially the same results through the operating band of the antenna for typical transmission lines. Transient responses of LPD antennas obtained from NEC results and convolution have been found to agree very well with measurements.

In the following sections the designs proposed by Yatskevich and Fedosenko to radiate a pulse with minimum distortion and to compress a linear FM signal are outlined and the transient responses obtained from NEC are compared with those in [1].

The Linear-Phase Antenna for Pulse Transmission

It is well known that when a transient signal is fed into a LPD antenna the radiated field is greatly distorted from the input pulse. Input of a short pulse, such as a Gaussian, results in a down-chirp radiated field. Yatskevich and Fedosenko note in [1] that this distortion is due to the nonlinear phase response of the standard LPD array. With the element ends subtending a constant angle, the distance in wavelengths of a resonant $\lambda/2$ element from the apex is constant. However, the radiated field changes phase by π radians when the frequency increases by a factor of τ due to the reversal of the transmission line between elements. Thus the phase of the radiated field varies as

$$\psi(\omega) = \frac{\pi}{\ln \tau} \ln(\omega/\omega_1).$$

Yatskevich and Fedosenko modified the antenna to produce a more linear phase characteristic. The resonant frequencies of successive elements in their antenna are related by an arithmetic progression with frequency increment $\delta\omega$, as

$$\omega_n = \omega_1 + (n-1)\delta\omega; \qquad n = 1, 2, \ldots, N$$

with element lengths

$$\ell_n = \ell_1/[1 + (n-1)\delta\omega/\omega_1]. \tag{3}$$

Since the elements in their antenna still subtend a constant angle α, the distance of the resonant element from the apex should remain constant over the band of the antenna. Thus the phase should change by π with a frequency increment of $\delta\omega$, so that

$$\psi(\omega) = -\pi\omega/\delta\omega.$$

This argument neglects the possible frequency-dependent phase velocity of the transmission line in the antenna, but results in [1] and here show that the antenna works reasonably well.

The linear-phase design for transmitting a pulse with minimum distortion was tested for a 18 element antenna. A standard LPD antenna was considered first, with longest element of length 0.88 m, and with $\tau = 0.915$, $\sigma = 0.168$ and $\alpha = 7.21$. This is an optimum design according to equation (2), covering a band of about 170 to 700 MHz. A comparable linear-phase antenna used 18 elements with the same largest and smallest elements, and the same α, but with element lengths determined from equation (3) with $\delta\omega/\omega_1 = 0.207$. The transmission line impedance in each case was 100 ohms. These two antennas are shown in Figure 2. The effect of scaling the elements by equation (3) rather than (1) is to crowd the elements toward the small end with increased spacing for the large elements.

The antennas were modeled at 10 MHz steps in frequency from 10 MHz to 1 GHz, with a source of 1 volt and a generator impedance of 50 ohms. The transfer function obtained for radiated field was then resampled, inverse transformed and convolved with a Gaussian input pulse with 1 ns FWHM. Comparison of the 18 element LPD and linear-phase antennas in Figures 3 and 4 shows a considerably more linear phase response for the modified antenna. The transient response in Figure 4 is compressed, and its peak amplitude exceeds that of the standard LPD antenna in Figure 3 by a factor of nearly two. The increased spacing of the elements with the linear-phase design is seen to degrade the low frequency performance, however.

The degradation at low frequencies can be partially overcome by increasing the number of radiating elements. A 30 element antenna analyzed in [1] gives a cleaner impulse response than the 18 element antenna. NEC modeling confirmed the effectiveness of the 30-element design.

Pulse Compression Antennas

Yatskevich and Fedosenko show that this concept of tailoring the phase response of the antenna can be generalized by selecting the resonant frequencies ω_n of the radiating elements to obtain a phase response

$$\psi(\omega_n) = \psi(\omega_1) - (n-1)\pi. \tag{4}$$

They apply this method to compress a linear FM signal of the form

$$u(t) = \begin{cases} u_0 \cos\left(\omega_0 t + \frac{\Delta\omega^2 t^2}{2B}\right), & \text{for } |t| \le t_u/2, \\ 0, & \text{for } |t| > t_u/2, \end{cases}$$

where ω_0 is the mean frequency, t_u is the duration of the signal, $\Delta\omega$ is the bandwidth and $B = \Delta\omega t_u$. The spectrum of this signal, assuming $B \gg 1$, is

$$U(\omega) \approx u_0 \frac{\sqrt{\pi B/2}}{\Delta\omega} e^{-j\frac{B(\omega-\omega_0)^2}{2\Delta\omega^2}} \tag{5}$$

over the frequency range $\omega_0 - \Delta\omega/2 < \omega < \omega_0 + \Delta\omega/2$.

The antenna is required to act as an optimum filter, with the conjugate phase response to (5). Thus

$$\psi(\omega) = B(\omega - \omega_0)^2/2\Delta\omega^2 - \omega t_0 \tag{6}$$

where t_0 is a time delay chosen to obtain a realizable antenna. Substituting (6) into (4) and solving for ω_n yields

$$\omega_n = \omega_0 + \frac{\Delta\omega t_0}{t_u}\left\{1 - \sqrt{1 - \frac{2t_u}{\Delta\omega t_0^2}\left[t_0(\omega_1 - \omega_0) - \frac{t_u}{2\Delta\omega}(\omega_1 - \omega_0)^2 + (n-1)\pi\right]}\right\}$$

Assuming $\omega_0 = \omega_1 + \Delta\omega/2$ as in [1], this result becomes

$$\omega_n = \omega_1\left[1 + \frac{\Delta\omega}{\omega_1}\left(0.5 + \gamma - \sqrt{(0.5+\gamma)^2 - 2\pi(n-1)/B}\right)\right]$$

where $\gamma = t_0/t_u$. Thus the element lengths scale as

$$\ell_n = \ell_1 \Big/ \left[1 + \frac{\Delta\omega}{\omega_1}\left(0.5 + \gamma - \sqrt{(0.5+\gamma)^2 - 2\pi(n-1)/B}\right)\right].$$

Yatskevich and Fedosenko consider a linear FM signal with $B = 40\pi$ and $\Delta\omega/\omega_0 = 1$. Their antenna uses 30 elements with $\alpha = 4°$ and $\gamma = 0.705$. The ratio of element radius to length was 0.005, and the transmission line impedance was 100 ohms. The antenna modeled here was scaled for a longest element of 0.88 m, so the resonant lengths of the largest and smallest elements were $f_1 = 0.170$ GHz and $f_{30} = 0.511$ GHz. The radiating elements of this antenna are shown in Figure 5.

The response of the antenna, obtained from NEC, is shown in Figure 6, where the radiated field is shown for one volt input and no generator impedance. The input linear FM signal and the resulting field radiated are shown in Figure 7. The radiated pulse is compressed, but not as well as that shown by Yatskevich and Fedosenko in [1]. One uncertainty in this comparison is the source impedance, since a value is not stated in [1]. In addition to the 50 ohms used for the results in Figure 7, we also tried 100 and 1000 ohms. The high impedance was tried because reference [4] mentions fixing the input current, which is equivalent to using a high impedance source. These variations in source impedance did not have a significant effect on the compression of the radiated pulse, although they did alter its amplitude.

The result of convolving the linear FM signal with the impulse response of the optimum filter, having the phase of equation (6) and a constant amplitude from $\omega_0 - \Delta\omega/2$ to

$\omega_0 + \Delta\omega/2$, is shown in Figure 8. This response is close to that shown in [1]. The transfer function of the antenna, computed by NEC, is compared with the ideal transfer function in Figure 9. The magnitude of the antenna response is seen to drop off sharply above about 0.34 GHz. This loss of high frequencies is also noted by Yatskevich and Fedosenko, and the gain in Figure 6b appears to be in close agreement with that shown in [1]. The phase of the antenna response is not plotted in [1], but it is stated that the phase is within ± 10 degrees of the quadratic relation of (6). The phase computed by NEC is close to that of (6) at the lower frequencies, but deviates substantially above about 0.32 GHz. This difference in phase apparently accounts for the reduced compression of the pulse. The phase characteristic is more difficult to obtain than the smoothly varying magnitude, since many samples are needed to avoid aliasing. The antenna response was computed with NEC at 5 MHz increments from 160 to 570 MHz and at 10 MHz increments over the rest of the band from 0 to 1 GHz. The results appeared to be well converged. Also, the radiated power, obtained by integrating the far field (computing average gain), was in balance with the input power minus power dissipated in the terminating load. The computation of the transfer function shown in Figure 6, from 0 to 1 GHz, required 12 hours of CPU time on a VAX 8650.

Conclusions

The concept of modifying a LPD array to produce a desired phase characteristic for transmitting or compressing a pulse appears to have considerable merit, although there are limitations on what can be achieved. The linear-phase modification proposed in [1] is effective for radiating a short pulse with minimum dispersion. However, more elements are needed to cover a given band than with the standard LPD array.

The antenna for compression of a linear FM pulse also is effective, although the radiated pulse obtained from the NEC model is not as clean as that shown in [1]. The reason for this discrepancy has not been determined, although it appears possible that the pulse shown in [1] could be the response of the ideal filter, which is then broadened by the reduced bandwidth of the antenna. Statements in [1] appear somewhat ambiguous on this point. Another possibility is that the result shown in [1] is for a different antenna than is described.

The simple analysis used in deriving the element spacings in [1] probably does not lead to a completely optimum design. The antennas might be further optimized by adjusting the elements to correct phase errors revealed by the numerical model, although the potential gain is not known. Also, an analysis in terms of $k - \beta$ diagrams for propagation on the locally-periodic structure might lead to a better understanding of the possibilities and limitations of these antennas.

References

[1] V. A. Yatskevich and L. L. Fedosenko, "Antennas for Radiation of Very-Wide-Band Signals," *Radio Electronics and Communication Systems*, Vol. 29, No. 2, pp. 62-66, 1986.

[2] R. Carrel, "The Design of Log-Periodic Dipole Antennas," *IRE International Convention Record*, Vol. I, pp. 61-75, 1961.

[3] G. J. Burke and A. J. Poggio, *Numerical Electromagnetics Code (NEC) - Method of Moments*, Lawrence Livermore National Laboratory, Rept. UCID-18834, Jan. 1981.

[4] V. A. Yatskevich and V. M. Lapitskij, "Exact and Approximate Methods of Calculating Log-Periodic Dipole Antennas," *Radio Electronics and Communication Systems*, Vol. 22, No. 5, pp. 64-67, 1979.

[5] E. K. Miller, A. J. Poggio and J. G. Burke, "An Integro-Differential Equation Technique for the Time-Domain Analysis of Thin Wire Structures, I. The Numerical Method," *Journal of Computational Physics*, Vol. 12, No. 1, May 1973.

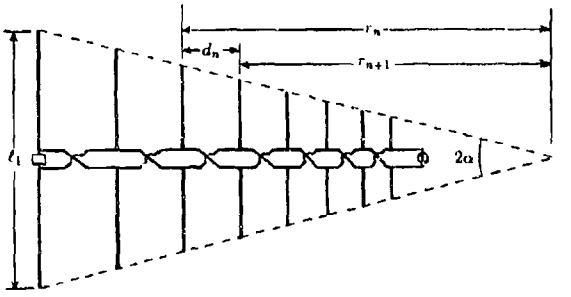

Fig. 1. Log-periodic dipole antenna geometry.

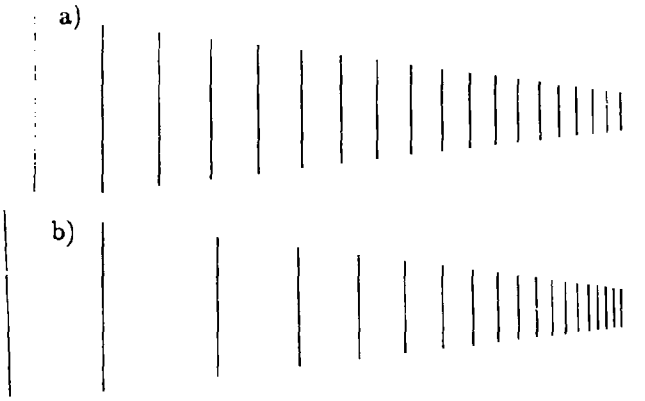

Fig. 2. Radiating elements of a) an 18 element LPD antenna with $\tau = 0.915$, $\sigma = 0.168$ and $\alpha = 7.21°$ and b) a similar linear-phase antenna with $\delta\omega/\omega_1 = 0.207$.

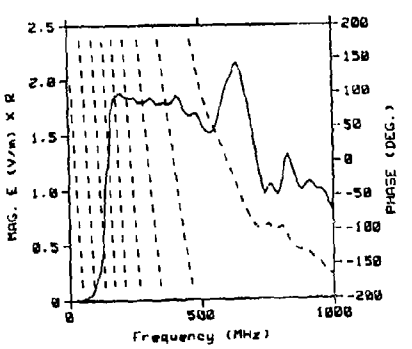

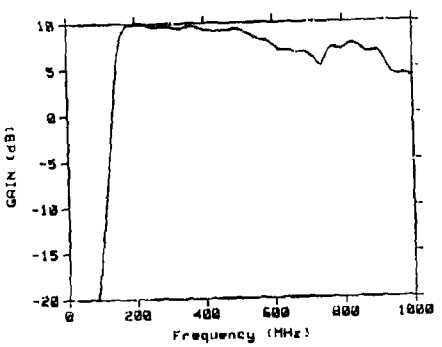

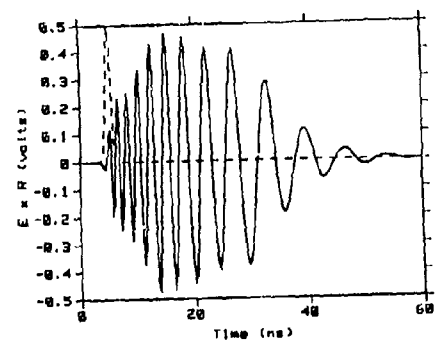

Fig. 3. Response of an 18 element log periodic antenna from Fig. 2, with $\tau = 0.915$. Shown are radiated field magnitude (———) and phase (– – –), power gain and transient response to a Gaussian pulse 1 ns FWHM.

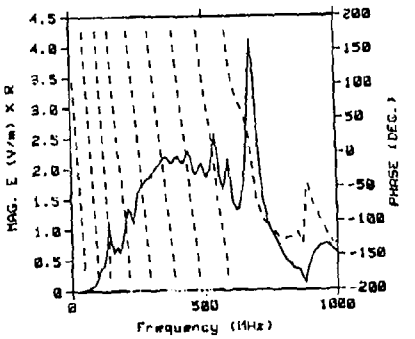

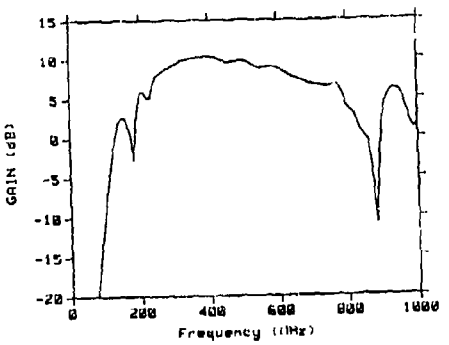

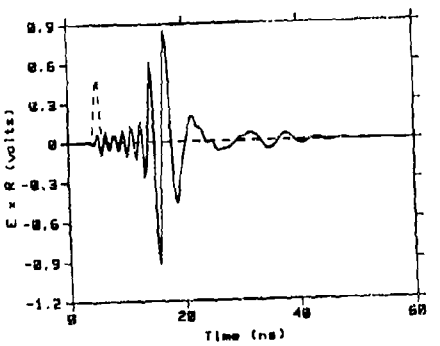

Fig. 4. Response of an 18 element linear phase antenna from Fig. 2. Shown are radiated field magnitude (———) and phase (– – –), power gain and transient response to a Gaussian pulse 1 ns FWHM.

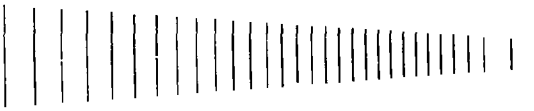

Fig. 5. Radiating elements of a thirty-element antenna for compressing a linear FM pulse, with $\Delta\omega/\omega_1 = 2$, $B = 40\pi$ and $\gamma = 0.705$.

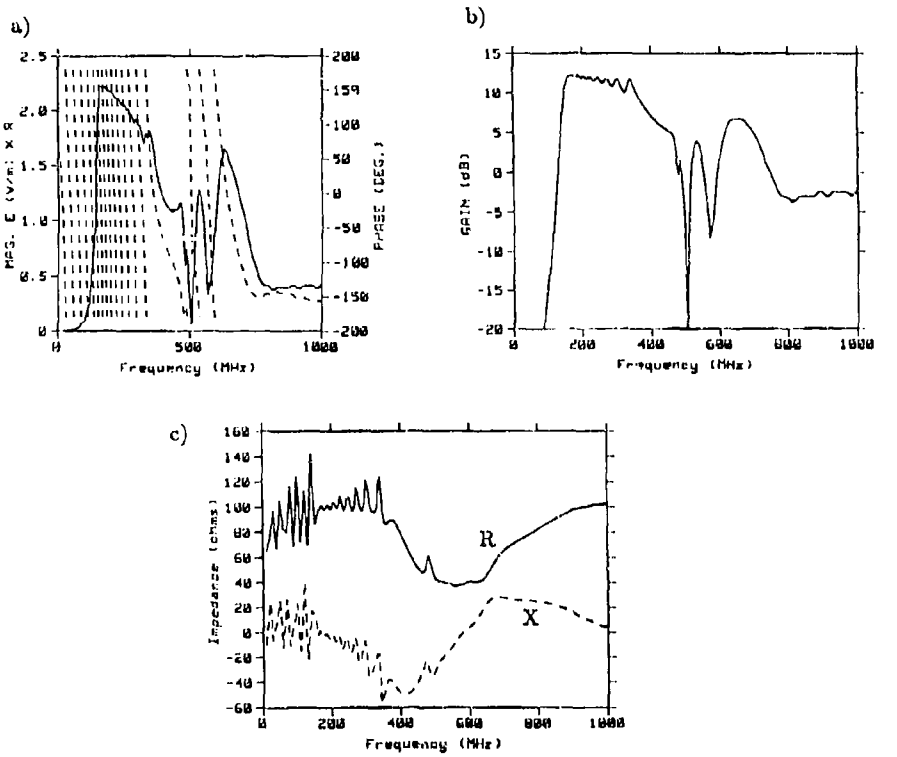

Fig. 6. Frequency response of the thirty-element antenna in Figure 5, showing a) radiated field magnitude (———) and phase (– – – –) on axis for one volt input, b) power gain relative to an isotropic source and c) input impedance.

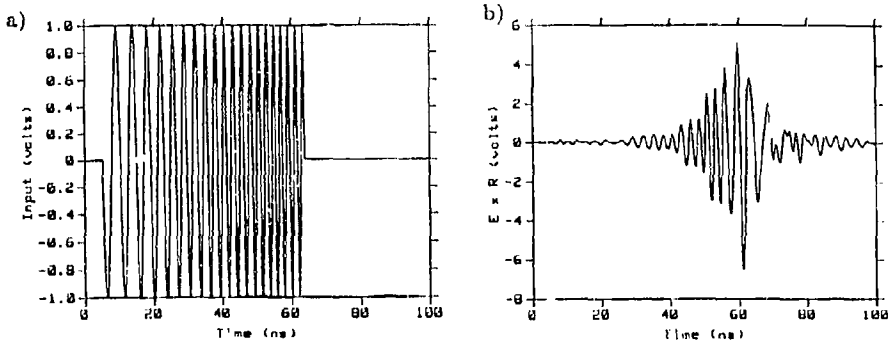

Fig. 7. Transient response of the pulse compression antenna of Figure 5 , showing a) linear FM input pulse with $f_0 = \Delta f = 0.34091$ GHz and $t_u = 58.667$ ns and b) radiated field of the antenna on axis.

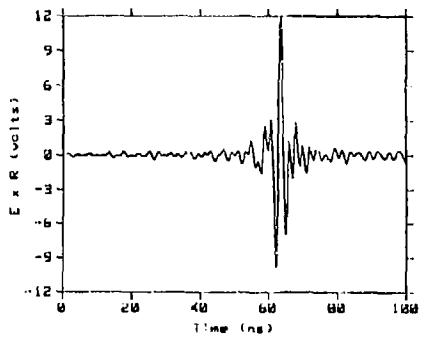

Fig. 8. Result of convolving a linear FM signal with $f_0 = \Delta f = 0.34091$ GHz and $t_u = 58.667$ ns with the optimum filter response having the phase of equation (6).

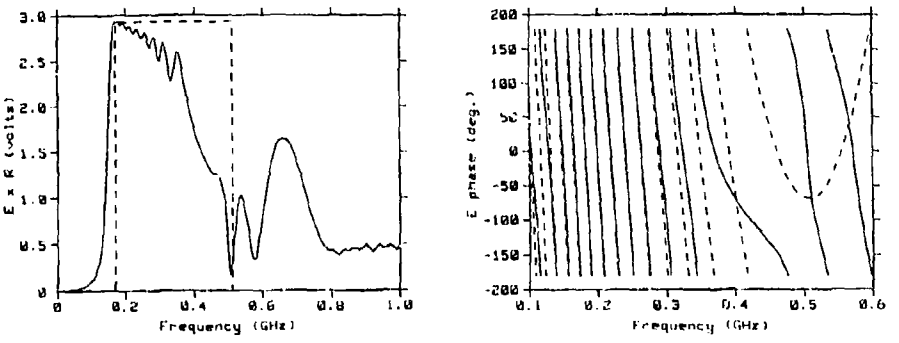

Fig. 9. Comparison of the response of the pulse compression antenna in Figure 5 computed by NEC for a 50 ohm source (———) with the optimum-filter response (– – – –).

The Pulsed Response From a Parabolic Reflector Antenna

G. R. Salo
BDM International, Inc.
Albuquerque, NM

INTRODUCTION

The radiated pulsed response of the parabolic reflector antenna system shown in figure 1 is presented in this paper. The emphasis of the current modeling effort was to determine the transmitted pulse characteristics of this antenna system, i.e., the peak amplitude, rise time, and pulse width of the transmitted pulse. It was initially hoped that an antenna system of this type would be able to transmit high gain, short pulses at large distances. Results from this initial phase of analysis are very encouraging. These results along with a detailed description of the models developed will be given.

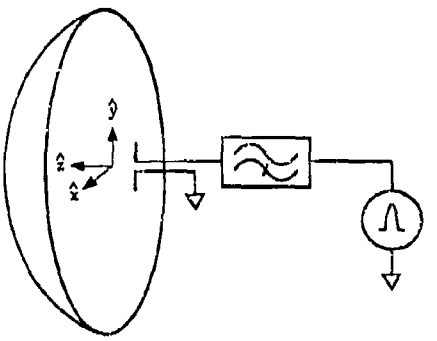

Figure 1. Parabolic reflector antenna system.

METHODOLOGY

This section discusses the methodology employed during the analysis and describes the models developed for each component of the antenna system. A goal of this analysis was to determine the transmitted field strength relative to the input signal level. For this reason, a complete characterization of the antenna system from the source to the radiated fields was necessary. As shown in figure 1, there are three major components in this antenna system - the source, feed, and reflector. Each of these components were modeled individually and are discussed in detail below.

The Source

The source was modeled as an ideal Gaussian voltage generator in series with a high pass filter. The waveform produced by the generator is given in equation 1 and plotted in figure 2. With $1/a$ set equal to 1 ns, a pulse width of 1.7 ns and a rise time of 1.2 ns is produced. In figure 2, t_0 was set equal to 25 ns to allow for easier viewing of the entire pulse.

$$v(t) = e^{-a^2 (t-t_0)^2} \qquad (1)$$

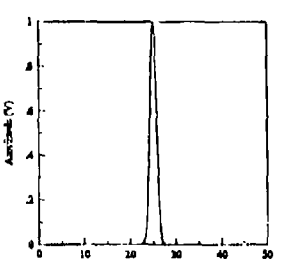

Figure 2. Waveform produced by Gaussian voltage generator.

The output of the voltage generator was fed directly into a high pass filter to remove the low frequency content of the voltage source. The model developed for the parabolic reflector (given below) is most accurate when the wavelength is small relative to the dimensions of the reflector. Therefore, removal of the low frequencies (large wavelengths), was performed to improve the overall accuracy of this analysis.

A single pole high pass filter with a lower cutoff frequency of 100 MHz was used in this analysis. Its frequency response is given in equation 2 while a plot of its magnitude and phase responses are given in figures 3 and 4.

$$F(\omega) = \frac{j\omega}{j\omega + 2\pi f_c} \qquad (2)$$

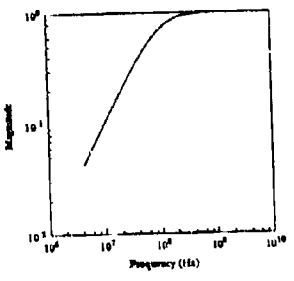

Figure 3. Magnitude response of the high pass filter.

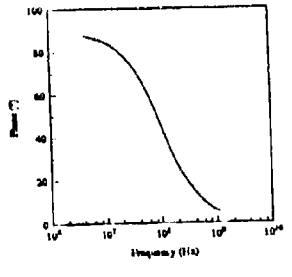

Figure 4. Phase response of the high pass filter.

The result of passing the Gaussian signal through the high pass filter is shown in figure 5. The rise time is essentially unchanged at 1.2 ns while the pulse width has increased to approximately 10 ns.

The Feed

The feed section (see figure 6) was modeled as a short dipole with resistive losses. To avoid any resonances with the feed, an extremely

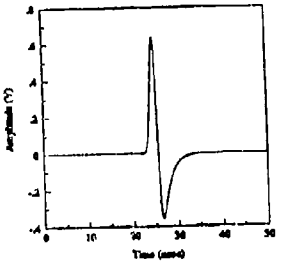

Figure 5. The Gaussian pulse after being filtered.

short, thin feed section was chosen. In this analysis, δl was set equal to 0.03 m while the ratio of $\delta l / d$ was set equal to 100.

The resistive losses of the dipole feed were assumed to consist of radiation and ohmic losses as given in equation 3[1]. A plot of $R(\omega)$ is given in figure 7 where σ is 50 Mmhos/m.

$$R(\omega) = \frac{\delta l}{\pi d}\sqrt{\frac{\omega\mu}{2\sigma}} + \frac{\omega^2\mu\sqrt{\mu\varepsilon}}{6\pi}\delta l^3 \qquad (3)$$

The current distribution on the dipole feed was assumed to be uniform and is given in equation 4, where $V(\omega)$ is the Fourier transform of the voltage source. Figures 8 and 9 are plots of $V(\omega)$ and $I_0(\omega)$.

$$I_0(\omega) = \frac{V(\omega)}{R(\omega)} \qquad (4)$$

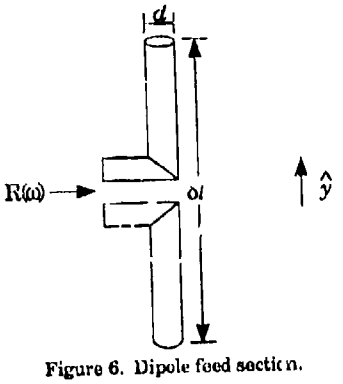

Figure 6. Dipole feed section.

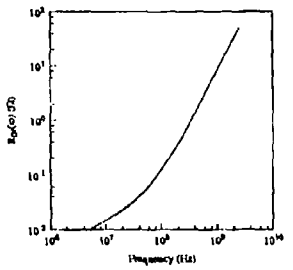

Figure 7. Dipole feed input impedance.

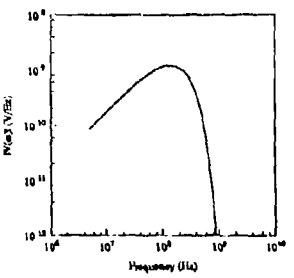

Figure 8. Fourier transform of filtered, gaussian pulse.

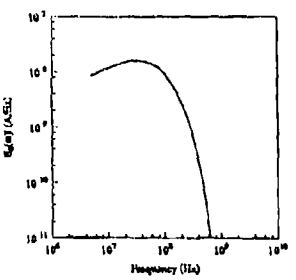

Figure 9. Fourier transform of the current on the dipole feed antenna.

The radiated far fields produced by the dipole feed are given in equation 5. It was assumed that these were the incident fields at the parabolic reflector's surface. This assumption is fairly accurate since the dipole feed is very short, the low frequencies have been attenuated, and the minimum distance (the focal length) to the reflector's surface is 10 m.

$$\vec{E} = -j\omega\mu I_0 \delta l \frac{e^{-jkr}}{4\pi r}\left(\hat{\theta}\cos\theta\sin\phi + \hat{\phi}\cos\phi\right)$$
$$\vec{H} = jkI_0\delta l \frac{e^{-jkr}}{4\pi r}\left(\hat{\theta}\cos\phi - \hat{\phi}\cos\theta\sin\phi\right) \quad (5)$$

The Reflector

The fields scattered off of the parabolic reflector are calculated by geometric optics[2]. The radiated electric far field produced by the short dipole feed antenna (located at the focal point) provided the excitation. Geometric optics was then used to calculate the scattered electric field in the xy plane that goes through the focal point of the parabolic reflector as given in equation 6 (where f is the focal length of the parabolic reflector). The fields are assumed to be zero outside of the parabolic reflector's projected area on this plane (i.e., outside of the circle described by the reflectors edge). Given these fields, equivalent magnetic sources are found through the equivalence principle (equation 7). These sources are then used to calculate the electric vector potential (equation 8), from which the electric and magnetic fields in the far field can be found (equation 9).

$$\vec{E}_{ap} = j\omega\mu f I_0 \delta l \frac{e^{-jk2f}}{\pi}\left(-\hat{x}\frac{2xy}{(x^2+y^2+4f^2)^2} + \hat{y}\frac{(x^2-y^2+4f^2)}{(x^2+y^2+4f^2)^2}\right) \quad (6)$$

$$\vec{M}_{ap} = 2\vec{E}_{ap} \times (-\hat{z}) \quad (7)$$

$$\vec{F} = \frac{e^{-jkr}}{4\pi r}\iint_{s'}\vec{M}(s')\,e^{jkr'\cdot\hat{r}}\,ds' \quad (8)$$

$$\vec{E}_{ff} = -\nabla \times \vec{F}$$
$$\vec{H}_{ff} = \frac{-1}{j\omega\mu}\nabla \times \vec{E}_{ff} \quad (9)$$

When calculating the electric field potential in equation 8, if one is only concerned with the fields along the boresight, the integration can be performed analytically and results in the expression given in equation 10. However, when off boresight angles are desired, the integration can no longer be performed analytically. To perform this integral, a fast Fourier transform (FFT) was used. Comparing a two dimensional Fourier transform integral to the integral in equation 8, it is readily found that equation 8 is of the same form as an inverse, two dimensional Fourier transform.

$$E_\theta = \omega\mu k I_0 \delta l f \left(\frac{d^2}{d^2 + 16f^2}\right) \frac{e^{-jk(r+\delta)}}{2\pi r} \sin\phi$$
$$E_\phi = \omega\mu k I_0 \delta l f \left(\frac{d^2}{d^2 + 16f^2}\right) \frac{e^{-jk(r+\delta)}}{2\pi r} \cos\phi \qquad (10)$$

Throughout this analysis, the parabolic reflector modeled had a focal length of 10 m and a diameter of 20 m.

RESULTS

The results will be presented in three parts. The first part will be the pulse characteristics along the boresight. A comparison between the analytically generated and numerically calculated data will be shown. This comparison is used to validate the numerical technique. The next two parts will show the transmitted pulse characteristics for the E and H planes. In each case, the transmitted pulse waveforms were calculated for a range of 1000 km. However, to make viewing of the waveforms easier, no time shifts (other than the 25 ns offset from the source) were included. Conclusions from these results are presented in the next section.

Boresight

As previously discussed, along boresight the electric vector potential integral (equation 8) can be calculated analytically. This has been performed and the results are shown in equation 10. Off boresight, however, a two dimensional FFT has been used to perform this integration. A comparison between the two methods (on boresight) is shown in figures 10 and 11. As is evident in the figures, the two methods give nearly identical results.

It should be noted that the polarization of the electric field on boresight is in the y direction. Since we are used to working in spherical coordinates when in the far field, the polarization on boresight can be a little confusing. θ and ϕ polarizations will change as our observation angle (ϕ) changes. This is simply an artifact of the spherical coordinate system when θ=0°.

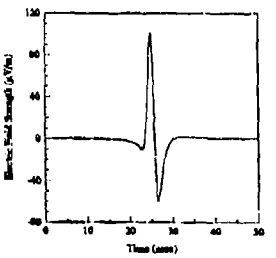

Figure 10. The electric field strength on boresight calculated analytically.

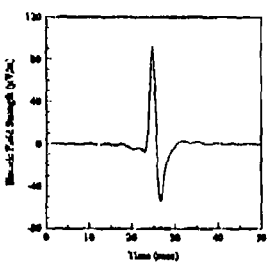

Figure 11. The electric field strength on boresight calculated numerically.

E-Plane

The E-plane is defined as the ϕ=90° plane. Figures 12 through 24 are plots of the electric field for different values of θ. Figures 12 through 18 are plotted on the same scale to allow visual inspection of the pulse amplitude changes as the angle off boresight is changed. Figures 19 through 24 are the same figures replotted to show in detail the pulse characteristics at each angle. At ϕ=90°, the ϕ component of the electric field is zero. Thus, only the θ component of the electric has been plotted.

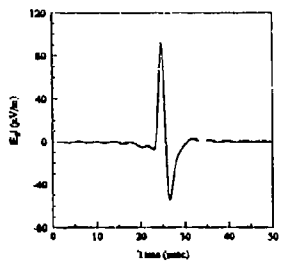

Figure 12. E-plane result for θ=0°.

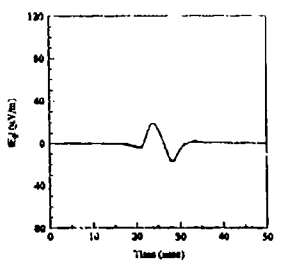

Figure 15. E-plane results for θ=5.4°.

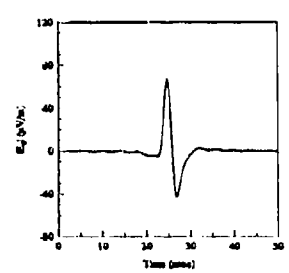

Figure 13. E-plane result for θ=1.8°.

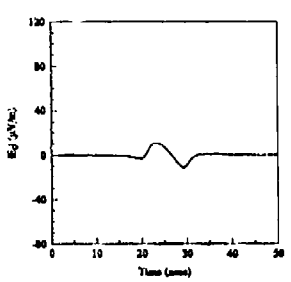

Figure 16. E-plane result for θ=7.2

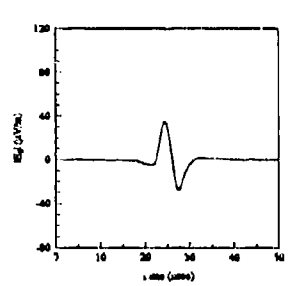

Figure 14. E-plane results for θ=3.6°.

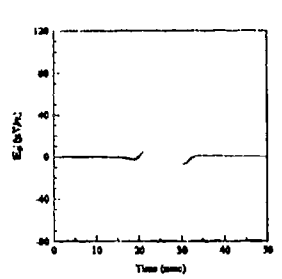

Figure 17. E-plane results for θ=9.0°.

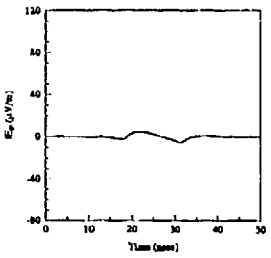

Figure 18. E-plane results for θ=10.8°.

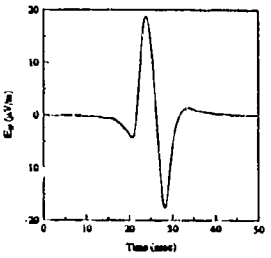

Figure 21. E-plane results for θ=5.4°

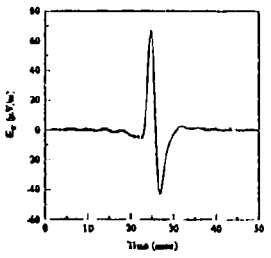

Figure 19. E-plane results for θ=1.8°.

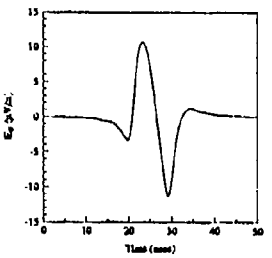

Figure 22. E-plane results for θ=7.2°.

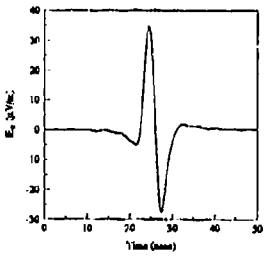

Figure 20. E-plane results for θ=3.6°.

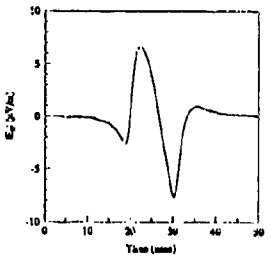

Figure 23. E-plane results for θ=9.0°.

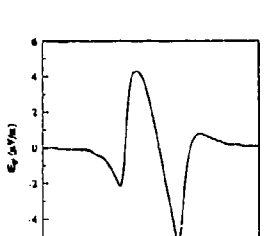

Figure 24. E-plane results for θ=10.8°.

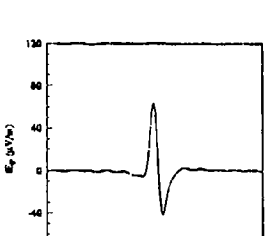

Figure 26. H-plane results for θ=1.8°.

H-Plane

The H-plane is defined as the ϕ=0° plane. Figures 25 through 37 are plots of the electric field for different values of θ. Figures 25 through 31 are plotted on the same scale, while figures 32 through 37 are plotted on different scales for the reasons discussed above. Since ϕ=0°, the θ component of the electric field is zero. Thus, only the ϕ component has been plotted.

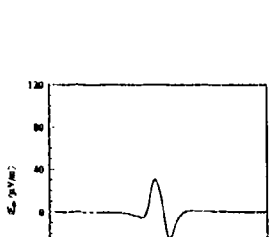

Figure 27. H-plane results for θ=3.6°.

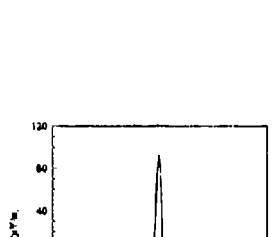

Figure 25. H-plane results for θ=0°.

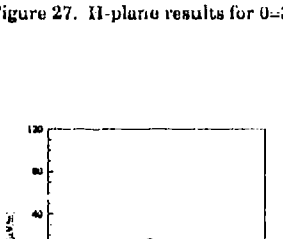

Figure 28. H-plane results for θ=5.4°.

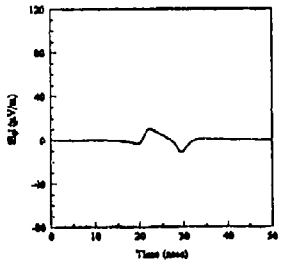

Figure 29. H-plane results for θ=7.2°.

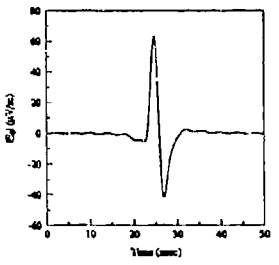

Figure 32. H-plane results for θ=1.8°.

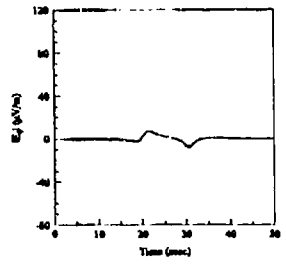

Figure 30. H-plane results for θ=9.0°.

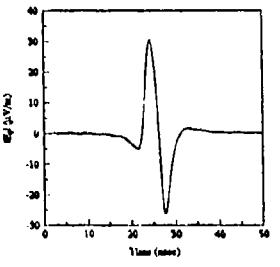

Figure 33. H-plane results for θ=3.6°.

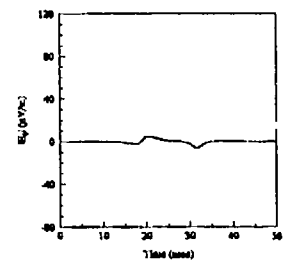

Figure 31. H-plane results for θ=10.8°.

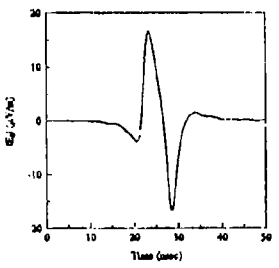

Figure 34. H-plane results for θ=5.4°.

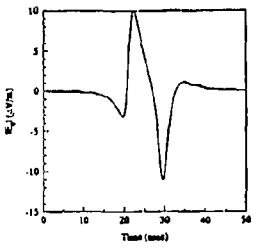

Figure 35. H-plane results for θ=7.2°.

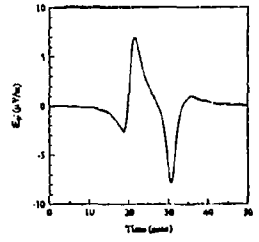

Figure 36. H-plane results for θ=9.0°.

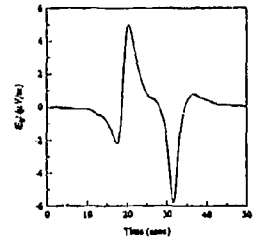

Figure 37. H-plane results for θ=10.8°.

CONCLUSIONS

From the results presented, it is easy to understand why the parabolic reflector antenna system looks to be very promising in its ability to transmit high gain, short pulses. Both the E and H plane results clearly indicate that the transmitted pulse is maximum along boresight and attenuates rapidly with angular deviation from boresight. At five degrees off boresight, the peak amplitudes have decreased approximately by a factor of 5. The amplitudes continue to decrease the further off boresight one goes, however, the assumption about the low frequency content made throughout this analysis begins to fail at extreme off boresight angles. The reason for this is simple. The parabolic reflector is a very high gain antenna at short wavelengths. Thus, the energy from the high frequencies is concentrated along boresight. However, at lower frequencies, the gain begins to broaden and the energy is distributed over a wider range of angles. At large angles off boresight, the relative content of low frequency versus high frequency will be greater than it is along boresight. Since the geometric optics approximation is inaccurate at low frequencies, the relative energy due to the long wavelengths must be small compared to the short wavelengths. Along boresight and near it, this condition is satisfied. However, at large angles off boresight, this condition is no longer true. Therefore, results for angles greater than 10° have not been included.

In addition to the pulse amplitude decreasing, the pulse width increases with angular deviation from boresight. Once again, this is due to the fact that the relative contribution of low frequencies increases as the angle off boresight increases.

RECOMMENDATIONS

Two enhancements could be made to improve the results that have been presented here. The first is to improve upon the feed section. A more realistic feed could be incorporated. This would complicate the analysis considerably and is why it was not performed in this analysis.

The second enhancement would be to improve upon the reflector analysis. Edge effects along with an accurate model for low frequencies could be developed.

REFERENCES:

(1) Warren L. Stutzman and Gary A. Thiele, *Antenna Theory and Design*, John Wiley and Sons, 1981

(2) *Antenna Handbook, Theory, Applications, and Design*, edited by Y.T. Lo and S.W. Lee, Van Nostrand and Reinhold Company, 1988

A RAY-TRACING MODEL TO PREDICT TIME-DOMAIN RCS PERFORMANCE OF A COMPACT RANGE

Norman Carey
Hughes Aircraft Company
El Segundo, California

Steve Brumley
Denmar Incorporated
Carson City, Nevada

Atul Jain
Hughes Aircraft Company
El Segundo, California

Abstract

Characterization of time-domain High Range Resolution (HRR) scattering returns is a valuable tool in evaluating performance of RCS compact range chambers. A code, based on geometrical optics modeling and empirical reflector and absorber data, is described. Results obtained using this computer model are compared with actual downrange RCS plots measured on the Hughes Aircraft Company dual-reflector Vokurka compact range chamber in El Segundo, California. Important mechanisms contributing to the downrange response and to measurement clutter in the sweet spot measurement zone are identified, indicating this to be a useful tool in chamber design and evaluation.

1.0 Introduction

The quality of measurements made in an indoor compact range depends to a large extent upon the level of background clutter in the time vicinity of the target. The background level is due to unwanted returns of similar path length, and to processing sidelobes of bright peaks elsewhere in the room. Before measures can be taken to reduce clutter, the paths involved must be identified, and the potential negative side effects of the design changes estimated.

Time-domain images of compact ranges show contributions from several mechanisms. Some of these can be deduced from the image and from knowledge of the range geometry. Certain comparatively simple effects can be estimated accurately; however, detailed calculations of higher-order interactions are cumbersome, requiring computer assistance. While a great number of versatile RCS prediction codes are available, they are generally unsuitable for modeling complex, electrically large, lossy cavities, such as a compact range. Specialized software exists to compute the near field of a compact range reflector in isolation, but the absence of interactions with other objects restricts its use to prediction of field strength in the quiet zone; clutter in the zone, as seen in time-domain images, cannot be predicted. Another approach approximates profiles of the quiet zone by summation of absorber backscatter components, computed using empirical data for the illumination pattern and absorber RCS [1].

A series of computer codes has explored the applicability of ray tracing to range analysis. The current iteration, Vuku5, employs an extended form of Geometric Optics (GO) to treat nonspecular scattering. Pure GO is quite restricted in its ability to predict calibrated background levels due to its exclusion of nonspecular mechanisms. In particular, the level in the quiet zone around the target cannot be calculated, since this depends on diffraction from the main reflector and backscattering from the side walls. Vuku5 provides facilities for graphical examination of specific paths in isolation

and graphical display of paths in both time and space domains. Design emphasis was placed on the flexibility of the model description language and on the extensibility of the code.

2.0 Theory

Pure GO approximates a wavefront with a set of rays, each of which represents a tube of flux. When a ray strikes a surface, it reflects at the specular angle. In Vuku5, surfaces are considered to be locally planar, so that the tube's cross-sectional area is conserved. Spreading from curved surfaces is then represented by the divergence of the reflected rays as a group, rather than individually. If the surface is lossy, it is described by a gain pattern -- the power of the reflected ray is just the incident power multiplied by the gain at the angle of incidence.

While Vuku5 retains specular reflection as an optional mechanism for metal objects, it extends GO by allowing nonspecular reflection. The spot on a surface illuminated by an incident ray is considered a point source from which ray cones emanate. By the use of ray cones, rather than ray tubes, the wavefront is represented by sections of spherical shells rather than sections of planes. Each ray's power is determined by the source power, the solid angle subtended by the ray, and the surface scattering gain. The gain pattern is determined empirically, usually by measuring the material's RCS per unit area; in general, it is a function of incident and reflected angles.

$$P_r = P_i \cdot G(\theta_i, \theta_r, \phi_i, \phi_r) \cdot \frac{\Omega}{4\pi}$$

where:

P_i	= power of incident ray
P_r	= power of reflected ray
G	= gain of surface
(θ_i, ϕ_i)	= angle of incidence
(θ_r, ϕ_r)	= angle of reflection
Ω	= solid angle of reflected ray

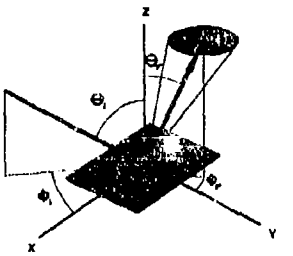

Pure GO calculation requires setting two parameters: angular ray sampling and minimum power threshold. (Equivalent parameterization schemes could certainly be used.) The transmit antenna emits a number of rays which will meet the sampling specified. Each ray then reflects off a number of surfaces until it either strikes the receiver or its power falls below the threshold. Extended GO uses similar parameters, but the angular sampling is used at every (nonspecular) reflection. Each surface illuminated by a ray is treated as a new transmitter. This cascade effect means that the choice of sampling becomes far more critical in determining the number of calculations required.

3.0 Implementation

A compact range is modeled as a set of heterogeneous elements. Each type of element is characterized by a different set of geometric and electrical properties. Geometric shape determines the endpoint of a ray incident on the object. If the object is not a perfect conductor, the electrical properties of its surface are condensed into one or more tables of gain as a function of incident and

reflected angles. For example, a wall is a triangle described by three vectors; it has a scattering gain pattern defining the absorber performance. Besides walls, there are feed horns, parabolic cylindrical reflectors, and plate targets. The code is modularized so that new object types can be added without disturbing existing parts of the program. A generic object's scattering behavior is expressed in a set of functions; versions of these functions are then written to characterize a specific type.

Fine control can be exercised over the scattering process. Angular ray sampling and minimum ray flux threshold can be set globally, with these global figures modified by factors for individual elements. Paths between particular element pairs can be explicitly disabled. Unnecessary shadowing checks can be eliminated on a case-by-case basis, resulting in substantial savings in run time.

Though following nonspecular paths entails substantially more computation time than pure GO, the surface sampling requirement is much less than that of low-frequency techniques such as the Method of Moments.

Ray segments are linked together in a binary tree structure. Retaining the solution in its original form allows portions of the illumination to be separated out based on path length, intersection with a specific volume (e.g. the quiet zone), or radiated power density. Additionally, illumination incident on a rectangular strip can be monitored as a postprocessing step. These analytical procedures are far cheaper, in terms of run time, than generation of the illumination.

Downrange profiles are generated from ray trees as histograms of terminal power versus path length. Actual measurements are typically made in the frequency domain and transformed to time domain after multiplying by a window function. To simulate the resulting peak sidelobes, the computed profile can be convolved with the transform of the window. Without this convolution, the profile simulates what would ideally be achieved with infinite bandwidth and an infinite, constant window.

Two different graphical displays are provided. Ray paths can be overlaid on an orthographic wireframe representation of the chamber, and the whole displayed in perspective with an arbitrary viewpoint, angle and scaling. Cartesian graphs show downrange profiles and illumination cuts with user-definable units, axis ranges, and titles. Graphics are generated by way of a low-level driver which can be easily reimplemented for new physical devices.

4.0 Results

Modeling emphasis was centered on Chamber 1 of the Hughes RCS measurement facility in El Segundo, California [2]. An interior view of the chamber is shown in Figure 1. An idealized model of this chamber was created and tuned with appropriate sampling and threshold factors. Figure 2 shows the model in roughly the same view seen in the photograph, with features shaded and labeled; the two cannot be overlaid due to differences in perspective rendering. Figures 3 - 6 show other views of the model. With the exception of Figure 1, all graphics were originally generated by Vuku5; in Figures 2 and 7, halftoning, arrows, and some text labels have been added using a commercial vector drawing package.

The absorber covered chamber walls were modeled using triangular plates. Tiling on the side walls followed the division between pyramidal and wedge absorber types. Measured RCS per unit absorber area data [3] was condensed into lookup tables for the plates. The March Microwave 3629B/S

reflector system was represented by two parabolic cylindrical mirrors, edged with a zone of isotropic scattering to roughly approximate the serrated edge treatment of the actual reflectors. Gain tables for the mirror center sections were used when necessary to simulate aperture diffraction.

As shown in the figures, the back wall is represented by three separate subwalls. This is necessary to properly model the downrange extent of the 24 inch pyramidal absorber, visible at the resolution of typical measured profiles. The net absorber RCS/area was divided into three separate gain patterns for the subwalls, according to studies of the distribution of returns along the axes of individual pyramids [4]. Vuku5's shadowing control allowed the subwalls to be considered as mutually transparent.

Since the complexity of the model forbad simultaneous computation of all possible paths, the background level was computed as the sum of several particular scattering mechanisms. This technique also facilitated interpretation of the results. The computed and measured background curves at Ku band are shown in Figure 7. Selected components are shown in Figures 8 - 10.

Calibration to dBsm was determined by placing a -13dBsm target (visible in Figures 2 and 3) in the center of the quiet zone and computing its response, analogously to the procedure for a physical compact range. To simulate processing sidelobes, the results were convolved with the transform of the Kaiser-Bessel window used by the HP8510 network analyzer. Since the strong interhorn coupling can affect adjacent levels through the signal processing, an empirical approximation to this term was added.

It will be noted that the interhorn coupling and back wall peaks are translated slightly in range. This effect is thought to be due to differences between the planned and actual locations of the focal point of the reflector system. When the mirrors and feeds are installed in a range, their alignment is adjusted for maximum performance. Thus, blueprint coordinates can only be approximations. Determining the actual positions after installation is difficult in practice, and is considered to be rather less important than ensuring smooth quiet zone illumination. Presumably, this discrepancy affects other peaks as well, but the simplified nature of the model prevents precise peak overlay.

To explore the effects of target/sidewall coupling, a later test series placed a 1 meter square metal plate in the quiet zone, pitched up at 45 degrees to illuminate the ceiling. The effect on the downrange profile is shown in Figure 11; the single peak expected from a plate at broadside is replaced by multiple peaks further downrange. Naturally, the coupling effects from a more typical target (such as an aircraft model) would be less -- the large plate area deliberately exaggerates the effects. The illumination incident on the ceiling is shown in Figure 12; power per 0.1 square meter cell is given as a function of distance from the near end (North) wall. A portion of that illumination is shown in perspective in Figure 13. Note that two separate peaks appear in the downrange profile, since the illuminated spot on the ceiling is received both directly (nearer peak) and back through the plate (farther peak). The direct path (sub/main/plate/ceiling/main/sub) is weaker than the symmetric path (sub/main/plate/ceiling/plate/main/sub) since the gain of the reflector system falls off away from the main axis -- the plate/ceiling/main scattering is nonspecular.

Finally, to provide additional validation, a second compact range was modeled. This was the Hewlett-Packard range in Santa Rosa, California. This chamber resembles the Hughes range in overall design, and shows similar features. Results for X band are graphed in Figure 14.

The most important caveat in examining these results is the simplicity of the reflector edge model. Serrated edges are approximated here by rectangular strips with isotropic, lossless reradiation. The resulting inaccuracy is most noticeable in the reflector backscatter terms. Detailed, quantitative studies of edge-related mechanisms will require data on serration performance, either experimental or theoretical, which was unavailable at this writing.

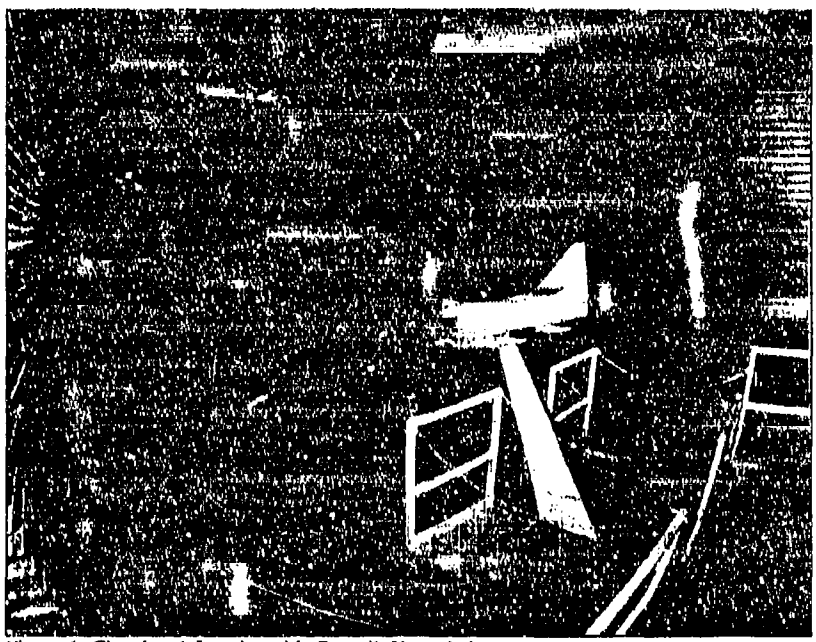

Figure 1: Chamber 1 Interior with Catwalk Extended

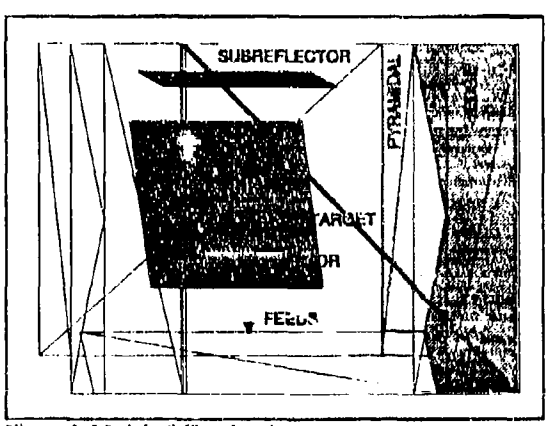

Figure 2: Model of Chamber 1

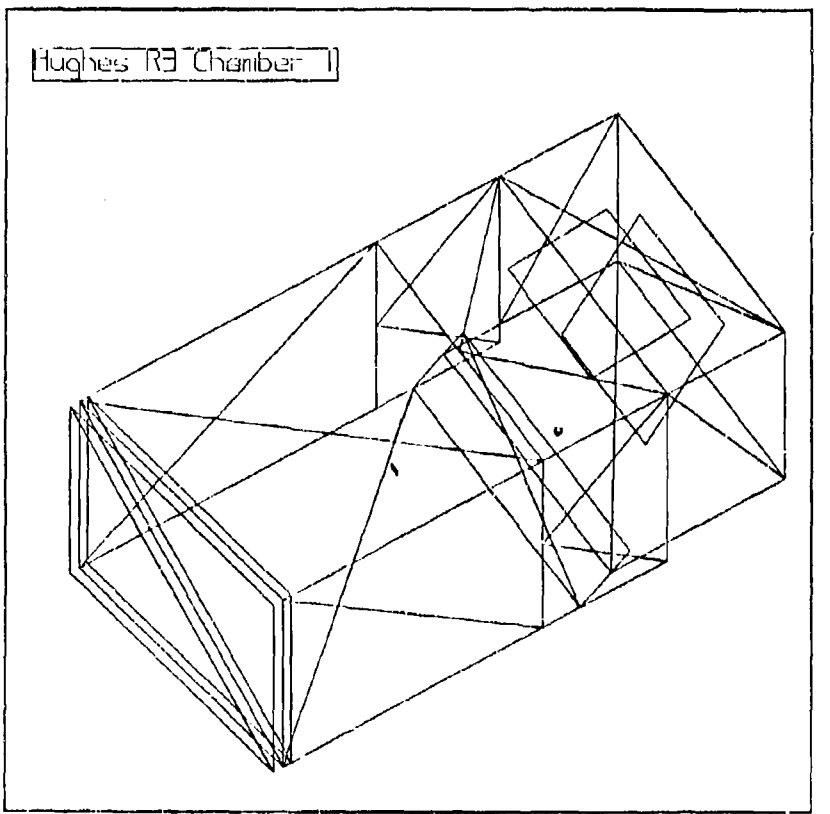

Figure 3: Compact Range Model

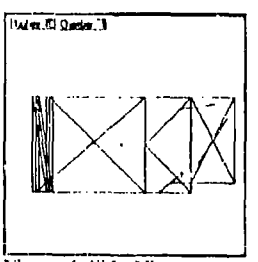

Figure 4: Side View

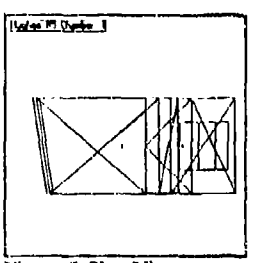

Figure 5: Top View

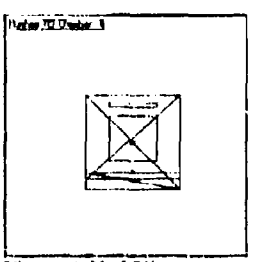

Figure 6: End View

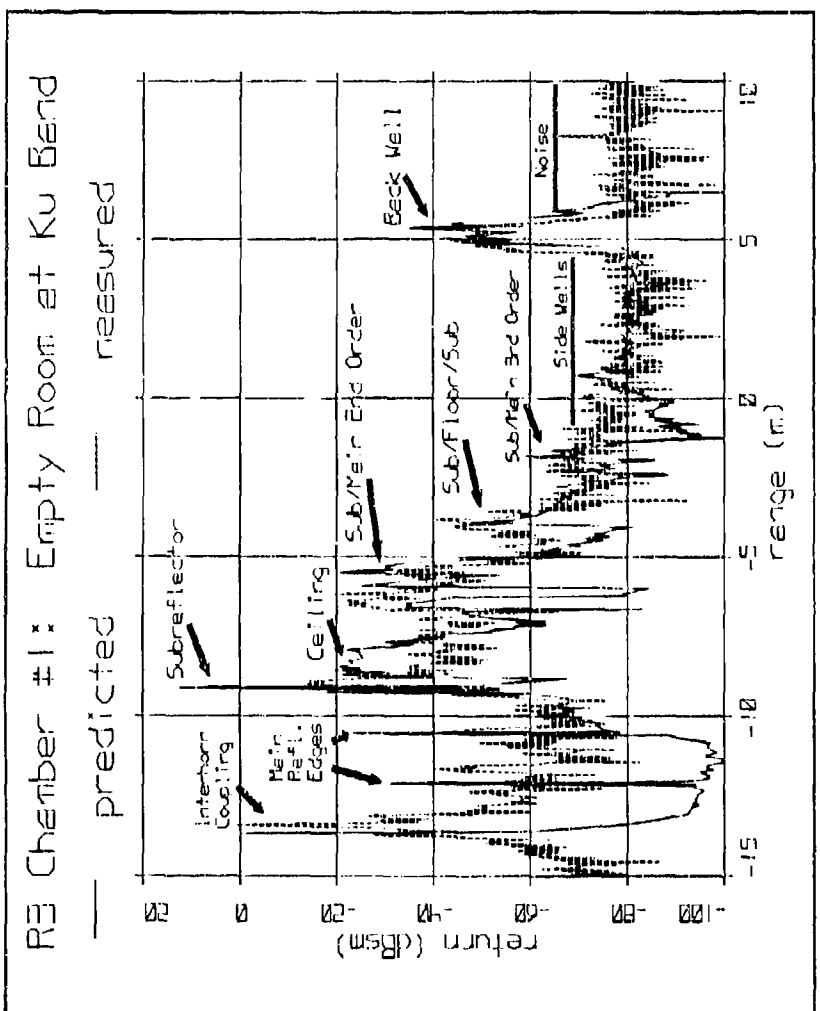

Figure 7: Total Downrange Profile

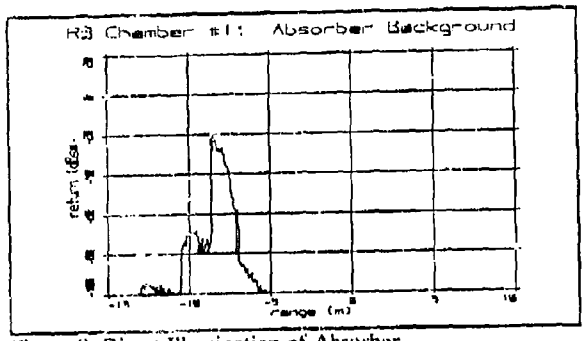

Figure 8: Direct Illumination of Absorber

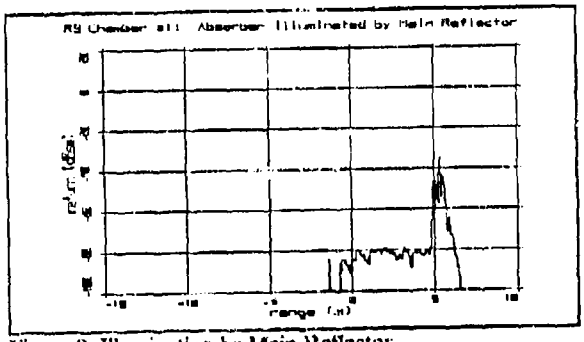

Figure 9: Illumination by Main Reflector

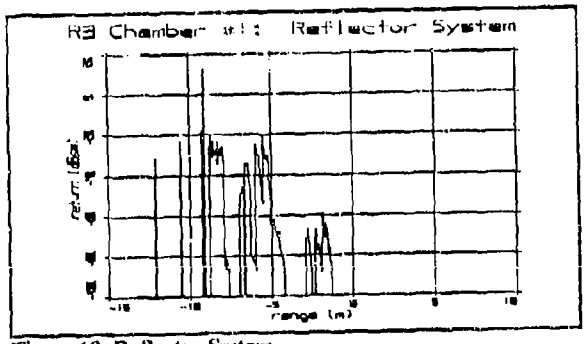

Figure 10: Reflector System

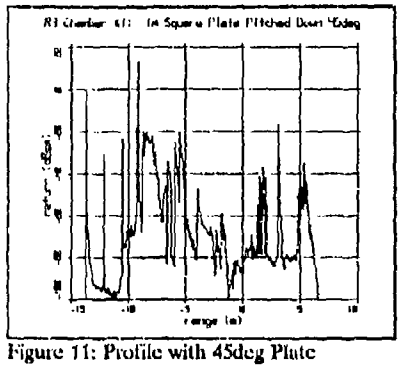

Figure 11: Profile with 45deg Plate

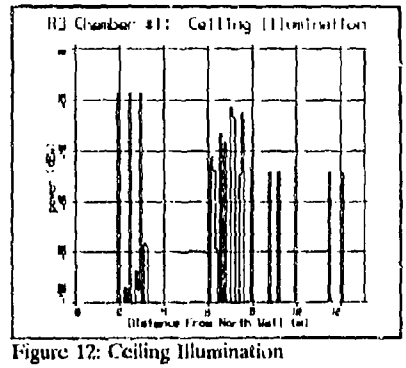

Figure 12: Ceiling Illumination

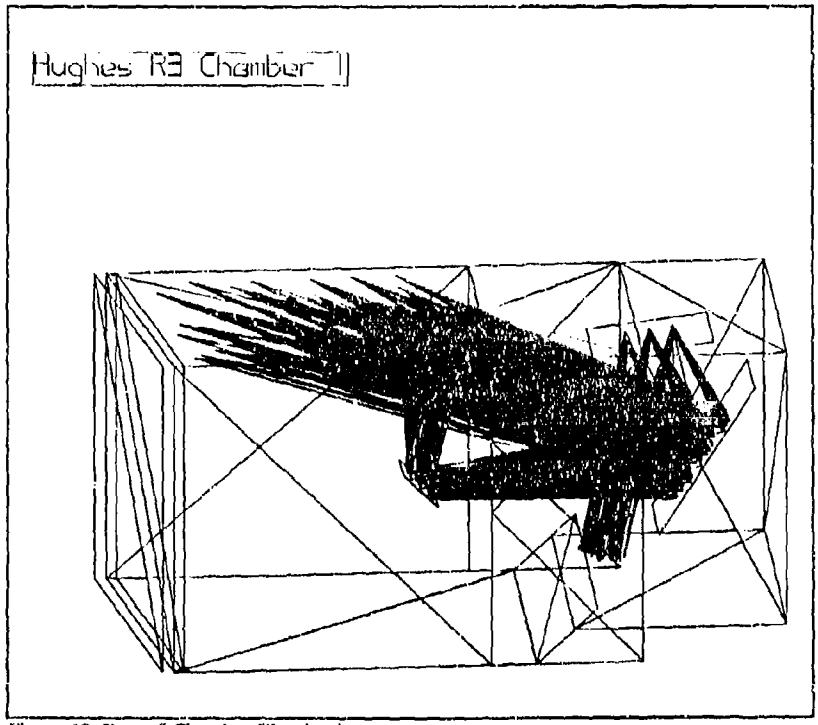

Figure 13: Part of Chamber Illumination

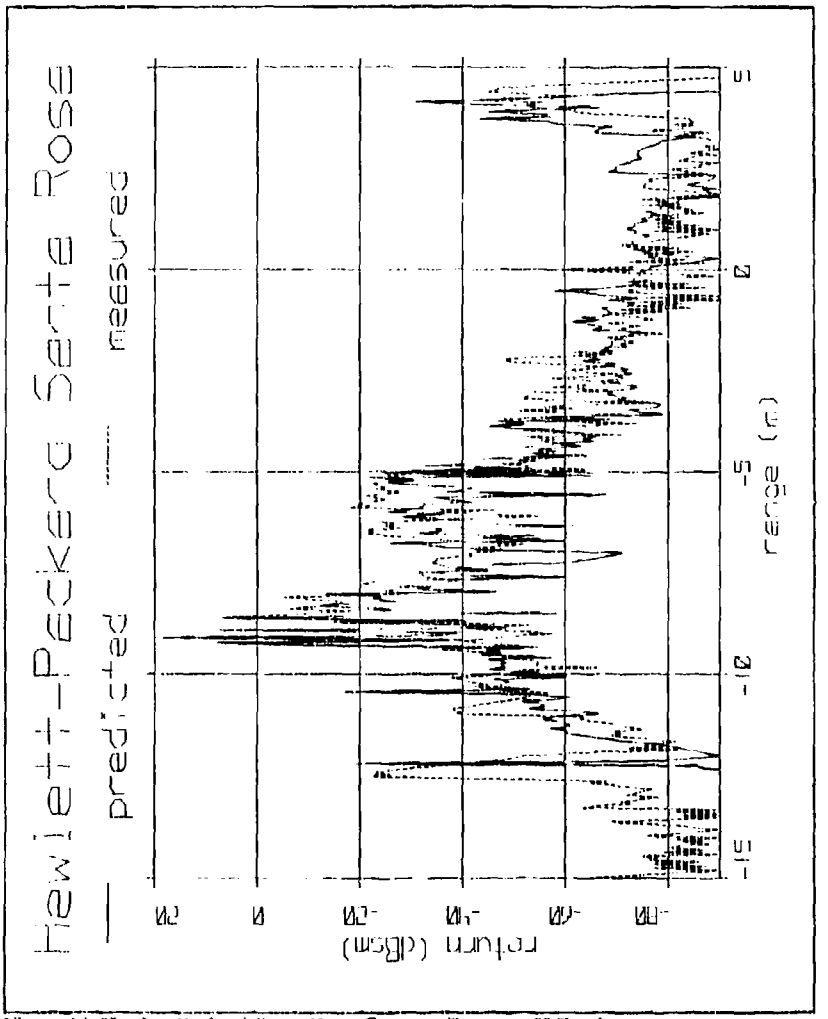

Figure 14: Hewlett-Packard Santa Rosa Compact Range at X Band

5.0 Future Development

The simplest improvements to Vuku5 could come, not from modifications to the source code, but from better modeling. Characterization of reflector edges seems to be the highest priority, given the high path strengths involved. Accurate measurement of edge response in a physical compact range is difficult; modeling the edges in isolation using a general-purpose low-frequency RCS code would probably be more effective. Edge serrations pose a modeling challenge due to their above-resonant electrical size. (Similar considerations would hold for other edge treatments -- rolled, absorber-loaded, etc.) Additional bistatic absorber RCS/area data could be collected, though this is difficult with extant facilities due to the amount of data required and the necessary reconfiguration of monostatic ranges. Given the relatively low gain of typical absorber, the significance of absorber/absorber multibounce scattering is questionable. However, a study of a specific scattering mechanism in isolation could model finer details than have been attempted so far.

Vuku5 is written in highly modularized, ANSI-standard C for maintainability and portability. New types of elements (or modifications of existing ones) can be added straightforwardly; in fact, code stubs exist to support additional targets and target mounts. Paraboloidal reflectors could be added easily. The primary challenge for new elements is not writing code, but determining appropriate electrical properties; in particular, mount performance is difficult to characterize with any certainty. Graphics device dependence has been encapsulated at a low level. Support is provided for X.11, ReGIS, HPGL, and LN03 Plus protocols; practice has shown that adding support for new devices is a simple matter.

Experience with the program has suggested some significant improvements that could be made in future versions. While retaining the basic theory, data representations could be altered to better accommodate high resolution computations. Flux density analysis would be greatly streamlined by the capability to display two-dimensional images with contouring or pseudocolor techniques. Several modules would need extensive rewriting, but the most lengthy and difficult part of the development, validation of the scattering algorithms, need not be repeated.

Vuku5 now offers the unique capability to analyze multipath interactions in a compact range. It can be a valuable addition to conventional chamber design tools. As new demands arise, its functionality can be expanded.

6.0 Acknowledgements

The authors would like to gratefully acknowledge the support and contribution of: T.W. Ohnstad, G. Tanakaya, D.J. Lang, and C.R. Boerman, all of Hughes.

7.0 References

[1] S. Brumley, "A Modeling Technique for Predicting Anechoic Chamber RCS Background Levels", Proceedings of the Antenna Measurement Techniques Association, 1987

[2] A. Lamb, R. Immell, "Hughes Aircraft Company's New RCS Measurement Facility", Proceedings of the Antenna Measurement Techniques Association, 1990

[3] S. Brumley, R. Immell, "Characterizing the Bistatic Performance of Anechoic Absorbers", Proceedings of the Antenna Measurement Techniques Association, 1989

[4] S. Brumley, "Time-Domain Methods Silence Reflections in Anechoic Chambers", Microwaves & RF, July 1989, pp 109-113

SESSION 16- "TRANSMISSION LINE MATRIX (TLM) TIME DOMAIN APPLICATIONS"

Moderator: Lloyd Riggs

A TRANSMISSION LINE MATRIX (TLM) METHOD ANALYSIS OF THE SEPARATED APERTURE BURIED DIELECTRIC ANOMALY DETECTION SCHEME

Paul R. Hayes and Lloyd S. Riggs
Electrical Engineering Departmen
200 Broun Hall
Auburn University, Alabama 36849-5201

and

Charles A. Amazeen
U.S. Army Belvoir RD&E Center
ATTN: STRBE-NT
Ft. Belvoir, Virginia 22060-5606

ABSTRACT

In this paper, a numerical time-domain technique known as the transmission line matrix (TLM) method is used to analyze a the separated aperture buried dielectric anomaly (mine) detection technique. This mine detector is designed to operate in the frequency range from 600 to 1,000 MHz. As shown in Figures 1 and 2, the mine sensor consists of transmit and receive broadband dipole antennas. Each dipole antenna is contained within an open cavity and the cavities are connected by a metallic septum. When the detector is over a homogeneous earth little of the transmitted power is picked up by the receive dipole. There is a significant increase in received power when the detector is over a buried dielectric anomaly (mine). Recently, a fairly extensive experimental effort was carried out at Ft. Belvoir, Virginia to characterize the performance of this mine detector. Although the experiments clearly indicate how the performance of the detector changes with mine depth, sensor height, sensor position relative to the mine, etc., the experiments do not necessarily provide a clear understanding of the electromagnetic principles underlying the mine-detection process. The TLM analysis has been used to generate a video tape which shows how the wave radiated by the transmit dipole interacts with the buried mine and scatters back into the receive cavity. This video simulation lends considerable insight into the fundamental wave mechanisms which govern the detection process.

INTRODUCTION

The separated aperture buried dielectric anomaly detection scheme, shown in Figures 1 and 2, was discovered in the 1950's and studied experimentally [1]. It was shown to have superior detection and false-alarm rates when compared to other mine-detection techniques. One drawback noted was sensitivity to sensor height. A false-alarm occurred when the sensor septum was greater than approximately one-half wavelength above the soil surface. Although the separated aperture approach to mine detection is simple, it has certain desirable features that are not shared by other electromagnetic mine detection methods. Electromagnetic identification of buried mines requires a transmitter and receiver: energy from the transmitter penetrates the earth's surface, interacts with the buried anomaly, and is then coupled into the receiver for detection. Unfortunately, a rather large amount of energy can be directly coupled from transmitter to receiver or reflected from the soil-air interface and coupled into the receiver. Energy at the receiver which interacts with the anomaly (the signal) can be quite small in comparison with this direct and ground-reflected energy (the clutter). The advantage of the separated aperture approach over other electromagnetic detection techniques is that, under proper operating conditions, the direct and ground reflected signals are substantially suppressed in comparison with the return from the buried anomaly. The metal septum forms a waveguide with the soil surface and when the septum-surface separation is small, this waveguide is below cutoff resulting in an exponential attenuation of the direct and ground reflected signals and a vastly improved signal-to-clutter ratio. In fact, according to one source, the separated aperture sensor exhibited the best signal-to clutter ratio of any technique ever attempted [1].

Recently, the Belvoir Countermine Technology Division of the U.S. Army Belvoir Research, Development, and Engineering Center (BRDEC) decided to pursue an experimental and theoretical research program dedicated toward developing a thorough understanding of the operating characteristics of the separated aperture mine detector. To date, fairly extensive measurements (described in greater detail below) have been conducted with this detector in dry loam (a mix of sand and clay) [2], and in moist or saturated soils [3]. Because of its robustness, versatility, and utility, the transmission line matrix (TLM) method was

chosen as the preferred numerical tool with witch to carry out the theoretical research program.

The transmission line matrix (TLM) method (described in greater detail in a later section) provides a very general and powerful technique for the solution of wide variety of electromagnetic interaction problems involving arbitrary material parameters and complex geometries. The basic principle of the TLM method is the modeling of space using a mesh of interconnected transmission lines. This transmission line mesh is excited at time zero, and the voltages and currents at the nodes in the mesh are recorded as time is stepped. A well known equivalence between electromagnetic field quantities and transmission line voltages and currents is used to calculate the electric and magnetic fields as a function of time; thus, the TLM method provides a time-domain analysis of scattering.

Two-dimensional TLM simulations have been used to study the variation in transmission coefficient (i.e. S21 = ratio of the voltage at the receive dipole to the voltage at the transmit dipole) as a function of horizontal sensor position relative to the location of the buried anomaly (see Figure 3). Figure 6 shows a TLM simulation with a dip-peak-dip variation in the transmission coefficient as the sensor scans over the buried anomaly. This result agrees qualitatively with measured transmission coefficient versus position data shown in Figure 4. As previously mentioned, a video tape will be presented showing the time-domain electromagnetic fields in the vicinity of the sensor as the sensor scans over the buried anomaly. This particular means of presentation lends considerable insight into the fundamental wave mechanisms responsible for the dip-peak-dip response. It is interesting to note that although the experimental efforts employed here provide the "answer" (i.e. the sensor output, S21, as a function of the variables which define the electromagnetic system), the experimental data alone does not necessarily provide any deep insights into the electromagnetic wave phenomenon responsible for the "answer". The TLM analysis on the other hand, particularly the video generated from sequential "snap shots" in time of the field structure throughout the analysis grid, provides a very clear picture (literally) of the mechanisms responsible for the "answer".

EXPERIMENTAL RESULTS

Figure 1 shows a side and front view of the experimental data collection system which consists of a motorized three-wheeled cart, Hewlett Packard 8753 A network analyzer, Hewlett Packard Multi-programmer, and separated aperture sensor head. The height of the sensor head above the soil surface is adjusted using the hand crank and horizontal movement of the sensor is automatically controlled by a worm gear attached to a stepper motor. The test equipment is controlled by a Hewlett Packard 9000 model 236 desktop computer via a fiber optic link. Experimental data collected from the network analyzer is stored on a 3.5 inch floppy disk. Figure 2 shows a close-up of the 790 MHz sensor head (the broadband dipoles are designed to resonate at 790 MHz) which is composed of a transmit and receive broadband dipole pair separated by a metallic septum. Each broadband dipole resides within a corner reflector. The critical dimensions for this head are also shown in Figure 2.

An overview of the experimental test configuration defines the many variables which must be examined in order to develop a good understanding of the separated aperture dielectric anomaly detection scheme. Figure 3 is a scale drawing of the experimental configuration showing the 790 MHz broadband sensor parallel to and at a height H above the soil surface. A dielectric anomaly, usually a 12 x 12 x 3 inch nylon block, is buried at a depth D below the soil surface. For the experimental results presented here, the sensor head is scanned in 1.5-inch increments directly over the anomaly (receive dipole passes over the anomaly first). As shown in Figure 3, measurements are made at 27 positions for a total horizontal scan of 39 inches. At each horizontal position, the network analyzer is used to measure the transmission coefficient (S21), complex ratio of voltage at the output of the receive dipole to the voltage at the input of the transmit dipole, at 8 MHz intervals starting at 600 MHz and ending at 1,000 MHz —— 51 frequency samples over a 400 MHz band. Since the dipoles are resonant near 800 MHz, the transmission coefficient is measured fro. 200 MHz below resonance to 200 MHz above resonance. A 6-inch septum was used for all of the data taken with the 790 MHz broadband sensor.

Figure 4 shows the measured transmission coefficient (S21) as a function of position for various sensor heights (1,3,4, and 6 inches as indicated) as the sensor head is scanned over a nylon block (12 x 12 x 3 inches) buried just under the surface of dry loamy soil. The transmission coefficient is measured at 796 MHz, a frequency which is near the resonant frequency of the dipoles. Notice that for the three inch height, the response when the detector is directly over the anomaly is around 25 dB greater than the response when the detector is well away from the anomaly (over homogeneous background)! Notice also that the anomaly becomes less "visible" as the sensor height increases (see for example the relatively flat response for a sensor height of 6 inches). This flat response is a consequence of increased direct coupling from transmit to receive dipole which washes out (masks) the relatively week signal scattered by the anomaly. As previously explained, the increased direct coupling results when the septum-earth "waveguide" is no longer below cutoff.

TWO-DIMENSIONAL TLM SIMULATION OF THE SEPARATED APERTURE MINE DETECTOR

The relationship between electromagnetic field quantities and the currents on a transmission line were first described by Kron [4] in 1944. In 1971, Johns and Burle [5] utilized this relationship along with pulse propagation theory to develop a numerical method for solving two-dimensional electromagnetic problems in the time domain. Johns and Berle named this method the transmission line matrix method, which has become known as the transmission line modeling (TLM) method. The TLM method has a conceptual advantage over other methods in that it is a physical model (a network of transmission lines in space) with an exact numerical solution. Any inaccuracies in the method are due to approximations used in modeling the problem being simulated and not in the solution of the model. Unlike other numerical methods such as the method of moments (MOM) [6], the algorithm used in the TLM method does not have to be changed for each new problem. The TLM algorithm used to compute the data presented in this thesis is based on the symmetrical condensed node, developed by P.B. Johns in 1987 [7]. The computer program employed here was developed at Auburn University by the first listed author (Paul Hayes).

In practice, the problem geometry is specified as a series of boundary reflection coefficients and material constituents in a cartesian mesh. An impulse is then applied to the mesh of nodes at some excitation point. The mesh is then iterated allowing the impulses to propagate throughout the network of transmission lines. An output point is defined as a node at which the voltages are saved at each time step. This output sequence of voltages corresponds to the impulse response of the electromagnetic system and the sequence may be Fourier transformed to obtain the frequency-domain response of the "network" or convolved with an arbitrary time function to obtain the time-domain response.

Figure 5 shows the TLM problem space (rectangular boundary), separated aperture sensor, earth/air interface, and buried dielectric anomaly. The appropriate reflection coefficients must be applied along the boarder of the mesh so that waves which are incident on the mesh boundary do not artificially reflect back into the problem space. The excitation and output points are taken at the center of the left and right rectangular cavities respectively.

Figure 6 shows typical results from a TLM simulation. The sensor height is 3 inches and the anomaly is 3 inches deep. The earth was taken as lossless and nonmagnetic and was modeled using a relative permittivity of 2.88. The nylon block was also assumed lossless and nonmagnetic and was modeled using a relative permittivity of 3.33. The peaks and dips present in the experimental data (see Figure 4) are visible in the TLM simulation as well. In the TLM model, the dips occur when the transmit or receive dipoles pass over the edge of the anomaly. As expected, a peak occurs when the detector is positioned directly over the buried anomaly. The two-dimensional TLM model produces results which agree remarkably well with the measured data of Figure 4.

CONCLUSIONS

In this paper the fundamental operation of the separated aperture buried dielectric anomaly detection scheme was described. Experiments indicated that as the sensor is scanned over a buried dielectric anomaly the transmission coefficient between output and input dipoles exhibited a dip-peak-dip character. The transmission line matrix (TLM) method of electromagnetic analysis was described and used to perform a

two-dimensional simulation of the separated aperture mine detector. The transmission coefficient computed with the TLM analysis also exhibited this dip-peak-dip response. Furthermore, it was pointed out that the dips in the TLM computed response occur when the transmit and receive dipoles are positioned over the edge of the buried anomaly. The TLM analysis has been used to generate a video tape which shows how the wave radiated by the transmit dipole interacts with the buried mine and scatters back into the receive cavity. This video simulation lends considerable insight into the fundamental wave mechanisms which govern the detection process.

REFERENCES

[1] R. V. Nolan, H.C. Egghart, L. Mittleman, R. L. Brooke, F. L. Roder, D. L. Gravette, MERADCOM Mine Detection Program: 1960-1980, Belvoir RD&E Center [formerly MERADCOM], Fort Belvoir, VA 22060-5606.

[2] L. S. Riggs and C. A. Amazeen, "Research with the Waveguide Beyond Cutoff or Separated Aperture Dielectric Anomaly Detection Scheme," Technical Report A227-008, United States Army, Belvoir Research Development & Engineering Center, Fort Belvoir, Virginia 22060-5606

[3] L. S. Riggs and C. A. Amazeen, "Measurements in moist and wet soils with the waveguide beyond cutoff or separated aperture dielectric anomaly detection scheme," Final report under contract No. DAAL03-86-D-001, Delivery Order 1773, Scientific Services Program, administered by Battelle, P.O. Box 12211, Research Triangle Park, NC 27709-2211.

[4] G. Kron, "Equivalent Circuit of the Field Equations of Maxwell - I,"Proc. IRE, vol. 32, pp. 289-299, 1944.

[5] P. B. Johns and R. L. Burle, "numerical Solution of Two-Dimensional Scattering Problems Using a Transmission-Line Matrix," Proc. IEE, vol. 118, no. 9, pp. 1203-1209, Sept. 1971.

[6] R. F. Harrington, Field Computation By Moment Methods, Macmillan, 1968.

[7] P. B. Johns, "A Symmetrical COndensed Node for the TLM Method," IEEE Trans. Microwave Theory Tech., col. MTT-35, no. 4, pp. 370-377, April 1987.

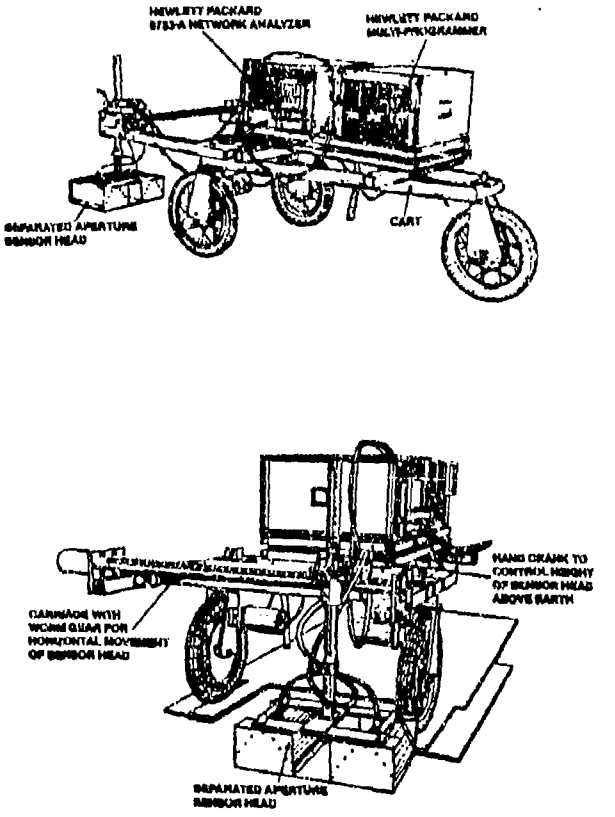

Figure 1. Side and front view of experimental test setup consisting of: motorized three-wheeled cart, Hewlett Packard 8753-A network analyzer and multi-programmer, separated aperture sensor head, hand crank to control height of sensor head above earth, and carriage with worm gear for horizontal movement of sensor head.

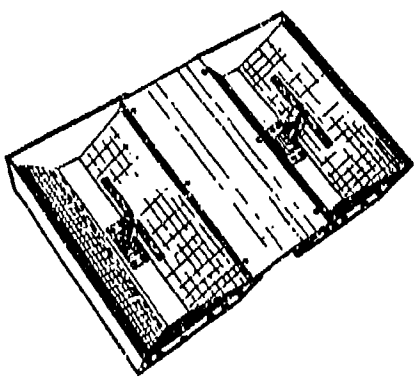

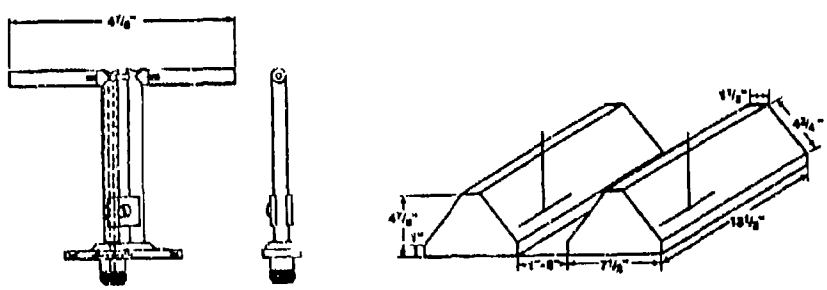

Figure 2. Close up and critical dimensions of the sensor head and broadband dipole. The dipole is designed to resonate at 790 MHz.

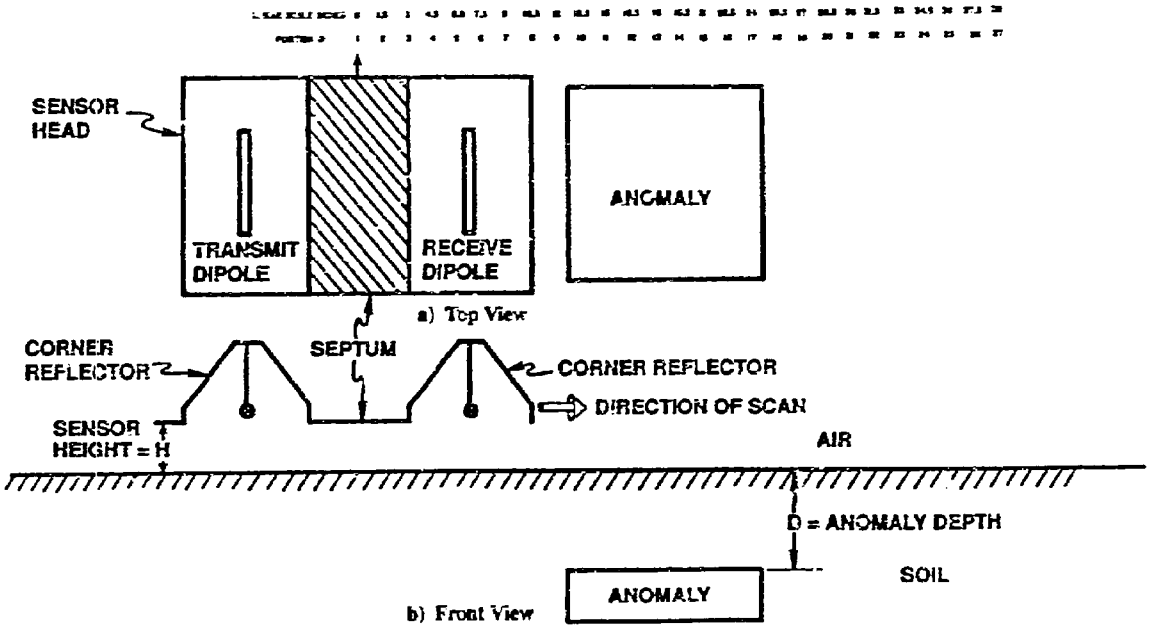

Figure 3. Scale drawing of experimental configuration showing 790 MHz sensor head parallel to and at a height H above the soil surface and dielectric anomaly (12 x 12 x 3 inches) buried at depth D below the soil surface. The sensor head is scanned directly over the anomaly in the direction shown (receive dipole passes over the anomaly first) in 1.5-inch increments for a total horizontal scan of 39 inches. The broadband dipoles are resonant at 790 MHz. The sensor head septum width is adjustable in 1-inch increments over a range from 1 to 6 inches; however, for the data shown here, the septum width is held fixed at 6 inches.

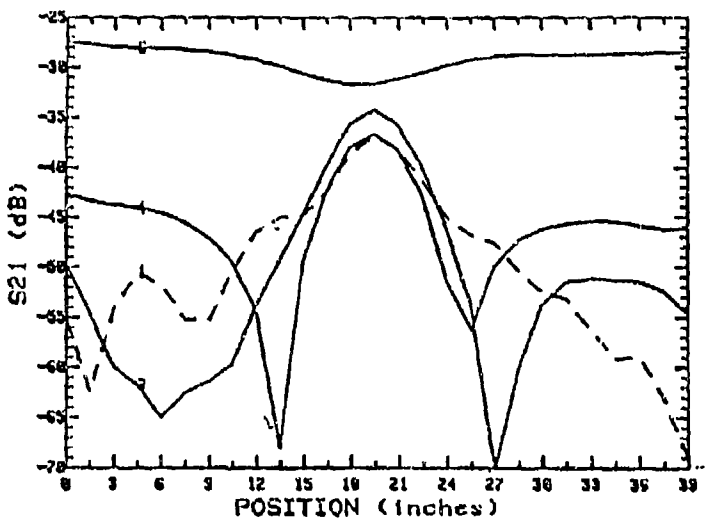

Figure 4. Measurement of transmission coefficient (S21 as a function of position for various sensor heights (1,3,4, and 6 inches as indicated) as the broadband sensor head is scanned over a nylon block (12 x 12 x 3 inches) buried just under the surface of dry, loamy soil. The receive dipole passes over the nylon block first. The transmission coefficient is measured near the resonance frequency of the broadband dipoles (790 MHz).

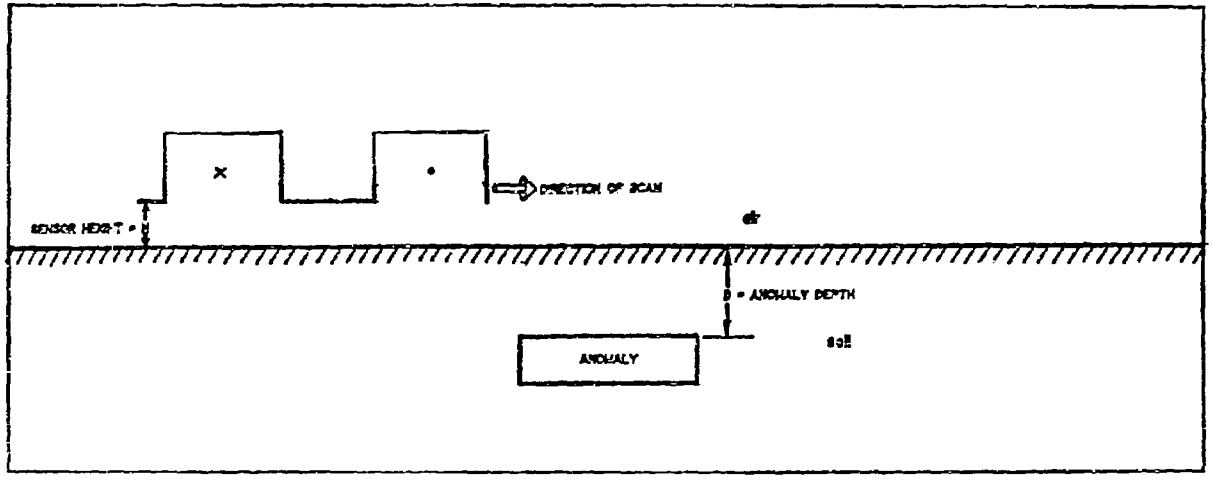

Figure 5. TLM problem space (rectangular boundary), separated aperture sensor, earth/air interface, and buried dielectric anomaly.

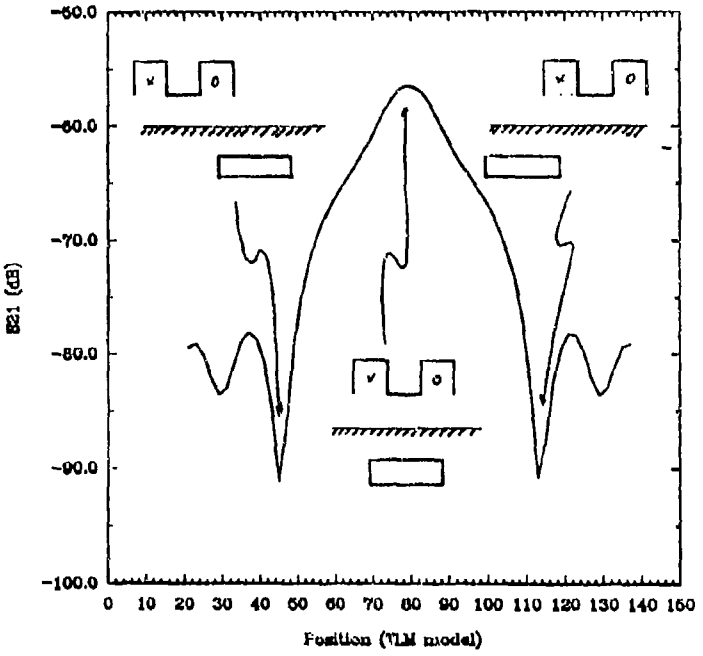

Figure 6. Transmission coefficient (S21) as a function of position computed with the two-dimensional TLM model. The transmission coefficient is computed at 790 MHz and the dielectric anomaly is buried 3 inches below the earth-air interface. (See text for further details.)

THE MODELING OF LOSSY MATERIALS WITH THE SYMMETRICAL CONDENSED NODE TLM METHOD

Fred J. German, G.K. Gothard and L.S. Riggs
Department of Electrical Engineering
Auburn University, AL 36849
(205)844-1864

ABSTRACT

Until recently, the symmetrical condensed node transmission line matrix (TLM) method has not been capable of modeling lossy materials. In this paper we present a new formulation for the symmetrical condensed TLM node which permits the modeling of materials which exhibit both electric and magnetic loss mechanisms. We test the validity of our formulation first by comparing the TLM calculated results for a plane wave incident on a lossy half-space to the exact solution of the lossy wave equation. In addition, we have applied the lossy node formulation to the analysis of wires coated with radar absorbent material (RAM). The TLM results for this problem will be compared with results from an exact series solution.

INTRODUCTION

The transmission line matrix (TLM) method is a well known technique for modeling physical processes with a mesh of interconnected transmission lines. A time domain impulse analysis of the transmission line mesh yields the time history of voltages and currents in the mesh. These voltages and currents are then used to compute the physical quantities of interest. For

electromagnetic applications several different versions of the TLM method have been developed. The most efficient and accurate of these various formulations is the symmetrical condensed TLM (SCTLM) method [1]. A single SCTLM cell is shown in Figure 1. Until recently, the SCTLM method was not equipped to model electromagnetic interaction problems which involved materials that exhibited electric and/or magnetic losses. In this paper, we reformulate the SCTLM method to include *both* electric and magnetic loss mechanisms. It should be pointed out that, although arrived at independently, the formulation that we present here is identical to that recently given by Naylor and Desai [2] for electric losses when there are *no* magnetic losses present in the material being modeled. The ability to model both electric and magnetic losses is important for many real materials such as radar absorbent material (RAM) where both the permittivity and permeability are complex.

FORMULATION

In order to model losses, six additional transmission line stubs have been added to the symmetrical condensed node; three to model electric losses and three to model magnetic losses. These additional stubs are considered to be infinitely long (or equivalently terminated into a matched load) so that none of the energy that couple into these stubs is returned to the mesh. Thus, a loss of energy is modeled by these stubs. Since the voltage pulses that couple into these stubs are not returned to the node, there is no need to store them in the computer, and thus the lossy node

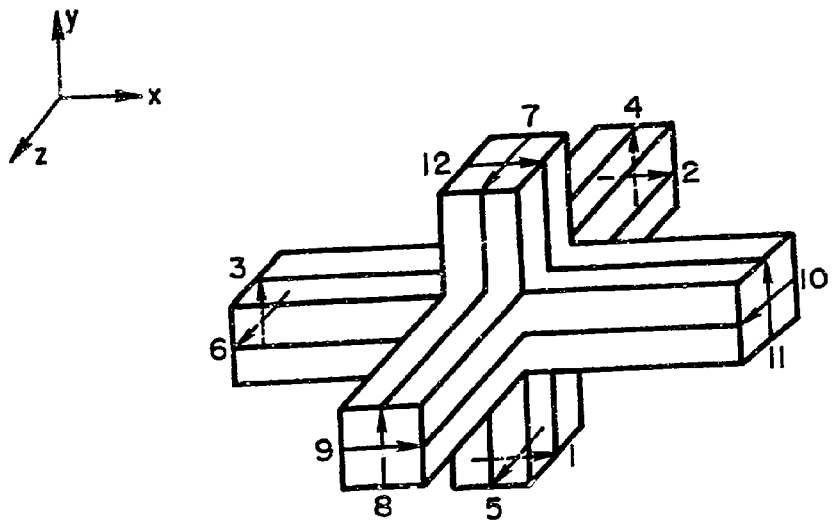

Figure 1. The Symmetrical Condensed Node With All Port Voltages Shown.

scattering matrix requires the same computer storage space as the node without losses.

To begin the derivation we let three of the stubs have normalized (with respect to 377Ω) characteristic admittances G_x, G_y, and G_z and couple only to the E_x, E_y and E_z electric field components, respectively. For magnetic losses, three stubs with normalized characteristic impedances R_x, R_y and R_z which couple only to H_x, H_y and H_z magnetic field components, respectively, are assumed. To obtain the scattering matrix for the lossy node, the structure of the scattering matrix given in [1] for the node with stubs is compared to the two-dimensional series and shunt TLM nodes [3]. These nodes are the basic building blocks for the expanded node TLM mesh. The shunt node is equipped with an open circuited permeability stub with normalized characteristic admittance Y_o and an electric loss stub of normalized characterized admittance G_o. Similarly, the series node has a permittivity stub with normalized characteristic impedance Z_o and a magnetic loss stub with normalized characteristic impedance R_0. The scattering matrices for these nodes are easily obtained from a simple lumped element equivalent network and are given by

$$\underline{S} = \frac{1}{4+Y_o+G_o}\begin{vmatrix} -(2+Y_o+G_o) & 2 & 2 & 2 & 2Y_o \\ 2 & -(2+Y_o+G_o) & 2 & 2 & 2Y_o \\ 2 & 2 & -(2+Y_o+G_o) & 2 & 2Y_o \\ 2 & 2 & 2 & -(2+Y_o+G_o) & 2Y_o \\ 2 & 2 & 2 & 2 & (Y_o-G_o-4) \end{vmatrix} \qquad \text{(1a)}$$

for the shunt connected node with the loss stub and without the loss stub is

$$\underline{S} = \frac{1}{4+Y_o}\begin{vmatrix} -(2+Y_o) & 2 & 2 & 2 & 2Y_o \\ 2 & -(2+Y_o) & 2 & 2 & 2Y_o \\ 2 & 2 & -(2+Y_o) & 2 & 2Y_o \\ 2 & 2 & 2 & -(2+Y_o) & 2Y_o \\ 2 & 2 & 2 & 2 & (Y_o-4) \end{vmatrix} \tag{1b}$$

For the series node with the loss stub we have

$$\underline{S} = \frac{1}{4+Z_o+R_o}\begin{vmatrix} (2+Z_o+R_o) & 2 & 2 & -2 & -2 \\ 2 & (2+Z_o+R_o) & -2 & 2 & 2 \\ 2 & -2 & (2+Z_o+R_o) & 2 & 2 \\ -2 & 2 & 2 & (2+Z_o+R_o) & -2 \\ -2Z_o & 2Z_o & 2Z_o & -2Z_o & (4+R_o-Z_o) \end{vmatrix} \tag{2a}$$

and

$$\underline{S} = \frac{1}{4+Z_o}\begin{vmatrix} (2+Z_o) & 2 & 2 & -2 & -2 \\ 2 & (2+Z_o) & -2 & 2 & 2 \\ 2 & -2 & (2+Z_o) & 2 & 2 \\ -2 & 2 & 2 & (2+Z_o) & -2 \\ -2Z_o & 2Z_o & 2Z_o & -2Z_o & (4+Z_o) \end{vmatrix} \tag{2b}$$

for the series connected node without the loss stub. It must be remembered that, in general, the scattering matrix for the symmetrical condensed node cannot be obtained from a lumped element equivalent circuit. However, by comparing the scattering matrix of the symmetrical condensed node with stubs with those of the shunt and series nodes with stubs some useful similarities can be observed which lead to the scattering matrix for the symmetrical condensed node with losses.

To begin, let us examine Johns' original scattering matrix [1] in some detail. The scattering parameters in the lossless SCTLM scattering matrix that are associated with the open circuited stub link line-to-stub transmission coefficients (i.e., they specify the amount of coupling into the open circuited stubs from pulses that are on the link lines connecting

the nodes in the mesh) are given by

$$e = \frac{4}{2(4 + Y)} \tag{3}$$

The scattering parameters that are the reflection coefficients for pulses traveling toward the node on the open circuited stubs are given by

$$h = \frac{(Y - 4)}{(Y + 4)} \tag{4}$$

They specify how much of the pulse is reflected back into the stub. Finally, the open circuit stub-to-link line transmission line coefficients which specify how much of a pulse couples from a stub to the link lines is given by

$$g = \frac{4Y}{2(4 + Y)} \tag{5}$$

Comparison with the scattering matrix for the two-dimensional shunt node with the Y_o stub, equation (1b), shows that the scattering parameters associated with link line-to-stub transmission, stub reflection, and stub-to-link line transmission are identical to equations (3), (4) and (5), respectively. This indicates that the open circuited electric field stubs in the symmetrical condensed node can be thought of as being shunt connected to the transmission lines which are associated with the corresponding field component.

Similarly, for the short circuited magnetic field stubs in the symmetrical condensed node, we can identify

$$f = \frac{4Z}{2(4 + Z)} \tag{6}$$

$$j = \frac{(4 + Z)}{(4 - Z)} \tag{7}$$

and

$$l = \frac{4}{2(4 + Z)} \tag{8}$$

as the entries associated with link line-to-stub coupling, stub reflection, and stub-to-link line coupling, respectively. Comparison with the scattering matrix for the two-dimensional series connected node with the Z_o stub (2b) shows that (7), (8) and (9) are identical to the corresponding terms in (2b) suggesting that the short circuited magnetic field stubs in the symmetrical condensed node mesh are connected in series with the link lines that are associated with the corresponding magnetic field component.

The correspondences between the stub coupling in the symmetrical condensed node TLM mesh and the stub coupling in the two-dimensional shunt and series node meshes which allows us to draw conclusions about the actual physical connection of the symmetrical condensed node stubs to the link lines, also allows us to easily obtain the scattering matrix for the symmetrical condensed node when the loss stubs are included.

Since the stubs associated with electric losses are shunt connected, their characteristic admittance G and Y (note that G and Y take subscripts appropriate to the field value with which they are coupling) are in parallel. Therefore, the symmetrical condensed node scattering matrix entries S_{IJ}, I and J from 1 to 12 are identical in form as before except that now the total stub admittance is taken to be (Y + G).

The other entries in the scattering matrix, namely, those associated with link line-to-stub coupling, stub reflection, and stub-to-link line transmission are obtained from the corresponding entries in the scattering matrices for the two-dimensional shunt and series connected nodes with loss stubs (1a) and (2a). The final form for the scattering matrix of the

symmetrical condensed node equipped with all twelve stubs is the same as that given in [1]. The new expressions for the scattering matrix elements for the fully equipped node are given by the following expressions:

$$a = -\frac{(Y + G)}{2(Y + G + 4)} + \frac{(Z + R)}{2(Z + R + 4)} \tag{9a}$$

$$b = -\frac{4}{2(Y + G + 4)} \tag{9b}$$

$$c = -\frac{(Y + G)}{2(Y + G + 4)} - \frac{(Z + R)}{2(Z + R + 4)} \tag{9c}$$

$$d = \frac{4}{2(Z + R + 4)} \tag{9d}$$

$$e = b \tag{9e}$$

$$f = 4d \tag{9f}$$

$$g = Y\,b \tag{9g}$$

$$h = \frac{Y - G - 4}{Y + G + 4} \tag{9h}$$

$$i = d \tag{9i}$$

$$j = \frac{4 + R - Z}{4 + Z + R} \tag{9j}$$

where the subscripts appropriate for G, R, Y and Z are determined from the field component to which they couple as explained in [1]. At this point, relationships must be derived which relate the loss stub immitances, G_l and R_l, to the electric and magnetic conductivities, σ_{el} and σ_{ml}, respectively, where l = x, y, or z. Consider a block of space with dimensions u, v, and w in the x, y, and z coordinate direction, respectively, with a diagonal electric conductivity tensor with entries σ_{ex}, σ_{ey}, and σ_{ez} and magnetic

conductivities σ_{mx}, σ_{my}, and σ_{mz}.

Consider as an example case the conductivity associated with the x-directed electric field, σ_{ex}. By definition, the resistance associated with this field component is

$$r_x = \frac{V_x}{I_x} \tag{10}$$

where

$$V_x = E_x u \tag{11}$$

and I_x is

$$I_x = \sigma_{ex} E_x vw \tag{12}$$

thus giving

$$r_x = \frac{u}{\sigma_{ex}(vw)} \tag{13}$$

Therefore, the characteristic admittance of the loss stub associated with E_x, normalized to the characteristic impedance of the link lines, Z_o is

$$G_x = \frac{\sigma_{ex}(vw)}{u} Z_o \tag{14a}$$

Similarly for the other electric field loss stubs we obtain

$$G_y = \frac{\sigma_{ey}(uw)}{v} Z_o \tag{14b}$$

$$G_z = \frac{\sigma_{ez}(uv)}{w} Z_o \tag{14c}$$

To relate the magnetic loss stub characteristic impedance to the magnetic loss tangent the dual of the above derivation is used which yields the following final results

$$R_x = \frac{\sigma_{mx}(vw)}{Z_o u} \tag{15a}$$

$$R_y = \frac{\sigma_{my}(uw)}{Z_o v} \tag{15b}$$

$$R_z = \frac{\sigma_{mz}(uv)}{Z_o w} \tag{15c}$$

Often, the electric and/or magnetic loss tangent of a material is specified. These are related to the equivalent conductivities by

$$\tan\delta_e = \frac{\sigma_e}{\omega\varepsilon'} \tag{16a}$$

and

$$\tan\delta_m = \frac{\sigma_m}{\omega\mu'} \tag{16b}$$

where $\tan\delta_e$ is the electric loss tangent, $\tan\delta_m$ is the magnetic loss tangent, ε' is the real part of the complex permittivity and μ' is the real part of the complex permeability.

Finally, the equations for calculating the nodal field values from the incident voltage pulses require modification in order to account for the charge that couples into the loss stubs without returning to the node. These slightly modified expressions are easily shown to be

$$E_x = \frac{2}{u(4 + Y_x + G_x)}(V_1 + V_2 + V_9 + V_{12} + Y_x V_{13}) \tag{17a}$$

$$E_y = \frac{2}{v(4 + Y_y + G_y)}(V_3 + V_4 + V_8 + V_{11} + Y_y V_{14}) \tag{17b}$$

$$E_z = \frac{2}{w(4 + Y_z + G_y)}(V_5 + V_6 + V_7 + V_{10} + Y_z V_{15}) \tag{17c}$$

$$H_x = \frac{2}{Z_o u(4 + Z_x + R_x)}(V_4 - V_5 + V_7 - V_8 - V_{16}) \tag{17d}$$

$$H_y = \frac{2}{Z_o v(4 + Z_y + R_y)}(-V_2 + V_6 + V_9 - V_{10} - V_{17}) \tag{17e}$$

$$H_x = \frac{2}{Z_0 w(4 + Z_s + R_x)} (-V_3 + V_1 + V_{11} - V_{12} - V_{18}) \qquad (17f)$$

Thus, the symmetrical condensed node completely equipped with three permittivity stubs, three permeability stubs, three electric loss stubs, and three magnetic loss stubs has been completely characterized.

NUMERICAL RESULTS

In this section, the lossy node formulation for the symmetrical condensed node with electric and magnetic loss stubs is tested. Three examples are presented: two which involve plane wave propagation in an inhomogeneous lossy space and one involving scattering from a RAM-coated cylinder.

As a first example, consider a 15 GHz plane wave to be normally incident on an infinite lossy half-space from free space. The lossy half-space has relative complex permittivity and permeability given by $\varepsilon_r = 10 - j5$ and $\mu_r = 3 - j2$. Figure 2 shows a plot of the electric field magnitude as a function of position. The material interface is located at 38mm. Comparison of the theoretical curve on the same plot shows that the TLM solution and the theoretical solution are virtually indistinguishable.

To examine the accuracy of the formulation for magnetic losses, we again look at the case of a normally incident plane wave on a lossy half-space. For this example $\varepsilon_r = 5 - j5$ and $\mu_r = 5 - j\mu_r''$ where μ_r'' is varied. The reflection coefficient from the lossy half-space is taken to be the ratio of reflected electric field to incident electric field. Figure 3(a) shows the TLM calculated reflection coefficient magnitude along with the theoretical values; again, excellent agreement is noted. Figure 3(b) plots

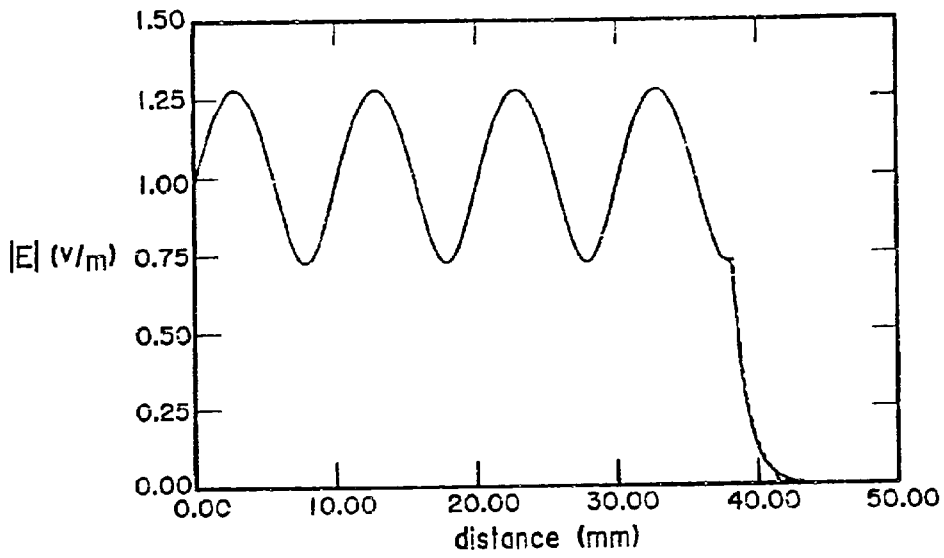

Figure 2. Electric Field Magnitude for a 15 GHz Plane Wave Incident on a Lossy Half-Space with $\varepsilon_r = 10 - j5$ and $\mu_r = 3 - j2$. (- - - TLM, —— Theoretical).

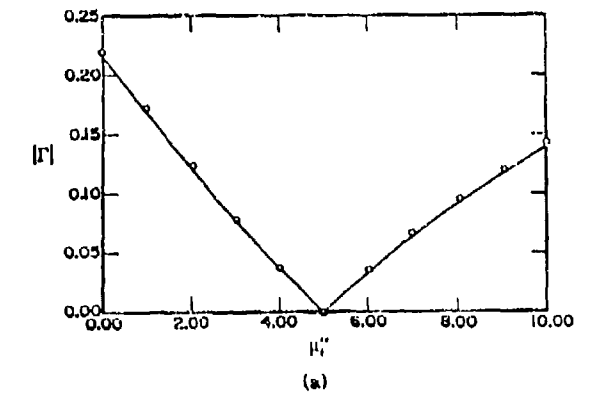

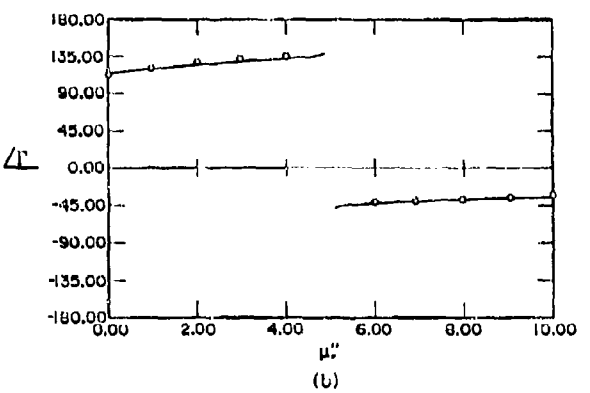

Figure 3. Reflection Coefficient. (a) Magnitude (b) Phase for $\epsilon_r = 5 - j5$ and $\mu_r = 3 - j\mu_r''$.

the TLM and theoretical reflection coefficient phase, referenced to the material interface, with excellent agreement observed.

Finally, we present calculations for scattering from a circular PEC cylinder coated with RAM. The radius of the PEC cylinder is 2.38125 mm and the radius of the wire and RAM coating is 4.643 mm. The material constants for the RAM were assumed constant over the frequency range of interest (8-12GHZ) and are given by $\varepsilon_r = 15.0 - j1.0$ and $\mu_r = 0.95 - j0.25$. Using the above loss formulation we have calculated the attenuation provided by the RAM coating on the wire. The attenuation is defined as follows:

$$(\text{Attenuation})_{dB} = (\text{RCS Uncoated Cylinder})_{dB} - (\text{RCS Coated Cylinder})_{dB} \qquad (18)$$

In Figure 4 the TLM results are compared to the results obtained from a series solution to the problem and fair agreement is observed. It is noted that the results match better at the lower end of the frequency band, and diverge somewhat with increasing frequency. There are two probable causes of this: one is that the inherent numerical dispersion of the TLM mesh increases with increasing frequency and the inclusion of the lossy material makes this error more pronounced. Secondly, the error caused by the approximation of the circular cylinder using a "stair-stepped" model on the cartesian TLM mesh is known to cause serious errors at higher frequencies.

CONCLUSIONS

In this paper a formulation of the SCTLM method which includes both electric and magnetic loss mechanisms is presented. Several examples have been presented to validate the formulation.

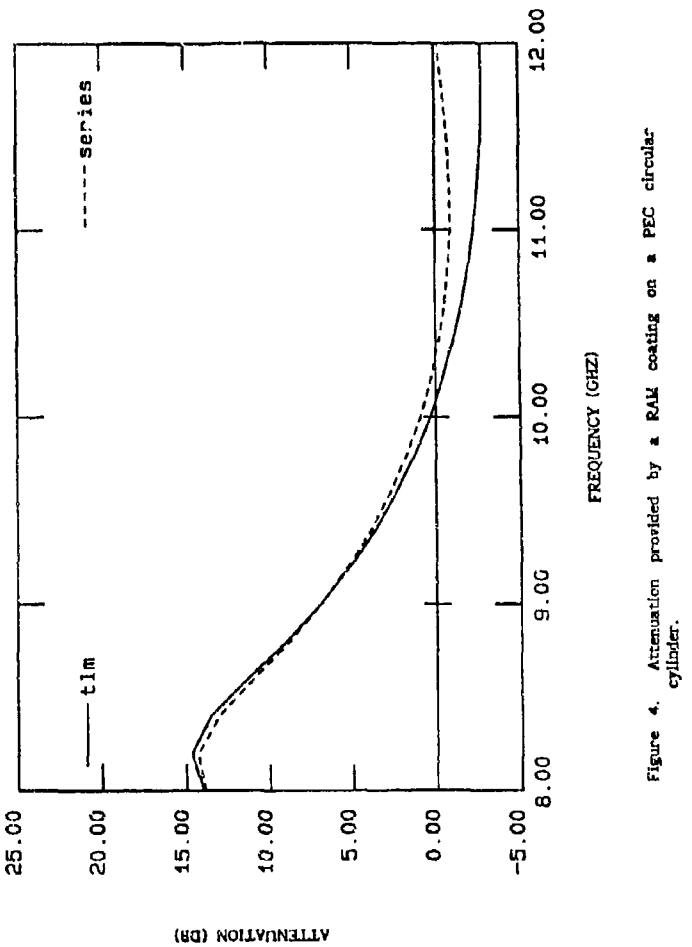

Figure 4. Attenuation provided by a RAM coating on a PEC circular cylinder.

REFERENCES

[1] P.B. Johns, 'A symmetrical condensed node for the TLM method', IEEE Trans. Microwave Theory and Tech., 1987, vol. MTT-35, no. 4, 370-377.

[2] W.J.R. Hoefer, 'The transmission line matrix method', in *Numerical Techniques for Microwave and Millimeter Wave Passive Structures*, T. Itoh, Ed. New York: Wiley, 1989.

[3] P. Naylor and R.A. Desai, 'New three dimensional symmetrical condensed lossy node for solution of electromagnetic wave problems by TLM', Electron. Lett., 1990, vol. 26, no. 7, 492-494.

THE ANALYSIS OF PASSIVE MICROWAVE COMPONENTS USING THE TLM METHOD

Patrick R. Conway, F.J. German, L.S. Riggs
Department of Electrical Engineering
Auburn University, AL 36849
(205) 844 - 1873

ABSTRACT

The increased use of computer aided design and analysis of circuits which transmit information at high frequencies has lead to a need for reliable computer modeling of microwave frequency circuit elements. In this paper a technique is developed using the TLM method to calculate the scattering matrix for a class of strip type passive microwave transmission lines. Single port and multi-port microstrip circuits with discontinuities are analyzed. The technique is shown to be a very accurate method for using TLM in this type of design analysis through comparison of measurements with the TLM calculated parameters.

INTRODUCTION

It has been shown [1] that the TLM method provides an accurate and convenient method of simulating microwave frequency circuits over a wide bandwidth. The accuracy of the TLM method is due to its ability to model inhomogeneous space and accurately reproduce the frequency dependent characteristics of such structures (including dispersion and radiation). The convenience of the TLM method is due to the fact that a reformulation is not necessary for every new problem. Only a change of the input file is required. The TLM method also produces, in a single run, the electric and magnetic field quantities in the modeled space over a broad frequency

range. These qualities make computer aided design a very practical application of the TLM method.

This paper will take advantage of the desirable characteristics of the TLM method to analyze several microstrip structures (See Fig. 1). Five practical microstrip structures containing discontinuities will be analyzed and four of the five circuits are multiport devices. Guidelines for modeling the microstrip structures will be presented. The method used to extract the time domain data from the TLM mesh and the procedure used to calculate the scattering parameters will be shown. The TLM extracted scattering parameters are compared with the scattering parameters from measurements, where available, and with calculated scattering parameters from other numerical methods when measured data is not available.

SCATTERING PARAMETER CALCULATION

A single row of elements in the scattering matrix for a microwave component may be calculated by taking the ratio of the voltage wave traveling outward from each port of the circuit element divided by the voltage wave traveling inward on the input port. The inward and outward traveling current may also be used in this calculation since both voltage and current may be considered as "normalized" power waves [2]. Both the electric and magnetic field values are available from the TLM simulation so both current and voltage are available. For the calculation of wide band scattering parameters the traveling voltage wave in the TLM cartesian mesh was used. For a given size volume and coarseness of the mesh the line integral calculation of the voltage for a given point on the transmission line would be more accurate than the closed line integral around the transmission line for the calculation of current.

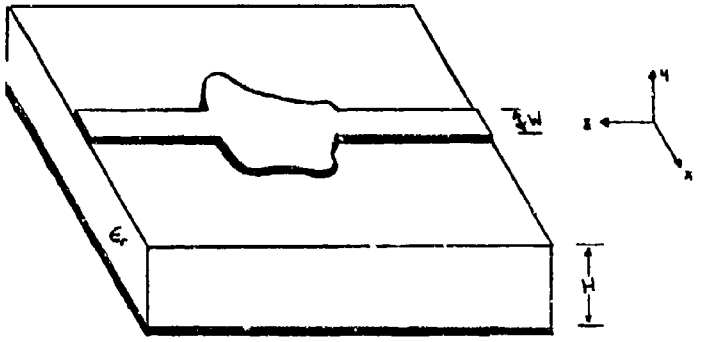

Figure 1 Microstrip Transmission Line Containing General Discontinuity

To obtain the voltage on a transmission line the impulse response along a line at an observation point is saved as the TLM simulation steps through time. The inward and outward traveling voltages at the observation point(s) are Fourier transformed and then the ratio of two traveling waves is used to produce the scattering parameters as a function of frequency:

$$S_{11}(f) = \frac{F[\, V_r(t)\,]}{F[\, V_i(t)\,]}$$

Where $V_r(t)$ is the outward (reflected in this case) traveling voltage at the input port as a function of time and $V_i(t)$ is the inward traveling voltage at the input port.

MODELING

In order to analyze a microstrip circuit accurately using the TLM method, the circuit itself and a finite volume of space surrounding the circuit must be included in the model. This volume, which is included in the model but is not part of the circuit itself, is a region above the circuit and a region normal to the direction of the propagation along the circuit. Both of these regions are included in order to ensure that the fields oriented in these directions have attenuated and that a TEM condition exists at the computational domain boundaries. This is necessary since the boundary conditions which were enforced at the limits of the TLM computational domain are designed to match TEM radiation. If a non-TEM wave is present at the boundary then partial reflection of the fields incident on the boundary would result. These reflections are non-physical and would corrupt the circuit simulation.

The number of cells used to model the regions above and to the side of each microstrip varied from circuit to circuit because of the type of discontinuities considered. In general though, for a straight microstrip transmission line only 2 times the number of cells required to model the thickness of the dielectric substrate is required to model the region above the transmission line. Outward from the transmission line a region 5 times the width of the strip was used to model this dielectric half space.

The quantity which will be used to calculate the scattering parameters is a sum of the electric field values along a line from the ground plane to the conducting strip. Because of this the TLM model should accurately reproduce the electric field values throughout this region. The number of cells used to model the width of a 50 Ω microstrip transmission line is four, in some cases, to take advantage of the geometric symmetry of the problem. This means the number of cells used to model the dielectric region is also four. It is possible to model the dielectric region with only three cells beneath the strip, and this was used in cases where symmetry was not available.

SIMULATION OUTPUT

The point used to observe the impulse response of the circuit should be chosen such that any higher order modes which exist on the transmission line due to the excitation and discontinuities present in the circuit have decayed. The decay of these modes determines the length of transmission lines connected to the microwave devices within the TLM model. For all of the circuits considered in this paper the excitation was chosen to be along a line from the ground plane to the conducting strip. The propagating mode did not fully develop until 20 to 30 cells away from this excitation. The

transmission line discontinuity was therefore placed at least 30 cells down the transmission line from the excitation. Due to the various circuits analyzed, the number of cells required to ensure that the higher modes around the discontinuities were fully decayed varied from circuit to circuit.

The extraction of the traveling voltage waves on the input port of the microwave device requires some extra attention. Both the inward and outward (reflected) voltages will be present on this port and a method for separating the two is needed. It has been reported [3] [4] that two models of the input port are needed to reparate the two voltages on the input port of a device. The method used here has only one model of the input port. This method models the input port such that it is long enough to allow the incident voltage to completely pass the observation point before the reflected voltage can return. This method seems more efficient since preparation and post processing time, along with computer requirements, in most cases, are reduced since only one input file is prepared and only one TLM simulation is run.

The number of time steps required for the calculation of the Fourier transform also varies from circuit to circuit. An accurate method for determining the number of time steps required is to calculate the Fourier transform for an increasing number of time steps (see Fig 2). When the traveling wave has not yet passed the observation point, the frequency response is seen to vary as a function of the number if time steps used in the calculation. When the wave does completely pass the observation point the frequency response remains constant as a function of time steps.

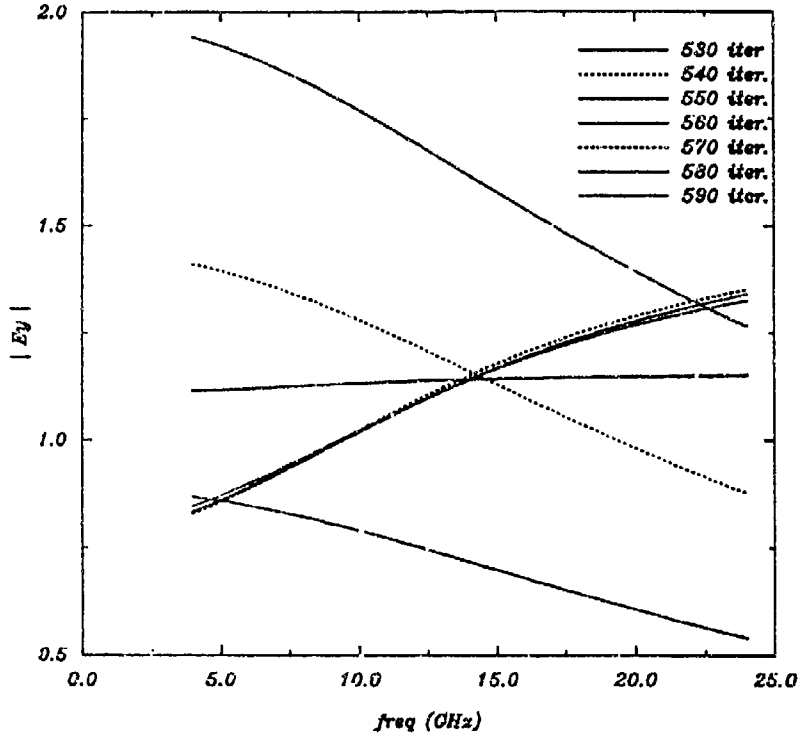

Figure 2 Fourier Transform of Voltage Impulse Traveling On a Microstrip Transmission Line Versus Time Steps

NUMERICAL RESULTS

Open-Ended Microstrip: The scattering parameters for a single port device are presented first. The microstrip (shown in Fig. 3) is a 50 Ω transmission line (W = 0.6mm, W/H = 1.0) on an alumina substrate (ε_r = 9.6) terminated into an open (a single port device). The results from the TLM analysis are compared with that of [4] which are from an FD-TD analysis of the same structure (See fig. 4). It is seen that the two techniques agree very well over a very broad bandwidth.

Microstrip Side Coupled Filter: A microstrip side coupled filter was modeled next. It is shown in Fig. 5. Because this a resonant structure a large number of time steps was required to ensure that the impulse response of the filter was complete. The filter has 50 Ω transmission lines (W = 1.272mm, W/H = 1.0), ε_r = 10.0 for the substrate and the gap between each of the strips D = 1.272mm. Figure 6 shows that the TLM calculated scattering parameters compare very well with those of [5].

Microstrip Radial Stub: A microstrip radial stub filter was modeled next (See Fig. 7). The structure has two ports with W = 0.61mm, H = 0.635mm, the radius R = 3.253mm and the gap G = 0.61mm. This is also a highly resonant circuit and required a large amount of simulation time for convergence. The results from the TLM analysis of the radial stub are presented in Figure 8 and compared with measured data [6]. It is seen that good agreement between the TLM results and the measured data is achieved.

Microstrip T-junction: The next microstrip structure analyzed was the microstrip t-junction, shown in Figure 9. The microstrip is modeled as a 50 Ω (W = 25 mil, W/H = 1.0) on a substrate with ε_r = 9.9. Good agreement was obtained between the TLM analysis of the microstrip t-junction and measured data [7] (See Figure 10).

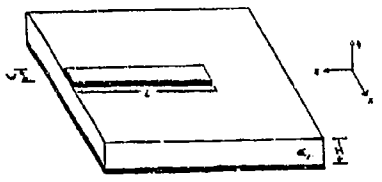

Figure 3 Microstrip Open End.

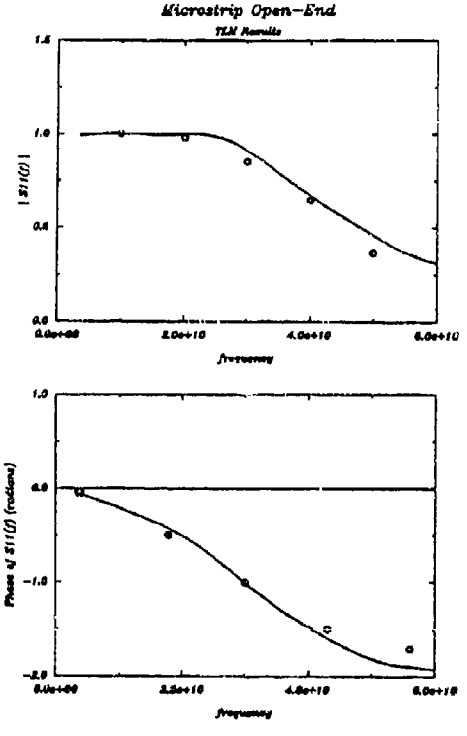

Figure 4 Scattering Parameters for the Open-Ended Microstrip.
(---TLM, o o o Reference 4)

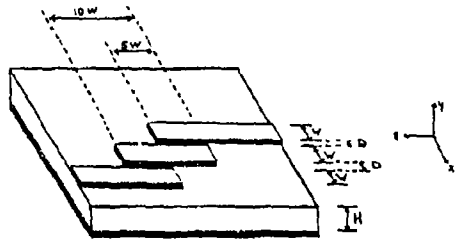

Figure 5 Microstrip Side Coupled Filter.

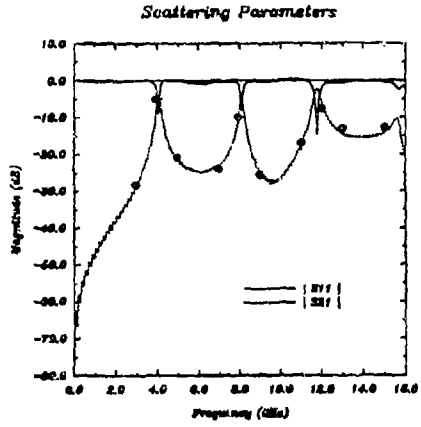

Figure 6 Scattering Parameters for the Microstrip Side Coupled Filter.
(---TLM, o o o Reference 5)

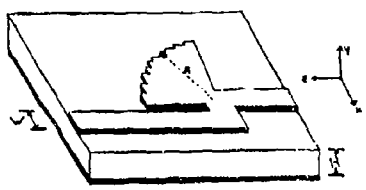

Figure 7 Microstrip Radial Stub.

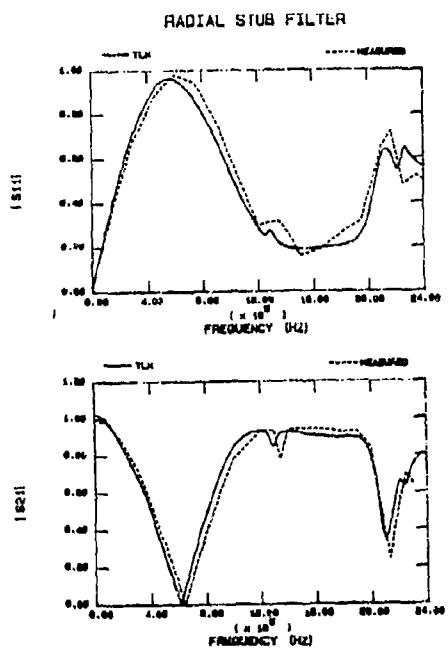

Figure 8 Scattering Parameters for the Microstrip Radial Stub.
(——TLM, --- Reference 6)

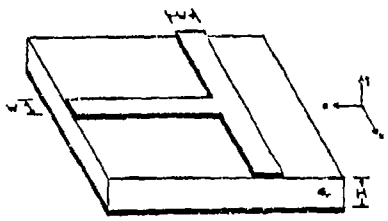

Figure 9 Microstrip T - Junction.

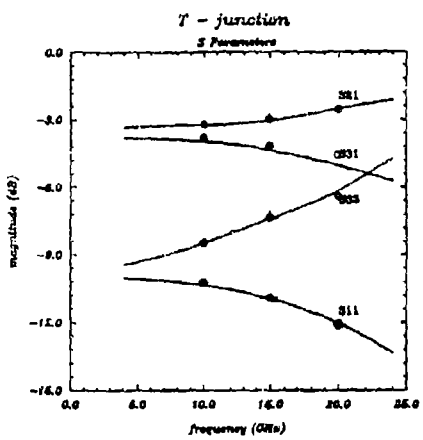

Figure 10 Scattering Parameters for the Microstrip T Junction.
(---TLM, o o o Reference 7)

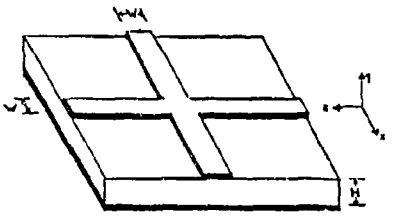

Figure 11 Microstrip Symmetric Right Angle Crossing Junction.

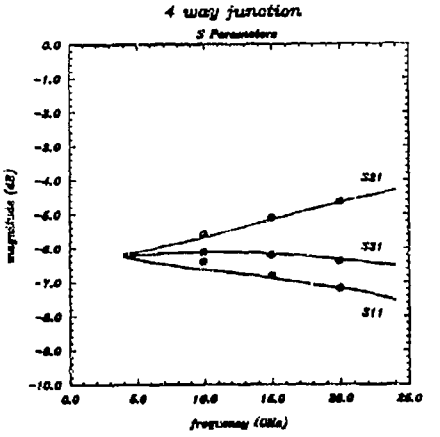

Figure 12 Scattering Parameters for the Microstrip Symmetric Right Angle Crossing Junction.
(---TLM, o o o Reference 7)

Microstrip Cross Junction: The next structure modeled, and shown in Figure 11 , is the microstrip cross junction. The TLM results are compared in Figure 12 to a Method of Moments solution based on the EFIE [7] and show good agreement. The microstrip is modeled as a 50 Ω transmission line (W = 25 mil, W/H = 1.0) with ε_r = 10.2 for the dielectric substrate.

CONCLUDING REMARKS

A method was developed which used TLM calculated data to extract scattering parameters for single-port and multi-port microstrip devices. General rules were also presented for modeling this type of microwave transmission lines. The results of using these rules with a TLM simulation were presented and the application of this method to resonant, as well as nonresonant microstrip structures was shown to produce accurate scattering parameters over a wide frequency range.

REFERENCES

[1] F.J.German, H.D. Williams, L.S. Riggs, and M.E. Baginski, "Three Dimensional Full-Wave Analysis of Passive Microstrip Components Using The TLM Method", ACES Conf. Proc., 1989, 63-77.

[2] P.A. Rizzi, The Scattering Matrix, Appendix D, *Microwave Engineering Passive Circuits*, Prentice-Hall, Englewood Cliffs, New Jersey, 1988.

[3] J. Uher, S. Liang and W.J.R. Hoefer, "S-Parameters of Microwave Components Computed With The 3D Condensed Symmetrical TLM Node", IEEE MTT Symp., 1990, 653-656.

[4] X. Zhang and K.K. Mei, "Time-Domain Finite Difference Approach To The Calculation of the Frequency-Dependent Characteristics of Microstrip Discontinuities", IEEE Trans. Microwave Theory Tech., 1990, vol. 36, no. 12, 1775-1787.

[5] T.Shibata, T.Hayashi and T. Kimura, "Analysis of Microstrip Circuits Using Three-Dimensional Full-Wave Electromagnetic Field Analysis In The Time Domain", IEEE Trans. Microwave Theory Tech., 1990, vol. 36, no. 6, 1064-1070.

[6] M. Wertgen and R. H. Jansen, "Efficient Direct and Iterative Electrodynamic Analysis of Geometrically Complex MIC and MMIC Structures", Int. J. Numerical Modelling, 1989, vol. 2, 153-186.

[7] S.-C. Wu, H.-Y. Yang and N.G. Alexopoulos, "A Rigorous Characterization of Microstrip Cross and Tee Junctions", IEEE MTT Symp., 1990, 1151-1154.

SESSION 16- "FINITE ELEMENT AND FINITE DIFFERENCE TIME DOMAIN SOLUTIONS"

Moderator: Raymond Luebbers

A New Weighted Residual Finite Element Method for Computational Electromagnetics in the Time Domain

John Ambrosiano and Scott T. Brandon
L-95, Box 808
Lawrence Livermore National Laboratory
Livermore, CA 94550

Rainald Löhner
CMEE School of Engineering and Applied Science
The George Washington University
Washington, DC 20052

Abstract

Engineers and scientists have become increasingly interested in calculating electromagnetic effects in the time domain. For example, the time domain is especially convenient for studying short (wide band) pulses. For such methods to be generally useful, they must be free of the severe geometric restrictions imposed by traditional finite difference methods.

In our research into methods for plasma simulations in realistic geometries, we have developed finite element methods for electromagnetics in the time domain on unstructured grids. Unstructured grids provide maximum flexibility in fitting sample points to the problem, both on boundaries and in the interior. Finite elements provide the most convenient framework for the mathematics as well as for the implementation.

We will present a new finite element method for computational electromagnetics on unstructured grids. The method is fast, easy to implement, and 2nd-order accurate. Although we use low-order elements, the method can be shown to preserve the divergence constraints ($\nabla \cdot \mathbf{B} = 0, \nabla \cdot \mathbf{E} = 0$ in vacuum). We also present a numerical benchmark.

1. Introduction.

There has been great interest in recent years in calculating electromagnetic fields in the time domain. The time domain is especially convenient for modelling wide-band pulses or for understanding transient effects.

To be truly useful, a good method must be geometrically flexible. This requirement has motivated many successful research efforts using both finite elements and finite volumes[1-8]. These methods allow solutions to be computed on boundary-conforming structured meshes or on unstructured meshes. The freedom to choose these more general meshes over the traditional rectilinear finite difference meshes is crucial for geometric flexibilty. We have concentrated exclusively on unstructured meshes of triangles. We feel this provides maximum flexibility in fitting sample points to the problem, both on boundaries and in the interior.

In the process of designing methods for plasma simulation, we have investigated several approaches. We have previously reported our experience with the Taylor-Galerkin technique applied to electromagnetics[3]. The Taylor-Galerkin (TG) method is a general high-order method for hyperbolic systems that has been used sucessfully in fluid dynamics[9]. Accurate computations using TG have been reported for electromagnetic scattering applications[10] and we have successfully implemented a plasma particle code based on the technique[11]. The TG schemes are highly accurate and relatively free of dispersion. However, we have found that they are substantially more expensive than traditional finite difference time domain (FDTD) methods. In addition, there is nothing in the conforming Galerkin formulation to guarantee additional constraints that are often important in electromagnetics. For example, while our TG computations are globally quite accurate, they nonetheless produce spurious local divergence errors. Although these errors are bounded by the order of the method to relatively small values, they are potentially troublesome for certain applications, particularly those that seek to incorporate charged particles.

Our search for a better particle code field solver has led us to some unconventional approaches. One of the most appealing has been described by Nedelec[4] who constructs special elements appropriate to vector fields on which constraints are imposed. Nedelec's elements have specific degrees of freedom which constrain the vector field represented by them to conform to the special Hilbert spaces $H(div, \Omega)$ or $H(curl, \Omega)$. A variational formulation

may then be applied directly to the vector components. This yields a finite element formulation which satisfies the desired constraints. On Nedelec's elements, the tangential or normal components are constant on, and therefore continuous across, interelement boundaries. It is this property that causes them to be conformal in the $H(div, \Omega)$ or $H(curl, \Omega)$ spaces.

The method of Nedelec, while appealing, has certain drawbacks in our opinion. It uses a complicated variational formalism which is awkward to interpret in the usual way (i.e., in terms of shape functions and test functions) and awkward to implement. We have endeavored to obtain a simpler method based on weighted residuals by using non-conforming shape functions. We regard our method as the non-conforming equivalent of Nedelec's formulation. The new method retains the divergence-conserving properties of Nedelec and is fast and easy to implement. In addition, our method becomes identical to finite differences on an equilateral triangular mesh (with its dual regular hexagonal lattice) and thereby makes good contact with traditional FDTD techniques.

2. Non-conforming elements in $H(div, \Omega)$ and $H(curl, \Omega)$.

Our non-conforming formulation relaxes the requirement of continuity of the tangential or normal vector components across the interelement boundaries. These components are required only to be midpoint-side continuous. A suitable shape function for any linear interpolation represented by sample values at the midpoint of the sides can be uniquely derived. This shape function is pictured in Figure 1. Consider the standard mapping of an arbitrary triangle onto the lower-left half of the unit square in the two-dimensional (ξ, η) space (Figure 2). We may define two types of elements. An element that is non-conforming in $H(curl, \Omega)$ (Figure 2a) expresses the vector $\mathbf{v} = (v_\xi, v_\eta)$ in the form:

$$\begin{aligned} v_\xi &= -A\xi - B\eta + C \\ v_\eta &= D\xi + A\eta - C \end{aligned} \tag{1}$$

where

$$A \equiv \sqrt{2} v_{t3}; \qquad B \equiv \sqrt{2} v_{t3} + 2 v_{t2}$$
$$C \equiv v_{t2} + \tfrac{1}{\sqrt{2}} v_{t3}; \qquad D \equiv \sqrt{2} v_{t3} + 2 v_{t1} \tag{2}$$

and $v_{t1}\hat{\tau}_1, v_{t2}\hat{\tau}_2, v_{t3}\hat{\tau}_3$ are the tangential vectors at the midpoint of each side. In terms of shape functions

$$S_1 = 1 - 2\xi$$
$$S_2 = 1 - 2\eta \tag{3}$$
$$S_3 = 2(\xi + \eta) - 1$$

$\mathbf{v}$ is expressible as

$$\mathbf{v} = v_{t1}\hat{\tau}_1 S_1 + v_{t2}\hat{\tau}_2 S_2 + v_{t3}\hat{\tau}_3 S_3 \tag{4}$$

One can readily see from (1) and (2) that this element has the following properties: (i) the curl of $\mathbf{v}$ (in the z-direction out of the page) is a constant in the element and equal to the sum of each tangential component times the length of its respective side divided by the area of the triangle, (ii) $\nabla \cdot \mathbf{v} = 0$.

With the same kind of representation as (4), but this time using the normal projections $\{v_{ni}\hat{\nu}_i : i = 1, \ldots, 3\}$ as degrees of freedom as in Figure 2b, we obtain the non-conforming element corresponding to $H(div, \Omega)$. Its properties are: (i) the divergence of $\mathbf{v}$ is the sum of each normal component times the length of its respective side divided by the area of the triangle, (ii) $\nabla \times \mathbf{v} \cdot \hat{\mathbf{z}} = 0$.

3. Weighted residual formulation — TE polarization.

Once the unknowns are expressed in terms of their basis set and degrees of freedom, the weighted residual (WR) method obtains finite element relations by multiplying the

residual by a "suitable" test or weighting function, setting it to zero, and integrating over the problem domain. For non-conforming representations, the loss of interelement continuity requires that the integrals be performed elementwise.

By using a WR formulation we gain the necessary freedom to satisfy additional constraints. However, this freedom means that it is possible to derive a bad method by choosing "unsuitable" test functions. A successful WR method is often found by serendipity or by trial and error. Unlike variational methods or Galerkin's method, a WR formulation is normally justified *a posteriori* by examining special cases and, of course, by performing computational benchmarks.

For the TE polarization pictured in Figure 2a, let the electric field's degrees of freedom be its tangential projections at the midpoint of the sides and its basis functions be the set of side functions $\{S_i : i = 1,\ldots,\mathcal{N}_s\}$, where $\mathcal{N}_s$ is the number of sides. Let B_z be constant within an element so that its basis is the set of constant element shape functions $\{P_e : e = 1,\ldots,\mathcal{N}_e\}$ with $\mathcal{N}_e$ being the number of elements. Faraday's law

$$\frac{\partial B}{\partial t} = -\left[\nabla \times \mathbf{E}\right] \cdot \hat{\mathbf{z}} \tag{5}$$

becomes

$$\sum_e \dot{B}_e P_e = -\left[\nabla \times \sum_i S_i E_i \hat{\tau}_i\right] \cdot \hat{\mathbf{z}} = -\sum_i E_i \nabla S_i \times \hat{\tau}_i \cdot \hat{\mathbf{z}} \tag{6}$$

To select a particular element e' we choose as our weight function $P_{e'}$. We then multiply (6) by $P_{e'}$ and integrate. Clearly, the only contribution is from the element e' and the sides connected to it. Thus we obtain

$$\dot{B}_{e'} = -\frac{1}{\Delta_{e'}} \sum_{i \in e'} E_i \ell_i \tag{7}$$

The notation $i \rightleftharpoons e$ is taken to mean side i connected to element e. $\Delta_{e'}$ is the area of element e' and ℓ_i is the length of side i. Equation (7) obviously makes good physical sense. It states that the rate of change of the element value of B is minus the circulation of E.

Next consider Ampere's law:

$$\frac{\partial \mathbf{E}}{\partial t} = c^2 \nabla \times B\hat{\mathbf{z}} \tag{8}$$

Its form in the chosen representation is

$$\sum_i \dot{E}_i S_i \hat{\tau}_i = c^2 \nabla \times \sum_e \mathcal{B}_e P_e \hat{\mathbf{z}} \tag{9}$$

Let us leave the exact form of the weight function unspecified for the moment and assume that there exists a function W_j of bounded support which is constant on side j and vanishes outside the elements which have side j in common. The WR prescription is

$$\sum_i \dot{E}_i \left(\int_{\Omega_j} W_j S_i d\Omega_j \right) \hat{\tau}_i = c^2 \sum_e B_e \left(\int_{\Omega_j} W_j \nabla P_e d\Omega_j \right) \times \hat{\mathbf{z}} \tag{10}$$

where Ω_j is the support of W_j. We see that the right-hand side of (10) is ill-defined since the gradients of P_e vanish elementwise. Thus we integrate by parts obtaining

$$\begin{aligned} \sum_i \dot{E}_i \left(\int_{\Omega_j} W_j S_i d\Omega_j \right) \hat{\tau}_i = -c^2 \sum_{e \rightleftharpoons j} B_e \left(\int_{\Omega_j} P_e \nabla W_j d\Omega_j \right) \times \hat{\mathbf{z}} \\ + c^2 \sum_{e \rightleftharpoons j} B_e \left(\oint_{\Gamma_j} W_j P_e d\Gamma_j \hat{\mathbf{n}} \right) \times \hat{\mathbf{z}} \end{aligned} \tag{11}$$

where Γ_j is the boundary of the support of W_j and $\hat{\mathbf{n}}$ is normal to Γ_j. One natural choice for W_j is the non-conforming linear basis function S_j. However, we have found that this choice is incorrect and causes signals to propagate at the wrong speed. The correct choice is a similar function $\tilde{S}_j$ which has 1/2 the slope of S_j. That is, S_j is equal to one on side

j and goes to zero on a line joining the midpoints of the remaining two sides, while $\tilde{S}_j$ is one on side j and goes to zero at the vertex opposite side j. The left-hand-side of (11) contains a matrix expression which may be lumped. The lumped mass contribution from each of the two elements is $\Delta_e/3$. Multiplying by $\hat{\tau}_j$ and carefully evaluating the interior and the surface contributions yields:

$$\dot{E}_j = c^2 \left(\frac{3}{2}\right) \frac{(B_{j+} - B_{j-})}{(\Delta_{j+} + \Delta_{j-})} \ell_j \tag{12}$$

Relative to side j, + (−) refers to the element in (opposite) the direction $\hat{z} \times \hat{\tau}_j$. We may also replace the areas associated with the mass matrix with expressions in terms of the altitude lengths h_{j+},h_{j-} obtaining:

$$\dot{E}_j = c^2 \frac{(B_{j+} - B_{j-})}{\frac{1}{3}(h_{j+} + h_{j-})} \tag{13}$$

In this form it is plain that if the mesh were equilateral, the update on the tangential component of E would simply be c^2 times the difference between values of B at the Voronoi points of the two triangles common to that side.

4. Weighted residual formulation — TM polarization.

For the TM polarization pictured in Figure 2b, let the magnetic field's degrees of freedom be its normal projections at the midpoint of the sides — again letting its basis functions be the set $\{S_i\}$. Let E_z be linear within an element as interpolated from values at the vertices so that its basis is the set of linear element shape functions $\{N_n : n = 1, \ldots, \mathcal{N}_v\}$ with $\mathcal{N}_v$ being the number of triangle vertices. Faraday's law in this polarization

$$\frac{\partial \mathbf{B}}{\partial t} = -\nabla \times E\hat{z} \tag{14}$$

becomes

$$\sum_i \dot{B}_i S_i \hat{\nu}_i = -\nabla \times \sum_n E_n N_n \hat{\mathbf{z}} \tag{15}$$

The appropriate test function for a side j is again the test function $\tilde{S}_j$ although in this case no error occurs if S_j is used instead. Integrating we obtain

$$\sum_i \dot{B}_i \left(\int_{\Omega_j} \tilde{S}_j S_i d\Omega_j \right) \hat{\nu}_i = -\sum_n E_n \left(\int_{\Omega_j} \tilde{S}_j \nabla N_n d\Omega_j \right) \times \hat{\mathbf{z}} \tag{16}$$

In this instance the lumped mass matrix contribution to side j from each element e is $2\Delta_e/3$. After taking the scalar product with $\hat{\nu}_j$, we notice that, on the right-hand side, the only vertex contributions are from those joined directly to side j. Evaluation of (16) eventually leads to the very simple expression

$$\dot{B}_i = -\frac{(E_{i+} - E_{i-})}{\ell_i} \tag{17}$$

where + (-) refers to the vertex in (opposite) the direction $\hat{\mathbf{z}} \times \hat{\nu}_j$. Once again we have an expression that makes good physical sense. It states that the update on the normal component of **B** at the midpoint of a side is just equal to the difference between the values of E_z at each end divided by the length.

We next turn to Ampere's Law in this polarization:

$$\frac{\partial E}{\partial t} = c^2 \left[\nabla \times \mathbf{B} \right] \cdot \hat{\mathbf{z}} \tag{18}$$

In terms of the basis functions:

$$\sum_n \dot{E}_n N_n = c^2 \nabla \times \left[\sum_i B_i S_i \hat{\nu}_i \right] \cdot \hat{\mathbf{z}} \tag{19}$$

We choose as our weighting function the linear vertex shape function N_m. Because our non-conforming element representation for **B** has vanishing elementwise curl, we must integrate by parts in this case as well. Thus we have

$$\sum_n \dot{E}_n \left(\int_{\Omega_m} N_m N_n d\Omega_m \right) = -c^2 \sum_{i \rightleftharpoons m} B_i \left(\int_{\Omega_m} S_i \nabla N_m d\Omega_m \right) \times \hat{\nu}_i \cdot \hat{\mathbf{z}}$$
$$+c^2 \sum_{i \rightleftharpoons m} B_i \left(\oint_{\Gamma_m} N_m S_i d\Gamma_m \hat{\mathbf{n}} \right) \times \hat{\nu}_i \cdot \hat{\mathbf{z}} \tag{20}$$

where Ω_m is the support of N_m and Γ_m is the boundary. The mass matrix contributions in this instance are the familiar lumped mass contributions associated with conforming linear elements. That is, each element e contributes $\Delta_e/3$. Although somewhat tedious, careful evaluation of (20) yields the uncomplicated expression

$$\dot{E}_m = \left(\frac{2}{3} \right) \frac{\sum_{i \rightleftharpoons m} B_i (\Delta_{i+} + \Delta_{i-})/\ell_i}{\sum_{e \rightleftharpoons m} \Delta_e/3} \tag{21}$$

where + or - refers to elements to the right or left respectively of side i. Using the relation between the area of each triangle and the length of the altitude along the normal directions $\hat{\nu}_i$ one may develop a straightforward interpretation (21) for an equilateral mesh. In that case the sum in the numerator is the sum of the normal component B_i times the distance between the Voronoi points of the two adjacent triangles. Dividing this sum by the enclosed area yields a reasonable approximation to the curl about vertex m.

5. Implemention and benchmark.

Equations (7), (12), (17), and (21) constitute the new weighted residual method. In the spirit of traditional staggered finite difference methods, we use a leapfrog approximation to the time derivatives. Given a list linking elements with vertices and elements with sides, the WR equations require only straightforward gather and scatter operations for implementation. The electric fields are expressed at timelevel k and magnetic fields at timelevel $k + \frac{1}{2}$. Although space does not permit it here, it may be shown that these equations have the required symmetry properties that preserve the divergences of **E** and **B** exactly (to roundoff) in the vacuum. The degrees of freedom representing the fields

are natural for enforcement of boundary conditions. Specifically, boundary conditions are enforced by setting E_i (E-tangential) and B_i (B-normal) at the midpoint of boundary faces and by setting E_n (E-tangential) at boundary nodes.

We present a numerical benchmark showing that the WR method obtains reasonably accurate results for a scattering problem. Figure 3a shows a portion of the mesh around a circular obstacle. For this test a plane wave of wavenumber k is incident from the left. Relative to the radius a of the circle, $ka = 5$. The observation point is one radius ahead of the circular boundary on a line joining the center. The Courant number is 0.25. Figure 3b compares the computation with the analytic result. We can see that the computed solution has some dispersion and a small phase error, but is a reasonably good approximation to the true result.

We have presented a new finite element method for triangle grids that has many useful properties in common with traditional staggered-mesh finite difference schemes. Indeed, it reduces to a straightforward finite difference scheme on an equilateral mesh. Unlike many methods that have been proposed, it is simple to implement and fast. It does not require a Voronoi-Delaunay mesh or any other special mesh. Benchmarks thus far suggest that the method is 2nd-order accurate for smooth meshes; i.e., the same relative accuracy as standard FDTD methods.

Acknowledgement.

We wish the thank several colleages for their suggestions and comments. We thank Rick DeVore, Scott Ray, Bruce Langdon, Peter Rambo, Dale Nielsen, Alain Adolf, and Bruno Scheurer. This work was performed under the auspices of the U. S. Department of Energy by Lawrence Livermore National Laboratory under contract no. W-7405-Eng.-48.

References.

1. Niel K. Madsen and R. Ziolkowski, *Wave Motion*, **10** (1988).
2. Robert L. Lee and Niel K. Madsen, *J. Comput. Phys.*, 88, 284 (1990)

3. J. Ambrosiano, S. T. Brandon, and Rainald Löhner, "Electromagnetic Propagation on an Unstructured Finite Element Grid," Proceedings of the 6th Annual Review of Progress in Computational Electromagnetics, Monterey, California, January, 1990.

4. J. C. Nedelec, *Numerische Mathematik*, **35**, 315 (1980).

5. P. Degond, F. Hermeline, P. A. Raviart, and J. Segre, "A Coupled Particle-Finite Element Method for the Approximation of Vlasov-Maxwell Equations," (Unpublished).

6. F. Hermeline, "Two Coupled Particle-Finite Element Methods Using Delaunay-Voronoi Meshes for the Approximation of Vlasov-Poisson and Vlasov-Maxwell Equations," (Unpublished).

7. James Eastwood, "Virtual Particle Electromagnetic Particle-Mesh Algorithms," Culham Laboratory Report CLM-P870, 1990.

8. M. E. Jones, "Electromagnetic PIC Codes with Body-Fitted Coordinates," Proceedings of the 12th Conference on the Numerical Simulation of Plasmas, San Francisco, California, September, 1987.

9. R. Löhner, K. Morgan, and O. C. Zienkiewicz, *Int. J. for Num. Meth. in Fluids*, **4**, 1043 (1984).

10. C. R. DeVore, R. Löhner, and J. Ambrosiano, "Electromagnetic Scattering Calculations Using a Finite-Element Solver for the Maxwell Equations," Proceedings of the 1990 Free-Lagrange Conference, Jackson Lake, Wyoming, June 3-7, 1990.

11. J. Ambrosiano, S. T. Brandon, and R. Löhner, "Electromagnetic Particle Codes on Unstructured Grids," Proceedings of the 1990 Free-Lagrange Conference, Jackson Lake, Wyoming, June 3-7, 1990.

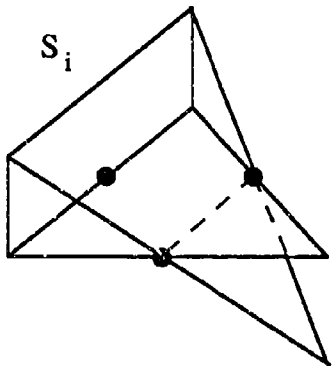

Figure 1

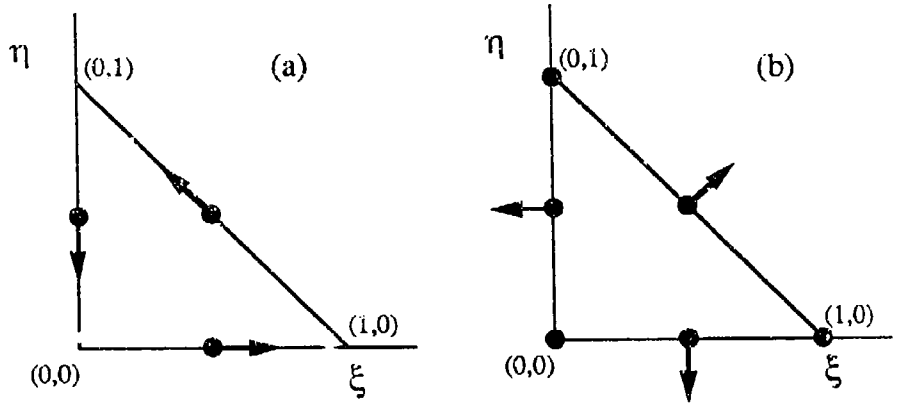

Figure 2

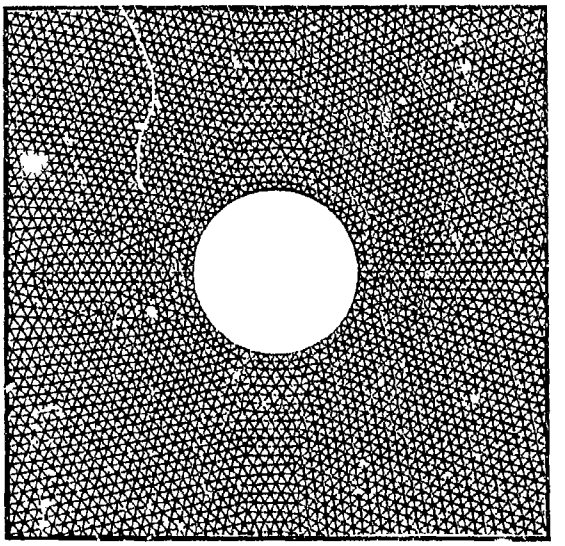

Figure 3a

Figure 3b

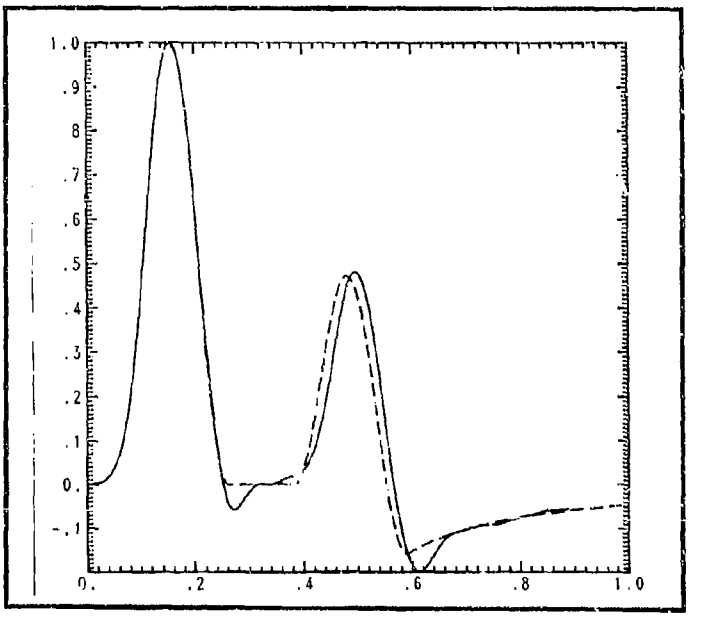

1991 ACES Symposium, Monterey, California, March 1991

'Virtual Particle' Electromagnetic Particle-Mesh Algorithms for Microwave Tube Modelling

James W. EASTWOOD

AEA Technology, Culham Laboratory,
Abingdon, Oxon. OX14 3DB, England

Abstract

Virtual Particle algorithms are new charge conserving finite element PIC schemes which combine good physical accuracy, geometrical flexibility and computational speed. Their derivation is outlined and illustrated by a 2-D polar example. Numerical noise control is used to reduce the number of superparticles needed. Dispersion analysis shows less mesh dependence and better numerical stability than conventional PIC. Some illustrative application, including video animations, are given.

1 Introduction

The 'Virtual Particle' particle-mesh algorithms provide a new approach to solving the relativistic Vlasov-Maxwell equations. They differ from the usual Particle-in-Cell (PIC) schemes in that they are derived using finite elements in both space and time. Virtual particles, from which current is assigned to element nodes, are placed at special points interpolated between particle positions at successive timelevels; this procedure automatically leads to charge conservation, so eliminates the need to refer to charge density and to Poisson's equation in the main calculation loop. The advantage of the new schemes over PIC is that they combine good physical accuracy, geometrical flexibility and computational speed – indeed, they are well suited to parallel computer architectures.

2 Derivation

The mathematical model we consider is the relativistic Maxwell-Vlasov set. If the distribution function is represented by a set of sample points (i.e. superparticles)

$$f(\mathbf{x},\mathbf{p},t) = \sum_s N_s \delta(\mathbf{x} - \mathbf{x}_s(t))\delta(\mathbf{p} - \mathbf{p}_s(t)) \qquad (1)$$

where $(\mathbf{x}_g, \mathbf{p}_g)$; $g \epsilon [1, N_p]$ are the coordinates of the N_p superparticles, each of mass $M = N_s m_0$ and charge $Q = N_s q$, then the Maxwell-Vlasov set may be written in terms of the action integral

$$I = \int dt dr \left(\frac{\mathbf{D} \cdot \mathbf{E} - \mathbf{B} \cdot \mathbf{H}}{2} - \rho\phi + \mathbf{j} \ \mathbf{A} \right) - \int \sum_g \frac{Mc^2}{\gamma_g} dt \tag{2}$$

where $\mathbf{B} = \nabla \times \mathbf{A}$ and $\mathbf{E} = -\nabla\phi - \frac{\partial \mathbf{A}}{\partial t}$. Treating I as a functional of the vector potential $\mathbf{A}$, the scalar potential ϕ and particle coordinates $\{\mathbf{x}_g\}$ leads to Euler-Lagrange equations which reduce to Maxwell's equations and the relativistic equations of motion. More extensive discussions of this are given in references [5, 6].

The finite element approximations to the Maxwell-Vlasov equations are obtained by substituting test function approximations for potentials ϕ and $\mathbf{A}$, and particle coordinates $\mathbf{x}_g$ into Eq.(2) and taking variations with respect to the unknown nodal amplitudes.

Variations *wrt.* to ϕ yields a discrete form of Gauss' Law, plus a prescription for charge assignment. Variation *wrt.* $\mathbf{A}$ gives Ampere's Law and the current assignment prescription, and variations *wrt.* particle coordinates give discrete equations of motion and the prescription for force interpolation. Explicit reference to $\mathbf{A}, \phi$ and charge density ρ can be eliminated by using the homogeneous Maxwell equations. The result is a fast and accurate timestepping scheme where ρ need not be accumulated, and charge conservation corrections such as Poisson equation solutions for longitudinal electric field correction [3] or "pseudocurrents" [4] are not required.

A whole family of virtual particle schemes may be generated by choosing appropriate element geometry and trial functions. If the procedure is correctly followed, these schemes will automatically have the charge conserving property.

3 A 2-D Example

We use a two dimensional polar (r, z, t) transverse magnetic (TM) model and the lowest order conforming rectangular brick elements to illustrate the practical realisation of the method outlined in section 2. On a uniform net of elements, this choice leads to a numerical scheme similar to that using the usual interlaced TM finite difference mesh [2].

For clarity, we work with units which give length unity sides to elements and $\mathbf{E} = \mathbf{D}, \mathbf{B} = \mathbf{H}$. The potential and field trial functions become a mixture of piecewise linear (L) and constant (C) functions of the coordinates (r, z, t). Fields (E_r, E_z, E_θ) are respectively (C, L, C), (L, C, C) and (C, C, L) in (r, z, t). This choice leads to node locations shown in figure 1. Variations *wrt.* ϕ and element assembly give the global discrete approximation to Gauss' Law

$$\partial_z(r\alpha_r E_z) + \partial_r(r\alpha_z E_r) = q \tag{3}$$

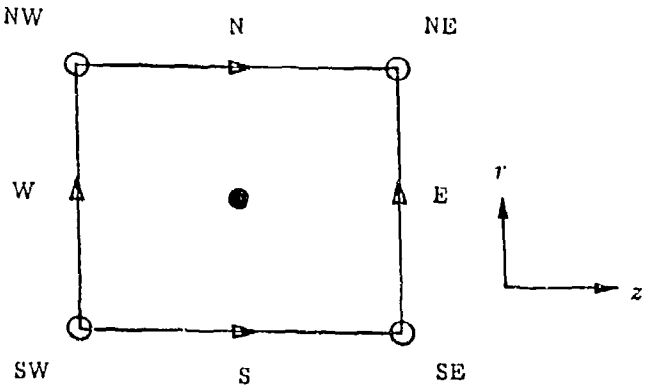

Figure 1: *Location of element nodes. Values of ρ and ϕ are stored at corners, (E_z, E_r) and (I_z, I_r) at sides and B_θ at the centre.*

where difference operator ∂_z and ∂_r (and averaging operators α_z and α_r) respectively act on the indices ℓ and m:

$$\partial_z f_{\ell,m} = f_{\ell+1/2,m} - f_{\ell-1/2,m} \quad ; \quad \alpha_z f_{\ell,m} = (f_{\ell-1,m} + 4f_{\ell,m} + f_{\ell+1,m})/6 \tag{4}$$

Similar expressions hold for ∂_r and α_r on index m and ∂_t and α_t on the time index n. In Eq.(3), the choice of (L, L, C) support for ϕ implies that q is accumulated using CIC (Cloud In Cell) in r and z, and NGP (Nearest Grid Point) in t [1]

Variations *wrt.* A and assembly give the discrete approximations to the components of Ampere's Law

$$\partial_t(r\alpha_r E_z) = \partial_r(r\alpha_t B_\theta) - I_z \quad ; \quad \partial_t(r\alpha_z E_r) = -\partial_z(r\alpha_t B_\theta) - I_r \tag{5}$$

and the NGP/CIC virtual particle current assignment prescription. Faraday's Law becomes

$$\partial_t B_\theta = \partial_r E_z - \partial_z E_r \tag{6}$$

Note that these equations for the fields differ from the usual finite difference equations only in the appearances of the averaging operators in Eqs.(3) and (5).

To maintain explicit forms for the equations of motion we assume that particle positions are constant over the interval from timelevel $n - 1/2$ to $n + 1/2$, and use a weak approximation for the momentum. This yields the usual finite difference expression

$$\mathbf{p}^{n+1/2} - \mathbf{p}^{n-1/2} = Q\Delta t \left[\mathbf{E}^n(\mathbf{x}^n) + \bar{\mathbf{v}}^n \times \frac{(\mathbf{B}^{n+1/2} + \mathbf{B}^{n-1/2})}{2}\right] \tag{7}$$

where $\bar{\mathbf{v}}^n = (\mathbf{v}^{n+1/2} + \mathbf{v}^{n-1/2})/2$ and

$$\mathbf{x}^{n+1} = \mathbf{x}^n + \mathbf{v}^{n+1/2}\Delta t \tag{8}$$

The fields at particle locations are the value of the finite element fields at that point. Thus, for this example, E_z is the NGP in z and CIC in r interpolant of the nodal values, E_r is CIC/NGP and B_θ is NGP/NGP , etc.

The choice of trial functions prescribe the charge and current assignment schemes. For a unit charge at position (z,r) *wrt.* the SW corner of a unit side element, the charges assigned are:-

$$\begin{array}{llll} \delta\rho_{NE} = zr & \delta\rho_{NW} = (1-z)r \\ \delta\rho_{SE} = z(1-r) & \delta\rho_{SW} = (1-z)(1-r) \end{array} \tag{9}$$

Currents assigned from a trajectory segment of length $(\Delta z, \Delta r)$ and mean position $(\bar{z},\bar{r})$ are:-

$$\begin{array}{llll} \delta I_N = \bar{r}\Delta z & \delta I_S = (1-\bar{r})\Delta z \\ \delta I_E = \bar{z}\Delta r & \delta I_W = (1-\bar{z})\Delta r \end{array} \tag{10}$$

It can be shown that assignment according to Eqs. (9) and (10) identically satisfies the charge conservation law, $\partial_t q = -\partial_z I_z - \partial_r I_r$.

The timestep loop for this example comprises:-
(1) advance positions using Eq. (8)
(2) accumulate currents using Eq. (10)
(3) update fields using Eqs. (5)-(6)
(4) update momenta using Eq. (7)
(5) go to (1).

4 Noise Control using TCA

The algorithms derived using the variational time centred formulation are lossless, apart from radiation and particle fluxes through the boundaries. The small number of simulation superparticles and discontinuous current assignment enhances current fluctuations above those in the physical counterpart. The noise radiation field depends on all past fluctuations and can rapidly mask collective phenomena being studied. The obvious expedients of increasing the number of particles and refining the current assignment are unattractive because of larger computational costs. The transverse current adjustment (TCA) scheme allows computations to be successfully undertaken with particle numbers which, in its absence, would be too small to keep noise levels acceptable.

The idea behind TCA is to introduce a dissipative solenoidal current, $\mathbf{j}_d$, which attenuates noise generated by particle graininess but leaves collective modes and charge conservation unaffected. One choice which has proved both simple and effective is

$$\mathbf{j}_d = |\beta|\,\nabla_d \times \nabla_d \times \mathbf{E}(= -|\beta|\,\nabla_d \times \Delta_t B) \tag{11}$$

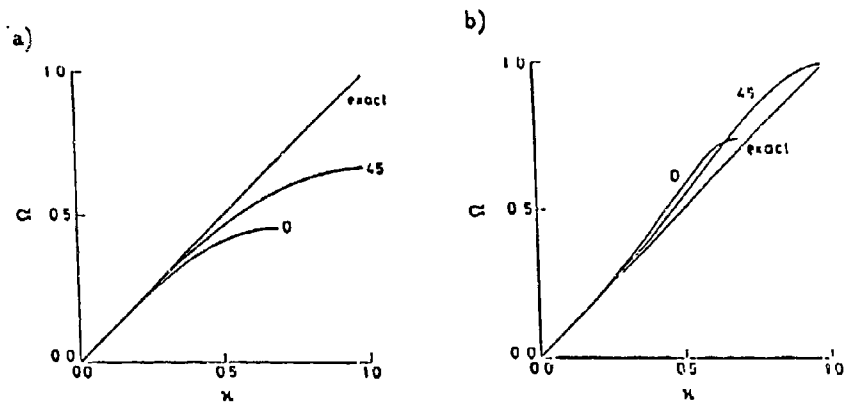

Figure 2: *(a) frequency Ω versus wavenumber κ for plane EM waves on a FD mesh for wavevectors along a mesh axis* (0°) *and mesh diagonal* (45°) *using Courant number 0.5. (b) As (a), but for the FE net. The curves labelled 'exact' are those followed in the absence of numerical errors.*

where ∇_d is the discrete gradient operator and Δ_t is the backward time difference operator. Equation (11) may be interpreted physically as a magnetization current or numerically as a small adjustment to the time centring of the magnetic field.

5 Dispersion

The finite element approximations obtained in section 3 have, like their finite difference counterparts a Courant stability condition $c\Delta t/\delta < 1$, but give much improved dispersion. Figure 2a shows the dispersion of light waves on a uniform cartesian net for the standard TM fda [2]: there is strong anisotropy and $\Omega < \kappa$ introduces the possibility of numerical Cerenkov instability [7]. Figure 2b shows that the corresponding FE scheme has greatly improved isotropy and no Cerenkov instability ($\Omega > \kappa$).

6 Final Remarks

The FE formulation outlined here provides a systematic approach to obtaining efficient and accurate charge conserving algorithms for solving the coupled Maxwell Vlasov equations. The method applies equally well in 1, 2 or 3-D, in general coordinates and for general element shapes. Already 1-D and 2-D implementations have been used to study diodes, MITLs, MILOs, TWTs and multipaction. Video illustrations at this conference include MILO and multipaction simulations(cf. Figure 3). Currently, work is being undertaken on developing

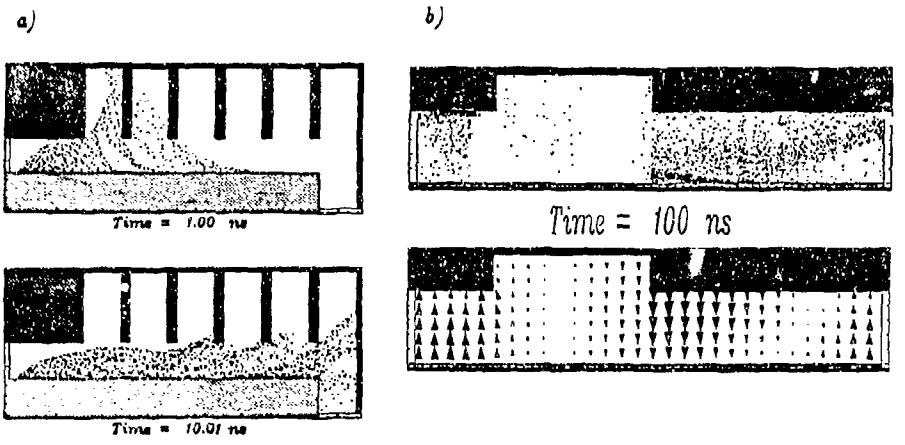

Figure 3: *(a) electron density scatter plots taken from the startup phase of the video animations of a 6 cavity MILO device and (b) electron density and electric field vectors in a multipacting coaxial transmission line.*

3-D software and in studying the implementation of the VP method on parallel architecture machines.

References

[1] R. W. Hockney and J. W. Eastwood, "Computer Simulation using Particles", McGraw-Hill (1980) (student edn. Adam-Hilger, 1988).

[2] C. K. Birdsall and A. B. Langdon, "Plasma Physics via Computer Simulation", McGraw-Hill (1985).

[3] J. P. Boris, Proc. 4th conf. Num. Sim. Plasmas, (N.R.L., Washington, 1971), p3.

[4] B. M. Marder, J. Comput. Phys. 68 (1987) 48.

[5] H. R. Lewis, Meth. Comp. Phys. 9 (1970) 307.

[6] H. Goldstein,"Classical Mechanics", Addison-Wesley, (1950).

[7] B. B. Godfrey, J. Comput. Phys. 15 (1974) 504.

[8] J. W. Eastwood, "Virtual Particle Electromagnetic Particle-Mesh Algorithms", Culham preprint CLM-P780 (1990), *to appear* Computer Phys. Commun.

A New Magnetic Field Analysis For Dynamical Problem Involving Relative Displacement With Time

C. HAMAMURA, M. OKABE, T. OHMURA and K. SATO
MITSUBISHI ELECTRIC CO. MATERIALS & ELECTRONIC DEVICES LAB.
1-1-57, MIYASHIMO, SAGAMIHARA, KANAGAWA, 229 JAPAN

Abstract In order to understand the magnetic performance of the rotating machines in more detail, a new analytical technique for simulating the device including moving parts is proposed. A concept named " supplementary region" being newly introduced allows these machines to be analyzed by FEM taking the relative motion of a rotor into account. This technique is now applied to an induction motor, and results in that calculated torque characteristic depends on the rotor position and that its mean value is in good agreement with measured one. In this paper, the new concept and the computational result are presented. The technique reported here is one of the promising technique to calculate the more interesting issue of the transient rotational motion of the rotor with eddy current .

Introduction

The magnetic field simulation techniques are one of the most efficient means for understanding the detailed electromagnetic performance of many devices. Among simulation techniques, a finite element method (FEM) has been widely used for the sake of its high applicability in the non-linear and the anisotropic characteristics of a magnetic material. However, there is few report on the application of the method to magnetic devices including moving electromagnetic parts (rotating machine, linear motor, magnetic recording system, and so forth), because of the difficulty in generalizing the modification of the mesh division at each time step. In the case of an induction motor that has a slip characteristic, the computed results are not satisfied with the experimental if an analysis technique does not take the rotor movement relative to the stator into account. Therefore, to generalize the analysis technique based on the FEM for such a dynamic problem is an important theme.

Several investigations on the analysis technique for the dynamic problems have been presented in the literature. [1] They can be roughly classified into a few methods. For the method using FEM, three techniques are proposed as follows: [2] [3] The first technique is to introduce the movement in the expression of the field equation. But it is not applied to the rotating machines, because its reluctance is strongly dependent on the position of the rotor, although this equation just holds in the applications where the reluctance of the moving part does not vary during the movement. The second is the combined analysis technique with a boundary element method (BEM). [4] The technique can take any movement into account, but it is pointed out that some problems are left to be solved in terms of the accuracy adjacent to the air gap and an increase in CPU time due to non-symmetrical coefficient matrix. A local re-meshing is the third technique for this dynamic problem. It has the advantages of taking any movement into consideration without failing the symmetrical characteristic of the matrix. Especially a technique using a moving boundary is useful in

that the mesh distortion caused by the relative movement can be avoided. [5] [6] But even in this technique, the CPU time increases in changing the boundary condition at each time step. Therefore, there are still some problems to be improved.

In this paper, we propose a new efficient technique for solving the dynamic problems. By introducing a new concept named "supplementary region", the FEM can be applied to the problems that has a non-linear magnetic characteristic including eddy current and a mechanical problem with the relative motion. The principle of this method and numerical simulation results for a three-phase induction motor are described.

Method of Analysis

In the magnetic field simulation on the rotating machines, such factors as the magnetic saturation, relative motion between rotor and stator and the coupling field formulation with the external circuits should be taken into consideration. Furthermore, data modification is required as less as possible for every rotor angular position.

Outline of the technique

Figure 1 shows a general dynamic model. Usually, an analyzed region Ωa can be divided into two regions: the moving region expressed by the dotted part Ωr and the stationary region Ωs such as machine stator. Here, a closed path Γ shown by broken line surrounds the moving region Ωr, and it must be chosen large enough to allow the displacement of moving object.

To simplify the calculation, a region Ω_0 that is named " supplementary region " in this paper is introduced. The region covers a moving range of moving object for a period of analysis as illustrated in Fig.1-(b). By using this supplementary region, the conditions for calculating on the region Ωr is determined at each time step. If a set of the selected data on Ω_{r_0} has the same number of nodes on the boundary as that on Γ, and also the same number of elements as that in the region Ωr, the coefficient matrix is not needed to be recalculated at each time step. It is clear that the restricted geometric condition is satisfied in the most of rotating machines. Figure 2 shows a reconnecting process near the path Γ. Since the elements and nodes in the stationary part are not changed at each time step, they are left out of the illustration.

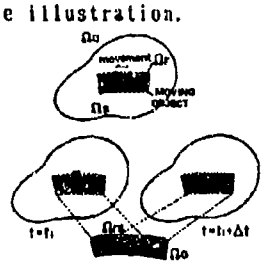

Fig.1 Relationship between an analysis and supplementary region

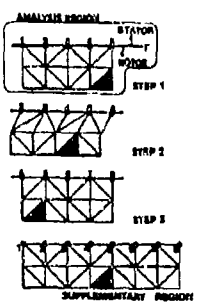

Fig.2 Discretization process near the Γ

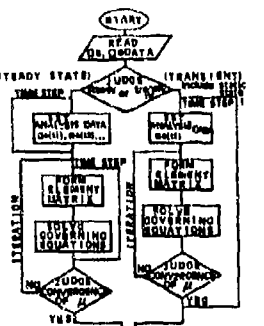

Fig.3 Flow diagram

The selected elements in the supplementary region determine the mesh division in the moving part. Each number expresses the relationship between two region. The flow diagram of modifying the mesh division is shown in Fig. 3.

Governing equation

In the magnetic field analysis, the governing equation is often expressed by $A-\phi$ method derived from Maxwell's equation.

$$\mathrm{rot}\left(\frac{1}{\mu}\,\mathrm{rot}\,A\right) = J_0 + \nu\,\mathrm{rot}\,M - \sigma\left(\frac{\partial A}{\partial t} + \mathrm{grad}\,\phi\right), \qquad (1)$$

where A is the magnetic vector potential, ϕ the electric scalar potential, μ the permeability, σ the conductivity, J_0 the exiciting current density and M the magnetization. A time-derivative term is substituted for the discreteme based on the variation method. The non-linear equation including the magnetic saturation characteristics of magnetic materials is solved by the Newton-Raphson iteration technique. [7] [8]

When the distribution of exciting current J_0 is not known, it is necessary to add Kirchhoff's equation, that expresses a relationship between the terminal voltage Ec and electromagnetive force induced by the change of the magnetic fluxΦ in the stator conductor. [8]

Simulation of Actual Performance of an Induction Motor

Description of analyzed machine

The procedure outlined above is applied to the case of an induction motor with three-phase four-poles, operated at 50Hz and squirrel-cage rotor. Figure 4 illustrates the analyzed area on a quarter of a whole cross-section of the motor. The laminated core material is non-oriented silicon steel 50A800. The gross core length is 175[mm]. The outside diameter of the stator is 210[mm] and the inside is 134[mm]. The air gap length is 0.45[mm]. The type of rotor cage is a cast aluminium, and its conductivity is 2.88×10^7 [s/m] at 20 ℃.

Field model

The analyzed magnetic field on the cross-section of machine core is assumed to be two-dimensional. The electric scalar potential has the constant value in the field, because the secondary conductor is connected to an end ring at the sides of rotor. The laminated core is treated as a non-conductor, and the magnetic non-linearity of the material is expressed by use of an initial magnetization curve. The shaft material S35C is also assumed to be non-conductor.

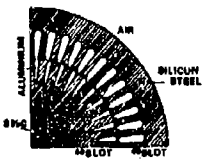

Fig.4 Analyzed field

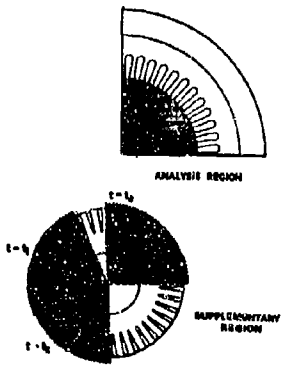

Fig.5 Analysis and supplementary region

An analyzing period $N\pi$ is the time required to be duplicate both the magnetic field and the analysis shape. If the stator has Ns slots, and the slip value and the pole number is S and P, respectively, the following relationship in terms of the integral number N in the steady state is satisfied

$$N \frac{2\pi S}{P} = M \frac{2\pi}{Ns}. \tag{2}$$

where M is also a integral number.

Motion of the rotor

In the rotating machine, either the stator or the rotor can be used as the supplementary region. In the present model, the whole cross section of the rotor with the air gap are used as the supplementary region. Figure 5 illustrated the regions.

Figure 6 shows the variation of magnetic flux distribution with time and the enlarged element division near the gap on the periodic boundary line at slip=0.05. The enlarged figure indicates that the mesh division of the rotor changes in relation to the rotor position at each time step without modifying the nodes given the boundary condition. The time required to generate the analysis condition at every time step (18 steps) is 0.20[sec], that includes the time for an input of the initial data.(The computer used IBM 3090.)

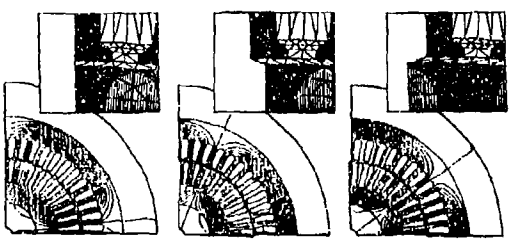

Fig.6 Magnetic flux distribution at slip 5%
(a) ωt=0 ° (b) ωt=60° (c) ωt=120 °

Torque characterisict

For calculating the electromagnetic force or torque, Maxwell's stress method are commonly used. However, it has been known that the method has a disadvantage that the calculated value often depends on the selected surface. [11] So in this paper, the value per unit meter T is calculated as the change in magnetic flux Φ multiplied by the eddy current Ie [12] :

$$T = Ie \frac{\partial \Phi}{\partial \theta} = -\sigma \iint_s \left(\frac{\partial A}{\partial t} + \text{grad } \phi \right) ds \frac{\partial \Phi}{\partial \theta}, \tag{3}$$

where θ is a rotational angle.
To find the magnetic flux difference term in eq.(3), use the formula:

$$\frac{\partial \Phi}{\partial \theta} \fallingdotseq \frac{A(\theta + \theta s) - A(\theta - \theta s)}{2\theta s}, \tag{4}$$

where θs is an angle between two slots of the rotor.

Figure 7 shows the computed result of the torque T at slip=0.05. It is

clear that the torque values depend on not only the exiciting current but also the rotor position. In this figure, the broken line shows the mean value through an analysis period and an open mark is measured one for comparison with the computed. The calculation value is in good agreement with measured one.

Figure 8 shows a calculated torque value at another slip value. The arbitrary slip value can be treated by changing the analyzing period, or time required to be duplicate the magnetic field.

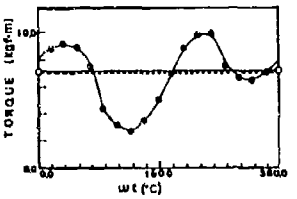

Fig.7 Torque values in a period at slip 5%

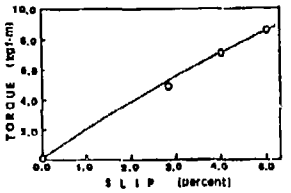

Fig.8 Torque characteristic

Conclusion

A new analysis technique allows to solve the problem including moving parts. The advantages of the concept of the supplementary region newly introduced are that the symmetrical characteristic of matrix is preserved at each time step and no re-meshing is required.

The usefulness of the technique is shown in the case of an induction motor. The time required to modify the mesh division is negligible in comparison with the time required to solve the coefficient matrix . This technique is also efficient for the magnetic recording device. The simulation being taken the hysteresis characteristic into account is implemented by regarding the recording medium as the supplementary region.

Reference

1) S.Mukherjee, G.E.Adams and R.Hoft, IEEE Power Engineering Review :Winter Meeting, vol.9, p.43, 1989
2) B.Davat, Z.Ren and M.Lajoie-Mazenc, IEEE Transactions on Magnetics, vol.MAG-21, pp.2296-2298, 1985
3) A.A.Abdel-Razek, J.L.Coulomb, M.Feliachi and J.C.Sabonnadiere, IEEE Transactions on Magnetics, vol.MAG-18, pp.655-659, 1982
4) M.Burnet Fauchez, IEEE Transactions on Magnetics, vol.24, pp.475-477, 1988
5) Z.Ren, B.Davat and A.Lajoie-Mazenc, presented at 1984 MODELEC Conf., La Grande Motte, France
6) Tang Renyuan, Hu Yan, Lu Zhanheng, Yang Shiyou and Miao Lijie, IEEE Transactions on Magnetics, vol.26, pp.1042-1045, 1990
7) P.Silvester, H.S.Cabayan and B.T.Browne, IEEE Transactions on Power Apparatus System, vol.PAS-92, pp.1274-1281, 1973
8) T.Nakata and N.Takahashi, Transactions on IEE(Japan), vol.104-B, pp.380-386, 1984
9) T.Nakata and N.Takahashi, IEEE Transactions on Magnetics, vol.MAG 22, pp.526-528, 1986
10) M.V.K.Chari and P.Silvester, IEEE Transactions on Power Apparatus System, vol.PAS-90, pp.2362-2372, 1971
11) J.Penman and M.D.Grieve, IEEE Proceeding B., vol.133, pp.212-216, 1986
12) M.Okabe and T.Ohmura, Transactions on IEE(Japan), vol.107-D, pp.1236-1242, 1987

A Time Domain Approach to Calculating Radar Cross Sections

D. W. Harmony and G. R. Salo
BDM International, Inc.
Albuquerque, NM

The potentially large benefits of using finite difference techniques to calculate the radar cross section of complex, composite targets will be discussed. Finite differencing in the time domain will be used to calculate the near fields scattered from a perfectly conducting cube and a solid dielectric cube. A broadband, short duration, plane wave pulse will be used as the excitation. The scattered near fields will be transformed to the far field and then Fourier transformed to calculate the radar cross section as a function of frequency. Numerically generated results for the perfectly conducting case will be compared to measured data. In addition, a short discussion on the numerical benefits and limitations of the approach will be presented.

A 2-D Finite-Volume Time-Domain Technique for RCS Evaluation

by
Richard Holland, Vaughn P. Cable and Louis Wilson

ABSTRACT

This paper describes and tests a method for computing electromagnetic scattering from 2-D metallic bodies using a generalization of the FDTD Yee algorithm, in which a nonorthogonal piecewise-linear conforming mesh may be applied. Results for 2-D TE and TM scattering from a shorted s-curved parallel plate region, and from a 2-D circular ojive are presented. In both cases, solutions were obtained using a structured quadrilateral mesh. A method for obtaining scattering by a circular cylinder using the same basic finite-volume formulation with a fully structured mesh is also discussed. The circular cylinder, while seemingly simple, is actually a stressing case of the meshing algorithm which stretches a cartesian grid to fit a curved geometry.

The primary goal of this work is to model oblique or curved surfaces in the time-domain without staircasing. Examples are presented for edge-on TE illumination of an ojive which demonstrate that 120 cells/λ are required for 1 dB accuracy when staircasing is used, but only 15 cells/λ are needed with conformal meshing. The conformal-mesh model of the curved parallel plate region accurately predicts the first 10 depth resonances and the first 2 width resonances for TE illumination directly into the aperture. Also, TM scattering from the curved parallel plate model retains some fidelity with as few as 4 cells/λ, while staircased models require at least 20 cells/λ.

INTRODUCTION

The majority of published work on modeling curved surfaces in time domain calculations has been by descretizing the curvature into stairsteps, where each step corresponds to a cartesian cell in the Yee FDTD algorithm [1]. The inadequacies of this approach have been well documented [2] and work toward fixing this problem is progressing in a number of directions. These include; the expression of Yee's algorithm in curvilinear coordinates [3,4]; the selective application of Ampere and Faraday contour integration to "sliced" Yee cells [5]; and the generalized oblique-cell rendition of Yee's algorithm [6,7]. The examples and work presented in this paper are an extension of the latter approach; the Yee dual-mesh algorithm is rewritten for a 2-dimensional quadrilateral mesh with full corrections for oblique cells.

The algorithm has previously been tested on problems of scattering by a 2-D circular cylinderusing an unstructured mesh [2]. In this paper, the algorithm is tested using a structured mesh on a shorted, s-shaped, parallel plate region, and a 2-D circular ojive. All of these objects were modeled as perfect electrical conductors (PEC).

The effectiveness of the method is demonstrated by the reduction in mesh density from the staircased method necessary for a given accuracy. For TE scattering by the PEC ojive, the structured mesh required 15 cells/λ to achieve 1 dB accuracy using the oblique cells, whereas, up to 120 cells/λ were needed when staircasing was used. For the s-curved parallel plate model, some resonances were predicted with as few as 4 cells/λ, while the staircased model required at least 20 cells/λ to achieve the same fidelity.

2-D FINITE VOLUME TIME-DOMAIN (FVTD) EQUATIONS

The following equations are a 2-dimensional implementation of the FVTD method in a structured quadrilateral mesh. Figure 1 illustrates the mesh-coordinate relationships used; e.g., S_{Pn} are primary cell

Richard Holland is at 1625 Roma NE, Albuquerque, NM 87106.

Vaughn P. Cable and Louis Wilson are with Lockheed Advanced Development Company, Box 551, Burbank, CA 91520.

edge tangent unit vectors, $\mathbf{N}_{Pn}$ are primary cell edge normal unit vectors, and $\mathbf{S}_{Dn}$ are dual cell edge tangent unit vectors. The 2-D structured mesh axes correspond to $n = 1, 2$.

The basic relationships used for the free-space advancement of $\mathbf{E}, \mathbf{H}$ are

$$\iint_{A_P} \mu_0 \frac{\partial \mathbf{H}}{\partial t} \cdot \mathbf{N_P} dA = -\oint_{\partial A_P} \mathbf{E} \cdot \mathbf{ds} \tag{1}$$

and

$$\iint_{A_D} \epsilon_0 \frac{\partial \mathbf{E}}{\partial t} \cdot \mathbf{N_D} dA = \oint_{\partial A_D} \mathbf{H} \cdot \mathbf{ds} \tag{2}$$

where ∂A is the contour which bounds primary (dual) cell face, having unit normal vector $\mathbf{N_P}$ ($\mathbf{N_D}$) and area A_P (A_D); this same face is pierced by a dual (primary) cell edge having unit tangent vector $\mathbf{S_D}$ ($\mathbf{S_P}$). This corresponds to the classical Yee cell notation; i.e., $\mathbf{E}$ is associated with primary cell edges and $\mathbf{H}$ is associated with dual cell edges.

A reduction and simplification of (1) and (2) to 2-D yields

$$\mu_0 A_P \frac{\partial (\mathbf{H} \cdot \mathbf{S_D})}{\partial t} = \mu_0 A_P \left[\frac{\partial (\mathbf{H} \cdot \mathbf{N_P})}{\partial t} (\mathbf{N_P} \cdot \mathbf{S_D}) + \frac{\partial (\mathbf{H} \cdot \mathbf{N_{P\perp}})}{\partial t} (\mathbf{N_{P\perp}} \cdot \mathbf{S_D}) \right] \tag{3}$$

and

$$\epsilon_0 A_D \frac{\partial (\mathbf{E} \cdot \mathbf{S_P})}{\partial t} = \epsilon_0 A_D \left[\frac{\partial (\mathbf{E} \cdot \mathbf{N_D})}{\partial t} (\mathbf{N_D} \cdot \mathbf{S_P}) + \frac{\partial (\mathbf{E} \cdot \mathbf{N_{D\perp}})}{\partial t} (\mathbf{N_{D\perp}} \cdot \mathbf{S_P}) \right] \tag{4}$$

In (3), a first order approximation to cell-obliqueness is obtained by using only the first term. The second-order correction comes by adding the second term, where $\mathbf{N_P} \times \mathbf{N_{P\perp}} = \mathbf{i}_z$, in which case $\mathbf{N_{P1\perp}} = \mathbf{S_{P2}}$ and $\mathbf{N_{P2\perp}} = -\mathbf{S_{P1}}$. Also, in (4), for the 2-D case, $\mathbf{N_{D\perp}}$ is parallel to dual-cell edge $\mathbf{S_D}$, with A_D being the appropriate dual-cell face area.

Figure 2 illustrates the field locations for the TM case, and the FVTD stepping equations with second-order corrections are

$$\frac{(\mathbf{H} \cdot \mathbf{S_D})_1^{n+1}(I,J) - (\mathbf{H} \cdot \mathbf{S_D})_1^n(I,J)}{\Delta t} = -(\mathbf{N_{P1}} \cdot \mathbf{S_{D1}})(I,J) \frac{E_z^{n+\frac{1}{2}}(I,J+1) - E_z^{n+\frac{1}{2}}(I,J)}{\mu_0 D_{P2}(I,J)} + \Delta_1 \tag{5}$$

$$\frac{(\mathbf{H} \cdot \mathbf{S_D})_2^{n+1}(I,J) - (\mathbf{H} \cdot \mathbf{S_D})_2^n(I,J)}{\Delta t} = (\mathbf{N_{P2}} \cdot \mathbf{S_{D2}})(I,J) \frac{E_z^{n+\frac{1}{2}}(I+1,J) - E_z^{n+\frac{1}{2}}(I,J)}{\mu_0 D_{P1}(I,J)} + \Delta_2 \tag{6}$$

$$\begin{aligned} \frac{E_z^{n+\frac{1}{2}}(I,J) - E_z^{n-\frac{1}{2}}(I,J)}{\Delta t} = & \\ & \frac{(\mathbf{H} \cdot \mathbf{S_D})_2^n(I,J) D_{D2}(I,J-1) - (\mathbf{H} \cdot \mathbf{S_D})_2^n(I-1,J) D_{D2}(I-1,J-1)}{\epsilon_0 A_D(I-1,J-1)} \\ & - \frac{(\mathbf{H} \cdot \mathbf{S_D})_1^n(I,J) D_{D1}(I-1,J) - (\mathbf{H} \cdot \mathbf{S_D})_1^n(I,J-1) D_{D1}(I-1,J-1)}{\epsilon_0 A_D(I-1,J-1)} \end{aligned} \tag{7}$$

where the second-order corrections in (5) and (6) are given by

$$\Delta_1 = \frac{[\mathbf{S_{P2}}(I,J) \cdot \mathbf{S_{D1}}(I-1,J)][C_P(I-1,J) + C_P(I,J)]}{\mu_0 [A_P(I-1,J) + A_P(I,J)]} \tag{8}$$

and

$$\Delta_2 = \frac{[\mathbf{S}_{P1}(I,J)\cdot\mathbf{S}_{P2}(I,J-1)][C_P(I,J-1)+C_P(I,J)]}{\mu_0\,[A_P(I,J-1)+A_P(I,J)]} \qquad (9)$$

In (8), $C_P(I-1,J)$ is the contour integral of $E_z(S_{P2x}(I,J)dx + S_{P2y}(I,J)dy)$ on the face boundary of primary-cell $(I-1,J)$ having face area $A_P(I-1,J)$; $C_P(I,J)$ is the contour integral on the face boundary of primary-cell (I,J) having face area $A_P(I,J)$; and S_{P2x} and S_{P2y} are the x-y components of unit vector $\mathbf{S}_{P2}$. The $C_P(I-1,J)$ contour integration is given by

$$\begin{aligned}
C_P(I-1,J) = {} & \\
& [S_{P2x}(I,J)(P_x(I,J)-P_x(I-1,J)) + S_{P2y}(I,J)(P_y(I,J)-P_y(I-1,J))] \\
& \cdot \frac{[E_z(I,J)+E_z(I-1,J)]}{2} \\
& + [S_{P2x}(I,J)(P_x(I,J+1)-P_x(I,J)) + S_{P2y}(I,J)(P_y(I,J+1)-P_y(I,J))] \\
& \cdot \frac{[E_z(I,J+1)+E_z(I,J)]}{2} \\
& + [S_{P2x}(I,J)(P_x(I-1,J+1)-P_x(I,J+1)) + S_{P2y}(I,J)(P_y(I-1,J+1)-P_y(I,J+1))] \\
& \cdot \frac{[E_z(I-1,J+1)+E_z(I,J+1)]}{2} \\
& + [S_{P2x}(I,J)(P_x(I-1,J)-P_x(I-1,J+1)) + S_{P2y}(I,J)(P_y(I-1,J)-P_y(I-1,J+1))] \\
& \cdot \frac{[E_z(I-1,J)+E_z(I-1,J+1)]}{2}
\end{aligned} \qquad (10)$$

and $C_P(I,J)$ is obtained in a similar manner. Here, $P_x(I,J)$ and $P_y(I,J)$ are the x-y coordinates of the primary cell corners. This is also the location where $E_z(I,J)$ is calculated. Similarly, the explicit terms in (9) are based on adjacent primary cells (I,J) and $(I,J-1)$ with common-edge unit vector $\mathbf{S}_{P1}(I,J)$ (see Figs. 1 and 2), and $C_P(I,J-1)$ and $C_P(I,J)$ are obtained from a procedure similar to (10).

The above expressions assume the second-order corrections to $(\mathbf{H}\cdot\mathbf{S}_D)_1$ and $(\mathbf{H}\cdot\mathbf{S}_D)_2$ are uniform over $A_P(I-1,J)$, $A_P(I,J)$ and $A_P(I,J-1)$, and that E_z varies linearly around face edges which bound areas $A_P(I-1,J)$, $A_P(I,J)$ and $A_P(I,J-1)$. Note, primary cell (I,J) is common to both correction calculations.

Finally, the second-order TE equations are obtained in a similarly complex, but straightforward manner [8].

2-D NUMERICAL RESULTS

In order to test the formulation documented here, calculations were made on a 2-D numerical space consisting of approximately 6600 cells and used approximately 2000 time steps in each case. These time-domain results were then transformed into the frequency domain, and then into the far-field. In all cases, a time-differentiated, plane wave, Gaussian pulse was used to illuminate the obstacle.

In the first application, the parallel-plate region was illuminated with the TE mode with $\mathbf{k}_0$ along the $\hat{\mathbf{i}}_x$ direction (i.e., $\phi^{inc} = 0$). In this case, the parallel-plate region supports TEM propagation. The scattering cross section, $\sigma(\omega)$, was computed using each of the near-to-far-field integration contours of Fig. 3; the inner-loop is adjacent to the curved plates and the outer-loop is purposely placed outside the region of nonorthogonal meshing. A comparison of the two results determines the fidelity of electromagnetic waves propagated across the nonorthogonal mesh. Overlaid curves of $\sigma(\omega)$ for both integration contours appear in Fig. 4, and the agreement is seen to be very good, at least up to 600 MHz.

The nominal size of the mesh cells used in this case is $\frac{\lambda}{16}$ meter along each edge, which at 600 MHz corresponds to 8 cells per wavelength. We can conclude that the nonorthogonal mesh with the second-order correction to the FVTD equations propagates electromagnetic simulation possibly even better than the original orthogonal Yee scheme. This curious result was also noticed by Madsen and Ziolkowski [9].

The resonances at which the parallel-plate region is $\frac{\lambda}{4}, \frac{3\lambda}{4}\cdots\frac{19\lambda}{4}$ deep are clearly visible in Fig. 4, as are the very sharp resonances at which it is $\frac{\lambda}{2}$ and λ wide. These transverse resonances imply that cross

coupling has occured between the original TEM mode and a parallel plate waveguide mode in the curved region.

Fig. 5 compares $\sigma(\omega)$ for the TM case, as evaluated on the same two integration contours. Agreement is again better than 1dB at virtually all frequencies below 600 MHz. For the TM case, the parallel plate region will not support TEM propagation, thus the TM results are free of resonant behavior until the parallel region is at least $\frac{\lambda}{2}$ wide, where the first TE_{0n} waveguide mode can propagate. Fig. 5 clearly shows the first nine depth resonances of this propagating mode.

Additionally, scattering in the TM case was computed for illumination from above ($\phi^{inc} = -90°$) and below ($\phi^{inc} = +90°$). Results for the inner and outer integration contours appear in Figs. 6 and 7. Resonances principally occur where the conducting plate path is $\sim n\lambda$ around (duct is $\sim n\frac{\lambda}{2}$ long). Note, the $\phi^{inc} = +90°$ case involves electromagnetic propagation across 20 cells which are 8 cm=$\frac{\lambda}{4}$ long at 600 MHz.

Calculations for scattering by an ojive-cylinder 10 meters long and 1 meter thick at the midpoint have also been performed using the second order formulation. Figure 8 shows the overall conformal mesh with inner and outer integration contours, and Fig. 9 illustrates the details near the left tip of the ojive. Results for edge-on TE scattering appear in Fig. 10. Results from a staircased analysis of this TE configuration, the dotted curve, become disastrous at the point which corresponds to 120 staircased cells/λ. Conformal cells for the FVTD model are about 8 centimeters on a side (9.3 cells per wavelength at 400 MHz), and good agreement is seen using inner and outer loop near-to-far field transformation contours at frequencies up to 250 MHz (15 cells per wavelength) for the TE case. The TM edge-on results in Fig. 11 deteriorate at a slightly lower frequency. Note, Fig. 11 shows considerably more amplitude (dB) resolution than Fig. 10.

CONCLUSIONS AND RECOMMENDATIONS

The purpose of this work is to validate the FVTD approach in 2-D, and thus, to reduce the risks before proceeding with the truly monumental task of developing a 3-D FVTD algorithm. The results presented here indicate that the FVTD approach is well suited to modeling curved surfaces and the payoff for its extension to 3-D is, therefore, likely be worth the effort. As a closing note, the FVTD approach is still not expected to ease the fundamental problem of turning a physical problem space into a successful solution mesh, and significant work in this area is continuing.

REFERENCES

[1] K. S. Yee, "Numerical solution of initial boundary value problems in isotropic media," *IEEE Trans. Antennas Propagat.*,vol. AP-14, pp. 302-307, May 1966.

[2] R. Holland, "The case against staircasing," Conference Proceedings, 6th Annual Review of Progress in Applied Computational Electromagnetics, Monterey, CA, pp. 89-95, 19-22 March 1990

[3] R. Holland, "Finite-difference solutions of Maxwell's equations in generalised nonorthogonal coordinates," *IEEE Trans. Nuc. Sci.*, vol. NS-30, pp. 4589-4591, Dec. 1983.

[4] M. Fusco, "FDTD algorithm in curvilinear coordinates," *IEEE Trans. Antennas Propagat.*, vol. AP-38, pp. 76-89, Jan. 1990.

[5] A. Taflove and K. Umashankar, "The finite-difference time-domain (FD-TD) method for numerical modeling of electromagnetic scattering," *IEEE Trans. Magnetics*, vol. M-25, pp. 3086-3090, Jul. 1989.

[6] N. K. Madsen and R. W. Ziolkowski, "A modified finite-volume technique for Maxwell's Equations," Lawrence Livermore National Laboratory, UCRL-98495, 26 Feb. 1988

[7] R. Holland and K. S. Cho, "Radar cross-section evaluation of arbitrary cylinders," Applied Physics Inc., API-TR-120, Albuquerque, NM, 12 Sept. 1986.

[8] R. Holland, V. P. Cable, and L. Wilson, "RCS calculation by finite-volume time-domain (FVTD) techniques", Lockheed Aeronautical Systems Co., Report # LG-90ER0131 , Nov 1990.

[9] N. K. Madsen and R. W. Ziolkowski, "A 3D modified finite-volume technique for Maxwell's equations," *Electromagnetics*, vol. 10, pp. 147-161, Jan. 1990.

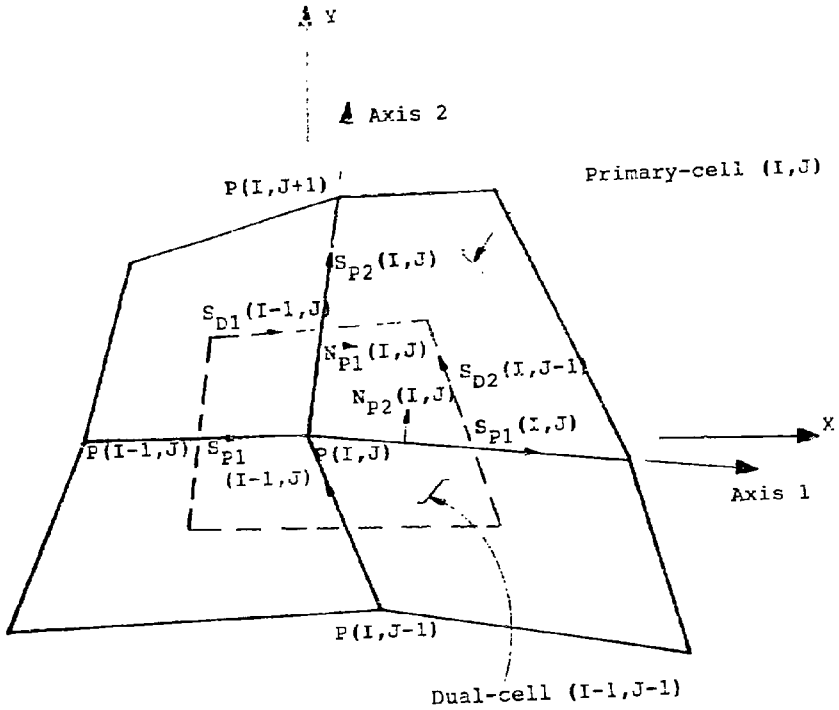

Figure 1. 2-D structured, quadrilateral mesh, where connectivety information is index-based along oblique axes 1 and 2.

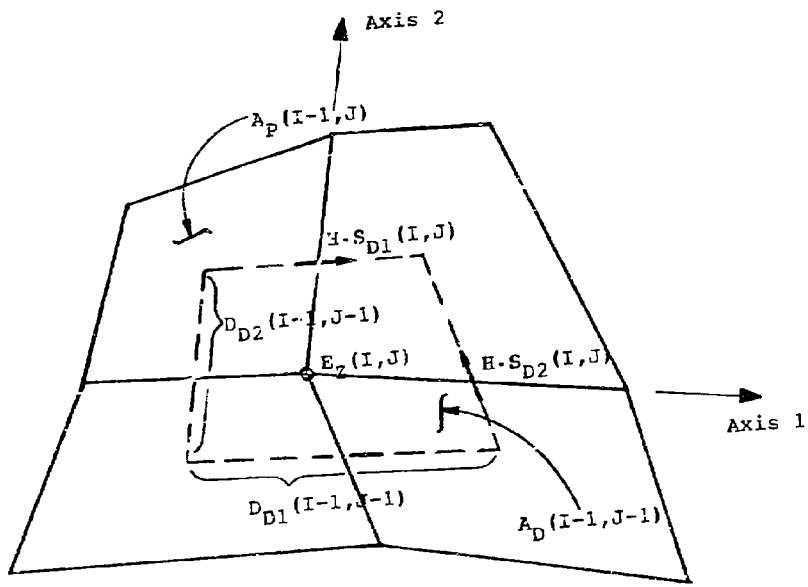

Figure 2. Field locations, cell-face areas, and integration path lengths.

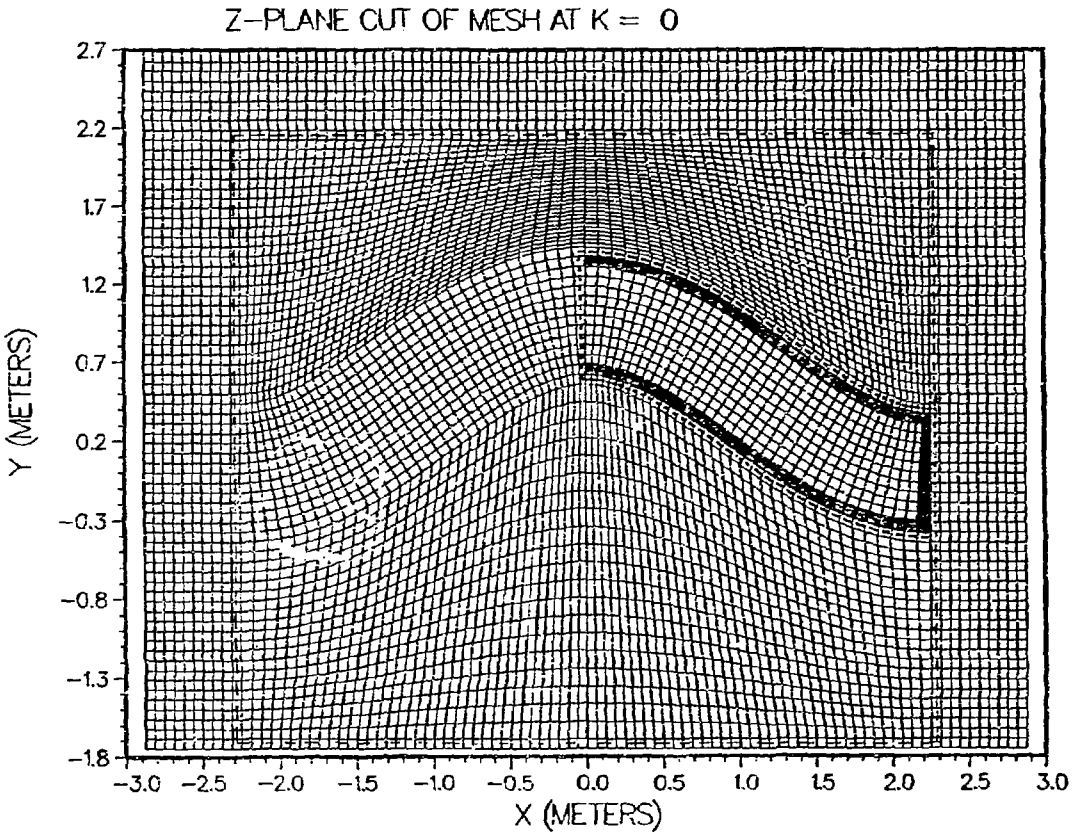

Figure 3. Inner and outer integration contours for near-to-far field transformation with a shorted s-curved parallel plate region.

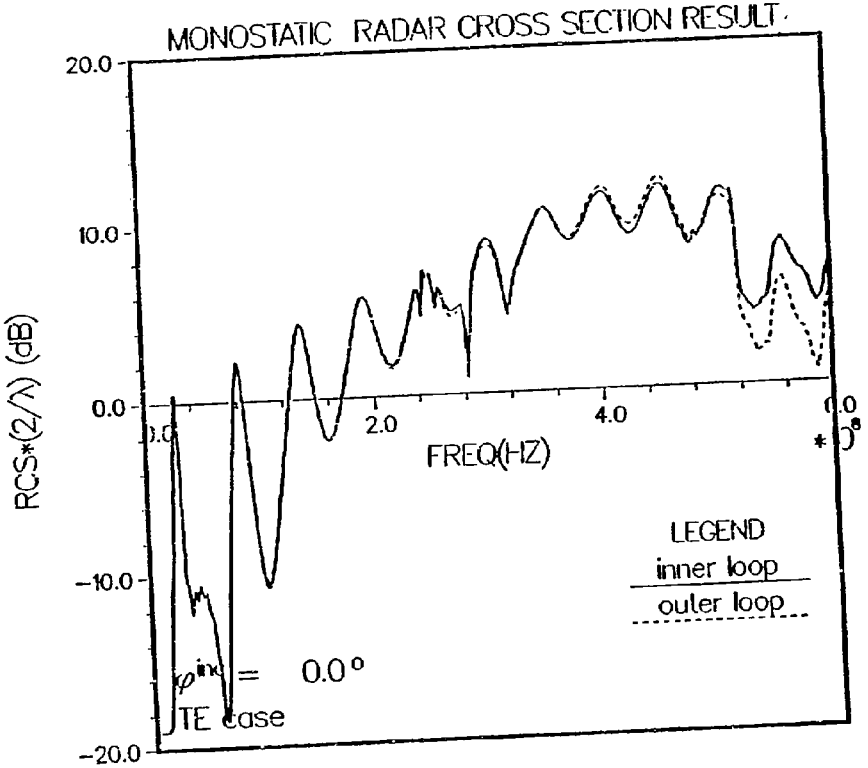

Figure 4. TE RCS of s-curved parallel plates evaluated over the two contours. The nonorthogonal mesh appears to propagate the scattered fields without significant noise or distortion up to frequencies near 400 MHz.

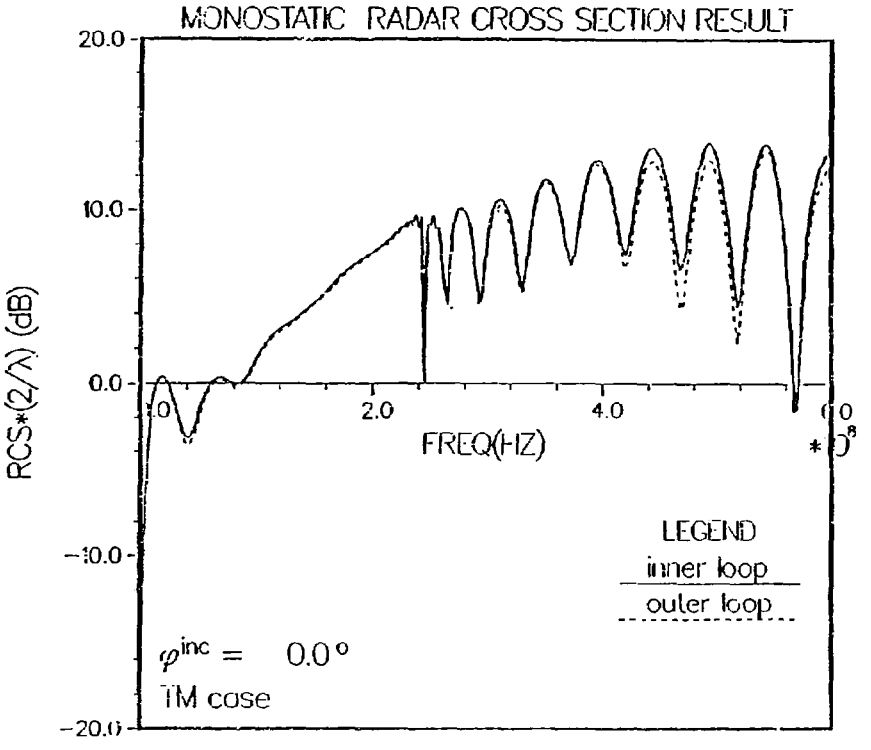

Figure 5. TM RCS of s-curved parallel plates evaluated over the two contours. The nonorthogonal mesh appears to propagate the scattered fields with little or no noise or distortion to frequencies above 400 MHz.

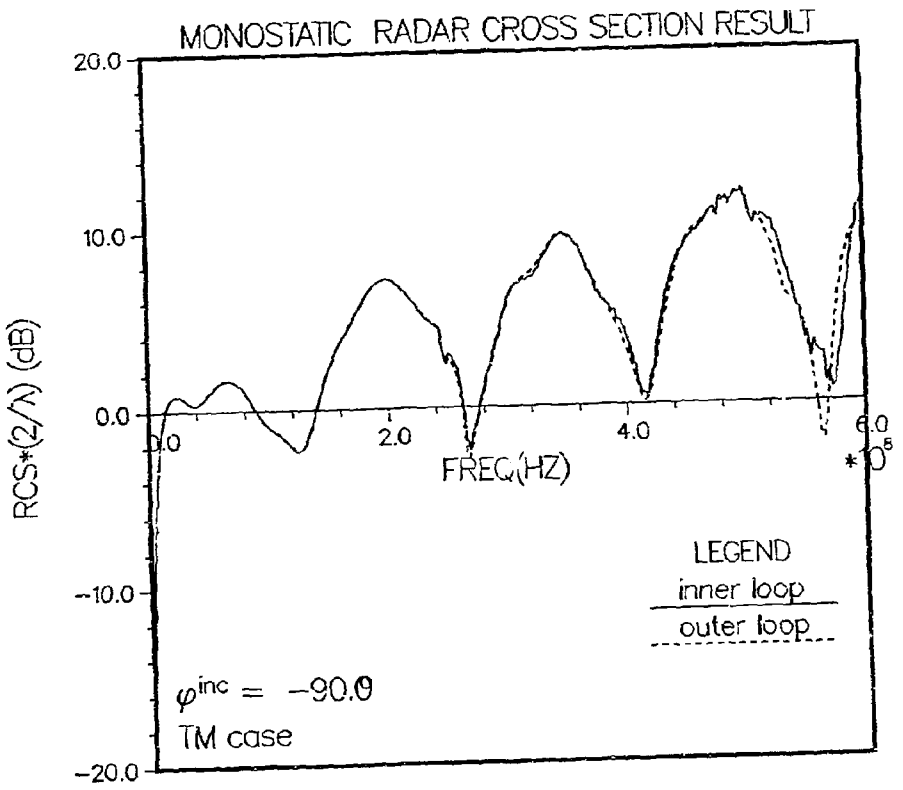

Figure 6. TM RCS of the s-curved parallel plates evaluated over the two contours. For illumination from above, the scattering appears to be dominated by the external length characteristics of the geometry.

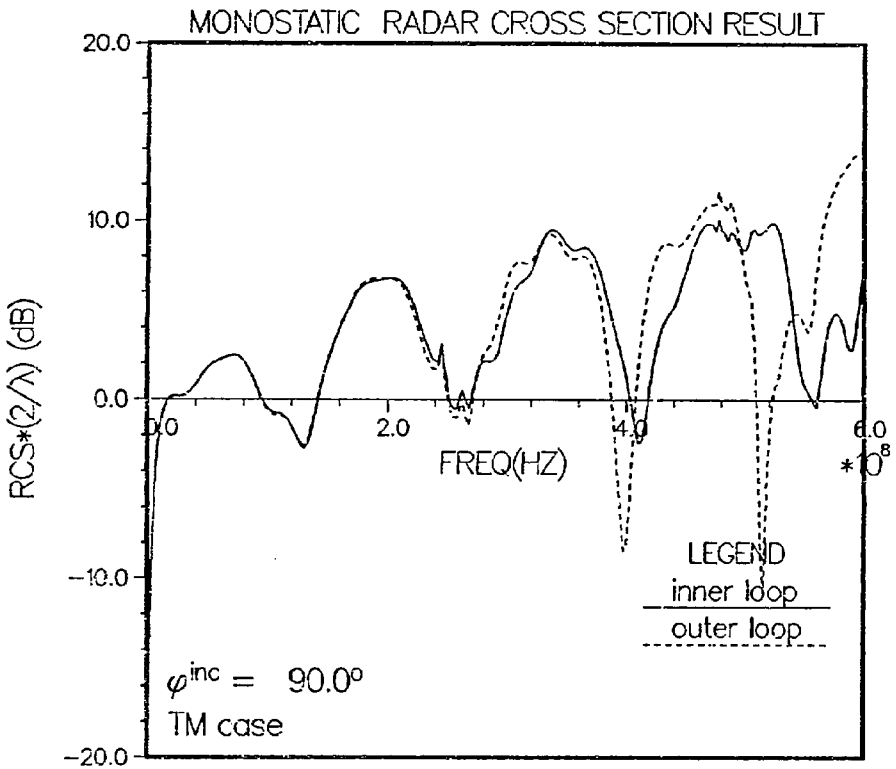

Figure 7. TM RCS of the s-curved plates when illuminated from below. At 600 MHz, the scattered fields must pass through 20 cells which are 1/4 wavelength long (see Fig. 1). The fidelity achieved with this mesh size is very encouraging.

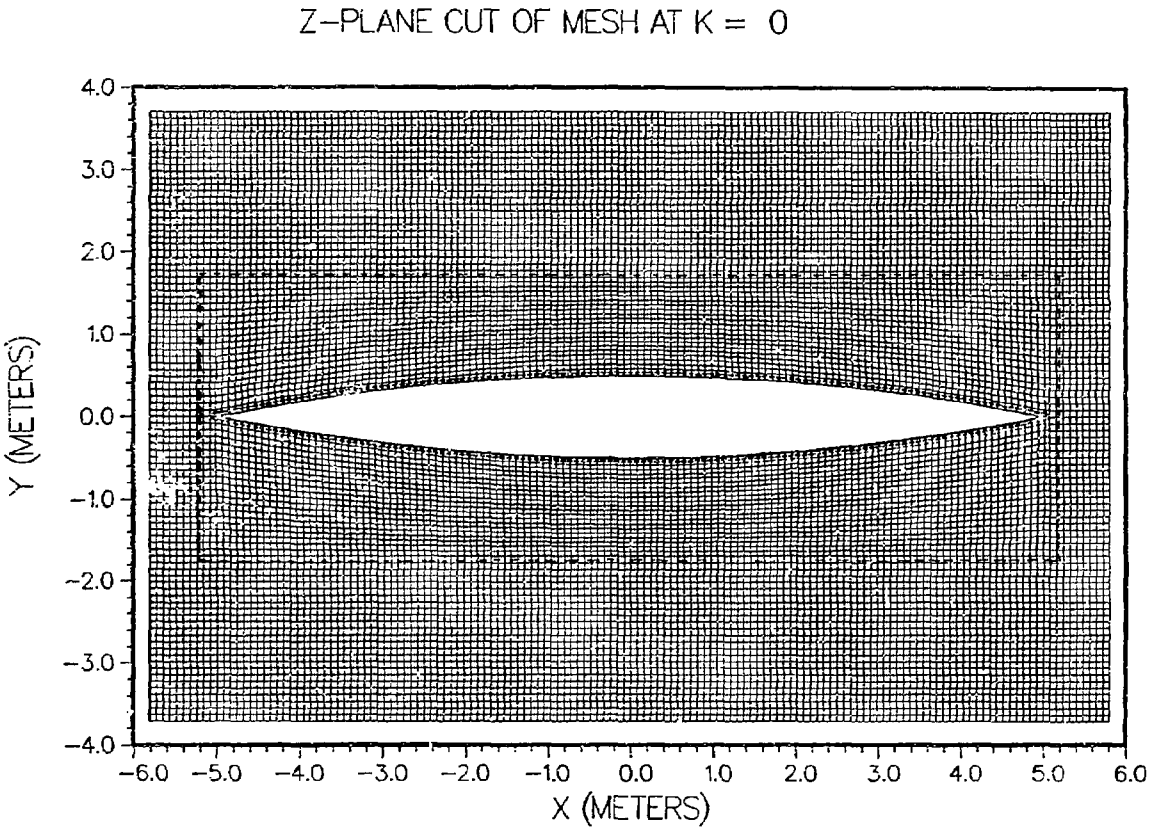

Figure 8. Inner and outer loop integration contours for near-to-far field transformation with an ojive.

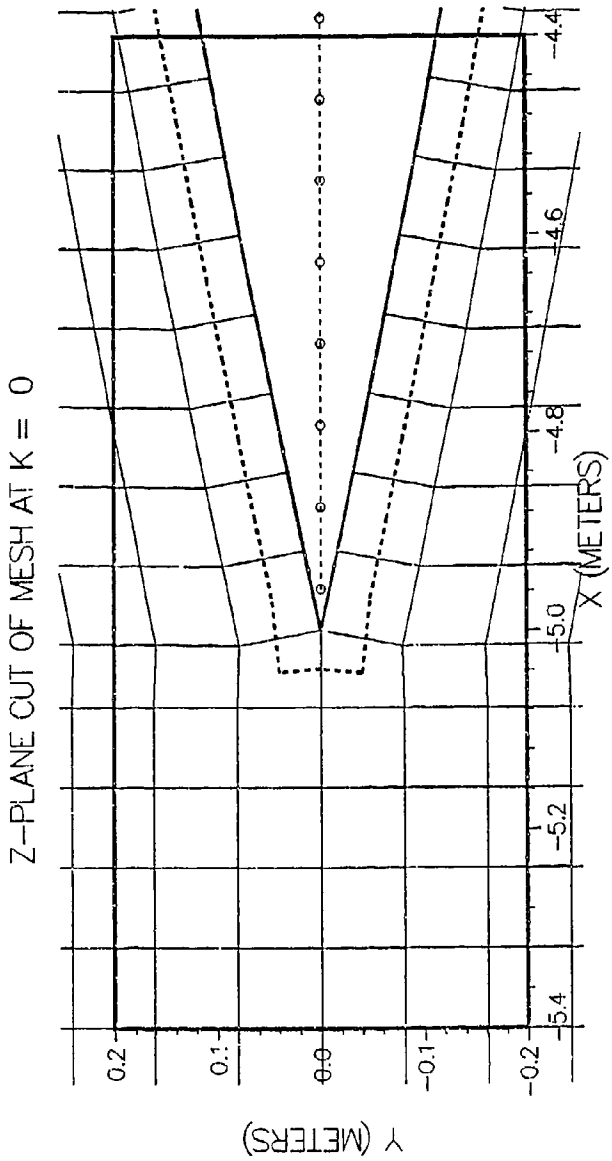

Figure 9. Details of ojive tip and inner loop contour.

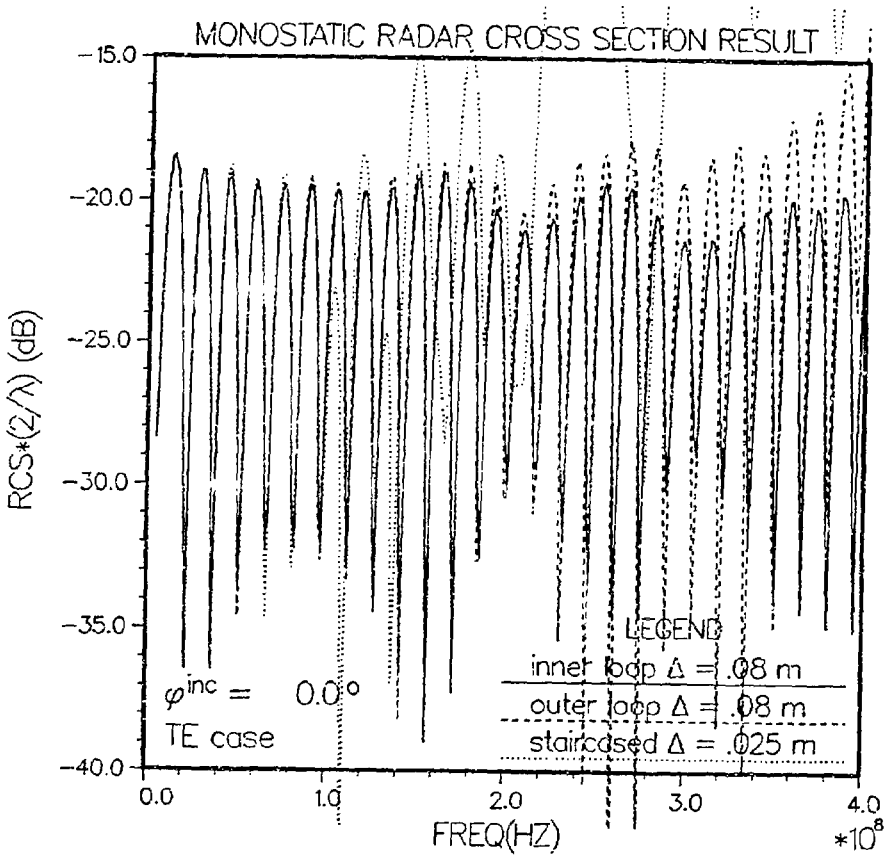

Figure 10. TE RCS of ojive illuminated edge-on, as computed by staircased mesh with 2.5cm cells and by conformal mesh with 8cm cells. For the conformal mesh, 10 cells per wavelength corresponds to 375 MHz.

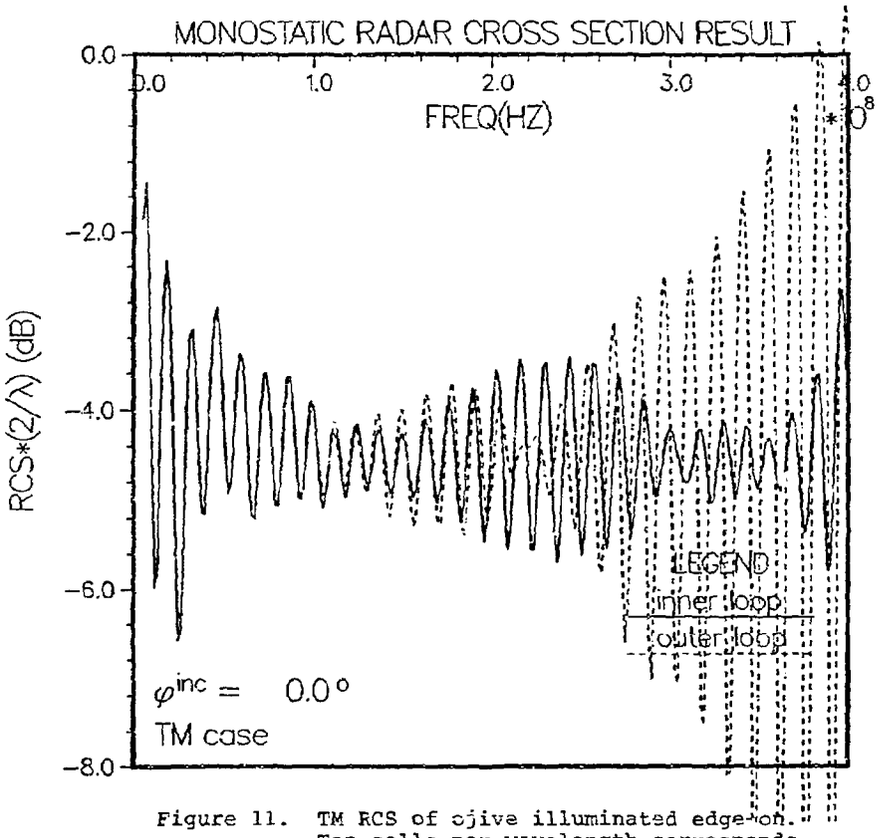

Figure 11. TM RCS of ojive illuminated edge-on. Ten cells per wavelength corresponds to 375 MHz. Note expanded dB scale.

RCS Calculation for Smooth Bodies of Revolution using FDTD

by

R. Luebbers, D. Steich, K. Kunz, and F. Hunsberger
Electrical and Computer Engineering Dept.
The Pennsylvania State University
University Park, PA 16802
Tel (814) 865-2362
Fax (814) 865-7065

Abstract

The objective of the research reported here was to determine if FDTD, using cubical cells, could be applied successfully to computation of RCS for smooth bodies of revolution composed of lossy dielectric materials. The bodies considered were a sphere, an oblate spheroid, and a sphere-cone-oblate spheroid. These shapes were chosen to provide a challenge to the FDTD method, and also because results computed using other methods were available for comparison. These shapes were modeled in three dimensions using cubical cells, and RCS calculations were made by Fourier transform of the far zone time domain scattered fields computed by FDTD.

The results were compared with the Mie series for the sphere, and with T-matrix results for the other objects. The agreement was quite good, indicating that, at least for the examples considered, the FDTD method with cubical cells produced satisfactory RCS results for smooth bodies of revolution.

Introduction

The Finite Difference Time Domain (FDTD) method has seen increasing application in the prediction of Radar Cross Section (RCS) of targets with a wide variety of shapes and material composition. While good results have been reported for simple targets, such as perfectly conducting flat plates [1], difficulties with targets which include smooth surfaces have been reported, especially when these are modeled using cubical computational cells. This "staircase" effect can be a serious problem in calculating low level RCS from some targets, and considerable effort is currently be expended in solving this problem [2-4].

While recognizing that staircasing errors can be significant, it was conjectured that for many RCS calculations, especially for penetrable targets, the staircasing errors should be small since much of the scattered energy would come from inside the scatterer volume. In addition, even for perfectly conducting scatterers, except for certain pathological situations, the staircasing effect would tend to average out, providing a good estimate of the RCS level for the target. The purpose of this paper is to demonstrate the accuracy of "staircased" cubical cell FDTD for some particular examples. The geometries considered here are a sphere, an oblate spheroid, and a sphere-cone-oblate spheroid.

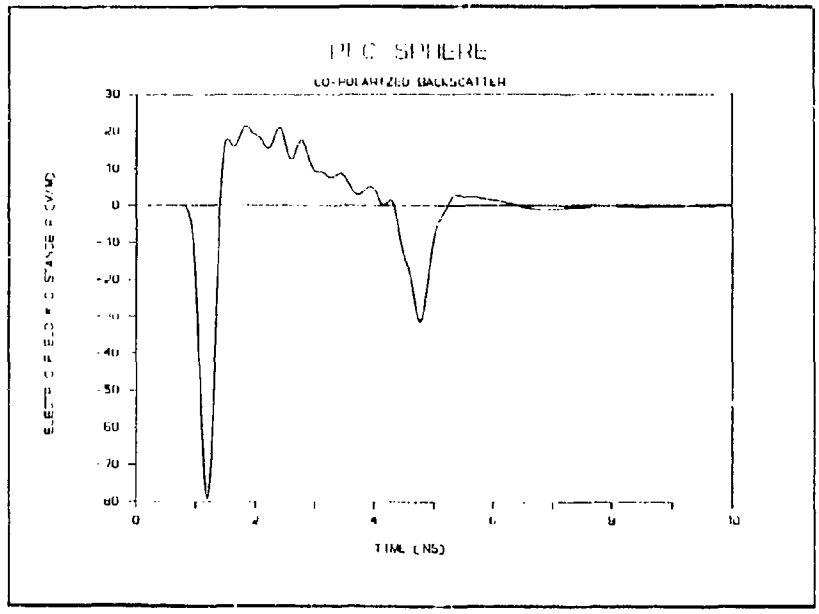

Figure 1 Time domain far zone electric field scattered by a 20 cm radius PEC sphere using FDTD.

Results

The first example is scattering from a 20 cm radius sphere composed of either perfect electrical conductor (PEC) or lossy dielectric. In both cases the sphere is modeled using 1 cm FDTD cubical cells.

Figure 1 shows the FDTD computation of the far zone time domain scattered electric field from the PEC sphere. The 1/R dependence (where R is measured from the sphere center) of the far zone fields is suppressed. There is an initial (negative) scattered pulse as the incident pulse strikes the front surface of the sphere, (positive) scattered energy from the curved sphere surface, and then a final (negative) pulse due to creeping waves traveling around the sphere. This far zone wide bandwidth time domain result was obtained using the approach described in [1].

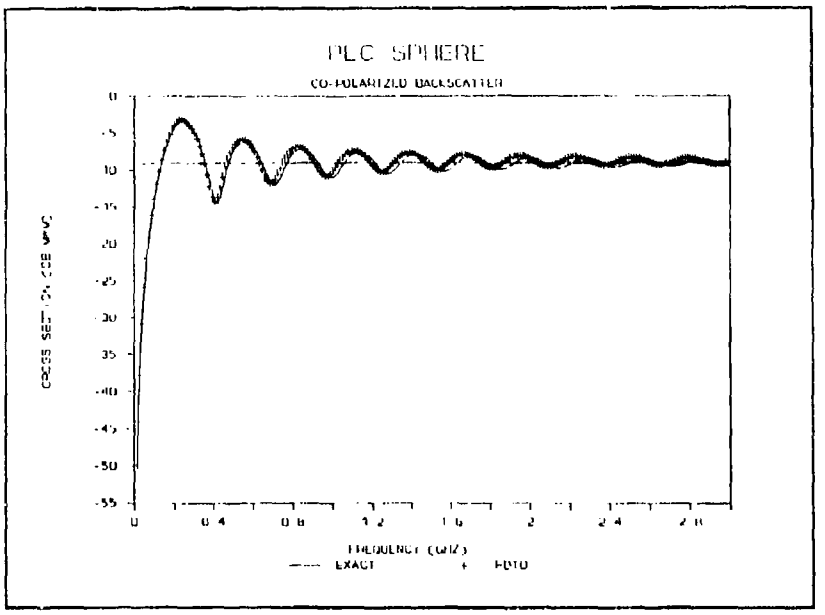

Figure 2 Back scatter cross section of 20 cm radius PEC sphere computed using FDTD compared with the exact solution.

Figure 2 shows the FDTD radar cross section of the sphere (determined by taking the Fourier transform of the time domain result in Figure 1 and dividing by the Fourier transform of the incident pulse) compared with the exact solution. The agreement is excellent at low frequencies, and even at higher frequencies tracks the exact solution reasonably well. More accurate results could be obtained by using more cells to model the sphere, or by utilizing conformal meshing techniques to reduce the staircasing error [2-4].

While the focus of this paper is FDTD scattering calculations from bodies of revolution, the next example also

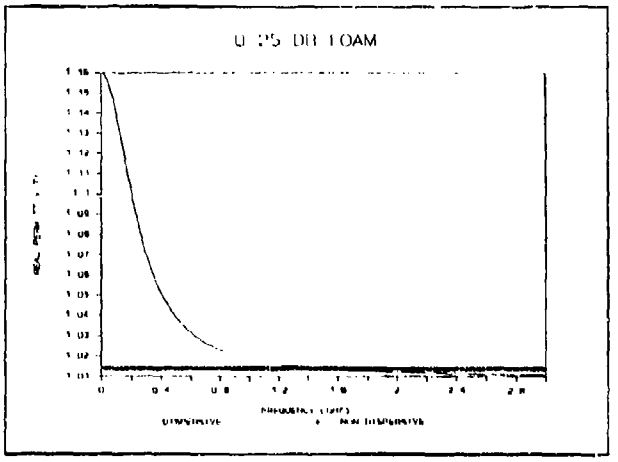

Figure 3 Real part of complex permittivity of 0.25 dB foam absorber showing actual dispersive variation and usual FDTD approximation taking value at 1.5 GHz.

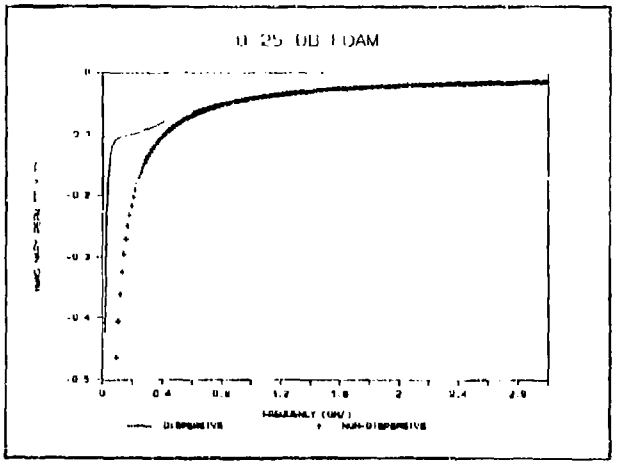

Figure 4 Imaginary part of complex permittivity of 0.25 dB foam absorber showing actual dispersive variation and usual FDTD approximation taking value at 1.5 GHz.

illustrates the ability of the FDTD to compute scattering from lossy dispersive materials. A sphere made of 0.25 dB (the attenuation rate) dielectric low loss absorbing foam was considered. The complex permittivity of the absorbing foam material is shown in Figures 3 and 4. The actual behavior of the material with frequency is labeled "DISPERSIVE". The dispersive nature of the material was approximated in the FDTD computations using the method described in [5]. The curves labeled "NON-DISPERSIVE" indicate how FDTD codes which do not include the dispersive effects of materials would approximate the behavior of this material.

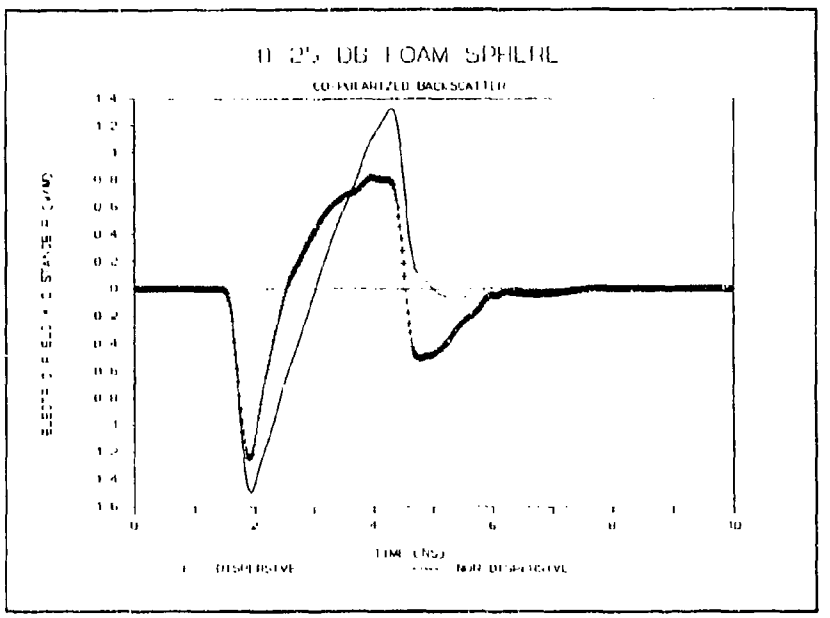

Figure 5 Time domain far zone electric field scattered by a 20 cm radius 0.25 dB absorbing foam sphere using both dispersive and non-dispersive FDTD.

The far zone time domain scattered electric field from a 20 cm radius absorbing foam sphere made of the material of Figures 3 and 4 and modeled using 1 cm cubical FDTD cells is shown in Figure 5. Results calculated with both dispersive and non-dispersive FDTD are shown. It is evident from the figure that the scattering behavior is clearly different depending on whether or not the material's dispersive behavior is included in the FDTD calculations.

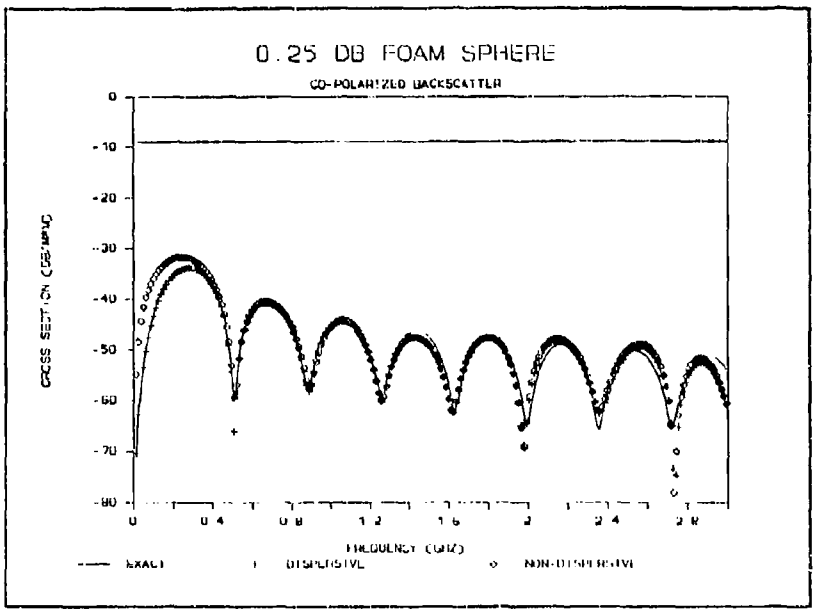

Figure 6 Back scatter cross section of 20 cm radius 0.25 dB low loss dielectric foam sphere computed using both dispersive and non-dispersive FDTD compared with the exact solution.

Figure 6 compares the two FDTD cross sections (obtained from Fourier transforms of the data in Figure 5) with the exact solution (which is for the actual dispersive material). Considering the "DISPERSIVE" FDTD calculation, the improvement in accuracy relative to the PEC data of Figure 2 can be seen. The explanation for this is that a significant portion the scattered energy is coming from the interior of the sphere, so that "stair case" errors in modeling the surface do not introduce as great an error as for the PEC sphere where all of the currents are on the sphere surface.

Note also that the FDTD method has accurately predicted the approximate 40 dB reduction in cross section relative to the perfectly conducting sphere (the high frequency limit of the corresponding PEC sphere is shown by the solid line at approximately -9 dB), illustrating the wide dynamic range of the method.

The next geometry is an oblate spheroid. Again it is modeled using 1 cm cubical FDTD cells. The major and minor axes are 0.48 and 0.288 meters. The material composing the oblate

spheroid has relative permittivity 2, conductivity 0.1 S/m. These parameters were chosen so that the T-Matrix solution used to validate the FDTD results [6] would converge. The incident field is phi-polarized from a direction 22.5 degrees off the major (z) axis. The computational space is 75 x 75 x 57 cells, and 2048 time steps were run, taking about 4 hours on a Silicon Graphics 4D220 GTX work station. The T-Matrix calculations also required approximately 4 hours of computer time on the same work station.

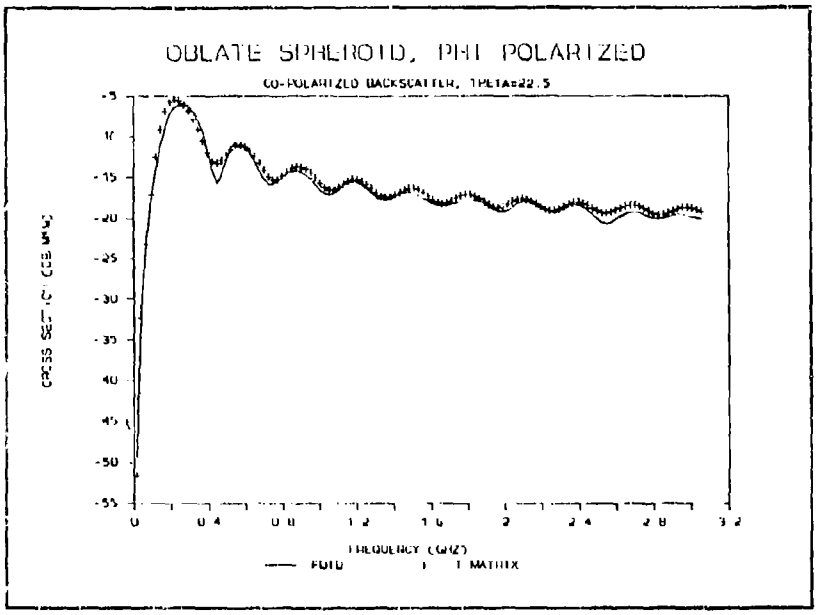

Figure 7 Scattering from oblate spheroid target computed using FDTD and compared with a T-Matrix solution. The oblate spheroid has relative permittivity 2, conductivity 0.1 S/m.

Frequency domain scattering results for the oblate spheroid obtained from Fourier transform of FDTD time domain results are shown in Figure 7 and compared with T-Matrix calculations. The results show good agreement.

The final body of revolution scatterer to be considered is a sphere-cone-oblate spheroid, this time modeled using 2 cm FDTD cells. The oblate spheroidal end cap has a diameter of 0.82 meters and is nearly spherical, the spherical end cap a diameter of 0.246 m, the total length is 0.702 m, and the cone angle is 85

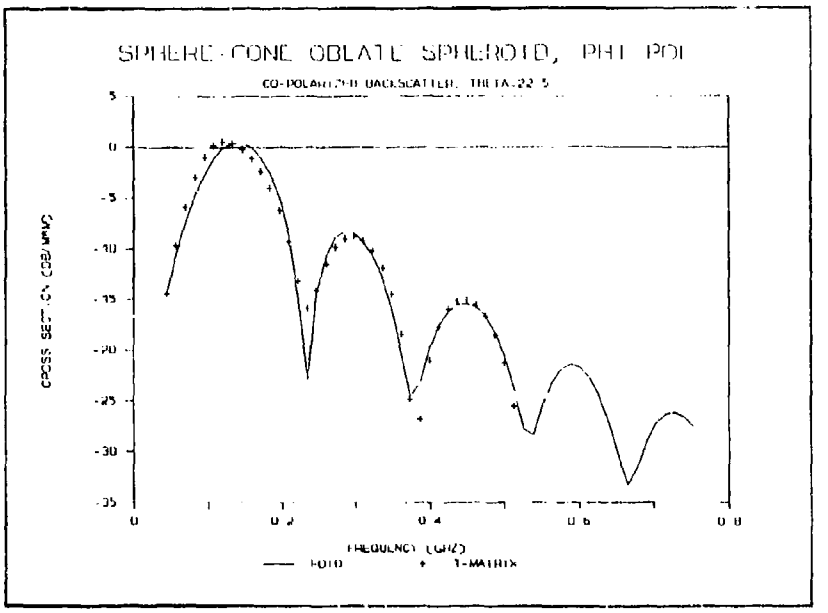

Figure 8 Scattering from sphere-cone-oblate spheroid computed using FDTD and compared with a T-Matrix solution. The sphere-cone-oblate spheroid has relative permittivity 2, conductivity 0.1 S/m.

degrees. The incident field is phi-polarized from a direction 22.5 degrees off the smaller end (spherical) of the major (z) axis. The material again has relative permittivity of 2, conductivity of 0.1.

In Figure 8 the frequency domain scattering cross section computed using FDTD is compared with T-Matrix results. While the T-Matrix validation code would not converge for higher frequencies, the agreement is good over the frequency range where comparisons can be made.

Conclusions

Staircasing errors due to modeling smooth surfaces with cubical FDTD cells can be significant. The purpose of this paper is not to deny this fact, but rather to point out that, for many geometries involving smooth surfaces, RCS results of reasonable accuracy can be obtained using "staircased" FDTD. This is especially true for scatterers composed of electromagnetically penetrable materials. Results presented in this paper showed

reasonable accuracy over a broad bandwidth for three different bodies of revolution, with the FDTD cell size being approximately 0.1 wavelength on a side at the highest frequency considered.

Improved accuracy can be obtained by using conformal meshing methods. However, it should be kept in mind that these methods require considerable more resources both in time and effort to mesh the object and in computer time needed for the finite difference calculations. The results presented here were obtained using a relatively inexpensive work station, and no advantage of symmetry was taken to reduce the computational requirements.

References

[1] R. Luebbers, K. Kunz, M. Schneider, F. Hunsberger, "A Finite Difference Time Domain Near-Zone to Far-Zone Transformation", accepted for publication in IEEE Trans. Ant. Prop.

[2] N. K. Madsen and R. W. Ziolkowski, "Numerical solution of Maxwell's equations in the time domain using irregular nonorthogonal grids," Wave Motion, vol. 10, pp. 583.596, 1988.

[3] Richard Holland et al, "RCS Evaluation and Reduction by an Interactive System," Report Number API-TR-171, Applied Physics, Inc., 5353 Wyoming Blvd., NE, Suite 3, Albuquerque, NM, 87109, October 1989.

[4] M. Fusco, "FDTD Algorithm in Curvilinear Coordinates," IEEE Trans. Ant. Prop., vol. AP-38, pp. 76-89, Jan. 1990.

[5] R. Luebbers, F. Hunsberger, K. Kunz, R. Standler, and M. Schneider, "A frequency-dependent finite difference time domain formulation for dispersive materials," IEEE Trans. Electromagnetic Compat., vol. EMC-32, pp. 222-227, Aug. 1990.

[6] K. Aydin et al, "Differential radar scattering properties of model hail and mixed-phase hydrometeors," Radio Science, vol. 19, pp 58-66, Jan-Feb 1984.

FDTD Waveguide Coupling Modeling and Experimental Validation

by

P. Alinikula, K. S. Kunz and R. J. Luebbers
Electrical and Computer Engineering Dept.
The Pennsylvania State University
University Park, PA 16802
Tel (814) 865-2362
Fax (814) 865-7065

Abstract

Coupling of electromagnetic fields into the interior of complex aerospace systems is a problem of continuing interest and study. At least three features of this coupling must be successfully treated whether the treatment is experimental, analytical or computational. The features are:

- highly resonant behavior of the interior response in particular the current response of any interior wires
- coupling between interior partitions or cavities in particular via waveguide-like geometries
- effects of dense interior fill in particular large cable bundles

In an earlier effort to characterize interior coupling computationally with the Finite Difference Time Domain (FDTD) Technique the highly resonant response of interior wires has been demonstrated. In this effort the same technique is applied to coupled waveguide geometries and the predictions compared against experiment to validate the technique's capability in this area. The technique does indeed accurately model coupling between waveguides. The next effort will be to successfully model dense interior fill. When this is accomplished it is expected that FDTD can be used with reasonable confidence to model interior coupling on a real world complex aerospace system. We therefore view validation of coupling between waveguides as a necessary and important step in establishing confidence and credibility in the use of the FDTD technique in interior coupling modeling.

Introduction

Waveguide coupling through an aperture is a fundamental electromagnetic problem. It has been approximated reasonably well with Bethe small hole theory [1], and with some more recent modifications of it [2]. However, these analytic solutions do not apply to arbitrary shaped complex waveguide coupling structures. Instead, numerical methods have to be used.

Finite Difference Time Domain (FDTD) method has proven to be a very promising technique for time-domain analysis of passive microwave and millimeter wave structures. FDTD's strength is in its capability to model any volumetric structure with rectangular cells. No requirements for symmetry or smooth surfaces are needed. Better modeling is of course achieved by using more cells. Additionally, the FDTD code can handle complex materials; lossy and anisotropic dielectrics as well as ferromagnetic materials are currently included in the code and some feasibility studies have been conducted with nonlinear dielectrics and chiral materials.

Recently, FDTD has been used in modeling microstrip structures [3], [4] and in predicting aperture coupling for a shielded wire [5]. These results suggest that FDTD could be successfully applied to waveguide coupling problems.

The objective of this paper is to model coupled waveguides using FDTD. The forward and backward couplings are predicted for two geometries: a single circular aperture and a dual circular aperture. The single aperture coupler simulations are performed using different mesh dimensions and different simulation durations to observe the model's sensitivity and by that means determine the setup for FDTD waveguide simulations. The dual aperture geometry, however, is selected to be the same as in [2] in order to be able to compare the calculated results with measurements.

FDTD Description

The FDTD field formalism is by now well known ([6],[7]), and will not be presented here. Only the introduction of the field into the waveguide requires discussion. The electric wall approach is used for the wave launching. An incident transverse electric field is allowed to appear spatially only at a transverse plate in other end of the lower waveguide. The amplitude of the field has a sinusoidal distribution across the plate resulting in a wave that approximates the TE_{10} mode. Temporally the incident field appears in the shape of a truncated gaussian envelope about a sinusoidally varying signal. The CW blocks the DC power and shifts the frequency band of the pulse higher. However, a truncated pulse has always an infinite frequency band and therefore some energy is forced inside the waveguide at frequencies below cutoff. This energy is kept to a minimum by using a relatively long gaussian envelope.

Model of Coupled Waveguides

The problem space, shown in figure 1 consists of 4 sides that are defined to be perfectly conducting, i.e., the tangential electric field components on these planes are forced to be zero. The remaining two sides, the ends of the waveguides, are open.

Electric fields on these sides fulfill Mur's first order approximate absorption condition [8]. This condition produces some reflection for waves that are not normal to the boundary. In a waveguide problem, however, the wave is more or less normal and the first order Mur condition is sufficient.

The metal plate between the two waveguides is defined to be infinitely thin, but effectively it has an approximate thickness of half the cell. Circular apertures are approximated with square cells. Several different diameters 8, 12, 13, and 16 were used. Naturally, the actual shape is modeled more accurately when more cells are used. The distance of the aperture from the source launcher was selected so that the whole pulse can fit inside the guide before the aperture is encountered. The test locations of the electric field components in the backward and forward propagation directions were selected to be 1/4 of the aperture diameter away from the edges of the aperture. Transversely the test locations are in the middle of the upper waveguide. The coupling coefficient was calculated as the ratio of electric field at the test location inside the upper waveguide and the electric field inside an undisturbed single waveguide.

Two aperture geometries that were analyzed are shown in figure 1. The first one consists of a single centered coupling aperture with circular shape and relatively large size. The diameter of the aperture is 0.375a, where a is the broad side dimension of the waveguide. All the waveguides have a 2:1 ratio between the sides. Three different mesh dimensions were used: 22 x 16 x 55, 32 x 16 x 80, and 43 x 16 x 108 in $\hat{x}$, $\hat{y}$, and $\hat{z}$ directions respectively. The corresponding diameters of the apertures were 8, 12, and 16 cells. The second structure has two parallel circular coupling apertures that are slightly smaller in size. Mesh dimensions are 42 x 26 x 108 in $\hat{x}$, $\hat{y}$, and $\hat{z}$ directions. The diameter of the apertures is 13 cells. This geometry was constructed to be identical to one in [2] in order to be able to compare the results.

Results

Single aperture coupler simulations showed that after 8192 timesteps the remaining energy in propagating waves was so small that truncation had negligible effect for the fast Fourier transformed response. The forward and backward coupling coefficients for 32 x 16 x 80 -cell geometry with 12 cell hole diameter are shown in figures 2a and b.

The model's sensitivity for mesh dimensions was conducted by comparing responses of the single aperture geometry with three different mesh dimensions. The forward and backward coupling coefficient comparisons at a narrower frequency band are shown in figures 3a and b. The results show significant difference between the 22 x 16 x 55, and 32 x 16 x 80 and 32 x 16 x 80 -cell geometries, whereas the responses for 43 x 16 x 108 and 32

x 16 x 80 -cell geometries are very close. The results indicate that 32 cells is sufficient for modeling the broad side of the waveguide and 12 cells for the aperture diameter respectively.

The forward and backward coupling coefficients for a coupler with two apertures is shown in figure 4. The experimental forward coupling results from [2] for the same structure are also shown. The forward coupling coefficient is a very close match to the experiment. Except for the band edges, the simulation results fall inside the measurement accuracy range. Moreover in [2] it was observed that the directivity (forward/backward coupling) was larger than 3 dB. Simulations support this with a minimum of approximately 2 dB directivity.

Conclusion

Simple waveguide coupling problems were successfully analyzed using the FDTD method. A sufficient setup for waveguide modeling was determined. Results, that showed little sensitivity to either mesh dimensions or simulation duration, were achieved using 32 cells for the broad side of the waveguide, 12 cells for the aperture diameter, and 8192 timesteps. With a well modeled geometry an accuracy inside measurement error range was achieved. Although these simple problems can be approximated reasonably well with analytical expressions, the results show FDTD method's potential in solving more complicated waveguide problems. Combinations of dielectric and metal screws and slabs as well as waveguide junctions can be analyzed in the same manner and with the same resource.

References

[1] H. A. Bethe, "Theory of diffraction by small holes," Phys. Rev., vol. 66, pp. 163-182, Oct. 1944.

[2] R. Levy, "Improved single and multiaperture waveguide coupling theory, including explanation of mutual interactions," IEEE Trans. Microwave Theory Tech., vol. MTT-28, pp. 331-338, Apr. 1980.

[3] D. M. Sheen, S. M. Ali, M. D. Abouzahra, J. A. Kong, "Application of the three-dimensional Finite-Different Time-Domain method to the analysis of planar microstrip circuits," IEEE Trans. Microwave Theory Tech., vol. MTT-38, pp. 849-857, July 1990.

[4] J. Moore, H. Ling, "Characterization of a 90° microstrip bend with arbitrary miter via Time-Domain Finite Difference method," IEEE Trans. Microwave Theory Tech., vol. MTT-38, pp. 405-410, Apr. 1990.

[5] K. Kunz, D. Steich and R. J. Luebbers, "Low frequency shielding characteristics of cylindrical shell with a varying size aperture," IEEE Journal of Electromagnetic Compatibility, (submitted).

[6] K. S. Yee, "Numerical solution of initial boundary value problems involving Maxwell's equations in isotropic media," IEEE Trans. Antennas Propagat., vol. AP-14, pp. 302-307, May 1966.

[7] K. S. Kunz, K. M. Lee, "A three-dimensional finite-difference solution of the external response of an aircraft to a complex transient EM environment: Part I-the method and its implementation," IEEE Trans. Electromagn. Compat., vol. EMC-20, pp. 328-333, May 1978.

[8] G. Mur, "Absorbing boundary conditions for the finite-difference approximation of the time-domain electromagnetic-field equations," IEEE Trans. Electromagn. Compat., vol. EMC-23, pp. 377-382, May 1981.

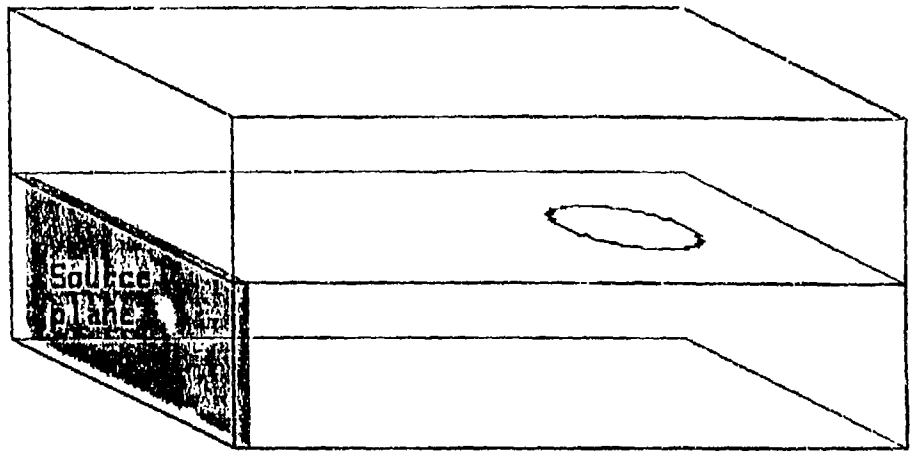

Figure 1a : Coupled Waveguides, Single Aperture (16 cell diameter hole shown)

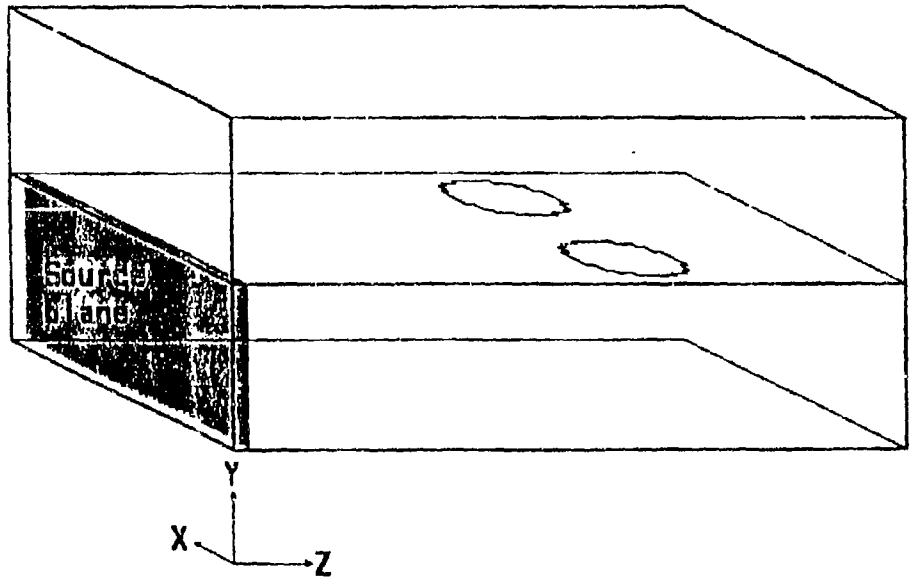

Figure 1b: Coupled Waveguides, Double Aperture Coupling (16 cell diameter holes shown)

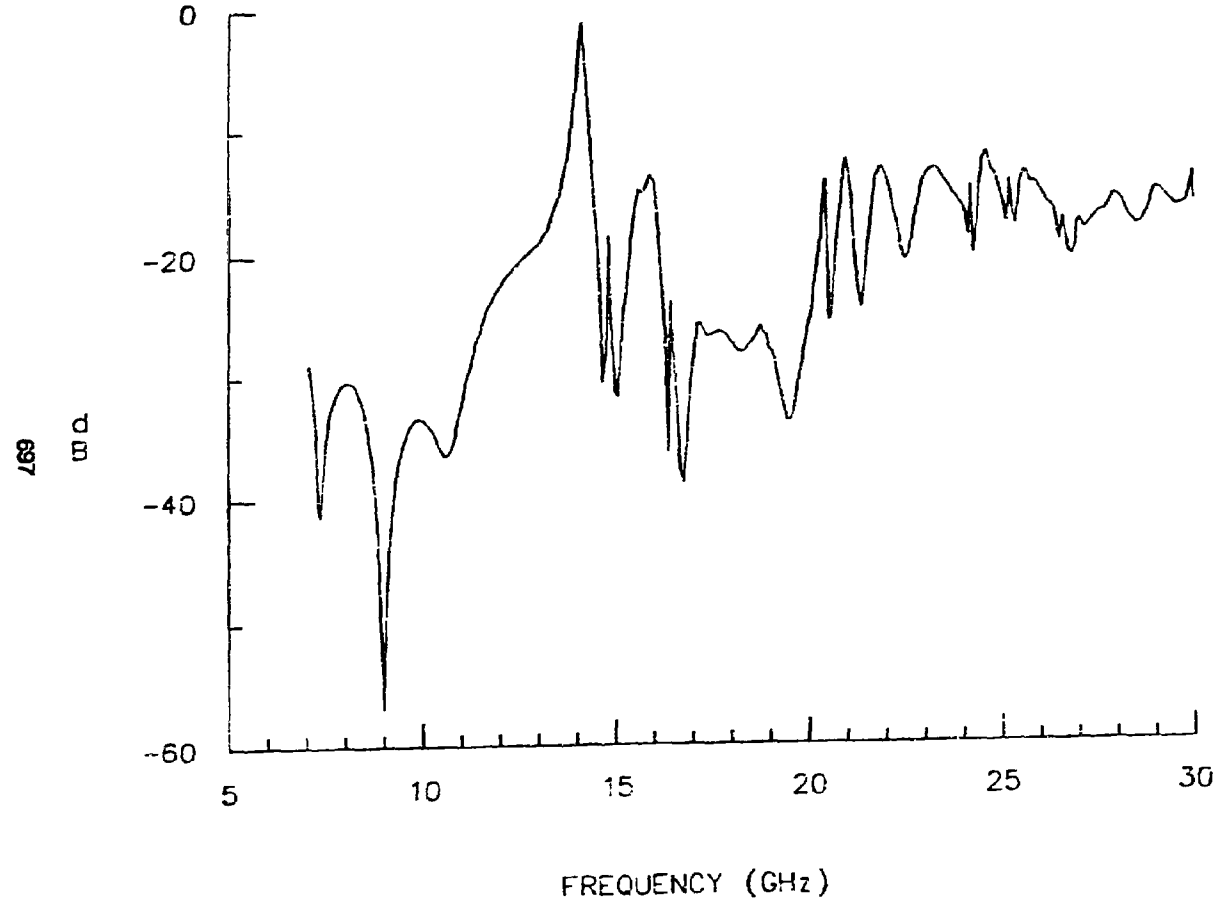

Figure 2a: Forward coupling 16 x 80 cells, holes 12 cells

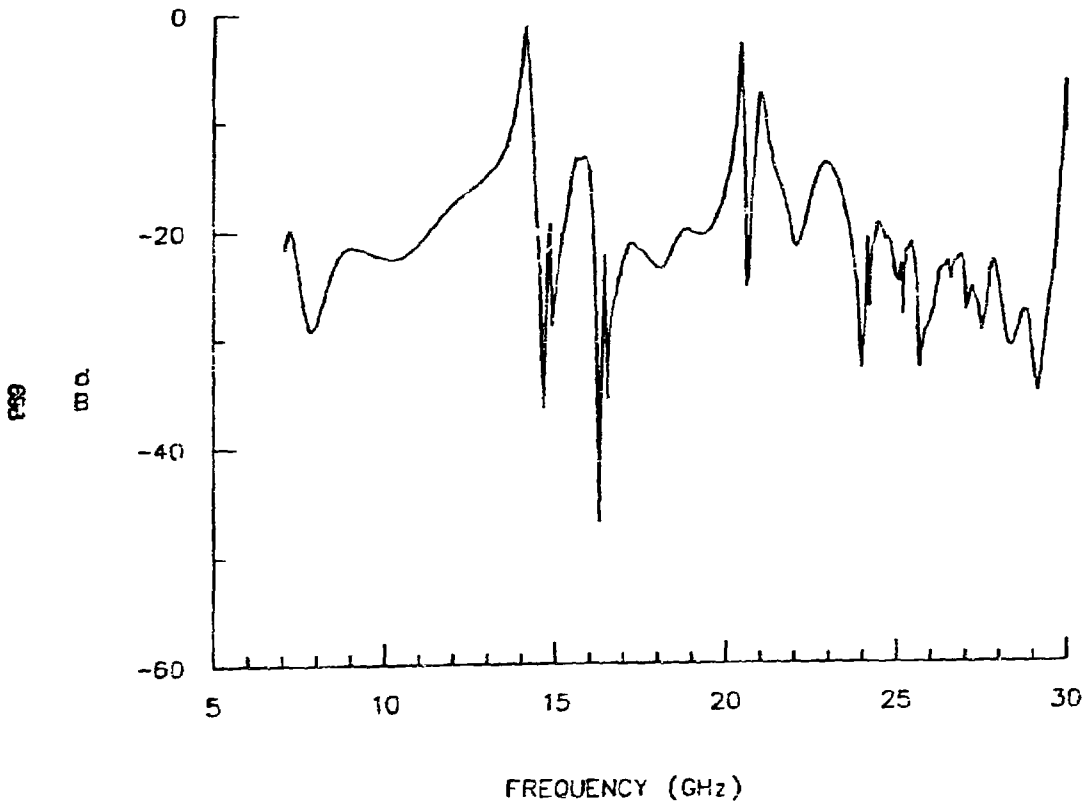

Figure 2b: Backward coupling, 32 x 16 x 80 cells, hole 10 cells

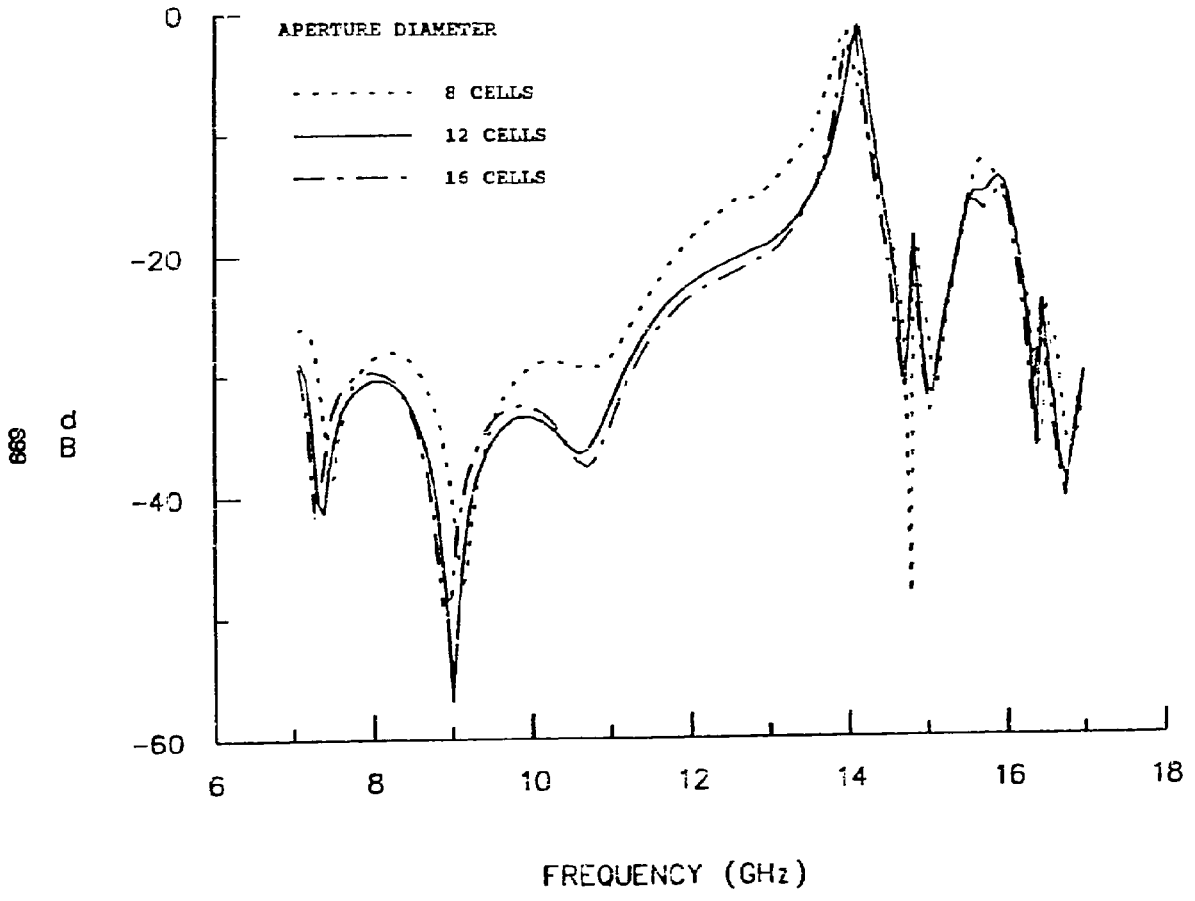

Figure 3a: Forward coupling, 8, 12, 16 cell holes comparison

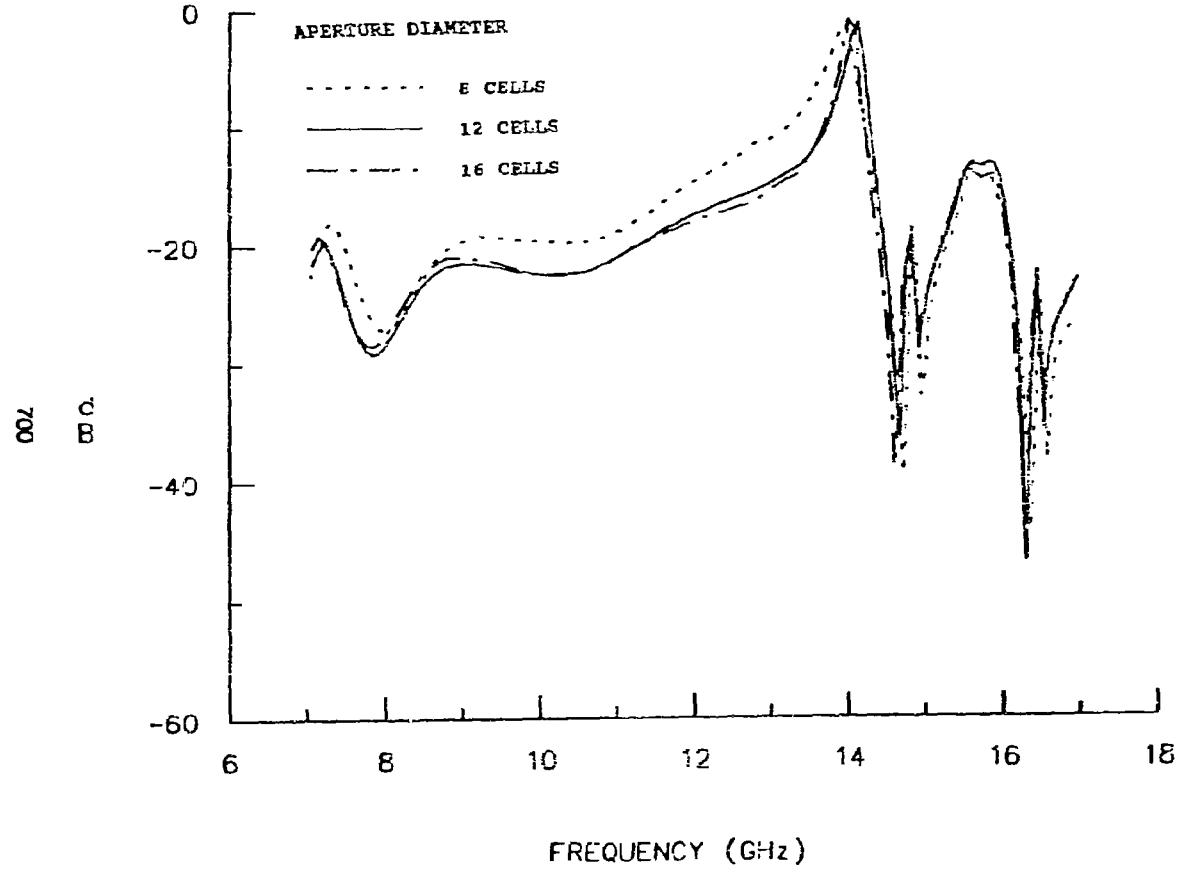

Figure 3b: Backward coupling, 8, 12, 16 cell holes comparison

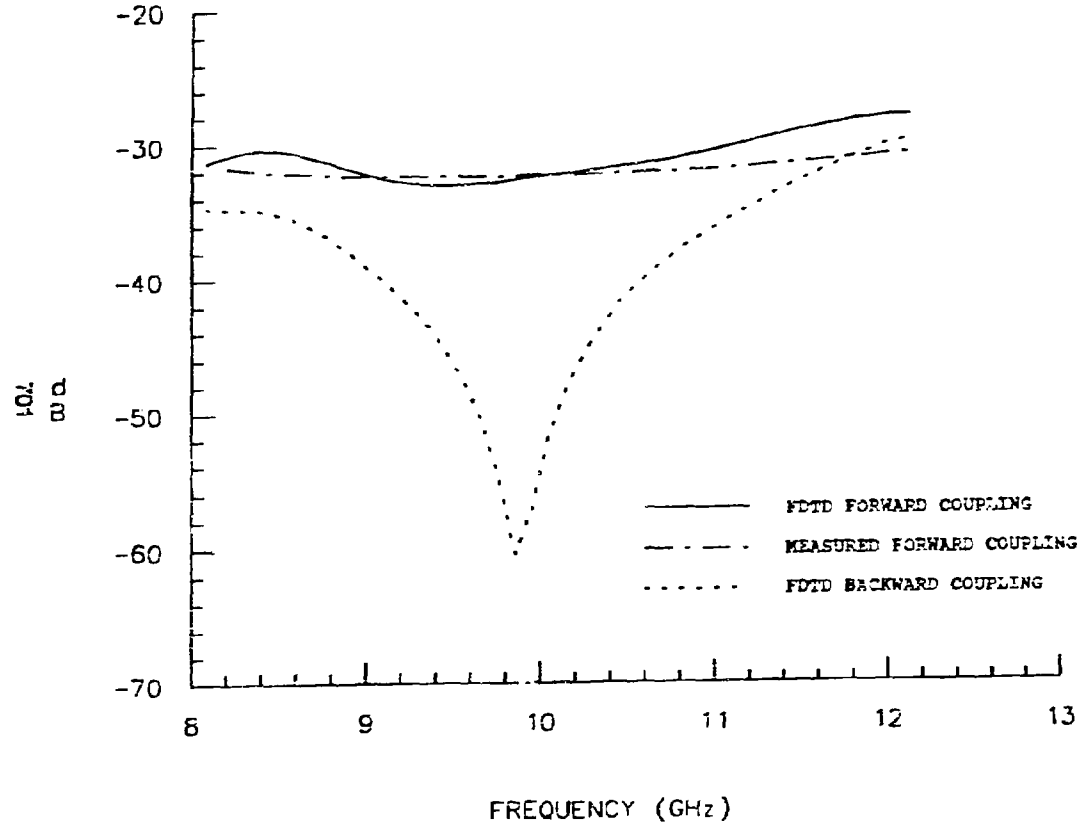

Figure 4: 2-hole coupler: FDTD results and measurements

AUTHOR INDEX

Author	Page
Agar, K.H.	320
Ahn, B.C.	265
Alinikula, P.	691
Amaseen, C.A.	699
Ambrosiano, J.	642
Armanious, A.F.	1,451
Arruda, S.R.	540
Bala, C.V.	534
Balanis, C.A.	10
Barber, E.L.	432
Barber, G.C.	10
Barbosa, A.M.	190
Bastos, J.P.A.	540
Bhattacharyya, A.K.	344
Boulhinon, M.	396
Boyse, W.E.	160
Brandon, S.T.	642
Brandow III, W.F.	487
Brim, B.	57
Brown, R.T.	146
Brumley, S.	586
Buccari, A.M.	139
Burke, G.J.	567
Burke, J	59
Bussey, P.E.	29
Cable, V.P.	667
Carey, N.	586
Cheney, M.	74,79,87,94
Cheng, Z.	551
Chew, W.C.	278
Choi, J.	10
Coffey, III, E.L.	20,68
Cole, R.	73
Conway, P.R.	627
Correia, L.M.	190
Craiu, O.C.	534
Daher, J.K.	520
Demarest, K.R.	254
Dornfest, J.	329
Eastwood, J.W.	655
Elliot, P.	567
Engel, J.	56
Ewing, P.D.	456
Excell, P.	1,446,481
Fanning, M.D.	507
Faust, D.L.	507
Fazarinc, Z.	67
Fehrer, R.	20
Gao, B.	551
German, F.J.	612,627
Glaser, D.	87
Gleason, A.W.	265,320
Goble, J.C.	87
Gotthard, G.K.	612
Guo, Y.J.	446
Gurel, L.	278
Haack, G.	493
Haffa, S.	244
Hamamura, C.	661
Hancock, R.J.	98
Harmony, D.W.	666
Haupt, R.L.	487
Haus, H.A.	72
Hayes, P.R.	599
Heid, J.S.	389
Herd, K.G.	235
Herkert, R.M.	520
Herper, J.C.	139
Hill, A.	59
Hohlfeld, R.	203
Holland, R.	667
Hollmann, D.	244
Hubing, T.	516
Huret, F.	403
Hunsberger, P.	652
Hussain, M.A.	419
Isaacson, D.	74,79,87
Isaacson, E.	74
Iskander, M.	57
Jain, A.	586
Jenn, D.C.	432
Jones, O.C.	94
Kalfas, D.	320
Kalbasi, K.	254
Kamerel, M.	396
Kennis, P.	403
King, M.B.	507
Kohlberg, I.	567
Kollermann, P.I.	649
Kong, J.A.	38
Kottapalli, K.	59
Koyama, L.	474
Krull, O.	73
Kubina, S.J.	369,380
Kunz, K.	682,691
Lamont, G.B.	130
Lebaric, J.E.	66
Lehman, T.H.	222
Leuchtmann, P.	198
Li, K.	38
Li, X.	545
Lin, J.H.	278
Lin, J.T.	94
Lorner, R.	642
Luebbers, R.	682,691
Lynch, D.J.	184

Mader, T.	292
Mahadevan, K.	265
Mahmood, A.	184
Marhefka, R.	21
Marrison, A.J.	409
McCormack, C.J.	487
McKee, M.	419
Melcher, J.	72
Mellon, M.	56
Mertz, E.	139
Millard, D.P.	520
Miller, E.K.	222
Mishra, S.R.	369
Morega, M.I.	529,534
Morega, A.M.I.	529
Moyer Jr. T.	234
Newell, J.C.	87
Nguyen, Q.H.	184
Noble, B.	419
Ohmura, T.	661
Okabe, M.	661
Ovacik, L.	94
Peng, J.	10
Pogorzelski, R.	174
Philipp, L.D.	184
Pribetich, P.	403
Putnam, J.M.	304
Qiu, Y.	545
Riggs, L.S.	599,612,627
Ruff, B.	351
Salazar, R.	396
Salo, G.R.	577,666
Sandri, G.	203
Salo, G.R.	577,666
Sandri, G..	203
Sato, K.	661
Schroeder, E.	234
Seidl, A.A.	160
Shin, R.T.	38
Singer, H.	292
Somersalo, E.	74,79
Sparangnia, S.M.	203
Speciale, R.	428,471
Stelch, D.	682
Suhr, S.	130
Suzuki, H.	94
Tassoudji, M.	30
Taylor, R.W.	29
Terjuoli Jr. A.J.	118,130
Theodossiou, G.	235
Timmerman, T.	20
Trueman, C.W.	369,380
Wang, J.	551
Wang, W.	545
Wang, Y.M.	278
Wheless Jr. W.P.	320,607
Wiesbeck, W.	244
Wilson, L.	667
Woody, J.A.	520
Xiao, G.	545
Ye, C.	551
Young, D.J.	118
Zahn, M.	72
Zhang, D.	551
Zhang, Q.	545
Zheng, J.	170